NUI MAYNOOTH

Ollscoil na hÉireann Má Nuad

Advanced optical calibration of the Herschel HIFI heterodyne spectrometer

A Thesis submitted for the degree of
Doctor of Philosophy

Presented by

Daniel Ronan Higgins, B.Eng, M.Sc

Department of Experimental Physics
NUI Maynooth
County Kildare
Ireland

Research supervisor
Dr. Neil Trappe

Head of Department
Prof. John Anthony Murphy

February 2011

Contents

Abstract

The Heterodyne Instrument for the Far-Infrared (HIFI) was launched aboard the Herschel Space Observatory on the 14th of May 2009. HIFI's frequency range is spread over 7 mixer bands. Bands 1-5 (480-1270 GHz) use Superconducting-Insulator-Superconducting (SIS) mixer technology while bands 6 & 7 (1410-1910 GHz) use Hot Electron Bolometer (HEB) mixer technology. HIFI is a double side band instrument and hence contains both the upper and lower side band of the down converted sky signal. The gain in the upper and lower side band is not always equal. This effect introduces a calibration uncertainty that must be understood in order to achieve the HIFI calibration goal of 3%.

To determine the frequency dependent side band ratio for each mixer band, a gas cell test set up was developed. During the instrument level testing a number of simple (^{12}CO, ^{13}CO and OCS) and complex (CH_3CN and CH_3OH) molecules were observed using the HIFI instrument. Using a radiative transfer model with the measured pressure and optical path length of the gas cell and molecular line parameters taken from the JPL and HITRAN catalogs, model spectra can be generated. By comparing the generated spectra with the observed spectra the side band gain can be determined.

In order to extract the side band ratio a number of additional instrumentation effects must first be understood. Bands 1 and 2 shows good performance and the side band ratio was extracted for these bands. The data showed good agreement with predicted antenna response. Bands 3 and 4 had significant IF gain effects due to a diplexer mistuning problems. Band 5 had spurious LO signals at certain frequencies making the data observed unusable. Bands 6 & 7 had significant standing wave issues due to a non-optimal IF chain design. These instrument effects are discussed in detail in this thesis.

The final part of the thesis details the first step in the analysis of the methanol (CH_3OH) data. This dataset makes up 80% of all data taken during the gas cell test campaign. Unfortunately the pressure broadening (variation of line width with pressure) was not known before the analysis. This was extracted from the data using a 2 parameter fit where the side band ratio was the other free variable. This approach was shown to be problematic with multiple viable solutions possible. It was proposed to use the analysis of the simpler molecules to constrain the pressure broadening extraction process. The methanol pressure broadening parameters were extracted from the data and showed some frequency dependence. The values extracted were in reasonable agreement with the values predicted in other publications. A first pass extraction

of the side band ratio was undertaken at the lower edge of band 2, there was a large degree of scatter in the measured data but an encouraging agreement was seen with the side band ratio values extracted from the other simpler molecules.

Acknowledgments

I would like to thank my supervisor Neil Trappe for his support and encouragement over the course of the last 4 years. My PhD followed an unconventional route through 3 countries and multiple trips abroad for meetings, conferences and summer schools, without the support of my supervisor this would not have been possible. I would also like to thank Tully Peacocke for his supervision during the first year of my PhD and also for providing a wall to bounce ideas of throughout my time in Maynooth. Thanks to the head of the experimental physics department Prof. Anthony Murphy for his encouragement over the course of the thesis. Thanks to Science Foundation Ireland for funding this research through the ESA prodex grant.

My PhD started in February 2007, after 3 months in Maynooth I relocated to Groningen to work on the HIFI ground test campaign. SRON Groningen is an exceptional place to work. From my first days there I was made feel very welcome and was quickly incorporated into the HIFI test team. This welcoming atmosphere doesn't occur by accident and it is a credit to the HIFI management of Thjis de Graauw and Pjotr Roelfsema and later Frank Helmich and Russ Shipman for creating such a pleasant environment to work in. I would like to thank David Teyssier for incorporating me in the gas cell work from my first days in Groningen. From an early stage David saw the potential of the gas cell test data, his encouragement and belief were crucial to this thesis.

The early stages of my time in Groningen were spent learning the ropes of HIFI and data analysis in the HCSS environment. The best way of learning anything is by asking questions of the experts. From the software perspective I would like to thank all the HCSS developers who work tirelessly in the background to provide a working data processing pipeline and analysis tools. I would like to particularly thank Bertand, Kevin, Andrea, Martin, Werner and Eduardo for their coding examples and advice and beer drinking company. I would like to thank the HIFI engineering team for their time over the last 4 years. In particular I would like to thank Jacob Kooi for our collaboration on the HEB standing wave problem and also Pieter Dieleman, Rob Huisman, Willem Jellema and Wouter Laauwen.

Analysis of the gas cell data forms the core of this thesis. The gas cell analysis and data acquisition would not have being possible without the gas cell team. Thanks to David, Bertrand, Emmanuel Dartois, Charlotte, Patrick, Claudia, Steve, Adwin, Colin from the gascell test team for all their support thoughout this thesis. I would also like to thank the standing wave group of Jonathan and Fabrice. Thanks to the HEB standing wave group led by Max and supported

by Chris, Kirill, Leanne and Meltem for helping implement and test the HEB standing wave correction routine developed in this thesis. I would also like to thank Yuan Ren and Jian Gao from TU Delft. Our collaboration on the QCL gas cell work was hugely beneficial to the gas cell analysis in this thesis. Thanks also to Michael, Tony, Volker, Pat, Christoph, Carolyn, Emmanuel, Raphael, Albrecht and Do for their help at various stages during the past 4 years.

The addition of the HIFI 'trainees' during the commissioning phase was welcomed by all in the over worked HIFI consortium. I would particularly like to thank those I lived with at the ICC house for some memorable times, thanks Elvire, Robin, Mikhel, Tom, Per, Nathan and Susanna. Thanks to the administrative staff, Engelien, Petra, Karina and Femke, at SRON Groningen for their help throughout my PhD thesis. Thanks in particular to Russ, Femke and Ylva for helping organise the Herschel ground segment meeting at Maynooth in September 2009.

Fortunately, my time in Groningen wasn't all work. I was lucky to meet with some exceptional people outside of work. Cheers to Jan who brought me to some great places including the cinema in a squatted hospital and concerts in a motorway underpass. Thanks to Stephanie and Christophe for introducing me to Cognac and to Giuliana for the great meals in Poelestraat. Thanks to the staff at Cafe de Minaar for their fine beer selection and generous whiskey glasses which were enjoyed in the company of Pourya, Isabel, Angel, Elif, Sandra, Fiona, Femke, Esra, David, Sander, Giambattista, Caroline, Parisa and many others. Thanks to the SRON crew (Rob, Martin, Jarno, Jan and Pourya) for the card games and Chinese takeaways.

After one and half years at SRON Groningen, I spent six months at Caltech. Thanks to Steve Lord and John Pearson for putting together the funds for my travel and salary. In particular I would like to thank John for his enthusiasm for my PhD project and the potential of the gas cell dataset, without his vision and support this thesis would have turned out a lot different. I would like to thank the two Mary-Ellens and Alesia at IPAC for helping me navigate the choppy waters of Caltech administration. Thanks to Pamela for some memorable L.A. day trips and introducing me to Jesper and Michelle. Cheers to Mick, Matt, Colin and Pat for some memorable times in the Athenum followed by less rememorable times at the Colorado. Thanks to Geoff for some interesting nights out using only yelp.com as a compass and Amanda for some nice evenings in old Pasadena. I returned to L.A. in November 2010 for a consortium meeting. This meeting was at a crucial time in the thesis write up. I would like to thank John, Steve, David and Christophe for taking the time to discuss my thesis and its structure. It was at this point that finishing it finally seemed possible.

I returned to Maynooth in December 2009 and began the arduous task of thesis writing. This was helped considerable by my fellow post grads, Brian, Ronan, Mairead, Dave, Dan, Donnacha and Rob. Thanks in particular to my office mates at various times of Leanne, Mark, Stephen and Enda. Thanks to the entire staff at the experimental physics department, in particular I would like to thank Grainne for her help during the final administrative steps of the thesis. I would also like to thank John for his IT support over the course of my time at

Maynooth.

I would like to take this opportunity to thank my old office mates from my masters in Galway who I learned so much from (SoF2 box jumping). Thanks to James in particular for his incredible patience in answering my sincere programming questions like "What's an if loop?". Thanks to Gregg, Rob and Steve for a legendary weekend in Groningen in 2009. Um grande abraço a todos meus amigos em Porto, thanks Tommy, Carlos, João and Joca for some great weekends over the last 4 years. Thanks also to my friends from UL in particular Tommy, Gavin and Ciara. Thanks to UL rowing club for teaching me the meaning of the word perseverance. Thanks to Nick for some of the random trips we had over the last years and for not reading my thesis. Thanks to my old colleagues and friends from Bremen where I enjoyed some nice weekends over the last 4 years, in particular the 30th of John and the wedding of Lars and Kirsten and seeing Dort and Cindy's new baby Emma. Over the last 4 years I had the opportunity to attend 3 summer schools however the one I won't forget is the Alpbach Astrobiology summer school. In 2007 I spent 10 days in Austria surrounded by some exceptional people. In particular I would like to thank fellow Irish PhD students Paul and Christine for some memorable dinners around Dublin.

My friends from home are a much neglected bunch but are always up for a pint and a chat and were always a welcome release from the drudgery thesis writing can be. Thanks to Rob, Aidan, Eoin Og, Tomas, Catriona and baby Cormac. Thanks to Mary my flatmate in Maynooth for always being up for a chat and a cup of tea especially in the last months of thesis writing. Thanks to Ciara for those evenings in the cinema and occasional dinners.

Thanks to Julia for her support during this thesis and for bringing some perspective to the PhD journey.

I would like to thank my immediate and extended family. Thanks to my Aunt Phil for a memorable visit to Chicago in May 2009. Thanks to my godmother Anne and cousins Edel and Louise for their support. Thanks to my brother David and his wife Ruby for their encouragement over the 4 years. It was one of the highlights of the last 4 years to be joint best-man at their wedding. Thanks to my brother Jonathan for his help over the last four years (and also for the PS3 purchase). Finally, I would like to thank my parents John and Catherine for their unbounding support throughout. Without their support none of this would have been possible.

Ronan Higgins, Maynooth, April 2010

Dedicated to the memory of my sister Karen

Chapter 1

Introduction

The discovery in 1800 of infrared radiation from the Sun by William Herschel opened a new era in astronomy. Astronomy was no longer confined to the optical wavelengths seen by the eye but was expanded into new regions of the electromagnetic spectrum. Each wavelength regime tells the astronomer something different about the astronomical source. Gamma rays are seen from the most extreme reactions in nature while the 21 centimeter line hydrogen probe subtle changes in the spin relation between a proton and electron in a hydrogen atom and each wavelength in between tells the observer something unique about the source of emission.

New discoveries in astronomy have been made through the development of new instruments. With each generation of astronomers new instruments and larger telescopes are developed further pushing the boundaries. In the 20th century astronomers pushed the envelope further by placing larger telescopes at higher altitudes to get above the atmosphere and further still onto aircraft and balloons. The launch of Sputnik in 1957 provided a new platform for astronomical observatories.

The Herschel Space Observatory follows the pattern of larger telescopes operating at previously unobserved frequency ranges in space. Herschel flies with 3 state of the art instruments each fulfilling in a unique role.

1.1 Herschel Space Observatory

The Herschel Space Observatory was formally proposed to ESA in 1982 and was incorporated into the 'Horizons 2000' long term programme for implementation as one of the four cornerstone missions. The project was originally called Far InfraRed and Submillimetre Space Telescope (FIRST) but this was later changed to the Herschel Space Observatory in line with the ESA policy of naming science satellites after famous European scientists. In 1993 the satellite got the official go ahead and work began on developing this ambitious satellite. For time line of the development of the Herschel satellite see [98].

The Herschel Space Observatory carries a 3.5m diameter passively cooled Cassegrain tele-

Figure 1.1: *Left:* Herschel satellite showing primary mirror and cutaway of cryostat showing the 3 instruments *Center:* Close up of cyrostat showing the 3 instruments on top of the Helium tank *Right:* Photo of Herschel satellite during ground testing at ESTEC[98]

scope. The primary mirror is mounted on a superfluid helium cryostat inside which the 3 instruments are found, see figure 1.1. The cryostat has a capacity for 2367 liters of liquid cryogen which depending on consumption should provide enough cooling for a 3.5 year mission lifetime. The satellite electronics are housed at the base of the satellite and control all aspect of the satellite operation. The telescope operates in an orbit around the L2 Lagrange point, 1.5 million kilometers from Earth. The Herschel Space Observatory was successfully launched aboard an Ariane 5 rocket on 14 May 2009 at 13:12 (UTC).

The final configuration of the Herschel space telescope flew with 3 instruments. The Photodector Array Camera and Spectrometer (PACS) was developed by a consortium led by the Max-Planck-Institut für extraterrestrische Physik (MPE) Garching[100]. The PI of the instrument is Albrecht Poglitsch. The Spectral and Photometric Imaging REceiver (SPIRE) was developed by a consortium led by Cardiff university[41]. The PI of the instrument is Matt Griffin. The Heterodyne Instrument for the Far-Infrared (HIFI) was developed by a consortium led by SRON Groningen[22]. The PI of the instrument is Frank Helmich. The calibration of HIFI is the topic of this thesis. Table 1.1 provides an overview of main characteristics of the three instruments.

Table 1.1: Overview of instruments on the Herschel space telescope[98].

HIFI	Heterodyne spectrometer
Wavelength coverage	157-212 & 240-625 μm
Field-of-view (FOV)	single pixel on sky
Detectors	5×2 SIS* & 2×2 HEB* mixers
Spectrometers	auto-correlator & acousto-optical
Spectral resolving power	typically 10^6
PACS	2-band imaging photometer
Wavelength coverage	60-85 or 85-130, 130-210μm
Field-of-view (FOV)	0.5 $F\ \lambda$ sampled $1.75' \times 3.5'$
Detectors	$64 \times 32 \times 32 \times 16$ pixel bol. arrays
PACS	integral field spectrometer
Wavelength coverage	55-210 μm
Field-of-view (FOV)	(5 $\times$ 5 pixel) $47'' \times 47''$
Detectors	two 25×16 pixel Ge:Ga* arrays
Spectral resolving power	1000-4000
SPIRE	3-band imaging photometer
Wavelength bands ($\lambda/\Delta\lambda \sim 3$)	250,350,500 μm
Field-of-view (FOV)	2.0 $F\ \lambda$ sampled $4' \times 8'$
Detectors	139, 88 & 43 pixel NTD* bol. arrays
SPIRE	imaging Fourier transf. spectrometer
Wavelength coverage	194-324 & 316-671 μm
Field-of-view (FOV)	2.0 $F\ \lambda$ sampled circular $2.6'$
Detectors	37 & 19 pixel NTD bol. arrays
Spectral resolving power	370-1300 (high) / 20-60 (low)

* Acronyms relating to detectors: superconductor-insulator-superconductor (SIS), hot electron bolometer (HEB), gallium-doped germanium (Ge:Ga), and neutron transmutation doped (NTD)

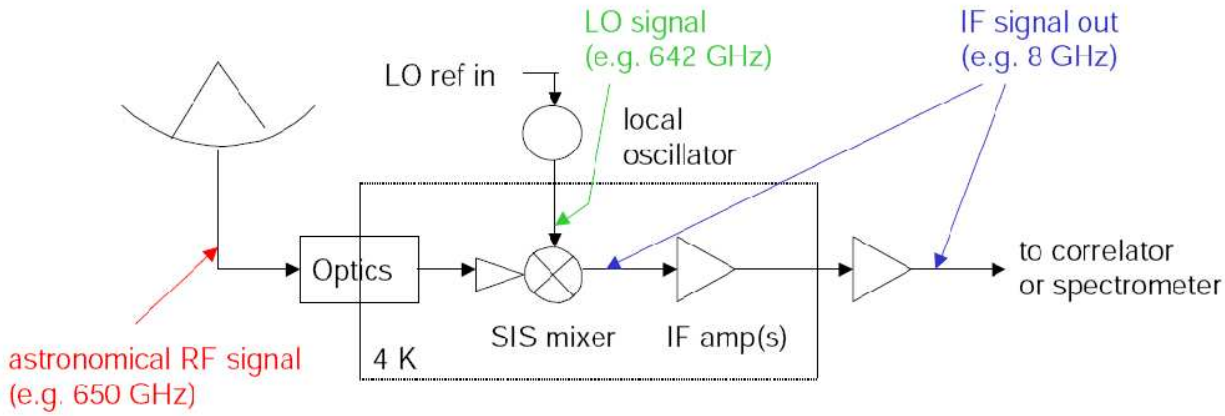

Figure 1.2: Sketch of sub-mm astronomical heterodyne receiver

1.2 The HIFI instrument

1.2.1 Introduction

In this section a brief overview of the HIFI instrument is given. The major components are briefly described and references provided for further reading.

1.2.2 Heterodyne principle

The heterodyne principle is based on the property that the multiplication of 2 signals of slightly different frequencies results in a set of new signals, the frequency of one of these new signals is the difference in frequency between the 2 original signals. The heterodyne principle is commonly used in commercial radio to upconvert a signal to a higher frequency for transmission, the signal is then down converted to the original frequency at the radio receiver end by coupling the sky signal to a local signal of similar frequency, this is tuning that is common to anyone who has used a radio.

The heterodyne principle is used in astronomy to down convert high frequency sky signals to lower frequencies where the signal can be amplified and sampled using conventional electronics thus providing spectral resolution not possible when directly observing the sky signal. Figure 1.2 provides an overview of a typical heterodyne astronomical receiver. The broadband sky signal is mixed together with the local monochromatic signal. The down converted beat frequency is then fed to the backend spectrometers.

By changing the local oscillator signal, different sky frequencies can be down converted and fed to the backend spectrometer. Only small bands of the broadband sky signal can be down converted. Depending on the mixer type this varies from 4-8GHz for the low frequency bands to 2.4-4.8 GHz for the higher frequency bands. Another feature of the heterodyne principle is that 2 bands either side of the local oscillator signal are down converted, these 2 bands are known

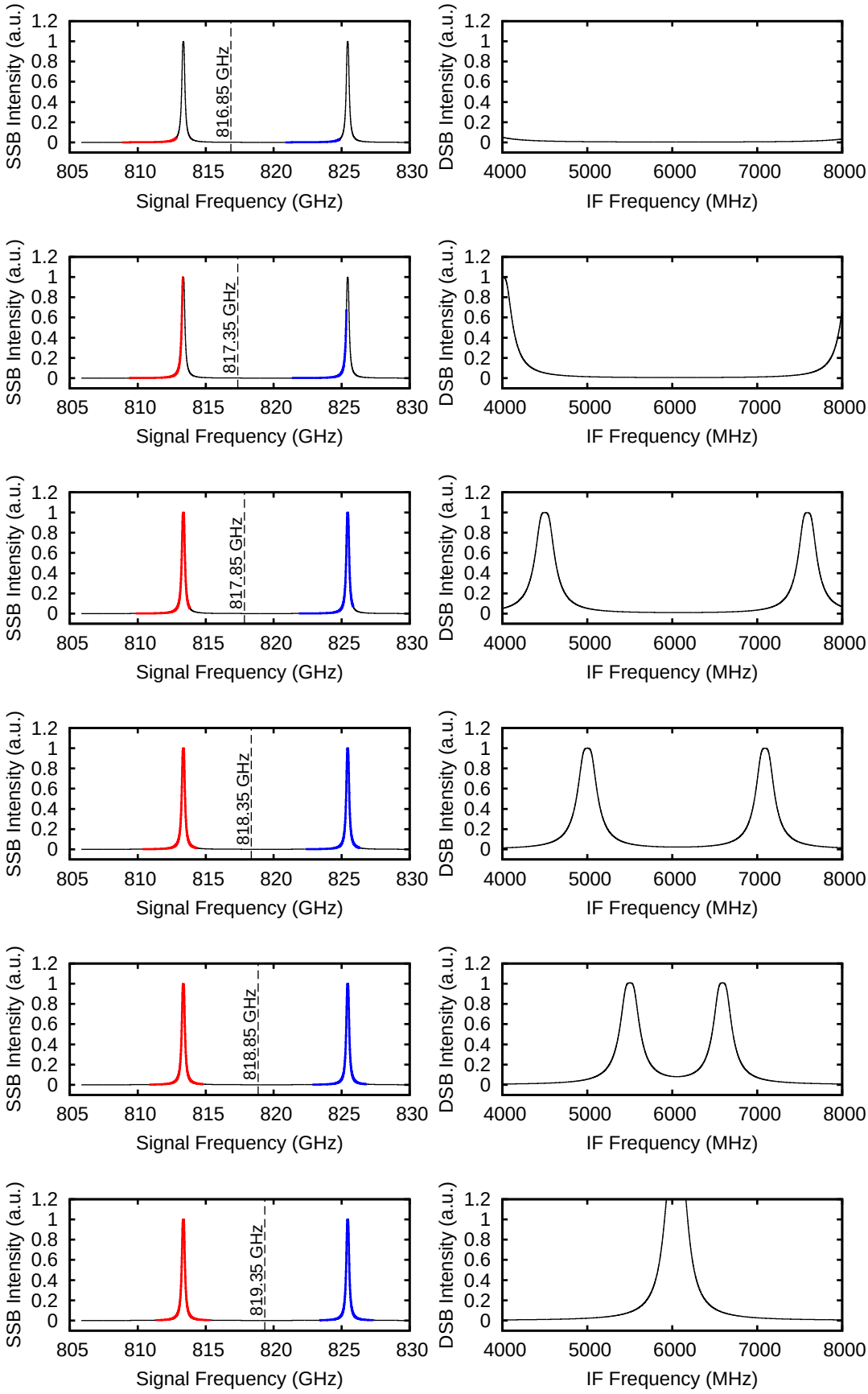

Figure 1.3: *Left:* OCS spectra from 805 to 830 GHz at different LO frequencies, red denotes the lower side band coverage, blue denotes the upper side band coverage. *Right:* Double side band OCS spectra

as the side bands. Both side bands are added together in the down converted signal. Figure 1.3 shows an example of this process using a model spectrum of the OCS spectra. The left hand side of figure 1.3 is the spectrum for OCS as seen between 805 and 830 GHz. The right hand figures show what the double side band spectra look like for different LO frequencies. Notice how lines from the upper and lower side bands move in opposite directions with changing LO frequency.

1.2.3 HIFI optics

Figure 1.4(a) provides an overview of the HIFI optics. The HIFI optics couples the signal from the Herschel telescope to the mixer focus. The beam size varies greatly over the HIFI frequency range and hence 7 different channels are evident in the optical set up, see Trappe et al. [121] for further information. The chopper and the diplexer are the only 2 moving parts in the optical path. Moving mechanical components are avoided in satellites as they increase the chances of failure in the system. The chopper is shown in figure 1.4(b). The chopper is used to switch the beam between 5 preset positions. 3 sky positions are available, looking at the M3 center, left of centre and right of center. These 3 sky positions are used for point sources allowing for quick swapping between the ON and OFF. These off centre sky positions are also used in the dual switch observation mode. The final 2 chopper positions are the hot and cold calibration loads which are vital for the intensity calibration of sky observations. The chopper mechanism has a certain degree of redundancy designed in with a backup actuator able to move the chopper in the event of a failure. Furthermore the chopper mechanism has a default position that points to the center of M3 mirror, this is achieved through the use of a leaf spring.

The Martin-Pupplet diplexer is another moving component in the HIFI signal chain. The diplexer is used to combine the LO and sky beams together in bands 3,4,6 and 7. The other bands use a beamsplitter combination to couple the sky and LO signals onto the mixer. The beamsplitter bands have ample LO signal power and hence can afford a poor coupling the LO unit. The diplexer bands were originally expected to have problems producing the required amount of LO power and hence the need for a more efficiency LO coupling process. Figure 1.5(a) shows a schematic of signal combining process for a beamsplitter and diplexer setup.

The diplexer achieves a high coupling by delaying one polarized beam relative to another, then combining the 2 signal at the mixer focus. The phase delay between the 2 beams results in the rotation of the polarization angle of the combined signal. The angle of polarization is rotated until the polarization angle of the mixer is achieved. The diplexer consists of 2 arms with rooftop mirror at each end. One roof top mirror has a slightly longer path length which is set depending on the center IF band frequency. For the SIS band with an IF bandwidth of 4-8 GHz, the IF center is at 6 GHz which corresponds to an additional path length of 12.5mm. The HEB bands have an IF bandwidth of 2.4-4.8 GHz, hence the IF band center is at 3.6GHz which corresponds to an additional path length of 20.833mm. In addition to the fixed offset between

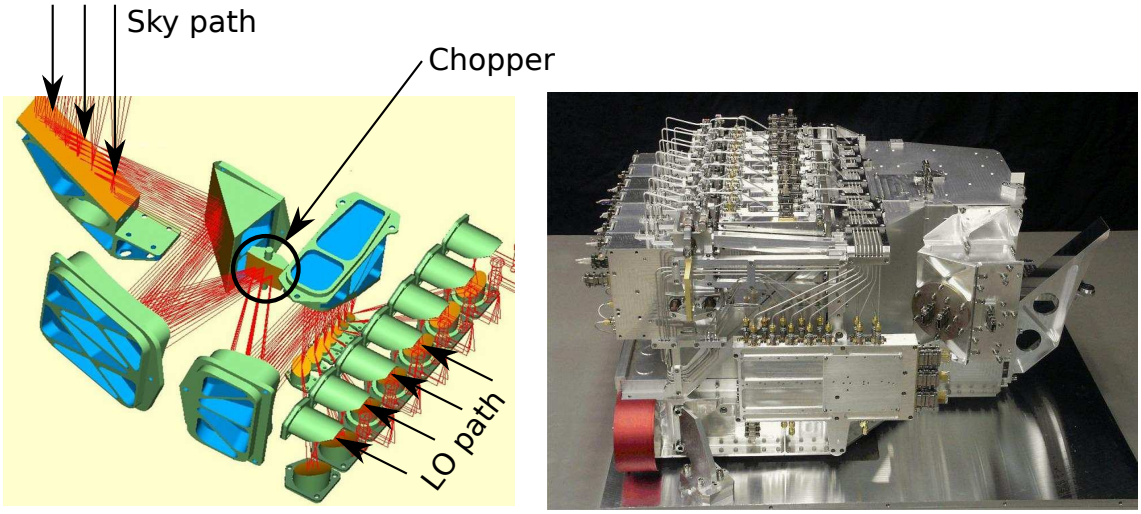

(a) *Left:* Schematic of HIFI optics showing sky and LO paths. *Right:* Photo of HIFI taken before integration with Herschel

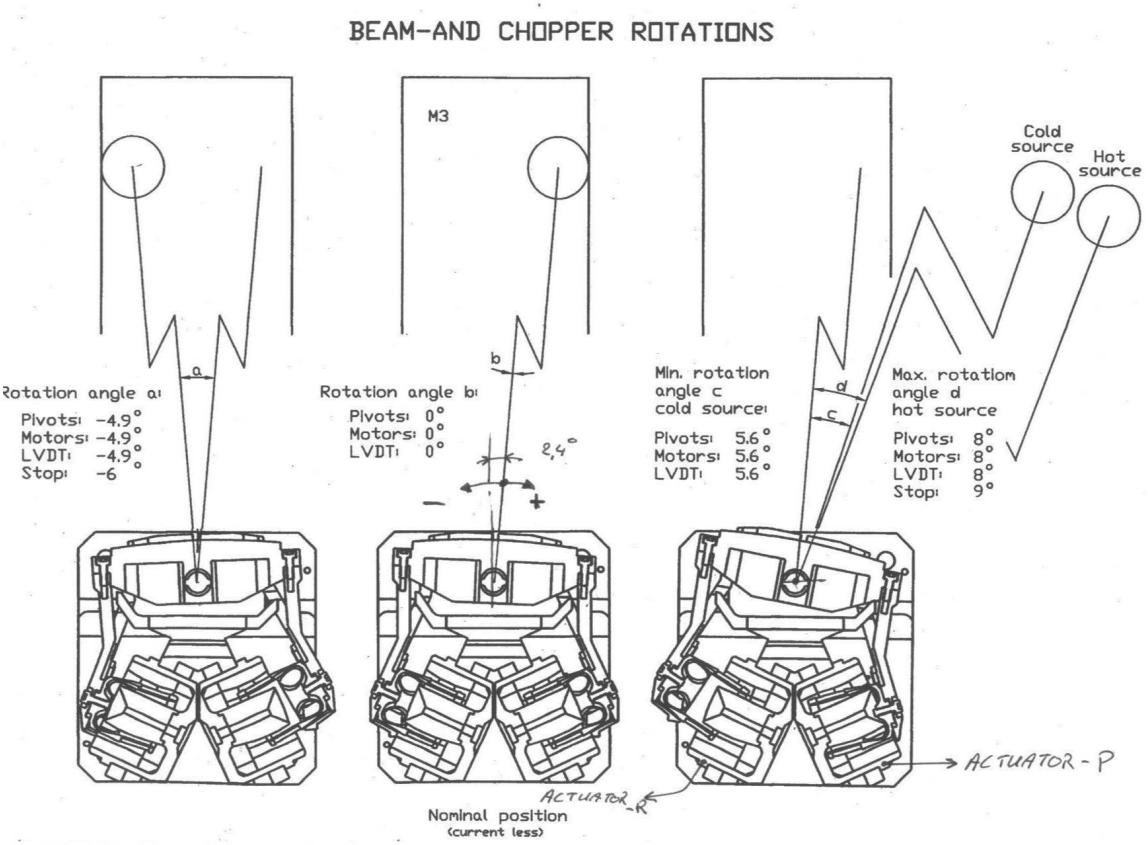

(b) Chopper positions

Figure 1.4: Overview of HIFI optics[78]

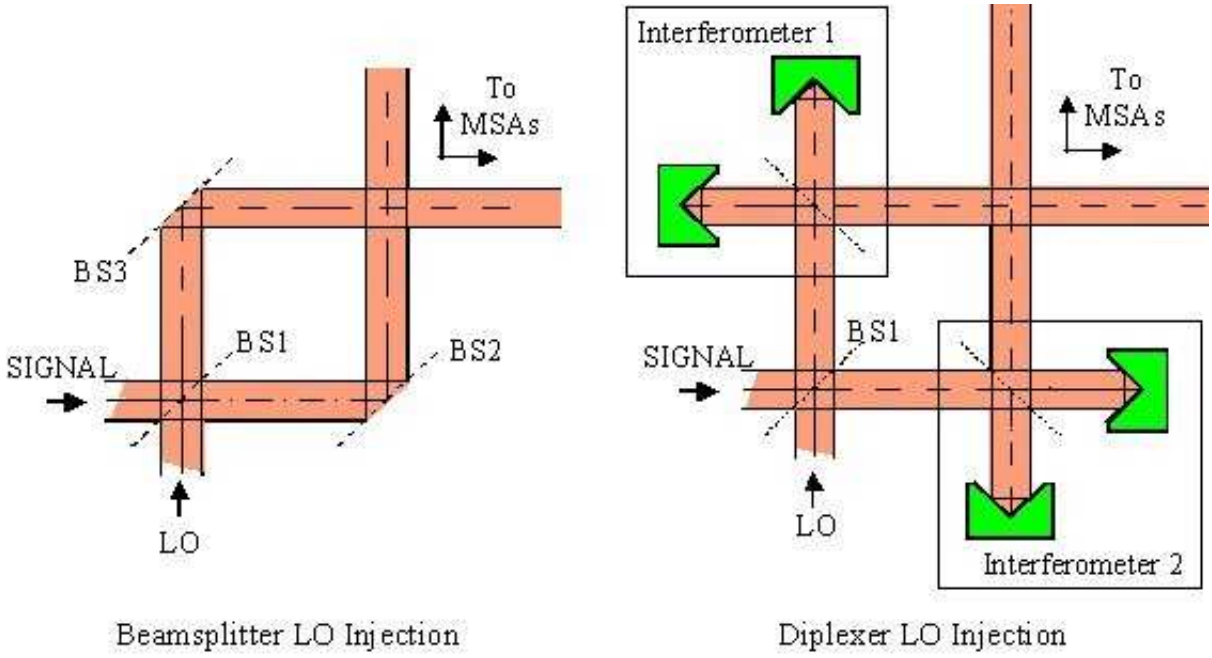

(a) *Left:* Beamsplitter signal injection.*Right:* Diplexer signal injection

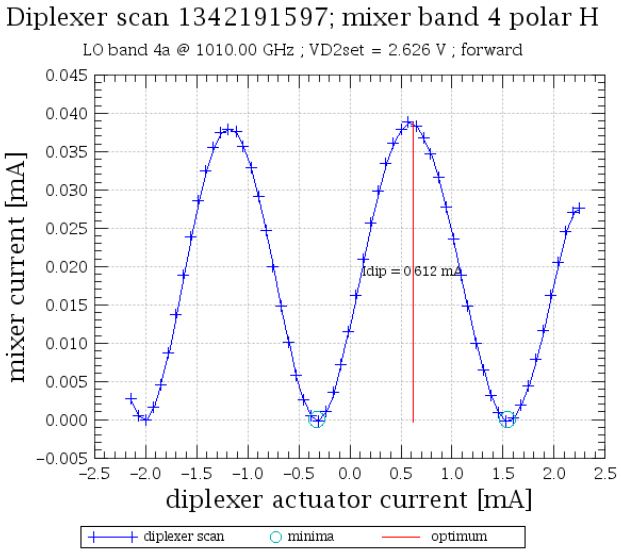

(b) Mixer current vs diplexer position for a band 4a diplexer scan at an LO frequency of 1009.998 GHz

Figure 1.5: Overview of beam combining mechanisms in HIFI

Mixer band/Beam Combiner/Laboratory	Frequency range (GHz)	Mixer element	Matching circuit	Feed and coupling Structure
1 (Beamsplitter) (LERMA/IRAM)[25]	480-640	SIS Nb-Al_2O_3-Nb	Nb on Nb microstrip	corrugated horn and waveguide
2 (Beamsplitter) KOSMA[116]	640-800	SIS Nb-Al_2O_3-Nb	Nb on NbTiN microstrip	corrugated horn and waveguide
3 (Diplexer) SRON/TUD[24]	800-960	SIS Nb-Al_2O_3-Nb	Al on NbTiN microstrip	corrugated horn and waveguide
4 (Diplexer) SRON/TUD[24]	960-1120	SIS Nb-Al_2O_3-Nb	Al on NbTiN microstrip	corrugated horn and waveguide
5 (Beamsplitter) Caltech/JPL[56]	1120-1250	SIS Nb-AlN-NbTiN	Au on Nb microstrip	lens and twin slot planar antenna
6 (Diplexer) CTH/JPL[16]	1410-1703	HEB NbN Phonon cooled		lens and twin slot planar antenna
7 (Diplexer) CTH/JPL[16]	1703-1910	HEB NbN Phonon cooled		lens and twin slot planar antenna

Table 1.2: Overview of mixer materials and implemented antenna technology[22].

the two rooftop mirrors the path length difference between the diplexer arms can be adjusted further using an actuator on one of the arms. By moving one mirror and keeping the other fixed the polarization angle can be rotated. Figure 1.5(b) shows a typical diplexer scan. The diplexer is moved through all positions and the mixer current recorded. From the figure one can see that the mixer current is modulated by the tuned diplexer position. In this example there are 2 diplexer positions which provide the correct polarization angle. This diplexer setting is frequency dependent and scans such as that shown in figure 1.5(b) are used to generate a look up table to determine the setting for other LO frequencies.

Unlike the chopper, the diplexer mechanism itself it not redundant. The redundancy comes from the availability of 2 separate mixer units detecting the same signal albeit at different polarizations. If one diplexer were to fail the other mixer unit band would be able to operate at the same frequency hence no loss in frequency coverage.

1.2.4 Mixer units

HIFI uses two types of mixer technologies. Superconductor-Insulator-Superconductor (SIS) mixers are used in bands 1-5 (480-1250 GHz) and Hot Election Bolometer (HEB) mixers in bands 6-7 (1410-1910 GHz). Both mixers use superconducting principles to mix the incoming terahertz sky signal with the LO signal, albeit with completely different mechanisms. HEB mixer technology was first proposed in the early 1970's[93] but was superseded by the development of SIS mixer technology in the 1980's. SIS mixers however have an upper frequency limit which is set by the energy gap of the superconducting material. Below 1THz SIS mixers are a key technology in submillimeter astronomy[132, 64]. At the time of HIFI development HEB mixers were the only mixer available about 1.25 THz. Table 1.2 provides an overview of the

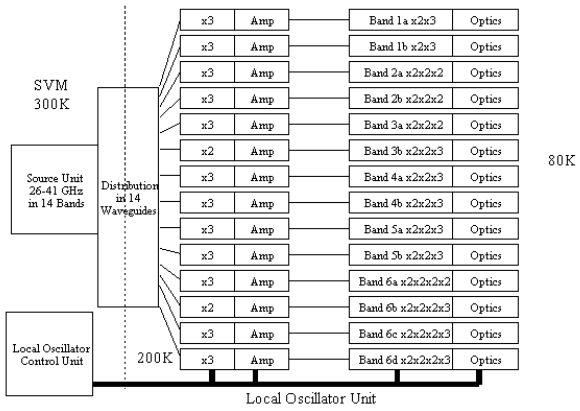

(a) LO multiplier chain configuration[22]

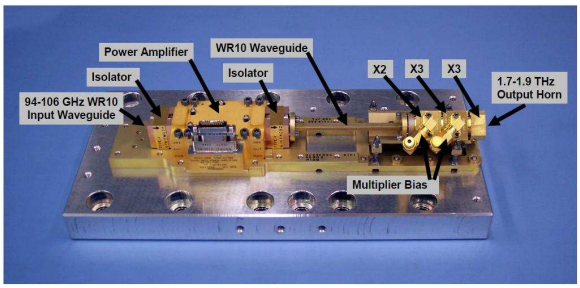

(b) Picture of band 7b LO chain[123]

Figure 1.6: LO signal chain

mixer technology used in HIFI. The laboratories associated with each mixer unit and the key reference associated with the mixer are also given.

1.2.5 LO signal chain

The LO signal provides frequency coverage from 480-1250 GHz and 1410-1910 GHz[91]. This coverage is spread over 14 bands. The cover of each of the mixer band is split between 2 of the LO bands. The LO signal starts from a high quality low frequency synthesizer. This signal is fed into multiple stages of frequency multiplication until the final THz signal is produced. Figure 1.6 provides an overview of the signal multiplication process.

1.2.6 Backend spectrometers

The down converted IF signal is fed from the mixer through a signal amplification chain to the backend spectrometers. There are 2 types of backend spectrometers, the wide band spectrometer (WBS) and the high resolution spectrometer (HRS). The wide band spectrometer is an acousto optical spectrometer. The IF signal is split into four bands and each of these bands is fed to a pizeoelectric actuator which induces an acoustic wave into a Bragg cell. A laser is passed through the Bragg cell and the density fluctuations induced on the Bragg cell by the IF modulated actuator cause the laser direction to change. The laser shines on a CCD strip. The output of this CCD is then integrated over the a period of time and this is taken as the IF output. Numerous graphs of this raw CCD output will be seen over the course of this thesis. The WBS has a lower resolution than the HRS at 0.55 MHz but provides full coverage over the entire 4 GHz IF band[109].

The HRS backend is an auto correlator spectrometer. The HRS has 4 options for spectral

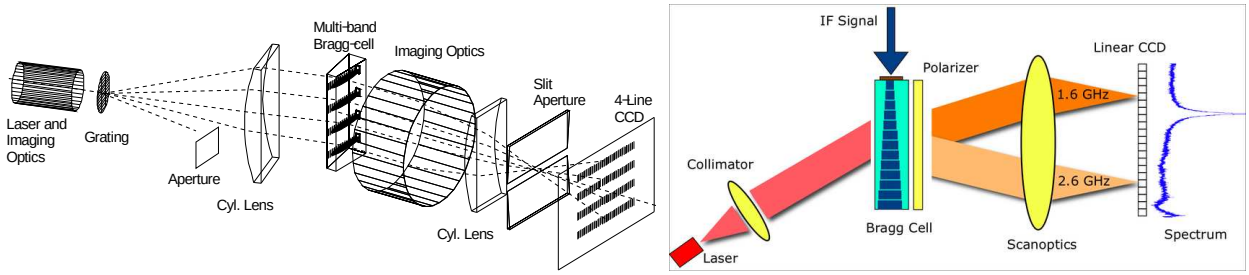

(a) Sketch of HIFI WBS spectrometer[109]

(b) Acousto optical spectrometer operation[125]

Figure 1.7: Wide band spectrometer layout and operation

resolution varying between 125kHz, 250kHz, 500kHz and 1000kHz. As the resolution increases the band width decreases. The HRS bands can be placed any where in the band so knowledge of the frequency region of interest must be at hand when the observation is submitted. For a 125KHz resolution observation a single 230 MHz band is available, for the 250KHz setting this increases to 2 bands of 230MHz, the 500kHz resolution has 4 23OMHz bands available and finally the 1000kHz resolution has 4 bands of 460MHz. For more information on the operation of the HRS backend see [4].

1.3 Thesis overview

The core of this thesis is the analysis of the considerable amount of data taken during the ground test campaign, examples from flight data are also discussed. The central theme of the thesis is the analysis the gas cell data and the extraction of the side band ratio. In order to extract this information a number of additional instrument effects must be over come before the true side band ratio is extracted.

The thesis is laid out as follows. Chapter 2 provides a theoretical background on the intensity calibration of HIFI. In this chapter the various sources of uncertainty in the determination of the intensity from a stellar source are described. The background to the side band ratio is described and some examples are provided. Other sources of intensity uncertainty are also discussed such as the load coupling efficiency, diplexer mistuning effects and standing wave effects. The standing wave discussion presents a more general discussion and describes some of the ancillary effects of standing waves in addition to the typical continuum modulation.

Chapter 3 details one of the dominant instrumental effects in HIFI, the HEB band standing wave. In this chapter the background to the HIFI HEB band development in described and the origin of the standing wave in the electronics are detailed. The behavior of the standing wave is detailed based on examples from the gas cell data. Standard standing wave removal tools are applied to the data and it is shown how the standard standing wave removal approaches fail. Two approaches to removing the standing wave are proposed. One is based on an electrical

model of the HEB and IF chain. The second approach uses large catalog of standing wave profiles to correct the data. This catalog approach is applied to the gas cell and 2 flight observations with considerable success.

Chapter 4 introduces the concept of using a gas cell as a calibrating instrument. The dimensioning, design and manufacturing of the gas cell are described. The rationale behind the gas selection and the test procedure are summarized. A typical gas cell test observation is detailed and the calibration procedure used to convert the raw data into transmission spectra is shown. The latter half of chapter 4 is concerned with processing and analysis of molecules which saturate in the gas cell setup. The preprocessing and filtering of the data is described and then the side band ratio results themselves are presented. The presentation of results follows a gas by gas approach. At the end of the chapter all gases are plotted together for comparison.

The analysis in chapter 4 is on saturated lines only. Chapter 5 looks at the extraction of the side band ratio from un-saturated lines. In order to extract this information a spectral line model of the gas opacity must be developed. In this chapter the main processes in the spectral line profile shape are detailed. From this theoretical framework a model code is developed which is used to extract the side band ratio from saturated lines. The analysis follows the same approach as chapter 4 and the results are presented on a gas by gas basis. From the data it was apparent that additional effects were affecting the data in addition to the side band ratio, the most dominant effect being a diplexer induced IF gain slope. The latter half of chapter 5 is concerned with the analysis of the methanol data. Methanol is an important gas in the gas cell campaign and accounts for 80% of all observations. The final section of chapter 5 describes the application of the gas cell spectral line code developed in this chapter to gas cell observation at 2.9156 THz using a prototype quantum cascade laser (QCL).

Chapter 6 provides the conclusions of the thesis.

Chapter 2

HIFI calibration

2.1 Introduction

The development and operation of a space telescope is a costly endeavor and great efforts are made to maximize the time and data returned from these missions. Before the launch of the Herschel space observatory great efforts were made to have a working telescope as soon after launch as possible. From an early stage in the Herschel mission an observation planning infrastructure, inherited from the Spitzer mission, was used to help the astronomers plan observations [33]. From the data analysis perspective the instrument data processing pipelines were operational on the launch date allowing the calibration teams to quickly establish the state of the instruments 2 weeks after the launch. The first data taken with Herschel using the PACS was taken 1 month after launch and was processed using the instrument data processing pipeline. Previous space telescopes would develop a large amount of the processing software during the flight stage of the satellite.

The calibration of the Herschel space telescope also far exceeds the efforts of its predecessors. From an early stage in the satellite development ambitious calibration accuracy goals were set for each instrument. Extensive instrument level testing (ILT) campaigns were undertaken for each instrument to investigate and quantify sources of error in the system. To fulfill these calibration requirements custom test facilities and equipment were developed for each instrument [7, 17, 27].

The calibration of a heterodyne instrument, such as HIFI, involves the conversion of the spectrometer units (CCD counts, IF voltages) into a unit of source intensity which can be compared with other telescopes and with astrophysical models. To achieve this instrument independent intensity measure a complete understanding of the instrument response must be at hand. Any unknowns in the instrument response to the sky signal leads to uncertainties which must be understood or at least quantified so reliable errors can be attached to any measurements.

HIFI calibration is split into 3 main areas:

- Intensity calibration
- Frequency calibration
- Spatial response calibration

In this chapter we will concentrate on intensity calibration of the instrument and follow the calibration equations detailed in Ossenkopf [86]. This chapter will describe the calibration in the most general sense starting at the telescope efficiency and describing the process of converting the backend spectrometer response into units of intensity. The following sections will describe the main sources of intensity calibration error and the role of gas cell measurements in resolving these sources of error.

2.1.1 Author's contribution

In this chapter the author was extensively involved in analysis and interpretation of the standing wave data presented at the end of the chapter. The mixer RF gain analysis is also the work of the author. The diplexer model was based on a report by Willem Jellema[50]. The aperture and forward efficiency work is based on the report of Raphael Moreno[80].

2.2 Radio telescope calibration

A radio telescope nominally consists of an antenna, a receiver and a backend. For HIFI the antenna is the Herschel telescope. The Herschel mirror has a certain field of view or beam size which samples a portion of the sky and feeds the signal to the receiver. HIFI itself can be described as the receiver. HIFI is a heterodyne receiver which means a local monotonic signal is coupled to the sky signal collected by the antenna. The 2 signals are combined together using a mixer. The mixer is sensitive to the beat signal between the local signal and sky signal. A band of signal is down converted to GHz frequency where it is propagated to the backend spectrometers. The spectrometer digitizes the IF broadband signal converting it into spectrometer specific units. The basic calibration process aims to convert these spectrometer units into intensity units which can used to verify astrophysical models or compare with observations from other telescopes. To extract telescope independent intensity values the effect of each telescope component on the sky signal must be understood.

The astronomer is interested in the intensity distribution of an astronomical object in both the spatial and frequency domain. The antenna samples the spatial domain of the intensity distribution. Each antenna has a unique gain profile or point spread function that is convolved with the sky signal. At its simplest the telescope samples a portion of the sky equal to the area of its collecting surface. However, due to diffraction effects antennas can be sensitive to power coming from other directions. Furthermore, due to the support structure of the secondary mirror and manufacturing flaws in the mirror this causes the overall intensity detected to deviate

from the ideal case. These deviations are summed up through a variety of efficiencies which are multiplied by the detected intensity to convert the measured intensity into the original stellar source intensity.

Three efficiencies are normally used to summarize the telescope performance [42, 77]. They are the aperture efficiency, η_a, the forward efficiency, η_l and the main beam efficiency, η_{mb}.

2.2.1 Aperture efficiency

The aperture efficiency is the ratio of the effective telescope collecting area from the geometrical telescope collecting area . In an ideal case all signal from the sky signal is coupled to the detector however due various optical and manufacturing effects this perfect coupling is impossible. The deviation from this ideal case is described by the aperture efficiency. The aperture efficiency can be written as the ratio of the effective collecting area compared to the geometrical area:

$$\eta_a = \frac{A_{eff}}{A_{geom}}. \tag{2.1}$$

Knowledge of the aperture efficiency is necessary when converting from antenna temperatures to flux density units such as Jansky. During an antenna commissioning a point source of known flux (solar system object) is observed and from this the aperture efficiency can be determined. A number of effects couple together to reduce the aperture efficiency, in order of importance they are the illumination efficiency, the spillover efficiency, the blockage efficiency and the Ruze losses due to mirror surface variations.

The main component in the aperture efficiency is the illumination efficiency. The illumination efficiency or taper efficiency is one of the first considerations when designing the telescope and instrument optics. One of the first decisions in the design of a telescope system is size and focal lengths of the primary and secondary mirrors. The instrument optics are then designed around this so the beam profiles of the detectors are matched in size to the instrument telescope optics. The instrument optics want to avoid having a beam waist larger than the primary mirror where signal is lost over the mirror edges (spillover). However the beam size should kept large enough maximize the collecting area. The square of the ratio between the Gaussian beam radius, w_a on the primary mirror and the mirror radius, r_a is known as the taper ratio and is written as:

$$\alpha = \left(\frac{r_a}{w_a}\right)^2 = 0.115 T_e(\mathrm{dB}). \tag{2.2}$$

T_e is commonly used to describe an optical system and is normally quoted in units of dB[36]. An illumination efficiency, η_i, can be derived as a function of the taper ratio such that

$$\eta_i = \frac{2}{\alpha}\frac{[1 - exp(-\alpha)]^2}{1 - exp(-2\alpha)}. \tag{2.3}$$

A spillover efficiency, η_s, can also be derived from the taper ratio such that:

$$\eta_s = 1 - exp(-2\alpha). \tag{2.4}$$

For more background on these relationships see chapter 6 of Goldsmith [36]. The relationship between the taper ratio and illumination and spillover efficiency is shown in figure 2.1. For HIFI the taper ratio was designed to be 11dB.

Another significant effect on the aperture efficiency is the level of obscuration due the secondary mirror and support structure on the primary mirror. This effect must also be included in the aperture efficiency as this causes further deviation from the optimum collecting area. From Goldsmith [36] the degree of obscuration is defined by a blockage factor, f_b, where:

$$r_{bl} = f_b r_a, \tag{2.5}$$

r_{bl} is the radius of a circle of area equivalent to the total blockage area. Herschel was designed to have a maximum 7.7% obscuration ratio of the total mirror area which is made up of the following components[97]:

- M1 central hole 2.91%
- 3 Hexapode I/F holes 0.5%
- shadow of hexapode legs + M2 barrel 1.73%
- shadow of hexapode legs (path from M2 to M1) 2.54%.

The obscuration ratio is a ratio of radii and is directly comparable to f_b defined in equation 2.5. Hence an obscuration factor of 7.7% yields a blockage factor of 0.077. From Goldsmith [36] blockage efficiency, η_{bl}, can be calculated as a function of the taper ratio, α, and blockage factor, f_b, where

$$\eta_{bl} = \frac{[exp(-f_b^2\alpha) - exp(-\alpha)]^2}{[1 - exp(-\alpha)]^2}. \tag{2.6}$$

Figure 2.1 shows a comparison of an ideal case of no aperture blockage due to a secondary mirror, $f_b = 0$. The effect of the 7.7% blockage, $f_b = 0.077$, is also plotted. For the 11dB edge taper this yields an aperture efficiency of 0.8. Following a more rigorous optical modeling of the Herschel primary mirror the aperture efficiency which included truncation, aberration and support structure blockage effects, the aperture efficiency was calculated to be 0.71 ($f_b = 0.18$) [55]. This efficiency is also plotted in figure 2.1.

Another significant effect which reduces the aperture efficiency is the effect of the surface accuracy. Unlike the taper and blockage effects the surface roughness is a frequency dependent efficiency and has a greater effect at shorter wavelengths. For Herschel a wave front error of 6μm was designed[97]. This error is made up of 2 components, the level of polishing possible

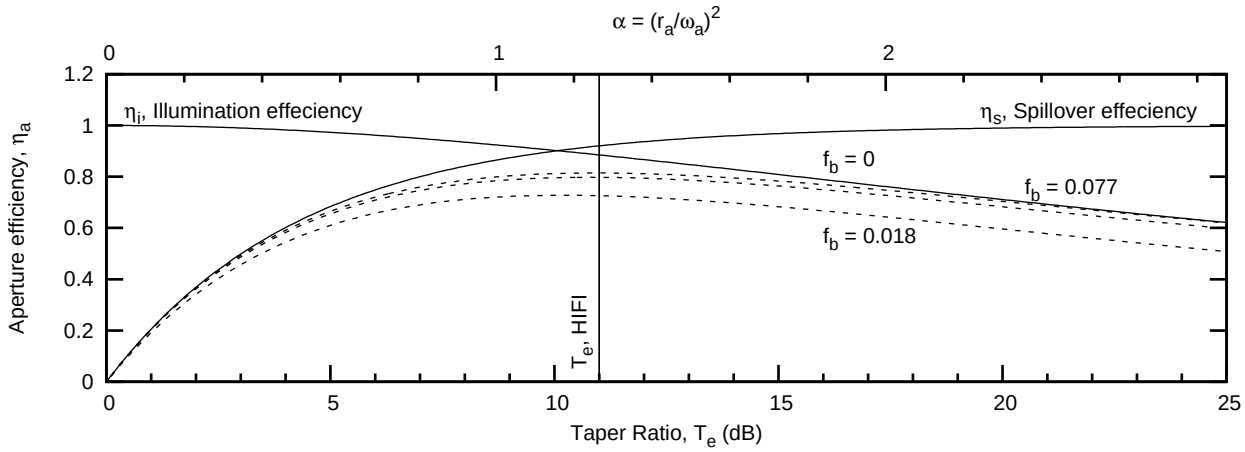

Figure 2.1: Aperture efficiency for different taper ratios and levels of aperture obscuration.

(3.4μm) and cool down distortions (1.5μm). A 6μm wave front error translates into a 3μm surface error. The level of surface error can be converted into an efficiency using the Ruze formula:

$$\eta_e = exp(\frac{4\pi\epsilon}{\lambda})^2. \tag{2.7}$$

where λ represents the signal wavelength and ϵ represents the RMS surface accuracy of the dish. Figure 2.2(a) compares the efficiencies of 3 surface finishes. It is apparent from this plot the need for high quality mirror surfaces towards higher frequencies.

The final aperture efficiency is the product of the four efficiencies.

$$\eta_a = \eta_i\eta_s\eta_{bl}\eta_e. \tag{2.8}$$

The final efficiency for the HIFI frequency range is given in figure 2.3. There are a number of second order efficiencies which can also can be considered but are beyond the scope of this thesis, see Baars [1] for further discussion.

2.2.1.1 Forward efficiency

The forward efficiency, η_l, describes the fraction of the radiation received from the forward hemisphere of the beam compared to the total radiation received by the antenna. This can be written as

$$\eta_l = \frac{\int_{2\pi} P_n(\Omega)d\Omega}{\int_{4\pi} P_n(\Omega)d\Omega}. \tag{2.9}$$

where P_n is the beam pattern normalized to the peak maximum and Ω is the solid beam angle. For ground based telescope η_l is calculated by taking measurement of the blank sky at various elevation angles also known as sky dips. The output is then compared to an atmospheric model and from this the forward efficiency can be calculated. For HIFI the sky dips option is unavailable. OFF calibrations combined with an assumed radiation temperature for the telescope are

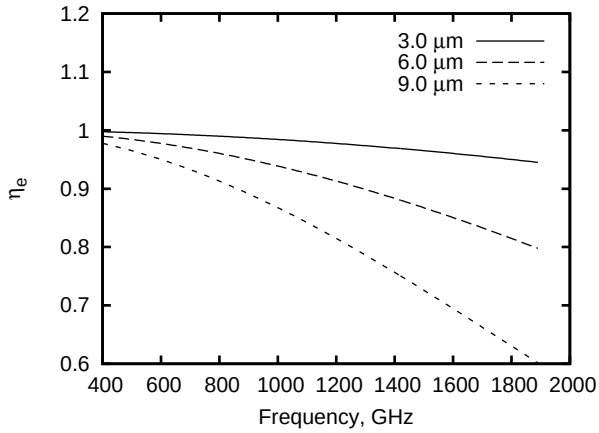

(a) Losses due to mirror surface quality

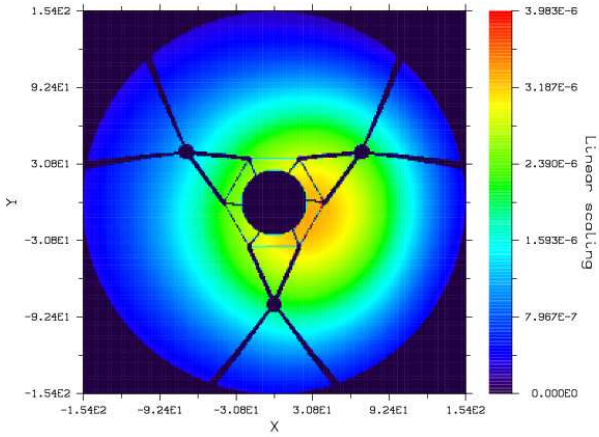

(b) Blockage of primary mirror due to secondary mirror support structure

Figure 2.2: Sources of loss affecting the aperture efficiency

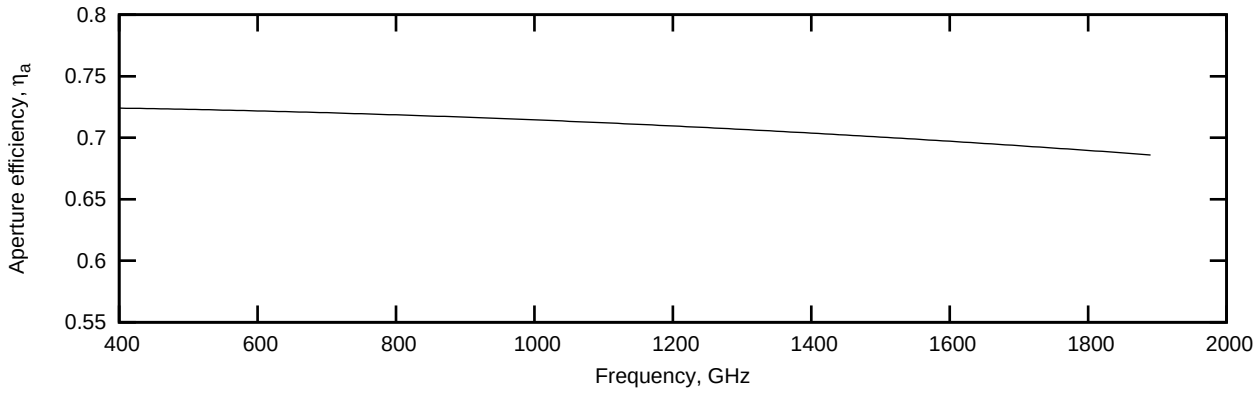

Figure 2.3: Final aperture efficiency for a edge taper, T_e, of 11dB, a blockage factor, f_b, of 0.18 and a surface roughness of 3μm

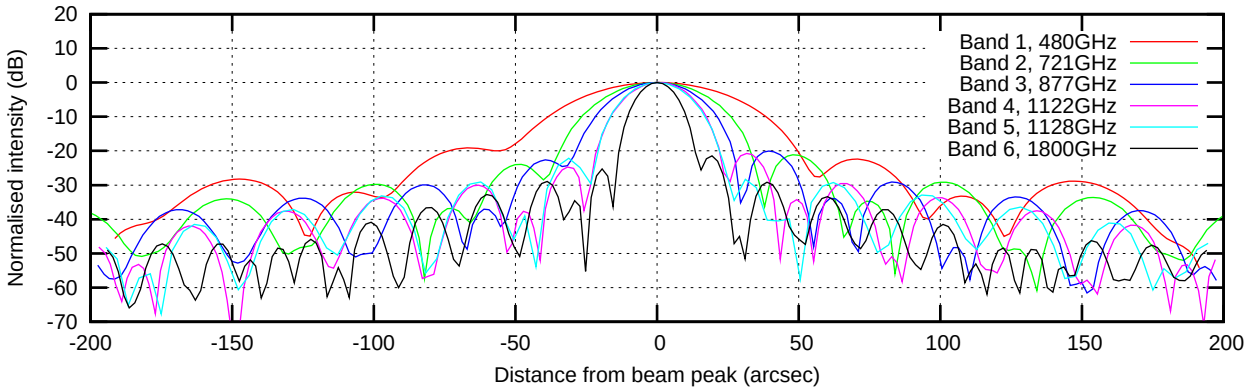

Figure 2.4: Normalized beam patterns for HIFI bands 1-6[89]

used in flight. From these observations a forward efficiency, η_l, of 0.96 is calculated[81].

2.2.1.2 Main beam efficiency

The final efficiency to be considered in the antenna calibration is the main beam efficiency, η_{mb}. The main beam efficiency describes the fraction of the total signal included by the main beam:

$$\eta_{mb} = \frac{\int_{\Omega_{mb}} P_n(\Omega) d\Omega}{\int_{4\pi} P_n(\Omega) d\Omega}. \tag{2.10}$$

The main beam solid angle, Ω_{mb}, is defined as the angular distance between the first nulls in the antenna power diagram and is frequency dependent, see figure 2.4. Hence the main beam efficiency is the defined as the percentage of power entering the main beam between the first nulls. For HIFI a quasi optical model of bands 1,4,6 was developed to determine the main beam efficiencies and main beam angles for various focusing scenarios[88]. This analysis found a main beam efficiency of 0.72 which has a scatter $\pm$ 1% for secondary mirror focusing errors of $\pm$ 15mm.

The discussion so far has concentrated on the theoretical determination of the antenna efficiencies. It is necessary to also measure these efficiencies during the commissioning phase of the telescope. Determination of the beam efficiencies form a key part of the commissioning and performance verification phase of the HIFI mission. Both the aperture and main beam efficiencies are determined through observation of solar system objects with well known source intensities and size.

The primary calibrating source for the main beam efficiency is Mars. An intensity model of Mars is available along with detailed source size information based on previous observations[71]. The main beam efficiency can then be estimated using point observations of Mars and comparing the measured antenna temperature, T_A^*, with a double side band Mars model temperature, T_{mrj},

at the same sky frequency such that

$$T_A^* = \frac{T_{mrj}}{F}\frac{\eta_{mb}}{\eta l}. \tag{2.11}$$

here F is the geometrical dilution factor and is defined as:

$$F = \frac{1}{1 - 2^{-(\theta_s/\theta_t)^2}}. \tag{2.12}$$

where θ_s is the source size and θ_t is the telescope beam size. The main beam temperature, T_{mb}, commonly quoted by astronomers is equal to T_{mrj}/F. Rough approximations of the beam size can be calculated using the following approximation[80]:

$$\theta_t = (1.019 + 0.0134 * T_e) * \lambda/D. \tag{2.13}$$

However this is a theoretical value and a more accurate measure of the telescope beam size for each observing frequency must be determined.

The beam size is calculated by observing a point source and moving the telescope beam over the source. For HIFI this was undertaken using a raster map observation of Mars for all bands through which both the main beam efficiency and main beam size can be determined. The calculation of the beam size and main beam efficiency is best described using an example. The following data was described in the commissioning phase beam efficiency test report[80].

As an example we take the band H polarization 1a observation at an LO frequency of 491 GHz(obsid 1342194179[1]). This observation contains 49 map points which are separated by 23 arcminutes and orientated into a square map centered on the planet mars, see figure 2.5. The central position acts as the point observation used to calculate the main beam efficiency. To determine the main beam size all map positions are used, see figure 2.6(a). By fitting a 2D Gaussian to the map intensity data and extraction the full width half maximum the main beam size can then be determined. The full width half maximum (FWHM) of the fitted Gaussian can be related to the beam size or half power beam width using the following formula[80]:

$$\theta_t = \sqrt{\sigma_{fit}^2 - (0.6 * \theta_s)^2}, \tag{2.14}$$

where σ_{fit} is the full width half maximum of the fitted Gaussian. Fitting a 2D Gaussian to figure 2.6(a) returns a value for σ_{fit} of 43.52 arcseconds which yields a telescope main beam size, θ_t, at 491 GHz of 43.22 arcseconds assuming the angular size of Mars as 8.5 arcseconds. Now that the beam size has been determined the main beam efficiency can be calculated using equation 2.11. T_A^* is taken as 3.7K, the mean intensity across the IF band for the map position centered on Mars. The geometrical dilution is calculated from measured main beam size using equation

[1]Each observation has a unique obsid. This obsid can then be used to quickly search the observation database, for further discussion of the Herschel data structure see reference [31].

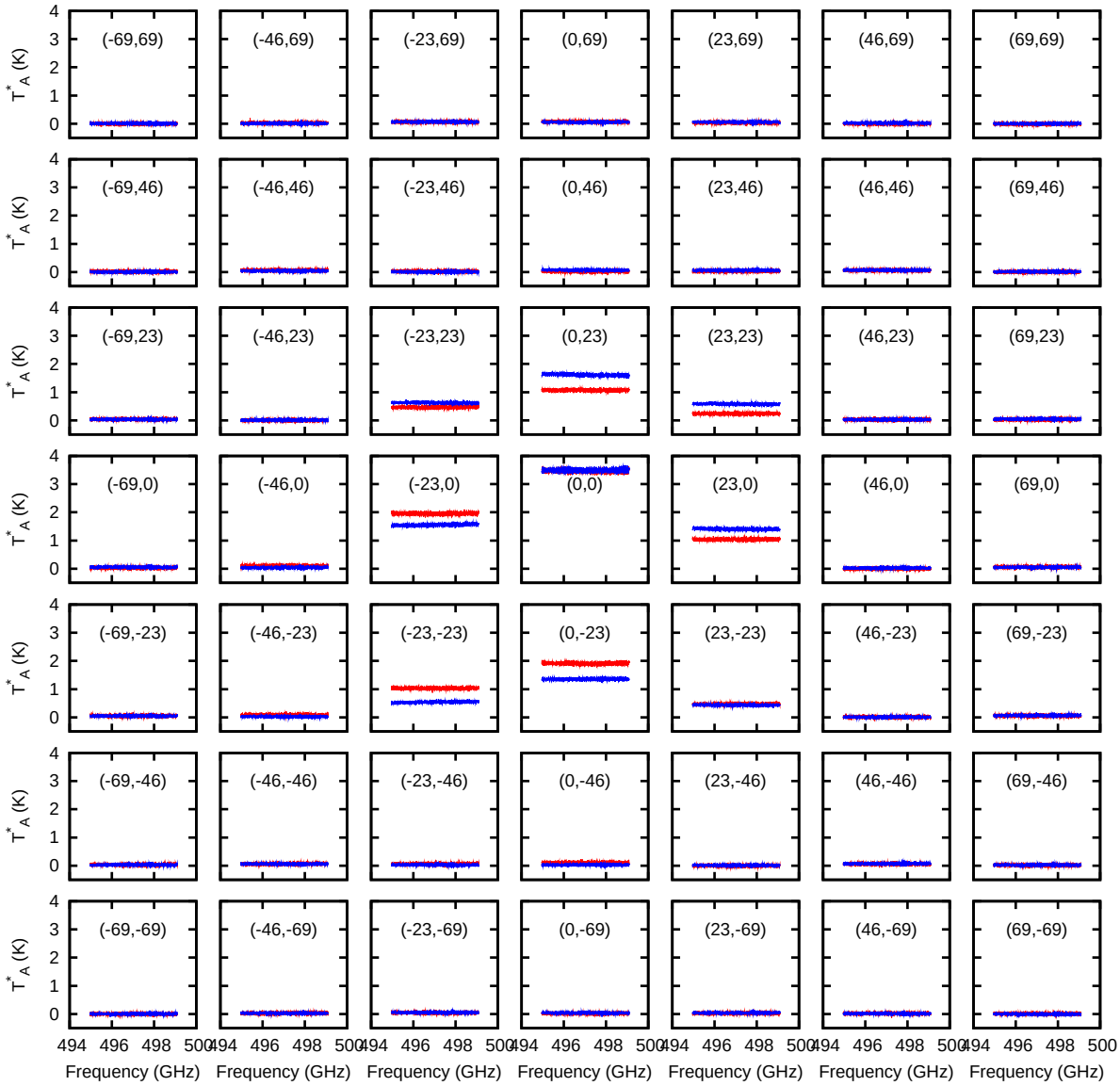

Figure 2.5: Main beam map observation of Mars taken at an LO frequency of 490.975 GHZ. The H polarization is plotted in red while the V polarization is shown in blue. Mars is seen at the center of the map. The right ascension and declination offsets from the center of the map are plotted for each spectrum in units of arcseconds.

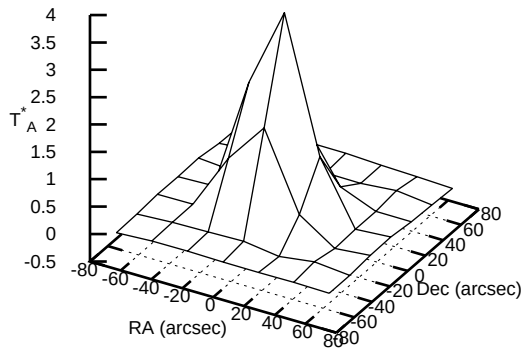

(a) Band 1a, 491 GHz

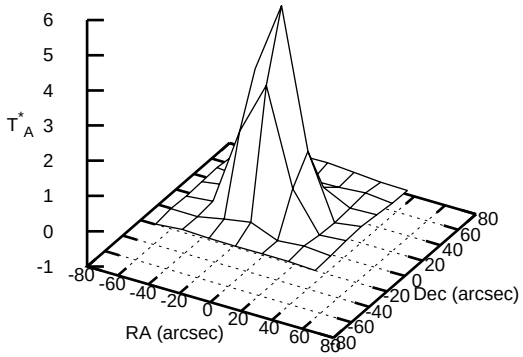

(b) Band 2a, 648 GHz

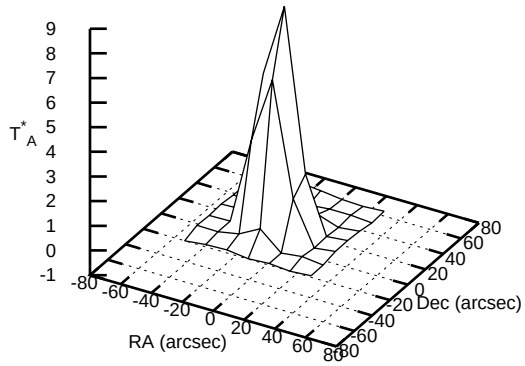

(c) Band 3a, 828 GHz

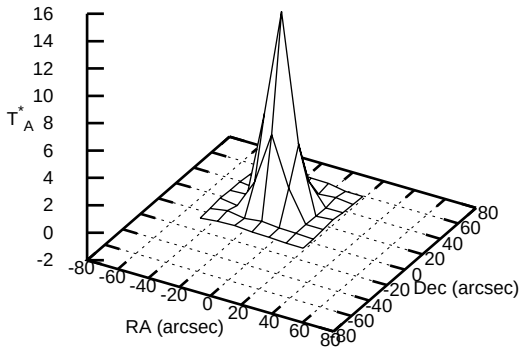

(d) Band 4a, 1012 GHz

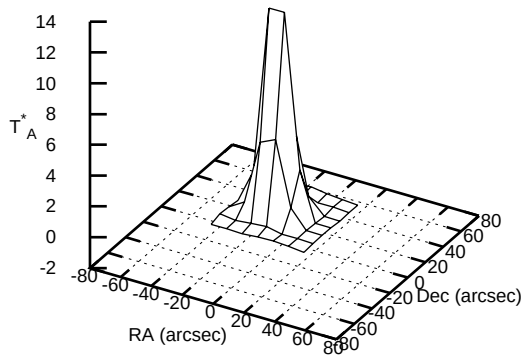

(e) Band 5a, 1127 GHz

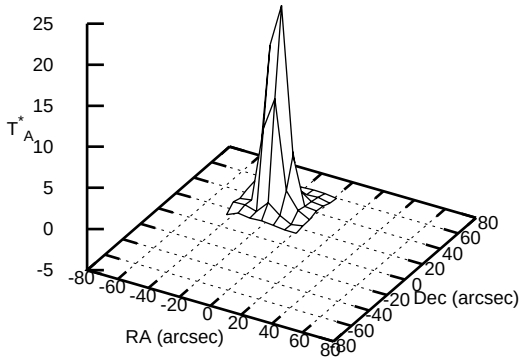

(f) Band 6a, 1483 GHz

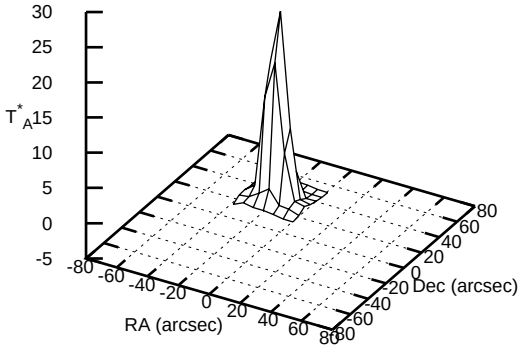

(g) Band 7a, 1703 GHz

Figure 2.6: Raster map of mars for the H polarization LO bands 1a-7a. Each map contains 49 map points however the sampling between map points is decreased to match the decreasing beam size with increasing frequency.

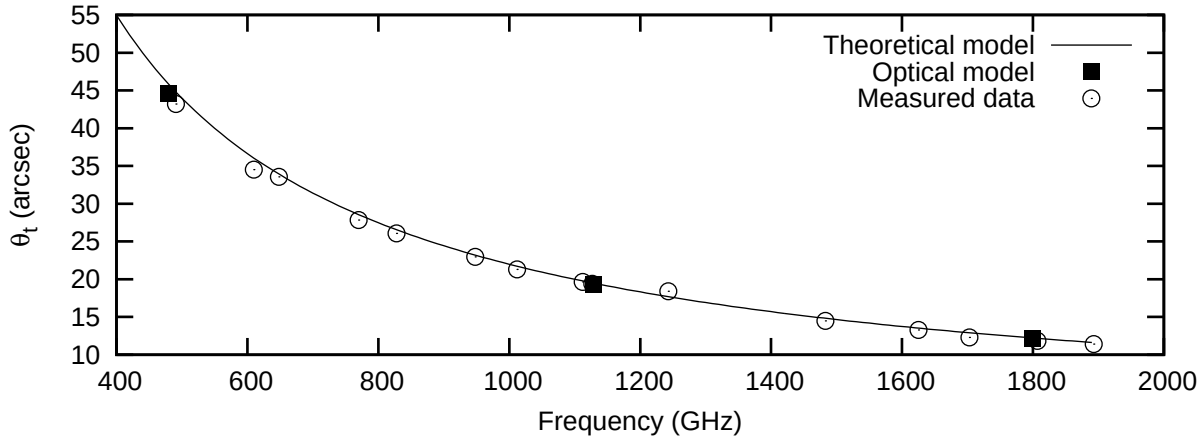

Figure 2.7: Comparison of main beam angle calculated from the empirical relationship described in equation 2.11, the optical tolerancing model from Peacocke [88] and the raster map observations of Mars.

2.12 giving a value of 38.022. Using the Mars brightness temperature model the brightness temperature (T_m in equation 2.11) at a sky frequency of 491GHz is 188.048K. Rearranging equation 2.11 for the main beam efficiency we find:

$$\eta_{mb} = \frac{\eta_l T_A^* F}{T_{mrj}} \tag{2.15}$$

assuming a forward efficiency, η_l of 0.96 returns a main beam efficiency of 0.718 for the H polarization of band 1a at an LO Frequency of 491GHz.

For each of the 14 LO bands a raster map of Mars was taken during the commissioning phase, see figure 2.6. The same process of extracting the beam size by fitting a 2D Gaussian is applied to all Mars maps. A dilution factor is calculated which is combined with the expected brightness temperature of Mars to generate an expected main beam temperature for the HIFI optical setup. By comparing the measured and the model main beam temperature the efficiency can be calculated. Figure 2.7 shows the measured main beam sizes plotted against frequency. The measured data is compared to the empirical relationship given in equation 2.11 and the optical model of Peacocke [88].

Figure 2.8 shows the final main beam efficiency determined from the raster map observations of Mars. The main beam efficiencies calculated by [88] are also plotted for comparison. The error bars for the optical model are based on different focusing scenarios. The error bars for the measured main beam efficiencies are based on the ideal calibration accuracy for HIFI of 3%. From figure 2.8 it is apparent that there is a large degree of scatter in the measured efficiencies. A number of sources of error are present in the system which must be investigated further to reduce the scatter in the beam efficiencies calculation. The instrument pointing must be considered in the determination of the beam intensities and this must be factored into the beam calculation. Furthermore there are a number of instrument effects within HIFI which must be carefully considered such as side band ratio, diplexer mistuning and standing

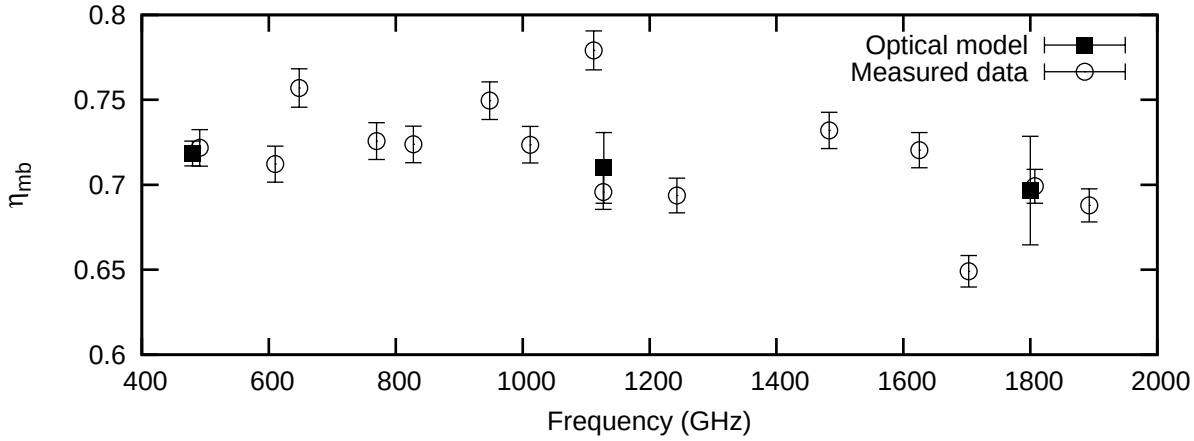

Figure 2.8: Comparison of main beam efficiencies from the optical model including Ruze surface losses and the main beam efficiencies determined through raster map observation of Mars. The optical model error bars are calculated for various secondary mirror defocusing scenarios. The measured data assumes an ideal calibration accuracy of 3% and has being corrected for surface error losses as the optical model is based on an ideal mirror surface.

waves. The next sections will discuss these sources of error which have a two fold effect for the astronomer in that the beam efficiencies used to determine the source temperature have an undefined error and the observed data itself calibrated using the same process as the beam efficiencies has the same error.

2.3 HIFI intensity calibration

The chapter so far has discussed the conversion of the detected antenna temperature to a source temperature. In this section we take a step back and discuss how the antenna temperature is calculated. Unfortunately the output units from the backend spectrometer are not Kelvin. Furthermore the output from the spectrometer looks nothing like the flat baseline presented in figure 2.5 on page 21. The raw spectrometer output is dominated by the spectrometer and IF chain behaviour and the sky signal is only a small portion of the output signal, these instruments effect are known as the band pass. Fortunately the band pass is normally stable over the course an observation and the subtraction of a reference position is used to remove these effects. The data shown in figure 2.5 is the combination of a 4 phase calibration routine known as the chopper wheel calibration [68, 46].

In this routine 4 phases are observed. The HOT and COLD phases are taken by observing the hot and cold internal calibration loads. The ON and OFF phases are taken looking though the telescope primary mirror. The ON phase is taken on the target object and the OFF phase is taken on a blank portion of sky. The 4 phases are then combined together using the following equation:

$$\frac{c_{ON} - c_{OFF}}{c_{HOT} - c_{COLD}} \tag{2.16}$$

If the ON source had an intensity equal to the difference between the hot and cold load the calibrated spectrum would have a value of 1. In order to convert this ratio to an equivalent antenna temperature the HOT and COLD spectra are converted to their Rayleigh-Jeans black body equivalent temperatures using the following equation:

$$\gamma_{rec} = \frac{c_{HOT} - c_{COLD}}{J_h - J_c}, \tag{2.17}$$

where J_h and J_c are the hot and cold equivalent Rayleigh-Jeans black body radiation temperatures. γ_{rec} is known as the band pass. For a given black body temperature the equivalent black body intensity at a given frequency, ν, is

$$J = \frac{h\nu}{k} \frac{1}{exp(\frac{h\nu}{kT}) - 1}. \tag{2.18}$$

The final temperature calibrated spectra is determined by dividing the difference between the ON and OFF phases by the temperature calibrated band pass as follows:

$$T_A^* = \frac{c_{ON} - c_{OFF}}{\gamma_{rec}}. \tag{2.19}$$

Figure 2.9 shows an example of calibration for source with a high continuum intensity. The data presented is from the central pixel of the Mars raster map shown in figure 2.5. From the figure 2.9(a) it is apparent that the raw data is dominated by the instrument pass-band. The central panel shows the small difference between the COLD and ON,OFF phases. The bottom panel shows the final calibrated spectrum. The calibrated spectrum is plotted in both units of antenna temperature and the ratio output of equation 2.16. From this one can see that the ratio of the difference between the ON and OFF responses is 0.044 of the difference between the HOT and COLD. This then equates to an antenna temperature of ∼3.5K.

Figure 2.10 shows an example of the calibration of a source with a strong line emission at the center of the IF band. From figure 2.10(b) one can see that the ON and OFF data have the same value bar instrument noise except at the line emission frequency where an higher CCD count is seem for the ON source. After the cross calibration, the spectral line is apparent with a corresponding antenna temperature of 5K.

The discussion so far has presented the basics of HIFI calibration. At this stage we will discuss 3 major sources of error in the HIFI intensity calibration, the calibration load coupling, standing wave effects and the side band ratio effects. These sources of error were anticipated during the design of HIFI and the investigation and categorization of these effects formed a core component to the HIFI ground testing. The next sections in this chapter will discuss these topics. The concept of side band ratio and its effect on the intensity calibration is discussed here. The determination of the side band ratio is the primary goal of this thesis

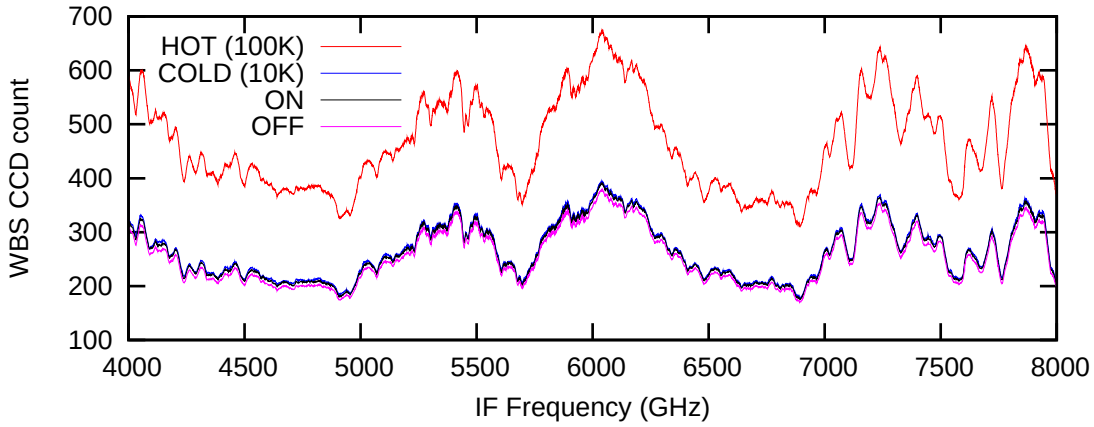

(a) WBS raw data for 4 observation phases

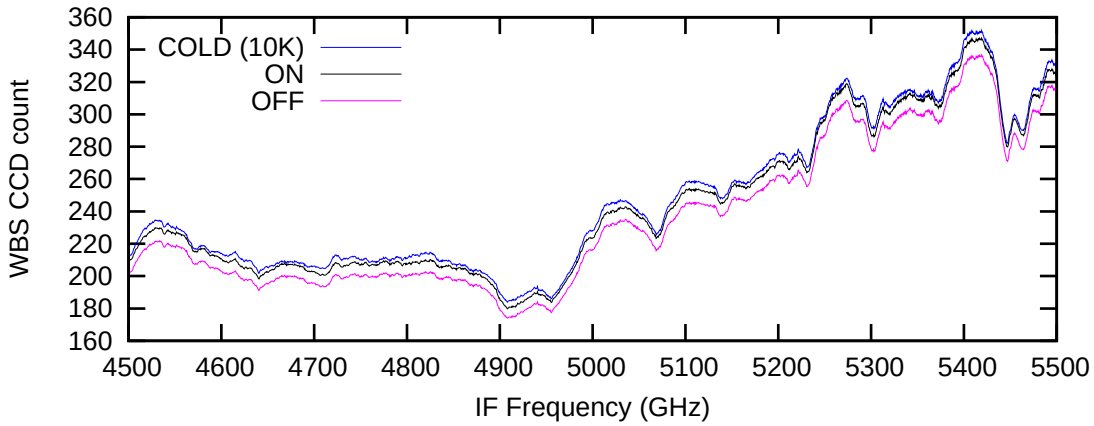

(b) Central IF region showing WBS raw data for ON, OFF and COLD phases

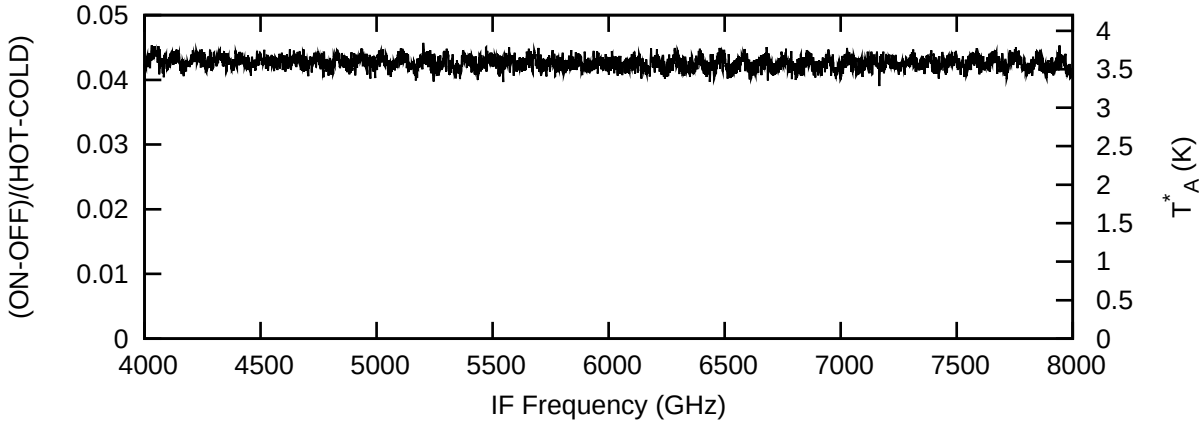

(c) (ON-OFF)/(HOT-COLD) ratio and Rayleigh Jeans temperature calibrated data

Figure 2.9: Example of intensity calibration and band pass removal for central pixel of the Mars map shown in figure 2.5 for the H polarization WBS data at an LO frequency of 490.975 GHz (Obsid 1342194179). The difference between the ON, OFF and COLD phase is of the order of a few percent and is shown on a smaller scale in figure (b). The final calibrated spectrum is shown in the figure (c). The calibrated data is presented in both the ratio form (left axis) and in intensity calibrated form (right axis).

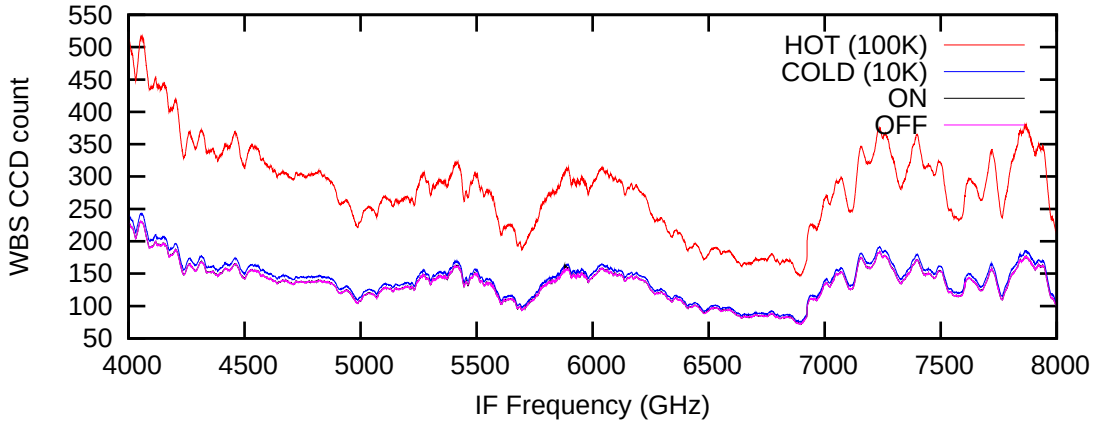

(a) WBS Raw data for 4 observation phases

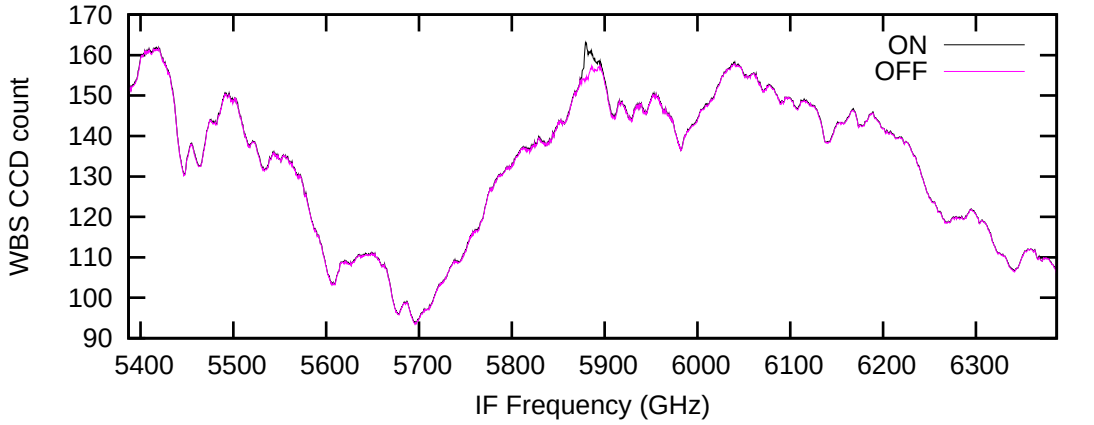

(b) Central IF region showing WBS Raw data for ON,OFF and COLD phases

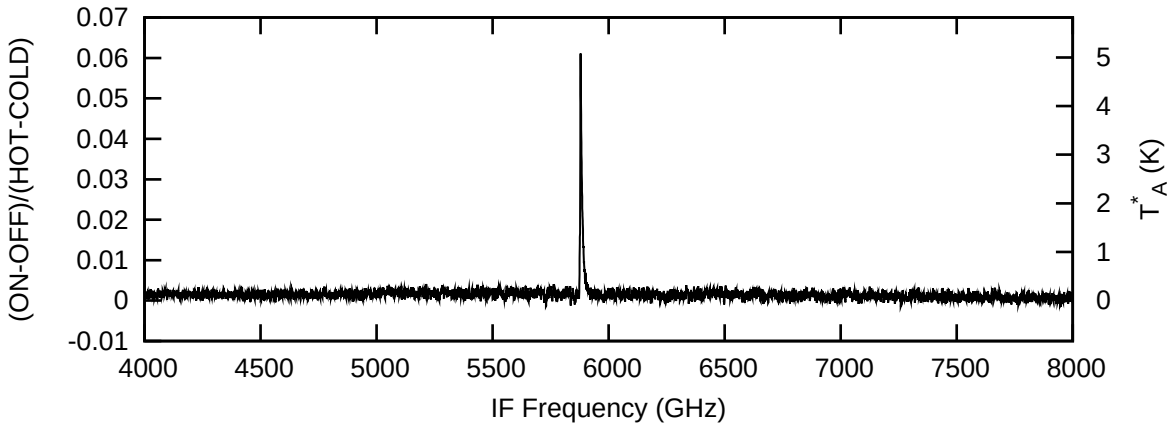

(c) (ON-OFF)/(HOT-COLD) ratio and Rayleigh jean temperature calibrated data

Figure 2.10: Example of intensity calibration and pass band removal for a strong with ^{12}CO(5-4) line emission at a sky frequency of 576.267GHz (Obsid 1342181161). The observation was taken at an LO frequency of 570.02 GHz placing the CO line at the center of the IF band.

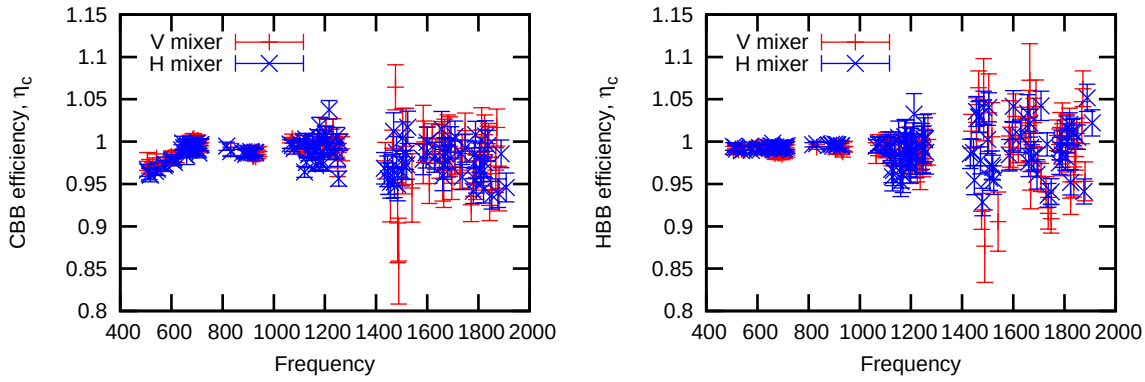

(a) Cold load coupling efficiency, η_c

(b) Hot load coupling efficiency, η_h

Figure 2.11: Overview of hot and cold load coupling efficiencies calculated during the HIFI ground test.

2.3.1 Calibration load coupling

The observation of the HOT and COLD load are an essential component in the conversion of the sky signal from instrument units into physical units. Hence the accuracy of the calibration load measurement must be established and included in the calibration process. The need to establish the accuracy of the load measured was foreseen during the conception of the HIFI ground test campaign. A set of external HOT and COLD loads were designed for comparison with the internal HOT and COLD loads. The external loads were designed such that the source size was larger than the HIFI beams. The external loads are observed through the same optical path as the sky signal. By comparing the external load measurements to the internal load measurements the efficiency of internal load path compared to the sky path can be established. In an ideal setup the detected signal from the external and internal loads would be identical. However due to the different optical paths for the internal hot and cold loads a residual factor is present. These are then called the coupling efficiencies.

Figure 2.11 shows the results of the ground test campaign to establish the calibration load coupling efficiencies for the hot and cold internal loads [70].From the measured data it is apparent there is a large degree of scatter toward higher frequencies in particular the HEB bands. This scatter is due to the poor baseline behaviour in these bands. This topic is discussed in detail in chapter 3 and is due to reflection IF power in the electrical amplification chain of the HEB bands. The resulting uncertainty in the coupling factor is propagated into the antenna temperature uncertainty. From the intensity calibration document [86], the hot load coupling efficiency, η_h, and the cold load coupling efficiency, η_c, are included in the band-pass equation 2.17 as follows:

$$\gamma_{rec} = \frac{c_{HOT} - c_{COLD}}{(J_h - J_c)(\eta_h + \eta_c - 1)} \tag{2.20}$$

where η_c is the cold load coupling efficiency and η_h is the hot load coupling efficiency. Figure 2.12 shows data before and after the application of the load coupling efficiency. For

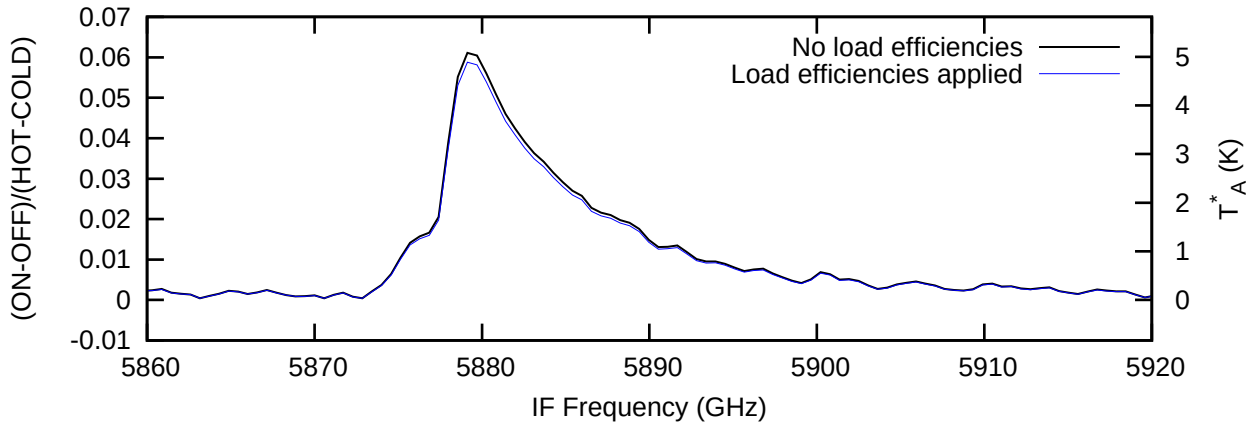

Figure 2.12: Calibrated data with and without Load efficiency correction. ^{12}CO data taken at an LO frequency of 570.020 GHz with the H polarization mixer. The data shown here is the same as that shown in figure 2.10.

an LO frequency of 570.020 in band 1b, η_h is 0.991 and η_c is 0.97. From ground test data the degree of uncertainty in the SIS bands for the coupling efficiency is estimated to be 0.2%. For the HEB band the certainty is estimated to be 10%. This degree of uncertainty has a significant effect on the calibration accuracy of the final data. Ossenkopf [86] analyzed the effect of various calibration errors on the final calibration accuracy. Through an error analysis of equation 2.20 it was shown that a 1% error results in a 1% calibration error. So while the SIS bands (bands 1-5) remain within the specification of 3% the HEB bands are outside of the specified calibration accuracy and this is before the additional calibration errors are considered.

The degree of uncertainty in the determination of the coupling efficiency in the HEB bands is primarily due to large standing waves in the HEB bands. This topic is discussed in detail in chapter 3. The methods developed for correction of standing waves in the HEB bands in the gas cell data can potentially be applied to the load coupling ground test data, see figure 3.13 on page 87. A overview of the calibration load coupling as used in version 2.6.0 of the data processing pipeline is given in table 2.1.

Table 2.1: Hot and Cold calibration load coupling efficiencies for H and V polarization as determined in the instrument level test campaign[70].

Band	LO Freq., GHz	H, η_h	H, η_c	V, η_h	V, η_c
1a	480.0	0.991	0.959	0.991	0.959
1a	640.0	0.991	0.98	0.991	0.98
1b	480.0	0.991	0.959	0.991	0.959
1b	640.0	0.991	0.98	0.991	0.98
2a	640.0	0.993	0.993	0.993	0.993
2a	800.0	0.993	0.993	0.993	0.993
2b	640.0	0.993	0.993	0.993	0.993
2b	800.0	0.993	0.993	0.993	0.993
3a	800.0	0.996	0.988	0.996	0.988
3a	960.0	0.996	0.988	0.996	0.988
3b	800.0	0.996	0.988	0.996	0.988
3b	960.0	0.996	0.988	0.996	0.988
4a	960.0	0.997	0.995	0.997	0.995
4a	1120.0	0.997	0.995	0.997	0.995
4b	960.0	0.997	0.995	0.997	0.995
4b	1120.0	0.997	0.995	0.997	0.995
5a	1120.0	0.987	0.993	0.987	0.993
5a	1280.0	0.987	0.993	0.987	0.993
5b	1120.0	0.987	0.993	0.987	0.993
5b	1280.0	0.987	0.993	0.987	0.993
6a	1420.0	0.994	0.982	0.994	0.982
6a	1710.0	0.994	0.982	0.994	0.982
6b	1420.0	0.994	0.982	0.994	0.982
6b	1710.0	0.994	0.982	0.994	0.982
7a	1420.0	0.998	0.97	0.998	0.97
7a	1710.0	0.998	0.97	0.998	0.97
7b	1420.0	0.998	0.97	0.998	0.97
7b	1710.0	0.998	0.97	0.998	0.97

2.3.2 Side band ratio

2.3.2.1 Introduction

HIFI is a double side band receiver. The mixer detects radiation from 2 4-8GHz (2.4-4.8GHz for HEB bands) windows on either side of the LO frequency. The detected signal is then the addition of the 2 signals in the upper and lower side band also known as the image and signal bands. The double side band (DSB) antenna temperature can be written as:

$$T^*_{A,DSB} = T^*_{A,ISB} + T^*_{A,SSB} \tag{2.21}$$

where:

$$T^*_{A,SSB} = \frac{c_{ON} - c_{OFF}}{\gamma_{rec} G_{ssb}} \tag{2.22}$$

$$T^*_{A,ISB} = \frac{c_{ON} - c_{OFF}}{\gamma_{rec}(1 - G_{ssb})} \tag{2.23}$$

G_{ssb} is known as the normalized side band ratio is the fraction of the total signal which is the signal (upper) side band or in terms of the band pass signal:

$$G_{ssb} = \frac{\gamma_{ssb}}{\gamma_{rec}} = \frac{\gamma_{ssb}}{\gamma_{ssb} + \gamma_{isb}} = \frac{1}{1 + R_G} \tag{2.24}$$

γ_{rec} is the total receiver double side band response and is the sum of the image and signal band band-passes. The normalized side band ratio can be rewritten in terms of the actual side band ratio, R_g, where R_g is the gain ratio between the image and signal side band or G_i/G_s. For a gain balanced mixer G_i equals G_s which leads to a side band ratio, R_g, of 1 which returns a normalized side band ratio, G_{ssb}, of 0.5. Hence in a gain balanced mixer each spectrometer channel has a equal portion of upper and lower side band intensity.

Unfortunately the gain across the upper and lower side bands are not equal and this leads to calibration errors when calculating a line intensity in a given side band. It is normally assumed that the mixer is gain balanced and that simply doubling the double side band intensity returns the single side band intensity. However if a gain imbalance exists this assumption leads to an uncertainty in the line intensity. The resulting uncertainty in the upper side band intensity can be expressed as:

$$\frac{\Delta T^*_{A,SSB}}{T^*_{A,SSB}} = 2(G_{ssb,act} - G_{ssb,nom}) \tag{2.25}$$

and for the lower side band can be written as:

$$\frac{\Delta T^*_{A,ISB}}{T^*_{A,ISB}} = 2(G_{ssb,nom} + G_{ssb,act}) \tag{2.26}$$

where $G_{ssb,nom}$ is the nominal normalized side band ratio for a balanced mixer, 0.5, $G_{ssb,act}$ is the measured normalized side band ratio.

Table 2.2: HIFI mixer type and antenna configurations

Band	**Frequency range (GHz)**	**Mixer type**	**Probe**	**Waveguide**
1	480-640	SIS Nb-Al_2O_3-Nb	Strip line	Corrugated Horn
2	640-800	SIS Nb-Al_2O_3-Nb	Strip line	Corrugated Horn
3	800-960	SIS Nb-Al_2O_3-Nb	Strip line	Corrugated Horn
4	960-1120	SIS Nb-Al_2O_3-Nb	Strip line	Corrugated Horn
5	1120-1250	SIS Nb-AlN-NbTiN	Double slot	Si Lens
6	1410-1703	HEB NbN	Double slot	Si Lens
7	1703-1910	HEB NbN	Double slot	Si Lens

The following sections will discuss the main drivers resulting in an unbalanced mixer. An example of the effect of an unbalanced mixer on the final science data is also presented here.

2.3.2.2 Mixer RF gain

The RF gain of a mixer unit is primarily determined by the mixer antenna design. For HIFI 2 families of antenna were used to focus the signal from the instrument optics to the mixer chip. For bands 1 to 4 a horn antenna was used to couple the HIFI optics to a strip line wave guide probe. The mixer chip is then mounted on the strip line wave guide probe, see figure 2.13. Above 1THz the size of horn wave guides become prohibitively small and difficult to accurately manufacture. Hence for bands 5-7, a quasi optical lens antenna is used to couple the instrument optics to the detector. The detector is mounted on a double slot wave guide probe which couples the lens signal to the mixer, see figure 2.14. Table 2.2 summarizes the wave guide types and probes used to couple the wave guide signal to the mixer.

The design and manufacture of the mixer antenna has a direct effect on the mixer RF gain across its frequency range. Careful design and manufacture of the wave guide probes is needed to optimally couple the mixer to the telescope optics (both the local oscillator and sky signal). The mixer antenna is designed to have the best coupling at the band center frequency. The wave guide is dimensioned based on this band central frequency which leaves frequencies toward the band edges to be less optimally coupled to the mixer. For a complete discussion of antenna design see Rebeiz [102].

For each mixer a direct detection test was undertaken using a local oscillator as a source. The response of the mixer at various frequencies was measured using a Fourier transform spectrometer (FTS). These tests were undertaken at a component level and as such provide only a measure of the detector antenna response and not of the entire mixer band with all the HIFI optics included. The FTS measurements provide a rough estimate of the gain variation across the band and provide a first order estimation of the effect of gain variation between the

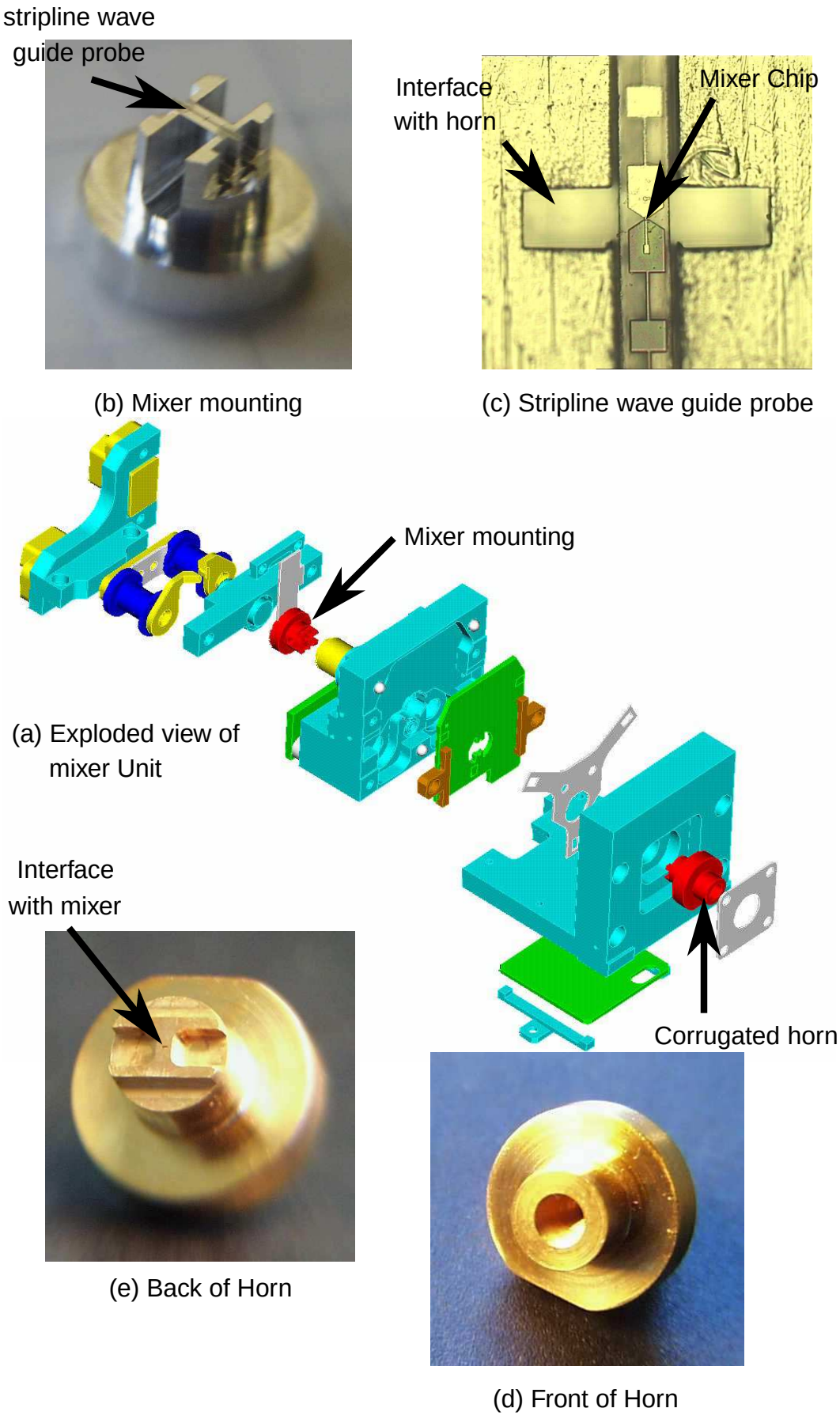

(b) Mixer mounting

(c) Stripline wave guide probe

(a) Exploded view of mixer Unit

(e) Back of Horn

(d) Front of Horn

Figure 2.13: Band 4 mixer unit[24]

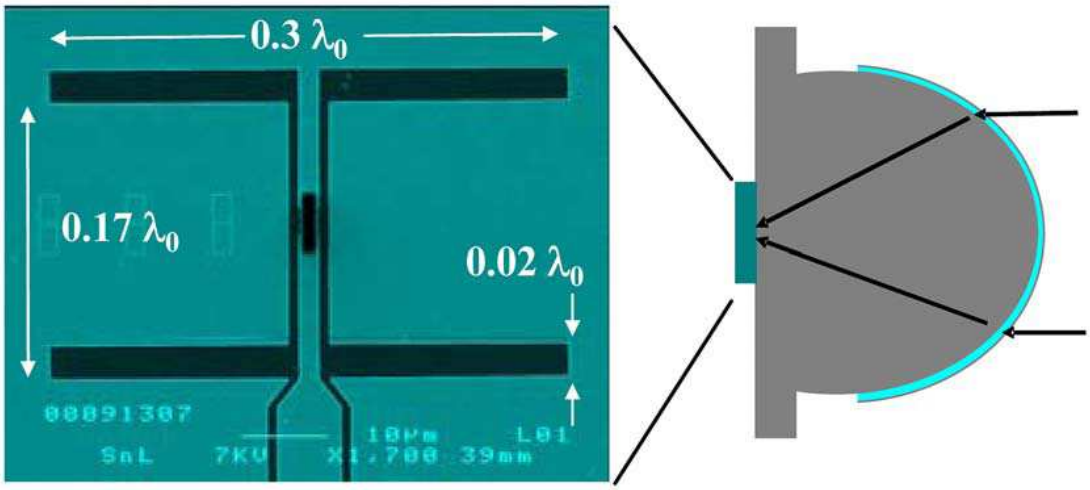

(a) Scanning Electron microscope image of the Band 6 Double slot antenna and a schematic of Silicon lens operation. Double slot antenna is glued directly to the back of the lens.

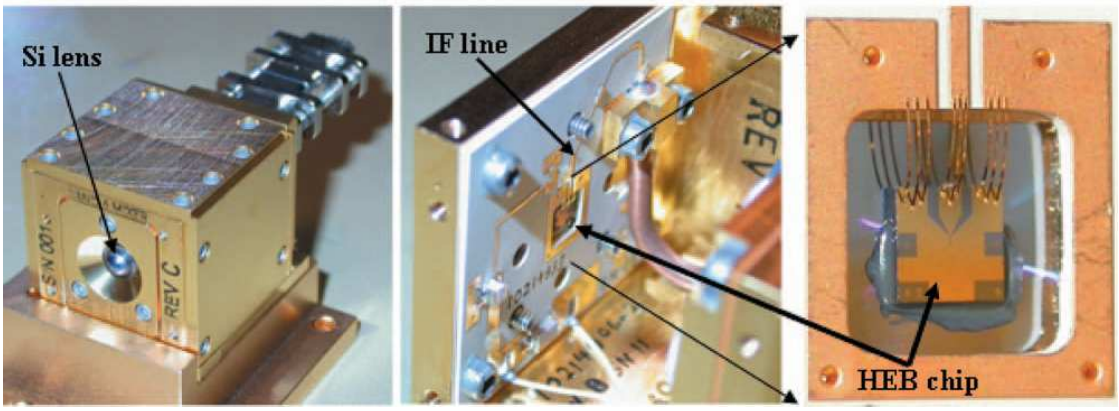

(b) Photographs of mixer unit showing final mixer unit and Silicon lens, the IF boards with mixer chip and the mixer chip glued to back of Silicon lens

Figure 2.14: Band 6 mixer unit[16]

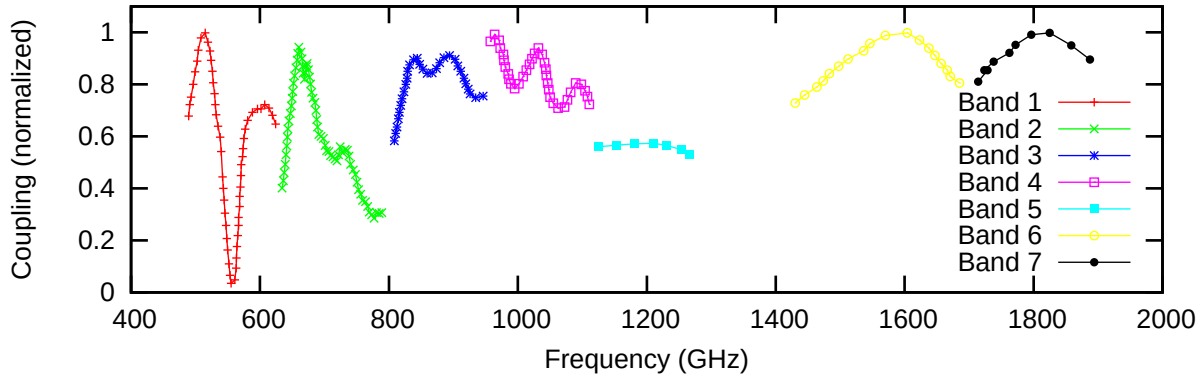

Figure 2.15: Normalized signal coupling for mixer bands 1-7 determined through FTS observation in direction detection mode. The data for band 1 is taken from Delorme et al. [25], band 2 band is from [116], for bands 3 & 4 is from de Lange et al. [24], band 5 is from Karpov et al. [56] and the data for bands 6 & 7 is taken from Cherednichenko et al. [16].

upper and lower side bands. The response of the instrument is expected to vary from when in a heterodyne detection mode and hence the need for further testing to determination the heterodyne response. Figure 2.15 for an overview of the direction detection FTS measurements. References to the mixer performance papers for each band are also given.

From the figure it is apparent that a large degree of variation exists for each band. A number of these extreme points can be explained away by the FTS test setup. The band 1 FTS test was undertaken under atmospheric pressure and hence the close to 0 coupling at 550 GHz due to the water transition line $1_{10} - 1_{01}$ at 557GHz [25]. Furthermore the oscillations seen in band 3 and 4 are due to standing waves in the FTS set up which induce a 70GHz modulation on the measurement[24]. The data shown for band 5 is smoothed, the original measured data was very noisy with an error of $\pm$ 10%[56]. The band 6 and 7 data was taken from Cherednichenko et al. [16] and compare well with the antenna model prediction. The band 2 coupling efficiency also compares well with the model data presented in [116].

From the RF gain profiles shown in figure 2.15 the resulting double side band gain can be calculated. The normalized side band ratio is determined using equation 2.24 on page 31. Figure 2.16 shows an example of the side band ratio for three different LO frequencies. From the figures it is apparent that a range of side band gain ratios across the IF band are possible. Figure 2.17 gives another perspective on the variation of side band ratio across the IF band with changing LO frequency. Figure 2.17(a) shows a contour plot of the variation of side band gain with LO frequency. Figure 2.17(b) shows the maximum side band ratio of each IF channel for band 2, this plot is calculated from the contour plot. From this figure it is apparent that the largest variation in side band ratio is at higher IF frequencies. This conclusion is expected given that USB and LSB channels are closer together in the lower IF frequencies than higher IF frequencies.

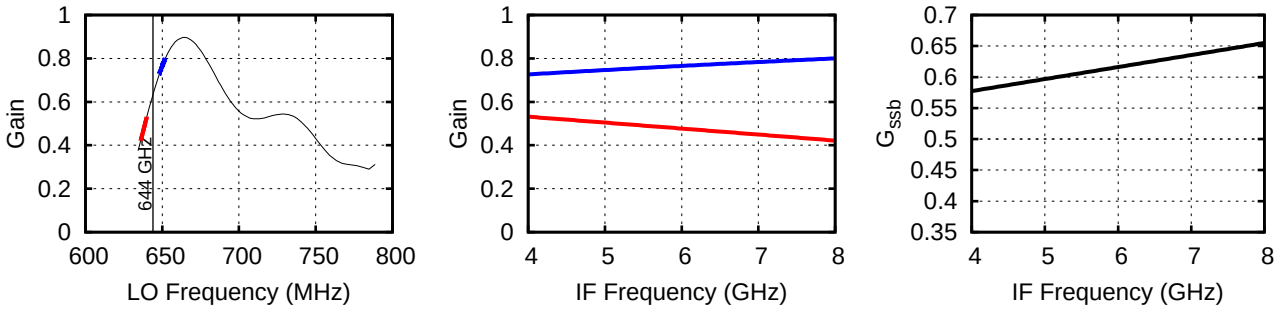

(a) Band 2 side band gain ratio example at 644 GHz

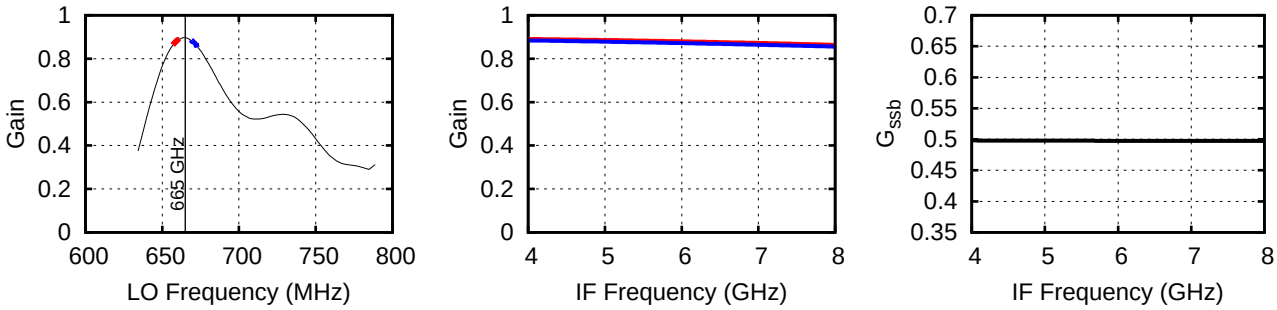

(b) Band 2 side band gain ratio example at 665 GHz

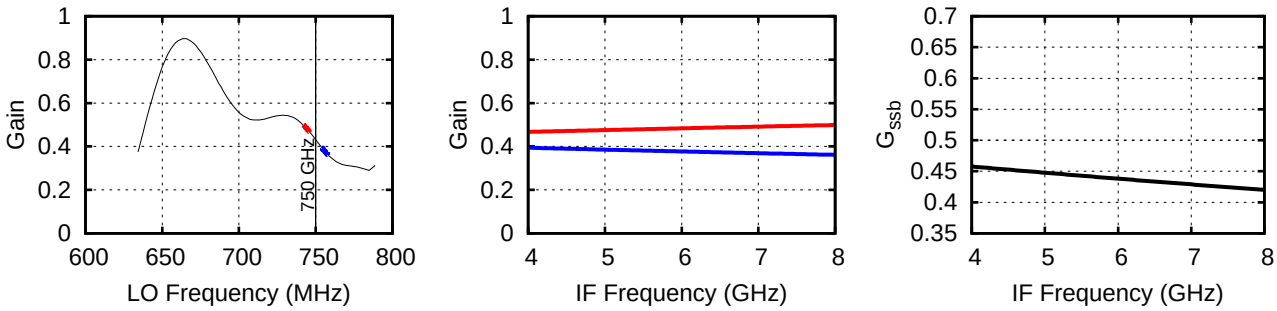

(c) Band 2 side band gain ratio example at 750 GHz

Figure 2.16: Variations in the side band gain ratio at different LO frequencies for band 2. The panel on left show the upper and lower side band gains on the overall mixer gain for a given LO frequency. The center panel figures show upper and lower side band gains as they appear on the IF band with the lower side band gain folded onto the upper side band gain. The right most figures show the resulting normalized side band ratio, G_{ssb}.

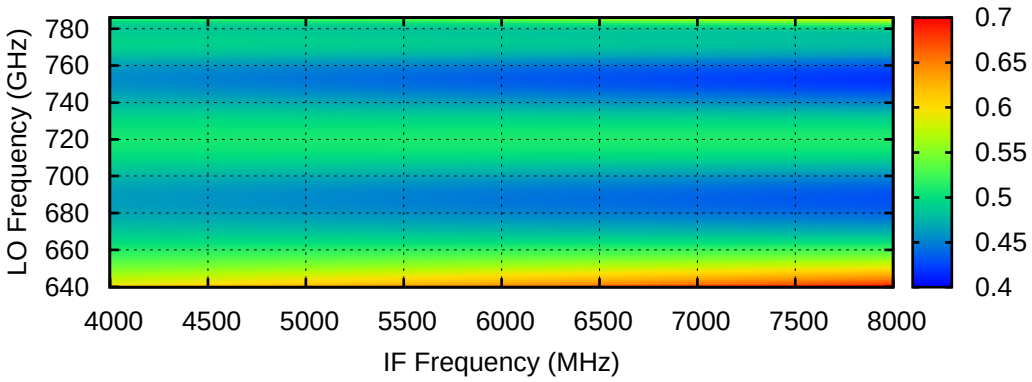

(a) Map plot showing normalized side band ratio variation across the IF band for band 2

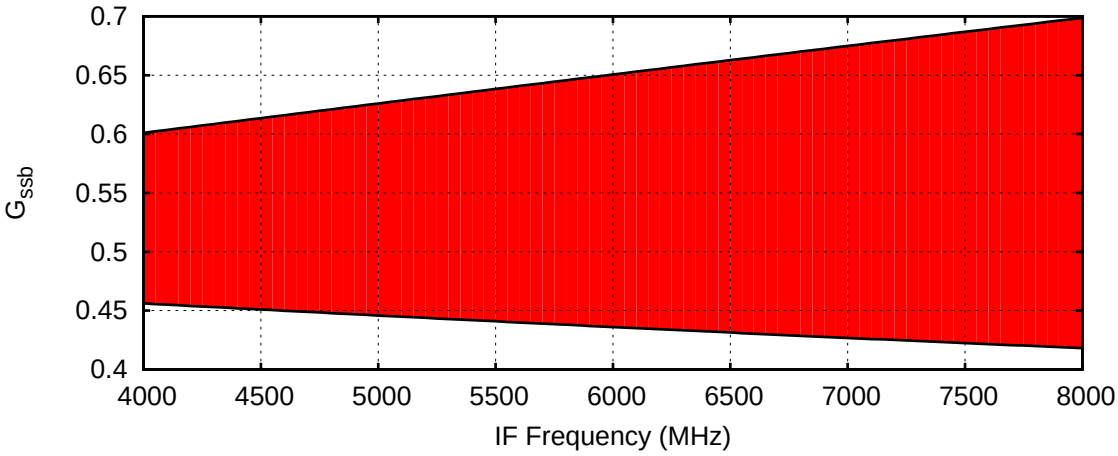

(b) The maximum and minimum normalized side band ratio value possible for each IF channel for band 2

Figure 2.17: Plots showing the variation of normalized side band ratio for band 2

2.3.2.3 IF Gain (Diplexer tuning/misalignment errors)

IF gain commonly refers to the gain across the IF band. IF gain is usually associated with the IF electrical amplification chain. For HIFI the amplifiers were carefully designed to provide an uniform gain across the IF band. The supplied amplifiers meet these requirement hence gain variations due to the amplification chain are not considered significant in HIFI calibration.

Another source of IF gain variation is in the diplexer signal coupling mechanism used in bands 3 and 4 and band 6 and 7. As discussed in section 1.2.3, a diplexer is used in these bands due to a perceived lack of LO power during the early development of the HIFI LO chains. The diplexer allows a larger of the LO signal to be coupled to the mixer as opposed to a beamsplitter set up which couples just a fraction of the LO power.

The diplexer is based on a polarizing Martin-Puplett interferometer. The incoming signal is split into 2 orthogonal polarization components and directed to 2 roof top mirrors. The 2 roof top mirrors are separated by a path length equal, L, calculated from the center IF frequency:

$$L = \frac{c}{4\nu_c}. \tag{2.27}$$

where ν_c is the central IF frequency. For the SIS bands, with an IF center frequency of 6GHz,there is a separation of 20.8mm and for the HEB bands, with an IF center frequency of 3.6GHz, there is a separation of 12.49mm. One of the diplexer mirrors is adjustable. By moving the adjustable mirror a phase difference between the two signals is introduced. Depending on the phase difference the polarization angle of the combined signal is rotated. The adjustable diplexer arm is moved until the combined signal has the same polarization angle that the mixer is sensitive to. This process of moving the diplexer arm to rotate the polarization angle is known as diplexer tuning.

The diplexer is optimized to provide the optimum coupling at the center of the IF band. The IF gain profile for the sky signal can be expressed as:

$$G_{sky} = 1 - \cos\left(2\pi\frac{\nu_c}{\nu_{if}}\right)/2, \tag{2.28}$$

and the IF gain profile for the LO signal is written as:

$$G_{LO} = 1 + \cos\left(2\pi\frac{\nu_c}{\nu_{if}}\right)/2, \tag{2.29}$$

The gain profile can be rewritten in terms of the diplexer path length, L, described in equation 2.27 such that:

$$G_{sky} = 1 - \cos\left(2\pi\frac{c}{4(L+\delta L)\nu_{if}}\right)/2. \tag{2.30}$$

Figure 2.18 provides an overview of the various diplexer tuning scenarios. Figure 2.18(b) shows an example of a perfectly tuned diplexer which each IF gain for both the upper and

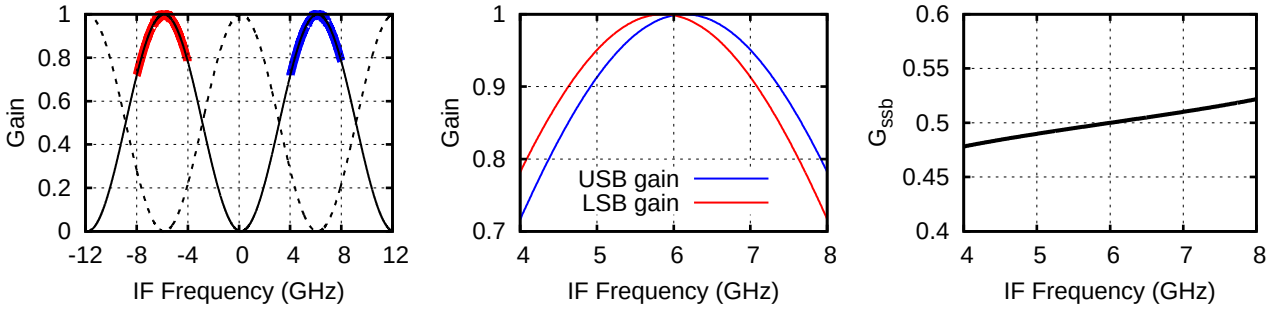

(a) Mistuning of diplexer by -3μm

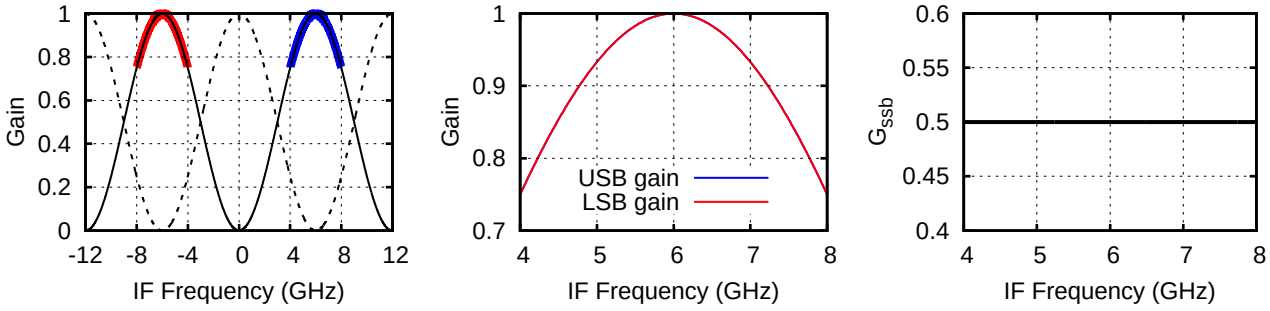

(b) Correctly tuned diplexer

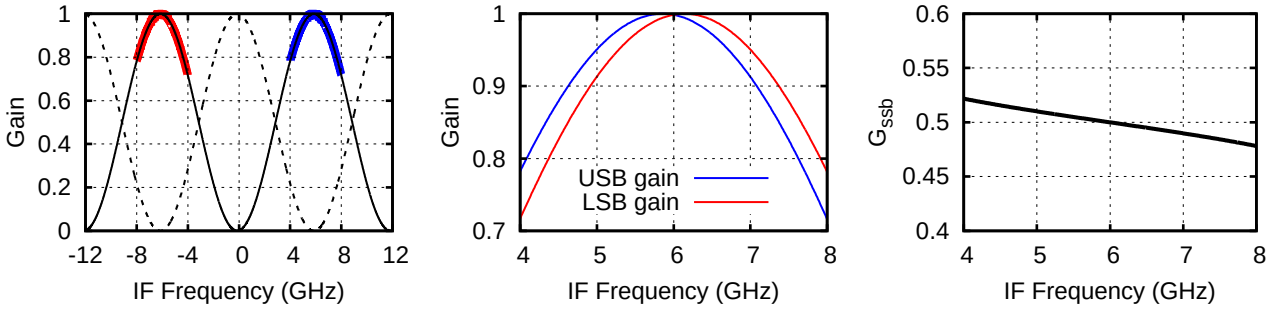

(c) Mistuning of diplexer by 3μm

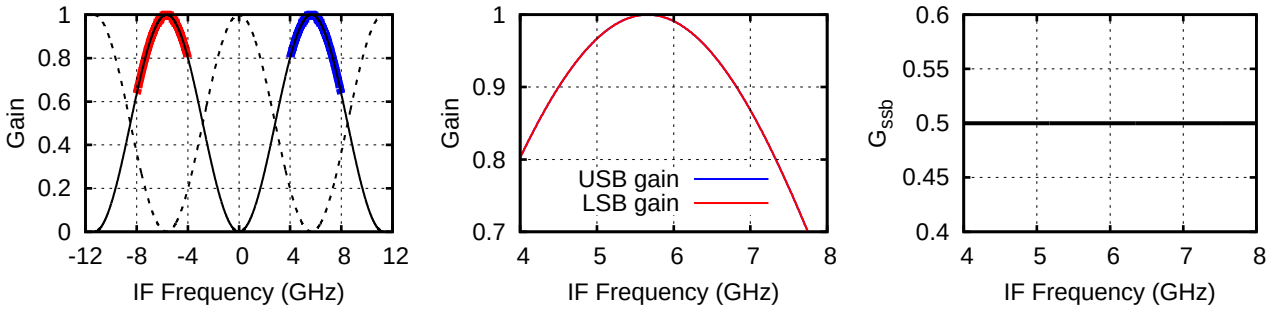

(d) Tuning diplexer to third nearest optima, mistuned by 749μm

Figure 2.18: Effect of diplexer mistuning on the side band gain ratio for an SIS diplexer band with a 4 - 8 GHz IF band

lower side bands. The diplexer tuning is however susceptible to errors. The diplexer tuning is based on a diplexer model which is generated from spot measurements where a diplexer scan is undertaken at a multiple LO frequencies. The response of the mixer is measured through the mixer current. During a diplexer scan the optimum polarization angle is seen at multiple diplexer settings. However there is a measurement error of up to 3μm on the model[50]. Figures 2.18(a) and 2.18(c) show the effect of a diplexer mistuned by 3μm. From the side band gain ratio it is apparent that a significant slope is across the IF band with deviations from an ideal side band ratio of up to 5% seen at the band edges.

Another issue with the diplexer model is that there are multiple diplexer settings which will optimally couple the LO power to the mixer however there is only one diplexer setting that will provide the optimum coupling at the center of the IF band. Care must be taken during the generation of the diplexer model that the correct diplexer positions are selected. Figure 2.18(d) shows an example of a diplexer position which provides the optimum LO coupling but has the optimum sky coupling at a lower IF frequency. This results in non-optimum coupling for the higher IF frequencies which results in higher noise in these regions. Additional noise towards band edges is an issue in the diplexer bands. Due to the nature of its operation optimum coupling is only possible at a single IF frequency however having the optimum gain at the center of the IF band can minimize the problem.

The end effect of the diplexer mistuning on the side band ratio is similar to the RF gain effects discussed in the previous section. However side band ratio variation with RF gain changes are LO frequency dependent as shown in figure 2.16 on 36 while the effect of diplexer misalignment is LO frequency independent and depending on the degree of misalignment results in a constant slope across the IF band for all LO frequencies.

2.3.2.4 Effect on line intensity

In the previous section we have presented some of the instrument effects which result in a side band gain imbalance in the mixer response. As has been stated numerous times the mixer is sensitive to 2 side bands either side of the LO frequency. The sky signal is calibrated by observing 2 internal loads. Each channel in the down converted signal contains signal from both side bands. The problem for the astronomer arises when trying to determine the intensity of a line which occurs only in one side band. A priori knowledge of the side band ratio is required in order to accurately determine the line intensity in one side band. If it is assumed that the mixer has a balanced side band gain ratio this results in an uncertainty in the measurement. Figure 2.17(b) on page 37 demonstrated the range of values possible for a typical mixer RF gain profile. In this section the effect of these extremes on a line intensity is demonstrated.

Figure 2.19 shows an example of the effects of side band ratio on line intensity. The data presented is a double side band observation of the molecule OCS. OCS is a useful molecule for this illustration as it has spectral lines approximately every 12GHz. By careful selection

of the LO frequency one line can be placed at the upper end of the IF band and one in the lower. For this example the LO frequency is set at 721.3 GHz which places the OCS lines at 716.546 GHz at an IF frequency of 4.754 GHz and the 728.654 GHz an IF frequency of 7.354 GHz. Figure 2.19(a) shows the single side band spectra of the line before down conversion while figure 2.19(c) shows the IF line positions for the down converted signal.

Another useful trait of the OCS molecule is that subsequent lines have very similar line intensity. For the 2 lines shown in figure 2.19 there is a 6% difference in line intensity. The 716.546 GHz line has a integrated intensity of 0.0034 nm^2.MHz while the 728.654 GHz line has an integrated intensity of 0.0032 nm^2.MHz, the units of integrated intensity are as defined in the JPL catalog[94]. The OCS line profile is generated assuming a gas cell setup of 1mBar pressure and a optical path length of 128cm. This model generation will be described in detail in chapter 4.

Figure 2.19 shows 3 different side band ratio profiles. The 3 profiles are generated from the band 2 mixer RF gain profile shown in figure 2.16 on page 36. The green profile shows the double side band response for a gain balanced mixer or where G_{ssb} is equal to 0.5 for all IF channels or to put it more simply where the fraction of the signal which is from the upper side band is half the total double side band signal for all IF channels. The resulting OCS double side band spectra show that the lines are almost of equal intensity consistent with single side band intensity shown in figure 2.19(a). The blue profile corresponds to the band 2 side band gain ratio response for an LO frequency of 644.0 GHz. This shows an example of a mixer setting where the fraction of double side band response that is from the upper side band is greater than the lower side band intensity i.e. $G_{ssb} > 0.5$. From this example one can see that the intensity of the line in the upper side band (at the higher IF frequency) has now a greater intensity than the lower side band line. The astronomer ideally wants to get back to the single side band spectra shown in figure 2.19(a) and must make an assumption on the side band ratio. It is nominally assumed that an equal portion of the double side band intensity is from the upper and lower side band. On this assumption the intensity is simply multiplied by 2 to return the single side band intensity. For this example where the side band ratio for the upper side band spectral line is 0.63 using equation 2.24 the over estimation of the line intensity is 26%. Similarly for the side band ratio less than 0.5, highlighted in blue in 2.16, the side band ratio of the upper side band side is 0.43 resulting in an underestimation of the line intensity of 14%.

From this example it is apparent that a 5% uncertainty in the side band ratio leads to a 10% uncertainty in the line intensity. The need for accurate a priori knowledge of the side band ratio was seen as crucial in achieving the 3% calibration goal envisaged for HIFI. To determine the side band ratio for HIFI a gas cell test set up was proposed during the instrument level testing of HIFI prior to launch. For this test setup known gases would be observed at a known pressure, temperature and optical depth. The gas molecules were carefully chosen to saturate in the gas cell set up. Using this principle measurement of the side band ratio could be taken. The test setup, measurement procedure, analysis and results will be discussed in detail in chapter 4.

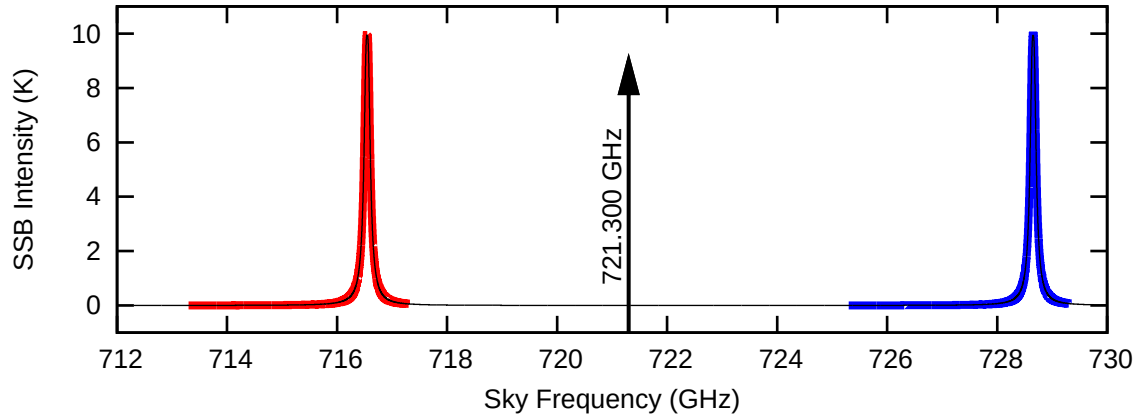

(a) OCS spectra shown between 712 and 730 GHz. The resulting upper and lower side bands are highlighted in blue and red respectively when observing with an LO frequency of 721.3 and an IF bandwidth from 4-8 GHz

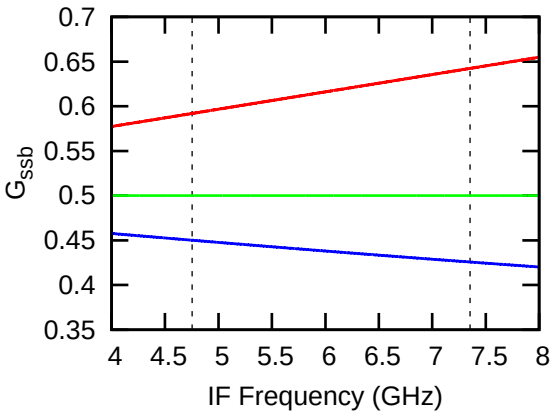

(b) Normalized side band ratio taken from the examples in figure 2.16 on page 36

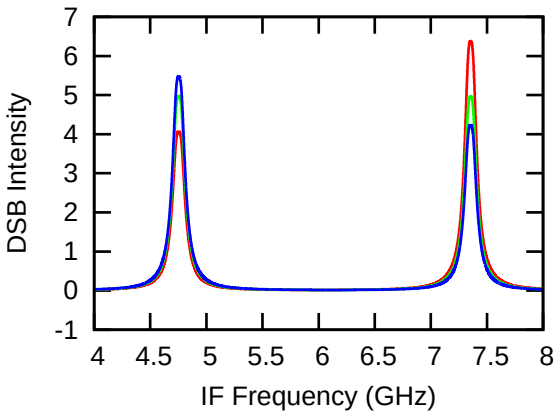

(c) Double side band spectra applying gains shown in figure 2.19(b)

Figure 2.19: The effect of side band ratio on double side band line intensity for the molecule OCS observed at 721.3 GHz.

2.4 Standing waves

2.4.1 Introduction

Standing waves are discussed here in a dedicated section of their own. Standing waves introduce an uncertainty in the intensity calibration and as such should be included in the intensity calibration section. However they have a number of ancillary effects on the calibration which merit further discussion.

Standing waves are a common source of calibration error in radio telescopes. Since the wavelength of the signal is comparable with the telescope optics internal reflections in the instrument optics leads to a frequency modulation of the signal. Standing waves typically manifest themselves as a modulation in the baseline of the broadband detected signal such as the Mars observation shown in figure 2.9, page 26. However the data shown in spectral line data shown in figure 2.10 also has a calibration uncertainty even though the continuum is standing wave free. Standing waves appear in a number of other forms in the HIFI data. As we have seen in the load efficiencies section, electrical standing waves in the HEB IF chain have a detrimental effect on the calibration accuracy of the HEB bands. Standing waves also affect the LO signal power pumping the mixer. This effect is particularly apparent in frequency switch observation modes. The origins of the electrical standing wave, its behaviour and the methods to remove it from the data are discussed in detail in chapter 3. In this section standing waves in the optics and the knock-on effects on the instrument operation and spectra are discussed. The tests undertaken to investigate standing waves are also detailed in this section.

2.4.2 Standing waves in a double side band receiver

Standing waves occur when the incoming signal is not completely absorbed by the mixer, part of the signal is reflected back out the optical path. The reflected signal is further reflected off another surface and a fraction of the signal is reflected back along the signal path towards the mixer. The mixer then detects the superposition of 2 signals; the full sky signal and a reflected sky signal. The 2 signals interfere at the mixer focus and depending on the phase difference between the 2 signal add constructively or destructively. When this is seen from a broadband perspective a frequency dependent modulation of the signal is seen. The amplitude of the resulting modulation is function of the reflectivity of the 2 cavity surfaces. The period of the modulation is a function of the distance between the 2 cavities and can be calculated using the following relationship:

$$d = \frac{c}{2P}, \tag{2.31}$$

where d is the distance between the reflecting surface, P is the period of the modulation and c is the speed of light. For further reading on standing waves in a sub-mm system see Trappe et al. [120].

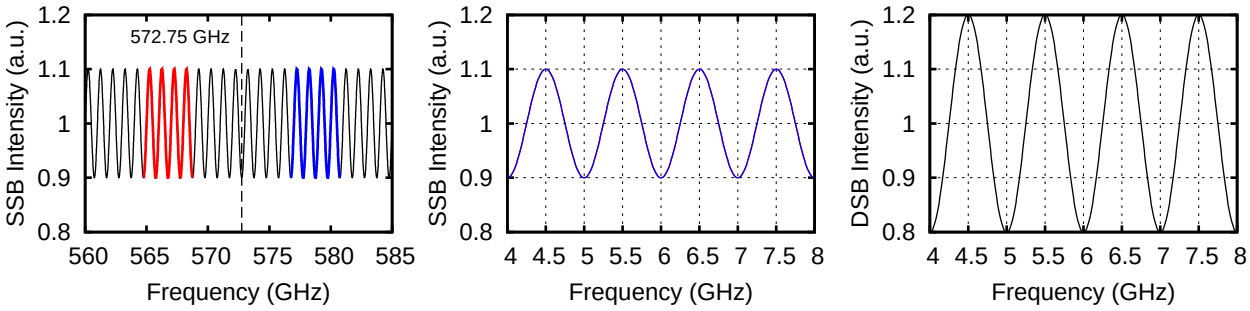

(a) Constructive interference, 572.75 GHz

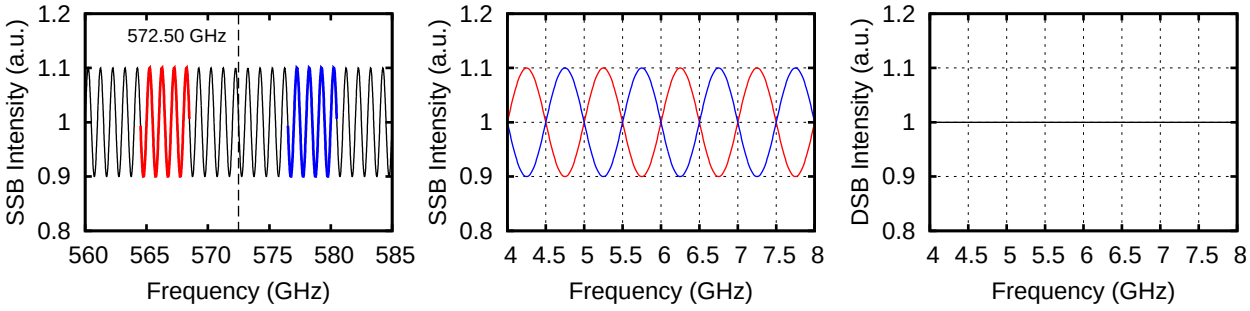

(b) Destructive interference, 572.5 GHz

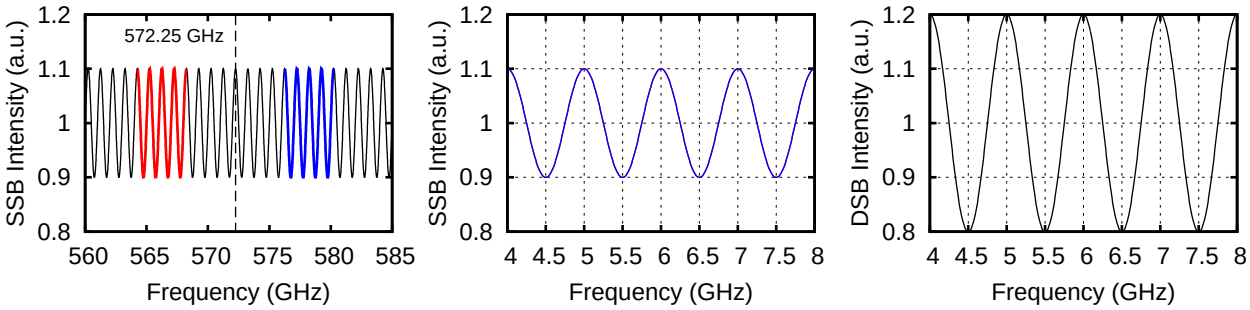

(c) Constructive interference, 572.25 GHz

Figure 2.20: Varying degree of interference between the upper and lower sideband for a 1 GHz period standing wave. The left hand side figure shows the sky frequency standing wave with the LO frequency overlaid as a dashed line and the upper and lower side bands are denoted by a blue and red line respectively. The center figures shown the upper and lower side band standing wave before addition into the DSB spectra. The right hand side figures shows the addition of the upper and lower side bands shown in the center column.

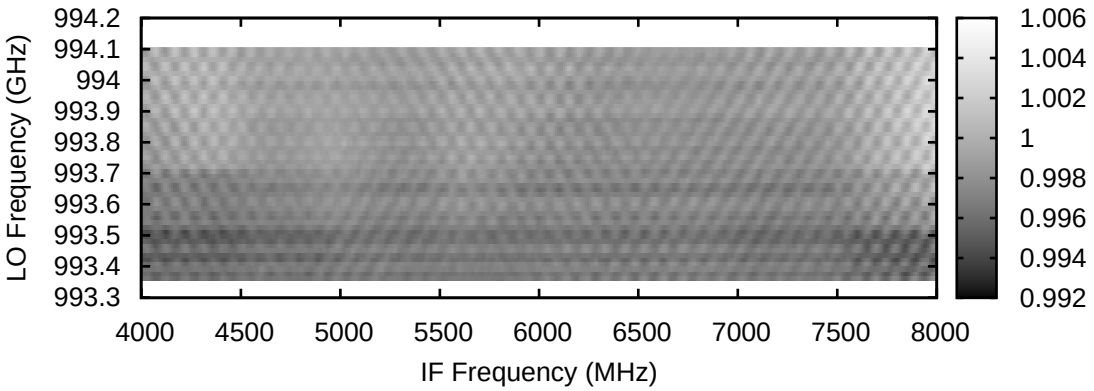

Figure 2.21: Standing wave test data showing the checkered pattern of a 90 MHz standing wave in instrument optics. The checkered pattern is caused by the interference between the upper and lower side band standing wave which is LO frequency dependent.

Standing waves in a double side band system such as HIFI have an added layer of complexity due to the double side band nature of the detected signal. HIFI down converts 2 bands of 4-8GHz (2.4-4.8 for HEB bands) of sky signal around the LO frequency. The output IF signal contains the addition of the upper and lower side bands. Depending on the phase difference between the upper and lower side band standing wave, the detected standing wave seen in double side spectra can constructively or destructively interfere. The appearance of standing waves in the double side band spectra is dependent on where the LO frequency intersects the standing wave in the sky frequency domain.

Figure 2.20 shows a model of double side band behaviour for different LO frequencies sampling the same sky signal standing wave. A standing wave period of 1.0 GHz is simulated. No such standing wave period exists in HIFI, this period is chosen for illustrative purposes. The point to note from figure 2.20 is that while the standing amplitude seen in the sky signal is the same for all settings the double side bad amplitude detected is seen to vary with LO frequency. This is due to the interference between the upper and lower side band. The interference between the upper and lower side band is dependent on the LO frequency intersection with the phase of the sky signal. The 3 LO frequencies plotted in figure 2.20 are separated by a quarter of the standing wave period. From this one can see side band interference goes from constructive interference to destructive interference to constructive interference. Figure 2.21 shows a grayscale plot of multiple spectra taken with an LO frequency spacing smaller than the standing wave period seen in the data. From the plot one can see the changing phase and amplitude of the 90 MHz standing wave due to the side band interference.

The end result of this side band interference is that each LO frequency effectively has a unique set of standing waves as the reflectivity of the standing wave cavities will most likely be frequency dependent. The side band ratio will also have an effect on the standing wave profile.

For most observation types the standing waves cancel in the cross calibration. However the

presence of standing waves can produce poor quality data in the frequency switch mode. The frequency switch mode uses a spectrum taken at a different LO frequency as an OFF phase calibration. This can produce significant standing waves if the frequency step is not a multiple of the standing wave period. Standing waves can also be an issue for high continuum sources such as Mars, see figure 2.9.

2.4.3 Standing wave tests

Standing wave tests are a key component in the test routine of the HIFI instrument. At each phase of the instrument development a series of standing wave tests were undertaken to measure the standing waves present in the system. The author was extensively involved in these tests and helped develop the test procedures and analysis scripts to interpret the tests. The basic layout of a standing wave test consists of a series of spectra taken at small LO frequency steps of 15MHz around a central LO frequency. The LO power is tuned to this central LO frequency. The chopper is then set at a fixed position and a spectrum is taken at each LO frequency step.

The data is then calibrated by dividing all spectra by the last spectrum in the series. This removes the band pass and returns a calibrated spectrum of sorts. With this calibration routine the standing waves are exaggerated since different LO frequencies are combined together. The standard 4 phase calibration would have the same LO frequency in all phases (with the exception of the frequency switch observation) and any common standing wave would cancel in the cross calibration. For the standing wave tests, the goal is to identify the standing waves present hence the special calibration routine.

A standard standing wave test consists of 50 LO steps of 15MHz around a central LO frequency. Each spectrum is then divided by last spectrum and a spectrum with the pass band removed is returned. The standing waves for these calibrated spectra are the residual between the denominator spectrum and the numerator spectrum. It is difficult to extract the standing wave properties of a single raw spectrum as the pass band dominates the signal. Hence the need to divide by another spectrum at a different LO frequency. By keeping the calibrator spectrum constant for all spectra it allows an indirect observation of the standing wave behaviour.

Once a set of calibrated spectra is at hand the standing wave behaviour can be extracted. The author developed a method to automatically extract the standing wave behaviour from the data using Fourier transforms of the calibrated data. The Fourier transform of all spectra is first calculated and then a peak finding routine extracts the strongest periodic signals from the Fourier transform. Each of the peaks in the Fourier transform is then fitted with a Gaussian and the total power for that frequency is extracted, this process is repeated for all significant peaks in the FFT. By taking the fitted signal power as a fraction of the total power the standing wave amplitude in the signal domain can be determined. This is described in the following equation:

$$A = \frac{P_{fit}}{2\sqrt{2}NF_{han}}, \tag{2.32}$$

where A is the standing wave amplitude, P_{fit} is area under the fitted Gaussian, N is the number of frequency channels in the spectrum and F_{han} is a Hanning conversion factor 1.4657. The factor 2 accounts for the frequency folding in the FFT processing. Using this process the amplitude of each standing wave in the system can be determined and plotted against the LO frequency. While this is not an absolute measure of the standing wave amplitude at that LO frequency it does provide an accurate measure of the maximum standing wave amplitude possible.

Figures 2.22,2.23,2.24 and 2.25 show the standard output from the standing wave test analysis script. These figures provide an overview of an entire standing wave test. The source observed (sky path, hot load, cold load) is given in the plot title. A number of interesting points can be taken from the over view plots. Figure 2.22 shows a standing wave test undertaken while looking at the sky through the Herschel internal optics. From the FFT plot a number of weak components can be seen. A small signal can be seen which corresponds to the secondary mirror cavity. This feature is not seen for the other polarization (V mixer is plotted here). There is no visible evidence of the standing standing wave in the plotted spectrum. The spectrum shape is distorted slightly, this is due the mixer current difference between the 2 calibrating spectra. Figure 2.23 shows a standing wave test undertaken while looking at the internal cold load. From the FFT plot in the top left panel it is apparent that significant standing wave exist at a period of 98MHz. From the bottom left panel the variation of this standing wave versus LO frequency is seen. The amplitude is seen to vary periodically with the LO frequency showing the constructive and destructive interference between the side bands for different LO frequencies. Again the large scale variation on the baseline is due to the mixer current difference between the 2 spectra used in the calibration. This feature is an artifact of the calibration routine and is not seen in the calibrated data unless a large drift in LO power occurs over the course of an observation.

Figures 2.24 and 2.25 show plots of the standing wave seen in the diplexer band 3b. From the data there is a large standing wave at 680 MHz which is due to a straight edge between the diplexer root top mirrors. This will be discussed in the next section. The diplexer adds an additional level of complexity to the standing waves seen in the system. The diplexer adds a frequency dependent coupling to the sky and LO signals. The diplexer is designed so the sky signal has a maximum coupling $\pm$ 6 GHz (3.6 for HEB bands) from the LO signal frequency. Conversely the signal from the LO direction has a maximum coupling at the LO frequency and a minimum coupling at the $\pm$ 6 GHz from the LO frequency. This gain variation can be seen in the standing wave data. Standing waves coming from the LO direction are significant towards the band edges and disappear towards the IF band center. On the other hand standing waves coming from the sky signal direction such the cold loads have a maximum amplitude towards the band center.

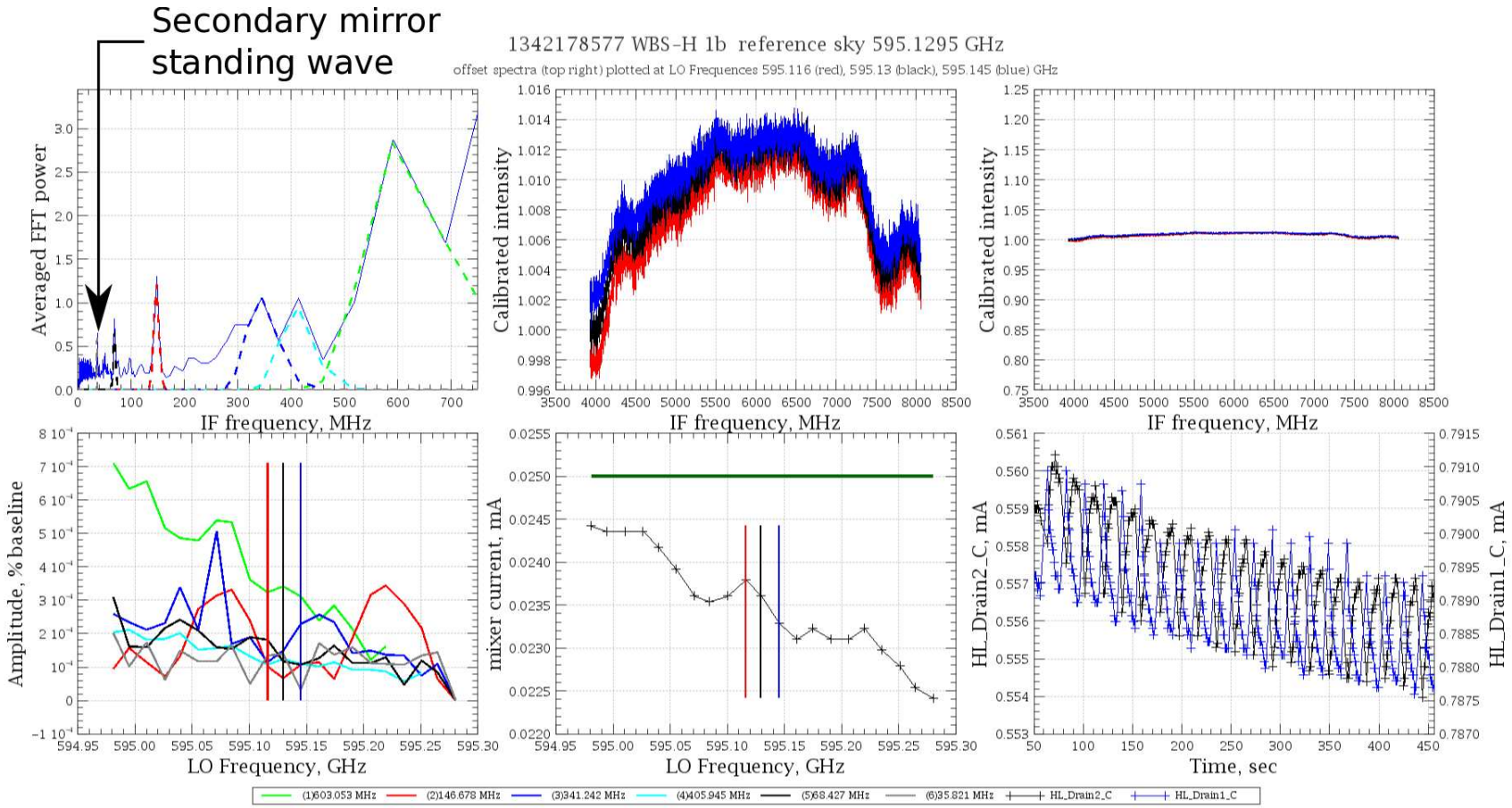

Figure 2.22: Example of the output from the standing wave analysis script. This is an example of a standing wave test at an LO frequency of 595.1295 GHz in band 1b looking at the sky through the Herschel primary mirror. Note the presence of a small signal at the secondary mirror cavity frequency, 34MHz. *Top left*: Average FFT plot of all data taken during test. *Top center*: Plot of 3 central spectra in the standing wave test series *Top right*: Same plot as the top center panel but with a fixed axis to allow for quick comparison between tests. *Bottom left*: Plot of standing wave amplitude vs LO frequency. The line color relates to a single standing wave period which is described in the legend. *Bottom center*: Plot of mixer current vs LO frequency. Green line represents the goal mixer current. Black, Red and Blue line mark the mixer currents for the corresponding spectra in the top center and top right panels. *Bottom right*: LO power vs observation time, this plot is used to determine if the power drifted during the observation.

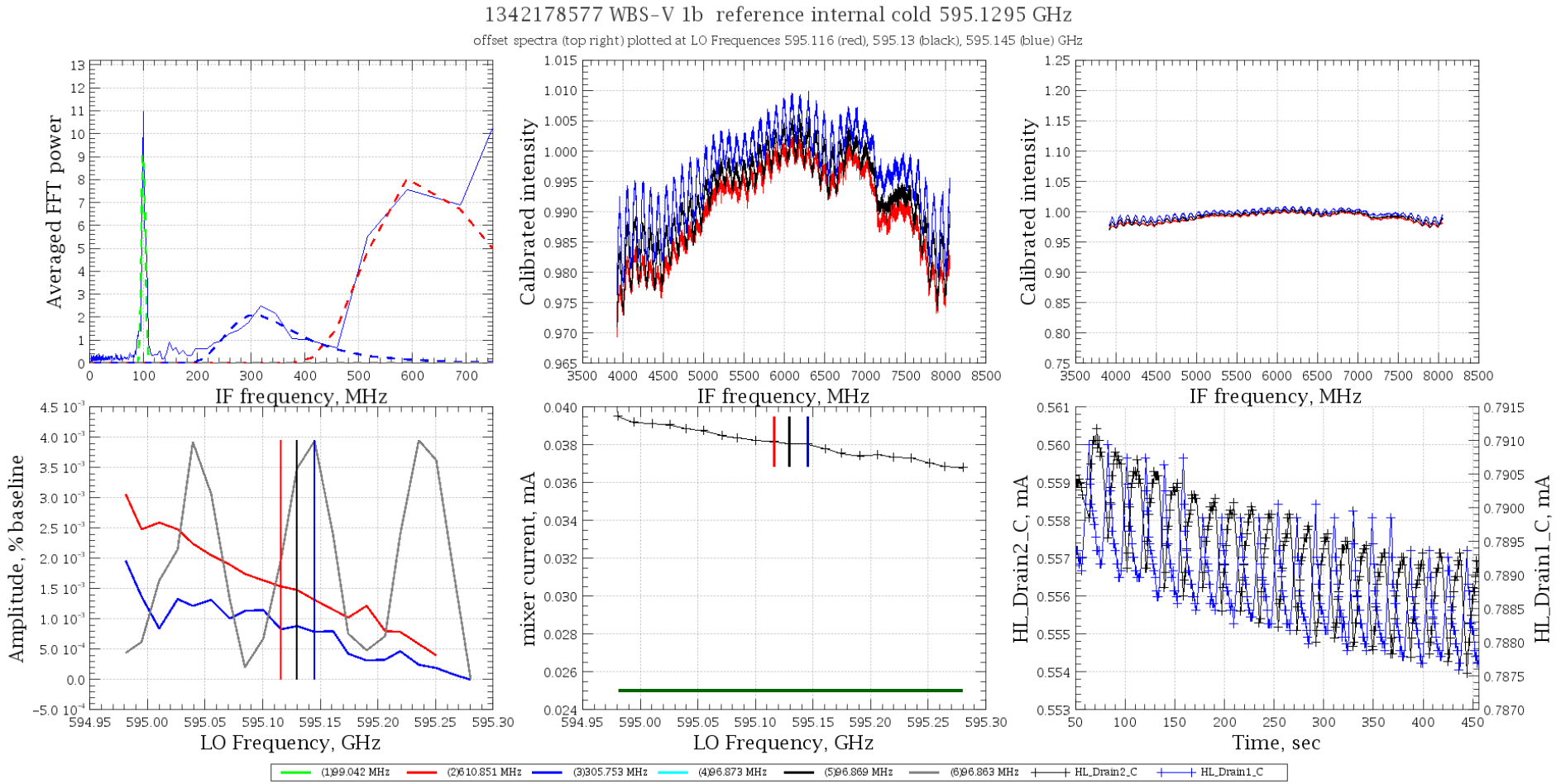

Figure 2.23: Example of output from standing wave analysis script. This is an example of standing wave test at an LO frequency of 595.1295 GHz in band 1b observing the internal cold load.

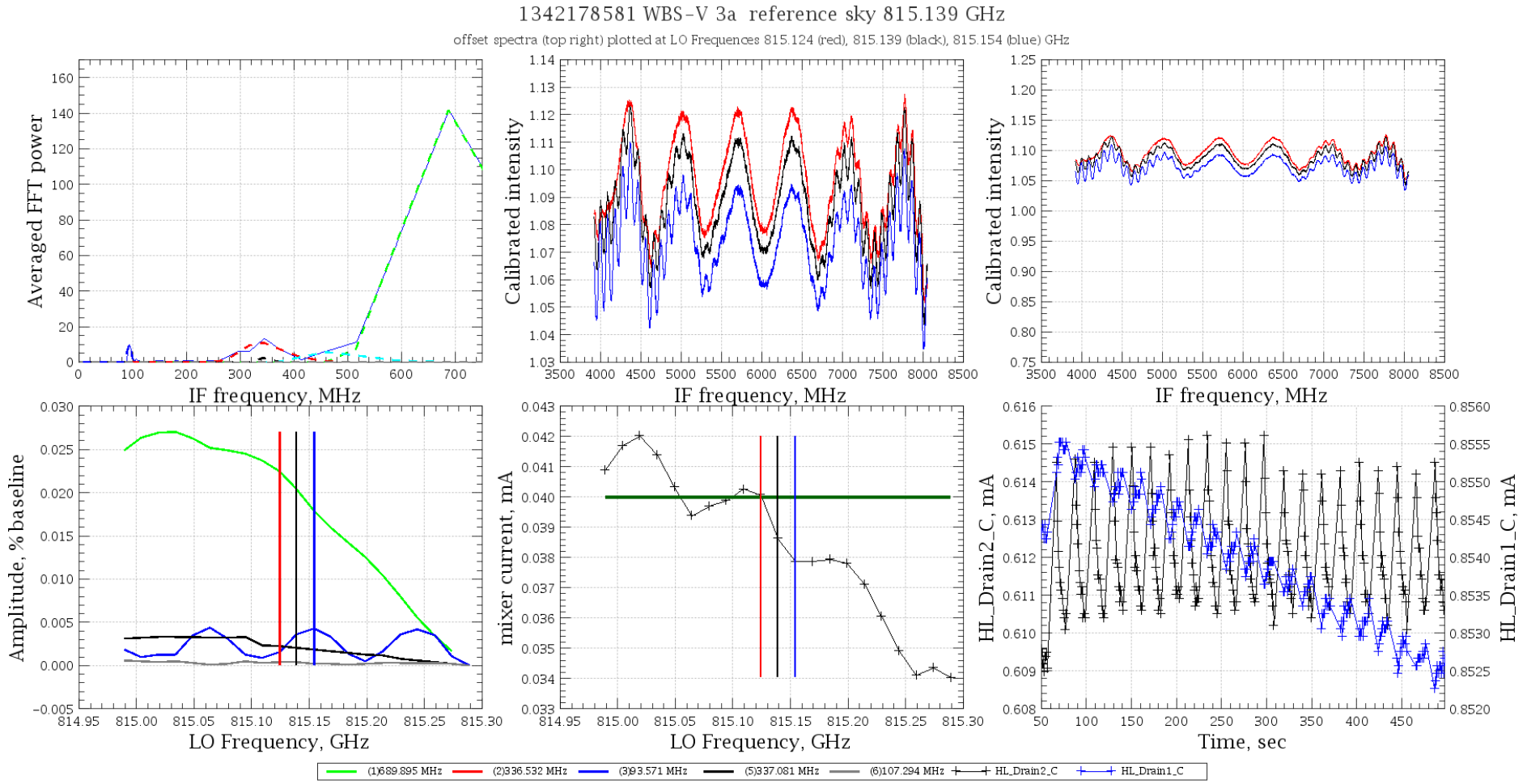

Figure 2.24: Example of output from standing wave analysis script. This is an example of standing wave test at an LO frequency of 815.139 GHz in band 3b looking at the sky through the Herschel primary mirror.

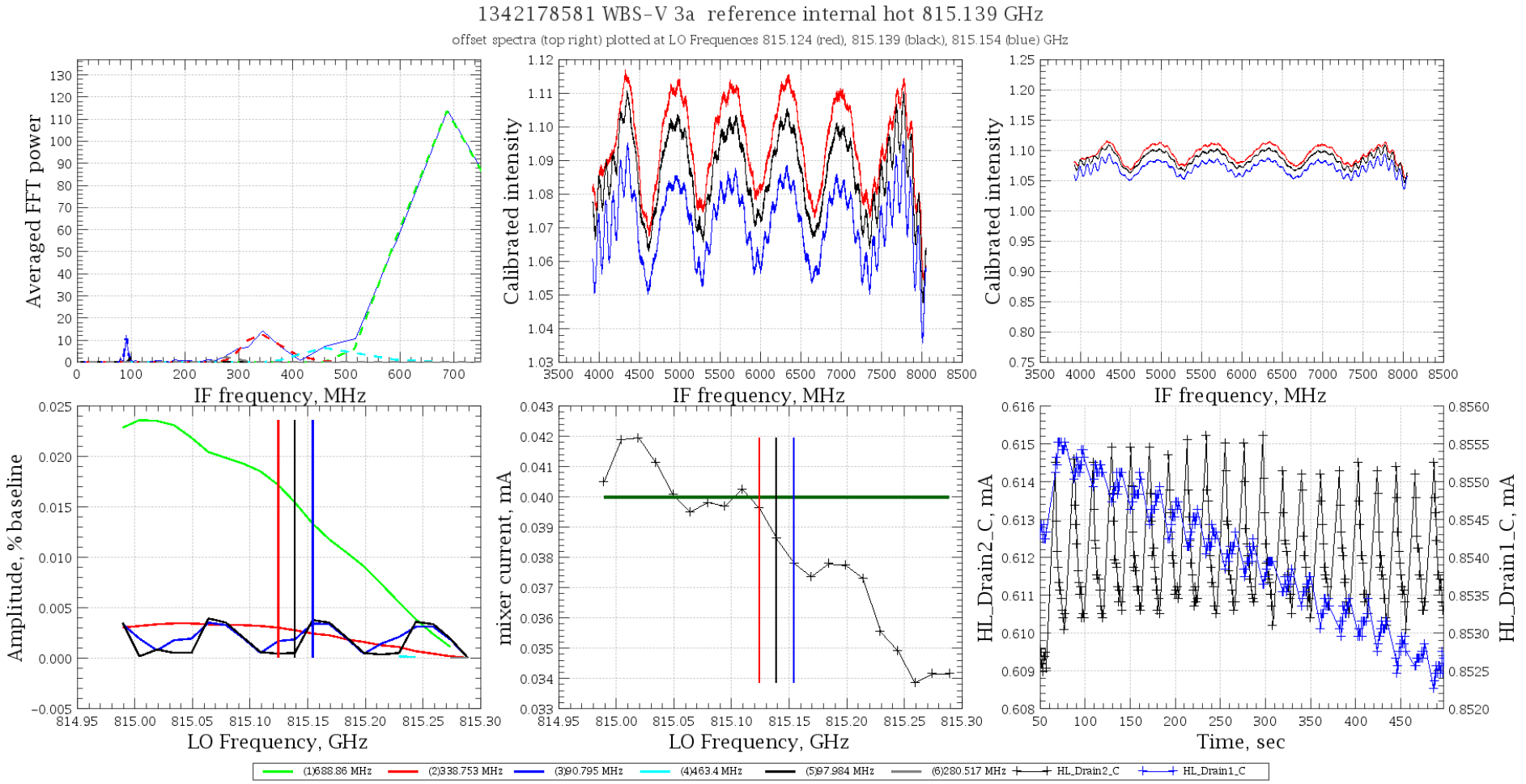

Figure 2.25: Example of output from standing wave analysis script. This is an example of standing wave test at an LO frequency of 815.139 GHz in band 3b looking at the internal cold loads.

Figure 2.24 shows data taken while looking through the Herschel optics, from the spectrum in the top right panel one can see that the 90 MHz standing wave is dominant towards the band edges and disappears towards the band center consistent with a standing wave in the LO direction. The period of the standing wave corresponds to the distance between the mixer and the LO signal horn. Figure 2.25 shows an example of data taken towards the internal cold load. From the spectra plot one can see that a standing wave now appears at the band center as well. The period of the standing wave is consistent with the cold load to mixer cavity. It appears that 2 standing waves at $\sim$ 90MHz exist in band 3 but from completely different sources, one from the cold load and one from the local oscillator unit.

The test data from bands 5,6 and 7 are not presented here. Band 5 is a non diplexer band shows similar standings behaviour to bands 1 and 2. Band 5 has a smaller beam size and a quasi-optical antenna as opposed to the wave guide antenna of bands 1 and 2, this leads to a reduction in reflections back into the optics. Furthermore the band 5 mixer units have a reduced sensitivity compared to the bands 1 and 2 mixer units and hence any standing wave can be dominated by the mixer noise. As stated earlier band 6 & 7 have significant electrical standing waves which are discussed in chapter 3 which dominate over any optical effects.

This section discussed the standing wave tests undertaken. The dedicated standing wave tests proved very useful in determining the standing waves present in the system. By combining the spectra observed in a non-optimum manner it helped exaggerate the standing waves in the system and provide some insight into the instrument behaviour which is not possible using a standard astronomical observation.

2.4.4 Sources of standing waves in HIFI

During the development of HIFI and the Herschel telescope great efforts were made to minimize the effects of standing waves in the instrument. In particular the secondary mirror and support structure were designed so that perpendicular surfaces to the optical path direction were avoided. The secondary mirror is a common source of standing waves when signal is reflected between the mixer horn and the the secondary. In order to avoid this a scatter cone was included at the center of the secondary mirror which minimizes the amount of light scattered back into the mixer. Figure 2.26 shows a sketch of the scatter cone shape and its effect on signal reflected back from the instrument. A photo of the scatter cone is also seen in figure 2.26, the scatter cone is noticeable through the distorted reflection seen in the primary mirror.

The inclusion of the scatter cone removes almost all traces of a standing wave between the secondary mirror and mixer focus. However there is still some evidence at the longer wavelength (larger beam) bands, as was shown in figure 2.22, however this is only seen when non standard calibration routines are used and for most observation routines the general astronomer should see no evidence of a standing wave from the secondary mirror.

Unfortunately not all sources of standing waves were foreseen in the development of HIFI

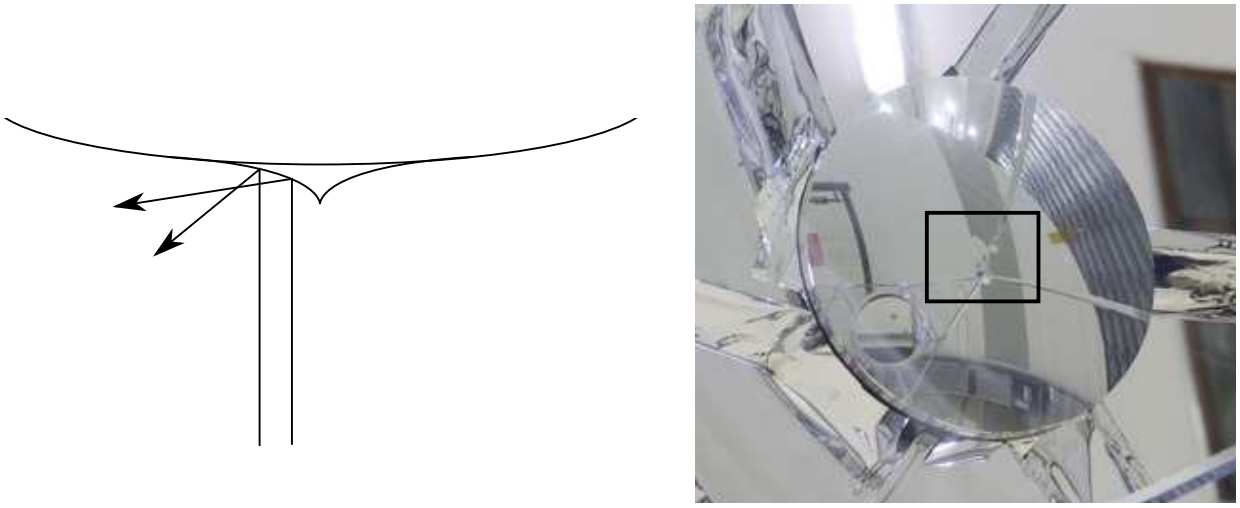

Figure 2.26: *Left*: Sketch of scatter cone on Herschel secondary mirror. *Right*: Picture of Herschel second mirror with scatter cone. Scatter cone is noticeable through the distortion of mirror reflection.

and 4 significant sources of standing waves still remain in the HIFI internal optics. The worst affected bands are those with the diplexer coupling (bands 3,4,6,7) which show evidence of all four standing waves in their data. Figure 2.27 shows a sketch of the diplexer optical set up showing the four sources of standing waves in the system namely the hot and cold loads, the diplexer rooftop mirror and the LO unit.

The most likely source of standing waves are the hot and cold loads as they have support structure which can induce standing waves, see figure 2.28. Even with careful design of the optics for the hot and cold loads and the painting of each source with anti-reflective coating standing waves are still significant. Figure 2.28 shows a photo of the hot black body with anti reflective coating. The standing wave period from the hot load is $\sim$ 92.0MHz while the standing wave from the cold load has a period of 98.0MHz. The periods are consistent with the locations of the loads. Returning to equation 2.31 the period of the standing wave is inversely proportional to the cavity size, hence the hot load positioned further from the mixer focus has shorter period standing of 92 MHz compared to the 98 MHz modulation seen from the cold load.

In order to investigate the standing wave from the loads further and determine the exact location of the reflecting surface on the calibration load structure a series of chopper scans were proposed by the author. These tests consisted of moving the chopper through its range of chopper angle scanning across the secondary mirror and onto the load structure. A spectrum was taken at a number of chopper positions. The data was calibrated much like the standing wave test. A single calibration spectrum was divided into all other spectra to remove the band pass. This calibrated data was then converted into Fourier space. The power at the FFT channels corresponding to 92 and 98 MHz were then plotted against the chopper voltage (angle). Figure 2.29 shows 3 examples from the chopper scan tests. From this one can see

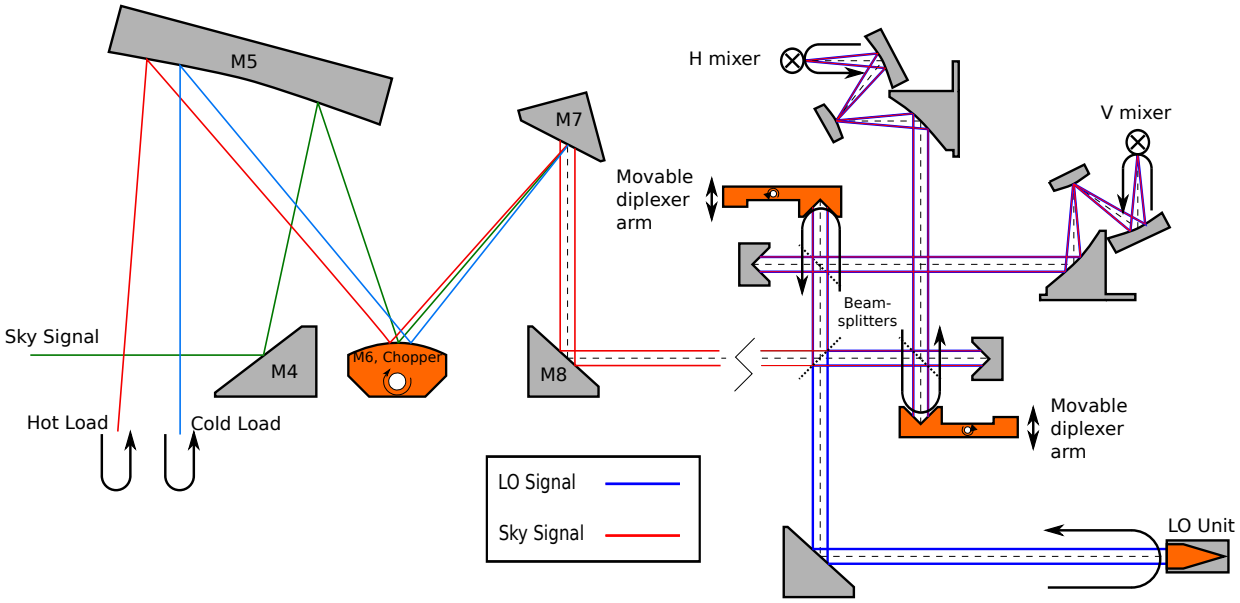

Figure 2.27: Sketch of diplexer band optical set up showing the 4 sources of standing wave in the system namely the hot and cold calibration loads, the diplexer rooftop mirror and the LO unit. They are highlighted with arrows showing a returned signal.

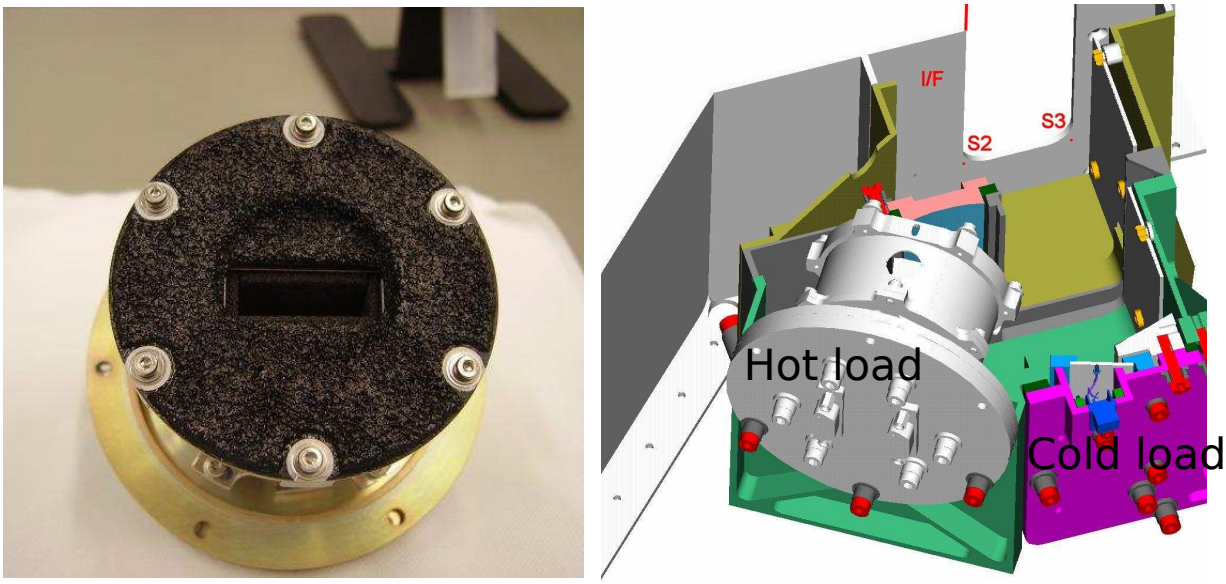

Figure 2.28: *Left:* Photo of hot black body calibration load showing anti reflective coating. *Right:* CAD drawing of calibration load layout.

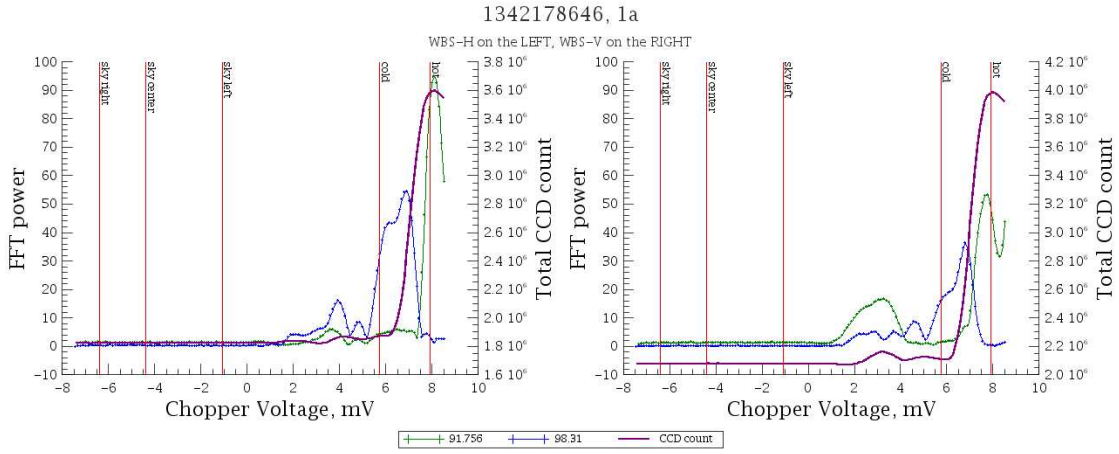

(a) Band 1a chopper scan

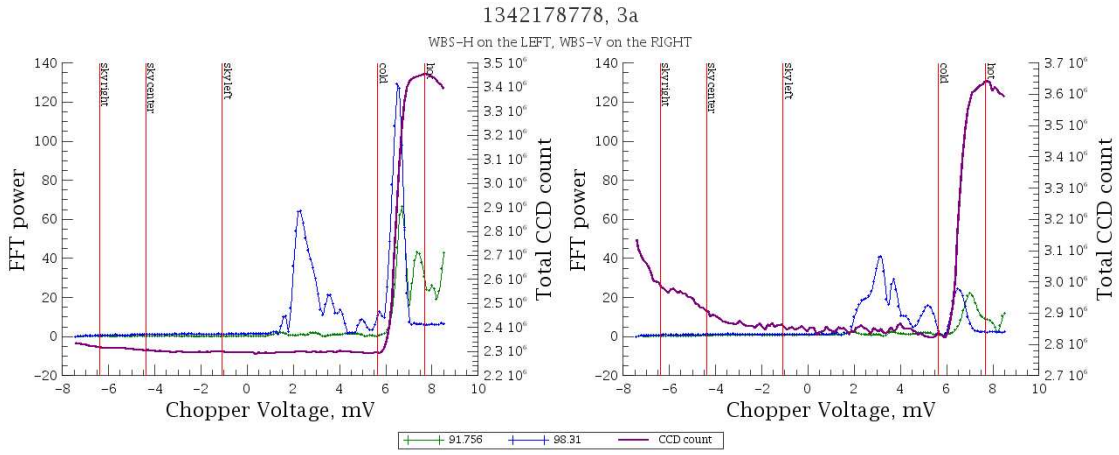

(b) Band 3a chopper scan

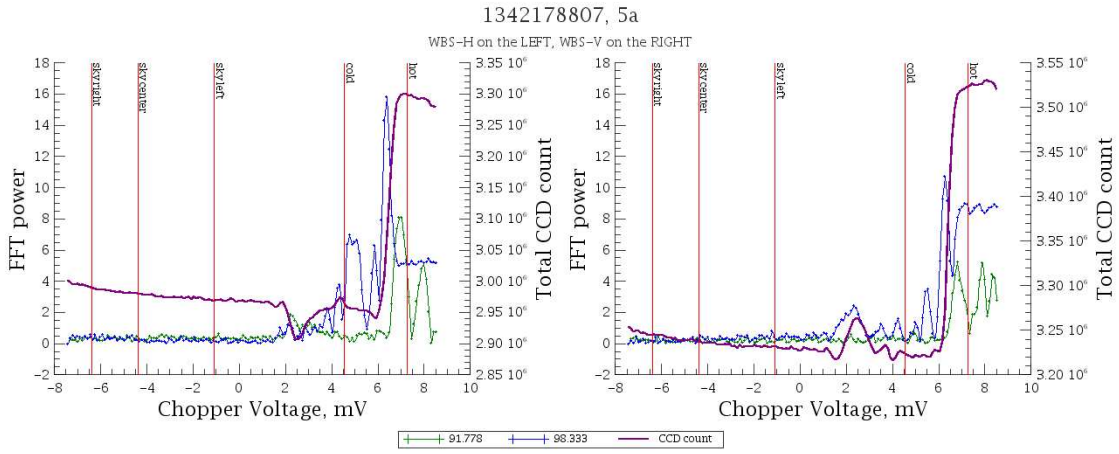

(c) Band 5a chopper scan

Figure 2.29: Chopper scan data showing the variation of different standing wave periods with chopper position. H mixer response is shown on the left and V mixer response on the right. The important chopper positions are marked on the figures with red vertical lines. The purple line is the average CCD for each chopper position, this is seen to rise as the beam moves over the hot load.

how the standing wave power is dependent on the chopper position. Note also the difference between the H and V mixer. The important chopper positions are also plotted on the figure.

The diplexer rooftop mirror standing wave is the most detrimental of all four standing waves seen in HIFI. This is apparent from the standing wave test plots shown in figure 2.24 and 2.25 where the 680 MHz diplexer standing wave has an amplitude ten times larger than the internal cold standing wave. The source of this standing wave is a flat edge at the center of the diplexer roof top mirror. Ideally this edge between the root top mirrors should be extremely sharp to minimize any flat regions facing the mixer. However due to manufacturing tolerances a flat edge was evident in the roof top mirror, see figure 2.30. Ideally the roof top mirror should be manufactured from 2 separate mirrors and then bolted together unfortunately the HIFI mirrors were machined from one block of aluminum hence the flat edge at the line center due to the milling process.

As the diplexer rooftop mirror is relatively close to the mixer unit this results in a long period standing wave of 680MHz such as that seen earlier. Reflections from the rooftop mirror also have a number of ancillary effects and can introduce some uncertainty into the instrument operation. The right hand plot in figure 2.30 shows a time line of the H and V diplexer movement and the corresponding response of the H and V mixer current. Ideally when the H diplexer is kept fixed and only V diplexer moved, only the V mixer current should react, however in the plot we see that both mixer currents reacted to the V diplexer movement.

The fundamental operation behind the operation of diplexer unit is that the roof top mirror rotates the polarization angle of the incoming single by 180° through reflection of 2 45° mirrors. By changing the path length difference between the 2 split signals the polarization angle of the combined signal can be rotated to suit the mixer polarization angle. However with a flat surface between the mirrors the signal is not rotated completely and a fraction of the signal instead of passing through the beam splitter is reflected away from the mixer unit, see figure 2.31. This signal is further reflected into the other mixer unit and enters into the diplexing process there. Hence moving the H mixer diplexer has an effect on the V mixer unit and vice versa. This cross talk between mixers limits the overall accuracy of any polarization studies, the extent of this uncertainty requires further analysis.

The 4th source of standing waves in the HIFI optics is from the local oscillator signal horn. Coincidentally the standing wave period from the local oscillator unit has a similar period to the cold load standing wave of ∼95 MHz. This standing wave is most significant in the diplexer band since the signal coupling here is high compared to the beamsplitter bands. As shown in figure 2.24 standing waves from the LO direction show up at the edge of the IF band and disappear towards the IF band center. The LO standing wave can also be seen to modulate the LO signal power through the mixer pump level. For most standing wave tests described in section 2.4.3 the LO power was kept fixed for a central LO frequency. While the LO frequency was changed the LO output power was kept constant. When the mixer current is then plotted against the LO frequency the 90 MHz modulation was apparent, this can seen in figure 2.22

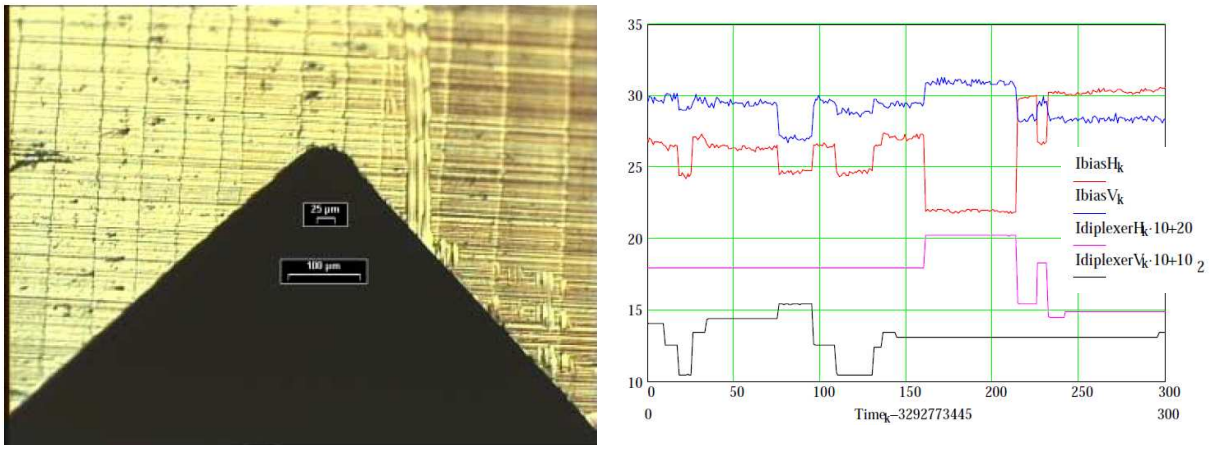

Figure 2.30: *Left:* Photo of diplexer roof top mirror showing a flat edge at center of roof top mirrors. *Right:* Timeline of diplexer and mixer response showing cross talk between the H and V mixers via reflected signal between from the diplexers[26].

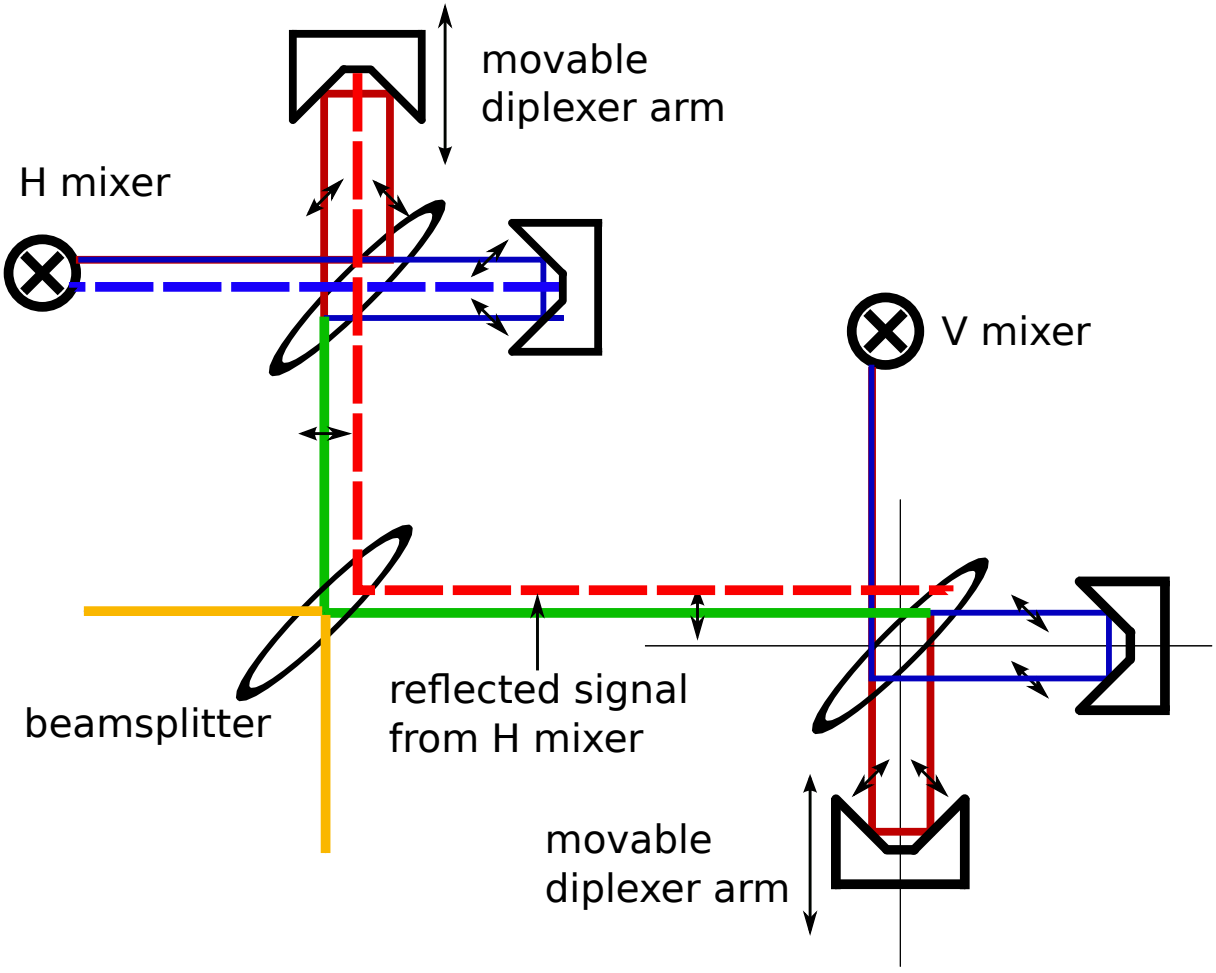

Figure 2.31: Sketch of cross talk between H and V mixer due to standing waves between the 2 mixers.

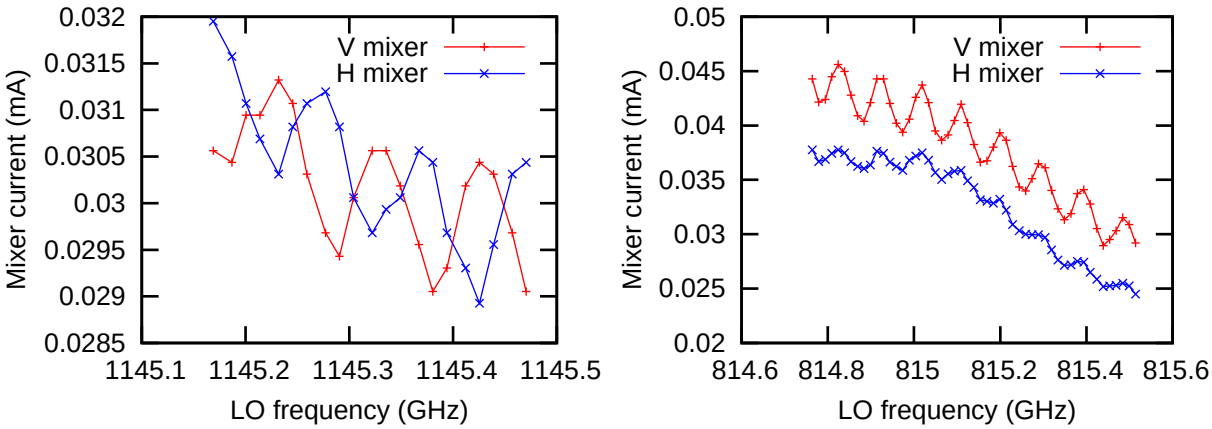

(a) Band 5a

(b) Band 3a

Figure 2.32: LO path standing wave at 90 MHz seen in pump level of the mixer when the LO power is kept constant and the LO frequency is changed.

on page 48 where the mixer current versus LO frequency is plotted in the bottom center panel. Figure 2.32 shows an example of mixer current versus LO frequency plots for both polarizations in bands 3a and 5a. From the data the 95 MHz period is apparent in both sets of data, however the amplitude in the diplexer band data is much larger than the beamsplitter band with a peak of trough modulation for V mixer of ∼10% with values close to ∼2% for the band 5 data. There is also a noticeable difference in amplitude between the H and V mixer in the diplexer band. The H mixer has almost half the V mixer standing wave amplitude, indicating different standing wave behaviour between the 2 polarizations.

2.4.5 Standing wave effects

2.4.5.1 Introduction

The standing wave discussion so far has concentrated on the dedicated standing wave tests where the data is calibrated in a way that exaggerates the standing wave behaviour. For a standard observation the calibration routine is designed to minimize standing wave effects. However in certain scenarios standing waves persist. In this section examples of standing wave in calibrated data are presented.

2.4.5.2 Strong continuum sources

For most observations the standard calibration procedure with the subtraction of an OFF reference position is sufficient to remove all standing waves in the data. However when the source target has bright continuum this can lead to standing waves from the loads appearing in the data. This is confusing on first inspection, why aren't standing waves from the loads there for all observations since the loads are observed for all observations? The 4 phase calibration is a ratio of the ON-OFF phases divided by the HOT-COLD phases. For sources with a

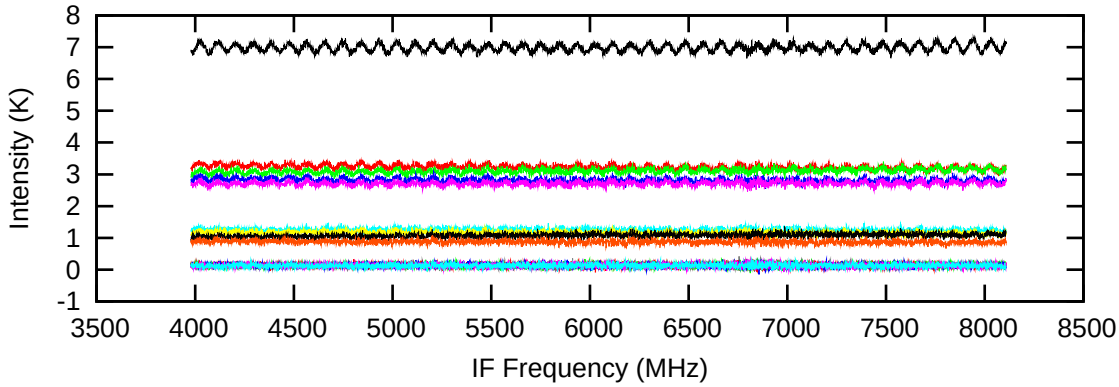

Figure 2.33: Plot of spectra taken during a Mars map observation showing the dependence of the standing wave amplitude on the continuum brightness.

low continuum and only spectral line emission the ON-OFF phase is close to zero outside of the regions of line emission. Hence when dividing the ON-OFF phase by the HOT-COLD denominator the standing wave is not seen outside of the region of line emission. Hence standing waves are only seen across the IF band when there is a strong continuum that is when the ON-OFF difference is significant. Figure 2.33 shows an over plot of a selection of map points from the Mars observation previously shown in figure 2.5 on page 21. From this figure it is apparent that the standing wave amplitude increases when Mars is at the center of the beam and the signal is brightest.

2.4.5.3 Line intensity modulation

From the previous section describing standing waves in a high continuum, it is apparent that the standing waves scale with brightness of the source being observed. The example shown in figure 2.33 has a broadband emission. Spectral lines on the other hand are bright over a small frequency range but they too have standing wave effects. However they are more subtle than those shown in the Mars example and it is only when a spectral line is tracked through the IF band that the modulation of the line intensity becomes apparent. This effect was described in detail in the paper of Siebertz et al. [113]. In this paper, OCS lines were tracked in very fine LO steps across the IF band and the line intensity was seen to modulate with the standing wave period.

Similar tests were undertaken during the flight test of HIFI. A bright spectral line was tracked across the IF band in small LO frequency steps of 35MHz. In the diplexer bands the spectral line intensity was seen to modulate with changing LO frequency consistent with the diplexer roof top mirror standing wave, see figure 2.34. As the source had a weak continuum no standing waves were seen outside of the line emission. From the max intensity plots shown in figures 2.34(b) and 2.34(c) it is apparent that the line intensity in both the H and V mixers vary by up $\pm$ 3% about the mean peak intensity. The calibration and removal of this effect may be possible although it would require extensive observation to extract the phase and amplitude

of the standing wave and using a model standing wave correct the data. Without this a priori knowledge of standing wave behaviour a 3% error due to standing wave modulation must be added to calibration uncertainty in band 4a. Other test were undertaken for the other bands but are not discussed here.

2.4.5.4 LO power disparity

The modulation of the LO power is another subtle effect of standing waves in a heterodyne system. Standing waves modulating the LO power were shown in figure 2.32. For a standard observation the LO power is set to pump a master mixer to the optimum operating point. The other mixer is left to follow the LO power and some times may not be in an optimum pumped state. As illustrated in figure 2.32 the standing wave phase and amplitude can be very different between the 2 polarizations, this is most apparent in the band 5a data shown in figure 2.32(a). From the data in band 5a it is apparent that if the mixer is tuned to an LO frequency of 1145.3 GHz there is matching power between both mixers and hence they would have similar sensitivity and performance. However if the LO frequency was 1145.27, just 30 MHz away a disparity in pump level is seen.

The differences in band 5a pump level are quite minuscule and would have little effect on the final data however in bands 6 and 7 where the HEB mixer is quite sensitive to LO power modulation this disparity in pump level can have a detrimental effect on the data quality of the slave polarization. This effect is discussed in section 4.20. Careful selection of the LO frequency can mitigate the effect of standing waves in the LO path and provide the optimum LO power to both mixers, however again an a priori knowledge of the standing wave phase is needed before this approach can be applied.

Standing waves in the LO signal path have a detrimental effect on frequency switch observations also. A frequency switch observation observes the OFF phase at a different LO frequency as opposed to a position switch observation which observes the OFF position at a different sky position at the same LO frequency as the ON position. Ideally if the mixer pump levels for the ON and OFF positions are the same the data quality is of good. The LO power is set before observation for the 2 LO frequencies of the frequency switch observation. However like a standing observation the LO power is only set for one master polarization and the other polarization is left to follow. This can lead to large differences in pump level between the slave mixer frequency switch ON and OFF spectra which leads to poor data quality. Figure 2.35 shows an example of a the mixer current for a 6b frequency switch observation. For this observation the H mixer is the master polarization and this is apparent in mixer current data. The V mixer shows a large disparity in mixer pump levels between the 2 frequency settings which has a detrimental effect on the resulting data quality. The resulting effects on the data quality are discussed in chapter 3.

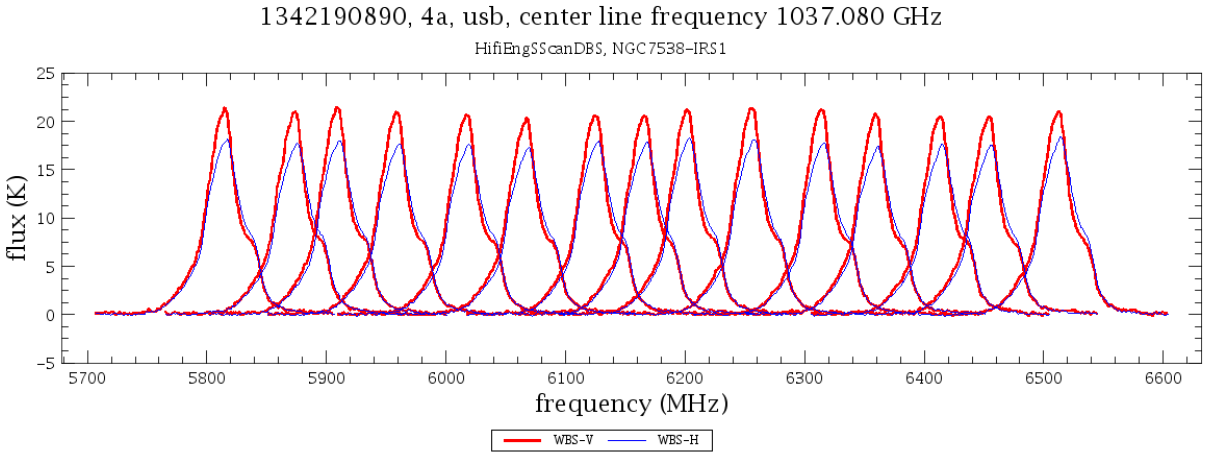

(a) H and V spectral lines at different IF positions

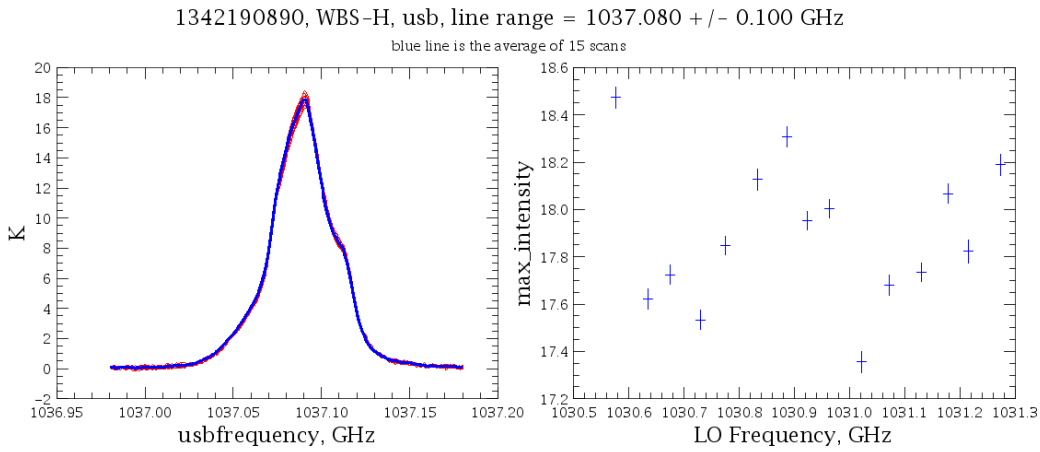

(b) *Left:* H line profiles overlaid, Blue line is the average profile, red line is the individual spectral lines *Right:* Peak line intensity versus LO frequency

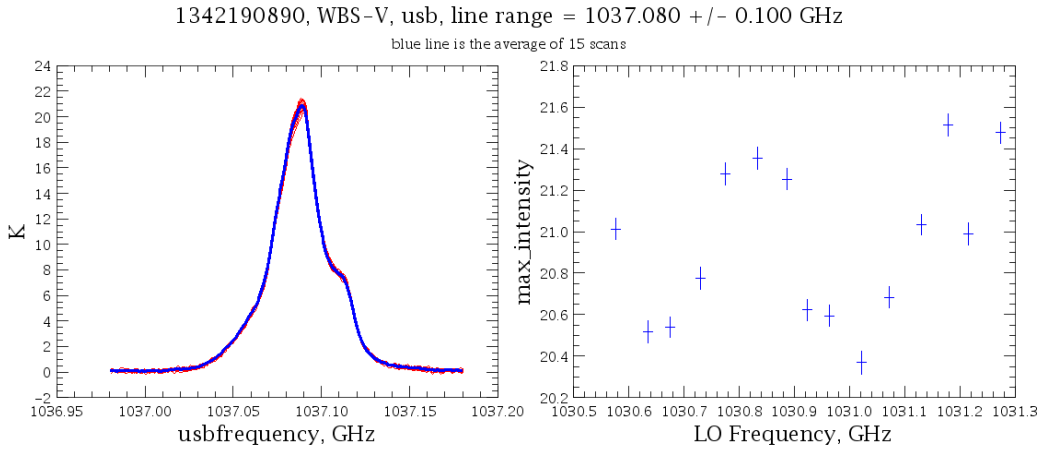

(c) *Left:* V line profiles overlaid, Blue line is the average profile, red line is the individual spectral lines *Right:* Peak line intensity versus LO frequency

Figure 2.34: Example of spectral line modulation due to the diplexer roof top mirror standing wave in band 4a at an LO frequency of 1037.08 GHz.

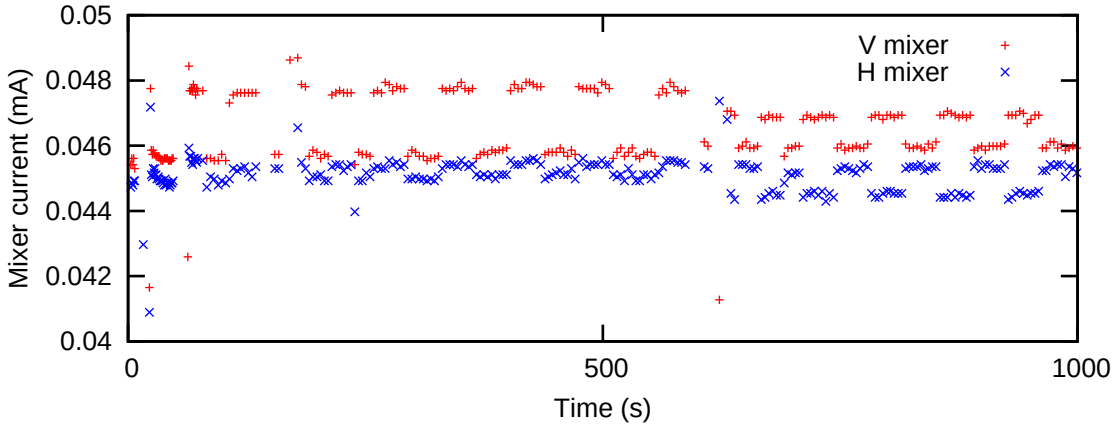

Figure 2.35: Instrument house keeping timeline showing H and V mixer current for a frequecny switch observation in band 6b at an LO frequency of 1666.933 GHz. For this example the H mixer is the master mixer for the LO power setting while the V mixer follows. Note the large disparity in mixer current settings for different LO frequencies.

2.5 Conclusions

In this section the intensity calibration of HIFI and the associated uncertainties were discussed. The antenna calibration and the procedure for determining the main beam efficiency and aperture efficiencies were described.

The intensity calibration of HIFI was described and the sources of uncertainty in the intensity measured were detailed. Side band ratio was discussed as one of the major source of intensity errors in the system. The 2 major sources of side band ratio irregularities, the mixer RF gain and diplexer mistuning, were discussed. The need for a priori knowledge of the side band ratio was mentioned at the end of this chapter. This is discussed in detail in the following chapter on the gas cell test campaign.

Standing waves in HIFI were discussed. The source of standing waves namely the hot and cold loads, diplexer root top and the LO horns, were detailed. It was shown that the standing wave amplitude on the spectrum baseline is dependent on the intensity of the source. Sources with bright continuums such as planets produce strong standing waves on the baseline. More subtle effects were also discussed such as the modulation of spectral line intensity with LO frequency which was shown to account for a 3% uncertianity in the intensity measured in band 4. The effect of standing waves in the LO signal path were also discussed and an example of the effect on the mixer pump levels in band 6 frequecny switch observation was shown.

Chapter 3

HEB Electrical Standing Wave

3.1 Introduction

At an early stage in the instrument level testing (ILT) of HIFI the HEB bands were seen to have poor baseline performance with high noise towards higher IF frequencies and large standing wave effects present. This degradation was eventually attributed to LO instability and an impedance mismatch between the mixer and the first low noise amplifier (LNA). This chapter discusses the source of this baseline degradation, the efforts made to model it and the final solution to be incorporated into the HIFI data processing pipeline.

As discussed in section 2.4, standing waves are a common effect in sub-mm instruments given that the radiation wavelength is comparable to the receiver optical component dimensions. The dominant standing wave seen in the HEB band however is not due to reflections within the instrument optics but due to reflections in the instrument electrical amplification chain (IF chain). Careful design of Herschel and HIFI optics in combination with optimized observation routines have reduced the impact of standing waves in the HIFI optics on the final calibrated data. Sources with high intensity are sensitive to standing wave effects but for the most part the effect of standing waves from the optics can be removed during the cross calibration and there occurrence and behaviour is mostly predictable.

The standing wave originating in the IF chain has a very different behaviour and its occurrence is less predictable. The appearance of the standing wave in the HEB is a function of the mixer state, LO thermal condition, which can't be predicted in advance. The HEB standing wave is the most destructive systematic effects seen in HIFI data with amplitudes of up to 20 Kelvin. The higher frequency HEB bands account for 33% of the observing time of the guaranteed time key programs[82] and operate at a frequency range that is almost completely opaque for ground based telescopes. Understanding and correction of this baseline effect is a crucial step in returning the maximum possible science from this unique observing opportunity.

There are five sections in this chapter. The first section is the introduction. The second section describes the development time line of the HEB mixer technologies for HIFI, some

of the problems encountered and their subsequent effect on the intermediate frequency (IF) amplification chain design. The third section details the behaviour of the standing waves seen in the spectra due to the impedance mismatch between the mixer and first LNA. The fourth section section describes the efforts to remove the standing wave from the data. 2 different approaches are described. The first approach starts from the device physics and develops an analytical model of the distorted baseline profile based on the HEB mixer and LNA impedance. This method is based on the HEB mixer impedance work of Jacob Kooi. A second approach is also presented. This approach, developed by author, uses a catalog of standing wave waves to correct the observed spectra. This approach is applied to gas cell data and 2 flight observations. The final section presents the chapter conclusions.

3.1.1 Author's contribution

The author was extensively involved since 2007 with the HEB standing wave working group. The author carried out analysis on the standing wave behaviour and established some of the key properties of the standing wave such as LO frequency independence and fixed phase. The author worked closely with Jacob Kooi (Caltech) in adapting his electrical model data to match gas cell observations. The baseline catalog solution was developed by the author and further improved by Kirill Tchernyshyov (Oberlin college).

3.2 HEB mixer development

3.2.1 Introduction

From the outset of HIFI development the instrument performance goals were unprecedented for a heterodyne instrument. Table 3.1 details the sensitivity goals and mixer technologies considered for the 7 HIFI bands. The sensitivity goals laid down in 1998 were largely met in the SIS bands. However in hindsight the HEB band targets were very ambitious and even by today's standards (Zhang et al. [131] achieved a DSB noise temperature of 900K) the HEB technology goals set in 1998 are beyond the current state of the art.

In the original HIFI design a third LO band was planned which would have covered a frequency range from 2.4 to 2.7THz. This band was eventually scrapped due to development issues with the gas laser LO source. HIFI optics were designed with 7 LO paths with each path being coupled to 2 LO units, which split the LO coverage. For example band 1a and band 1b describe 2 different LO chains. To reduce the impact on the optics design the 6L band frequency coverage was split into 2 bands with the 6L band providing LO frequency coverage for the lower end of the band, 1410–1703 GHz, and 6H for the upper end of the band 1703–1902GHz. Band 6L and 6H were later renamed bands 6 and 7.

When SIS mixers were proposed for bands 1–5 in 1998, they were already established as a

Table 3.1: Comparison of HIFI frequency ranges and mixer technologies as proposed in 1998[21] and the final flight configuration[23], SOAP stands for the State–Of–the–Art Performance as of 1998

Band	Range,	DSB Noise temperature, K			Mixer element technology			Antenna
	GHz	SOAP	Goal	Flight	SOAP	Goal	Flight	Type
1	480	80	70	74	Nb-SIS	Nb-SIS	Nb-SIS	WG
	680	130	110	85				
2	640	130	110	143	Nb-SIS	NbTiN-SIS	NbTiN-SIS	WG
	800	500	130	195				
3	800	500	130	230	Nb-SIS	NbTiN-SIS	NbTiN-SIS	WG
	960	700	160	233				
4	960	700	160	360	Nb-SIS	NbTiN-SIS	NbTiN-SIS	WG
	1120	1600	190	345				
5	1120	1600	190	988	Nb-SIS	NbTiN-SIS	NbTiN-SIS	WG
	1250	1900	210	1234				
6L	1410	2100	300	1555	Nb-HEB[a]	Al-HEB[a]	NbN-HEB[b]	QO
	1910	2100	300	1386				
6H[c]	2400	2500	450	N/A	Nb-HEB[a]	Al-HEB[a]	N/A	QO
	2700	2500	450	N/A				

[a] diffusion cooled
[b] phonon cooled
[c] The highest frequency band 6H with an LO frequency coverage from 2.4 - 2.7 THz was descoped in the final HIFI design.

key technology of sub-millimeter spectroscopy and had been used extensively in ground based telescopes[132]. Table 3.1 is a reflection of this maturity as the superconductor material and noise goals proposed in 1998 were largely met in the final HIFI configuration.

SIS mixer frequency coverage is limited by the energy gap of the superconducting material. Above this frequency the absorption loss in the superconducting material increases dramatically; for an all-Nb mixer the limit is 1.4THz, for NbTiN-Nb or NbN-Nb junctions operation above 1.6THz should be possible [132]. HEB mixers were seen as the only option for mixing above 1.25THz. Schottky diodes provide a mixing alternative above 1THz but require large amounts of LO power and have lower sensitivities when compared to HEB mixers.

3.2.2 HEB operation

HEB mixer technologies were still at a development stage when first proposed for HIFI. The concept of HEB mixing was first proposed in the 1970's [93] however it was superseded by the SIS mixer for ground based spectroscopy. The development of the HEB mixer gathered pace in the early 90's once the frequency limits of SIS mixer technology became apparent. One of the drawbacks of HEB mixers when first used in the 1970's was the small bandwidth of 100's of MHz. Hence early efforts in HEB development focused on increasing the IF bandwidth.

A mixer's IF bandwidth is defined as the IF frequency where the mixer gain drops 3dB from the gain at 0 IF frequency:

$$G(f_{if}) = \frac{G(0)}{1 + (f_{IF}/f_{3dB})^2}. \tag{3.1}$$

The -3 dB IF bandwidth is a function of the bolometric time constant, τ_{th}, or the time it takes heat to dissipate through the mixer

$$f_{3dB} = 1/(2\pi\tau_{th}) \tag{3.2}$$

Hence decreasing the time it takes for the mixer to cool will increase the IF bandwidth. A model of cooling mechanisms in superconducting films was proposed by Perrin, N. & Vanneste, C. [92] and was further expanded upon by Semenov et al. [110] and applied to NbN films. This model proposes that cooling in a superconducting HEB mixer occurs via 2 mechanisms, the electron phonon interaction and the phonon lattice interaction. The electron phonon interaction describes the transfer of energy from the Cooper pair fluid generated during the superconducting state and the superconducting material phonons. The phonon lattice interaction describes the phonon interaction with the material lattice on which the superconductor is mounted.

The electron phonon interaction time, τ_{e-ph}, is a function of the superconducting material and is dependent on the superconducting critical temperature, T_c, see figure 3.1. The phonon lattice interaction time, τ_{esc}, is a function of the HEB geometry and the direction of heat transfer depends on the length and thickness of the superconducting surface. Short HEB mixers with lengths typically less than 100nm and thicknesses ~10nm transfer heat through the metal

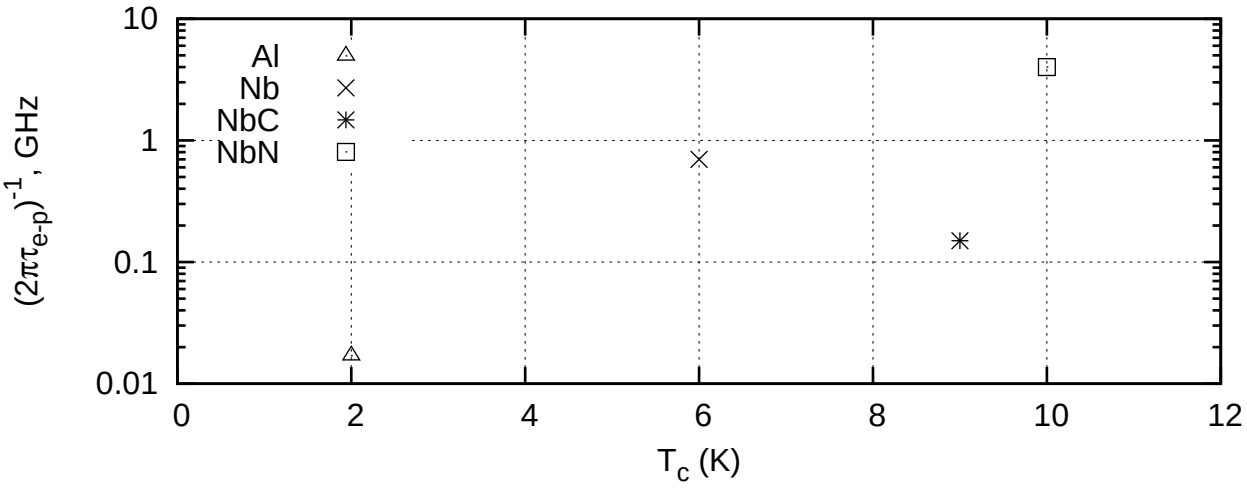

Figure 3.1: Typical values of the electron-phonon relaxation times for various superconducting materials used for HEBs [53].

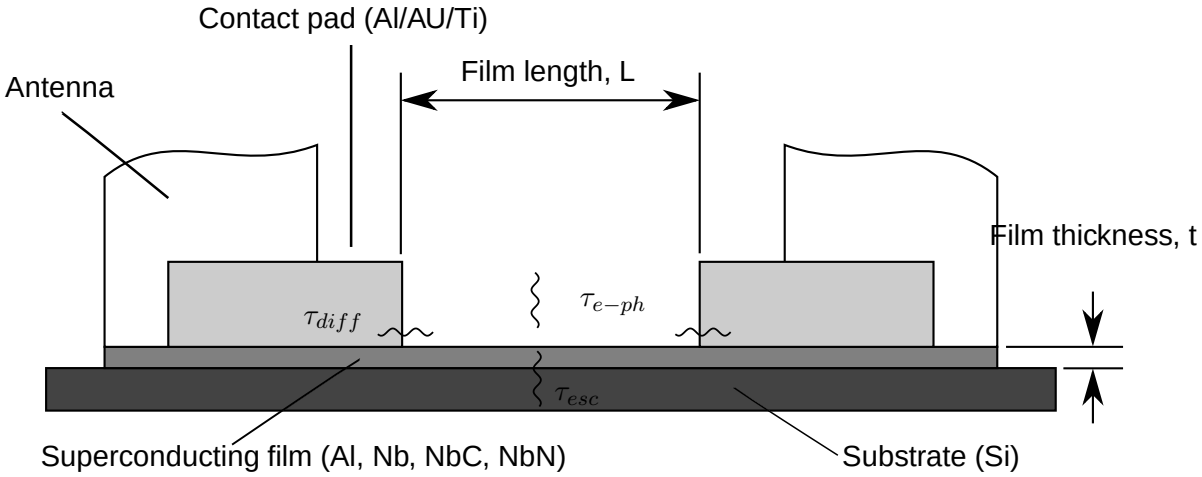

Figure 3.2: HEB mixer schematic showing the important dimensions determining the dominant HEB cooling mechanisms[62]

contacts on either side of the mixing surface, these are typical known as diffusion cooled HEBs. Thin HEB mixers with a thickness of less than 6nm transfer heat through the superconductor surface into the substrate the superconductor is adhered to, this type of HEB is called a phonon cooled HEB. See figure 3.2 for an overview of the key HEB mixer components and dimensions.

While both phonon and diffusion cooling is present in all HEB types the HEB geometry determines which mechanism is dominant. Karasik et al. [54] investigated the transition from phonon cooling to diffusion cooling for 20nm thick NbC films of variable lengths between 1.0 and 100.0 μm. Early attempts at HEB development concentrated on the thin film phonon cooled variation [84], however, the IF bandwidth limitations soon became apparent and the diffusion cooled version originally proposed by Prober [101] soon became the dominant HEB type.

At the time of HIFI development diffusion cooled HEBs were the only technology capable

of meeting the IF bandwidth, LO power and noise requirements for HIFI. When HIFI was proposed in 1998 the required LO power above 1 THz was difficult to achieve and the mixer design was constrained by this limitation. Diffusion cooled HEBs could be pumped by the LO power available. Burke [11] showed that for a diffusion cooled HEB the LO power required was given by the following expression:

$$P_{LO} = 4\mathfrak{L}(T_c^2 - T^2)/R, \tag{3.3}$$

where $\mathfrak{L}$ is the Lorenz constant [1], T is the bath temperature of the substrate on which the device is mounted, T_c is the superconductor critical temperature and R is the device resistance. From this equation it is apparent that the lower the material T_c is the lower the LO power requirement. Burke et al. [12] demonstrated that a short enough diffusion cooled HEBs could achieve large IF bandwidths. They showed that for the diffusion cooled mixer thermal relaxation time, τ_{th}, is a function of the mixer length, L, and superconductor material diffusion constant, D:

$$\tau_{th} = \tau_{diff} = L^2/(\pi^2 D). \tag{3.4}$$

They demonstrated that with a 10nm thick 80nm long Nb film IF bandwidths of >6GHz were possible. Furthermore Karasik et al. [53] compared various superconducting materials and showed that aluminum as a superconductor had the optimum diffusion properties for a practical mixer size and that single side band noise temperatures of 500K were achievable.

3.2.3 HIFI HEB mixer

Returning to table 3.1, based on the state of research at the time the HEB mixer technology goal was for a diffusion cooled Al HEB while a diffusion cooled Nb HEB was seen as the baseline. JPL were tasked with developing the diffusion cooled HEB into a working mixer unit which could be incorporated into the HIFI instrument. They developed a Al and Nb diffusion mixer in parallel. Unfortunately, a number of limitations to Al HEB mixer were discovered.

Siddiqi et al. [112] tested a batch of 14 different Al mixers with lengths varying from 0.2 to 1μ m. They found a lower limit to the superconducting film length due to the proximity of the normal resistive metal contact pads and the superconducting HEB film. This proximity either reduced the size of the superconducting region on the film or in the case of the 0.2μm film sample no superconduction occurred at all. This proximity effect provides a lower limit to the minimum super conducting film length and hence the maximum IF bandwidth possible. The maximum bandwidth for an Al mixer is still sufficient for most practical applications, however it does provide an upper limit to the relationship between τ_{diff} and film length published by

[1] The Wiedemann–Franz–Lorenz law states that the ratio of the electronic contribution to the thermal conductivity (k) and the electrical conductivity (σ) of a metal is proportional to the temperature (T) such that $\frac{k}{\sigma} = \mathfrak{L}T$ where $\mathfrak{L}$ is the Lorenz constant with units $\mathrm{W}\Omega K^{-2}$

Burke [11] and described in equation 3.4.

The most detrimental effect to Al HEB performance is from noise power saturation. Siddiqi et al. [112] showed that at microwave frequencies good noise and efficiency performance was possible through careful experimental setup to suppress background noise. However at THz frequencies the same performance wasn't possible given the larger antenna bandwidths and thermal noise present. Siddiqi et al concluded that noise saturation at THz frequencies was a major source of performance degradation. They described 2 types of saturation, input and output saturation.

Input saturation occurs when the background noise power is comparable with the LO signal power. The LO signal power is used in conjunction with the mixer bias to bring the mixer to its optimum performance. Siddiqi & Prober [111] showed that for moderate background temperatures the background noise power can be comparable with the LO power and pump the mixer to a state of non-optimum performance (low conversion efficiency, high noise temperatures). As an example, a background temperature, T_{bkgnd}, of 25K and a mixer RF bandwidth, B, of 500GHz (6L band as proposed in 1998) from the noise temperature equation $P = kTB$ results in a background noise power of 0.2nW. Siddiqi found the optimum LO power for Al HEB mixing to be $\sim$ 0.5nW. Output saturation occurs when the background noise is down converted into the IF band. Siddiqi et al. [112] showed that for a typical mixer set up the background noise can shift the mixer bias voltage up to 20 μV. This was shown to have a negative effect on the mixer performance as its range of optimum performance is over a small bias voltage region of ΔV_{opt} <10μV.

Increasing the mixer volume would have reduced the Al HEB's sensitivity to background noise however this would have reduced the mixer IF bandwidth. As HIFI was under a strict time schedule for component delivery, efforts to develop the diffusion cooled Al HEB mixer were abandoned and JPL concentrated on the Nb diffusion cooled mixer. Early results for the Nb mixers were promising but due to their small size they again suffered from saturation issues and never fully achieved the noise requirements outlined in table 3.1. Furthermore the Nb mixer suffered from a degradation of performance that was attributed to both environmental conditions and electrostatic discharge[57]. Fortunately in parallel to the diffusion cooled HEB research phonon cooled HEBs were also being developed.

In 1998, phonon cooled HEBs were not able to meet the IF bandwidth and LO power requirements of HIFI. However in the following 5 years phonon cooled HEB's became a viable alternative to the diffusion cooled variety. The development of 100's μW solid state compact LO sources above 1THz opened the door for space applicable phonon cooled mixers [75, 76]. The problem of IF band width was also overcome. Using reactive magnetron sputtering manufacturing techniques it was possible to consistently produce superconducting films with thicknesses between 3-6nm thereby decreasing the phonon to substrate time and therefore increasing the mixer IF bandwidth[129]. Ekström et al. [29] demonstrated IF bandwidths for an NbN film phonon cooled HEB up to 5GHz. From an early stage in phonon cooled HEB development

NbN has been the superconducting material due to to low electron phonon interaction time, τ_{e-p}, see figure 3.1.

Unfortunately the development of the HEB phonon cooled mixer was also problematic. While mixer IF bandwidths of up to 5GHz had been demonstrated previously the HIFI mixer batch was unable to meet the 4GHz HIFI design requirement. Due to the schedule restrictions of a space mission and the late change from a diffusion to a phonon cooled mixer, the project had no choice but to proceed with the manufactured film and settle for an IF bandwidth of 2.4–4.8 GHz. This had a number of knock-on effects for the instrument, the most significant being a redesign of the IF chain[124].

In the original HIFI design the IF chain design was common for all bands. However with the IF bandwidth change a new first and second LNA had to be developed to suit the reduced IF bandwidth[49, 74]. Furthermore, a 10.4GHz local oscillator was incorporated into the IF chain to up-convert the 2.4–4.8GHz IF signal to a spectrometer compatible IF bandwidth of 5.6–8GHz. The most significant effect of the the IF chain redesign was the exclusion of an electrical isolator between the HEB mixer and first amplifier. At the time of the redesign no space qualified 2.4 – 4.8GHz isolators were available. Additionally since the HIFI mechanical design was already at an advanced stage there was no space in the IF chain enclosure for a 2.4–4.8GHz isolator. Electrical isolators are designed for a specific IF frequency range[74] and their size scales inversely with frequency range, a lower IF frequency would have required a larger volume electrical isolator. The final IF chain design is shown in figure 3.3.

With the exclusion of the electrical isolator after the mixer unit the HEB band became susceptible to increased noise and broadband gain ripples. The component level testing of the mixer unit at Chalmers university was undertaken with an LNA with a reflection loss of more than 15dB [16], which demonstrated that the mixer performance was within the noise and standing wave amplitude limits. The flight LNA has a measured reflection loss of -10dB [74]. When the mixer unit was incorporated into the flight IF chain large peaks in the noise were seen as well as a significant ripple across the IF band consistent with power reflection between the mixer and first amplifier. On further investigation a large impedance difference was evident between the mixer and the LNA. A redesign of the mixer block resulted in a better IF match to the LNA and while the performance of the mixer was seen to improve, the IF ripple problem persisted[5].

The next section in this chapter will describe how the combination of instrument stability and the IF ripple affect the final calibrated data quality.

3.3 HEB standing wave behaviour

Standing waves are seen in all HIFI bands. The type discussed in this chapter occur due to reflections in the IF chain. The more common variety are those due to reflections between components in the instrument's optical path. Both types have a similar effect on the data

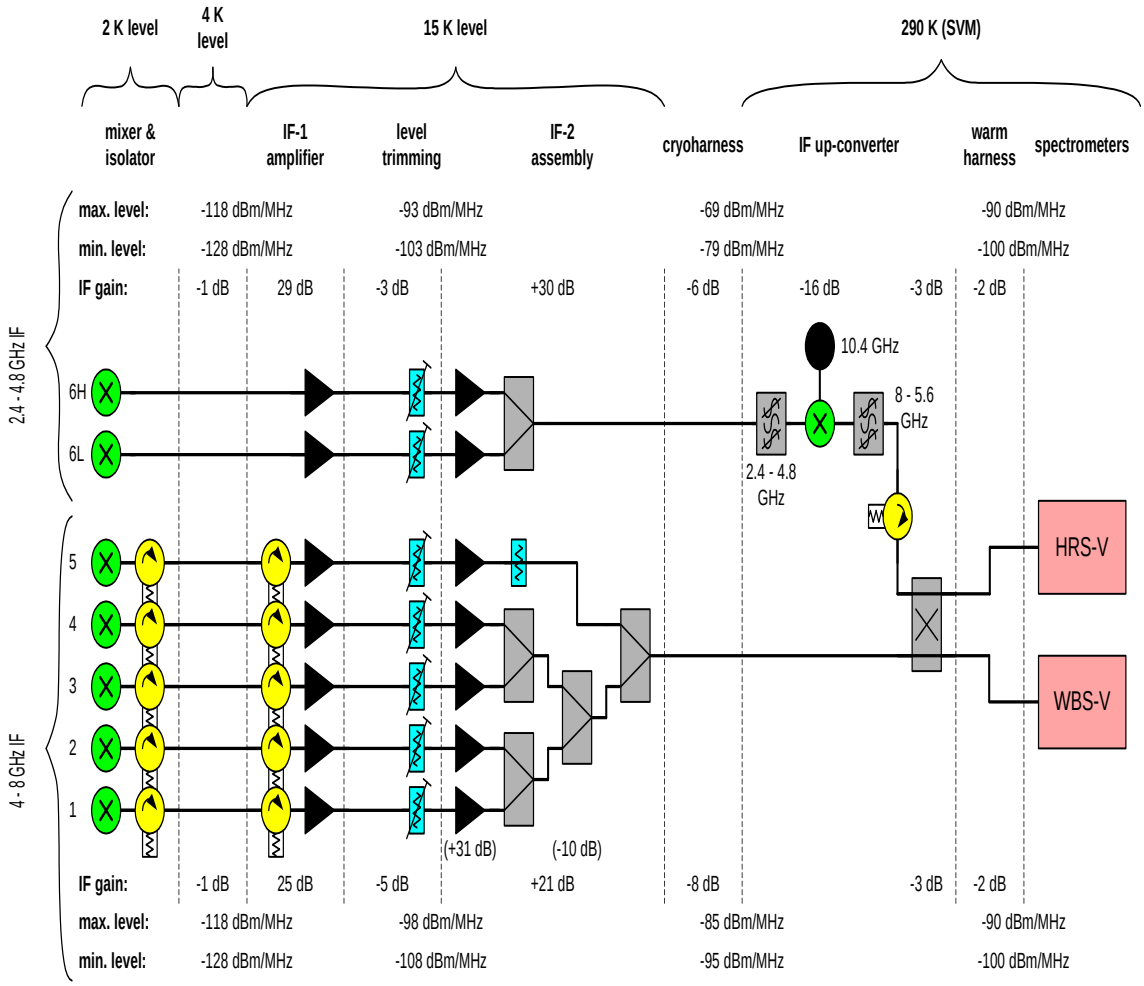

Figure 3.3: Block diagram of the HIFI IF chain showing all components between the mixer and backend spectrometers for the V polarization[23].

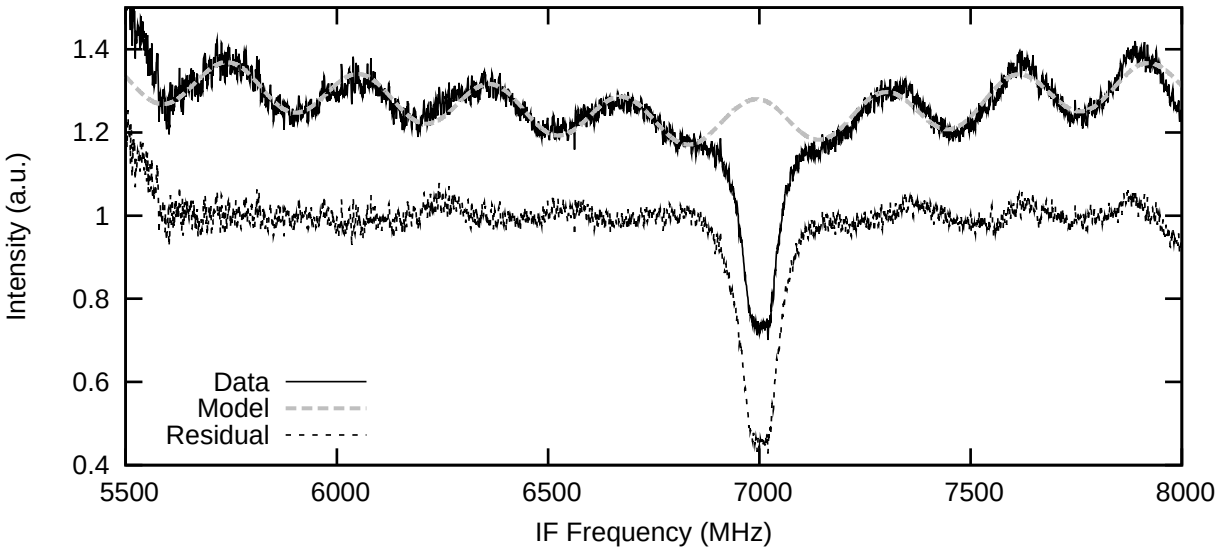

Figure 3.4: Plot of ^{12}CO gas cell WBS-V data for band 7a at an LO frequency of 1730.00475GHz. For an ideal observation the line minimum should have a value of 0.5 and the spectra baseline should have a mean value of 1.0. An approximate sine wave fit with a polynomial baseline fit is overlaid. This fit was generated using the fringe removal tool available in the HCSS environmental [59]. The residual minus the Sine model and polynomial baseline + 1.0 is also plotted.

quality however their behaviour is quiet different and in order to efficiently remove them from the calibrated data these differences should be appreciated.

The author was tasked with examining the HEB standing wave in the gas cell data in 2007. In this section the results of this exploratory work are outlined.

3.3.1 Standing wave profile

On first impressions the IF ripple is very much like a normal standing wave. However, when standard standing wave removal tools are used it becomes difficult to remove the standing wave and multiple iterations of sine fitting are needed before the ripple is sufficiently, if at all, removed. An example of a standing wave wave fit using the fit fringe tool developed by Kester et al. [59] is shown in figure 3.4.

Using the fit fringe routine it is possible to fit the IF ripple over a 0.5GHz band however outside of this region the fitted period and amplitude are no longer sufficient. From figure 3.4 it is apparent that the sine fit is adequate for the IF region from 5.6 to 6.1GHz but is slightly out for phase and has a lower amplitude than that of the data.

The IF ripple profile has a saw tooth shape which is difficult to fit with a simple sine wave profile. The model approach described by Kester et al. [59] however provides a good first order correction of data affected by standing waves originating in the instrument optics. The difference between the optical standing waves and the IF chain standing waves is the source of reflection. Optical components have smooth transmission properties over the mixer bandwidth.

An electrical component's transmission (electrical impedance) can vary significantly in a non-linear fashion across the IF bandwidth leading to the complicated profiles shown in figures 3.4 and 3.7(c).

3.3.2 Effect of changing LO frequency

Optical standing waves occur before the signal mixing in the optical path. The standing wave is a modulation of the sky signal due to some fraction of the signal being reflected between 2 components in the signal path. The reflected and incoming sky signal interfere at the mixer resulting in a broadband modulation of the signal detected. During the mixing process 2 bands of the sky signal are then down converted to IF frequencies. The signals from the upper and lower side-bands are summed together in the process. The 2 standing waves from the upper and lower side-band interfere and depending on the phase difference this interference can be constructive or destructive. The resulting double side-band standing wave amplitude and phase is then dependent on the relative phase between the upper and lower side band standing wave which is a function of the LO frequency. Figure 3.5(a) shows an example of the constructive and destructive interference of the upper and lower side band changing LO frequency.

Standing waves in the IF chain occur after mixing. The resulting double side band standing wave profile is then a function of the cavity length (coaxial cable length) and the reflection properties of the 2 reflecting components (mixer and LNA) and independent of LO frequency. From figure 3.5(b) one can see that the phase of the standing wave is fixed with changing LO frequency unlike the optical standing wave example in figure 3.5(a).

3.3.3 Instrument stability

Calibration measurements of an internal load or an OFF position are a common step in an astronomical observation sequence. HIFI has a number of different observation modes of varying complexity however at the core of all modes are 4 phases which when combined together form an intensity calibrated spectrum:

$$\frac{ON - OFF}{HOT - COLD} \tag{3.5}$$

In an ideal setup all systematic effects are removed from the spectra and only the intensity calibrated astronomical information is left. However, if differences exist between the 4 phases of the observation the final spectra quality will be degraded. Differences between spectra can be due to a number of factors.

The IF ripple seen in calibrated HEB spectra is due to differences in mixer impedance between the observation phases. As described in section 3.2, the IF ripple seen in the HEB bands is due to an impedance mismatch between the mixer and first LNA. The amplitude of the IF ripple is related to the degree of impedance mismatch between the mixer and LNA which is a function of the incident LO power. The LNA is the most stable component of the

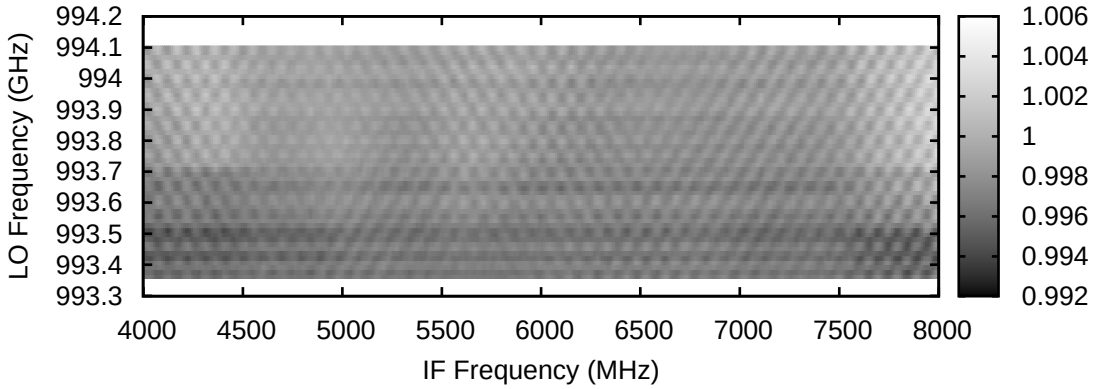

(a) Example of SIS baseline behaviour with 98MHz standing wave from reflections between the mixer and the cold internal. The checkered pattern of the data illustrates the changing phase with LO frequency typical of a standing wave in the optical path

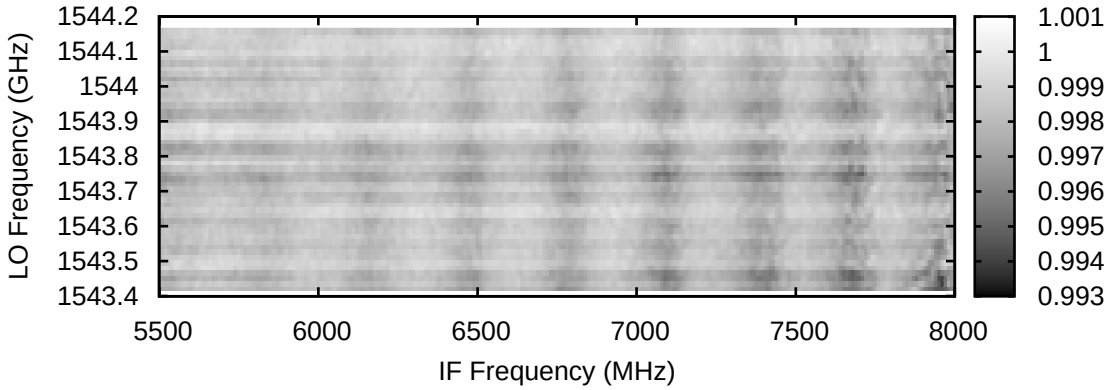

(b) Example of HEB baseline behaviour with 320 MHz IF standing wave from reflections between the mixer and the first low noise amplifier. The phase of the standing wave is the same for all LO frequencies indicating this is not an optical path standing wave.

Figure 3.5: An example of the different behaviour of a standing wave in the instrument optics and a standing wave in the IF chain. The data shown here is taken a standing wave test and is not representative of the amplitude seen in calibrated data. The serves to illustrate the fixed phase of the IF chain standing wave compared to the changing phase of the optical standing wave with changing LO frequency.

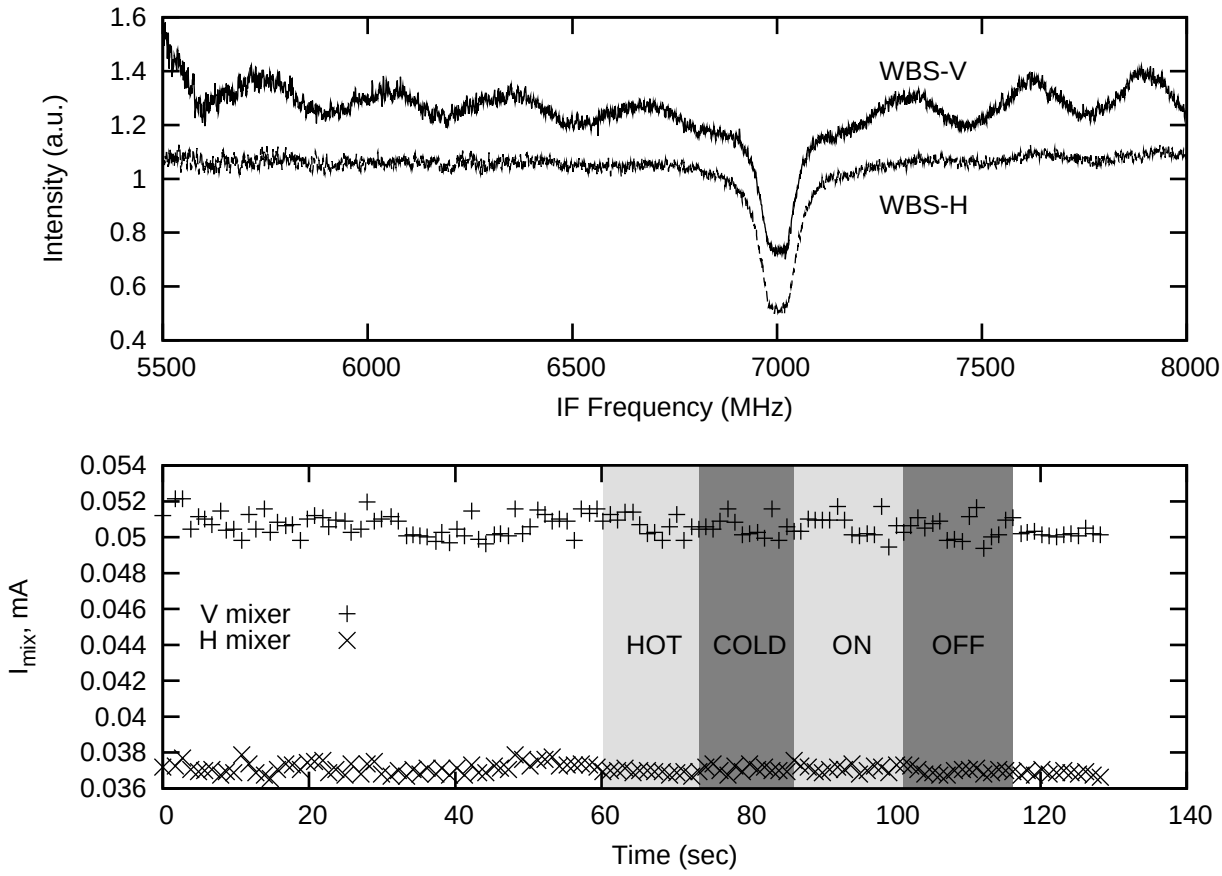

Figure 3.6: Calibrated ^{12}CO gas cell data at an LO frequency of 1730.01GHz showing both polarizations. Lower panel shows the associated mixer current for H and V mixer units. The V and H polarizations both show evidence of the IF standing wave with the V polarization being most effected. From the mixer current data it is apparent that there is a larger scatter for the V mixer (3.5% of mean mixer current) compared to the H mixer (1.5%).

pair as this is kept at a fixed voltage. However given the superconducting nature of the HEB mixer its impedance can be highly variable and dependent on a number of external influences. An integral part of HEB mixer operation is the pumping of the mixer by the LO chain. The HEB mixer impedance is driven by 2 components the mixer bias voltage and the LO power[64]. Variations in the LO power change the mixer pump level which in turn changes the mixer impedance and therefore the IF ripple amplitude. The HEB mixer impedance can also be sensitive to the temperature of the sky source be it the *HOT* or *COLD*. This effect is known as direct detection[3].

Figure 3.6 shows a comparison of baseline quality for the H & V polarizations taken at the same time. The V polarization was already presented in figure 3.4. From this figure one can see that the H polarization baseline quality is considerable better than the V polarization. The corresponding mixer current for each mixer is also plotted in the lower panel of figure 3.6. It is apparent that there is a larger degree of scatter/instability in the V mixer current than in the H mixer current.

Kooi et al. [63] investigated the various sources of instability in NbN phonon cooled HEB receivers. They looked at receiver stability from 2 perspectives, the inherent HEB mixer stability and the stability of the receiver set up as whole. They measured the stability using double difference Allan variance method commonly used to measure radio receiver stability[108]. The instrument setup used in their investigation was very similar to that used in the (instrument level testing) ILT setup and so their conclusions are directly applicable to the data presented here. They found that the sensitivity of the mixer to system instabilities varied depending on the pumped state of the mixer. This may explain the disparity in mixer current scatter between the V and H data presented in figure 3.6. It is apparent from the figure that the V mixer is pumped to a higher mixer current than the H mixer. HIFI HEB mixers have an optimum mixer current of 0.045mA. Above 0.045mA the mixer is tending towards a less stable fully superconducting state away from the transition state where the conversion efficiency is optimum. Below 0.045mA the mixer tends towards a normal resistive state and is less sensitive to LO power fluctuations and hence more stable however it also becomes less effective as a mixer.

Ideally both mixer currents should be around 0.045mA. Each mixer is coupled to the same LO source and the signal is polarized and directed to each mixer via a polarizing grid. Ideally the same LO power should couple at the H and V mixer focus but due to standing waves and other coupling effects one mixer receives more LO power than the other. Furthermore, the H and V mixer units are not identical and have different performance over the LO band due to differences in the manufacturing of the antenna and mixer. As a result of these differences, the LO power is set to optimally pump one mixer while the other mixer is left to follow. This leads to a situation like that shown in figure 3.6 where one mixer is optimally pumped while the other is left to follow, resulting in a disparity in baseline quality between the 2 polarizations.

The experimental setup used by Kooi et al. [63] was similar to the HIFI ILT setup. The LO unit was housed in a separate cyrostat to HIFI and the LO signal was transmitted through open air via 2 cryostat windows. Since the LO signal traversed air at sea level atmospheric conditions the power transmitted was modulated with the air turbulence in the room with noticeable degradation seen close to the water line frequencies.

In a stable mechanical environment standing waves in the LO path aren't particularly problematic but if the system isn't sufficiently mechanically stable and the optical path deviates over the course of the observation this will change the mixer pump level resulting in degraded baseline quality. Kooi et al. [63] showed that if the LO frequency is tuned to the peak of the standing wave this can reduce the receiver sensitivity to optical path changes. Unfortunately HIFI had multiple LO standing waves in the ILT setup making it difficult to find an optimum LO frequency. LO path mechanical stability was a significant problem during HIFI ground testing. Fortunately, one of the advantages of space is the thermal stability. Furthermore the Herschel telescope has few moving parts which can induce vibration in the system resulting in a stable operating environment.

The major source of instability is the LO unit itself. The LO chain is a complex unit which generates the local THz signal using various stages of frequency multiplication. As a byproduct of the signal multiplication heat is generated which in turn effects the LO chain performance and output power. When a chain is switched on initially a wait time of up to 1 hour is required before the power output stabilizes[65], figure 3.7(a) shows an example of a drift mixer current due to this effect.

3.3.4 Mixer current and standing wave amplitude

From the previous section it is apparent that changes in the mixer impedance as measured through the mixer current during the course of an observation result in a non optimum subtraction of the IF ripple between the mixer and LNA. The sources of these impedance changes were summarized in the previous section. In this section the relationship between the relative mixer current difference between observation phases and the resulting standing wave is detailed.

Figure 3.7 details the relationship between the percentage mixer current difference between 2 observation phases and the subsequent standing wave amplitude. The data is taken from a stability test taken during an LO chain warm up and since the LO has not completely settled the mixer current is seen to drift over the course of the observation, see figure 3.7(a).

This dataset is useful to gauge the impact of mixer current differences between observation phases on the resulting baseline standing amplitude. By dividing spectra at different mixer currents by each other, recording their mixer current difference and then measuring the resulting standing wave amplitude it's possible to measure the relationship between the standing wave amplitude and the mixer current difference between 2 phases. Figure 3.7(b) shows the percentage mixer current difference between 2 observation phases and the resulting standing wave amplitude. From this one can see there is a linear relationship between the mixer current difference and the resulting standing wave amplitude, such that a 10% change in mixer current results in a 1% amplitude standing wave.

Figure 3.7(c) shows some examples of the effect of mixer current difference between observation phases on the resulting baseline. From this figure one can see that not only is there is significant standing wave with increasing mixer current difference but also a significant baseline slope across the IF, with the effect most pronounced at the higher side of the IF band around 8 GHz. Note that the IF band plotted here is after the 10.4 GHz up converter (see figure 3.3) so the higher IF band here is in fact the lower side of the 2.4 to 4.8GHz IF band. This is consistent with other tests which show the HEB mixer has greater sensitivity in the lower region of the IF band. From figure 3.7(c) we can see that the baseline is more sensitive to changes in the impedance at these lower IF frequencies.

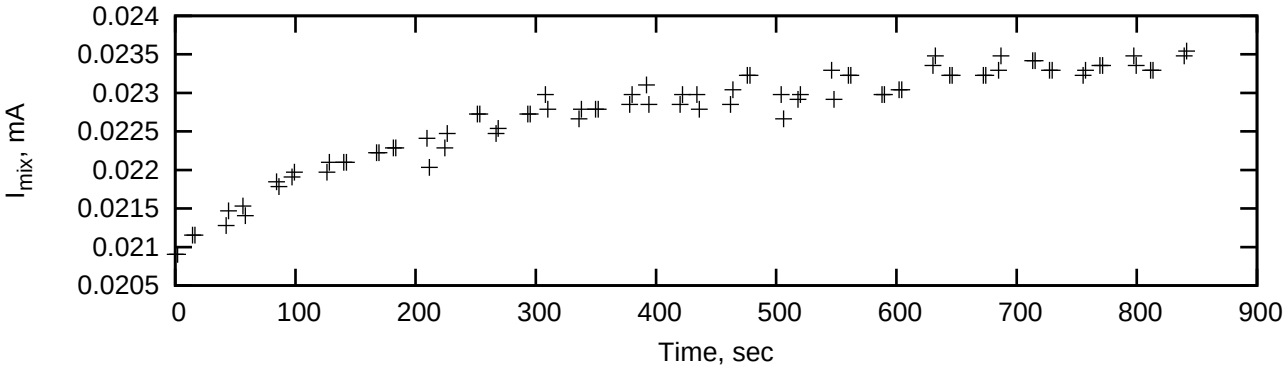

(a) Mixer current versus time during LO warm up

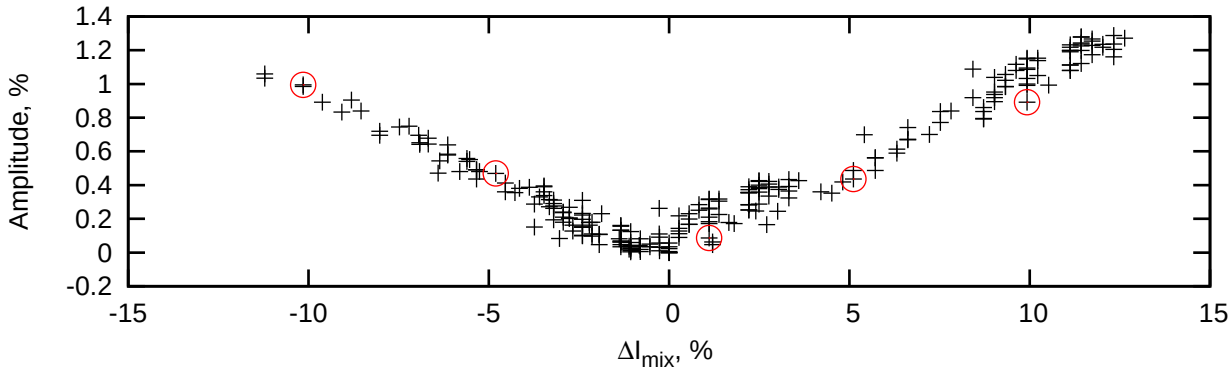

(b) Standing wave amplitude versus mixer current difference between 2 observation phases. ΔI_{mix} is defined as $\frac{I_{on}-I_{off}}{I_{off}}$, where I_{on} and I_{off} correspond to mixer current for the ON and OFF phases. The corresponding baseline for data points highlighted with a circle are plotted below.

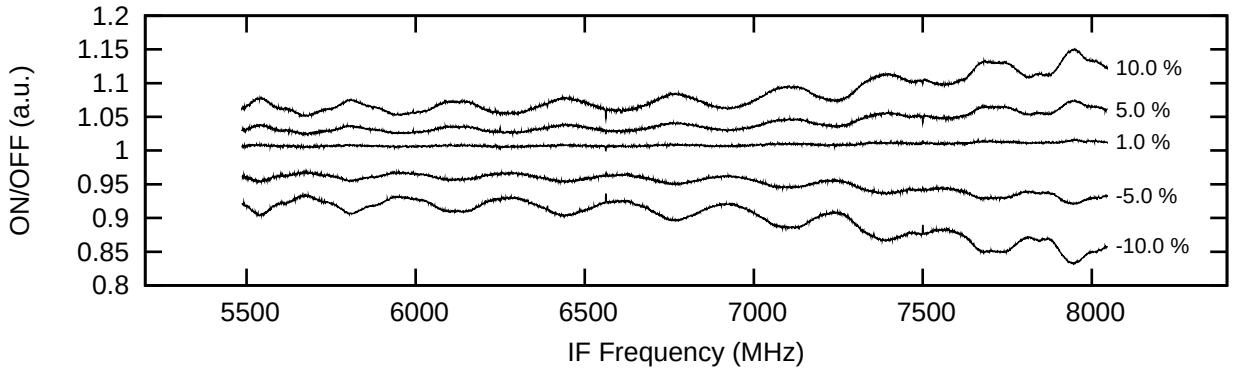

(c) Standing wave profiles for different percentage mixer current differences.

Figure 3.7: Figure showing relationship between standing wave amplitude and the mixer current difference between observation phases. The data presented here is from a stability test taken during the warm up phase of the LO band switch on in band 6a at an LO frequency of 1559.466 GHz. Data from V polar mixer unit is shown here.

3.4 HEB standing wave removal

While the physics of the HEB standing wave is a useful probe of the HEB mixer operation the main motivation for HIFI is to collect high quality data from which an astronomer can extract useful information about the cold universe. It is the role of the calibration scientist using their detailed insights of the instrument operation to provide this data. The HIFI calibration community were aware of the standing wave problem in bands 6 and 7 in early 2007 however at that stage the HIFI IF chain design was fixed and no hardware solution was possible. The solution to the HEB standing wave problem would have to be in the data processing pipeline post observation. Various methods were proposed from using variations of sine waves (as shown in figure 3.4) to wavelet analysis. In this section the 2 most efficient methods are presented.

3.4.1 Electrical model approach

One of the methods investigated as a method for standing wave removal was based on an electrical model of the IF chain. The 3 components considered in the model were the mixer unit, the LNA and the coaxial cable linking the 2 component. It was hoped that a model could be generated of the IF chain which could reproduce the standing wave profile seen in the data and this approach could then be used to correct the data.

The LNA transmission and reflection properties (impedance) were measured as part of an acceptance test and coaxial cable properties were also known. The mixer unit impedance was split into 2 components, those of the mixer unit support structure such as wiring and ports and the mixer device itself. After the redesign of the mixer unit to improve the impedance match a detailed electrical model of the support structure was available. Unfortunately, the impedance of the HEB mixer itself is still the topic of research which was discussed by Kooi et al. [64].

Building on the 2 temperature thin film cooling model of Perrin, N. & Vanneste, C. [92], Nebosis et al. [83] used a heat balance approach to model the temperature dependent impedance of a HEB mixer. Kooi et al. [64] showed that the impedance model proposed by Nebosis et al. [83] was consistent with the measured impedance. This model was dependent on the relaxation times, τ_{e-ph} and τ_{esc} (see figure 3.2), the heat capacities of the electron, c_e, and phonons, c_p, and the quasi particle temperature, T_e.

As discussed earlier τ_{e-ph} is a function of the superconducting transition temperature (see figure 3.1) and can be approximated by using the empirical relationship for for thin NbN film $\tau_{e-ph} \approx 500\ T^{-1.6}$[40]. τ_{esc} is a function of the super conducting film thickness, t, and can be approximated as $\tau_{esc} \approx 10.5t$[110]. The ratio of electron and phonon heat capacities for an NbN film can be approximated as $c_e/c_{ph} \approx 16.77\ T^{-2}$[110]. Using these empirical relationships it is possible to develop a model of the mixer impedance. Different pumping states of the mixer can then be generated by varying the device temperature.

Figure 3.8(a) shows the real and imaginary components of the HEB impedance generated using the approach of Kooi et al. [64]. From this figure one can see that there is a significant

complex impedance component which explains the saw tooth structure seen in the standing wave profile. Additionally, there is a significant variation in the impedance across the IF which is consistent with the variable standing wave amplitude and slope seen across the IF, see figure 3.7(c).

Figure 3.8 shows an electrical model of the electrical circuit between the mixer and the first amplifier. Using this electrical model in combination with a linear circuit simulator the overall gain of the system was calculated. This output could then be used to compare with actual data. As a test of the model, a gas cell spectrum was used with an impedance difference between 2 phases of the observation. One phase of the gas cell was observed with a cold load (77K) through a ^{12}CO filled gas cell (ON Phase) while the other phase observed the cold load through an empty gas cell (OFF phase). The resulting spectra is generated by dividing the ON by the OFF phase. Ideally the resulting spectra should have a flat baseline and a spectral line, however due to the impedance mismatch between the phase there is a standing wave present. In order to reduce the amounts of variables in the electrical model in the test only 2 phases of the gas cell spectra were used as opposed to normal 4 phases needed for calibration, see equation 3.5.

The modeled electrical spectra was generated by creating 2 separate electrical IF chain models and dividing their gain output by each other much in the same manner as the data calibration. The impedance of each phase was controlled by the relaxation times, t_{esc} and τ_{e-ph} and the specific heat capacity ratio, c_e/c_{ph}. The resulting best fit is shown in figure 3.9.

The electrical model approach improves significantly on the conventional sine wave fitting approach shown in figure 3.4. The approach recreates the saw tooth profile seen in the data and the amplitude variation across the IF band. However, the residual between the fit and the model is still significant. Furthermore, the method is computationally intensive. The example presented here has 3 free parameters for each observation phase. A standard intensity calibrated observation would contain 4 phases increasing the computation time significantly. However the quality of the fit generated using the electrical model of the IF gain provides a nice confirmation of the HEB impedance proposed by Nebosis et al. [83]. Unfortunately the fit is not sufficient for the level of baseline removal needed to meet the HIFI science requirements. Furthermore there are a significant number of higher frequency components present in the data which the model can't account for, see the 7-8GHz region of figure 3.7(c).

The electrical model presented here is primarily the work of Jacob Kooi as published in Kooi et al. [64]. The author worked closely with Jacob Kooi providing appropriate gas cell data to compare to the electrical model in an effort to model the residual standing wave seen in the gas cell data. This work was presented as a paper at an SPIE conference in 2008, see reference [44] for further information.

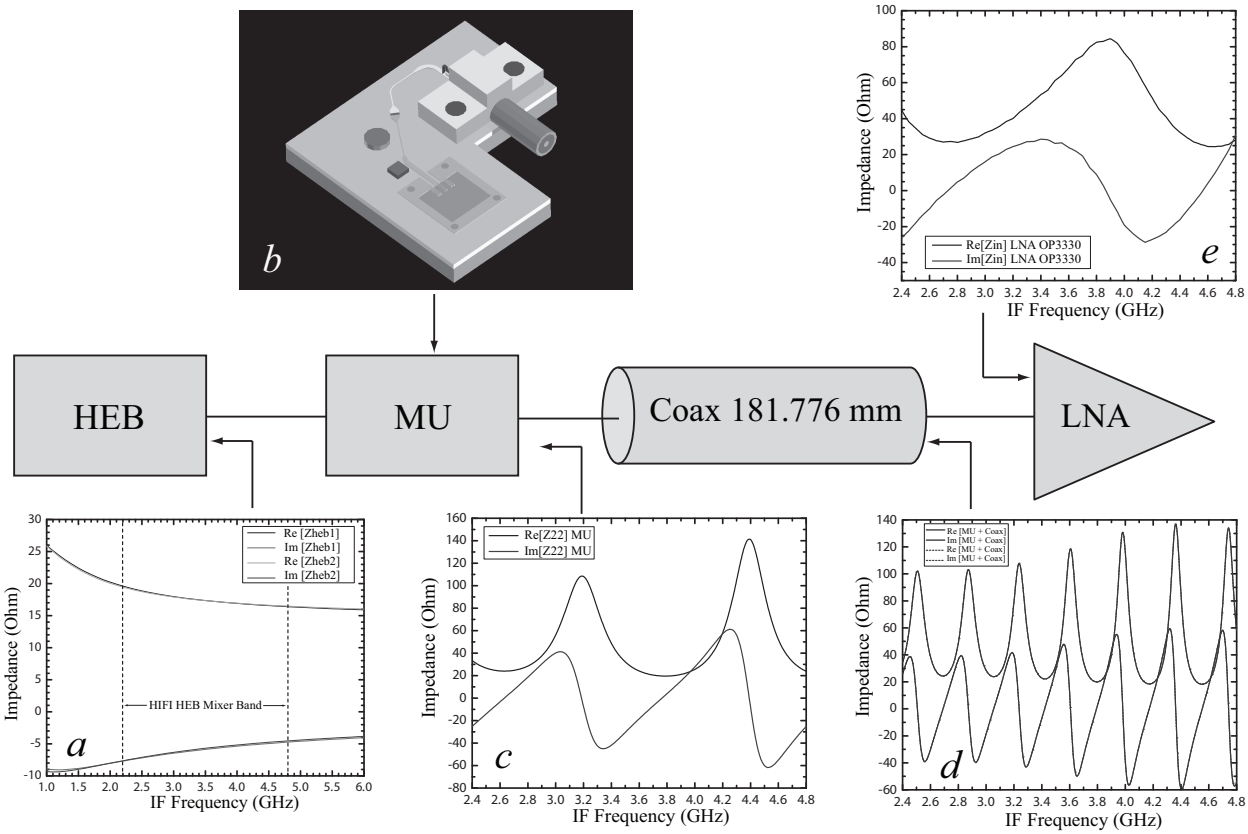

Figure 3.8: Electrical model of HEB band IF chain between the first low noise amplifier and the HEB mixer showing the electrical impedance at various junctions. *(a)* HEB mixer impedance as derived from Kooi et al. [64]. *(b)* schematic of mixer unit electrical model. *(c)* electrical impedance of mixer unit combining HEB mixer impedance with the mixer unit support structure. *(d)* Electrical impedance of mixer unit when coupled to 182mm of coaxial cable. *(e)* Electrical impedance of the LNA measured as part of an acceptance test. Figure taken from Higgins & Kooi [44]

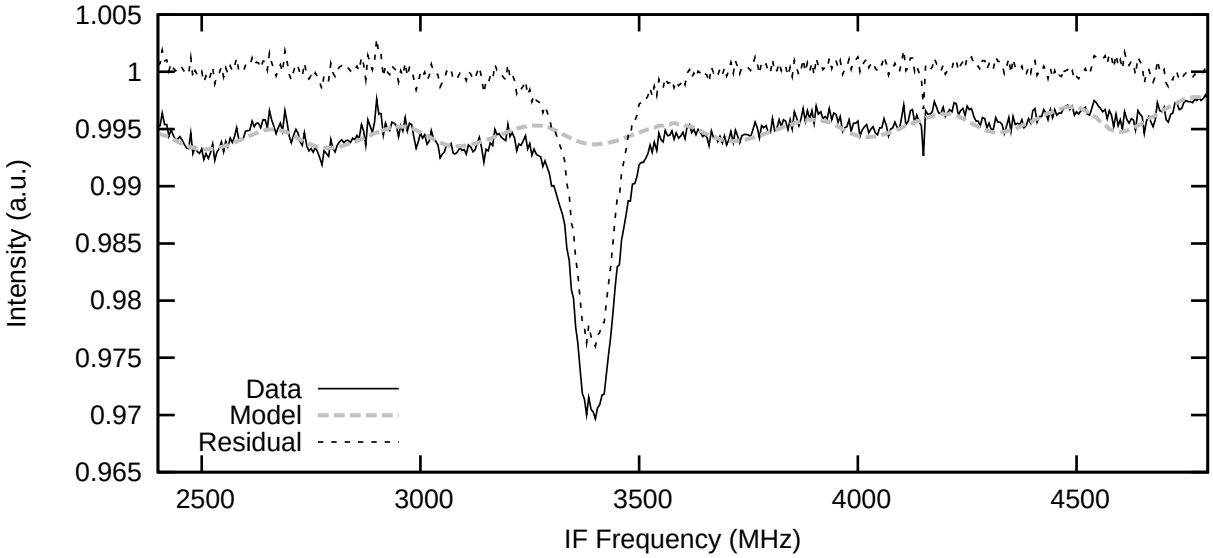

Figure 3.9: Comparison of measured and electrically modeled IF standing wave. Measured data was taken from gas cell campaign and shows the ^{12}CO(15-14) line at 1726.602 GHz observed with LO band 7a. The electrical model was generated by varying the impedance between 2 modeled mixer gains. The residual of the 2 model phases is overlaid in a dashed line.

3.4.2 Baseline catalog approach

Another baseline removal method investigated was to use a smoothed version of observed data itself to remove the standing wave. In section 3.3.4 it was shown that the standing wave amplitude is a function of the mixer current difference between the observation phases. Furthermore, it is apparent from figure 3.5 that the standing wave profile is independent of LO frequency. Given these attributes and the amount of HEB data taken during the course of HIFI operation, it is possible that for each observation with an impedance mismatch between observations phases that an equivalent mismatch was already observed. The catalog approach generates different standing wave profiles from the data by combining the OFF positions in different sequences. It is hoped that given the large amount of data available that for a given impedance mismatch seen in science data that an equivalent combination has already been observed or can be generated.

In this section, 3 examples of increasing complexity are presented and the methods used to generate a baseline catalog from the data are discussed.

3.4.2.1 Gas cell data

The experimental set up of HIFI during the gas cell campaign was far from ideal and the HEB bands were particularly sensitive to any temperature drifts or mechanical vibrations in the instrument set up and as such led to poor quality baselines in the final calibrated spectra. The gas cell data was the first real simulation of a science observation and hence was the first contact with HEB baseline problem in a real observation scenario.

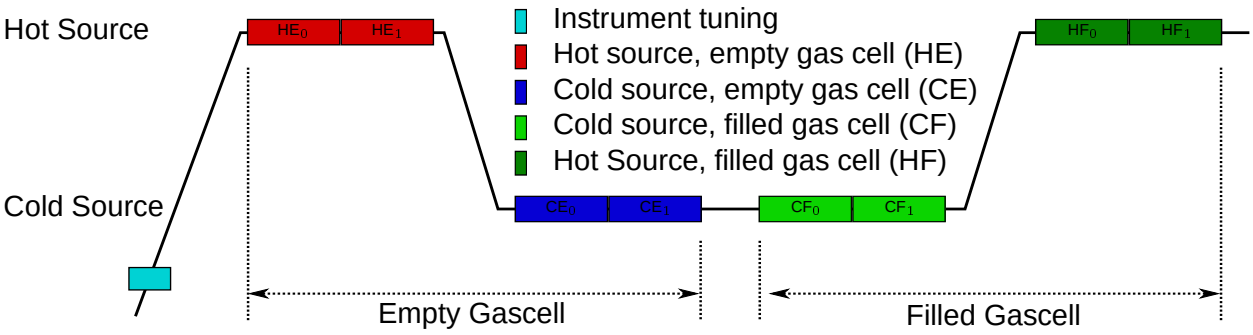

Figure 3.10: Gas cell observation time line

Gas cell data calibration

The gas cell observation routine is similar to the standard observation routine described by equation 3.5. The HOT and COLD observation phases are taken through an empty gas cell (HE,CE) with the HOT and COLD loads as a background source while the ON and OFF phases are taken through a full gas cell with the COLD and HOT loads as a background (CF, HE), see figure 3.10. Using the following equation a calibrated spectrum is generated:

$$\frac{OFF\ (\mathrm{HF}) - ON\ (\mathrm{CF})}{HOT\ (\mathrm{HE}) - COLD(\mathrm{CE})}. \tag{3.6}$$

The HOT, COLD loads in the denominator measure the signal transmission with no gas and the ON, OFF combination measures the signal transmission through the gas. The resulting spectrum is a measure of the signal transmission for a given gas column length, pressure and temperature, see figure 3.6(a).

Baseline catalog generation

Each observation phase (HOT,COLD,ON,OFF) has a four second integration time. To increase the signal to noise ratio multiple integrations of the same observation phase are taken. Hence each gas cell observation has at least 2 unique calibrated spectra using equation 3.6, which are then averaged together to reduce the noise, see figure 3.10. Correction of the baseline is undertaken before any averaging is done. Each calibrated spectrum is generated from 4 different observation phases which are assumed to have 4 different impedance states.

As stated previously, the standing wave seen in calibrated data is a result of a difference in mixer impedance between the observation phases. From section 3.3 it was shown that the resulting IF ripple is repeatable for a given mixer impedance difference between 2 phases and the IF ripple profile is independent of LO frequency. Using these properties it is possible to build a catalog of standing waves from which a suitable profile can be subtracted from the calibrated data.

For the gas cell data the baseline catalog is generated from gas cell data itself. As described in equation 3.6, a gas cell transmission spectrum is made up of 4 phases where the line data is

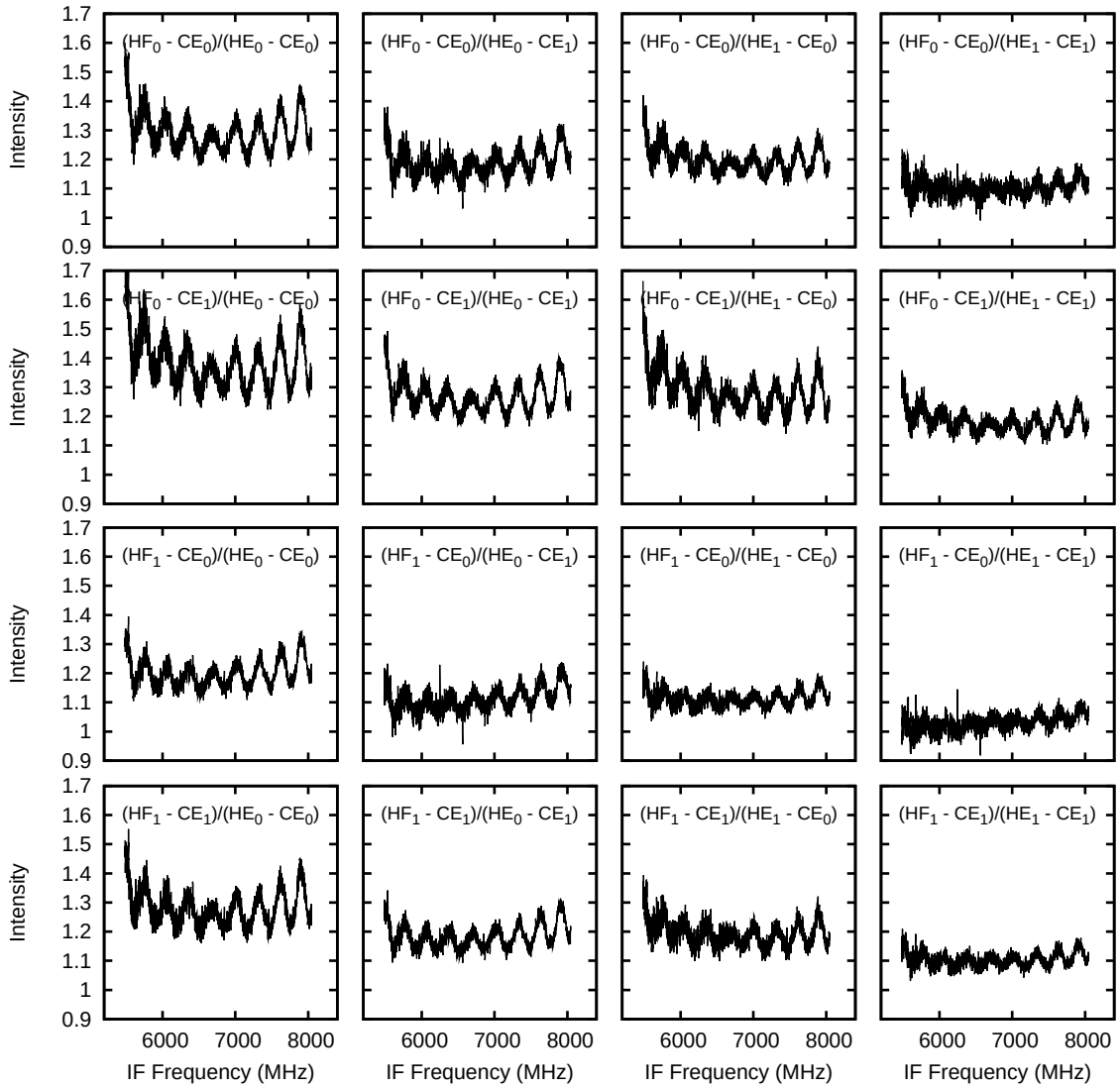

Figure 3.11: Example of baseline profiles possible by combining the phases in a gas cell observation containing no line data in different sequences. The data shown here is an observation of ^{13}CO at an LO frequency of 1764.0855 GHz with the V polarization mixer (Obsid 268477638).

contained in the observation phase looking at the cold source through the filled gas cell (CF). Line data is also contained in the observation phase looking at the hot source through the gas (HF) but since the hot source is at the same temperature as the gas itself no absorption is detected and its response is very much like the hot source empty gas cell phase. A baseline profile is then generated using a similar calibration equation to the gas cell but this time without the observation phase containing the line data:

$$\frac{HF - CE}{HE - CE}. \tag{3.7}$$

As each gas cell observation contains multiple observations of the same phase it's possible to generate multiple combinations of the impedance differences and hence multiple baseline

Band	6a	6b	7a	7b	Total
	1324	982	395	574	3275

Table 3.2: Distribution of gas cell HEB observations per LO band

shapes. Figure 3.11 shows an example of the different baseline shapes that can be generated by combining the gas cell observation phases containing no line data in different sequences. The example shown is for an observation where each gas cell phase is observed twice.

It is possible to generate 16 unique standing wave profiles for a single gas cell observation where each phase is observed twice. The amount of instability during the observation will effect the amount of variability in the baseline profiles created. A catalog is generated by applying the same matrix calibration to the each gas cell observation and then appending the baselines generated to a global catalog. A catalog is generated for each mixer unit as the standing waves will be slightly different since the associated IF chains are different. Table 3.2 gives an overview of the total number of gas cell observations per band which results in each mixer unit having a catalog with a minimum $\sim$ 5000 baselines.

Gas cell data baseline correction example

As described earlier, due to the higher noise in the HEB bands multiple integrations of each gas cell phase are taken to increase the signal to noise ratio. This results in a minimum of 2 unique calibrated spectra which are then averaged together. The catalog approach looks to correct the data before averaging as the spectra have a similar combination of 4 impedances to the spectra in the baseline catalog. After the averaging, the process of matching a suitable baseline from the catalog with the line spectra gets more complicated.

The basic premise of a catalog approach is that for each combination of impedance mismatch observed during a line observation an equivalent impedance mismatch has already being observed. It is hoped that the catalog contains all combinations of impedance observed. The final step in the catalog approach is to efficiently match the gas cell science spectra to an equivalent catalog spectra. This catalog spectra can then be subtracted from the science spectra removing the IF ripple and leaving just the line data.

Efficiently extracting a matching catalog spectrum from the large catalog database isn't trivial. The simplest approach would be to subtract the science spectra from all spectra in the catalog, analyze the residual spectrum and the residual with the least standing wave structure would be the best match. However, this method can be very taxing on computer resources given that a 5000 spectra catalog is over 2 Gigabytes of data and furthermore the amount of time required to subtract the science spectrum from all 5000 spectra make this approach prohibitively time consuming. The subtraction of the catalog spectra from the science spectrum is seen as final quality control for selection of the optimum catalog spectra however a subset of catalog spectra must first be selected to reduce the computation time.

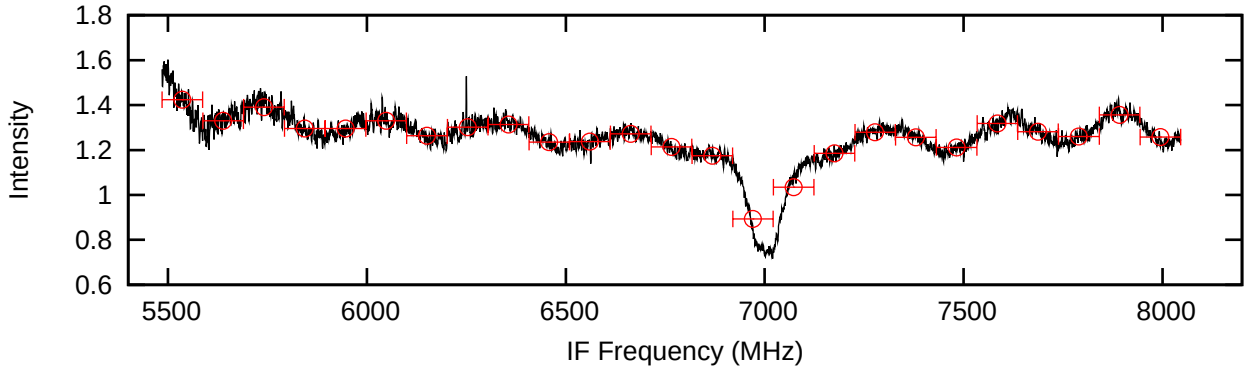

(a) Rebinning spectra into 100 MHz sections

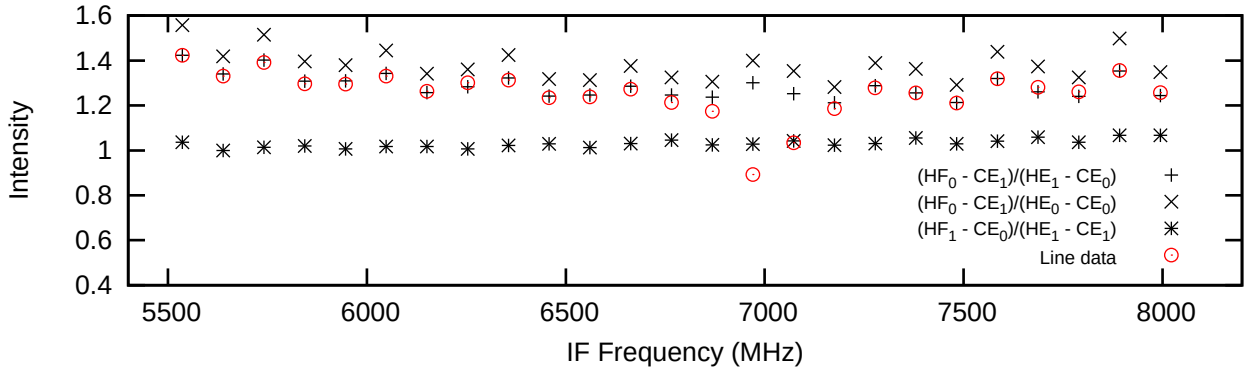

(b) Plot of rebinned gas cell spectra with 3 catalog spectra. The catalog examples shown here correspond to the spectra shown in figure 3.11.

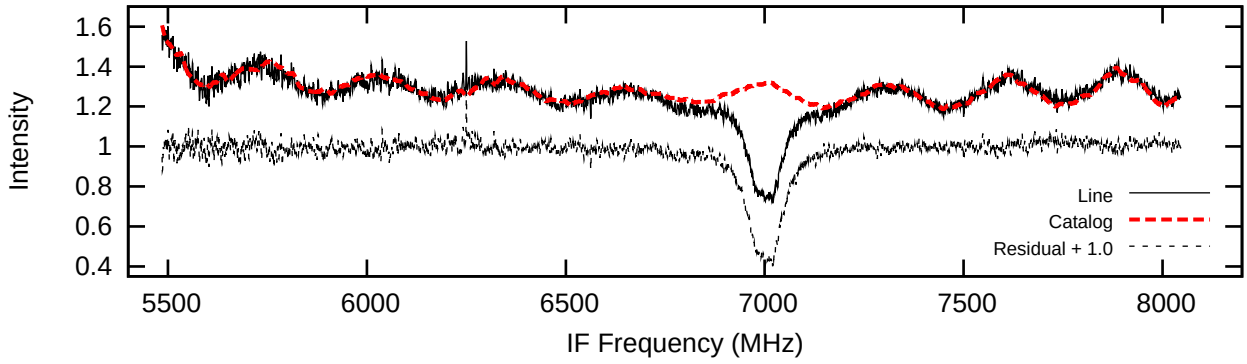

(c) Subtraction of optimum catalog spectra from line spectra.

Figure 3.12: HEB standing wave removal for ^{12}CO gas cell data at an LO frequency of 1730.01 GHz data (Obsid 268477562) using a baseline catalog. The best match baseline from the OFF catalog is from a gas cell observation taken at an LO frequency of 1764.086 GHz (Obsid 268477638).

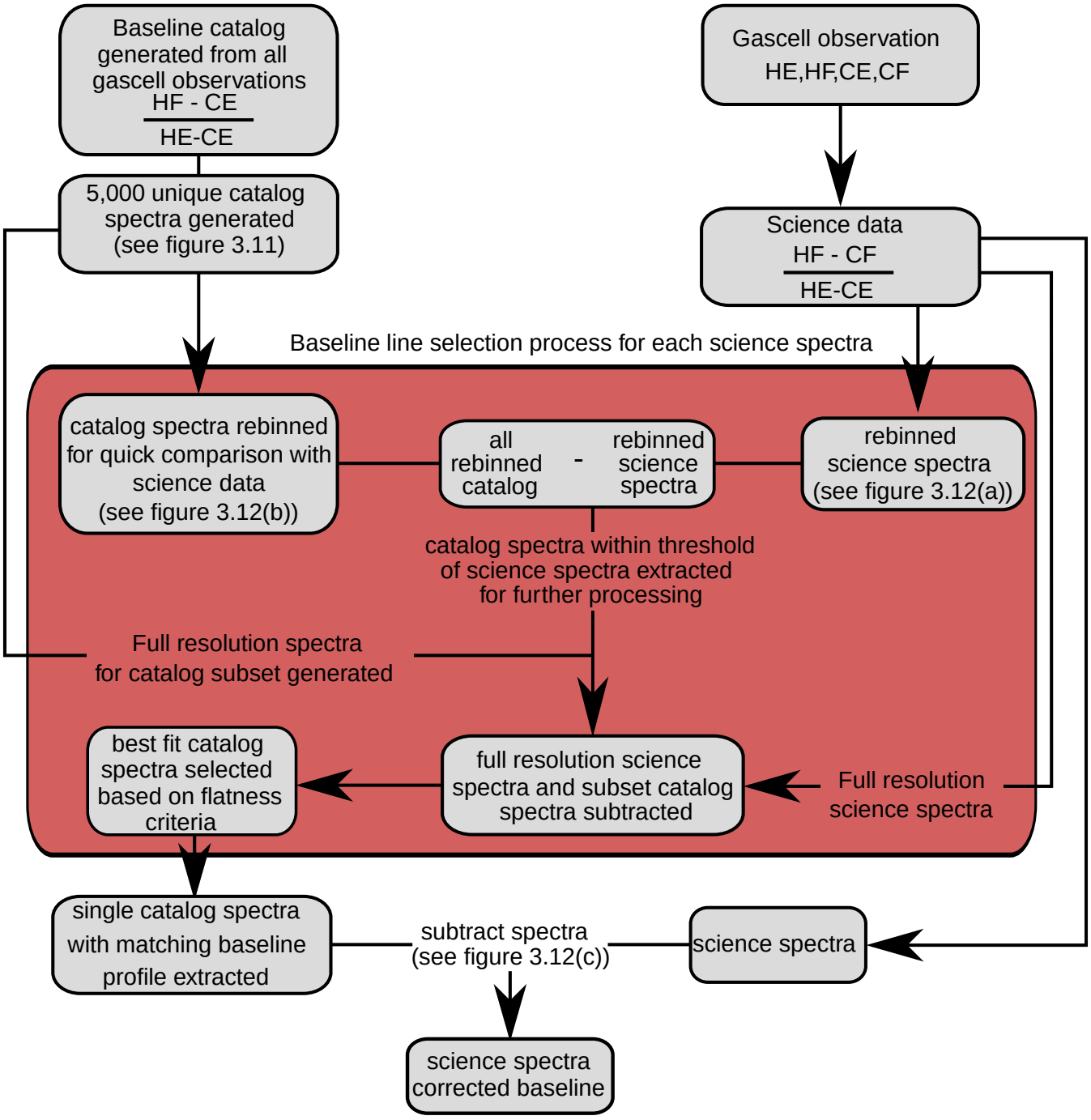

Figure 3.13: Flow chart showing the 2 step process of extracting the best matching baseline catalog profile for a gas cell observation.

To extract a suitable subset of spectra from the catalog an efficient means of categorizing the standing wave profile must be developed which can be used to extract suitable catalog spectra for further processing against the science spectra. An early approach was to calculate the FFT of each spectra and use the power at the 320MHz frequency channel (channel where standing wave power is concentrated) as a measure of the standing wave. This was then used to compare the catalog spectra with the science spectra. However this method proved inefficient and large thresholds had to be used to find a suitable match. Additionally if a strong line was present in the science data this added power around the 320MHz channel making it difficult to efficiently find a suitable catalog spectra.

The final solution is more elegant and involves less computer resources. The approach rebins each spectrum into 100MHz blocks[115], see figure 3.12(a). The flux over each block is then averaged and this rebinned spectra is taken as a measure of the standing wave profile. Each spectra is then defined by a 25 element array. Instead of subtracting each 4500 channel science spectra from every catalog spectra only the 25 element array of the catalog spectra and science spectra are subtracted. A threshold is then set and the number of elements in the residual array below this threshold are counted. Figure 3.12(b) shows a comparison of the rebinned line spectra and 3 rebinned baseline catalog spectra.

When a catalog spectra has a given amount of elements within the threshold this spectra is chosen as a candidate spectra. These candidate spectra are then further processed to determine which one ultimately provides the best baseline correction. The final step is to subtract the candidate spectra from the science spectra. A distance measure is used to determine which combination of candidate spectra with the line data spectra provides the flattest baseline. The distance measure is calculated on a smooth version of the line data spectra minus the candidate spectra. The distance is calculated as the sum of absolute difference between each consecutive flux channel. The spectra with the shortest distance is assumed to be the flattest spectra and this is candidate spectra is chosen as the best match from the baseline catalog. This 2 step process is then repeated for each science spectra. Figure 3.12(c) shows an example of the best match baseline catalog together with the line spectra, the distance measure is calculated on the residual spectra shown with a dashed line. A flow chart describing the entire process is shown in figure 3.13.

The example shown in figure 3.12 demonstrates one of the useful properties of the HEB standing wave. The final spectra chosen from the baseline catalog as a best match is taken at an LO frequency 14 GHz from the LO frequency of the line spectra being corrected. This demonstrates the LO independence of the standing wave profile which makes the catalog approach for the gas cell dataset feasible.

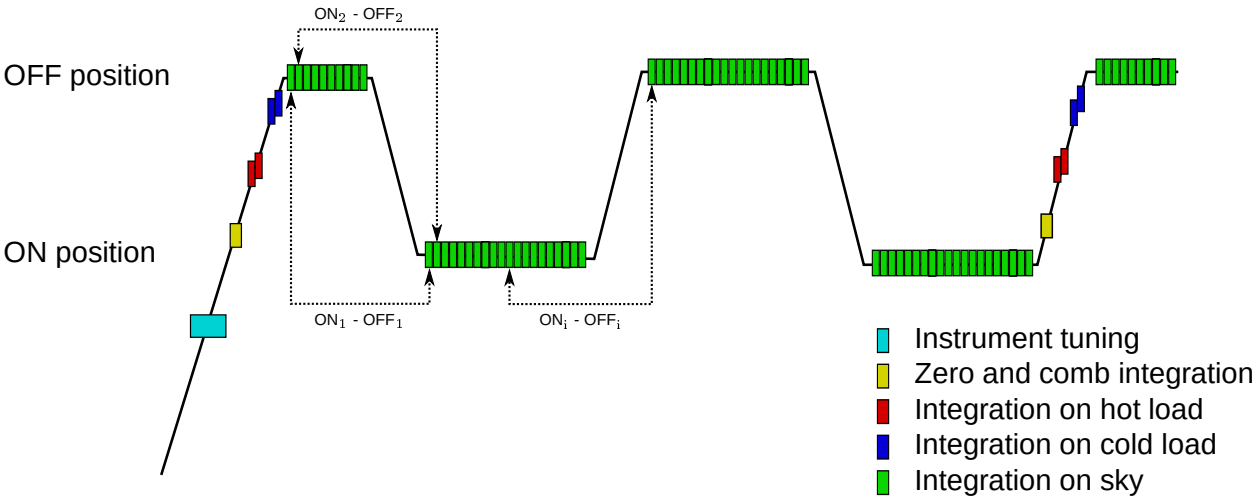

Figure 3.14: Position switch observation time line

3.4.2.2 Position switch flight data

While the mechanical stability is much improved in the vacuum of space the inherent LO mixer cavity stability are still comparable to the ground test conditions resulting in the same level of baseline degradation as seen in the gas cell data presented previously.

The gas cell test data is a useful environment to test the catalog approach since the test routine is identical for each observation allowing for a generic script to be applied to all observations taken. In-flight observations come in a variety of forms and separate scripts must be written to generate the baseline catalog for each observation. Furthermore, due to data download constraints the house keeping sampling rate is every 4 seconds for flight data which is considerably less than the ground test rate of every second. However a useful feature of flight data is the multiple integrations taken during a standard observation. To detect weak milli-Kelvin lines multiple integrations must be taken to improve the signal to noise ratio. Multiple integrations at the same LO frequency are useful for generating multiple combinations of impedance differences and hence increasing the baseline catalog size and the chances of finding a baseline profile to correct the line spectra.

In this section the correction of flight data with a weak broad line is presented. The AOT (Astronomical Observation Template) chosen is the position switch observation. This observation type is easiest to manipulate.

Position switch data calibration

A position switch observation consists of 4 observation phases of ON,OFF,HOT and COLD integrations. These phases are combined together using equation 3.5 returning an intensity calibrated spectrum. The OFF position is chosen by the astronomer and is normally the closest piece of blank sky to the ON source position, see figure 3.16(b). Position switch observations are normally used for sources with an extended region of emission (greater than 3 arcseconds).

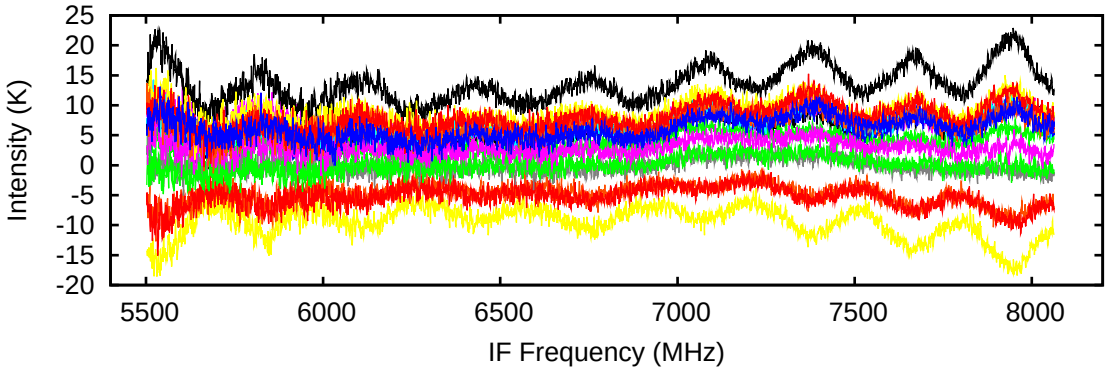

Figure 3.15: First 16 of 229 spectra from the position switch observation 1342192299 taken at an LO frequency 1494.276 GHz using the WBS H polarization backend.

For point sources the chopper mirror can be used to measure the OFF without having to slew the telescope, this mode, known as the dual beam switch mode, is discussed in the next section.

Figure 3.14 gives an overview of a generic position switch observation time line. The frequency of HOT COLD observation and ON and OFF slews are determined by the instrument stability (as measured by the Allan variance[87]) while the length of the integration time is determined by the signal to noise goals of the observation. Each ON observation is coupled to the nearest OFF observation as shown in figure 3.14 and intensity calibrated by the nearest HOT/COLD pair.

Baseline catalog generation

The baseline catalog generation follows much the same approach used for the gas cell observation, described in section 3.4.2.1. OFF positions are coupled together in different combinations and are calibrated using the different HOT/COLD pairs taken during the observation. Depending on the amount of OFF spectra taken during the observation a large catalog of baselines can be generated from within the observation.

Figure 3.16 provides an overview of the time-line for the position switch observation (obsid 1342192299) taken on the source Sagittarius A. This observation was taken during the performance verification phase. In total 228 ON/OFF pairs and 9 HOT/COLDS pairs were taken during the 3500 second observation. This observation, as expected, is beset with baseline problems which mask the broad ^{12}CO (13-12) line around 1496.923 GHz. Figure 3.15 shows the first 16 of 229 calibrated spectra. This observation was taken at an LO frequency of 1494.276 GHz which after the 10.4GHz up-conversion places the line in the upper side band at an IF frequency of 7.2GHz.

The baseline catalog is generated much like the gas cell baseline catalog described in the previous section. Observation phases with no line information in this case the OFF, HOT and

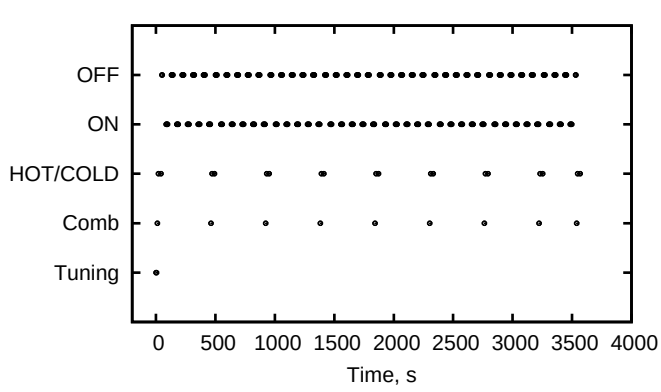

(a) Observation time-line

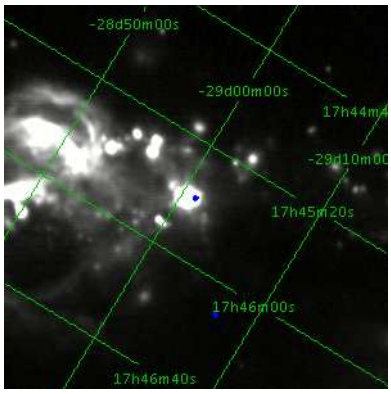

(b) ON/OFF Sky positions

Figure 3.16: Summary of the observation time line and sky position for the position switch observation 1342192299. The blue circles in the sky image represent the ON and OFF beam positions and size. There is a 9 arc-minute distance between the ON and OFF positions. The image shown is a 21.3μm image from the Mid-course Space Experiment (MSX) satellite archive [79] with the grid (Equatorial J2000) and beam positions added using the Herschel observation tool, HSpot[33].

COLD phases are coupled together using the following calibration equation:

$$\frac{OFF_i - OFF_j}{HOT_k - COLD_k}, \tag{3.8}$$

where for this observation k is from 1-9 and i, j are from 1-228. Unlike the gas cell baseline catalog generation, the HOT and COLD observations are kept in the same sequence as they are observed. For the gas cell observation there was up to 16 seconds between the HOT and COLD observations. For flight data the time between HOT COLD is kept to a minimum and is limited by the time taken to move the chopper between the 2 positions and the time it takes to record the data. This results in a time gap of 1 second between the acquisition of the HOT and COLD observation phases. The short time difference between the 2 observations minimizes the amount of drift possible during the observation and proves effective at minimizing the impedance change between the 2 phases.

Figure 3.17(a) shows the baselines when a single ON OFF pair are calibrated using the nine HOT COLD pairs taken during the observation (see the observation time-line in figure 3.16(a)). From these baselines it is apparent that the the choice of HOT COLD pairing has only a second order effect on the overall shape of the baseline profile. It is apparent there is little or no impedance difference between the HOT COLD pairing and the baseline ripple is due to the impedance difference between the ON OFF pairing.

Figure 3.17(b) shows an example of the effect of changing the OFF spectra while keeping the ON and HOT COLD pair fixed. From this figure it is apparent that there is a large degree of variability in the OFF spectra impedance compared to the ON spectra impedance. There

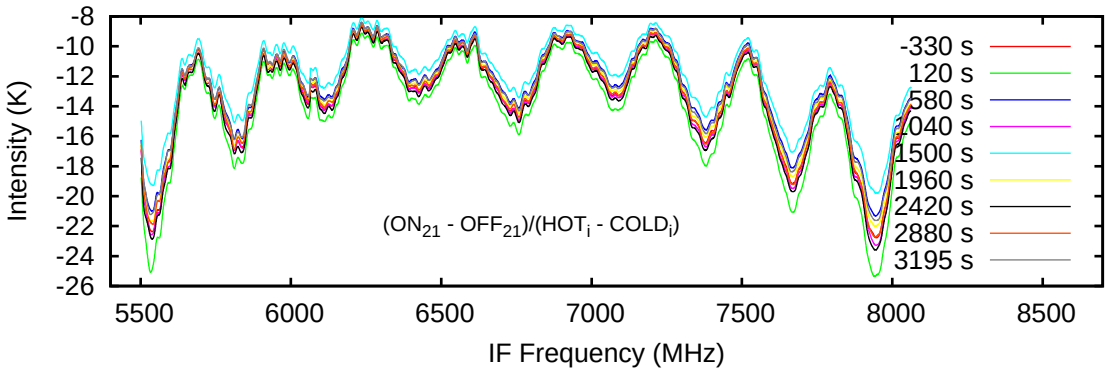

(a) Effect of using different HOT COLD pairs to calibrate the same ON OFF pair. The time difference between when the ON spectra and the HOT COLD pair were observed is shown in the legend.

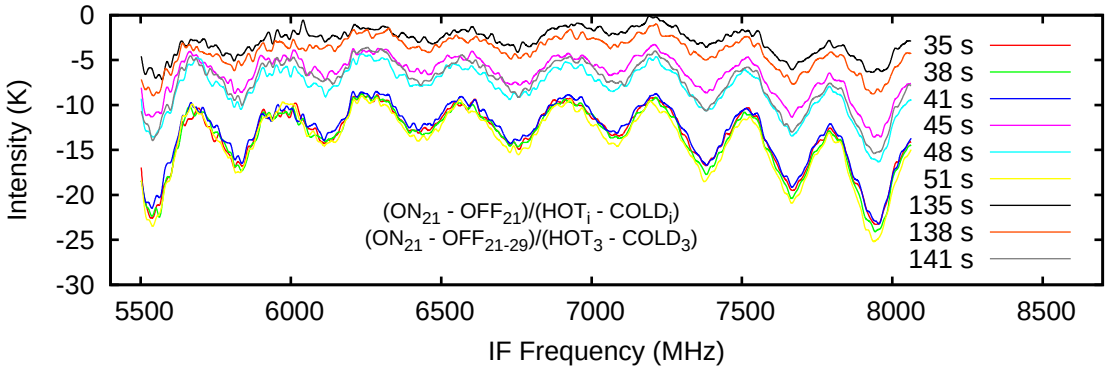

(b) Effect of using different OFF spectra while keeping the ON and HOT COLD spectra fixed. The time difference between the OFF spectra and the ON spectra is shown in the legend. The OFF spectra chosen are the nine nearest spectra in time. Note that the OFF spectra taken 135 seconds later provide a better baseline than the nearest OFF spectra at 35 seconds.

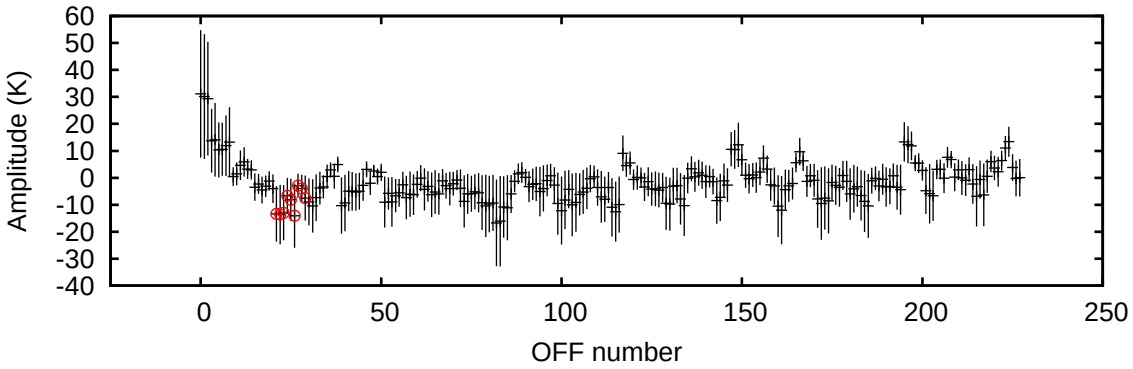

(c) Variation of standing wave amplitude when a spectrum is calibrated using different OFF spectra while keeping the ON and HOT,COLD spectra fixed. The data plotted is the mean baseline intensity for each spectra, the Y error bars represent the absolute difference between the maximum and minimum intensity values. The red circles on the plot highlight the nine spectra plotted in figure (b).

Figure 3.17: Effect of using different ON, OFF and HOT COLD pairs to generate calibrated spectra

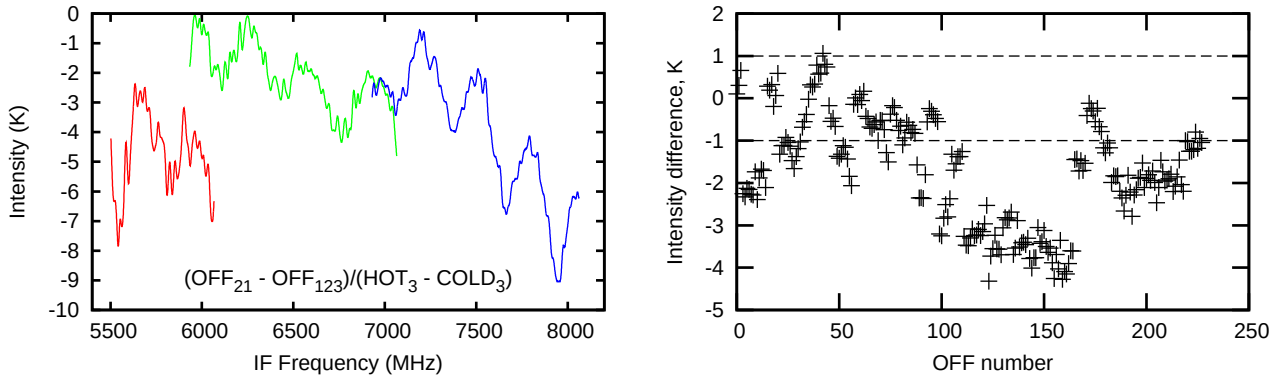

(a) Example of spectrum with platforming between the 2nd and 3rd sub-bands

(b) Mean intensity difference between overlapping region between the 2nd and 3rd sub-bands

Figure 3.18: Effect of platforming between sub-bands. The example data shown here has been smoothed using a 10MHz wide Gaussian filter to highlighted the flux difference otherwise the effect would be hidden by the noise. The summary data shown on the right is calibrated using a fixed OFF position (21st OFF) with all other 228 OFF spectra.

is a large impedance difference between the nearest OFF spectra at 35 seconds resulting in a large standing wave on the baseline. Figure 3.17(c) show the amplitude of the standing wave when the ON spectra is coupled to all OFF spectra available. The nearest nine spectra are highlighted with red circles. From this one can see that OFF spectra occurring much later in the observation time line can provide a better impedance match than the nearest OFF spectra and hence provide a lower amplitude standing wave.

While the basic concept behind the baseline catalog generation is similar for the gas cell data and the flight data other drift effects must be considered. For the gas cell data the baseline catalog is generated from short gas cell observations no greater than 2 minutes. All spectra are within at least 120 seconds of each other. For this example when all OFF spectra are considered there can be up to 3000 seconds between 2 OFF spectra which leads to other instrument problems.

This large time difference leads to other drift effects becoming significant. In particular the effect of platforming between the WBS spectrometer sub-bands. As described already the WBS splits the IF band into 4 equal 1GHz sub-bands, as the HEB band has a reduced IF bandwidth only 2 and half of these sub-bands are used. Platforming is the effect of a step in the baseline due to a sub-band gain difference between 2 different observation phases in this case the 2 OFF spectra. Figure 3.18 demonstrates the effect of platforming on the OFF catalog. Figure 3.18(a) shows an extreme example where a large difference is seen between the first subband and second subbands.

The effect of platforming must be removed from the OFF catalog as they can corrupt any baseline corrected when subtracted from a calibrated spectra with line data. The degree of platforming is measured by averaging the flux in the overlapping IF regions between the 2

sub-bands. A threshold of ± 1K is set and any spectra outside this threshold are excluded from the baseline catalog. Without the effect of platforming, over 400000 baseline combination would be possible given 228 OFF spectra and 9 HOT COLD pairs. However, when the effect of platforming is taken in account this reduces the amount of viable baselines to 200000. The effect of platforming can vary from observation to observation and depends on the stability state of the WBS backend. The final total of spectra in the baseline catalog is still more than enough to correct the baselines sufficiently as will be shown in the next section.

Position switch data baseline correction

Once the baseline catalog is generated the next step is to efficiently determine which baseline in the large catalog can be used to correct the baseline of calibrated spectra containing the line data. The approach follows the 2 step approach developed for the gas cell baseline correction detailed in section 3.4.2.1. Again each spectra in the baseline catalog and each of the 228 line data spectra is broken into 100MHz bins, see figure 3.12(a). Each spectrum is then categorized by an array of 25 numbers which can be quickly compared with each other, see figure 3.12(b). A subset of spectra are then selected which are more rigorously compared to the line spectra. A distance measure is calculated which determines the flatness of the residual between the candidate catalog spectra and the line spectra. The catalog spectra which produces the flattest residual spectra is chosen as the best match spectra and used to correct the line spectra. The flow chart in figure 3.19 provides an overview of the baseline correction routine.

Figure 3.20 shows the baseline correction of the first 16 spectra shown originally in figure 3.15. The average of the 16 corrected and uncorrected spectra is shown in figure 3.21 for comparison. It is apparent that there is a marked improvement in the base quality before and after baseline correction. The broad ^{12}CO line profile is clearly evident in both spectra, however the line profile shape is more apparent in the corrected spectra. Figure 3.22 provides a statistical overview of the first 100 spectra before and after baseline correction, the mean intensity of each spectrum is plotted and the error bars represent the absolute difference between the maximum and minimum intensity values and are a crude measure of the standing wave amplitude. From the plot one can see that the scatter in baseline quality is greatly reduced after baseline correction. Before baseline correction the data showed an average baseline intensity of 0.4K with scatter of ± 5.5K. For the corrected data the mean baseline offset is 0.4K with a greatly reduced scatter of ± 0.4K.

This is a significant reduction in the degree of baseline scatter seen in the data. While the example shown here was primarily concerned with spectral line observations other observations may require an accurate measure of the continuum for their science investigation. Large baseline scatter would be detrimental to the accurate measurement of the continuum intensity. Using the methods described the scatter can be greatly reduced.

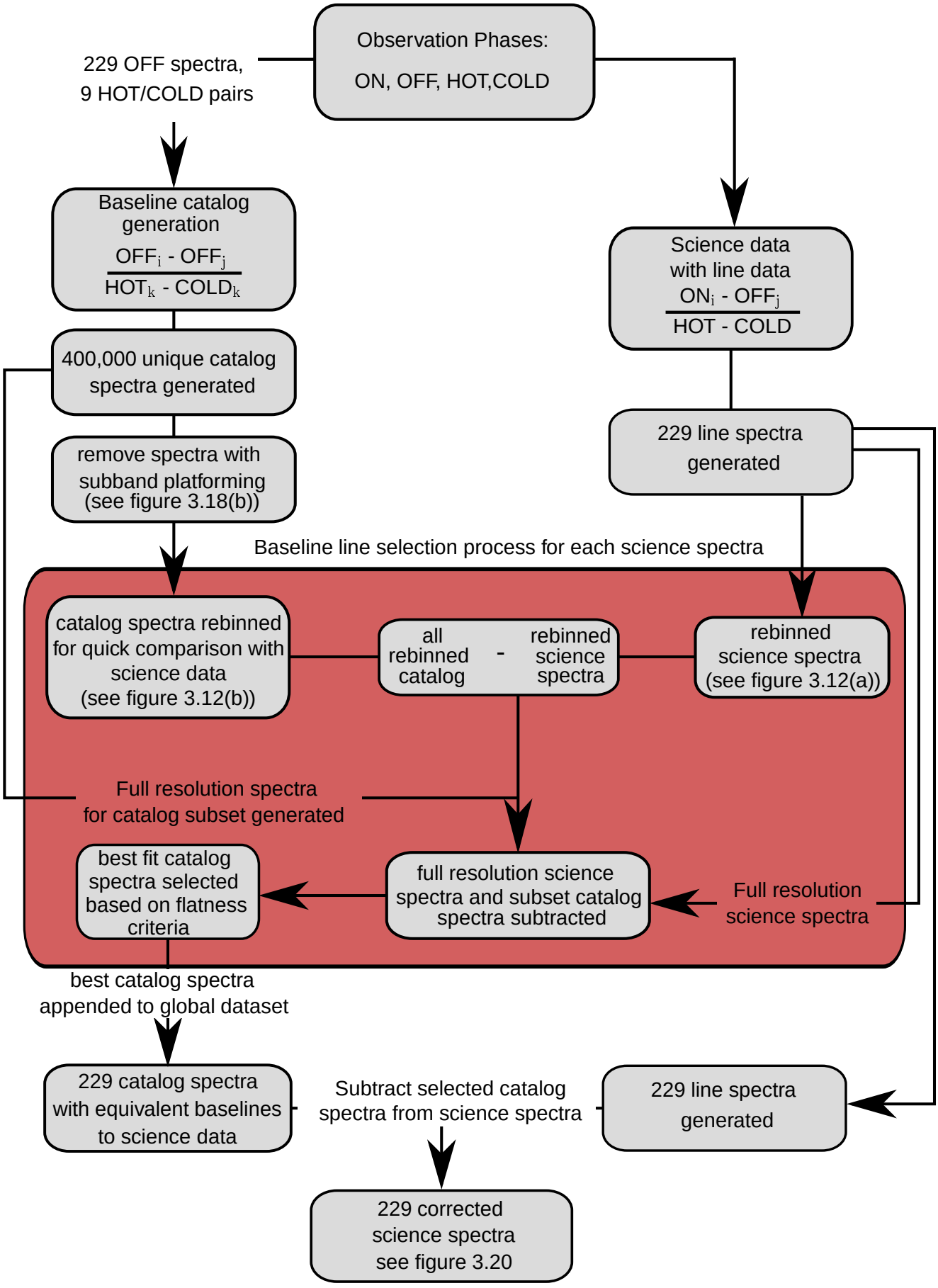

Figure 3.19: Flowchart describing baseline correction process for a position switch observation, in particular obsid 1342192299

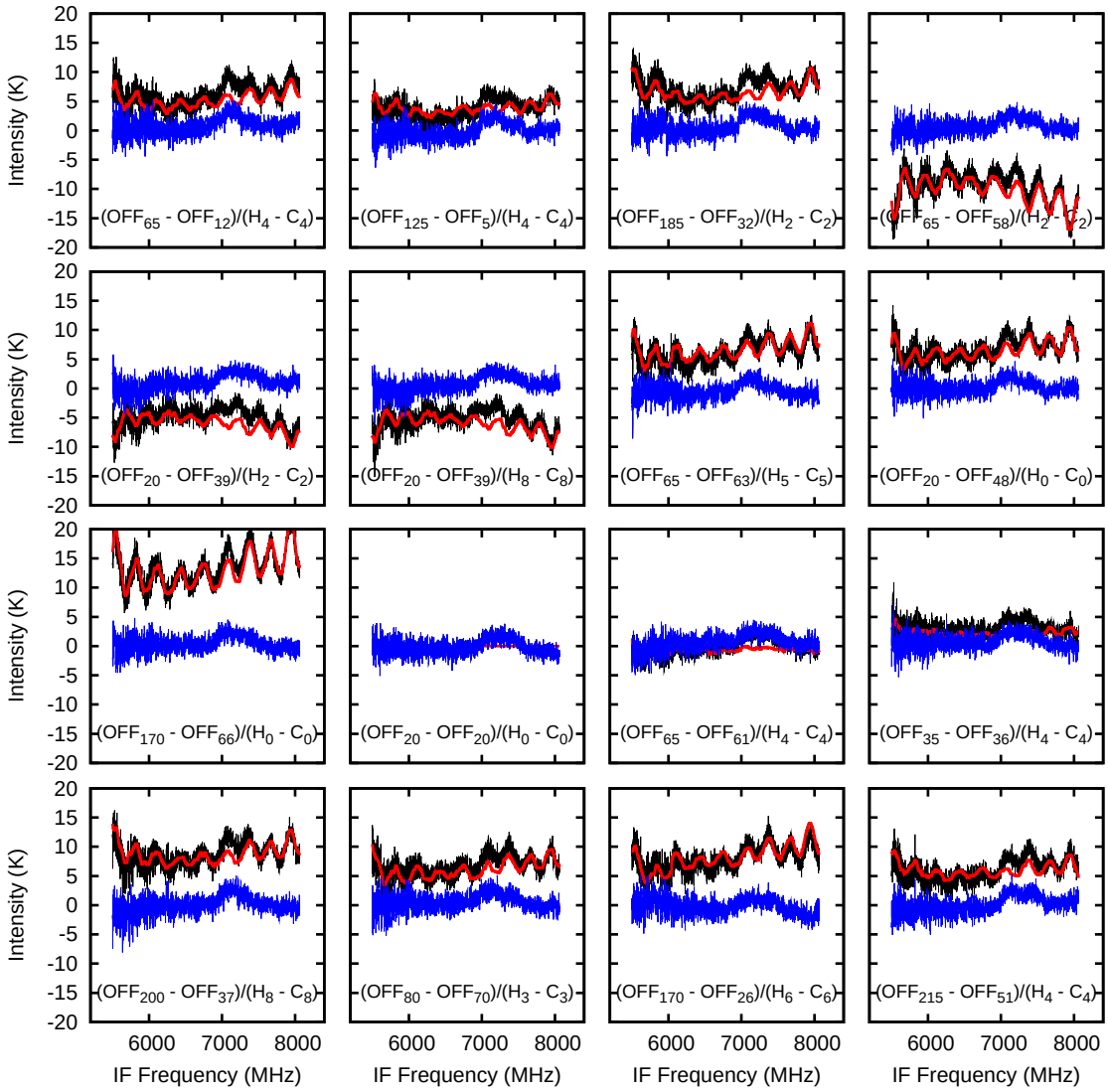

Figure 3.20: Baseline correction of the first 16 spectra. The original data is shown in black, the baseline spectra used to correct the standing wave is shown in red and the corrected data is shown in blue. The sequence of OFF spectra and HOT/COLD pair use to generate the baseline profile is labeled on each figure.

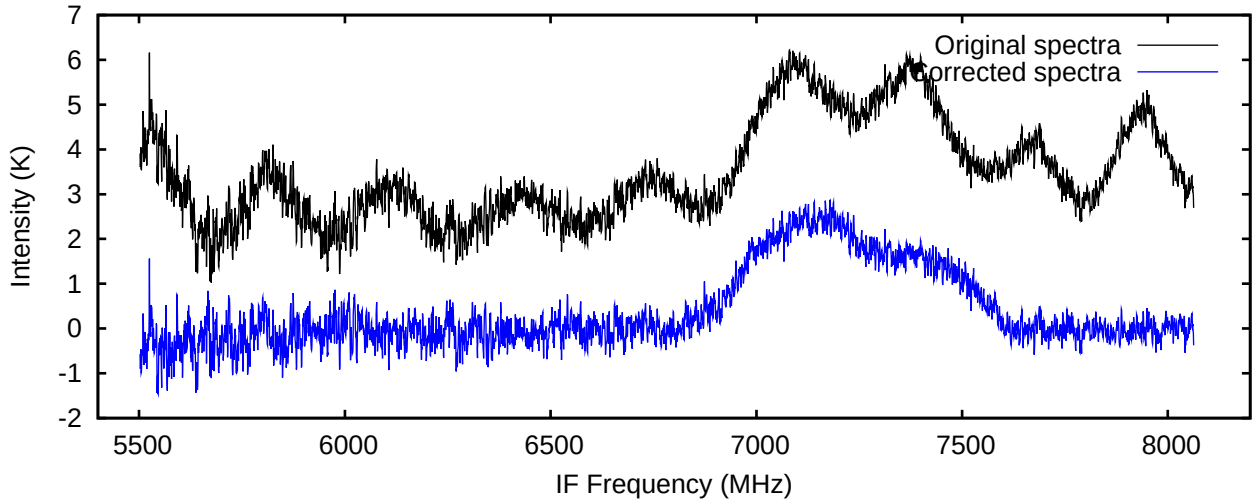

Figure 3.21: Average of first 16 spectra from obsid 1342192299 with and without baseline correction. With an LO frequency of 1494.276 GHz, the broad ^{12}CO (13-12) line at a sky frequency of 1496.923 GHz is seen in the upper side band. After the 10.4 GHz up conversion (see figure 3.3)) the line is observed over an IF region from 6800 MHz to 7600 MHz.

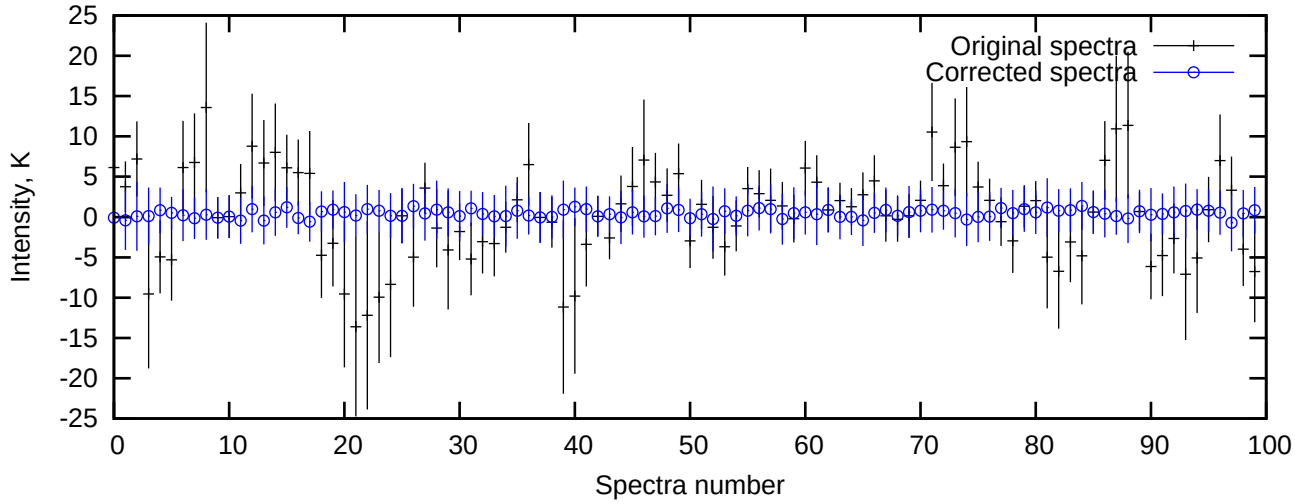

Figure 3.22: Comparison of baseline scatter for the first 100 spectra before and after baseline correction. The data plotted is the mean baseline intensity for each spectra, the Y error bars represent the absolute difference between the maximum and minimum intensity values.

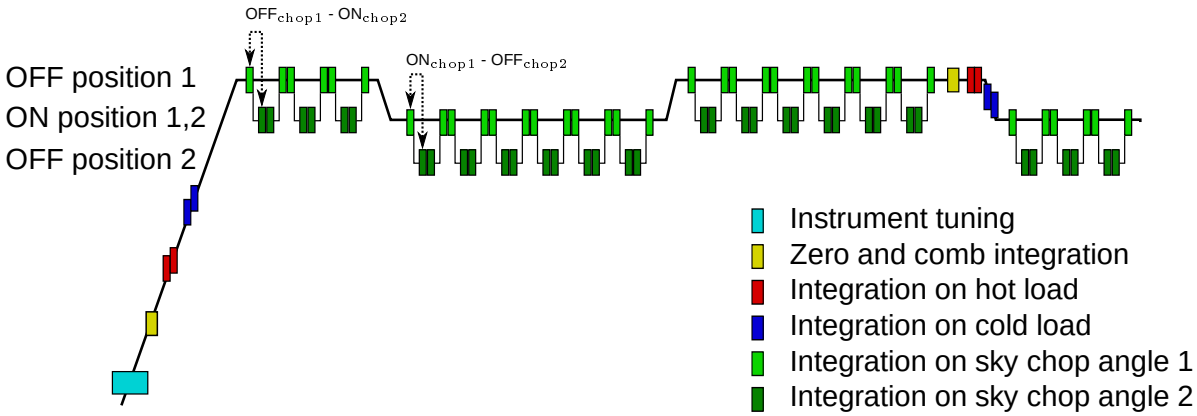

Figure 3.23: Dual beam switch observation time line

3.4.2.3 Dual beam switch data

Dual Beam Switch (DBS) mode is the most common mode used by the guaranteed time key programs. Over 75% of spectral scan and point observations are taken using this mode[82]. Dual beam switch mode uses the internal beam chopper to select the observed position on the sky. Instead of slewing the telescope to observe an OFF position like the position switch mode the chopper normally is used to switch between the ON and OFF positions, see figure 3.23. This decreases the time between ON and OFF observations which helps remove any drift effects between the 2 phases. The maximum chopper angle is 3′ so this observation mode is limited to point sources with no emission outside of 3′.

Since the optical path between the ON and OFF spectra is different optical standing wave effects can be significant. To reduce standing wave effects a second group of ON OFF pairs are taken with the reverse combination of chopper pairings. The Telescope is slewed 3′ so the source is at chopper position 1 and the OFF position is at chopper position 2, opposite to the fist slew position. Using this observation routine it is hoped that the standing waves between the 2 ON OFF pairs are opposite in phase and hence cancel during the double difference calibration.

The advantages of the DBS mode are quite apparent in the SIS bands where standing waves in the sky optical path can be quite significant. However for the HEB bands due to the beam sizes and quasi optical antenna coating the effect of optical standing waves is greatly reduced. For some LO bands there are strong standing waves from the calibration loads however alternating the sky beam has no effect on these standing waves. Further investigation is needed to determine the advantages of DBS mode in the HEB bands, a single beam switch model could be a more effective use of observing time. This topic is not discussed in this thesis.

The fast chopping between the ON and OFF source does help reduce the impact of the HEB standing wave on the data by reducing the amount of system drift between the 2 observation phases. While the baseline degradation is still apparent in the data it is much improved from the position switch data presented previously. Figure 3.24 shows the first 16 spectra taken for the DBS observation obsid 1342190743. The degree of baseline scatter is much improved when

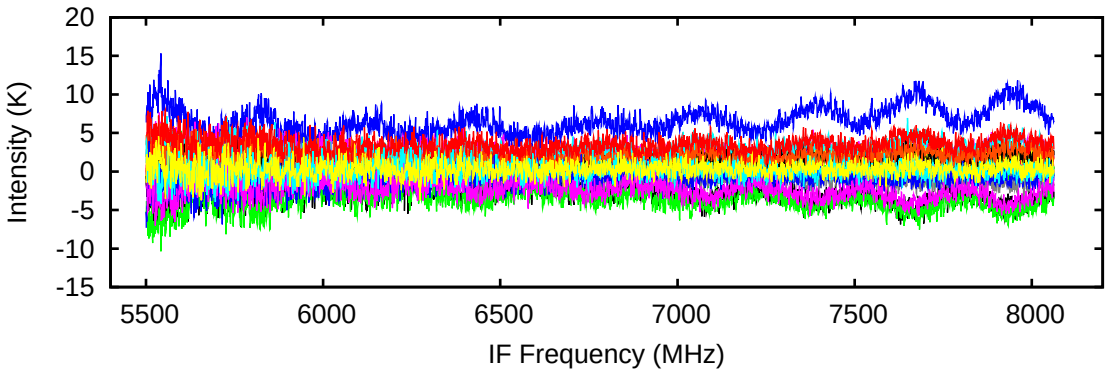

Figure 3.24: First 16 of 296 spectra from the dual beam switch observation observation 1342190743 taken at an LO frequency 1500.444 GHz using the WBS H polarization backend.

compared with the equivalent plot for the position switch observation, see figure 3.15.

Dual beam switch calibration

The final calibrated spectrum is known as a double differenced spectra. Unlike the position switch observation where only a single differencing (subtraction of OFF spectra, see equation 3.5) is undertaken here 2 subtractions are undertaken to remove systematic effects from the final calibrated spectra. The ON and OFF source is observed through 2 different optical paths and through the double difference subtraction it is assumed the standing waves will cancel.

Each ON OFF pair is divided by the nearest HOT COLD pair following the typical calibration equation 3.5. Each ON OFF pair is then subtracted from the nearest ON OFF pair with the opposite chopper sequence, see figure 3.23. The following equation gives an overview of the double differencing approach:

$$\frac{OFF_{chop1} - ON_{chop2}}{HOT - COLD} - \frac{ON_{chop1} - OFF_{chop2}}{HOT - COLD} \tag{3.9}$$

Baseline catalog generation

Given the short time between the ON and OFF observation the drift between the 2 phases is kept to a minimum. However baseline issues can still exist and given the large amount of observations using this observation mode it is necessary to have tools available to remove baseline effects should they arise.

The DBS catalog approach follows the same approach as that detailed in the previous sections for gas cell and position switch AOTs. The OFF spectra are combined together in different sequences with different HOT COLD pairs. For the DBS spectra there are 2 OFF types taken at different chopper positions. It is assumed that there are different optical effects between the 2 chopper positions so for the creation of the baseline catalog the 2 OFF positions are kept separate. Any optical effects for a given chopper angle should be canceled when subtracted from another OFF spectra at the same chopper position. Two baseline catalogs are

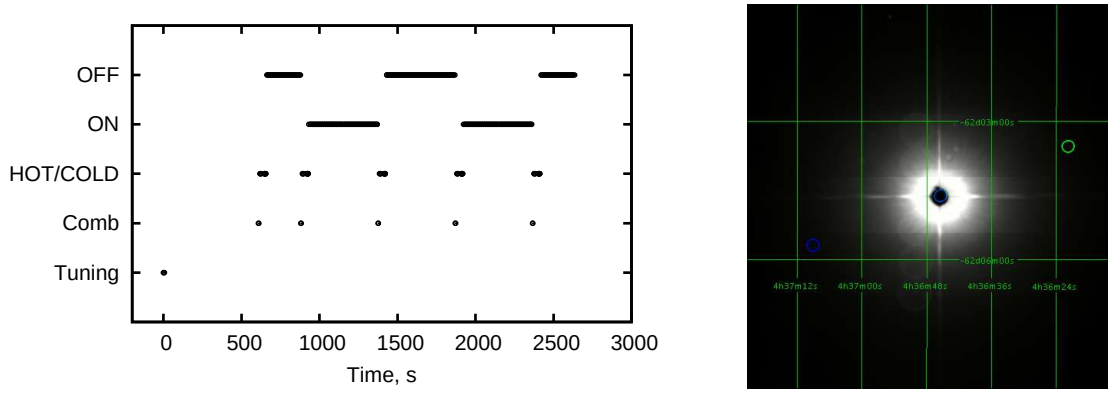

(a) Observation time-line

(b) ON/OFF Sky positions

Figure 3.25: Summary of the observation time line and sky position for the dual beam switch observation 1342190743. The blue circles in the sky image represent the ON_{chop1} and OFF_{chop2} beam positions and size while the green circle represent the ON_{chop2} and OFF_{chop1} positions. The image shown is a J band (1.25μm) image from the 2Mass survey[114] with the grid (Equatorial J2000) and beam positions added using the Herschel observation tool, HSpot[33].

then created which are appended together to create a larger baseline catalog. The baseline catalog equation for the 2 chopper positions looks like:

$$\frac{OFF_{chop1,i} - OFF_{chop1,j}}{HOT_k \quad - COLD_k}, \frac{OFF_{chop2,i} - OFF_{chop2,j}}{HOT_k \quad - COLD_k} \tag{3.10}$$

Dual beam switch baseline correction

The process of extracting a baseline profile from the baseline catalog, follows the same process as that detailed in the position switch flow chart shown in figure 3.19 except that for the baseline catalog generation the two OFF chop positions are kept separate. As before, each catalog and science spectra is rebinned for quicker comparison and a subset of catalog spectra are selected for further processing. A flatness measure is calculated of the residual between the science spectra and the subset of baseline spectra. The catalog spectra which produces the flattest residual is chosen as the best match spectra.

Figure 3.26 provides an overview of the baseline correction for first 16 spectra. The intensity range is comparable to the position switch data shown earlier in figure 3.20. It is obvious that the degree of baseline scatter is much less for the DBS mode compared with the position switch mode discussed earlier. Figure 3.27 shows the average of the first 40 spectra with the standard calibration routine and with the baselines corrected. From the average spectra one can see a weak ^{12}CO line. This example demonstrates the need for multiple integrations in order to reduce the system noise and detect weak lines previously masked by the system noise.

Figure 3.28 details the degree of baseline scatter seen for normally calibrated data and baseline corrected data. The points on the plot correspond to the mean intensity for each spectra across the IF band while the error bars represent the absolute difference between the

maximum and minimum intensity value. From this plot it is apparent that with the application of the baseline correction process the degree of baseline scatter and standing wave amplitude is greatly reduced.

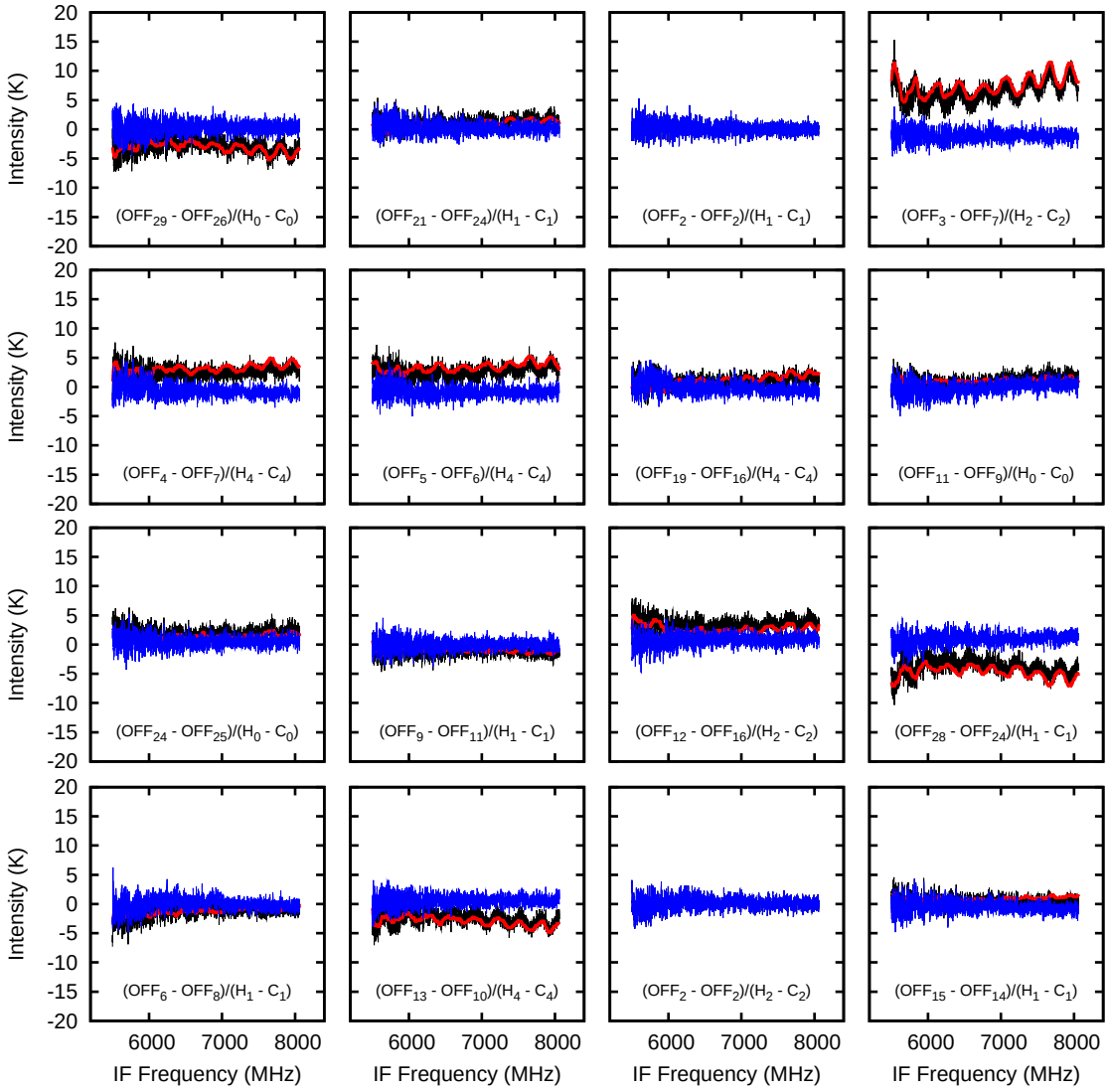

Figure 3.26: Baseline correction of the first 16 spectra for the dual beam switch observation with obsid 1342190743. The original data is shown in black, the baseline spectra used to correct the standing wave is shown in red and the corrected data is shown in blue. The sequence of OFF spectra and HOT/COLD pair used to generate the baseline profile is labeled on each figure. For this example all OFF spectra are taken from the same chop angle.

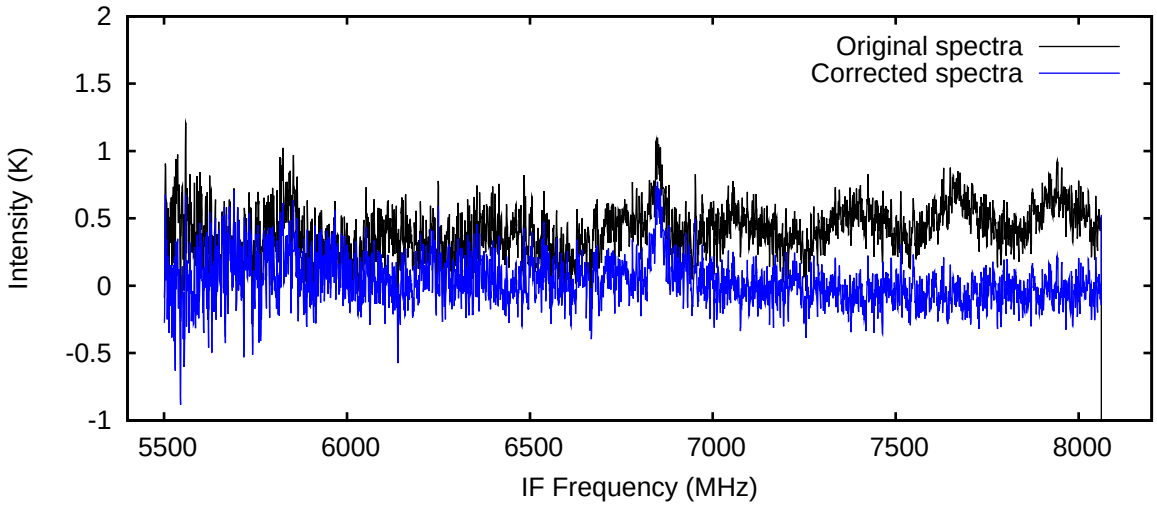

Figure 3.27: Average of first 40 spectra of the dual beam switch observation 1342190743 before and after baseline correction. The observation is taken at an LO frequency of 1500.444 GHz which places the ^{12}CO (13-12) with a frequency of 1496.923 GHz in the lower side band at an IF frequency of $\sim$ 6800 MHz (after the IF 10.4 GHz up conversion, see figure 3.3).

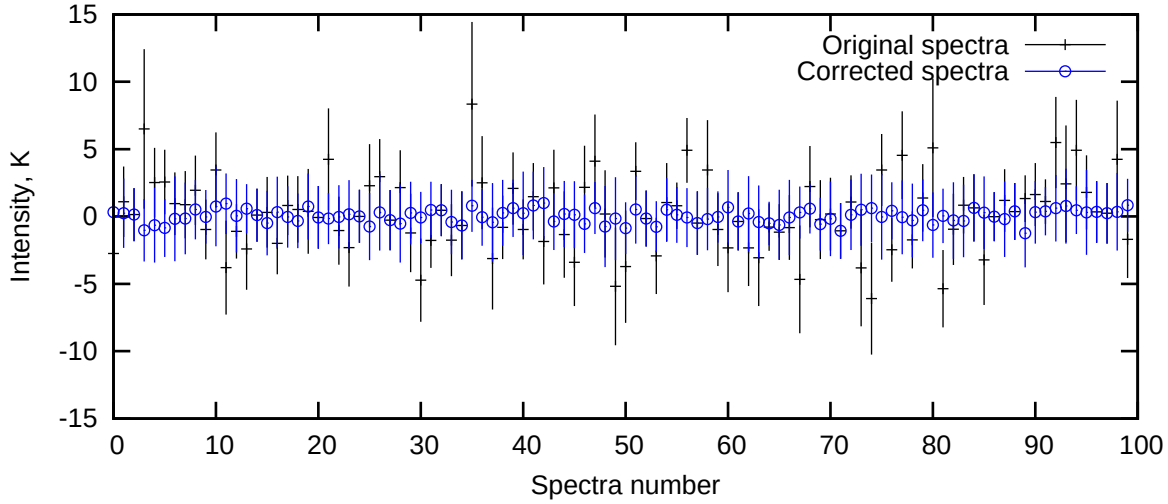

Figure 3.28: Comparison of baseline scatter for the first 100 spectra before and after baseline correction. The data plotted is the mean baseline intensity for each spectra, the Y error bars represent the absolute difference between the maximum and minimum intensity values.

3.4.3 Future work

The baseline catalog approach has been demonstrated for 3 different observation modes. The point observation and dual beam observations detailed in the previous sections had long integration times, which provided a useful sandbox to test the catalog approach. The baseline catalog was generated from the OFF observations within the observation and this was then used to correct the science data. The gas cell observation demonstrates a more generic approach to the baseline correction process. Since the gas cell data has a very limited amount of OFF spectra for each observation, the baseline catalog was generated from other observations taken at different times and at different LO frequencies.

A number of observation modes still remain untested, this section describes the observation modes still untested and summarizes the work needed to bring the baseline catalog approach from a prototype to a fully developed pipeline module capable of handling all observation modes.

3.4.3.1 Spectral scans

Spectral scans consist of multiple observations at different LO frequencies. They normally have short integration times at each LO frequency and rely on the deconvolution algorithm and the overlapping IF regions to reduce the noise. Baseline correction of spectral scan data will require an external baseline catalog as there will not be enough OFF spectra at the same LO frequency to generate a sufficient baseline catalog. Further work is needed to demonstrate the application of a baseline catalog generated at one LO frequency being applied to science data at another LO frequency. The gas cell baseline correction method has demonstrated that this is feasible. Figure 3.12 on page 86 shows an example where the baseline catalog spectra had an LO frequency of 1764.086 GHz and was used to correct data taken at an LO frequency of 1730.01 GHz.

3.4.3.2 Map observation

HIFI map observations can be taken using two different telescope slew modes. For the raster map mode the telescope is discreetly pointed at predetermined map points much like a point observation except multiple points are observed. For an on-the-fly (OTF) mode the telescope is slewed and the data is taken while the telescope is moving. Using the speed of the slew and the starting point the map can be reconstructed from the data. From a baseline correction point of view the approach is the same as that described already. Map observations normally take a suitable amount of OFF spectra which can be used to generate a baseline catalog from the data or alternatively the data can be corrected using an external catalog.

3.4.3.3 Frequency switch observation

The frequency switch observation mode is similar to the load chop observation in that it requires no slewing of the telescope when taking an OFF spectra. However, instead of observing the internal calibration load by moving the chopper the LO frequency is changed, this is known as a frequency switch. Depending on the width of the line being observed this frequency switch varies from 40 to 600 MHz. This mode is commonly used in ground based heterodyne receivers. It is a very efficient use of telescope time since the OFF spectra will also contain line data at a slightly different IF frequency.

The performance of this mode however has been beset with large standing waves and mixer pumping problems. Due to standing waves in the LO signal path the LO power reaching the mixer is frequency modulated. When the LO frequency is changed the LO power also changes, if the LO power pumping the mixer is not equal for both LO frequencies of the frequency switch an impedance mismatch appears resulting in a large standing wave. Careful selection of the LO frequencies can counteract this effect but this requires a priori knowledge of the standing wave behaviour.

Frequency switch mode is currently not recommended for use by the astronomer given the poor baseline quality returned by the instrument. The development of the baseline catalog approach would make this observation mode a viable alternative to load chop mode and also increase the observation efficiency of the instrument. Frequency switch is considered the most efficient observation mode as no slewing is needed and both the ON and OFF phase contains line information. The baseline catalog correction approach would follow the same process as that presented in figure 3.19. For Frequency switch data, ON,OFF,HOT and COLD spectra are taken at both LO frequencies. To generate a baseline catalog only data from the same LO frequencies should be coupled together. Spectra at different LO frequencies will have different optical standing wave behaviour. By coupling spectra with the same LO frequencies together this should remove the standing wave effect leaving only the impedance differences between the phases.

Correcting the baselines however is only part of the problem with the frequency switch mode, careful selection of the LO frequencies and LO pump power is essential to return viable data for baseline correction. LO settling times were quickly seen as a limiting factor in the performance of the frequency switch mode. During a frequency switch observation the LO frequency is quickly changed to reduce the drift time between ON and OFF observation phases. However, with each LO frequency change a settling time is required before data can be taken. If data is taken too early the mixer can be in an unpumped state and hence return corrupted data[43].

To summarize, the Frequency switch observation mode requires modification to both uplink (careful choice of LO frequencies, understanding of LO path standing wave) and downlink (baseline correction routine) before this mode can be recommended to the astronomer.

3.5 Conclusions

In this chapter the development of the HIFI HEB mixer unit was discussed. The various decisions made during the mixer development were detailed. The final mixer IF chain configuration was shown to be sensitive to impedance mismatches between the mixer unit and the first amplifier. This resulted in a significant standing wave seen in the data which was consistent with a cavity between the mixer and the first amplifier. The profile of this standing wave was shown to be LO frequency independent unlike the more common standing wave seen in the optics. The standing wave was shown to be dependent on the mixer state over the course of an observation. If the mixer state changed during the course of a observation this changed the standing wave amplitude resulting in a non optimum cancellation during the cross calibration.

Standard sine fitting standing wave removal techniques were ineffective at removing the standing wave profile and more elaborate removal methods were discussed. Using an electrical model developed by Jacob Kooi efforts were made to mimic a gas cell observation where by two separate mixer states were modeled and then the residual between the 2 states was compared to the residual between 2 gas cell states. The 2 model states were allowed to vary until the best fit to the measured data was reached. This showed a marked improvement over standard sine fitting standing wave removal. However the approach still had significant residuals.

The final approach was to use a catalog of baselines to correct the data. Due to the nature of the standing wave creation. The profile was shown to be quite repeatable and was purely a function of the impedance mismatch between the observation phases. The profile is however mixer unit dependent with each IF chain having a slightly different standing wave profile. This approach was developed using the gas cell test data as a test set. By combining spectra with no spectral line information it was possible to generate a catalog of baselines with no spectral line information. Spectra with significant standing waves could then be corrected by finding a similar standing wave profile in the baseline catalog.

The process of comparing the catalog to the science spectra went through a number of iterations before an optimum approach was found. The final process rebins each spectra from the catalog and science data in 100 MHz bins. This results in a 25 element array which describes each spectra. The arrays are then quickly compared to each other. A subset of catalog spectra that are within a certain threshold of the extracted and the full resolution catalog spectra are compared. The final step is to finalize the subset of catalog spectra which when subtracted from the science data provide the flattest spectra.

The process was developed for gas cell data correction and was also applied to 2 flight observations showing significant standing waves. Using a similar approach to the gas cell data a significant improvement in flight data was shown. For a position switch observation, the mean baseline scatter was reduced from $\pm$5K to $\pm$0.4K. A dual beam switch point observation was also analyzed. While the standing wave were less significant in the position switch observation there was a marked improvement over the original data quality.

The HEB bands make up 30% of the frequency coverage of HIFI and account for 33% of the observing time of the key program projects. The HEB bands also operate at frequencies not visible from ground based telescopes. Furthermore one of the key science goals of HIFI, the observation of the C^+ line at 1.9THz, is only observable in the HEB bands. The poor baseline quality is a major performance issue in these bands limiting the level of science possible. Using the techniques developed by the author in this thesis it is possible to recover a large amount of the data corrupted by poor baseline performance and maximize the science return from these important bands.

A prototype version of the baseline correction has been implemented by the GotC+ key program[69] and showed vastly improved baselines quality over the standard data processing pipeline[99].

Chapter 4

Gas cell test campaign: experimental setup and saturated line analysis

4.1 Introduction

The absence of atmosphere in orbit removes one of the main sources of calibration error for a ground based instrument. In order to take full advantage of this a comprehensive pre-launch instrument level and satellite level test campaign was undertaken to understand more subtle second order calibration uncertainties such as calibration load coupling, standing wave and side band ratio prior to launch. Furthermore given the limited lifetime of the Herschel mission it was necessary that a detailed understanding of the instrument operation and behaviour would be at hand prior to launch to maximize the telescope observing time and minimize the time needed for instrument commissioning and performance verification.

One of the key components in the HIFI instrument level ground test campaign was the gas cell test campaign. Gas cell tests are commonly used in the development and testing of heterodyne instruments [47, 104]. A variety of space missions have also used gas cells as part of a ground test campaign. SWAS (Submillimeter Wave Astronomy Satellite) was the first mission to measure the instrument performance using a gas cell[118]. Unlike the HIFI instrument testing, where the instrument is tested separately from the telescope, the SWAS gas cell tests were undertaken with the complete satellite. The Swedish Odin satellite used a gas cell filled with water vapor to provide a realistic signal source[34]. The TELIS Balloon mission also used a gas cell to determine the performance of its heterodyne spectrometer[130]. They observed OCS between 550 and 650 GHz using an SIS mixer unit similar to that used for HIFI.

The primary motivation for using a gas cell in the HIFI test campaign was the determination of the side band ratio. As detailed in chapter 2 a 5% uncertainty in the side band ratio leads to a 10% uncertainty in the single side band intensity. At the band edges large variations in side band ratio are expected. Knowledge of this variation is necessary to accurately separate

the double side band intensity into its upper and lower side band components. By observing known gases with strong emission lines at various LO frequency it is possible to measure the side band ratio. In addition to determining the side band ratio there are a number of additional instrument effects which can be investigated using the gas cell set up such as:

- Standing wave
- Direction detection
- LO spurs
- Frequency calibration
- Instrument broadening function
- Diplexer calibration

Furthermore the acquisition of a large data base of spectra for a variety of molecular species has a number of ancillary benefits for the operation of the HIFI instrument. Using the gas cell data it is possible to test the instrument pipeline, test data base procedures, developed user support tools (standing wave removal tools) and also test the Herschel Common Science System (HCSS). The commanding of HIFI's operation during a gas cell observation also provided a useful test ground for in flight operation of the instrument.

Observing line rich gases also provides a useful test data set for the side band deconvolution algorithm[20]. Using this algorithm it is possible to separate the upper and lower side band from the double side band spectra. By taking spectra at multiple LO frequencies and tracking the movement of the lines to higher or lower IF frequencies it is possible to deconvolve the spectral lines into their original side bands and produce a single side band spectrum. The deconvolution algorithm takes the side band ratio as an input to generate a more accurate separation of the side bands. However this method requires careful design of the observing routine to function properly.

In this chapter the development of the gas cell test apparatus and choice of test gases is discussed. The test time line for a typical gas cell observation is described. The data processing and calibration of the observed spectra is described. The instrumental effects discussed in the previous list are illustrated using examples from gas cell data.

The side band ratio results extracted from the analysis of molecules with saturated line emission is discussed in this chapter. The data is presented in a gas by gas manner and the instrument effects seen in the data are discussed through examples taken from observed spectra.

It should be noted that the gas cell was designed and built at the Institut d'Astrophysique Spatiale (IAS, Orsay) under a CNES contract, with contributions from E. Dartois, F. Boulanger, J-P Crussaire, D. Deboffle, Y. Longval. David Teyssier (ESAC) and Michel Perault from the École normale supérieure (LERMA, Observatoire de Paris) contributed to the original

gas cell design. David Teyssier led the integration and operation of the gas cell setup in the HIFI calibration setup at Space Research Organisation of the Netherlands (SRON, Groningen). Under his supervision the author was involved in the final stages of data acquisition in the Spring of 2007.

4.1.1 Author's contribution

The author was involved in the latter stages of the data acquisition at SRON Groningen in particular the water observations. The basic scripts for extracting the data and calibration were developed by Bertrand Delforge. The author developed an advanced suite of tools for spectral line analysis and bulk processing of the gascell dataset. The analysis and interpretation of results presented here is the work of the author.

4.2 Gas cell test apparatus

4.2.1 Gas cell design

The main driver for the gas cell dimensions was to provide saturated spectral lines for observation. A saturated spectral line occurs when the density of molecules is such that the radiation emitted for a given transition is absorbed before the radiation can escape the gas. Saturated lines are useful for probing the gain in a given side band. With the correct calibration routine the peak of a saturated line can be directly related to the side band ratio. Saturated lines can be achieved by increasing the pressure of the gas in the gas cell, increasing the temperature or increasing the column depth (optical path through the gas).

For the HIFI gas cell, based on the development of the SWAS gas cell setup[107], it was decided to have a low pressure gas cell and a relatively long optical path length cell of 102.54cm [117]. Typical gas cell path lengths in sub-mm region are 50cm[47, 104]. In order to avoid line blending in complex molecules the gas cell was designed to have a minimum pressure of 0.1 mBar. Figure 4.1 shows the variation in signal transmission for the spectral line peaks of ^{12}CO,^{13}CO and OCS for various gas cell pressures and path lengths. A saturated line is one with zero transmission. Figure 4.1(d) shows the line profile of the 5-6 transition of ^{12}CO at a frequency of 691473.0763MHz as it approaches saturation, note the flat top line peak indicative of a saturated line.

An additional requirement of the gas cell set up was to have a portable test apparatus which could be easily attached and detached from the HIFI main test cryostat. The gas cell was designed to be compact man portable apparatus. Standard gas cells are simply a cylinder with windows and valves attached on either side through which the gas is observed. For the HIFI gas cell internal optics were designed to maximize the optical path length while keeping the overall size to a minimum. Using an Offner system this maximizes the optical path length

through the gas while having little effect on the beam shape coming from the loads, see figure 4.2 for schematic of the gas cell optical layout.

The gas cell itself consists of a glass open ended cylinder with 2 port holes half way down its length, see figure 4.3. One porthole is used to pump the gas in and out of the system. The second port hole is used to insert temperature and pressure gauges. Based on the recommendation of the SWAS gas cell report[107], the gas cell is made from glass (Borosilicate glass DURAN) instead of metal to avoid contamination of the gas cell with "sticky" gases such as water or formaldehyde which would adhere to metal walls. The internal aluminum mirrors are gold coated to avoid corrosion of their surfaces. Furthermore the plumbing system for moving the gases into the cell is made from with glass joints and Teflon covered piping to avoid cross contamination between different gases.

The ends of the gas cell cylinder are sealed with 2 metal plates, see figure 4.3. The lower base contains the Mylar windows through which the signal transits. The windows and mirrors are designed to reduce the effect of standing waves in the system. This was achieved by avoiding directly perpendicular surfaces in the optical path with each window having a tilt to avoid reflected signal along the optical path. The top cover for the gas cell cylinder contains the internal gas cell optics with a curved primary mirror on the inside of the cover. The secondary mirror shown in figure 4.2 is attached to the top plate through two metal arms. All mirrors are made out of metal, with a gold+epoxy coating of surface accuracy of order 0.1μm allowing for operation at higher frequencies.

The gas cell is mounted after the Hot/Cold load source, see figure 4.3. The Hot/Cold load source contains a rotating mirror that is used to select the source signal that is seen by HIFI through the gas cell. The cold load, at a temperature of 80K, is mounted on top of the calibration load unit while the hot load, at a temperature of 300K, is mounted at the bottom. The gas cell output signal is directed into the HIFI re-imager. The re-imager mimics the Herschel telescope optics and presents a similar beam size and shape to the HIFI internal optics.

To achieve a vacuum pump level of 10^{-5} bar a two stage pump system is used. To go to 0.1mbar one primary pump is used (Adixen-Alcatel ACP 28) and a second stage turbo pump is to used to reduce the pressure to 10^{-5} bar (Adixen-Alcatel ATP 150). A 10^{-5} bar level is needed to measured the transmission through the gas cell with no gas present. An overview of the gas cell pump system is shown in figure 4.4(a). Figure 4.4(b) shows the sample holder for the gas cell sample.

4.2.2 Calibration gases

The choice of calibration gases was a trade off between 5 characteristics, were lines available in the HIFI frequency range, was the gas dangerous, was it lightly to corrode the gas cell and equipment, was it readily available (not difficult to source) and how well understood was the

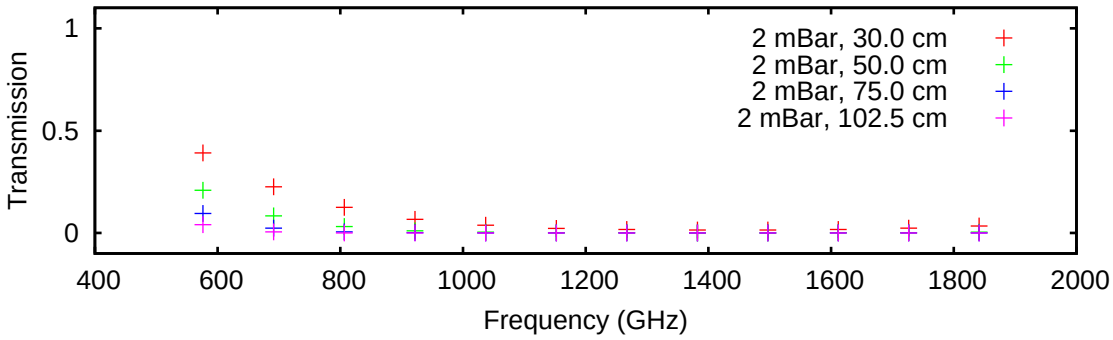

(a) ^{12}CO transmission

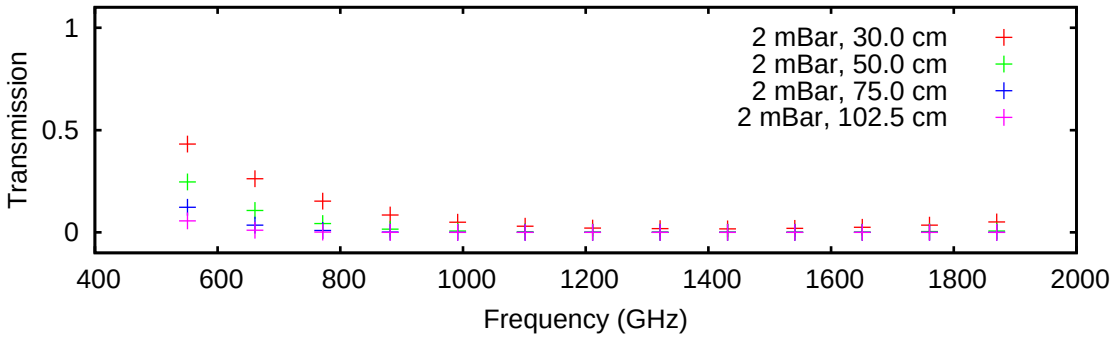

(b) ^{13}CO transmission

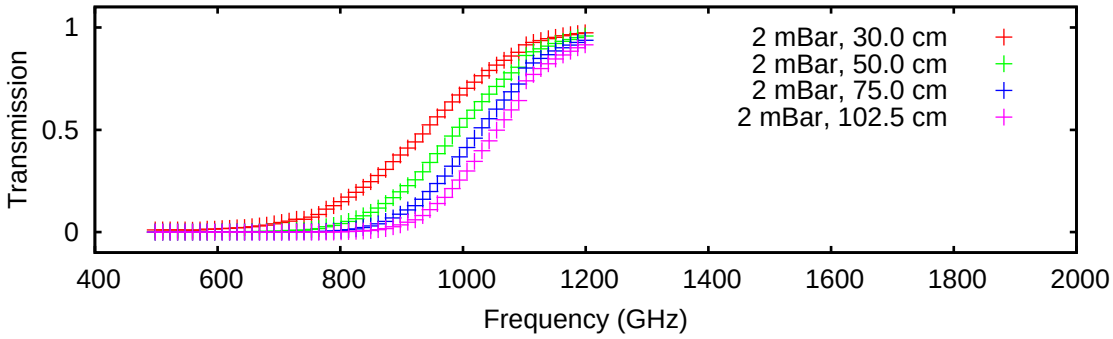

(c) OCS transmission

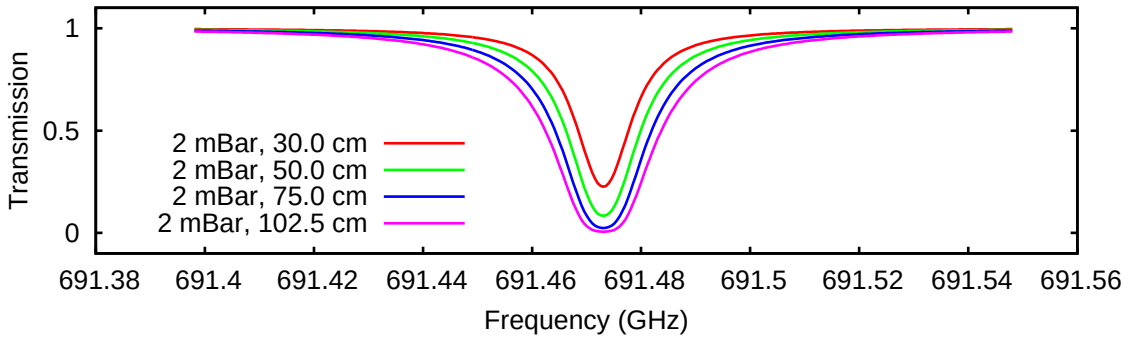

(d) Zoom on the 5 - 6 transition of ^{12}CO line (691.473 GHz) show the flattening of the line center as the line becomes saturated

Figure 4.1: Peak line transmission for ^{12}CO, ^{13}CO and OCS for a 2mbar gas cell pressure and a variety of gas cell path lengths. The transmission properties are modeled for a gas temperature of 296K.

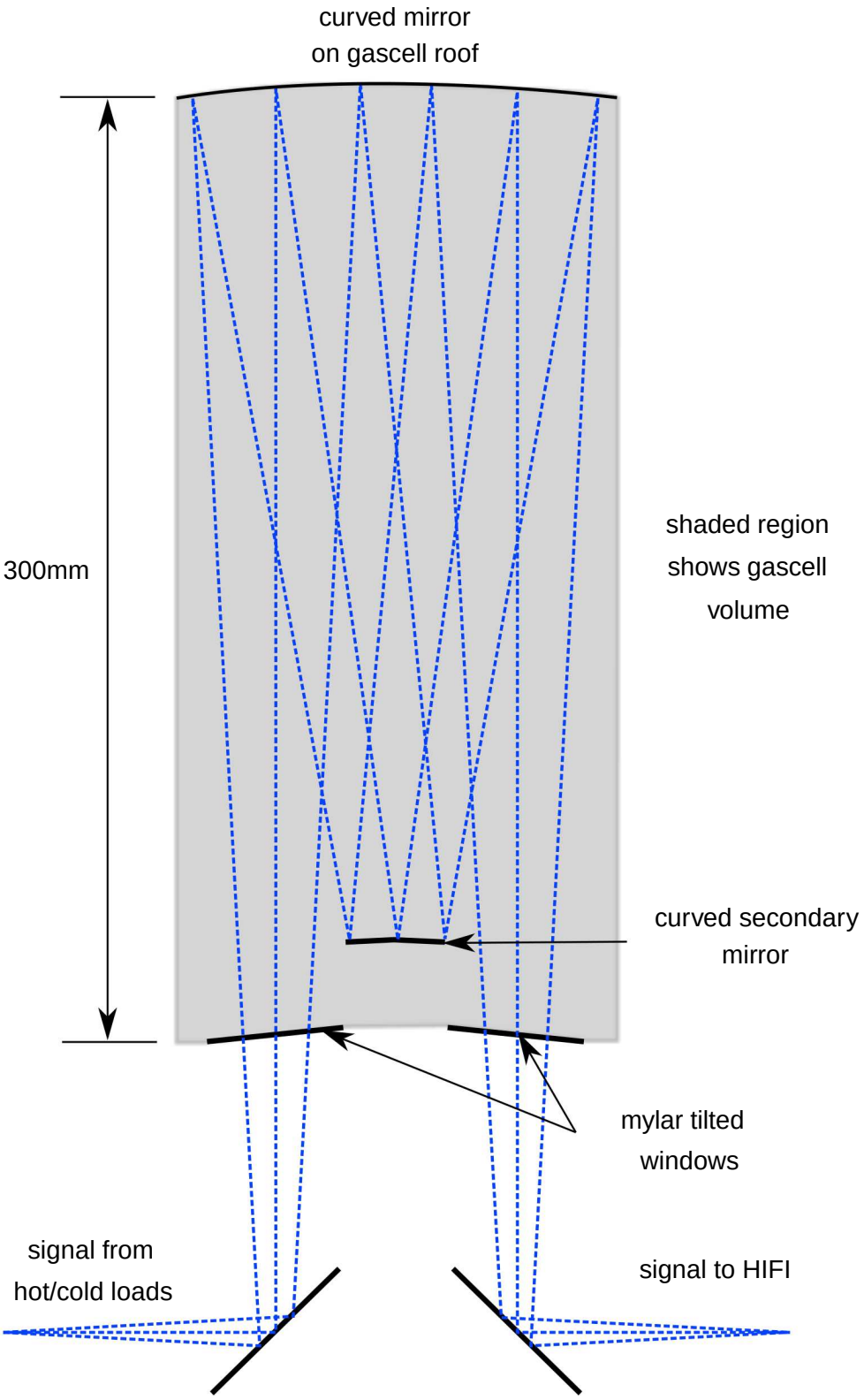

Figure 4.2: Gas cell Offner multiple optical path lay out

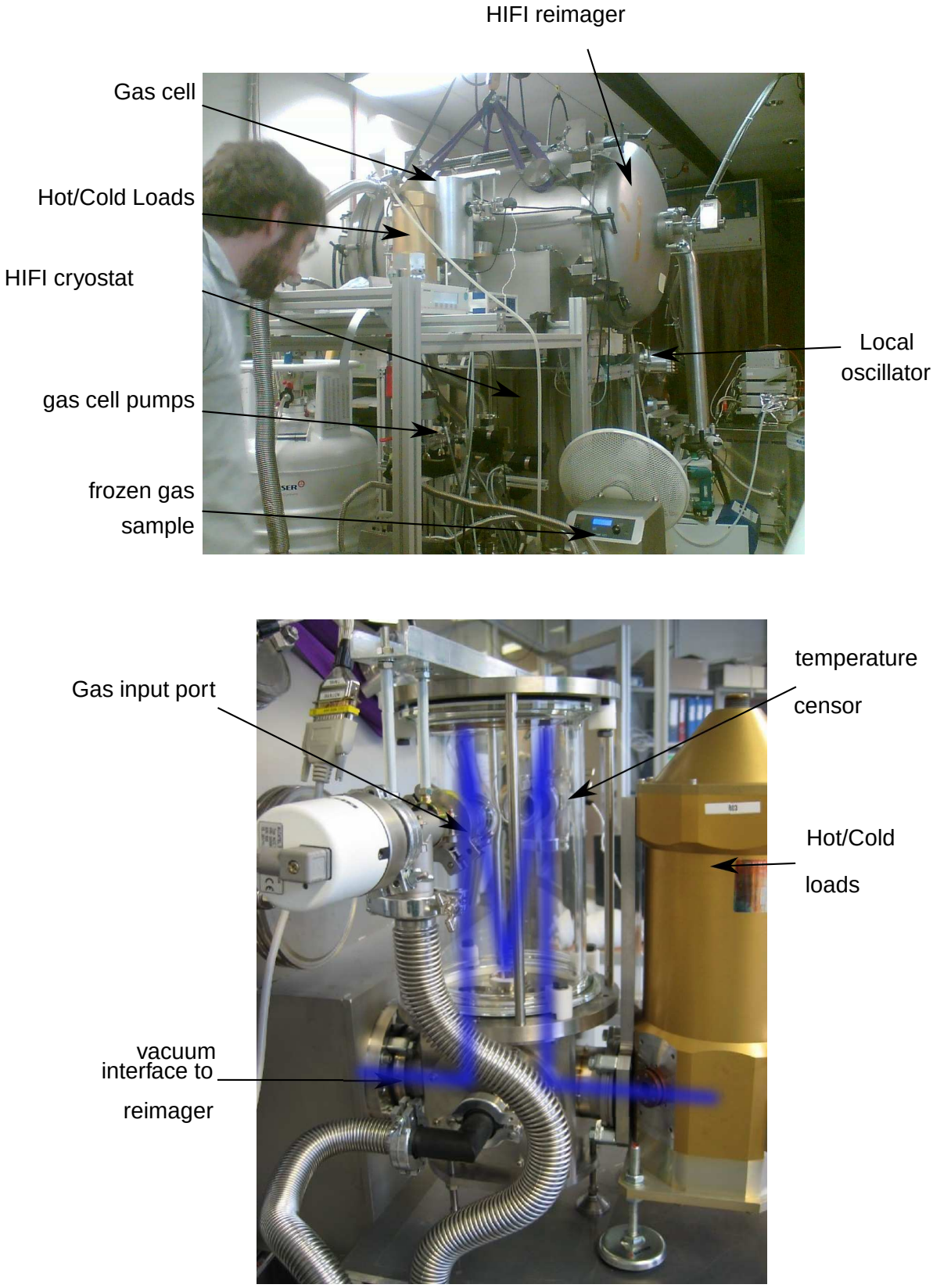

Figure 4.3: Images of gas cell test setup. Upper image shows a broad view of the test environment at SRON Groningen during the instrument level test campaign of 2007. The lower image shows a close up of the gas cell without its metal cover attached to the hot/cold source unit and the reimager

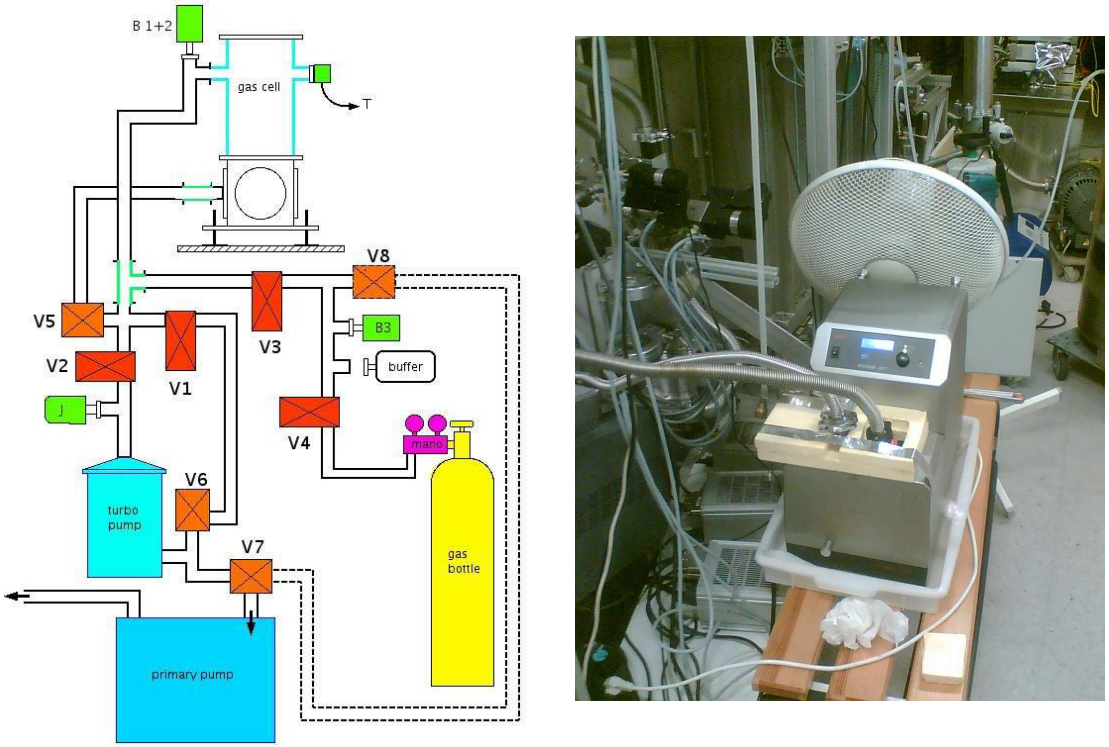

(a) Schematic of gas cell pump system

(b) Picture of gas cell sample holder

Figure 4.4: Gas cell pump system

molecule (complete line list, line intensity, pressure broadening parameters).

The gas cell test campaign was undertaken in 2 phases. The first gas cell test phase would use simpler linear molecules with saturated lines to provide a sparsely sampled first pass at measuring the side band ratio. This phase would provide limits to the range of side band ratios possible. The gases chosen were ^{12}CO,^{13}CO and OCS. Observing CO in the gas cell also had an astronomical significance as this is a common molecule observed in space and it was deemed necessary to investigate this portion of the HIFI range. The AOR investigation of Morris & Borys [82] showed that indeed CO and H_2O account for a large portion of the target molecules for map and point observations.

The second test phase would have a finer LO frequency resolution and attempt to cover the entire HIFI frequency converage with a gas cell observation. For this phase of the test campaign more complex line rich molecules were chosen to provide more points to sample the side band ratio. The gases chosen for this phase were CH_3OH,CH_3CN, H_2S and SO_2. However the transitions in the more complex molecules provide low line intensities resulting in little or no line saturation for the gas cell system designed. To extract the side band ratio from this data would require a more sophisticated modeling approach. Additionally for CH_3OH, which is the most used gas of the test campaign, the line frequencies, intensities and pressure broadening are a subject of research among the spectroscopy community and it would require a recursive approach to first extract the line information from the observed data and use this

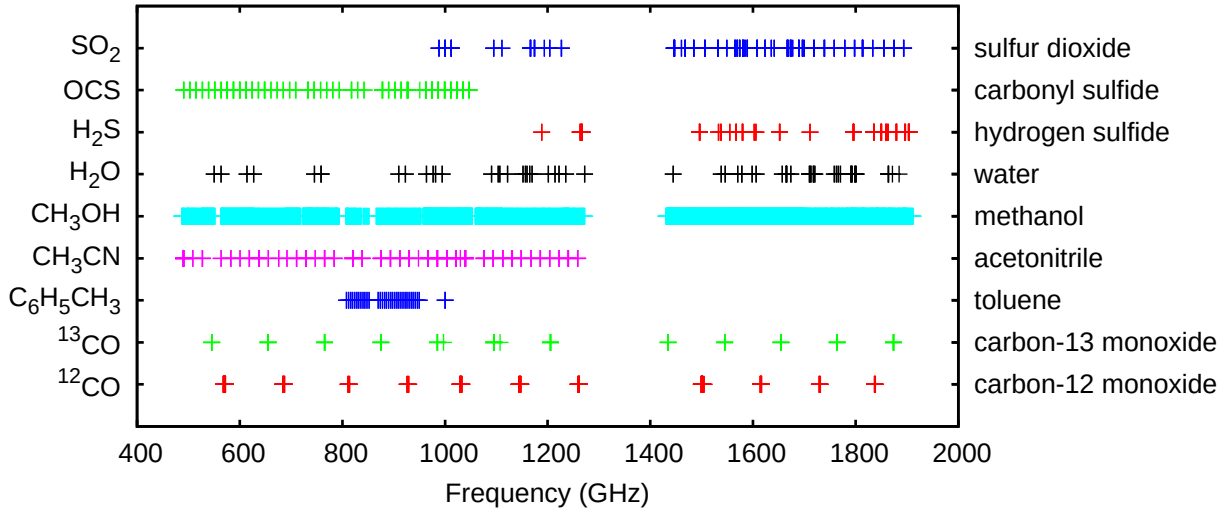

Figure 4.5: Summary of LO frequency coverage for all gases used during the gas cell testing. The common name of each molecule is given on the right hand side of the plot.

Molecule	Name	Safety	Gas cell effect	Observations
^{12}CO	carbon-12 monoxide	F+, T+	none	295
^{13}CO	carbon-13 monoxide	F+, T+	none	76
$C_6H_5CH_3$	toluene	F, Xn	none	69
CH_3CN	acetonitrile	F, Xn	none	192
CH_3OH	methanol	F, T	none	5370
H_2O	water	safe	"sticky"	116
H_2S	hydrogen sulfide	F+, T+, N	"sticky"	149
OCS	carbonyl sulfide	safe	none	165
SO_2	sulfur dioxide	T, C	corrosive	233

Table 4.1: Summary of gases used during the gas cell test campaign. The abbreviations in the safety column are based on the EU Dangerous Substances Directive (1967). F stands for flammable, T stands for Toxic, Xn for harmful, N is stands for Dangerous for the environment and C stands for corrosive. A plus proceeding the letter means highly for example T+ means highly toxic.

data to improve the line model and extract the side band ratio. In addition H_2O was included as a gas cell calibration gas, but was observed towards the end of the test campaign due to its "sticky" nature. Figure 4.5 gives an overview of the LO frequency coverage of each gas. From the figure the significance of methanol is apparent and accounts for 80% of all observations taken during the test campaign.

Table 4.1 provides an overview the number of observations taken with each gas as well as the safety and gas cell safety properties of each gas. The lab in Groningen was adapted to match safety standard particularly the highly toxic CO molecules and H_2S. An alarm was installed in the lab to warn the operator and the gas was exhausted out of the building through a chimney into the atmosphere away from any human contact.

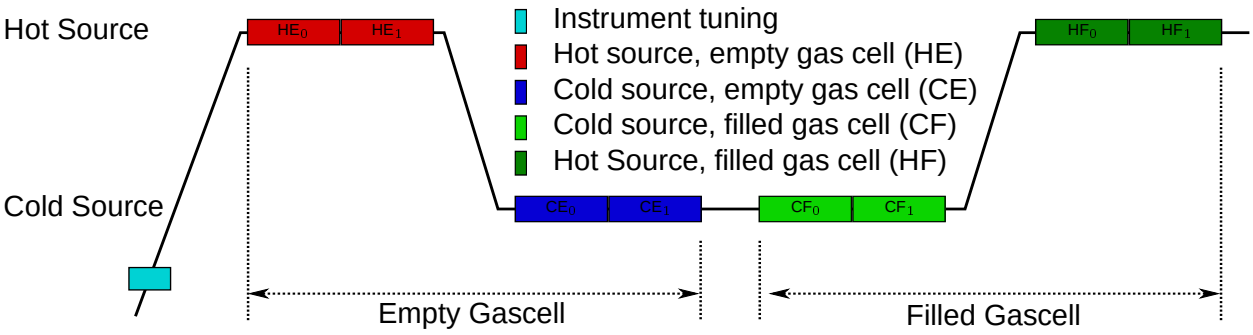

Figure 4.6: Gas cell observation time line

4.2.3 Gas cell operation

The gas cell operation was implemented much like a typical astronomical observation, a hot and cold measurement is taken followed by an observation of the point of interest and a suitable off position. For the gas cell observation the hot cold observations were taken looking at the external calibration loads through an empty gas cell. The gas was then pumped from the gas sample bottle into the gas cell and allowed to thermalize to room temperature. An observation was then made looking at the hot load and then the cold load through the gas at the required pressure. Each gas cell phase is observed for a minimum 4 seconds with higher observation times towards higher frequencies to reduce noise. Figure 4.6 gives an overview of a typical gas cell observation time line. Later observations incorporated the internal cold load to reduce the amount of drift in the system. Drift was especially problematic in the HEB bands resulting in poor baselines behaviour. This problem is discussed in detail in chapter 3.

4.2.4 Data calibration

The data calibration is also similar to a standard astronomical observation. The four phases observed during an observation are combined together to form a calibrated spectrum of sorts. The four phase calibration is necessary to remove the instrument band pass which dominates the recorded signal before the cross calibration, see figure 4.7(a). The difference between the gas cell and astronomical observation is that the data is not converted into units of intensity and is left as ratio of the signal transmission through the gas cell with and without the gas in the optical path. The gas cell spectrum is generated using the following formula:

$$\frac{OFF\ (\mathrm{HF}) - ON\ (\mathrm{CF})}{HOT\ (\mathrm{HE}) - COLD(\mathrm{CE})} \tag{4.1}$$

The resulting spectrum appears as an absorption spectrum, see figure 4.7. This can be confusing on first inspection. The spectrum is not a classic absorption spectrum where the radiation of a source is absorbed by a colder gas between the observer and the radiation source. The gas cell spectra appear in absorption due to the manner the observation phases are combined together in equation 4.1. For the gas cell spectrum the gas temperature is higher than the

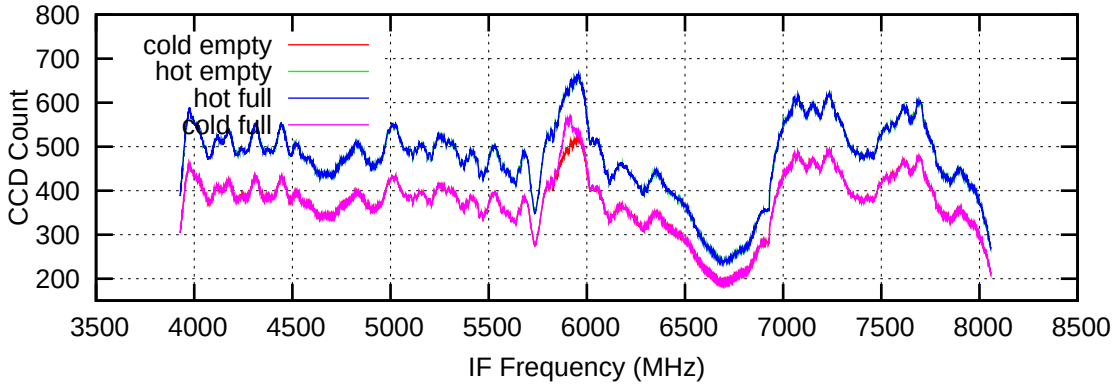

(a) WBS raw data for 4 observation phases

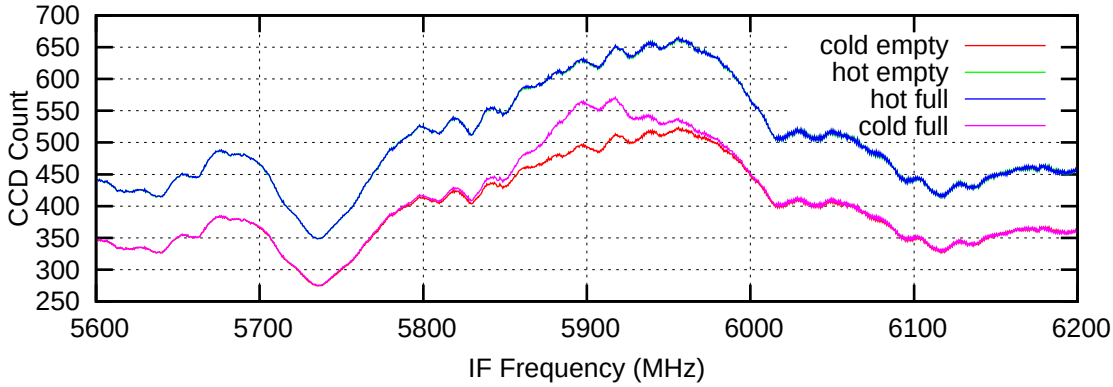

(b) Central IF region showing WBS raw data for ON, OFF and COLD phases

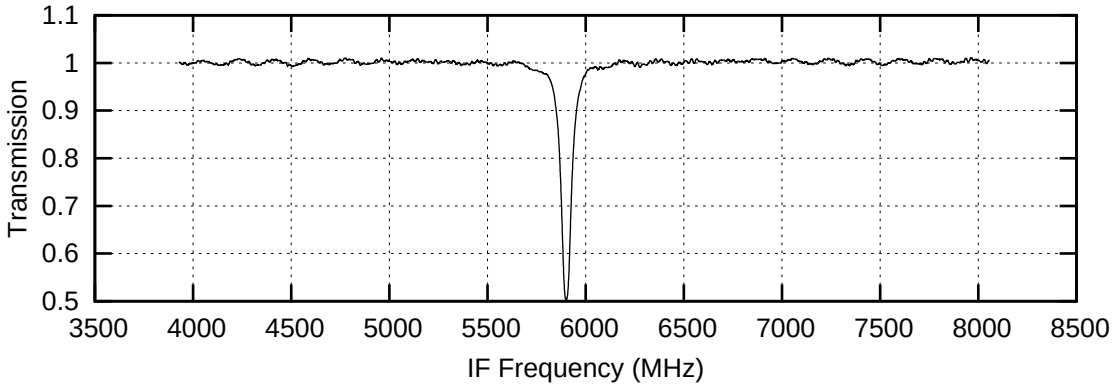

(c) Calibration gas cell data showing a saturated ^{12}CO line

Figure 4.7: Summary of gas cell data calibration showing an example of a saturated ^{12}CO (6-5) transition at a frequency of 691.473 GHz observed at an LO frequency of 685.572GHz. This example shows a side band gain balanced observation where the saturated line peak is at 0.5.

cold load temperature. The gas then appears in emission when viewed against the cold load, with the cold full phase showing both the emission from the cold load and gas, see figure 4.7(a). For the hot full observation phase, the gas emission is not visible as the hot load dominates the emission.

Calibrating the data in this way is useful, by observing a saturated line in one side band the side band ratio is readable directly from the line intensity peak. The example shown in figure 4.7 shows a saturated ^{12}CO (6-5) transition at a gas cell pressure of 4.7mbar observed in the upper side band. Note there are also 2 standing waves visible in the data, a 34 MHz and more prominent 170 MHz standing waves, these are discussed later in this chapter.The LO frequency is tuned to 685.572, the ^{12}CO line at frequency of 691.473 GHz is then down converted to an IF frequency of 5.9 GHz. The CO line observed here is saturated. Since the gas is at similar temperature to the hot load, a saturated line at that frequency is equivalent to the single side band hot load response. The hot load response is broadband and so is seen in both side bands. The line emission however is seen in only one side band. If the gain in the upper and lower side band is equal the peak line emission for a saturated line should be exactly half of the hot load response. Figure 4.7(c) shows that for this LO frequency the mixer gain at this IF frequency is balanced between both side bands.

By calibrating the spectrum as an absorption spectrum the side band ratio can be read directly from the line peak intensity. It must be known beforehand which side band the line is observed in. In the case of figure 4.7 the ^{12}CO line is in the upper side band with an IF frequency of 5.9 GHz. The line peak value of 0.5 is then equal to one minus the normalized side band gain or $1 - G_{ssb}$, where G_{ssb} was defined in equation 2.24 on page 31. If the line was from the upper side band the peak line intensity would be directly equal to G_{ssb}. Furthermore if the line peak in figure 4.7 was 0.4 this would corresponds to a G_{ssb} value of 0.6 i.e. the upper side band accounts for 60% of the total double side band intensity at this IF frequency.

This approach of observing saturated lines in the gas cell forms the basis of the gas cell test campaign. As stated previously the design of the gas cell and choice of calibration gases were driven by the requirement to provide saturated lines for observation. The following section describes the analysis of the data by extracting the peak line intensity of saturated lines and from that extracting the side band ratio.

4.2.5 Data storage

In total 6750 observations were taken during the gas cell test campaign. All the gas cell test data was stored in the same format and using the same procedures as real HIFI astronomical observations. This provided a useful test environment for database tools and security protocols. Initially assessing the database was difficult due to firewall and blocked ports either at SRON Groningen or at the home institutes of the gas cell test users. To overcome this obstacle a local database was generated by Bertrand DelForge which could be downloaded to a local computer

and then quickly accessed via a look up table which pointed to the location of each observation. One of the drawbacks of the online database was the querying facility which was extremely slow during the initial test campaigns. The development of the local database greatly increased the efficiency of the analysis process.

4.3 Gas cell data pre-processing

4.3.1 Introduction

The calibration process described in equation 4.1 and illustrated in figure 4.6 is designed to minimize the effect of drift on the final calibrated spectra and remove systematic effects from the system. However this approach is not always successful and depending on the stability of the system at that particular frequency the resulting spectrum can have a poor quality and maybe useless for calibration proposes. The correction of the data is a common task of the astronomer during a astronomical observation and the gas cell data analysis is no different. Due to the limited amount of frequency coverage great efforts were made during the data processing to recover as much bad data as possible. In this section we describe some of the effects seen in the data and the efforts made to recover the data. Some examples are also given of data that was irrecoverable.

4.3.2 Standing waves

Standing waves in the optics are discussed in detail in section 2.4 while standing waves in the HEB electrical amplification chain are discussed in chapter 3, in particular section 3.4.2.1 on page 82 discusses the process of correcting corrupted baselines in the gas cell data. In this section the topic of standing waves unique to the gas cell setup are discussed along with some examples.

The gas cell test setup was carefully designed to avoid having standing waves in the final spectrum. The optical design avoided having perpendicular surfaces in the optical path and also avoiding sources of vibration in the system. Unfortunately residual standing waves persisted in the system. Standing waves are normally associated with ripples on the continuum. However there are more subtle modulation effects on the spectral lines also. This effect is discussed in section 2.4.

On first inspection it was originally thought that the standing waves seen on the continuum were due to stability or vibration problems in the system. However on closer inspection the standing wave profile was consistent between observations taken at the same LO frequencies and gas cell pressure at different times. The standing wave profile was seen to change as the gas cell pressure was increased. This suggests that the introduction of the gas into the system changes the optical path resulting in the residual standing wave seen on the baseline.

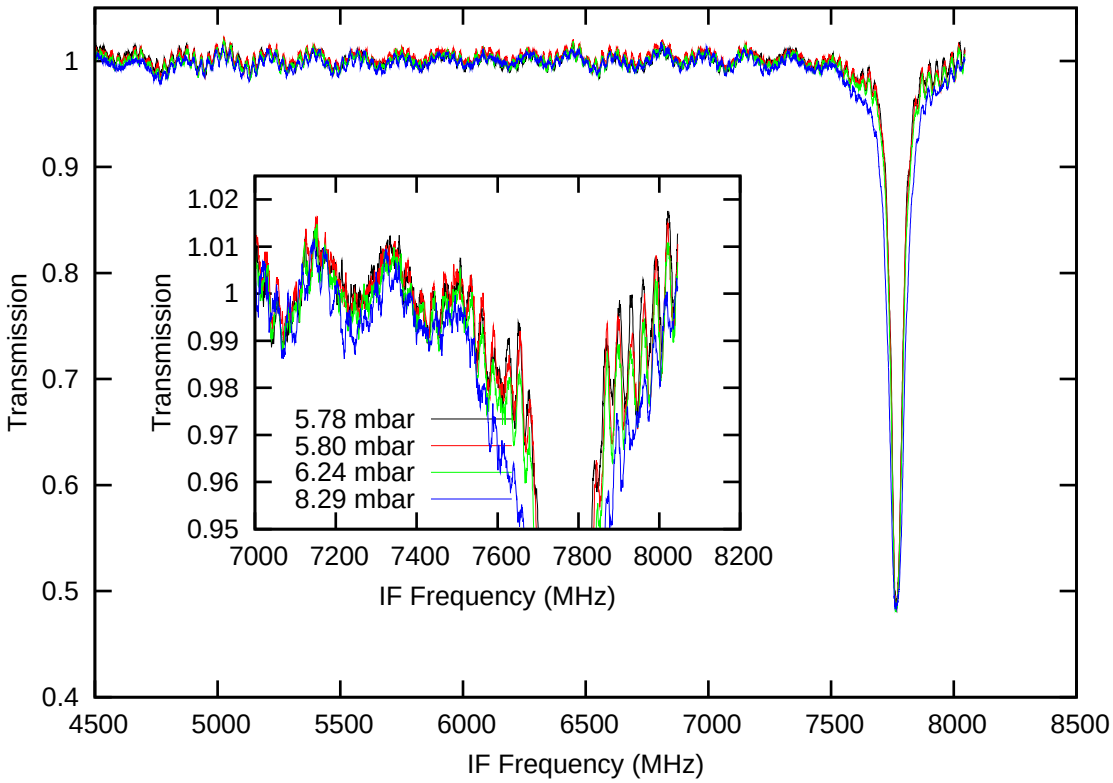

Figure 4.8: Spectra of ^{12}CO observed at an LO frequency of 568.5 GHz at different gas cell pressures. 2 standing waves are seen in the data, one with a period of 34MHz and a second larger amplitude standing wave with a period of 170MHz.

Unfortunately this effect was only realized after the gas cell test campaign had concluded and so a rigorous investigation of this effect was not possible. It may have been possible to determine the refractive index of the gas based on the phase shift between standing wave with and without the gas.

Figure 4.8 shows an example of ^{12}CO gas cell data observed at an LO frequency of 568.5 GHz with 2 standing waves, one with a 34 MHz period and a second stronger standing wave with a 170MHz standing wave. From the data it is apparent that the standing wave profile is consistent for different observations proving that the effect is systematic and not due to instability in the system. From the period of the standing waves it is possible to determine the corresponding cavity length generating the modulation using the following relationship:

$$L = c/2P. \tag{4.2}$$

The 34MHz period standing wave seen in the data corresponds to a path length of 440cm, assuming one half of the reflecting cavity is the mixer plane this places the culprit reflecting surface outside of HIFI and originating in the gas cell set up perhaps from the external calibration loads. The 170MHz standing wave corresponds to a cavity length of 88cm again assuming one half of the reflecting cavity is at the mixer plane the only viable cavity was determined to be the window between HIFI and the local oscillator unit.

The 2 main standing waves seen during the gas cell observation are the 34 MHz and 170MHz standing wave. These optical standing wave are most apparent at longer wavelength bands. Bands 1 & 2 are most effected as their larger beam sizes are more susceptible to the generation of standing waves. Standing waves are occasionally seen in band 3 and 4 also but these can be identified as stability related and are not reproducible between observations unlike the standing waves seen in bands 1 & 2, see figure 4.8. Due to the different quasi optical mixer antenna setup for Bands 5-7 standing waves in the optics are not as prominent. However, as described in chapter 3 bands 6 & 7 have other baseline problems.

The standing waves seen in figure 4.8 shows a worst case scenario of standing waves over the course of the gas cell campaign while the standing wave in the HEB bands are much worse, figure 4.8 is the worst example of the effect of standing waves in gas cell optics. Furthermore the standing waves seen in band 1 and 2 data have a stable amplitude and phase across the IF band which are easily removed using the standing wave removal tools developed by Kester et al. [59].

4.3.3 IF spurs

Spurs are discussed over 2 sections. In this section spurious response in the backend are discussed, LO spurs are discussed in the proceeding section. IF spurs are spiky features that appear in the calibrated data. Spurs can range from single pixels to whole sub-bands and depending on their location can be harmless or render an observation useless. The behaviour of the spur depends on the origin of the spur. IF Spurs can be split into 2 groups, those due to backend saturation and those due to a transient spur which moves over the course of an observation. By looking at the raw uncalibrated data the nature of the spur can be determined.

Saturation of the backend can occur when the attenuation setting of the backend is too low and this results in a saturation of the backend particularly in the acousto optical wide band spectrometer (WBS). Occasionally the local oscillator produces more than one signal. If this additional signal is within the IF bandwidth and has a large enough power it can saturate the backend output. These additional signals are known as LO spurs and are discussed in the next section. Figure 4.9 shows an example of backend saturation in the gas cell phases. In this example the backend is saturated for both the hot and cold load observations. When the data is then calibrated using equation 4.1 this results in a division by numbers close to zero and hence the large spiky signal at these IF channels.

Another source of spurious response in the IF is due to transient pixels in the backend particularly in the lower part of the IF band. These spurs are spread over multiple channels and can saturate some pixels at the center of the spike. These spurs change IF frequency in time also, this results in large residuals in the calibrated data which can corrupt lines that fall at these IF channels. Figure 4.10 shows an example of a ^{12}CO spectral scan. For this observation a spectrum was observed every 100MHz from 572.1 to 568.4 GHz. As the LO increases the

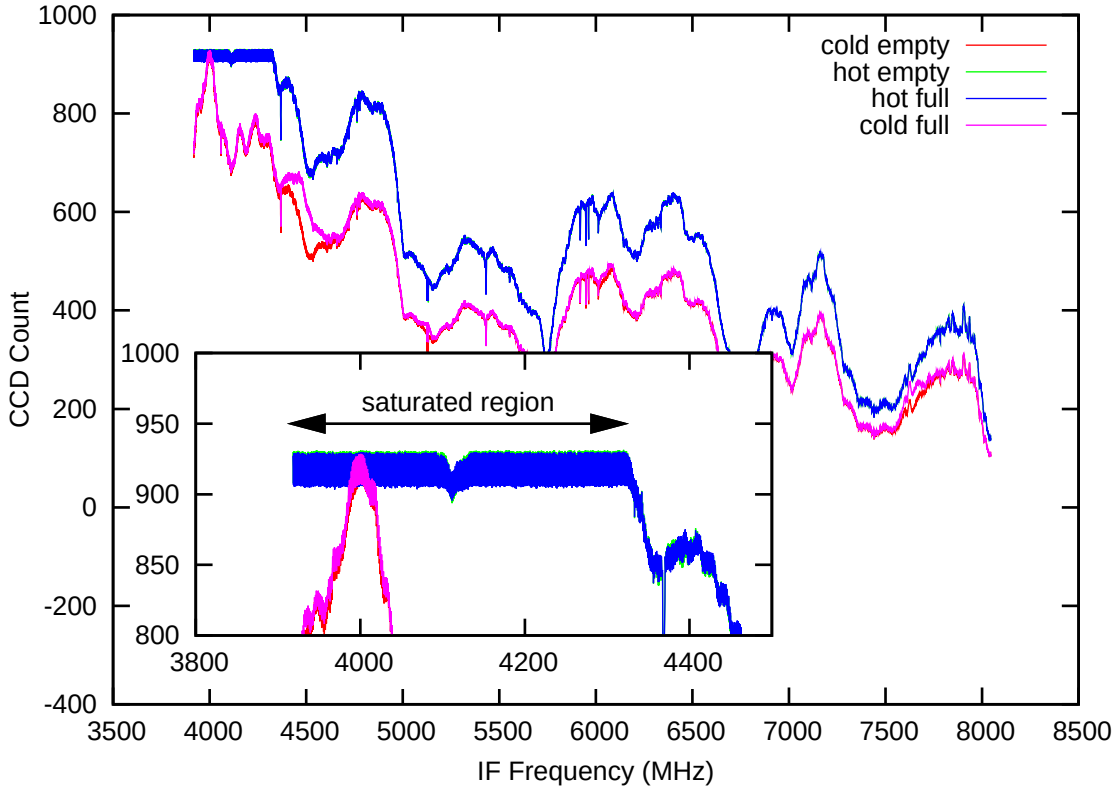

(a) Raw gas cell data showing saturated region between 3.95 and 4.3 GHz for the hot phase calibration. Cold load calibration shows a smaller saturated region centered at 4 GHz.

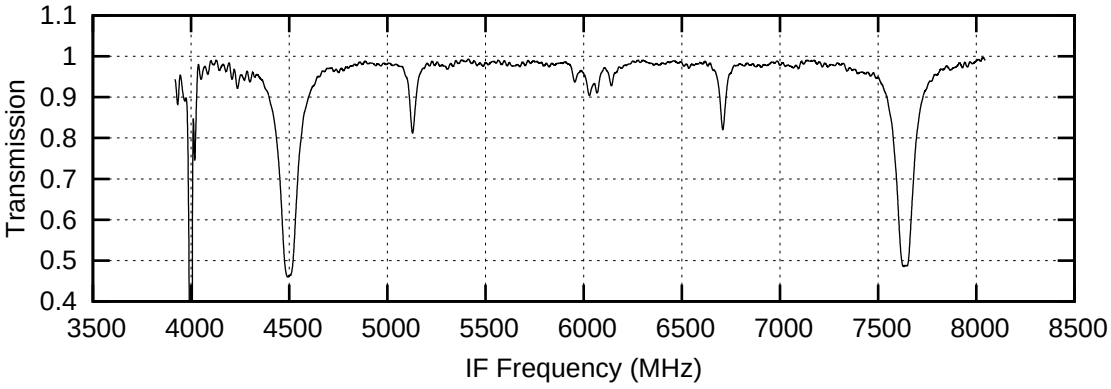

(b) Calibrated OCS spectrum observed at an LO frequency of 514.25 GHz showing spurious behaviour at lower IF frequencies centered on 4GHz.

Figure 4.9: Example of saturated gas cell data resulting in spurious calibrated data in an observation of OCS at an LO frequency of 514.25 GHz.

^{12}CO line at 576.267 GHz is seen to shift to lower IF frequencies, see the map plot in figure 4.10(c). The IF spur is seen to move in the lower IF band with no apparent correlation to the LO frequency.

The example presented in figures 4.9 and 4.10 are from simple molecule with a well known line positions making it easy to determine which IF feature is an actual spectral line and which is a spur. For more complex line rich molecules such as CH_3CN and CH_3OH differentiating between spectral lines and spurs can be difficult. In order to avoid this ambiguity a flagging system was developed by Borys et al. [8] to flag spur affected regions. By analyzing the empty phases of the gas cell data where no line emission is expected the spur regions are flagged. These flagged channels are then propagated into the calibrated data and can be ignored during the data analysis.

4.3.4 LO spurs

As mentioned in the previous section some of the spurs seen in the IF band are due to additional signal produced by the local oscillator unit other than the desired single LO frequency. In the previous section the effect on the final calibrated spectra was discussed. The spurs shown in the previous section were of relatively low power compared to the main LO signal. In the case where the extra LO signal is of comparable power to the main LO signal this can cause an additional down conversion of the sky signal and bring an additional set of upper and lower side bands into the down-converted spectra. This effect can make a line appear weaker that expected.

The source of these additional LO signals is a by-product of the LO signal generation, for a description of the process see Pearson et al. [91]. The LO signal starts from a lower frequency source unit of ∼30GHz and through various stages of amplification and frequency multiplication the required THz signal is produced. In an ideal scenario a single frequency tone of kHz width is produced. This signal is then mixed with the sky signal down-converting 2 side bands of signal to IF frequencies. At certain local oscillator settings additional frequency components are also produced, careful tuning of the multiplier and amplifier settings can remove these additional LO signals, however throughout the gas cell test campaign these spurious signals were present particularly in band 5b. Methods to detect these spurious signals through the LO house keeping data have since being developed to forecast multiple LO signal production[90]. These problematic LO regions have since been corrected through a rigorous in flight test campaign.

Figure 4.11 shows an example of a ^{12}CO spectrum in band 5b. As explained earlier a saturated line in a gain balanced mixer would have a line minimum at 0.5. However when an additional LO signal is produced the line intensity decreases. In figure 4.11 the line minimum is now at 0.75 which would represent an extreme departure from a gain balanced mixer. For this spectrum instead of 2 side bands there are in fact 4 sub-bands. A second LO signal has down converted at additional set of side bands. The side band with the line spectral emission

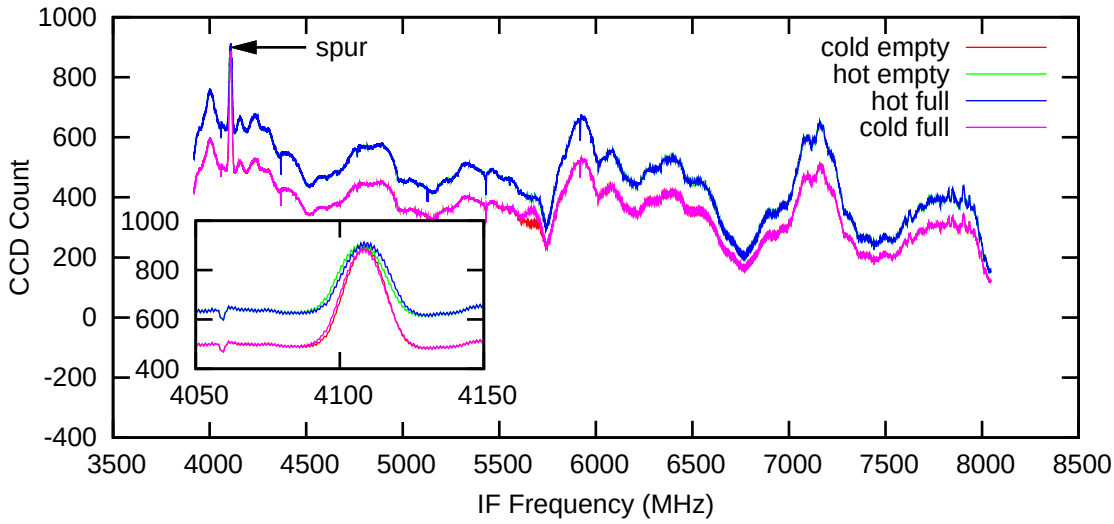

(a) Raw gas cell data showing a spur changing IF position over the course of a gas cell observation, the effect is most noticeable between the hot empty phase and hot full phase.

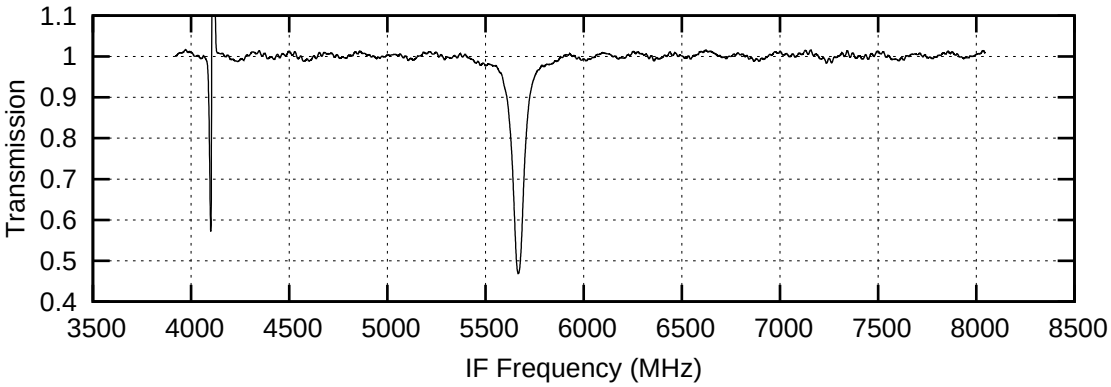

(b) Calibrated ^{12}CO spectrum observed at an LO frequency of 570.6 GHz with a transient spur seen at lower IF frequencies

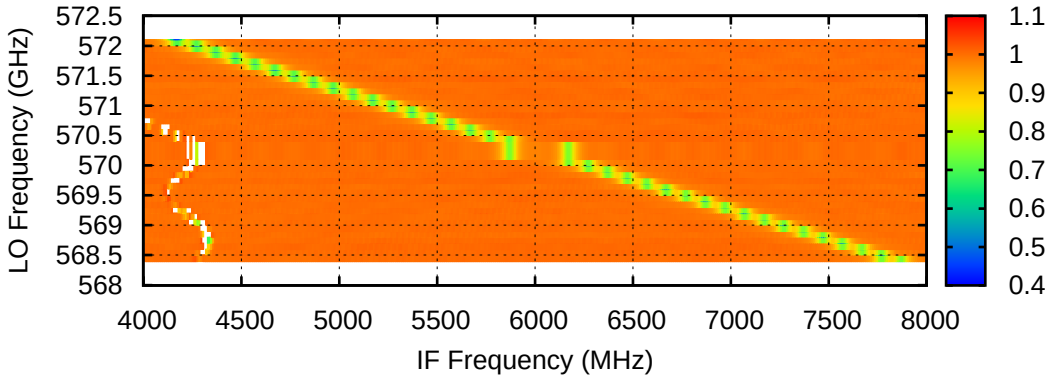

(c) Map plot of a spectral scan of ^{12}CO showing spectrum taken in LO steps of ^{12}CO ranging from 572.1 to 568.4 GHz. The spur can be seen in the lower portion of the IF band and is seen to move in the IF band with no apparent correlation to LO frequency.

Figure 4.10: Example of spur in ^{12}CO which moves in the IF band resulting in large peaks in the calibrated data in the lower part of the IF band.

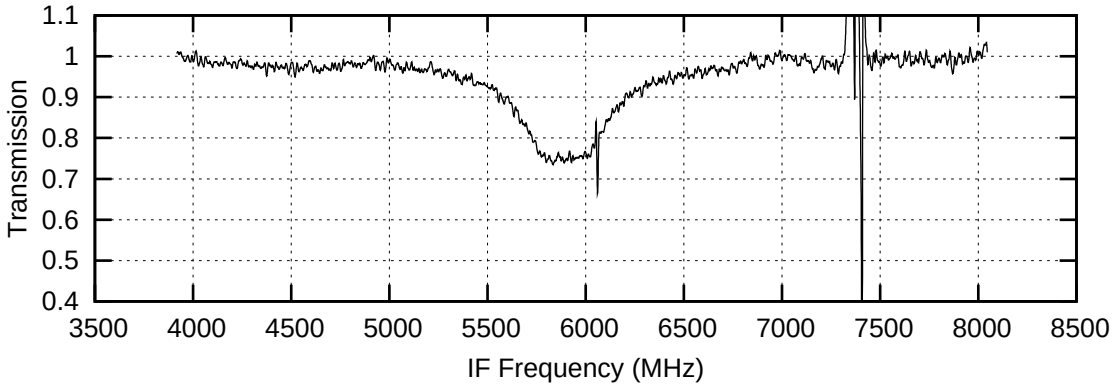

Figure 4.11: Spectra of ^{12}CO observed at an LO frequency of 1261.116 GHz. The line intensity is reduced due to an additional LO signal down converting 2 extra side bands into the IF band. The line peak minimum is seen at 0.75 instead of 0.5 for a gain balanced double side band mixer.

accounts for only a quarter of the total side band signal as opposed to half when the local oscillator is functioning nominally, hence the line minimum of 0.75. Another indication that something is wrong is the additional noise in the spectrum, the continuum noise is 6 times higher compared to other spectra with a nominally functioning LO unit.

The example shown in figure 4.11 illustrates the effect of spurious LO signals on the line intensity. Spurious LO signal can also have a dramatic effect on the number of lines present in the IF band. For line rich sources the addition of extra sub-bands from other LO frequencies can very quickly lead to a large amount of unknown lines appearing in the final spectrum. This could potentially deceive an observer into thinking they have detected a new molecule when in fact they are seeing lines from different frequencies down converted into the double side spectrum. This effect is best illustrated with an example.

CH_3OH was observed at the same LO frequency with 2 different LO chains, LO chain 5b had a significant LO spur problem while LO chain 5a operated nominally. Figure 4.12 shows a comparison between the correct spectrum and the LO spur spectrum. Using the CH_3OH line list one can overlay the expected spectral line positions. For the 5a spectrum the line positions are as expected for the commanded LO frequency. For the 5b spectrum, the spectral lines for the commanded LO frequency of 1241.001 GHz are observed, however numerous other unidentified lines are also seen. Furthermore the line intensities for the corrupted 5b spectrum common to both 5a and 5b have a 60% lower intensity. This suggests that there are potentially 2 different spurious LO signals in addition to the commanded LO frequency down converting the sky signal. Using the line list and a trial and error approach it was possible to determine the frequency of one additional LO frequency. In figure 4.12(a) the line positions for the commanded LO frequency are over plotted with black arrows, the lines positions for a secondary LO signal of 1243.4 GHz are plotted with red arrows. A number of additional spectral lines remain unidentified in the lower part of the IF band which suggest the presence of a third LO frequency as predicted from the reduced line intensities.

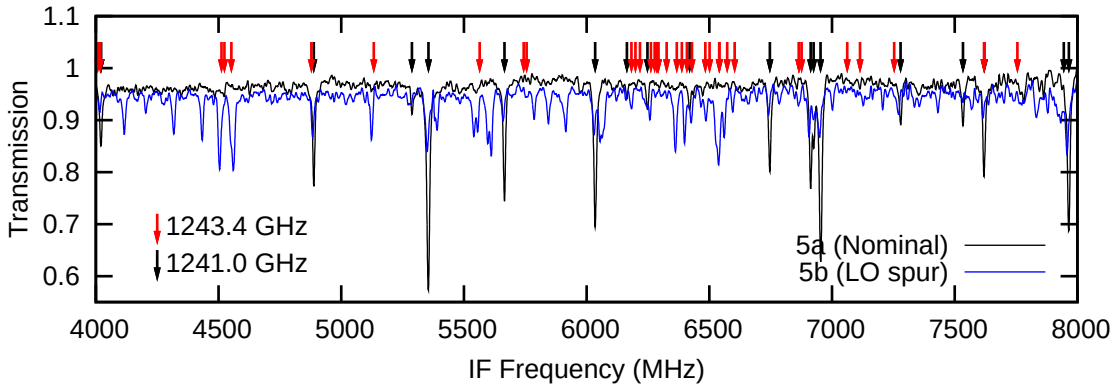

(a) CH_3OH taken with band 5a and band 5b at the same LO frequency of 1241.001 GHz

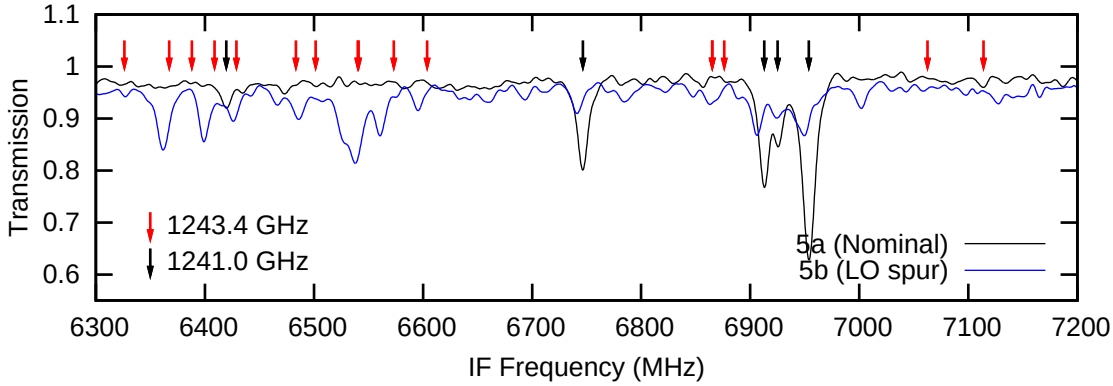

(b) Central region of IF band comparing CH_3OH data at the same LO frequencies but with different LO bands

Figure 4.12: 2 Observations of CH_3OH at an LO frequency if 1241.001 GHz using LO chain 5a and 5b. The 5a spectra shows the correct double side band spectra for methanol at this LO frequency. The 5b spectra shows additional spectral lines from other LO frequencies in addition to the desired LO frequency. Notice the line intensity is greatly reduced for the spur LO signal observation. Black arrows show spectral lines expected at an LO frequency of 1241.001 GHz, red arrows shows spectral lines for a secondary LO frequency at 1243.4GHz.

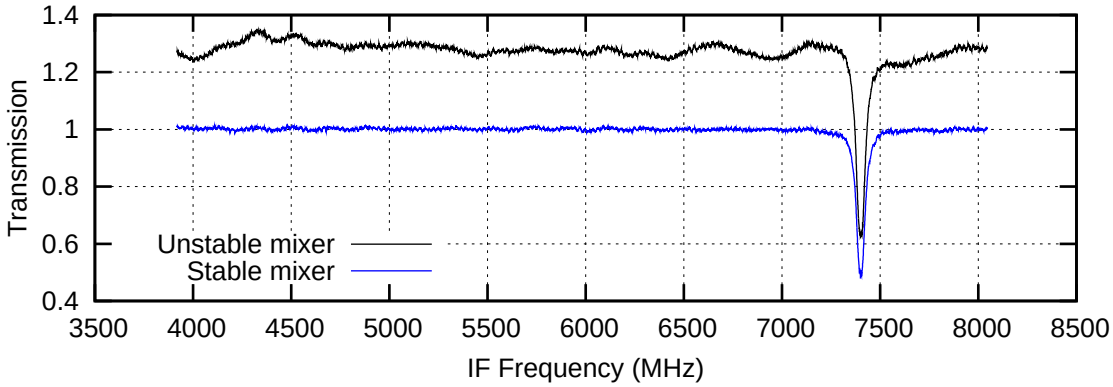

(a) Comparison of 2 spectrum for a stable and unstable system

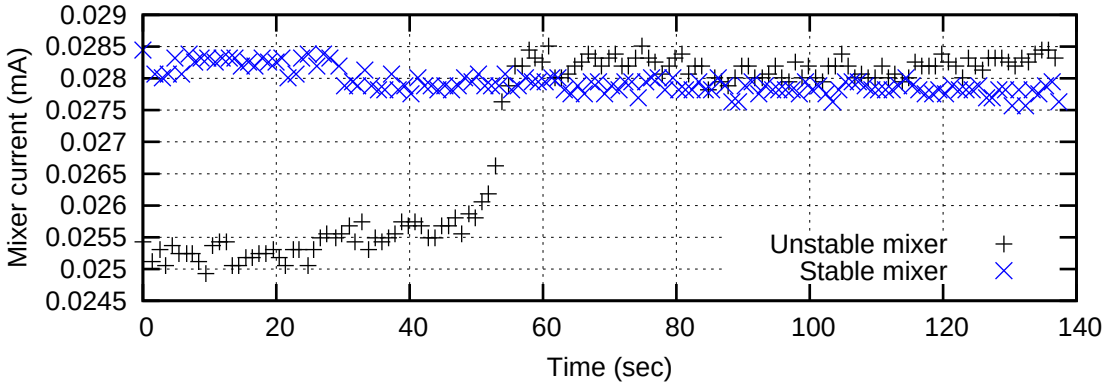

(b) Mixer current time series for a stable and unstable observation

Figure 4.13: Example of 2 ^{12}CO spectra taken with LO band 2a at an LO frequency of 684.072 GHz during a stable and an unstable period.

The main goal of the gas cell test campaign is the determination of the side band ratio for as large a frequency range as possible. Data with spurious LO signals aren't included in this analysis. As each LO frequency has a unique side band ratio for each LO frequency the task of extracting the side band ratio when multiple LO signal are present becomes impossible. Fortunately this effect of multiple LO frequencies observed in the same spectrum is confined to a small region of the band 5b. Unfortunately however the ^{12}CO spectra fall in this region however H_2O spectra were taken at multiple LO frequency throughout the band and provide an alternative source of saturated lines.

4.3.5 Mixer current stability

Having a stable instrument is crucial to returning good quality data. In some cases the instrument is not stable over the course of the observation and a mismatch between observation phases returns a poor quality final calibrated product. Instrument stability is frequency dependent with some bands being more stable than others. There is a general trend that the instrument is less stable at higher frequencies. This can be attributed to the increased complexity of HIFI

towards higher frequencies, the smaller beam sizes susceptible to mechanical oscillations and the decreasing size of the mixer towards higher frequencies. Instrument stability during the HIFI ground testing is discussed by Kooi [61].

System instability in the gas cell manifests itself as poor quality baselines. Figure 4.13(a) shows an example of 2 ^{12}CO spectra using LO band 2a taken during a stable and unstable period. From the mixer current house keeping data shown in figure 4.13(b) one can see the changing mixer current for the unstable spectrum. The resulting baseline distortion appears on first inspection as a standing wave problem, however the offset baseline points to a pass band mismatch between gas cell phases. In this case the LO power has increased during the course of the observation changing the pump state of the mixer and resulting in a change in pass band during the observation.

The sensitivity to change in LO power varies from band to band. The HEB bands are very sensitive to changes in LO power due to the IF chain setup and impedance mismatch between electrical components, this is discussed in detail in chapter 3. However these electrical effects are also seen in the SIS bands but at a much lower level. The same baseline catalog approach used to correct the HEB could be applied to the SIS bands however the amount of distorted spectra available is not sufficient. Perhaps over the course of the Herschel mission enough distorted spectra will be available to correct these effects. Corrupted spectra due to instability in the SIS bands are rare and account for about 5% of the total observations.

Figure 4.13(a) helps illustrate the usefulness of the mixer current housekeeping parameter to flag potentially problematic spectra. By setting a threshold on the standard deviation of the mixer current over the course of an observation it is possible to flag suspect spectra. Using this approach it is possible to automatically flag corrupted spectra and ignore them during the side band ratio analysis.

4.4 Saturated line analysis

4.4.1 Introduction

The previous sections have presented the gas cell design and operation, data acquisition and preprocessing of calibrated data. This section presents the determination of the side band ratio through an analysis of molecules with saturated lines.

Observing saturated spectral lines with HIFI was a critical goal of the gas cell campaign. The selection of gases and design of the gas cell vessel were driven by this requirement. Saturated lines provide a direct probe of the side band ratio. In a gain balanced mixer a saturated line peak in a double side band transmission spectra should have a line peak of 0.5. Any deviation from this points to a gain imbalance. By positioning various saturated lines at various frequencies throughout the HIFI frequency range a measure of the side band ratio can be generated.

Figure 4.5 on page 116 provides an overview of the gases observed. Of these gases only 5

provide saturated lines, ^{12}CO, ^{13}CO, OCS, CH_3CN and H_2O. In the case of OCS saturated lines are only seen up to 800 GHz (see figure 4.1(c)). In this section the process of determining the side band ratio of each of these molecules is discussed. The resulting side band ratios determined for each molecule are then presented for each mixer band.

4.4.2 Side band ratio extraction process

Figure 4.14 provides an overview of the analysis process developed by the author to extract the side band ratio. The first step in the determination of the side band ratio is the extraction of the desired data from the database. For this analysis each LO band was analyzed and processed separately.Using the local data base generated by Bertrand DelForge it is possible to quickly load the raw gas cell data for analysis.

The second step in the analysis is to determine the integrity of the raw data. During the gas cell operation occasionally some observations were taken while only looking at one load. Figure 4.7(a) on page 118 shows an example of the raw gas cell data for a correct gas cell observation. There is a distinct difference between the hot and cold phase CCD count. When there is no difference between the hot and cold load spectra this data is then discarded as no useful information can be taken from the calibrated spectra. Another problem observed in the data was that a phase of the gas cell was missing from the database, without the four phases of the gas cell observation a correctly calibrated spectrum is not possible. In this case the data is also discarded. From the raw CCD data the presence of IF spurs in the data can be established. Using the methods developed by Colin Borys[8] IF channels affected by spurious signals can be flagged and these flags are picked up later in the analysis and are ignored.

Once the integrity of the observation is established, the four phases of the gas cell observation are combined together using equation 4.1. The output is a calibrated spectrum similar to that shown in figure 4.7(c). A second stage of data inspection is then conducted looking at the effect of standing waves on the data. The standing waves seen in band 6&7 and bands 1-5 behave differently and must be treated separately.

For bands 1-5, the standing wave analysis methods developed by Do Kester[59] are used. Figure 4.15 shows an example of a ^{13}CO spectral line in band 1a showing the data before and after standing wave removal. From the figure one can see that the standing wave removal isn't completely effective. The limits of the standing wave removal tool are discussed in section 2.4. The data is finally Gaussian smoothed over 4 channels to remove excess noise in the data. For bands 6&7 the methods described in chapter 3 are used. This method uses a catalog of baselines generated over the course of the gas cell campaign to correct the data. Figure 4.16 shows an example of the baseline correction of a HEB spectrum.

For all the gases observed in the gas cell test campaign a comprehensive line list was available through the JPL[94] and HITRAN[106] line catalogs. The next step in the side band ratio extraction process is to determine which spectral lines are observed at a given LO frequency.

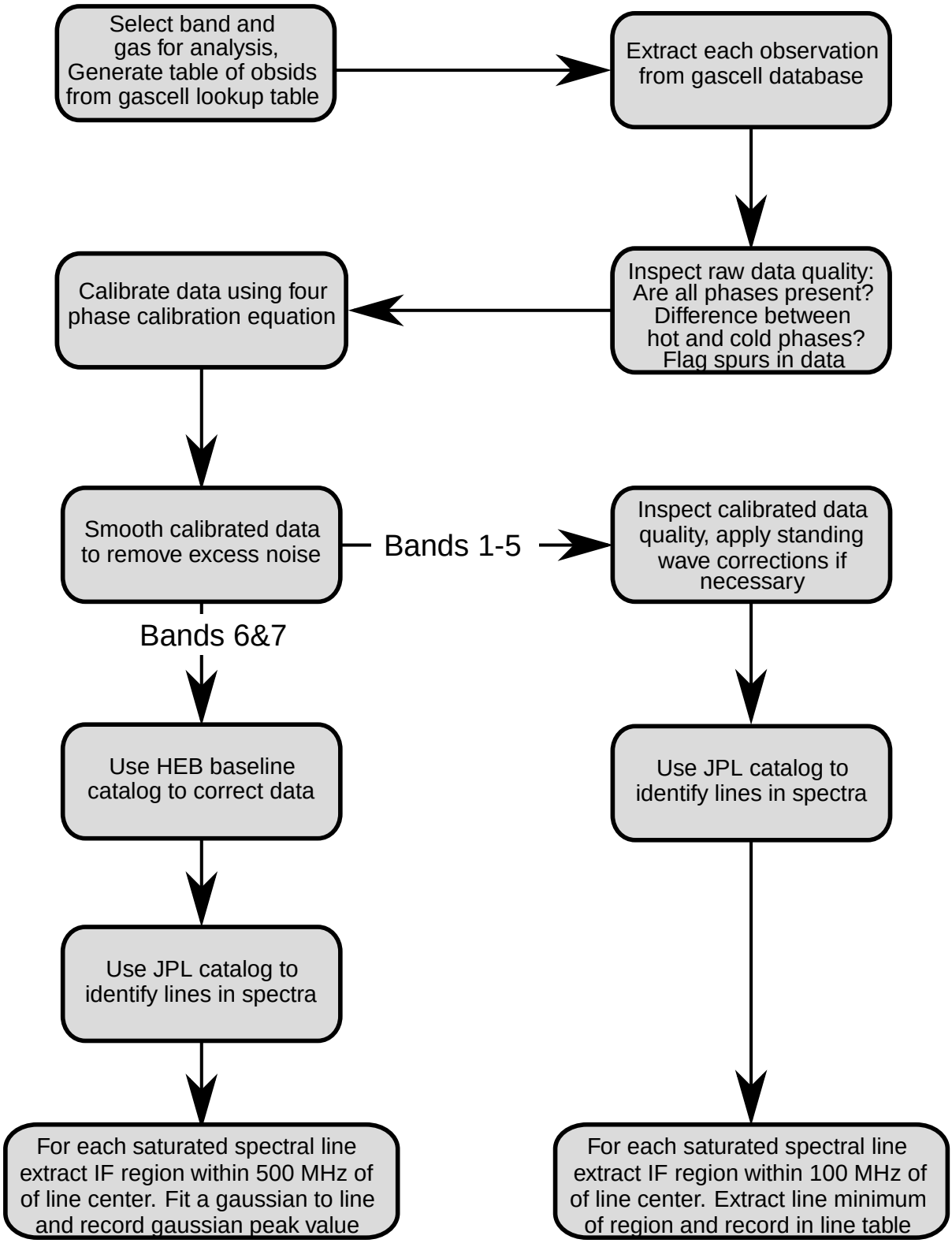

Figure 4.14: Flowchart describing extraction of side band ratio for saturated lines using a simply calculation of the line minimum of an IF region around the line center

This process is simple and involves subtracting the LO frequency from the line frequencies, any line where the absolute difference is between 4-8 GHz (for HEB bands, 2.4-4.8 GHz) is then taken for analysis. Figure 4.15 shows an example of a ^{13}CO observation at 545.249 GHz, the single spectral line at 550.926 GHz is then observed at an IF frequency of 5.677 GHz.

Once the spectral line IF position is determined the line peak and hence side band ratio can be extracted. Due to the high noise in bands 6&7 a Gaussian fit is used to determine the line peak value. For the SIS bands simply smoothing the data is sufficient and the line peak can be read directly from the data. Figure 4.15 shows an example of the procedure in the SIS band. Using the line list a region of 100MHz around the line center is analyzed. In this example the line peak is determined to be 0.513, as the line is the upper side band this corresponds to side band gain ratio, G_{ssb}, of 0.487 (1-0.513). Without baseline correction and data smoothing the line peak would have a value of $\sim$ 0.503. In this example the spectral line has a lower than expected intensity for a saturated line, ideally it should be 0.5 for a gain balanced mixer. To summarize, for this LO frequency and at an IF frequency of 5.677 GHz the fraction of the total signal that comes from the upper side band is 0.487. With this measurement comes a certain degree of uncertainty. For the analysis an error bar is calculated based on the surrounding baseline variability, taking the standard deviation of the baseline around the line position the uncertainty is calculated to be 0.5% of the calculated value. Using this approach poor quality data will have a large error bar allowing for quick identification of problematic observations.

Figure 4.16 shows an example of the procedure in the HEB band. In this example a region of $\pm$ 500 MHz around the line center is taken. A Gaussian is fitted to the shaded region and line peak of the fit is taken as the side band ratio. In this case the line peak is determined to be 0.462. The spectral line has a sky frequency of 1760.486 GHz, the LO frequency was 1764.086 GHz which places the line in the lower side band. Hence the normalized side band ratio, G_{ssb}, for this IF frequency at this LO frequency is 0.462. The normalized side band ratio is defined as the fraction of the total double side band intensity that is from the upper side band for each channel. For this example the fraction of the total intensity that is lower side band intensity was measured. Hence the upper side band fraction or G_{ssb} is 0.462.

The basic rule of thumb is that the line peak intensity for a saturated line observed in the lower side band corresponds directly to the normalized side band ratio, G_{ssb}. Conversely for saturated lines observed in the upper side band the peak line intensity corresponds to 1-G_{ssb}. The following sections describe the analysis of the following molecules, ^{12}CO, ^{13}CO, OCS, CH_3CN and H_2O using the methods described in this section. By combining the side band ratios extracted from these molecules a coarse sampling of the side band ratio across the HIFI frequency range is generated.

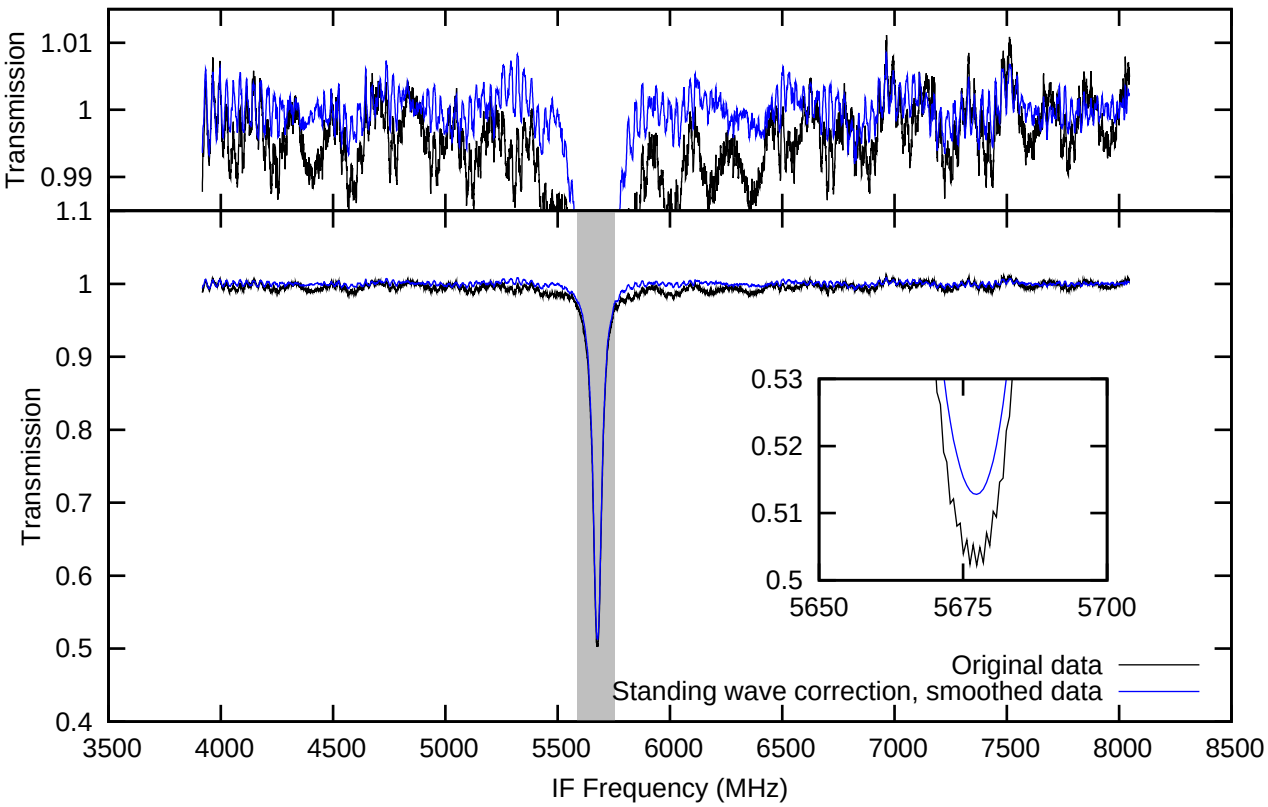

Figure 4.15: Spectrum of ^{13}CO at an LO frequency of 545.249 GHz, the ^{13}CO spectral line has a sky frequency of 550.926 GHz placing the spectral line in the upper side band at an IF frequency of 5.677 GHz. The shaded region highlights the portion of the IF band from which the side band ratio is determined. The peak line intensity is taken as 0.513, which corresponds to a normalized side band ratio, G_{ssb}, of 0.487.

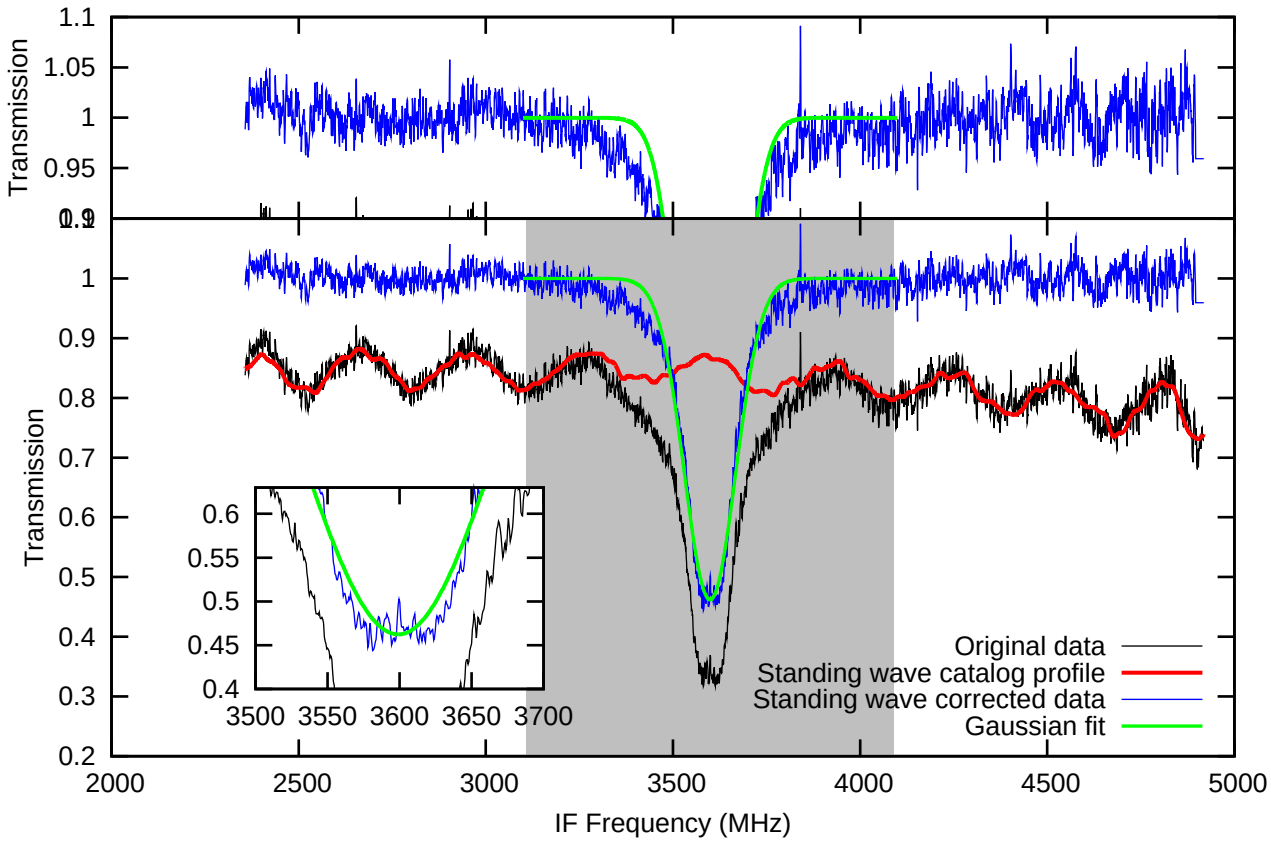

Figure 4.16: Spectrum of ^{13}CO line at 1760.486 GHz at an LO frequency of 1764.086. The spectrum is corrupted due to drift effects during the observation. The baseline is corrected using a matching baseline taken from a catalog of baselines. Due to the high noise in the HEB band the line is fitted with a Gaussian and the line peak of the fit is taken as the normalized side band ratio, G_{ssb}. In this case the side band ratio extracted is 0.462.

Line frequency (GHz)	LO band	observation count	Maximum LO (GHz)	Minimum LO (GHz)
576.268	1b	80	572.101	568.400
691.473	2a	20	687.372	683.574
806.652	3a	10	814.401	810.900
921.800	3b	9	929.552	926.050
1036.912	4a	30	1032.710	1029.110
1151.985	5a	24	1147.586	1144.084
1267.014	5b	25	1261.616	1259.114
1496.923	6a	51	1504.524	1499.274
1611.794	6b	25	1616.402	1614.398
1726.603	6b	10	1731.200	1729.249
1726.603	7a	10	1731.200	1729.249
1841.346	7a	11	1838.295	1836.796
1841.346	7b	11	1838.295	1836.796

Table 4.2: Summary of ^{12}CO gas cell converage showing observed line frequency, LO band coverage and number of spectra taken.

4.4.3 ^{12}CO analysis

^{12}CO is one of the key molecules observed in sub mm astronomy hence ^{12}CO was a key gas during the gas cell campaign. Unfortunately ^{12}CO is simple molecule and produces few spectral lines over the HIFI frequency range. In total 11 different ^{12}CO lines were observed at different LO frequencies and in different side bands, see table 4.2 for a summary. In particular, the (5-4) ^{12}CO transition at a frequency of 576.268 GHz was observed multiple times over the course of the gas cell test campaign at different gas cell pressures and LO frequencies. Figure 4.17(a) shows an example of this spectral line observed at same LO frequency but at different gas cell pressures. From this figure one can see the effect of pressure broadening on the line profile. This effect will be described in more detail in chapter 5. This example demonstrates one of the fundamental principles of the gas cell, that as the pressure is increased the line profile is seen to broaden.

Figure 4.17(b) shows a spectral scan of ^{12}CO taken in LO steps of 100 MHz from 568.4 to 572.1 GHz. In total 38 spectra are shown. For this example the spectral line is saturated. The line intensity is seen to increase toward lower IF frequencies indicating a changing side band ratio. This example is unique as the change in gain across the IF band is large and the number of spectra taken is the largest for any line transition observed during the gas cell campaign. Following the methods described in figure 4.14 the side band ratio is extracted and tabulated. The extracted side band ratio for each LO frequency is plotted in figure 4.17(c). From this figure it is apparent that over this LO frequency range that the side band gain, or the fraction of the upper side band making up the total side band, increases towards higher LO frequencies.

This process of side band ratio extraction is continued for all ^{12}CO lines observed in the

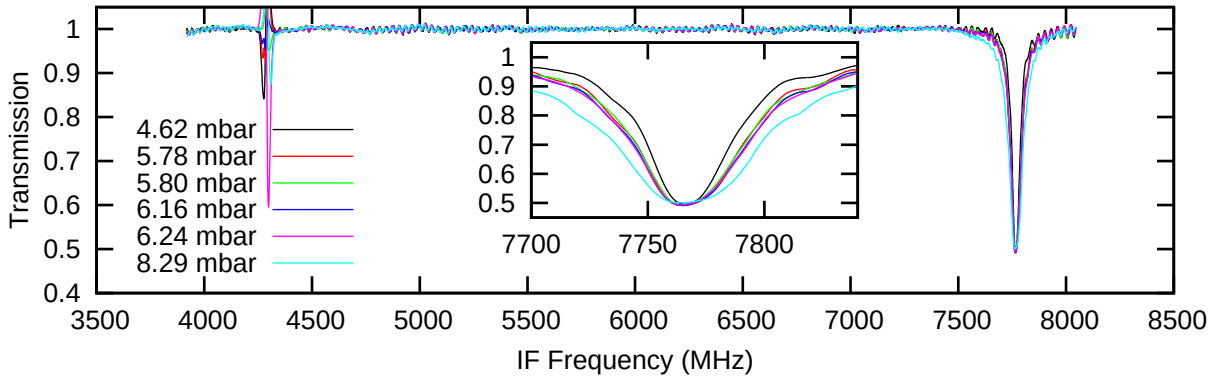

(a) ^{12}CO spectra taken at an LO frequency of 568.501 GHz showing the effect of increased gas cell pressure on the line profile. The line is saturated under these conditions and the peak line intensity is same for all gas cell pressure observed. Note the effect of standing waves on the line profile.

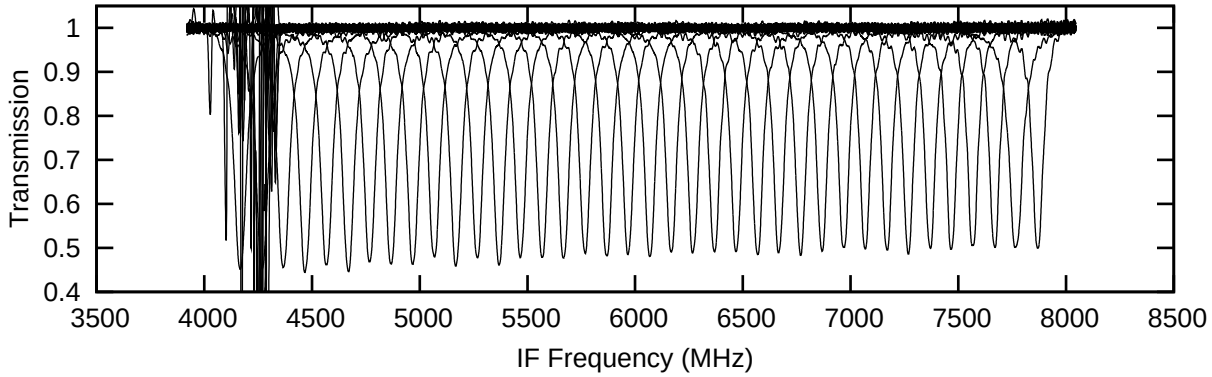

(b) ^{12}CO spectra taken during a spectral scan with LO steps of 100 MHz ranging in frequencies from 568.4 to 572.1 GHz

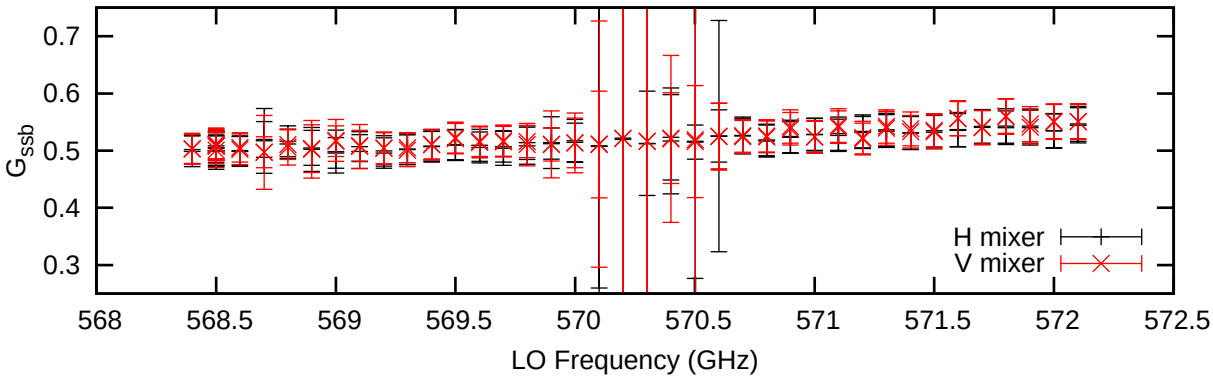

(c) Normalized side band ratio, G_{ssb}, calculated by extracting the line peak value. Error bars are calculated from scatter in continuum. The large error bars in the center are due to IF spurs corrupting the calculation.

Figure 4.17: Gas cell observations of the ^{12}CO spectral line at 576.268 GHz. A spur is seen in the lower part of the IF which disappears as the spectral line reaches that region of the IF band, see figure 4.11 for a map view of the spur position. Note the increasing line peak intensity towards lower IF frequencies indicated a changing side band ratio.

gas cell, Figure 4.18 provides a summary of the side band ratio measured for all bands. These plots provide a useful overview of the side band ratio value across the HIFI frequency coverage and help identify problematic areas. As summarized in table 4.2 each spectral line is observed multiple times at different LO frequencies. Based on analysis of the FTS measured mixer gain, see section 2.3.2.2 on page 32, it is not expected that the side band ratio ratio varies more than 10% over 4 GHz of LO frequency range. Any spectral lines showing extreme variation in side band ratio are flagged for further investigation. From figure 4.18 a number of suspect areas are identifiable. These areas are possibly effected by other systematic effects such as standing waves, poor data quality, under pumped mixers or in the case of the diplexer bands mistuning errors.

In the small regions of Band 2a and 5a measured the side band gain is balanced. The data quality here was excellent providing a solid first measurement in these bands. Band 1b has a steep variation in side band ratio with LO frequency however on close examination these variations appear to be intrinsic side band ratio effects. Similar slopes in gain for this LO frequency range were also seen in follow up in flight observations.

Band 5b has an extreme side band ratio of ~ 0.25 around 1260 GHz. Values like these require further investigation as they are not expected based on the FTS RF gain analysis. The culprit in this case is an impure LO signal leading to the multiple LO signal issue discussed in section 4.3.4 on page 124. An example of the resulting spectrum is shown in figure 4.11 on page 126. Extracting the side band ratio in these cases is almost impossible as one must consider not just the side band ratio at the primary LO frequency but also those at the secondary LO frequency. For these observations the data is discarded and it is hoped that the band is well sampled by other molecules at other frequencies.

Bands 3a, 3b and 4a have a large scatter in their measured side band ratios. Bands 3 and 4 are known to have large standing wave with a period of 680MHz due to a flat edge at the angle of the diplexer rooftop mirror, this is discussed in more detail in section 2.4. This standing wave differs from those discussed in section 4.3.2 in that it is internal to HIFI and not dependent on the gas presence and hence cancels on the continuum during the cross calibration. However the standing wave is still present in the spectral line profile and its effect is seen when the line is tracked across the IF band. Unfortunately the step size taken during the gas cell campaign is not sufficient to investigate this effect further with ^{12}CO however there are ^{13}CO and CH_3CN observations which show large variability in line intensity for spectra separated by 100 MHz in LO frequency this will be discussed later. Ideally for a standing wave period of 680 MHz a step size of 100 MHz would help establish perhaps the phase and amplitude of the standing wave and apply a correction to the data. Unfortunately a step size of 1GHz was taken.

In addition to the standing wave problem, bands 3 and 4 are also susceptible to diplexer mistuning and misalignment discussed in section 2.3.2.3 on page 38. Closer examination of the variation of peak intensity with IF Frequency indicates a diplexer mistuning. Coincidentally a useful pair of observations were taken in band 3b. 2 observations were taken at the same LO

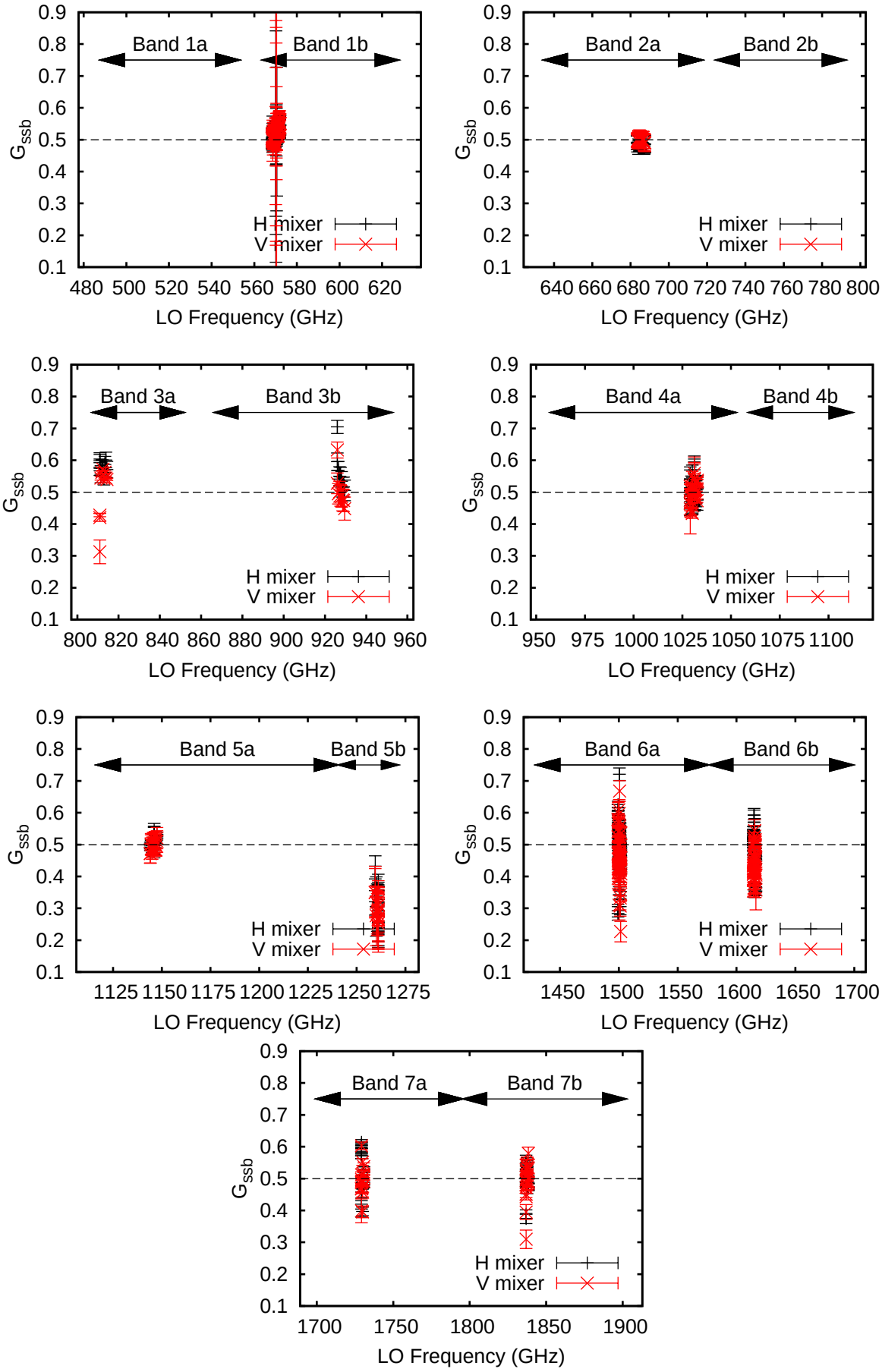

Figure 4.18: Overview of first pass determination of side band ratio from ^{12}CO observations.

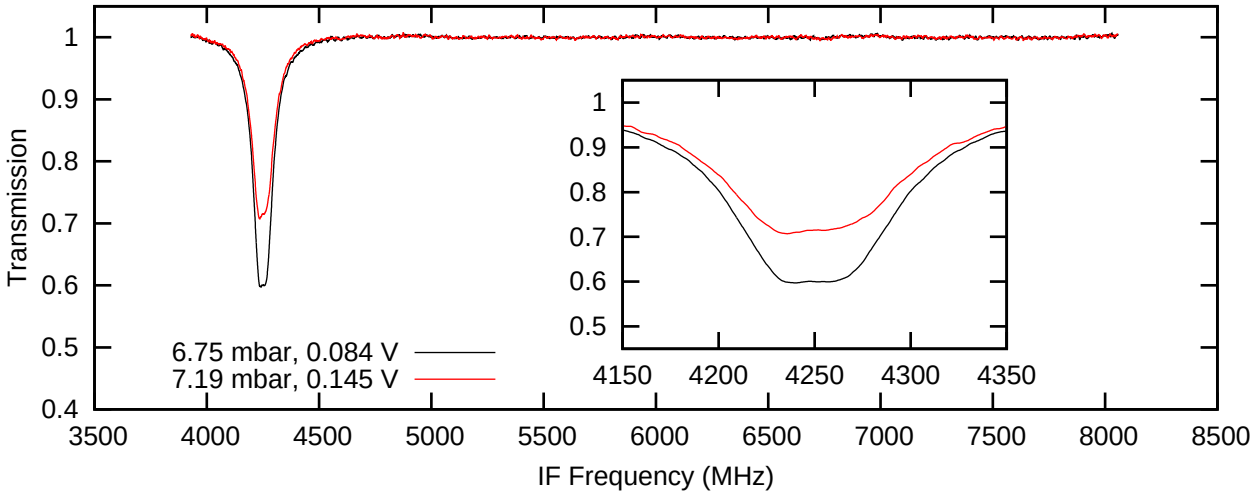

(a) ^{12}CO spectra taken at an LO frequency of 926.050 GHz showing the effect of a diplexer mistuning. The key shows the gas cell pressure and the diplexer actuator voltage. Both lines are saturated but have a different peak line intensity due to the side band ratio distortion introduced by the diplexer mistuning

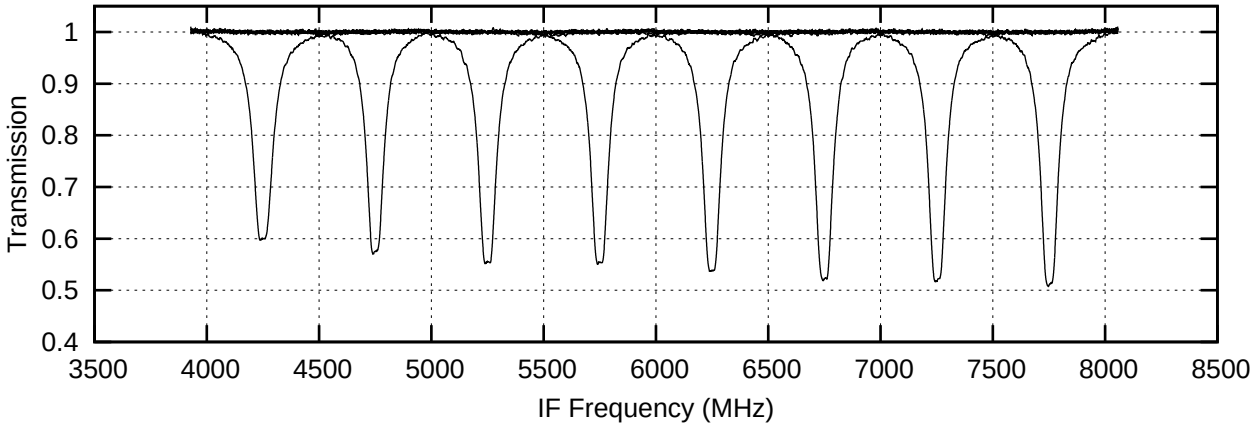

(b) Overview of ^{12}CO spectra taken in band 3b with the H polarization mixer showing the varying line intensity at different IF positions due to a diplexer mistuning

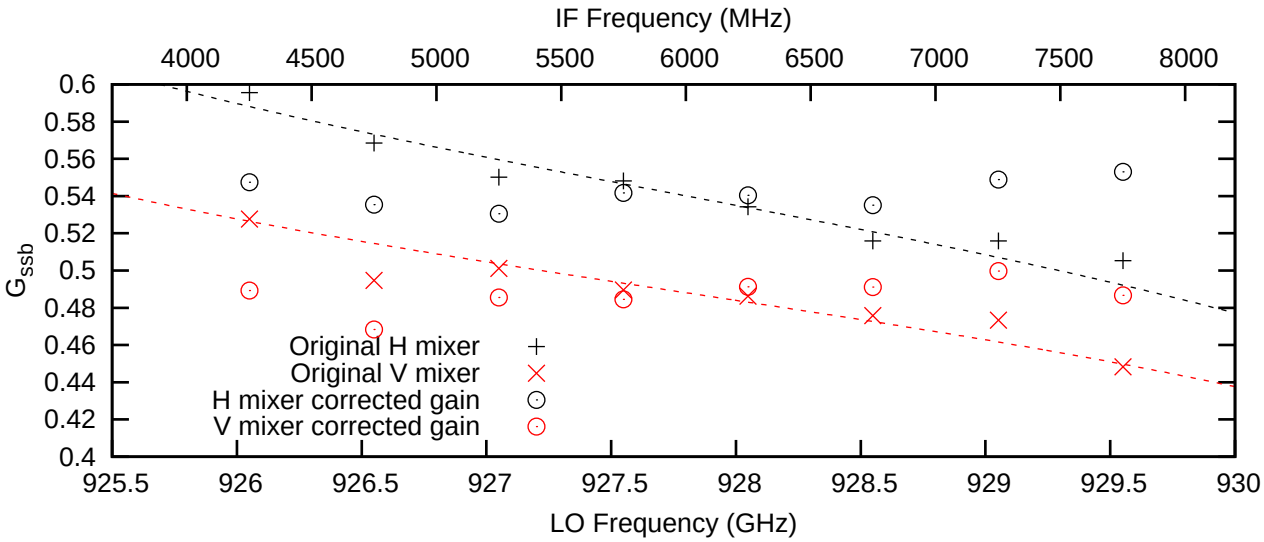

(c) Line peak intensity vs. IF frequency before and after correction for diplexer mistuning. H mixer had a -10μm mistuning while the V mixer had a -8μm mistuning. The diplexer gain model is shown with a dashed line.

Figure 4.19: Example of diplexer mistuning in band 3b.

frequency of 926.050 GHz placing the spectral line at 921.8 GHz at an IF frequency of 4250.8 MHz. One observation was taken at the correct diplexer setting while one was taken a mistuned diplexer setting. Figure 4.19(a) shows a comparison between the 2 spectra. The spectral lines are both saturated, which is apparent from their flat top spectral line profile, however due to the diplexer mistuning there is a 15% difference in peak line intensity. For side band ratio determination each observation must be taken in the context of the other measurements taken close by. For this example the weaker spectral line is discarded from the analysis.

Unfortunately there are further diplexer tuning problems in band 3b. Figure 4.19(b) shows ^{12}CO lines taken during a spectral scan. From this plot of the H mixer data it is apparent that the line intensity increases towards higher IF frequencies. A 20% increase in line intensity is seen across the IF band, this appears extreme. The variation in line intensity with IF frequency points towards a diplexer mistuning. Using the equations in section 2.3.2.3 it is possible to generate a model of possible diplexer misalignment tuning errors, see figure 2.18 on page 39 for some examples of various diplexer mistuning scenarios. Using the diplexer model equations one can determine the extent of diplexer mistuning and then use this model to correct the data. Figure 4.19(c) plots the line peaks from the H mixer data in figure 4.19(b) as well as the V mixer data. The dashed lines show the diplexer gain model estimation. From the model it is estimated that a -10 micron tuning error is present for the H mixer while a -8 micron error is seen for the V mixer. Applying the correction to the data reduces the scatter in line peak intensity for the H mixer from $\pm$11.2% to $\pm$2.8% and for the V mixer from $\pm$9.5% to $\pm$3.6%. The resulting scatter is assumed to be due to standing wave effects. Taking the mean of the gain corrected values returns a side band ratio of 0.48$\pm$0.01 for the V mixer and 0.54$\pm$0.02 for the H mixer.

From the example shown it is apparent that a diplexer mistuning can have quite real effects on the final calibration accuracy of the data. Depending on the IF position of a spectral line the intensity can vary up to 20%. For this example we have established the tuning error for band 3b and this can be used to correct this data and other data in this band. Unfortunately this correction can only be applied to the data taken during this test campaign. The gas cell data is spread over 3 test campaigns between which the test set up and instrument configuration was changed slightly and in most cases this included the diplexer look up table used to calibrate the diplexer. So the mistuning correction extracted from this 3b data can only be used on data with the same diplexer look up table. Fortunately there is no evidence of diplexer mistuning in bands 3a and 4a, with the large scatter seen in the side band ratio mostly due to standing wave effects. Follow up in flight observations of astronomical sources with strong line emission have shown that the in flight diplexer model was nominal for all bands proving that the mistuning seen in the band 3b data was due to a poor diplexer model.

The largest scatter seen in the side band ratio summarized in figure 4.18 is for the HEB bands. The band 6a measurement in particular has a large degree of scatter and requires an additional level of processing in addition to that described in figure 4.14. The HEB bands are

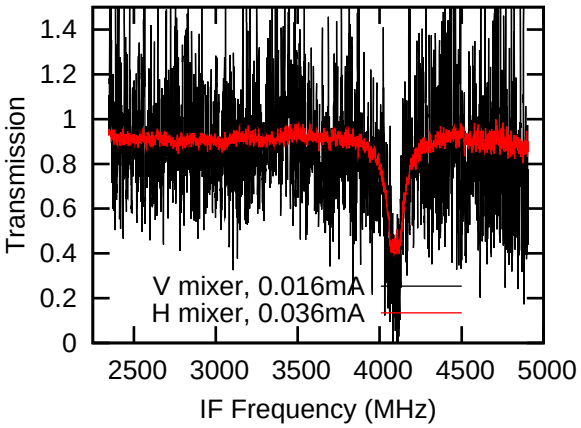

(a) Over pumped V mixer and optimally pumped H mixer at an LO frequency of 1501.020 GHz

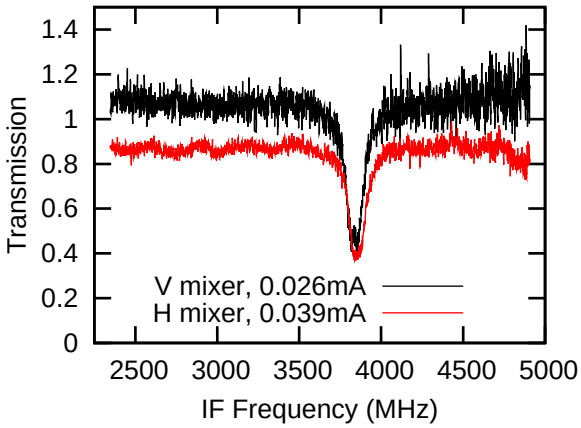

(b) Over pumped V and optimally pumped H mixer at an LO frequency of 1500.774 GHz

Figure 4.20: Example of over pumped V mixer compared to optimally pumped H mixer. An optimally pumped mixer has a mixer current between 0.035 to 0.045mA. A mixer current lower than this is considered over pumped as a result of excessive LO power. Alternatively a mixer current higher than this threshold is considered under pumped resulting in a mixer state prone to instability.

beset with baseline issues and while its possible to remove the standing wave from the baseline for some extreme cases the data is corrupted beyond repair. This data must be filtered from the dataset. The data presented in figure 4.18 takes all points with a reasonable quality baseline into account. A second phase of processing must filter this data and remove spectra that are beyond repair.

One method to filter poor HEB data is the mixer pump level. The HEB mixer has a small optimum operating range. The mixer is kept in an optimum state through a combination of the LO signal strength, mixer bath temperature and mixer bias voltage. The mixer state is most sensitive to LO power changes and hence the need for a stable LO chain for HEB operation. Both H and V mixers are pumped by the same LO chain, unfortunately the LO power can only be optimized for one mixer polarization. The other mixer unit is left to follow the required LO power for the other mixer. Due to differences in optics, mixer behaviour and standing waves, the "slave" mixer can be over pumped leading to higher noise in the data. In some cases the noise is prohibitively noisy and the data must be discarded. For band 6a, the H mixer is the "master" mixer and the LO power is set to place this mixer at the optimum operating point. The V mixer is the "slave" mixer and as a result the data quality is degraded.

Figure 4.21 shows an example of mixer data at different pump levels. Mixer current within a range of 0.035 to 0.045mA is considered optimally pumped with 0.4mA being the goal pump level when tuning the LO power. When the mixer current is below this level the mixer is considered over pumped due to excessive LO power. Alternatively if the mixer current is above 0.45 the mixer is under pumped which leads to an unstable mixer state resulting in saturated regions and corrupted data. Mixer current up to 0.055mA still return good quality data but

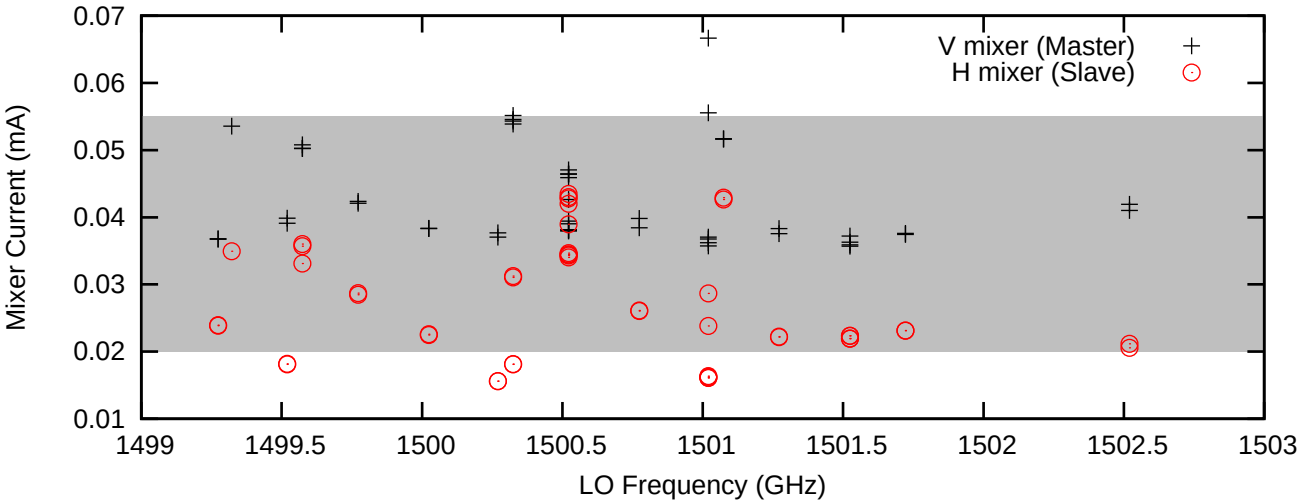

Figure 4.21: Overview of mixer pump level in band 6a. Note H mixer is closer to the goal mixer current of 0.04mA while the V mixer shows a large scatter in mixer current.

the mixer is more unstable in this region. Mixer currents down to 0.02mA return higher noise data but are still useful for side band ratio determination, figure 4.20(b) shows an example of the higher noise between a correctly pumped H mixer at 0.039mA and an over pumped V mixer at 0.026mA. Below the 0.02mA threshold data quality degrades significantly as illustrated in figure 4.20(a) and must be discarded. Figure 4.21 gives an overview of the pump levels seen for the H and V mixer for the band 6a ^{12}CO data. The variability between the "slave" V mixer and "master" H mixer is apparent. The region around 1500.5 GHz shows the best matched pumped level between the H and V mixers.

The variability in mixer current from frequency to frequency provides evidence of standing waves in the LO path. This topic is discussed in section 2.4. It should be noted that there are frequencies where both mixers are optimally pumped such as 1500.5 GHz however one must have a priori knowledge of the standing wave phases in both the H and V optical path. This can be established using specific standing wave tests prior to an observation. This approach is discussed in section 2.4.

In addition to the mixer pumping problem the HEB data has large standing wave issues. The baseline catalog approach used to correct the data is detailed in chapter 3. However even with the baseline catalog approach some data is still irrecoverable. Figures 4.22, 4.23 and 4.24 show examples of multiple gas cell spectra taken at the same LO frequency before and after baseline correction. From the data it is apparent that some baselines are not recoverable and have no equivalent baseline in the baseline catalog. Furthermore there is large scatter in the line peak intensity for some observations.

Figure 4.22 shows an example of data where the line peak intensity for 4 subsequent observations are within the baseline noise. The line peak intensity is close 0.5 consistent with a balanced mixer. On the other hand figures 4.23 and 4.24 shows a large degree of scatter in the line peak intensity even after baseline correction. Some line peaks fall around 0.5 indicating a

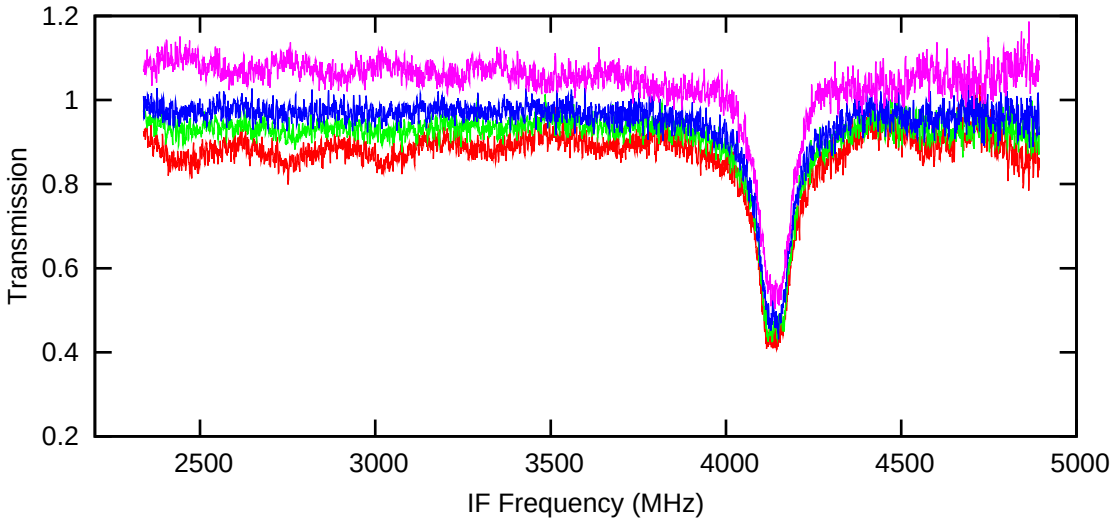

(a) ^{12}CO spectra observed at an LO frequency of 1501.074 GHz

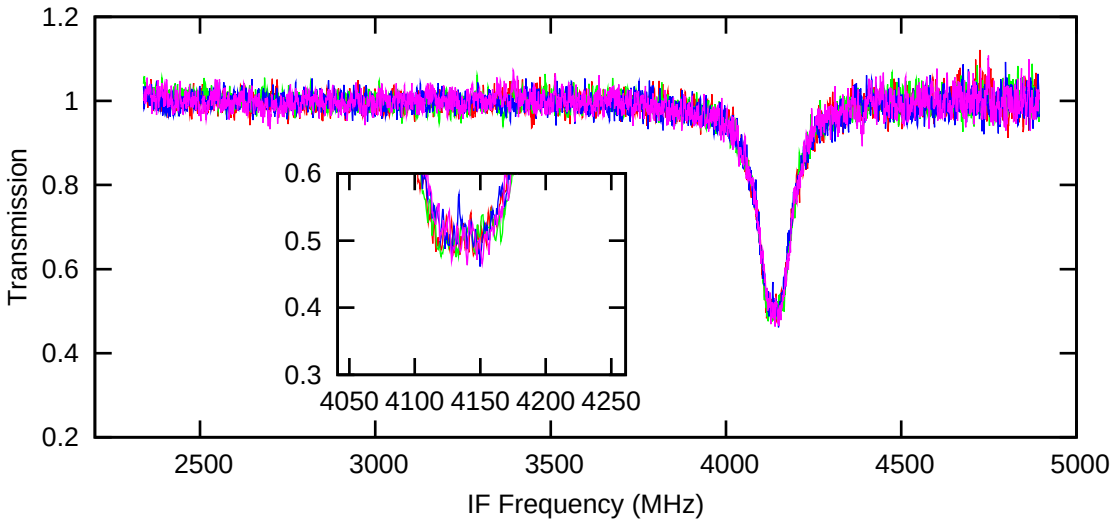

(b) Baseline corrected ^{12}CO spectra observed at an LO frequency of 1501.074 GHz

Figure 4.22: Example of HEB gas cell data taken at an LO frequency of 1501.074 before and after baseline correction. In this example the line peak scatter is within the noise and shows a balanced mixer gain.

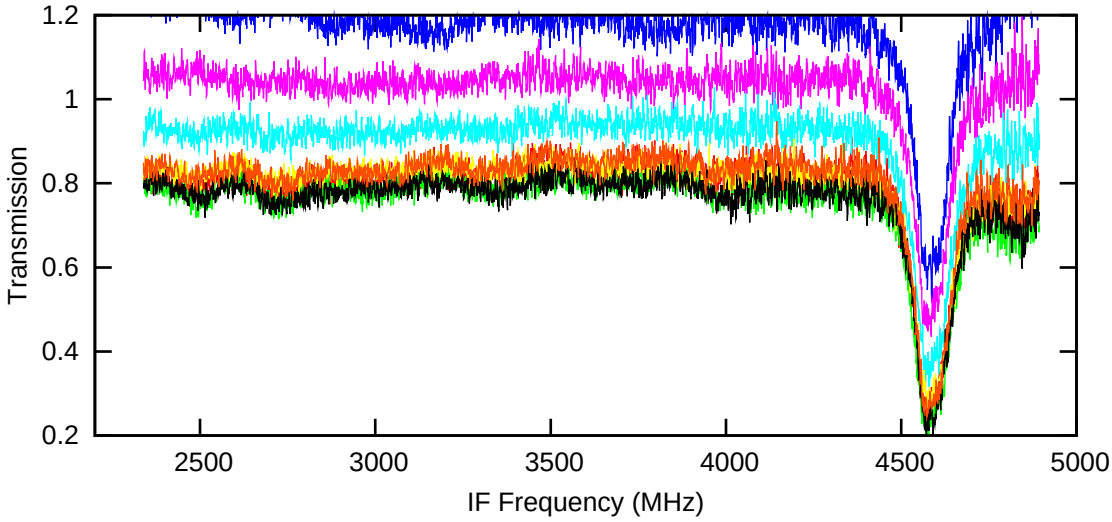

(a) ^{12}CO spectra observed at an LO frequency of 1501.524 GHz

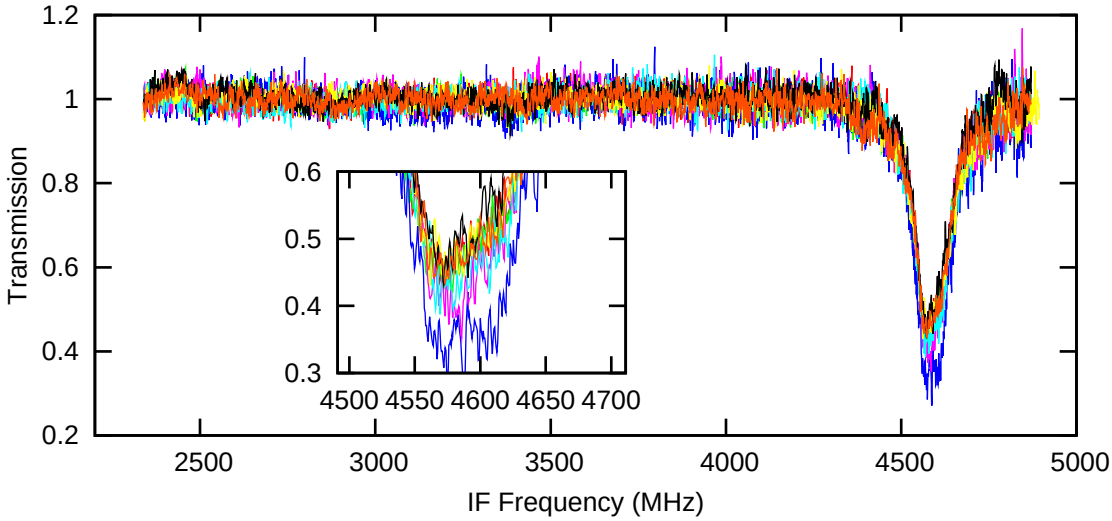

(b) Baseline corrected ^{12}CO spectra observed at an LO frequency of 1501.524 GHz

Figure 4.23: Example of HEB gas cell data taken at an LO frequency of 1501.524 before and after baseline correction. A large variation in line peak is seen in the data.

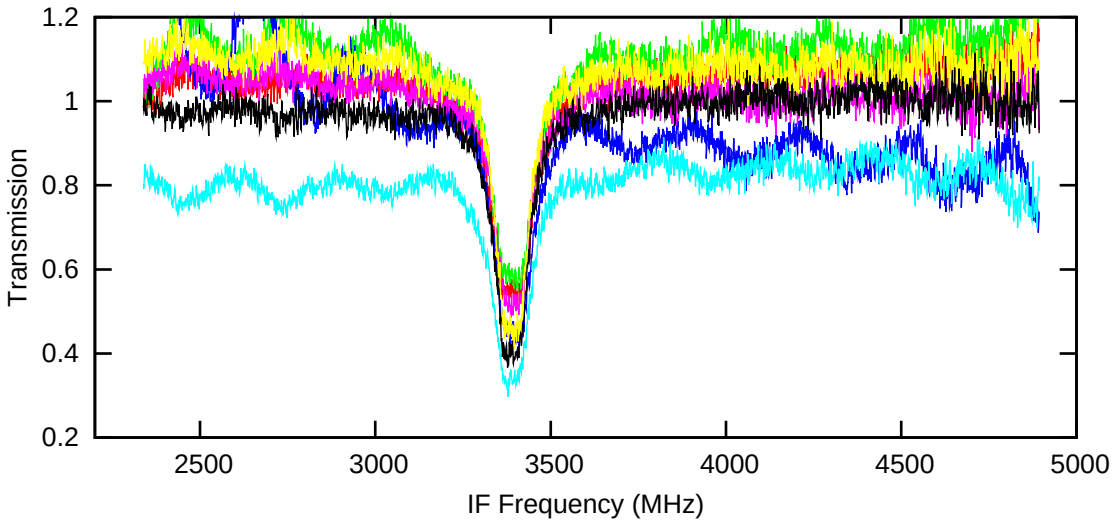

(a) ^{12}CO spectra observed at an LO frequency of 1500.324 GHz

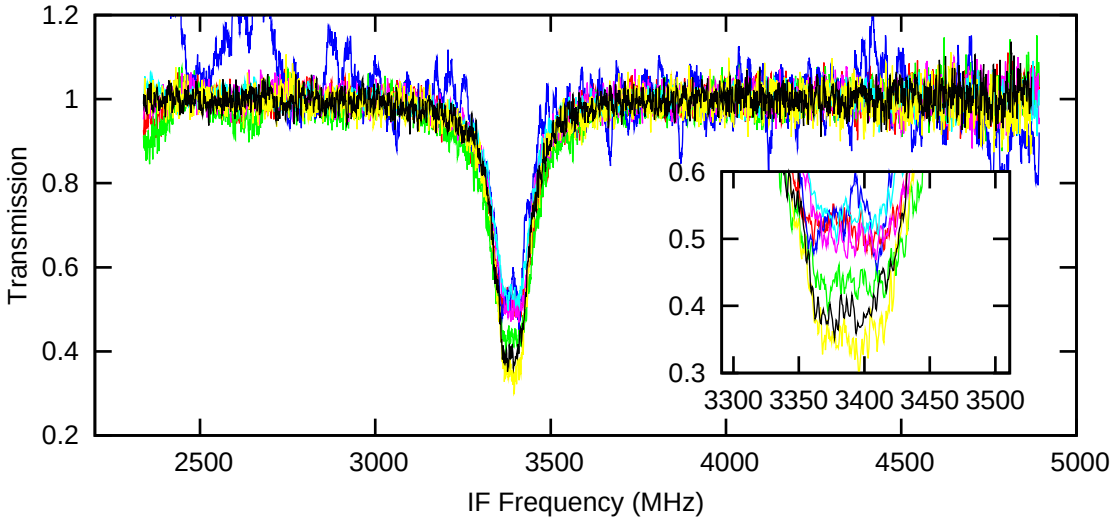

(b) Baseline corrected ^{12}CO spectra observed at an LO frequency of 1500.324 GHz

Figure 4.24: Example of HEB gas cell data taken at an LO frequency of 1500.324 before and after baseline correction. Note the degree of scatter seen in the line peak even after baseline correction.

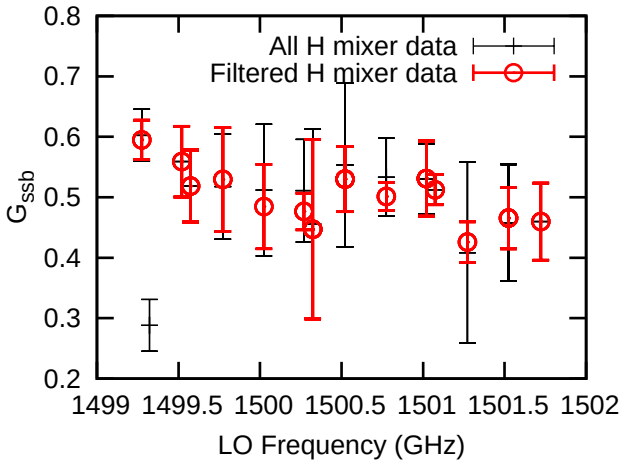

(a) H mixer G_{ssb} before and after filtering

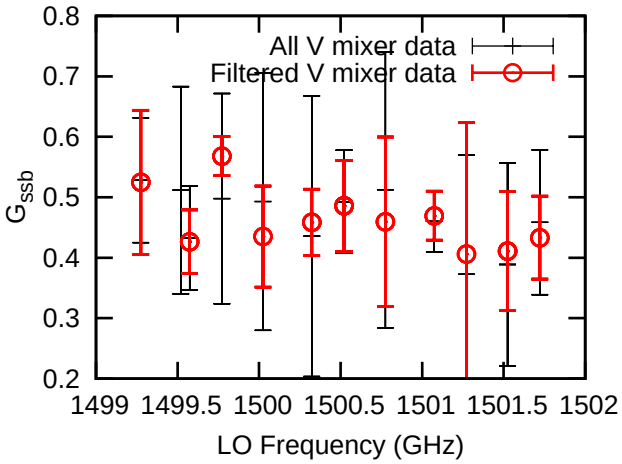

(b) V mixer G_{ssb} before and after filtering

Figure 4.25: comparison G_{ssb} before and after

gain balanced mixer for that observation. However some line peaks have lower values around 0.4. The obvious source to the problem is the method of baseline removal and using different baselines to correct the data can reduce the scatter however in some cases the line peak scatter persists. Given that multiple observations are taken at the same LO frequency the measured side band ratio can be averaged and level of scatter taken into account.

Returning to figure 4.18, the preceding discussion of HEB mixer problem explains the scatter seen in the measured side band ratio. The level of scatter in peak intensity can be reduced by ignoring extreme points with large standing waves and extreme mixer currents. Figure 4.25 shows an example of the measured side band ratio data before and after the data is filtered. For this example a mixer threshold is applied where any data with a mixer current below 0.02mA and above 0.055mA is ignored. An additional filter criteria is included such that any data with standing wave amplitude greater than 0.1 is ignored. Furthermore any data with RMS noise greater than 0.1 is ignored. Finally any spectra with a Gaussian residual less than 0.05 is deemed to be a poor fit and not included in the side band ratio data.

Figure 4.25 shows the resulting side band ratio data before and after application of the limits mentioned. From the plots one can see that the H mixer side band ratio scatter is reduced. From the data there is also possible evidence of a diplexer misalignment in the H band. Figure 4.25 contains data from 3 different test epochs with 3 different diplexer look up tables being used. Figure 4.26(a) contains the most complete dataset of the 3 test period, note the scatter in line peak intensity. From this figure one can see evidence of a possible diplexer misalignment similar to that seen in band 3a, see figure 4.19(c) on page 139. However given the large degree of line peak scatter seen in the data is difficult to conclusively prove the diplexer was mistuned.

The V mixer side band ratio data is plotted in figure 4.25(b). Even with the filtering of data based on the mixer current, standing wave amplitude, fit residual and RMS noise, there is still a large scatter at certain frequencies. This property of larger scatter for the V mixer is

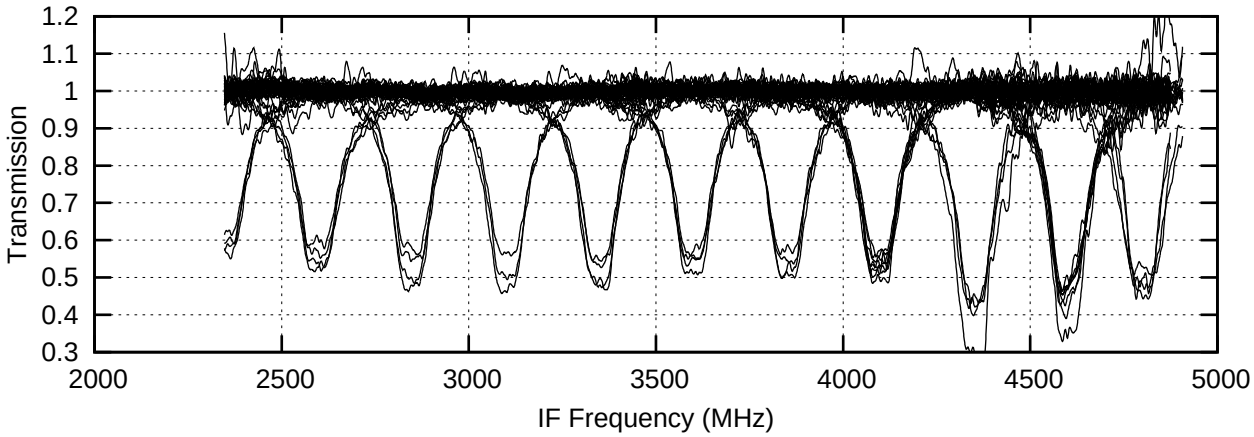

(a) ^{12}CO spectra taken during the same test period using the H mixer unit. This figure contains multiple spectra taken at the same LO frequency for an LO range from 1501.722 GHz to 1499.274 GHz. Note the possible diplexer mistuning with a 20% difference in line intensity between the spectral lines observed at the upper and lower edge of the IF band.

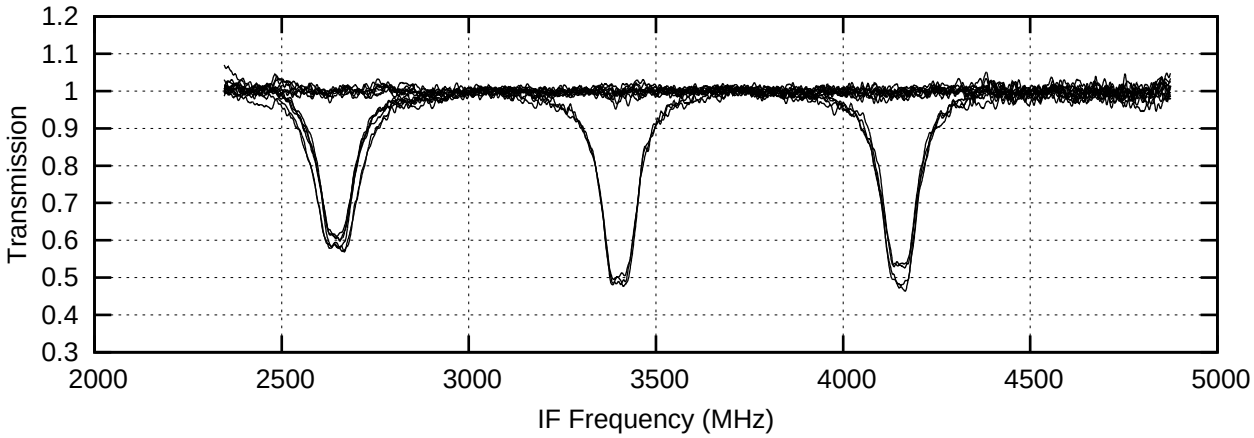

(b) ^{12}CO spectra taken using the H mixer at 3 LO frequencies ranging from 1730.754 GHz to 1729.249 GHz. The lower line intensity towards the IF band edge suggests a diplexer misalignment.

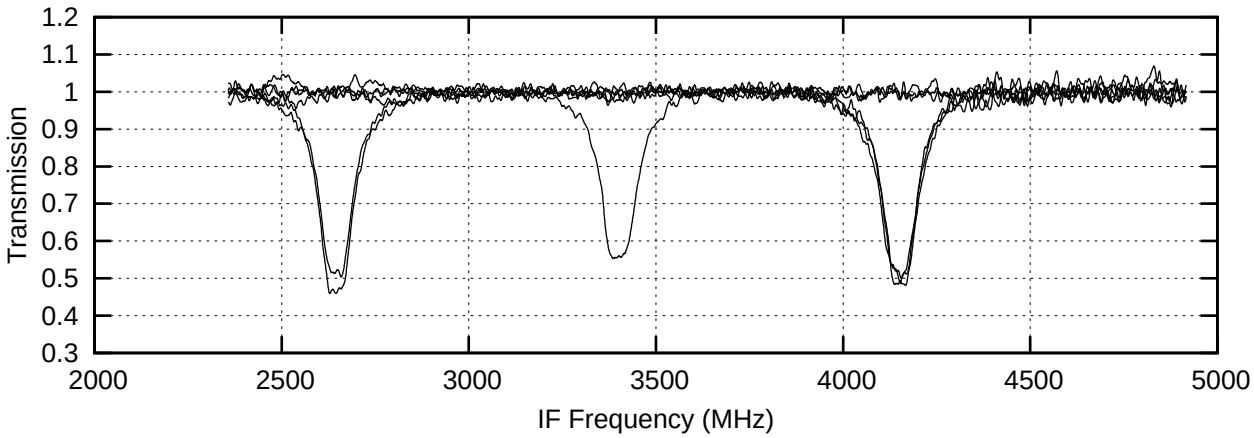

(c) ^{12}CO spectra taken using the V mixer at 3 LO frequencies ranging from 1730.754 GHz to 1729.249 GHz. The line intensity doesn't show any of the intensity variation seen in H mixer of the same band

Figure 4.26: Evidence of possible diplexer mistuning seen in H mixer for bands 6a and 7a. V mixer data for band 7a showing no diplexer mistuning is shown for comparison.

Line frequency (GHz)	LO band	observation count	Maximum LO (GHz)	Minimum LO (GHz)
550.926	1a	4	545.249	545.249
661.067	2a	6	655.251	655.251
771.184	2b	6	765.501	765.501
881.273	3b	5	874.998	874.750
991.329	4a	6	997.330	985.000
1101.350	4b	10	1107.351	1094.998
1211.330	5a	7	1205.330	1205.330
1431.153	6a	4	1434.756	1434.750
1540.989	6a	6	1544.598	1544.538
1650.768	6b	5	1654.371	1654.364
1760.486	7a	6	1764.086	1764.086
1870.141	7b	7	1873.746	1873.746

Table 4.3: Summary of ^{13}CO gas cell line frequency, LO band coverage and observation count

a knock on effect of the master and slave approach to LO power determination. As a result of this there may be a disparity between the achievable calibration accuracy of the V mixer and H mixer. Analysis of other gases in this band may help improve the calibration accuracy for the V mixer. It is not possible to determine the tuning state of the diplexer given the large amount of scatter in the data.

^{12}CO was also observed in LO bands 6b, 7a and 7b and shows similar H and V performance disparity. The level of peak line intensity scatter shows similar scatter to that shown for band 6a. The results however are encouraging with most spectral lines having peak value around 0.5 consistent with a gain balanced mixer. Band 7a also shows some evidence diplexer mistuning with line intensity seen to drop towards the IF band edges for the H mixer but not for the V mixer, see figure 4.26(b). The V mixer data is plotted for comparison in figure 4.26(c) showing less scatter and no drop in intensity towards the IF band edges however there is a drop in intensity for the line measured at the IF center.

4.4.4 ^{13}CO analysis

The usage of ^{13}CO as a calibration gas was less extensive than that of ^{12}CO, 316 ^{12}CO observations as opposed to 72 ^{13}CO, see table 4.3. Furthermore the LO frequency coverage around the spectral line was less broad with multiple observations taken at the same LO frequency as opposed to the line tracking approach used in the ^{12}CO observation. Multiple observations at the same LO frequency are useful in determining the accuracy of a measured side band ratio. However tracking a spectral line across the IF band is also a useful test to investigate standing wave or diplexer mistuning effects where applicable. The majority of ^{13}CO data were taken with the spectral line at the center of the IF band.

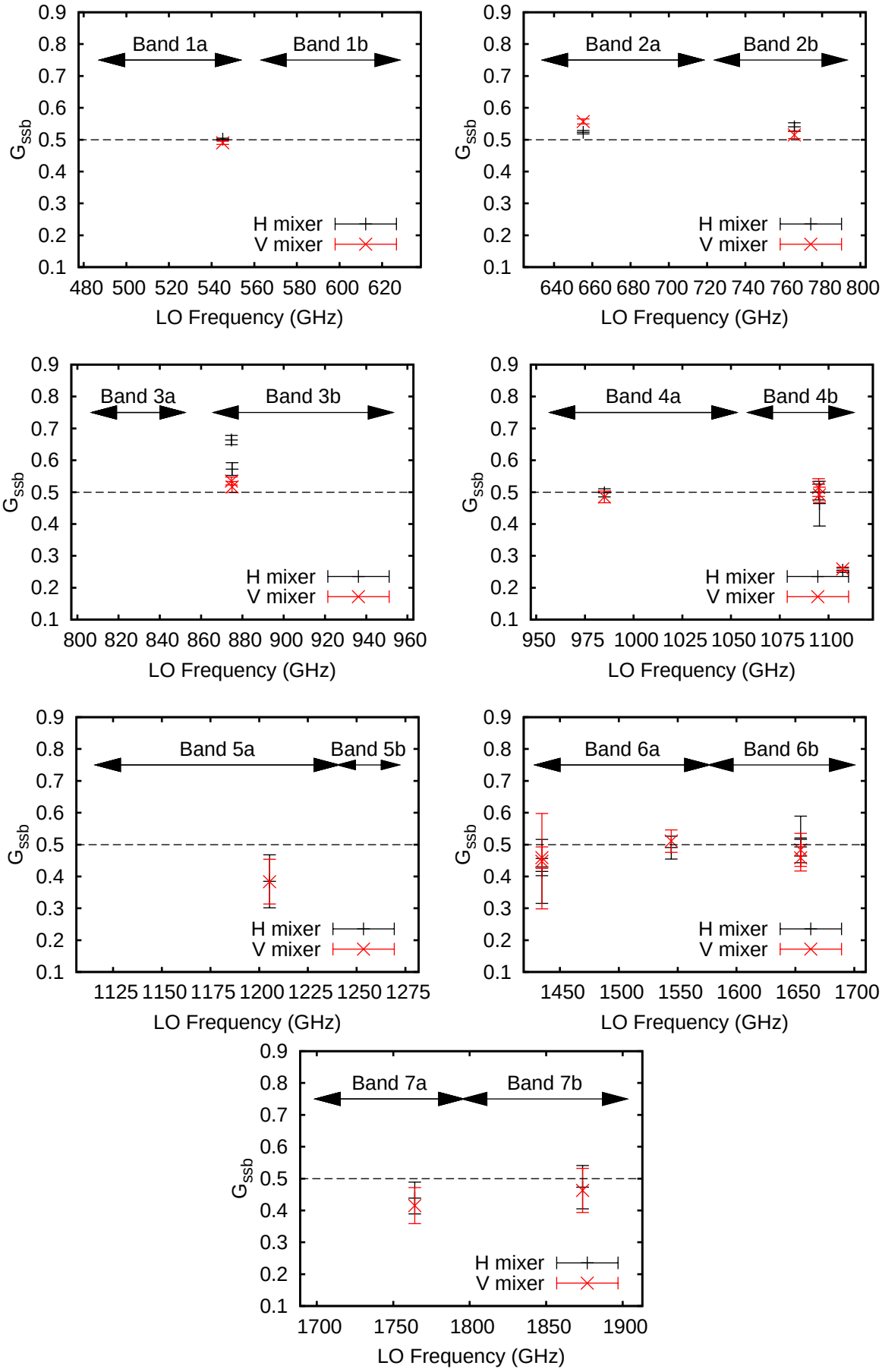

Figure 4.27: Overview of first pass determination of side band ratio from ^{13}CO observations.

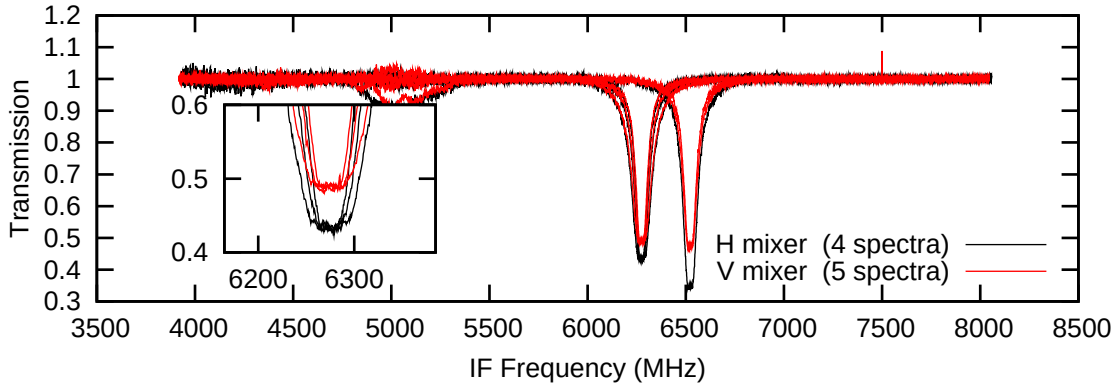

Figure 4.28: ^{13}CO line at 881.272 GHz observed at an LO frequency of 874.75 and 875 GHz placing the line in the upper side band at IF frequencies of 6.552 and 6.272 GHz respectively. Note the change in H mixer line intensity between the 2 LO frequencies.

The overall data quality in the SIS bands is comparable between the 2 calibration gases. The HEB data shows less scatter but this is probably more due to the sparse sampling than any difference in data acquisition.

Figure 4.27 provides an overview of the side band ratio determined through extraction of the line peak of saturated lines. The points shown in figure 4.27 are the averaged line peak intensities for all spectra observed at the same LO frequency. The error bars are generated through the addition of the line peak scatter and the RMS of the continuum around the line position. Bands 1 and 2 have excellent quality data, each spectrum was observed at least 4 times. Band 1a shows a gain balanced mixer with the spectral line having a peak intensity around 0.5. Bands 2a and 2b appear to have upper side band imbalance for the LO frequencies measured, with both spectral line measured having a normalized side band ratio, G_{ssb}, greater than 0.5.

Band 3b appears to have a larger scatter similar to that seen for ^{12}CO. Unfortunately the line is only observed at 2 LO frequencies separated by 250MHz so it is difficult to determine if a diplexer mistuning is seen in the data. The whole IF band needs to be sampled similar to the ^{12}CO observation seen in figure 4.19. In this example the scatter in line intensity is only seen for the H mixer. The V mixer line intensities are consistent between the 2 LO frequencies. For the H mixer, the line intensity observed at an LO frequency of 874.75 GHz is 15% larger than the line observed at an LO frequency of 875 GHz. Figure 4.28 shows the H and V mixer spectra at both LO frequencies. This scatter could possibly be due to diplexer misalignment in combination with a large standing wave. From dedicated standing wave tests it is known that a 680MHz period standing wave is present in this band. 250MHz corresponds roughly to half a period so this scatter in the H may indicate the extreme of the standing wave amplitude. A useful test here would be track the spectral line through the IF at very fine LO stepping of 50MHz, one would expect that the line intensity would be modulated by the underlying standing wave. For further discussion on the effect of standing waves on spectral lines see

section 2.4.

Band 4a and 4b had excellent baseline quality however for certain LO frequencies the H mixer was consistently noisier than the V mixer. This is a similar effect to that seen in the HEB band where one polarization is optimally pumped while the other polarization is left to float, although it is less dramatic for the SIS mixer bands as they are less sensitive to LO power changes. Figure 4.29(a) shows an example of an over pumped H mixer unit. In this example the H mixer had on average a mixer current of 0.0575mA while the V mixer had a 0.039mA. Unlike the HEB mixer where a low mixer current (0.02mA) denotes an over pumped mixer, for an SIS mixer a high mixer current denotes an over pumped mixer which can lead to high noise as we see here. Figure 4.29(b) shows an example of optimally pumped H and V mixer unit. For this example the mixer current for the H mixer is 0.044mA while the V mixer current is 0.029mA.

Figure 4.29(c) shows an example of an extreme line profile with a line peak at ~ 0.25. On first inspection, this may appear to be a standing wave problem however the line profiles for the H and V are almost exactly the same which is not consistent with a standing wave effect. Each polarization channel has a unique set of standing waves, in this case the 2 standing waves would have to have the same phase and amplitude which is not lightly. Perhaps this is a real RF gain effect as it is situated towards the band edge where extremes are expected. Observation of other gases at this frequency may help clarify the origin of this extreme gain variation.

From figure 4.27, band 5a exhibits an large imbalance in the side band gain ratio. A normalized side band ratio, G_{ssb}, of 0.38 ± 0.09 is seen for both polarizations. A scatter of this extreme merits further investigation. Figure 4.30 shows the line profile that went into the side band ratio ratio for the H and V profile. From this it is apparent there are 2 outliers generating the side band ratio scatter. One spectral line profile has an emission line at the line peak. This is the effect of not effectively removing the ^{13}CO gas from the empty phase of the gas cell test. From the line profile it is apparent that a residual of gas was left for the cold empty gas cell phase resulting in this line profile. This observation is flagged and is discarded from future analysis.

The second 5a outlier is a single spectrum taken an at earlier test phase. This spectrum shows a close to gain balanced line profile. The remaining spectra are all taken over the same gas cell test period and are consistent with each other. During the intervening period of testing new attenuators were introduced for all bands except band 5 so this provides no answer to this outlier. This could perhaps be another LO spur, however the line intensity is greater than 0.75, unlike in the band 5b example in figure 4.11 on page 126, this would require some side band gain ratio gymnastics to make this a viable scenario. This spectrum is flagged as an outlier and is ignored for future analysis.

The HEB band data was of better quality compared to the ^{12}CO data. At certain frequencies there is still a large scatter in the peak line intensity similar to that shown in figure 4.23. Even after applying the baseline correction the line peak has a large variability. In band 6a, 3

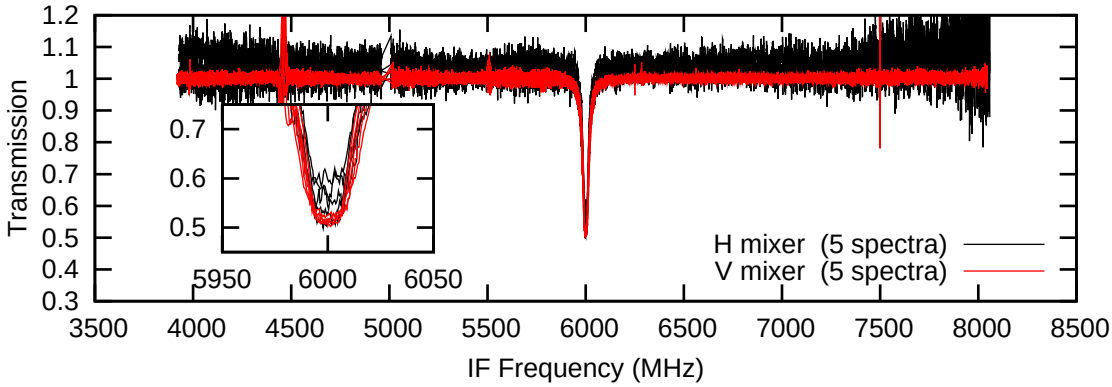

(a) ^{13}CO spectra observed at an LO frequency of 1095.350 GHz showing higher noise between the H and V mixer due to an under pumped H mixer.

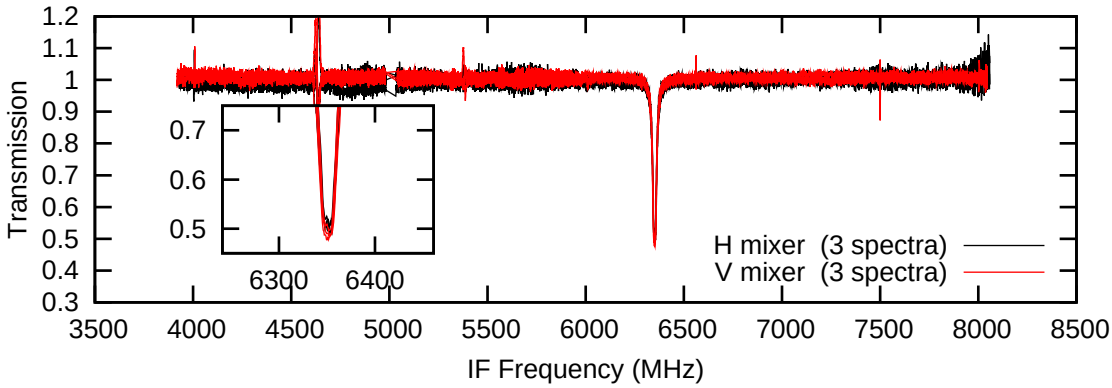

(b) ^{13}CO spectra observed at an LO frequency of 1095 GHz showing comparable noise in the H and V mixer

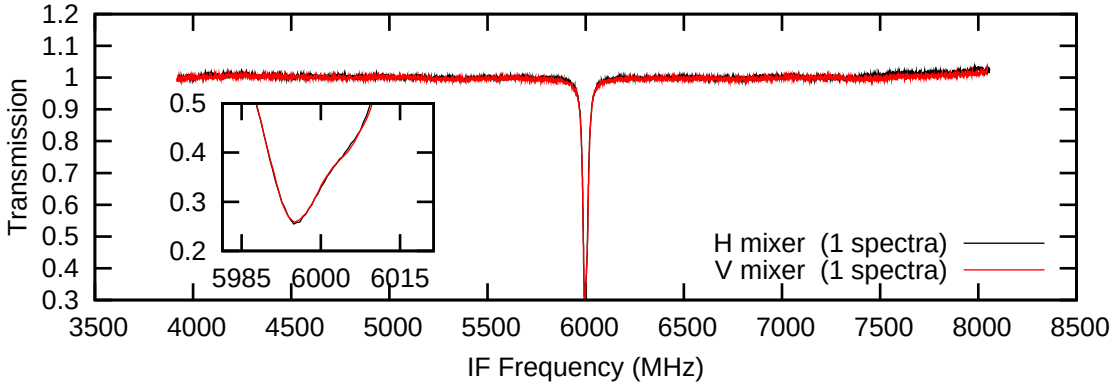

(c) ^{13}CO spectra observed at LO frequency 1107.351 showing extreme side band gain ratio. The effect is possibly due to standing wave or real antenna band edge effects or possibly both.

Figure 4.29: Examples of ^{13}CO spectra taken at LO frequencies 1094.998, 1095.350 and 1107.351 GHz.

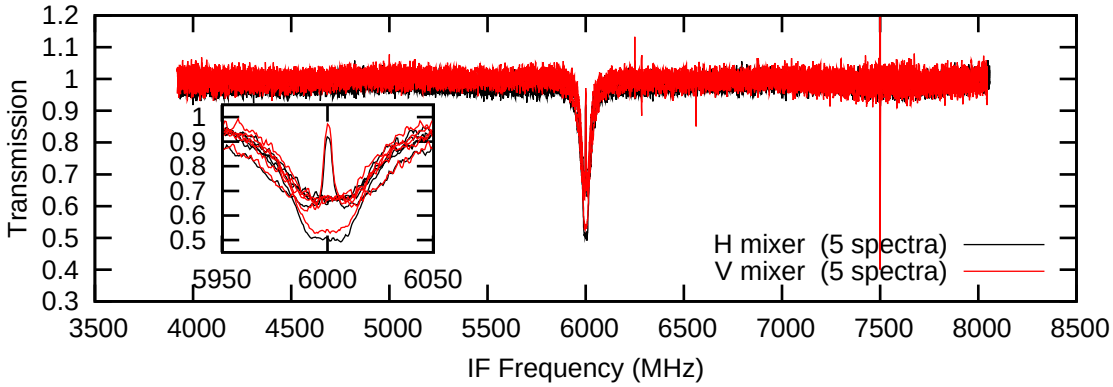

Figure 4.30: Observation of ^{13}CO spectral line at 1211.329 GHz at an LO frequency of 1205.3295 GHz placing the line in the upper side band at an IF frequency of 6.0 GHz. In this figure, an example of the spectral line profile seen when the gas cell is not fully emptied for the empty gas cell.

different LO frequencies were observed. Figure 4.31 shows the spectrum taken at each of the LO frequencies. There appears to be no correlation between the test period and the quality of data and is more dependent on LO frequency and possibly LO chain configuration.

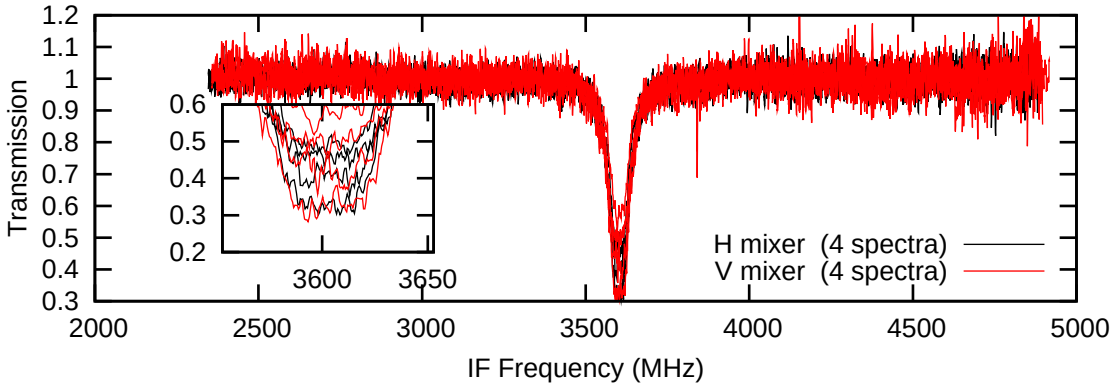

(a) ^{13}CO spectra observed at an LO frequency of 1434.756 GHz showing large line peak intensity scatter for consecutive observations

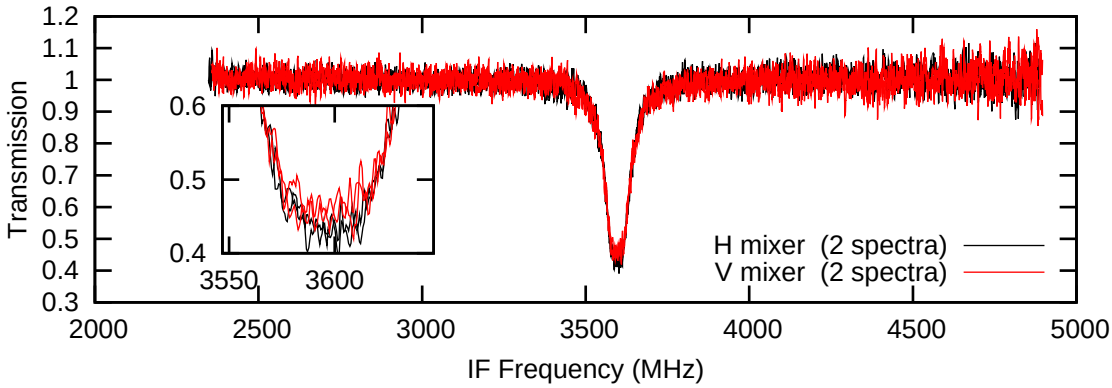

(b) ^{13}CO spectra observed at an LO frequency of 1434.75 GHz with a low line peak intensity scatter

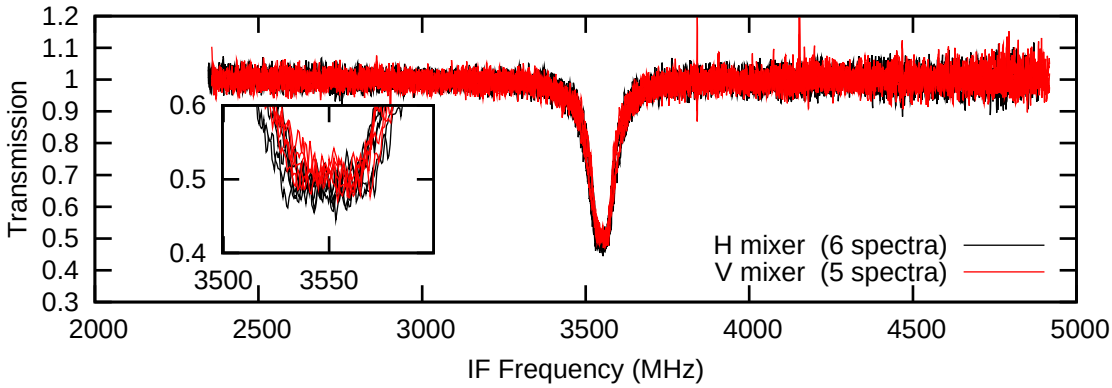

(c) ^{13}CO spectra observed at an LO frequency of 1544.538 GHz showing excellent quality data with consistent line peak intensity between observations

Figure 4.31: Examples of ^{13}CO spectra taken at LO frequencies 1434.756, 1434.75 and 1544.538 GHz.

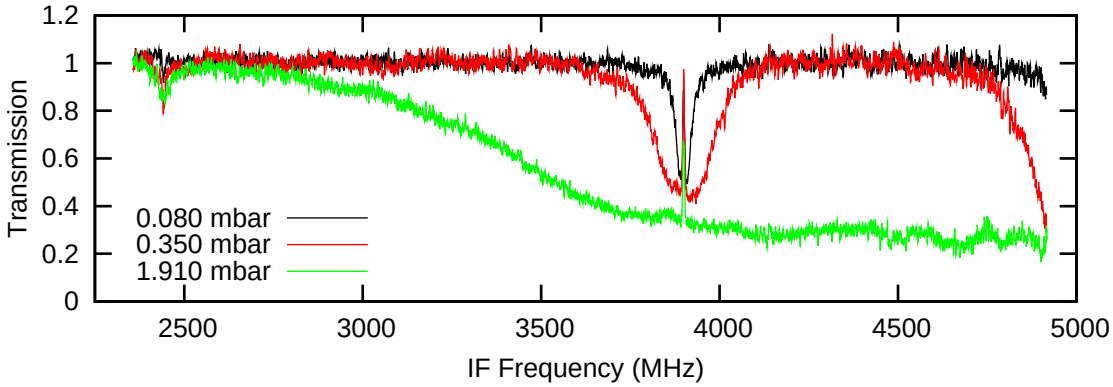

Figure 4.32: Observation of H_2O at an LO frequency of 1664.908 GHz at 3 different gas cell pressures. The central line is at a frequency of 1661.008 GHz, the wing of another line at a frequency of 1669.905 GHz is seen at the upper IF band edge. At higher pressure the 2 lines blend together making it difficult to apply the HEB baseline correction. All spectra have an emission line at the center of the absorption line indicating that the gas cell was not completely void of water during the empty gas cell phases.

4.4.5 H_2O analysis

The observation of water is one of the main goals of the HIFI instrument. In particular the 3 water lines ending in the ground states are essential for absorption studies of cold water. These lines are at frequencies of 556.936 GHz (band 1a), 1113.343 GHz (band 4b) and 1669.905 GHz (band 6b). The gas cell observations concentrated on these lines and they are observed multiple times in both the upper and lower side band. Other water lines are also observed however some lines were not strong enough to saturate in the gas cell set up and so were ignored in this analysis.

Water was observed towards the end of the gas cell campaign since water has a negative effect on the gas cell and tends to stick to the gas cell walls. As the data was taken in the final stages of HIFI testing the data is of high quality reflecting the experience gained over the test period. The data in the SIS band required little post processing. The HEB bands suffer from standing wave issues still but this was expected beforehand. Removing the HEB standing wave from the water data however was problematic given the width of the water lines at high pressure.

As described in section 3.4.2, the method of HEB baseline correction requires that some continuum is available so the spectrum can be compared to the catalog for a matching spectrum. For water observations the line can dominate the entire IF band making it impossible to find an appropriate matching catalog baseline for a high pressure spectrum. Figure 4.32 shows an example of a water observation at 1664.908 GHz at different gas cell pressures. In this example the line is at a frequency of 1661.008. The wing of another line is observed at 1669.905 GHz. At high gas cell pressure the 2 lines are blended together making it difficult to extract the side band ratio. For the gas cell water observation data was taken at various gas cell pressures. This redundancy with LO frequencies means high pressure spectra such as the 1.191 mbar spectra

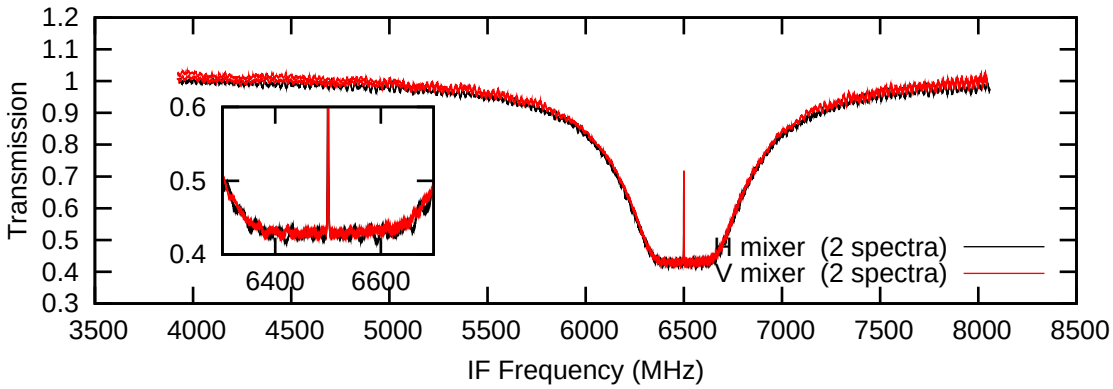

(a) H_2O spectra observed at an LO frequency of 563.436 GHz GHz showing a flat line peak.

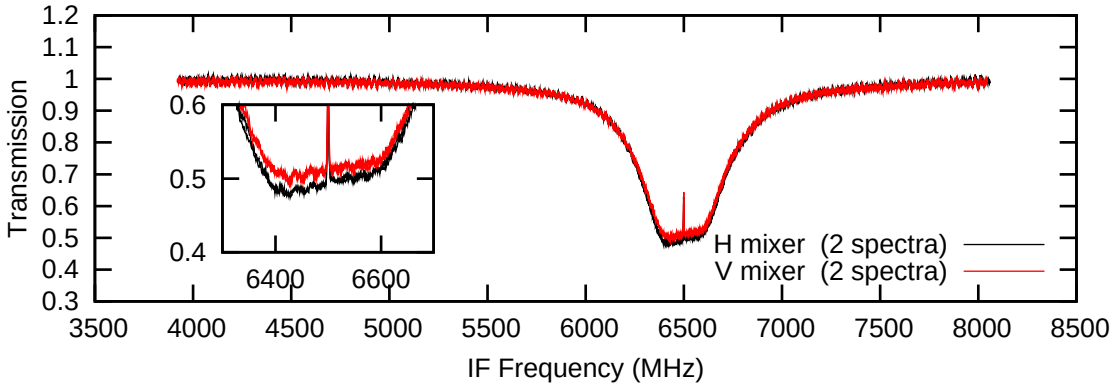

(b) H_2O spectra observed at an LO frequency of 981.428 GHz showing a large slope in the line peak

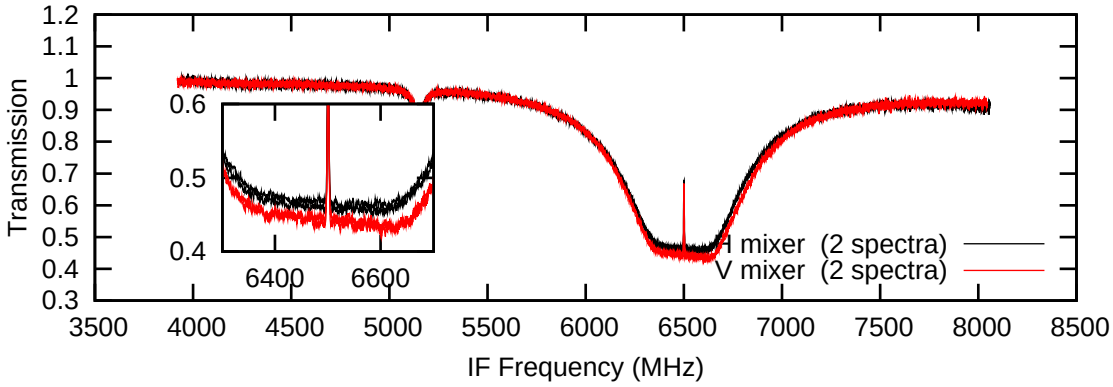

(c) H_2O spectra observed at an LO frequency of 1106.842 GHz showing a large slope in the line peak

Figure 4.33: Examples of standing wave effects on broad saturated line peaks. The standing wave between the diplexer roof top mirror has a period of 680MHz consistent with the slopes seen in the band 4 data. The feature at the line center is due to residual water vapor left in the gas cell during the empty gas cell phase.

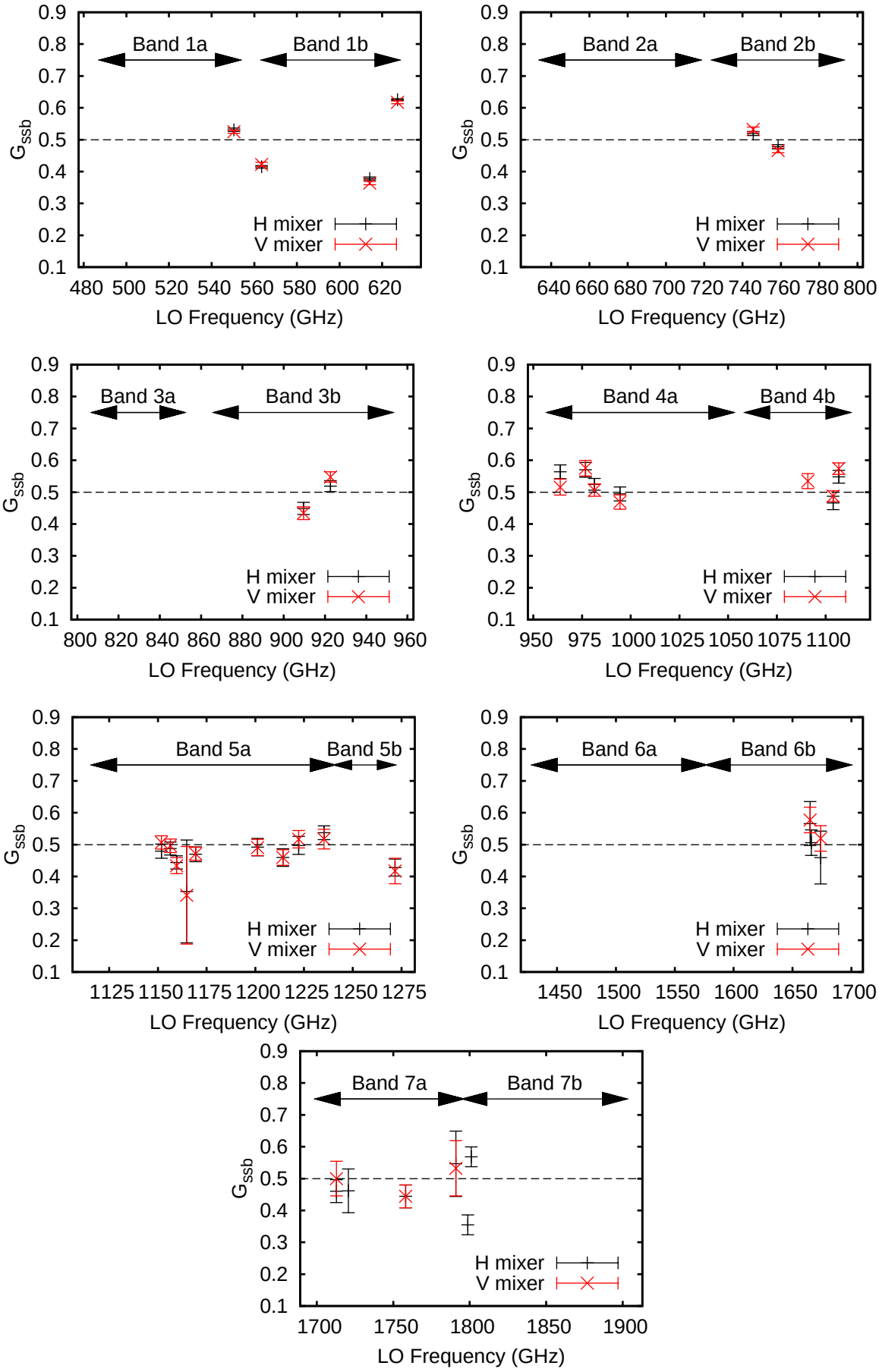

Figure 4.34: Overview of first pass determination of side band ratio from H_2O observations.

gas	H mixer	V mixer
^{12}CO	25%	44%
^{13}CO	25%	38%
H_2O	40%	60%

Table 4.4: Percentage of HEB spectra discarded due to large standing waves. Large standing waves are defined as those having an amplitude greater than 10% transmission.

in figure 4.32 can be ignored for the analysis without loosing a sample point in the side band ratio survey.

For the HEB band correction the broad water lines are problematic. However in the SIS bands the large saturated peaks reveal some interesting features in the data. In the SIS diplexer bands (band 3&4), where standing waves are significant, we see some large slopes in the saturated line peak. This is not seen in bands 1 and 2 data where standing waves in the optics are less. Figure 4.33(a) shows an example of a saturated water line in band 1a. The line peak is flat and has no significant slope. A short period standing wave can be see on the line peak plateau. Figures 4.33(b) and 4.33(c) show an examples of the effect of a long period standing wave on the link peak. The standing wave seen here is due to reflected signal between the mixer unit and the diplexer roof top mirror. This cavity produces a 680MHz period standing wave.

Figure 4.34 provides an overview of the side band ratio measured for saturated water lines. From the data it is apparent that there is little scatter seen in the SIS bands. Each side band ratio point in the SIS band was measured at least twice. In the HEB bands, a large number of spectra were discarded due to the extreme standing waves seen. Table 4.4 shows an overview of the amount of spectra discarded for both H and V mixer. There is a large disparity between H and V, most lightly due to the master and slave LO power acquisition approach where the H mixer is always pumped optimally and the V mixer is left to float. There is also a gap between the CO molecules and water observation. The CO molecule have less extreme standing waves. This increased amount of poor quality data may be a reflection of the LO stability at these frequencies. Operating the LO close to the water line can be problematic. As we saw in figure 4.32, even at low pressures and for a short gas column length the signal transmission can drop significantly. Turbulence in the air could have caused fluctuations in the LO power pumping the mixer. As discussed in chapter 3, slight changes in mixer pump level can have a large effect on the standing wave cancellation in the resulting spectra.

4.4.6 OCS analysis

OCS is a useful gas for calibration purposes. OCS has a strong spectral line every 12 GHz. Through careful selection of the LO signal, a spectral line can be placed in the upper and lower side band providing a useful probe of 2 IF positions simultaneously. Figure 2.19(a) on page 42 shows a simulation of the typical OCS double side band spectra. Unfortunately above 800 GHz OCS spectral lines are not saturated in the gas cell test set up. Hence the analysis of OCS is

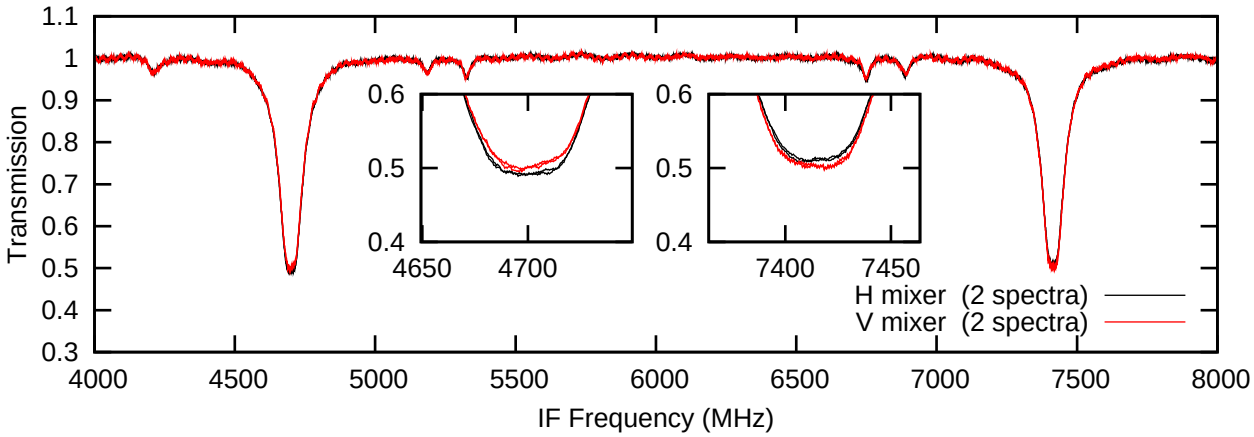

Figure 4.35: OCS spectra observed at an LO frequency of 684.912 GHz with a gas cell pressure of 4.4mbar. This example shows a balanced side band gain at this LO frequency at the IF frequencies of 4700 and 7414 MHz. The additional weaker lines are most probably isotopes of OCS.

only useful at frequencies below 800 GHz, see figure 4.1(c) for a summary of OCS line peak transmission for various gas cell path lengths.

For OCS the analysis approach described is changed slightly to that of the single line spectrum discussed in the preceding sections. Since there are now 2 lines in each spectrum, one in the upper side band and one in the lower each line is treated separately. Lines observed at the same IF and LO frequencies are then averaged together.

Figure 4.35 shows an example of a typical OCS spectrum taken during the gas cell test campaign. 2 OCS lines are seen in the spectrum. The lower IF band line is observed in the lower side band and has a frequency of 680.213 GHz. Which combined with the LO frequency of 684.912 GHz places the line at an IF frequency of 4700 MHz. Similarly the upper IF band line is at a frequency of 692.326 GHz and is placed at an IF frequency of 7414 MHz when combined with the LO signal. For this example both lines have a line peak at 0.5 suggesting there is equal gain between the upper and lower side band at this LO frequency.

There are some LO frequencies which vary significantly from a gain balanced mixer particularly towards the band edges. This was predicted by the analysis of the FTS RF mixer gain data see figure 2.16(a) on page 36. Figure 4.36 provides an overview of the side band ratios determined from OCS. For all observations the 2 OCS lines were observed at IF frequencies in and around 4.7 and and 7.4 GHz. The LO frequency is selected so the LSB line is seen at the lower IF frequency and the USB line is seen at the upper IF frequency. Figure 4.36 shows the side band ratio determined for both the upper and lower side band lines. From these observations one can get a picture of the slope in side band gain ratio across the IF band. Up to now, with the analysis of ^{12}CO, ^{13}CO and H_2O only a single frequency point on the IF band was measured. The advantage of OCS as a calibration gas is that 2 points at different IF frequencies are sampled simultaneously. LO frequencies with extreme side band ratio slopes across the IF band are easily identified as those with large differences between the side band

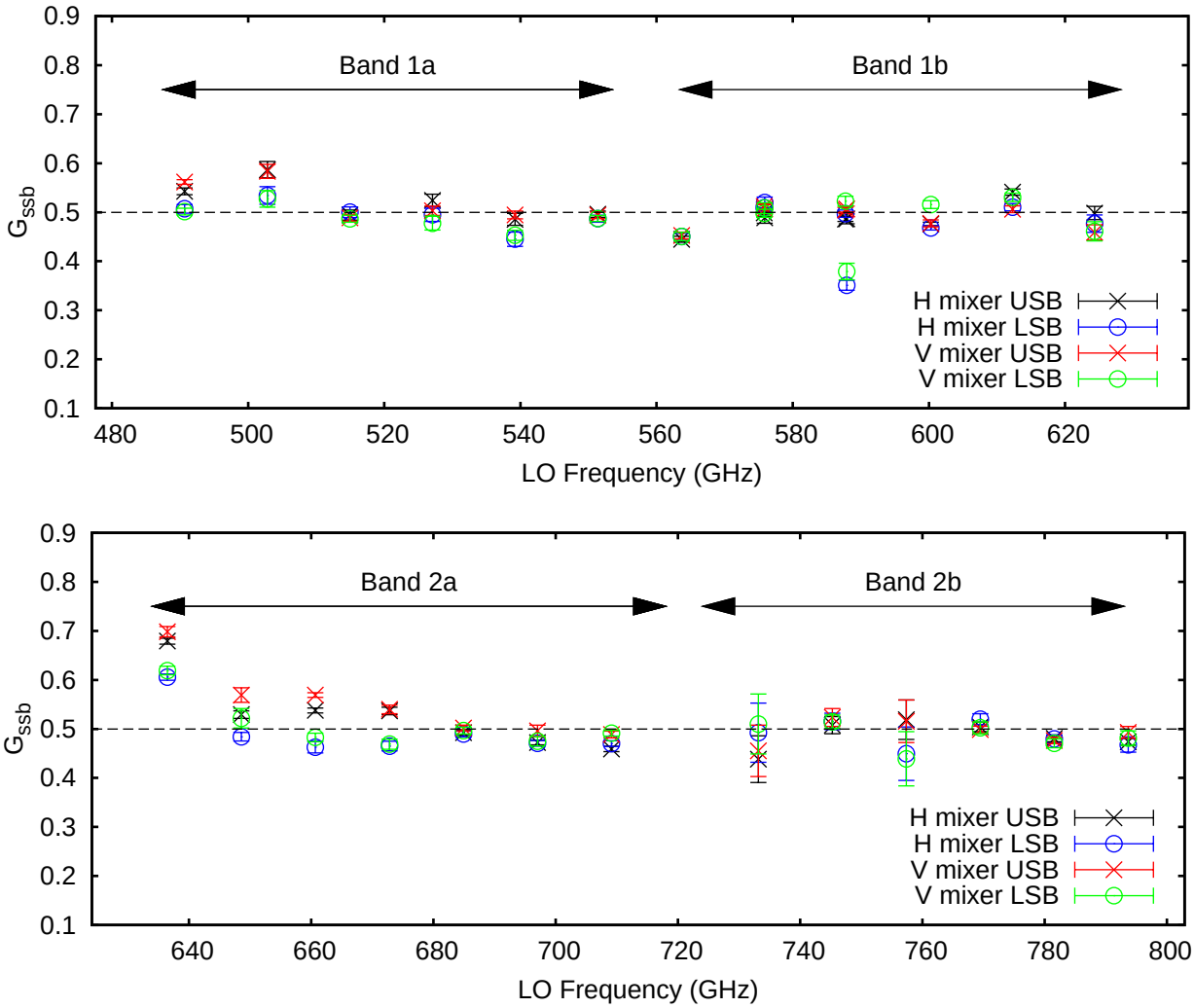

Figure 4.36: Overview of first pass determination of side band ratio from OCS observations.

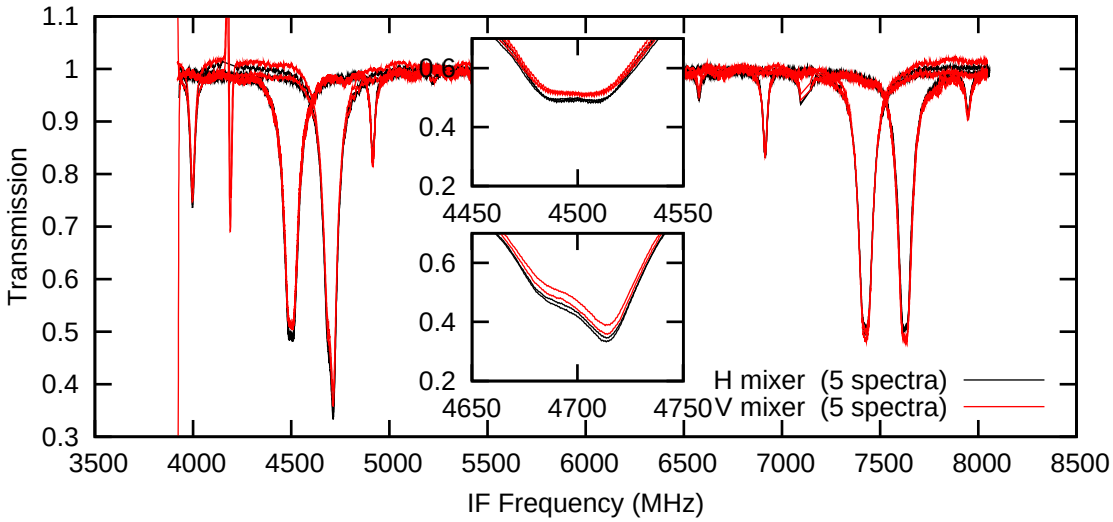

Figure 4.37: 2 OCS spectra taken at LO frequencies of 587.74725 and 587.9475 GHz. The LSB line at a frequency of 583.247 GHz shows an extreme variation in gain over a small change in LO frequency of 0.2GHz. The top inset figure shows a typical line peak at an LO frequency of 587.74725 GHz with a peak close to 0.5. The bottom inset plot shows the small line peak at an LO frequency of 587.9475 GHz with an extreme line profile and a line peak close to 0.35.

ratio determined for the USB line (cross symbols) and those determined for the LSB line (circle symbols). Examples of these extremes can be seen in band 1b at an LO frequency of 575.82 GHz and in band 2a at the LO frequencies 636.444, 648.561, 660.681 and 672.798.

There is another outlier point in band 1b at a frequency of 588 GHz. This outlier line is measured at twice at 2 LO frequencies separated by 200MHz, see figure 4.37. The line measured in the lower side band shows a large change in intensity over the short frequency step. The line measured in the upper side band shows no such change in intensity. Furthermore the line shape for the higher intensity line has a strange shape exhibiting behaviour similar to the 4a line peak peak shown in figure 4.29(c). For the band 4a example there are some feasible explanations such as diplexer mistuning or standing waves. However band 1b has no diplexer problem and standing waves are greatly reduced compared to bands 3 and 4. This type of behaviour maybe explainable through some peculiar LO behaviour however one would expect both OCS lines measured to be affected which is not the case. No explanation is forthcoming to explain this strange line behaviour. Further in flight tests are needed to determine if this behaviour is real or an artifact of the gas cell test setup.

On closer inspection of the side band ratio overview in figure 4.36 there are some points which are extreme. 660.681 and 672.798 GHz for example show extreme differences over a short IF frequency. At these frequencies, at an IF frequency of 4.7GHz the lower side band signal dominates the double side band signal ($G_{ssb} < 0.5$) while 3 GHz away the upper side band dominates the double side band signal ($G_{ssb} > 0.5$). This behaviour is extreme and isn't consistent with the side band ratio IF frequency variation determined from the FTS direct detection data in band 2, see the example figures on page 36. Figure 4.38 shows a comparison

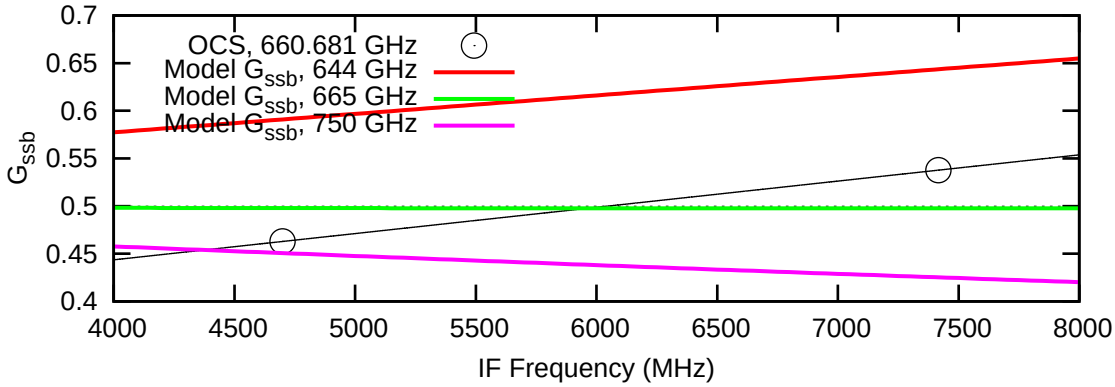

Figure 4.38: Extreme side band ratio profile determined from direct detection FTS measurement of mixer band 2 compared to measured OCS data at an LO frequency of 660.681 GHz.

between the most extreme side band ratio variations determined from the FTS data compared to the measured side band ratio data taken from the line peaks of OCS at an LO frequency of 660.681 GHz. The slope of the OCS measured side band ratio across the IF band is consistent with the 644 GHz FTS however the measured data shows a stark cross over between a lower side band dominated signal to an upper side band dominated signal. This stark variation was not seen in the FTS data.

Further investigation of the extreme points at 660.681 and 672.798 GHz reveal similar albeit less extreme line profile distortion to that shown in figure 4.37. Figure 4.39 shows a close up view of the line peak of the outlier spectrum taken at LO frequencies 660.681 and 672.798 GHz. A close up view of the 636 GHz spectrum taken at the band edge shows an extreme side band ratio but correct line peak behaviour is shown for comparison. Figure 4.39(a) shows the 660.681 GHz example. The inset plot focuses on the line peaks from which one can see the sharp peak on the lower side band line which distorts the side band ratio measured. This behaviour isn't only seen in the lower IF frequencies. The spectrum taken at 672.798 GHz shows similar behaviour for the upper side band line at an IF frequency of 7.4 GHz. Again a slope on the line results in an over estimation of the peak line value. Figure 4.39(c) shows a spectrum taken at the band edge where extreme side band ratio behaviour is expected. This example has a typical flat top line profile which is expected for a saturated line and such can be taken as an accurate side band ratio measure.

For this OCS analysis, lines with a pointed line peak such as that seen at LO frequencies 660.681 and 672.798 GHz in band 2a and 587.9475 GHz in band 1b (figure 4.37) are ignored for this analysis. The source of this distortion is not entirely clear. As stated earlier similar behaviour was also seen in band 4b at a frequency of 1107.351 (see figure 4.29(c)). This was a ^{13}CO observation and just one spectral line was observed hence this behaviour was attributed to standing wave or possibly diplexer behaviour. However for the OCS observation here we see similar behaviour in the beamsplitter SIS bands. Furthermore standing waves are not expected to be significant in these bands (see analysis in section 2.4). Finally if this was a standing wave issue one would expect both OCS lines to be affected but in the examples shown here only one

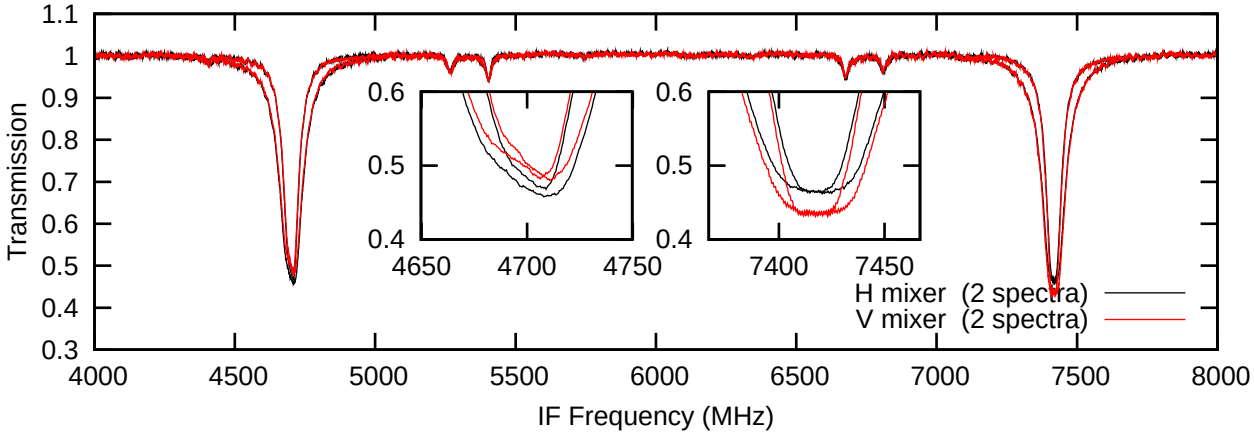

(a) OCS spectrum seen at an LO frequency of 660.681 GHz. The upper side band line, at a frequency of 668.098 GHz, is seen at 7.42GHz has regular flat line peak and is consistent with different pressures. The lower side band line, at a frequency of 655.981 GHz, has a sharp line peak different to the upper side band line.

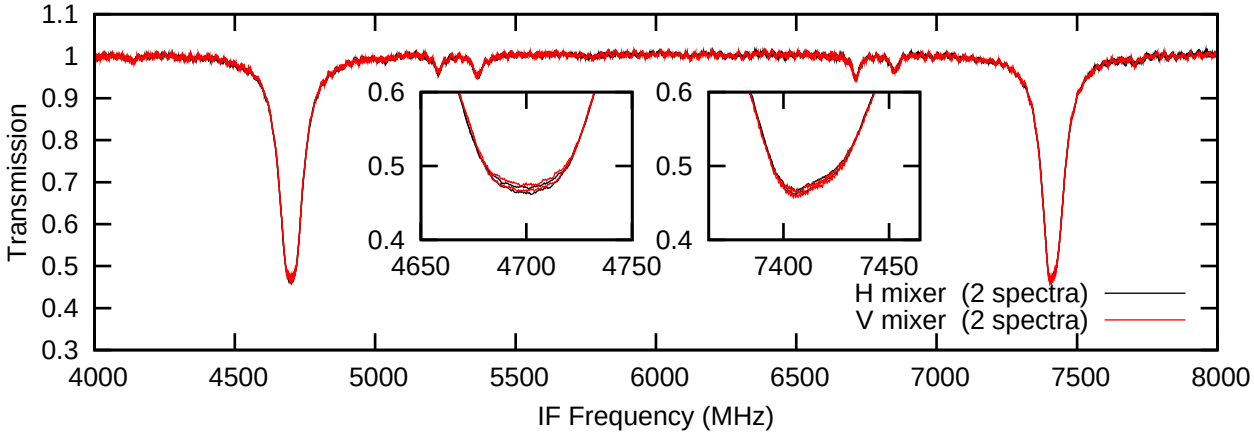

(b) OCS spectrum seen at an LO frequency of 672.798 GHz. The upper side band line seen at the higher IF frequency shows a similar sharp peak as that seen for the 660.681 GHz example above.

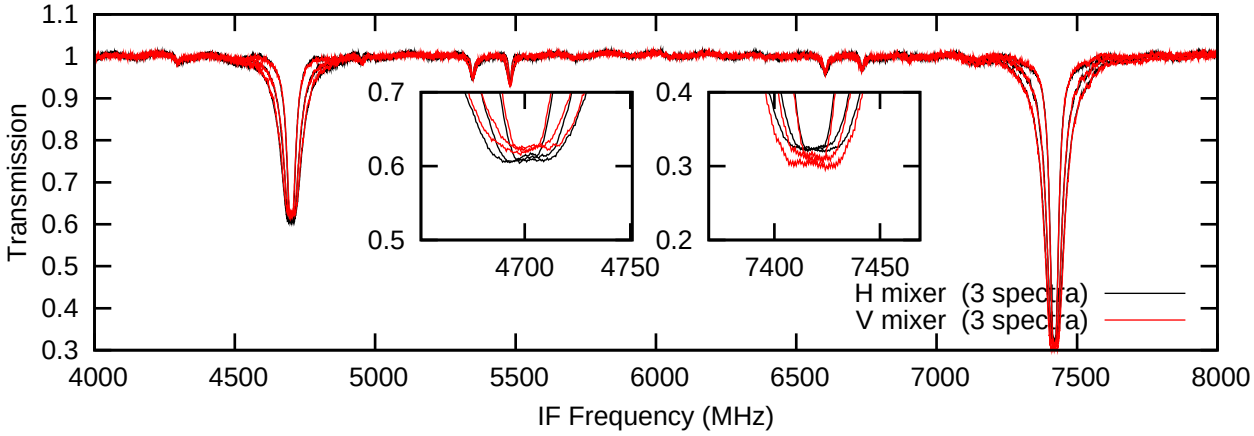

(c) OCS spectrum seen at an LO frequency of 636.444 GHz showing extreme side band gain imbalance towards the band edge. The average normalized side band gain, G_{ssb}, at this LO frequency is 0.65 (upper side band signal is on average 65% of the total double side band signal).

Figure 4.39: OCS spectra taken in band 2a showing examples of irregular line peak shape which distort the calculated side band ratio. The lower figure shows an example of an extreme but plausible side band ratio example at the band edge.

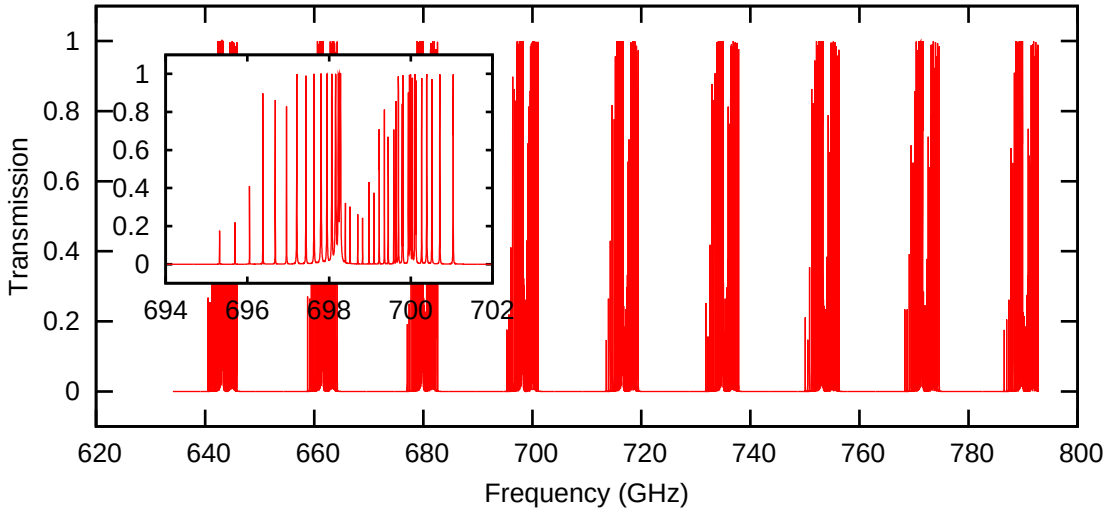

Figure 4.40: Model of CH_3CN spectra seen between 634 to 792.9 GHz (band 2). The inset plot is a magnification of the region between 694 and 702 GHz showing the fine spectral line structure.

spectral line has a distorted line shape.

4.4.7 CH_3CN analysis

CH_3CN is a more complicated molecule that those discussed so far. With more complicated molecules the number of spectral lines increases. However with more complex molecules the line transition intensities are reduced. For some complex molecules, such as CH_3OH, no saturated lines are seen in the gas cell spectra due to the lower spectral line intensity. However for CH_3CN this is not the case. Due to Nitrogen splitting 3 almost identical families of lines are superimposed on top of each other, see Cazzoli & Puzzarini [14] for further discussion. The combination of the superimposed lines provide saturated region at various IF frequencies. Another useful trait of the CH_3CN molecule is each branch of lines is separated by 18 GHz. Between these line branches no line emission is seen, see figure 4.40. This is useful for the determination of the side band ratio as there is no confusion between lines in the upper and lower side band.

The method of side band ratio extraction is similar to the previous molecules in that the peak of lines that are known to saturate are extracted. For CH_3CN a number of spectral lines are known to saturate in the center of the band. For simplicity the minimum line peak intensities are averaged together and this is taken as a single point side band ratio measurement for that LO frequency. Figure 4.41 shows an example of a CH_3CN spectrum taken at the same LO frequency of 490.406 GHz and varying gas cell pressures from 0.02 to 0.12mbar. From the figure one can see that the various lines are saturated for pressures greater than 0.07mbar. For this example the lines are observed in the upper side band. The 3 saturated lines chosen for analysis are shown in the inset plot in figure 4.41. The 3 line peak intensities are averaged together returning a value of 0.45 which corresponds to a side band ratio, G_{ssb}, of 0.55.

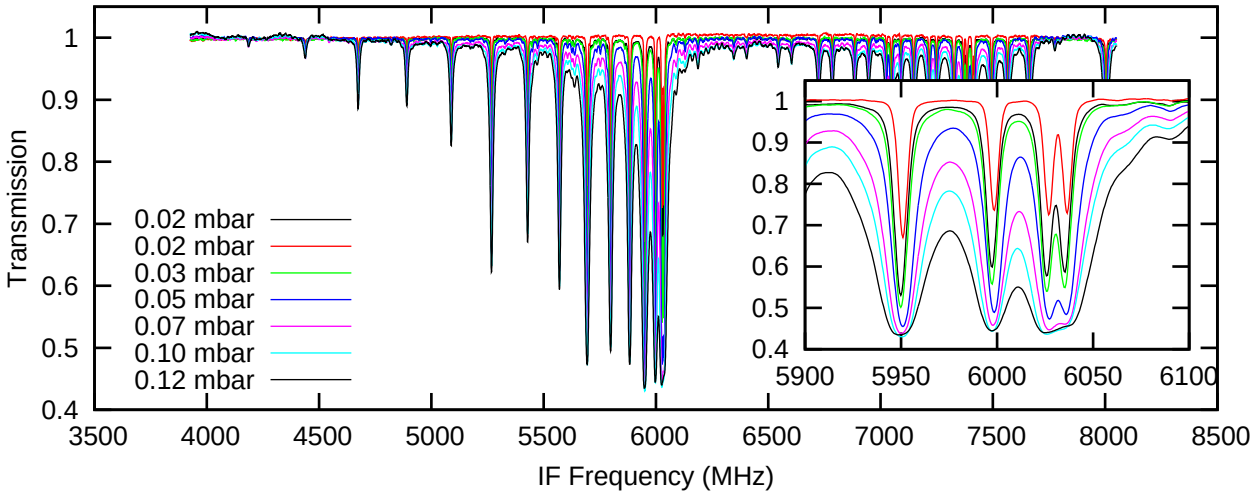

Figure 4.41: CH_3CN spectra taken at an LO frequency of 490.406 GHz with gas cell pressures varying from 0.02 to 0.12 mbar.

Figure 4.42 provides an overview of the side band ratio determined from the analysis of saturated CH_3CN lines. Each point is the average of 3 line peaks separated by 300 MHz. From the data one can see that the degree of scatter for each point is low. The edge of band 3b at 875 GHz shows some extreme behaviour and on closer inspection the data is of excellent quality suggesting that side band ratio determined is accurate. Figure 4.43 shows the spectra used to calculate the 875 GHz side band ratio point. The inset plot shows a magnification of the line region used to determine the side band ratio. From this data one can see that there is a large variation in the H mixer line peaks with IF frequency. This is not evident in the V mixer line intensities. The variation in the H mixer line intensity is consistent with the 680 MHz standing wave seen in diplexer bands. This standing wave however is not seen in the line intensities of other CH_3CN spectra and appears to be more evident at 875GHz. This is possibly linked to the diplexer setting which may have a stronger coupling to the standing wave reflecting surface at this setting. Similar standing wave behaviour was also seen at the same LO frequency for 2 ^{13}CO observations where the line intensity in the H mixer was seen to change up to 15% between 2 different LO frequencies for the H mixer but remained unchanged for the V mixer, see figure 4.28.

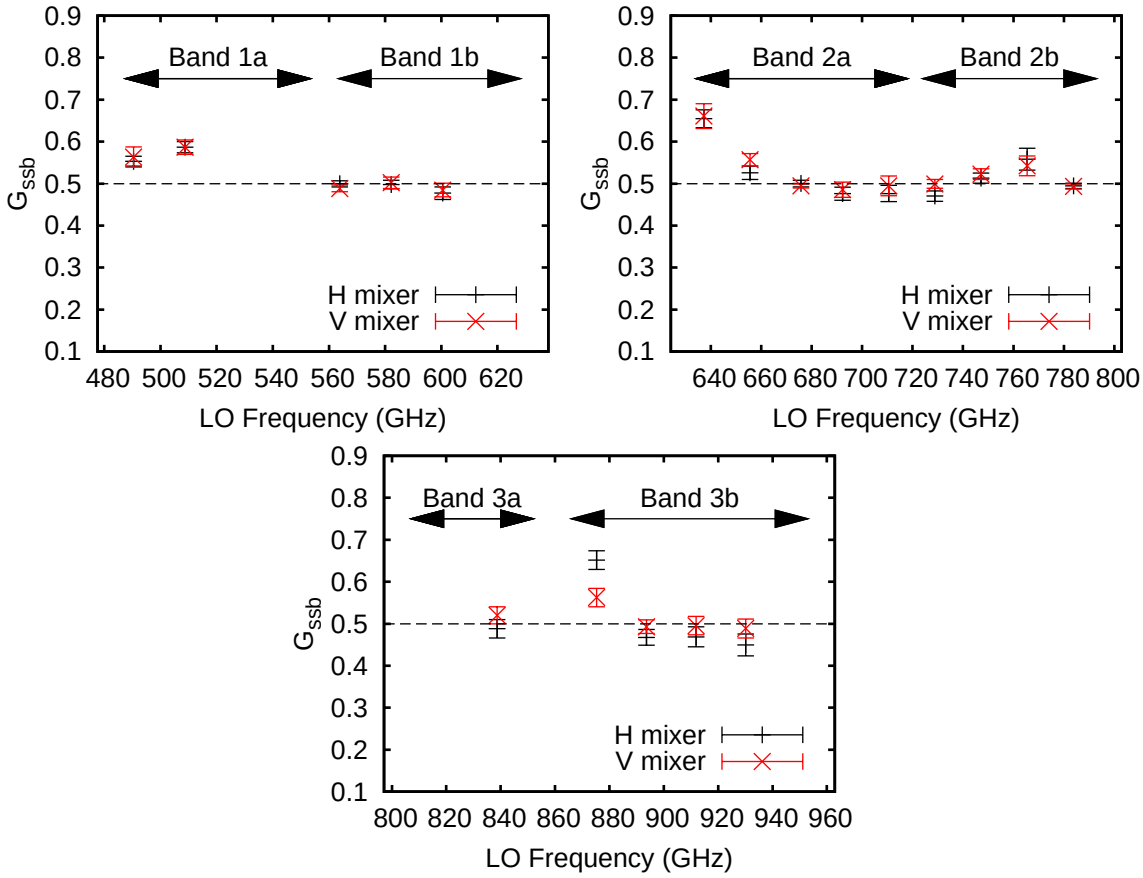

Figure 4.42: Overview of first pass determination of side band ratio from CH_3CN observations.

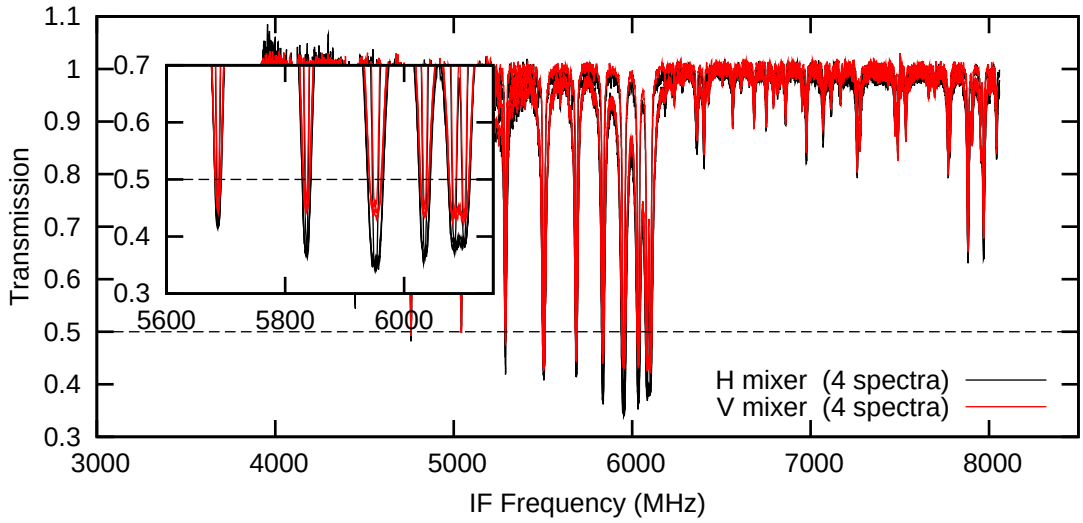

Figure 4.43: CH_3CN spectra taken at an LO frequency of 875.308 GHz showing a large side band imbalance for the saturated lines. A standing wave modulating the saturated line intensity is visible for the H mixer but not seen in the V mixer.

4.4.8 Summary

A summary of the side band ratio for the H and V mixer over the entire HIFI frequency range is given in figures 4.44 and 4.45 respectively. It is encouraging that different gases observed at the same LO frequency return similar side band ratios. For example the lower edge of band 2a shows extreme gain variation as measured by OCS. These results are supported by the CH_3CN observations which follows the trend of the OCS data. This agreement between the side band ratio extracted for different molecules is seen for most observations and supports the core goal of the gas cell campaign, that the side band ratio could be measured using different gases to sample different LO frequencies.

The side band ratio summary figures 4.44 and 4.45 provide an overview of problematic areas in the HIFI frequency range. Bands 1 and 2 provide excellent data quality except for a few spurious regions. The other bands however have there own unique problems which can be seen in the increased scatter in the measured side band ratio.

The baseline quality of the bands 3 and 4 data was comparable with that of bands 1 and 2, however the degree of scatter seen in the line intensity is indicative of more subtle effects. As shown in the ^{12}CO data for at least one test period of the gas cell test the diplexer was mistuned in band 3 while the data is recoverable using the diplexer gain model to correct the data this introduces and additional degree of uncertainty (see figure 4.19(b)). Diplexer mistuning was shown to have a large effect on the calibration accuracy with variations of 20% in line intensity seen for lines measured at the extremes of the IF bands. Unfortunately not enough gas cell data was taken when the spectral line was tracked across the IF band except for the ^{12}CO data so it is difficult to determine a diplexer mistuning in the other diplexer bands.

The SIS diplexer bands showed evidence of standing wave modulation of the spectral line. This is a subtle effect. Standing waves are normally associated with poor continuum modulation but in a stable system the continuum is devoid of standing waves. To measure the effect of standing waves on the spectral line, the line should be tracked across the IF band with a very fine LO stepping (depending on the standing wave period). For the diplexer band, it is known that a 680 MHz standing wave is present in the system. Unfortunately this was not known before the gas cell tests and this fine LO stepping approach was not undertaken in the diplexer bands.

The one incident where a spectral line was tracked finely across the IF band was for the ^{13}CO data at an LO frequency of 875 GHz. In this case only 2 observations were taken with the a 200 MHz difference between LO settings, see figure 4.28 on page 150. From this data it was apparent that there was a large increase in line intensity for the H mixer between the 2 LO setting while the V mixer line intensity was consistent between observations. This H and V mixer disparity was also seen in the CH_3CN data. The CH_3CN data was taken at just one LO frequency however since it has multiple saturated spectral lines over a range of 200 MHz the modulation of the spectral line by the standing wave could be seen, see figure 4.43 on page 166.

Ideally the saturated CH_3CN should have the same line intensity however due to the standing wave the line intensities are different. Similar to the ^{13}CO data taken at the same frequency the standing wave is more apparent in the H than the V mixer data.

No evidence of standing wave modulation of the spectral lines with IF frequency was seen in band 4, however the LO sampling was sparse and the quality of data was poor. Further investigation of these standing wave effects on the spectral line is needed. Following the 2 examples shown for ^{13}CO and CH_3CN, the calibration uncertainty for band 3 is close to 15%. This is not including the effect of side band variation across the band which will add further uncertainty to measured intensity. Further in-flight testing is needed to extract the standing wave properties modulating the spectral line intensity. It may be possibly with enough data to develop a routine to correct the spectral line data for the standing wave effect much like the diplexer model correction. To get to this model, one must understand the amplitude and phase variation of the standing wave across the band. The diplexer adds another level of complication to developing a model as the standing wave behaviour will most lightly be linked to the diplexer position which will vary from LO frequency to LO frequency.

The effect of diplexer misalignment and standing wave modulation of the side band ratio was expected. There are other effects seen in the analysis which are unexplained. For the OCS observation in band 1 & 2 a number of observation were discarded due to peculiar line profiles. A saturated line is expected to have a flat top line shape. In the diplexer bands a slope was seen in the water observation (see figure 4.33) due to standing wave or diplexer mistuning effects. However in the OCS data a number of lines showed sharp pointed line peaks (see figure 4.39). Furthermore these sharp peaks were only seen for one of the OCS lines while the other had a regular flat top saturated line. This behaviour was seen to alternate from the upper and lower side band. The shape of the pointed line profile was also similar for H and V data. If this was a standing wave effect one would expect both OCS lines to be effected and also a different response between H and V data. This sharp line peak was also seen in band 4b (see figure 4.29(c)). No explanation is forthcoming for this behaviour and lines exhibiting this behaviour were discarded from the analysis. Analysis of more data is needed to determine the origin of this effect.

The scatter in the side band ratio determined for the HEB bands is large. This is primarily due to the baseline quality seen in the data. The baseline correction routine is effective in removing the standing wave however there appears to be an inherent scatter in the HEB bands. Figure 4.26(a) on page 147 shows an example of ^{12}CO data taken in band 6a. Even after baseline correction there appears to be a large scatter in the line intensity.

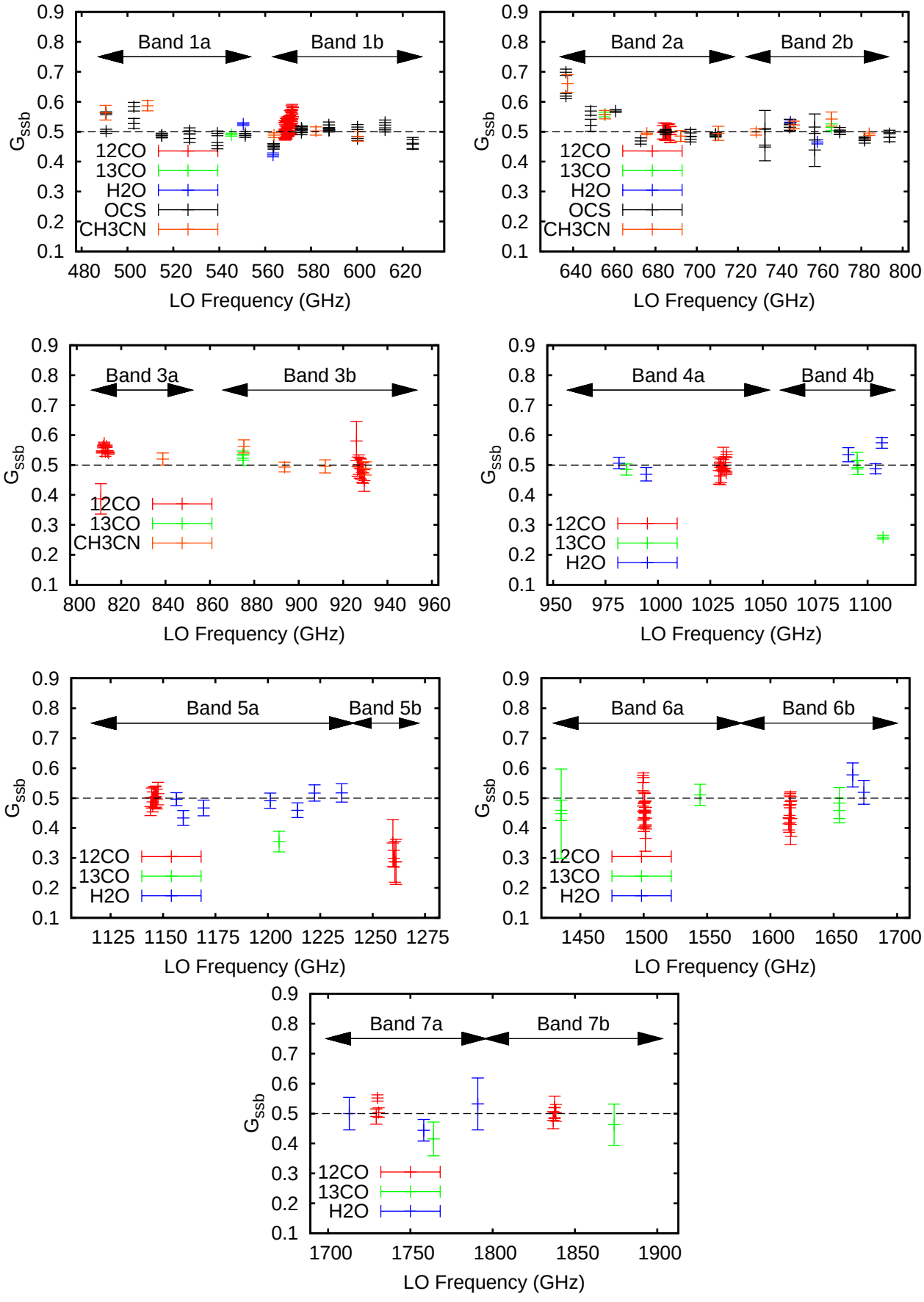

Figure 4.44: Overview of side band ratio for V mixer using ^{12}CO, ^{13}CO, H_2O, OCS and CH_3CN.

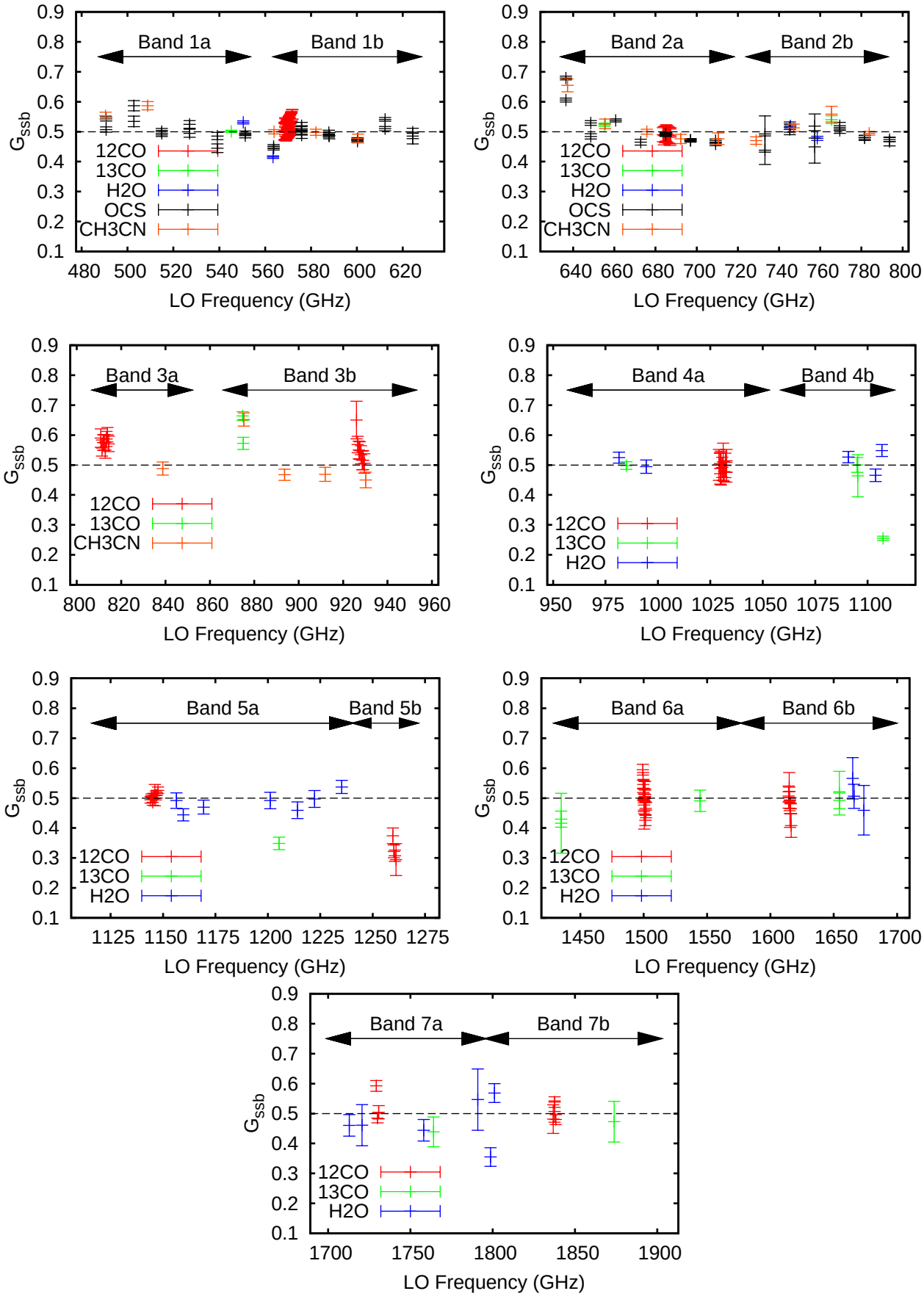

Figure 4.45: Overview of side band ratio for H mixer using ^{12}CO, ^{13}CO, H_2O, OCS and CH_3CN.

4.5 Conclusions

In this chapter the gas cell test campaign and the contributions of the author were discussed. The rationale behind the gas cell optical set up, the choice of calibration gases, the test procedure, calibration, processing and analysis was detailed. In this chapter the analysis of the saturated lines observed in the gas cell and the extraction of the side band ratio was described.

From the data a number of problems were uncovered. The analysis of HEB bands uncovered significant data quality issues due to an IF chain impedance mismatch. Chapter 3 describes the source of this problem and also the methods to correct the gas cell test data and also in flight data. Without the gas cell data the development of this HEB baseline correction routine would have being impossible.

The main goal behind the gas cell test campaign was the extraction of the side band ratio across the HIFI frequency range. For bands 1 and 2, this goal has been achieved over a sparsely sampled frequency range using four different molecules. However, bands 3-7 are only sparsely sampled by saturated line molecules. Towards the higher frequency bands the sampling is particularly coarse. Unfortunately the bands sampled the most (band 1 & 2) are also the bands with the least instrument problems. The SIS diplexer bands show considerable variation in line intensity due to standing wave and diplexer mistuning effects. Band 5 has LO purity issues. While bands 6 & 7 show a large degree of scatter in the determined side band ratios.

The higher frequency bands are less sampled because of the lack of saturated lines towards higher frequencies. As shown in figure 4.5 and table 4.1 a number of additional molecules were observed which don't saturate in the gas cell test setup. It is possible using a model the spectral line for a given temperature, pressure and optical path length. By comparing this model with the measured data it is possible to extract the side band ratio from a non saturated line. Furthermore using the more line rich molecules can help fill in the gaps in the side band ratio coverage in band 1 and 2. The next chapter will describe this second stage of side band ratio extraction using a line model instead of simply measuring the line peak as discussed in this chapter.

Chapter 5

Gas cell test campaign: spectral line model generation and CH_3OH analysis

5.1 Introduction

The extraction of the side band ratio so far has being limited to the analysis of saturated lines. Extracting the peak intensity of saturated lines provides a direct probe of the gain ratio between the upper and lower side band. Unfortunately molecules with saturated lines in the gas cell set up only sparsely sample the HIFI frequency range. For bands 1 & 2 the side band ratio is sampled multiple times by the simple molecules. However towards higher frequencies the line intensity of certain molecules drops off and are no longer saturated, OCS for example.

It is possible however to extract the side band ratio from spectral lines which are not saturated using a spectral line model to estimate the line opacity. One of the criteria in choosing a calibration gas was the availability of accurate line lists containing line frequencies, intensities and pressure broadening parameters. Using this information in combination with the gas cell properties such as gas pressure, gas temperature and optical path length of the gas cell it is possible to generate a model double side band spectrum which can then be compared with the observed spectra. The side band ratio is left as free variable in the model and fitted to the data.

The use of a spectral line model opens up the possibility of using CH_3OH to determine the side band ratio. Methanol was original envisaged as a test gas for the side band deconvolution algorithm however using a spectral line model it is also possible to extract the side band ratio. As summarized in table 4.1 on page 116 methanol accounts for 80% of the observations taken over the course of the gas cell test campaign. In total methanol has over 7000 spectral lines in the HIFI frequency range. At a gas cell pressure of 0.2mbar 1500 of these spectral lines are 20% opaque.

As stated previously one of the criteria for calibration gas selection was that a complete line list was available. However for methanol this wasn't entirely true, the line frequencies and

intensities were still the subject of research and during the gas cell test campaign it was hoped that through the analysis of methanol over the HIFI frequency range that the molecular model could be constrained and from this a more accurate line list could be generated. Furthermore the pressure broadening parameters were unknown before the test campaign and one of the initial goals of the methanol analysis was the retrieval these values. Once the pressure broadening parameters for each transition were established then the side band ratio could be extracted.

In this chapter the theory behind a spectral line profile shape is described. The process of converting a line list into a double side band spectrum using the gas temperature, pressure, optical path length is described. These methods are then applied to a ^{12}CO spectrum to demonstrate the feasibility of such an approach. By comparing the line model to the real data it is possible to extract the side band ratio. Using this model approach the side band ratio is extracted for the saturated molecules analyzed in previous chapter, namely ^{13}CO, OCS and H_2O.

The analysis of methanol is presented towards the end this chapter. The processing of methanol follows a iterative process whereby the pressure broadening parameters are first extracted from the data and then once this data is at hand a second modeling effort is undertaken to extract the side band ratio. Since the pressure broadening parameters are already known for ^{12}CO, ^{13}CO and OCS the method of pressure broadening extraction is first tested on this dataset. By comparing the extracted pressure broadening parameters with published data it is possible to calibrate the approach for methanol.

The last section of this chapter describes the use of methanol gas cell observations in the development of a new heterodyne receiver. In this section the application of the methods described in this chapter to the gas cell testing of a new Quantum Cascade Laser (QCL) heterodyne system are described.

5.1.1 Author's contribution

The author converted the radiative transfer code of Charlotte Vastel, originally written in IDL, to the HCSS environment. The analysis and interpretation of results in this chapter are the work of the author. The author developed a number of tools to investigate the diplexer mistuning problem seen in the data. The testing of the deconvolution algorithm on methanol data was done by Claudia Comito who kindly provided the data for presentation here. The QCL work was undertaken in collaboration with Yuan Ren and Jian Rong Gao from TU Delft. Yuan Ren was responsible for the experimental setup and data acquisition. The author use the HCSS gas cell code to model the measured data.

5.2 Spectral line shapes

5.2.1 Introduction

The following section describes the theory behind the generation of a model gas cell spectrum.

5.2.2 Natural line broadening

Spectral lines have an inherent line width independent of external influences such as relative motion and collision with other molecules. This line width is inversely proportional to the lifetime of a spectral line transition. In the THz regime transition lifetimes are usually very short and by Heisenberg's uncertainty principle, $\Delta E \Delta t \sim h/(2\pi)$, there is a corresponding uncertainty in energy or spread in energy seen for that transition giving rise to a corresponding broadening of the spectral line. This spectral line shape is best approximated by a Lorentzian profile. At these sub-mm frequencies the natural line width is of the order of kHz and is insignificant when compared to the more dominant pressure and Doppler broadening effects which are in the MHz range. For this analysis this broadening effect is ignored. For further reading see Gordy & Cook [39].

5.2.3 Doppler line broadening

Doppler broadening occurs due to the motion of a molecule as it emits radiation. Due to the motion of the molecule the frequency of the transition is shifted depending on the direction of the molecule relative to the observer. A molecule moving away from the observer will have a red shifted line (lower frequency) while a molecule moving towards an observer will have a blue shifted line. The frequency ν of line emitted from a molecule moving with velocity v_r in the line of sight is given by

$$\Delta\nu = \nu - \nu_0 = -(v_r/c)\nu_0, \tag{5.1}$$

where ν_0 is the rest frequency of the gas and c is the speed of light. Substituting in the Maxwell-Boltzmann distribution of particle speed in gases, this returns a unit Gaussian line shape such that:

$$\phi_\nu = \frac{1}{\sqrt{\pi}\delta\nu_D} e^{-ln(2)(\nu-\nu_0)^2/\delta\nu_D^2}, \tag{5.2}$$

where $\delta\nu_D$ is defined as

$$\delta\nu_D = \frac{\nu_0}{c}\sqrt{\frac{2ln(2)kT}{m}}, \tag{5.3}$$

where k is the Boltzmann constant (1.38×10^{-16} erg/K), T is the gas temperature in Kelvin, m is the molecular mass of the molecule, c is the speed of light and ν_0 is the line rest frequency. For a more detailed explanation of the above equations see Emerson [30].

5.2.4 Pressure/Collisional line broadening

Pressure broadening is the effect of increasing line width with increasing pressure. Collisional broadening is another name for this effect and is a more descriptive term for the broadening mechanism. The line broadening mechanism is similar to the natural line broadening in that the width of the line is determined by the time a molecule is in a given emission state. The state of the molecule is changed due to collisions or proximity to another molecule. The time between collisions determines the extent of the line broadening. The sensitivity of a molecular transition to collision or proximity with other molecules depend on the property of the molecule such as dipole moment and also the type of transition. The result of this is that each molecular transition has a unique pressure broadening variation. For further discussion of this topic see Emerson [30].

Similar to the natural line width, the line profile resulting from pressure broadening is best described by a Lorentzian line profile such that:

$$\phi_\nu = \frac{\delta\nu_L}{\pi((\nu - \nu_0)^2 + \delta\nu_L^2)} \tag{5.4}$$

where:

$$\delta\nu_L = \gamma_{self} P_{gas} \tag{5.5}$$

and P_{gas} is the gas cell pressure and γ_{self} is the pressure broadening parameter. The units of γ_{self} vary from publication to publication. The unit used in the HITRAN database[106] is cm^{-1}/atm. For the model code the unit of self broadening in changed as MHz/mbar since the frequency unit is the unit of choice for HIFI and up to now pressures have been quoted in mbar. For the methanol analysis both units are quoted to ease comparison with published data.

5.2.5 Opacity line broadening

Up to now the line broadening effects described were local effects due to motion or interactions of individual molecules. Opacity broadening is a non local effect and is due to the transmission of the signal through the gas sample. This effect of line broadening is also known as the Beer-Lambert law. The transmission of signal through a gas is a function of the column length and can be described by the following function:

$$\phi_\nu = e^{-\alpha L} \tag{5.6}$$

where L is the gas cell column length and α is the opacity of the gas sample is calculated from the Doppler, pressure broadening described in the previously sections in combination with the line strength.

5.3 Spectral line model generation

From the previous section it is apparent that 3 broadening mechanisms cause the line broadening we see in a gas cell spectrum. Doppler broadening has a Gaussian profile the width of which is a function of molecular mass, gas temperature and line frequency. The pressure broadening is a Lorentzian profile which is function of the gas pressure and the pressure broadening parameter for the transition of interest. The opacity broadening is a function of the column length of gas under observation. All these mechanisms combine together to produce a net line profile. In order to generate a model spectra we need to have a measure of the line intensity, line frequency and the pressure broadening parameter which we get from a combination of the JPL line catalog[94] and HITRAN database[106]. The JPL catalog is used for the line frequencies and intensities while the pressure broadening is taken from the HITRAN database.

The steps undertaken to generate a model spectrum are best illustrated through an example. For this example a ^{12}CO spectrum from band 2a is used. The band 2a dataset was selected as an example as it has a balanced side band gain ratio at the ^{12}CO (6-5) transition. The final profile is a convolution of the pressure broadening Lorentz profile and the Doppler broadening Gaussian profile. A convolution of a Gaussian and Lorentzian profile is known as a Voigt profile. For this analysis the Voigt profile is generated using a numerical approximation developed by Olivero & Longbothum [85] and expanded upon by Liu et al. [73]. A numerical approximation is used instead of a direct convolution as this reduces the computation complexity. For the CH_3OH data it is envisaged using a fitting routine that will extract the pressure broadening paramete, using a numerical approximation to generate the line profile reduces the computation time considerably.

The first step in generating a model double side band spectrum is to determine which lines are present in upper and lower sidebands. Each gas cell spectrum is taken at a given LO frequency. Using the LO frequency in combination with the line list a subset of lines which fall inside the IF band of the mixer is generated. Each line in this line list contains the line frequency, the IF frequency, the line intensity and the self broadening, γ_{self}, if its available. For each spectral line a profile is generated and this is then added to the global model. For ^{12}CO only one line is seen for a given LO frequency. For this example the observed data was taken at an LO frequency of 685.572 GHz, this places the 691.473 GHz spectra line in the upper side band at an IF frequency of 5.9 GHz.

Once the line list is generated and the IF frequency of each line in the spectrum is established a spectral profile is generated for each line. The first step in this process is to calculate the Doppler and pressure broadening widths for the transitions using equations 5.3 and 5.5. For the Doppler broadening the molecule weight of the molecular must be calculated, for ^{12}CO the molecular mass is 27.994914u[1] (^{12}C is 12.0u, O is 15.994914u). For equation 5.3 the atomic

[1] **u** is the unit of atomic mass where 1u is is defined as one twelfth of the rest mass of an unbound atom of carbon-12

mass is converted to grammes using the Avogadro constant, N_A. The Boltzmann constant, k, is in units of ergK^{-1}. An Erg is a unit of energy in centimetre-gram-second system of units. To keep the units consistent the speed of light is then quoted in units of cms^{-1}. Inserting all the values in equation 5.5 as follows returns the Gaussian half width:

$$\begin{aligned}
\delta\nu_D = & \frac{\nu_0}{c}\sqrt{\frac{2ln(2)kT}{m}} \\
= & \frac{691.473\times10^9}{2.997\times10^{10}}\sqrt{\frac{2ln(2)\times1.38\times10^{-16}\times296}{(27.99/6.022\times10^{23})}} \\
= & \frac{s^{-1}}{cms^{-1}}\sqrt{\frac{cm^2s^{-2}gK^{-1}K}{g}} \\
= & 8.1\times10^5 s^{-1} \\
= & 0.81\text{MHz}.
\end{aligned}$$

The calculation of the pressure broadening half width is less complicated but requires some care with units also. Gas cell results are presented in a wide variety of units depending on the wavelength regimes and the pressures under investigation. For this analysis MHz and mbar are the units of choice. As described in equation 5.5 the pressure broadening profile is a function of the pressure broadening parameter γ_{self} and the gas cell pressure. For ^{12}CO the pressure broadening parameter is available through the HITRAN database for all transitions observed. For this transition the pressure broadening parameter is 0.07 cm^{-1}/atm. The units of the pressure broadening are in cm^{-1}/atm and must be converted to MHz/mbar to suit the unit choice here. Converting the HITRAN cm^{-1}/atm to MHz/bar is as follows:

$$\gamma_{self}(\text{MHz/mbar}) = \gamma_{self}(\text{cm}^{-1}\text{/atm}) \times \frac{2.99\times10^{10}}{1.0135\times10^3\times10^6}. \tag{5.7}$$

The factor 1.0135 is the conversion from atm to bar (1atm = 1.0135bar), the fact 10^3 is to convert to mbar. The 10^6 factor converts Hz to MHz. Following from this the pressure broadening parameter in MHz/mbar is 2.065. Returning to the Lorentzian half width half maximum formula in equation 5.5 and applying the gas cell pressure for the observation of 5.54 mbar returns a pressure broadening width of 11.44 MHz.

For this observation, it is apparent that the pressure broadening width of 11.44 MHz is dominant over the 0.81 MHz value calculated for Doppler broadening. A Voigt profile generated from these 2 profiles will be closer to a Lorentzian than a Gaussian profile.

The numerical approximation for a Voigt profile uses the 2 widths of the constituent Gaussian and Lorentzian profile as starting point to generate an equivalent profile, see Liu et al. [73] for a detailed discussion of the Voigt profile and the following approximation. The first step in generating the equivalent Voigt profile is calculate the dimensionless weighing function, d, as

follows:

$$d = \frac{\delta\nu_L - \delta\nu_D}{\delta\nu_L + \delta\nu_D}. \tag{5.8}$$

From this equation, it is apparent that if the Lorentzian profile is dominant then $\delta\nu_L \gg \delta\nu_D$ and $d \rightarrow 1$. On the other hand where the Gaussian profile is dominant then $\delta\nu_D \gg \delta\nu_L$ and $d \rightarrow -1$ From this parameter, 2 weighing parameters are generated as follows:

$$c_l = \quad 0.68188 + 0.61293 \times d - 0.18382 \times d^2 - 0.11568 \times d^3 \tag{5.9}$$

$$c_d = \quad 0.32460 - 0.61825 \times d + 0.17681 \times d^2 + 0.12109 \times d^3. \tag{5.10}$$

For the extreme case where the Lorentz width dominates or d = 1, the constant $c_l \rightarrow 1$ and $c_d \rightarrow 0$. Where the Gaussian profile is dominant over the Lorentz width (d = -1), $c_d \rightarrow 1$ and $c_l \rightarrow 0$. These weighting factors are used to generate the numerical approximation of the Voigt profile from a weighed sum of a Gaussian and Lorentzian functions with an equivalent half width half maximum, $\delta\nu_V$, which is calculated from the pressure and Doppler half width half maximums as follows:

$$\delta\nu_V = 0.53456 \times \delta\nu_L + \sqrt{(0.2166 \times \delta\nu_L^2 + \delta\nu_D^2)}. \tag{5.11}$$

The final Voigt profile is then written as follows:

$$\phi_{\nu_V} = \frac{c_l(1/\pi)\delta\nu_V}{(\nu - \nu_0)^2 + \delta\nu_V^2} + c_d \frac{\sqrt{ln(2)}}{\sqrt{\pi}\delta\nu_V} * exp\left(\frac{-(ln2)(\nu - \nu_0)^2}{\delta\nu_V^2}\right). \tag{5.12}$$

From the equation it is apparent the numerical approximation is made up of a Gaussian and a Lorentzian profile with an equivalent width, $\delta\nu_V$. The 2 profiles are weighed with constants c_l and c_d calculated earlier. For the ^{12}CO transition under investigation, d is 0.87, c_l is 0.999 and c_d is 3.57×10^{-4}. For this line transition the Lorentzian component is dominant. The calculated equivalent Voigt width, $\delta\nu_V$, is 11.54 MHz which is very close to the pressure broadening width of 11.44MHz. For this example the inclusion of the Doppler width is not necessary, however for other gases the pressure is less dominant and also towards higher frequency the Doppler effect can be more pronounced.

From equation 5.12 we now have a unit area Voigt profile that describes the line shape for this transition. The next step is to scale this area using the integrated line intensity, I_{ba}, taken from the JPL catalog. The JPL catalog gives the line transition intensity as an integrated intensity in units of nm^2.MHz for a gas temperature of 300K. The Voigt profile distribution is scaled so the area is equivalent to the integrated intensity from the JPL catalog [122].

The Voigt profile is scaled by the line center absorption coefficient, α_{max}, which is calculated from the JPL line intensity. From Vastel [122], α_{max}, can be calculated from the line strength,

H, and the density of the gas, n (P/(kT)), such that

$$\alpha_{max}(\mathrm{cm}^{-1}) = H(\mathrm{cm}^2) \times n(\mathrm{cm}^{-3}). \tag{5.13}$$

The line strength H can be written as a function of the line integrated intensity, I_{ba} and the cross section of the Voigt profile described in equation 5.12 such that:

$$I_{ba} = H \times \left(\pi\delta\nu_L + \sqrt{\frac{\pi}{ln(2)}}\delta\nu_D \right). \tag{5.14}$$

rearranging the equation,

$$H = \frac{I_{ba}}{\pi\delta\nu_L + \sqrt{\frac{\pi}{ln(2)}}\delta\nu_D}. \tag{5.15}$$

Returning to equation 5.13, the absorption coefficient α_{max} can be rewritten in terms of I_{ba} as follows:

$$\alpha_{max} = \frac{I_{ba}}{\pi\delta\nu_L + \sqrt{\frac{\pi}{ln(2)}}\delta\nu_D} \times \frac{P}{kT}. \tag{5.16}$$

The absorption coefficient α_{max} is then applied to the Voigt profile to convert the unit area profile into a absorption line profile. The Voigt profile is normalized about it peak value and then multiplied by the line center absorption coefficient α_{max}. The final absorption spectra is described by the following equation:

$$\alpha_{line}(\nu - \nu_0) = \underbrace{\frac{10^{I_{ba}} \times 10^{-14}}{\pi\delta\nu_L + \sqrt{\frac{\pi}{ln2}}\delta\nu_D} \times \frac{P \times 10^6}{kT}}_{\alpha_{max}} \underbrace{\times \frac{\frac{c_l(1/\pi)\delta\nu_V}{(\nu-\nu_0)^2+\delta\nu_V^2} + c_d\frac{\sqrt{ln(2)}}{\sqrt{\pi}\delta\nu_V} * exp\left(\frac{-(ln2)(\nu-\nu_0)^2}{\delta\nu_V^2}\right)}{c_l/(\pi\delta\nu_V) + c_d\sqrt{(ln(2)/\pi)}/(\delta\nu_V)}}_{\text{normalized Voigt profile}}. \tag{5.17}$$

The JPL intensity is given as a base 10 logarithm and is written here to the power of ten. The factor 10^{-14} is introduced to convert the JPL integrated intensity units from nm^2 to cm^2 units. The factor of 10^6 is included to convert the pressure to ergs which is compatible with units used in the Boltzmann constant. The units of intensity for the above profile is cm^{-1}. For each spectral line the process is repeated and added to a global model of upper and lower side band.

Once a line profile has been generated for each spectral line and a model of the upper and lower side band is finished, the next step in the creation of a gas cell spectral line profile is the application of the opacity effect of the gas column length. This effect was described in equation 5.6. As described in the previous chapter the optical path through the gas cell is 102.54cm. The opacity is calculated using the following equation:

$$I(\nu - \nu_0) = exp(-\alpha_{line}(\nu - \nu_0) \times L). \tag{5.18}$$

The resulting model spectra is shown in figure 5.1. The ^{12}CO line is saturated at this pressure

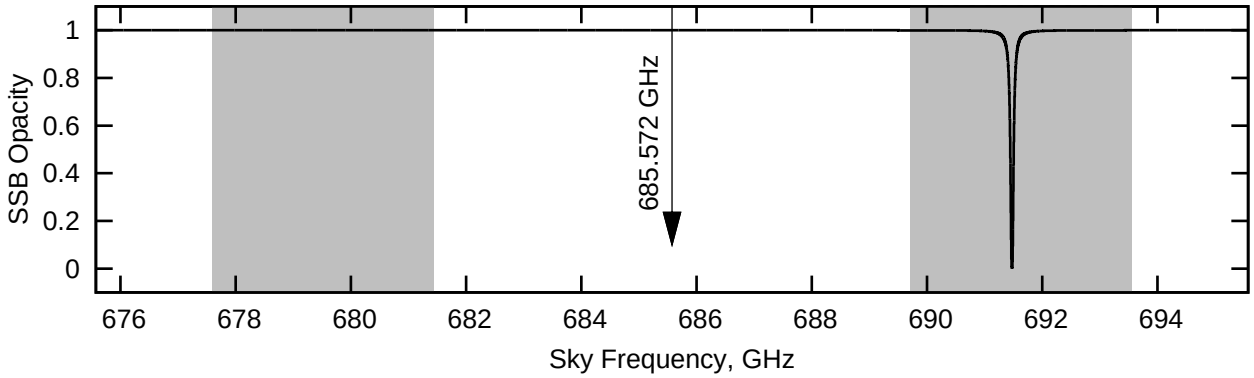

Figure 5.1: Model of upper and lower side band spectra for ^{12}CO line observed in band 6a at an LO frequency of 685.572 GHz. The side bands are highlighted in grey. No line is seen in the lower side band.

and one can see at the line peak that the single side band opacity is at 1. The final step is to convert the single side band transmission spectra shown into a double side band spectra. This is where the normalized side band ratio quantity, G_{ssb}, is introduced. The final transmission spectra is as follows:

$$I_{dsb} = I_{lsb}(\nu - \nu_0) \times (1 - G_{ssb}) + I_{usb}(\nu - \nu_0) \times (G_{ssb}). \tag{5.19}$$

For the application of the side band ratio the side band intensity is inverted so that the continuum is at 0 and the line peak at 1. The side band gain ratio, G_{ssb}, can then be applied directly. Care must be taken when adding the lower side band and upper side band intensities together. It should be remembered that LSB is folded onto the USB spectrum. So a frequency channel at 4000 MHz in the USB is added to a frequency channel at -4000 MHz in the LSB. In this example it's not important since there is no line emission in the lower side band, none the less care must be taken when combining the 2 side bands and applying the side band gain ratios.

At this stage in the analysis a double side band spectrum is generated which can be compared with the observed data. Figure 5.2 shows a comparison between a model spectrum generated using the methods described here. For this example an LO frequency was chosen where mixer gain was equal for both side bands, $G_{ssb} = 0.5$. Hence the line peak intensity is 0.5. The residual between the model and the data is plotted in black. From this one can see that the fit is excellent except for the line peak where a slight double dip is seen. This could be indicative of some uncertainty in the measured gas cell pressure. The residual however does show the ability of the methods described here to model a gas cell spectrum.

Figure 5.3 provides an overview of the process of generating a double side band spectral line model starting from a molecule line list, the LO frequency and the gas cell properties and conditions during the observation. Using this process it is possible to extract the side band ratio. By leaving G_{ssb} as free variable in equation 5.18 the model data can be fitted to the measured data. In the example shown the data is not fitted and a balanced side band gain is

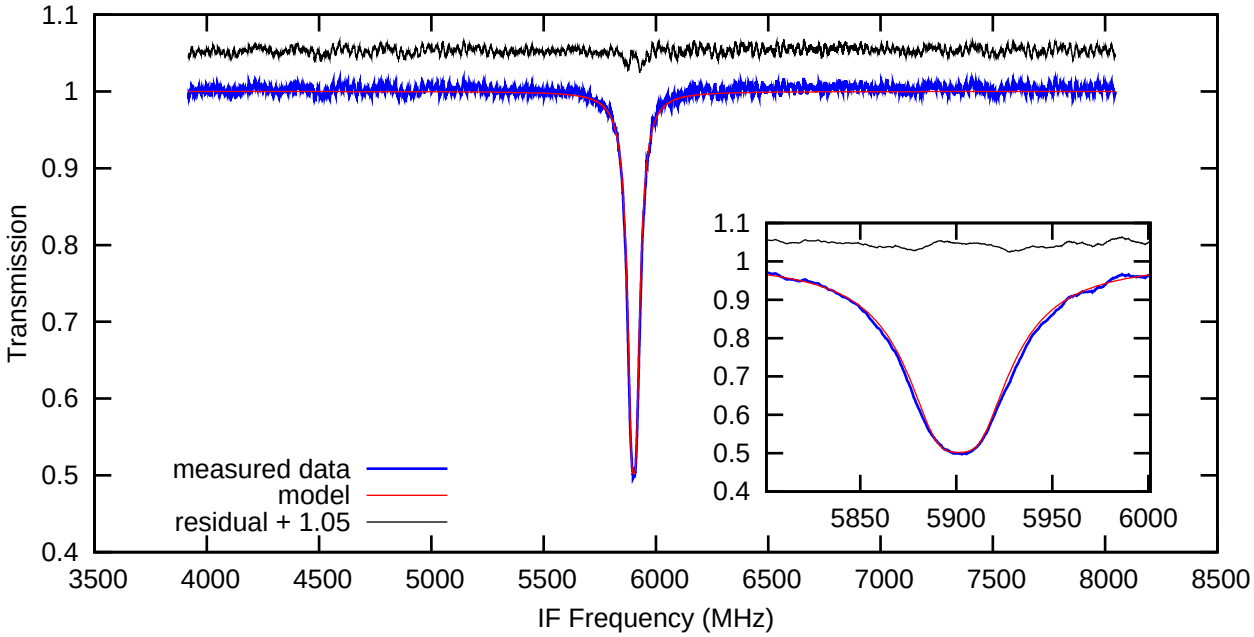

Figure 5.2: Double side band model spectrum for a ^{12}CO gas cell observation at a gas cell pressure of 5.54mbar. Spectrum was taken at an LO frequency 865.572 GHz. The residual between the model and observed data is shown in black with an offset of 1.05.

assumed. The next section presents the extraction of the side band ratio using the spectral line modeling approach on various gases measured during the test campaign.

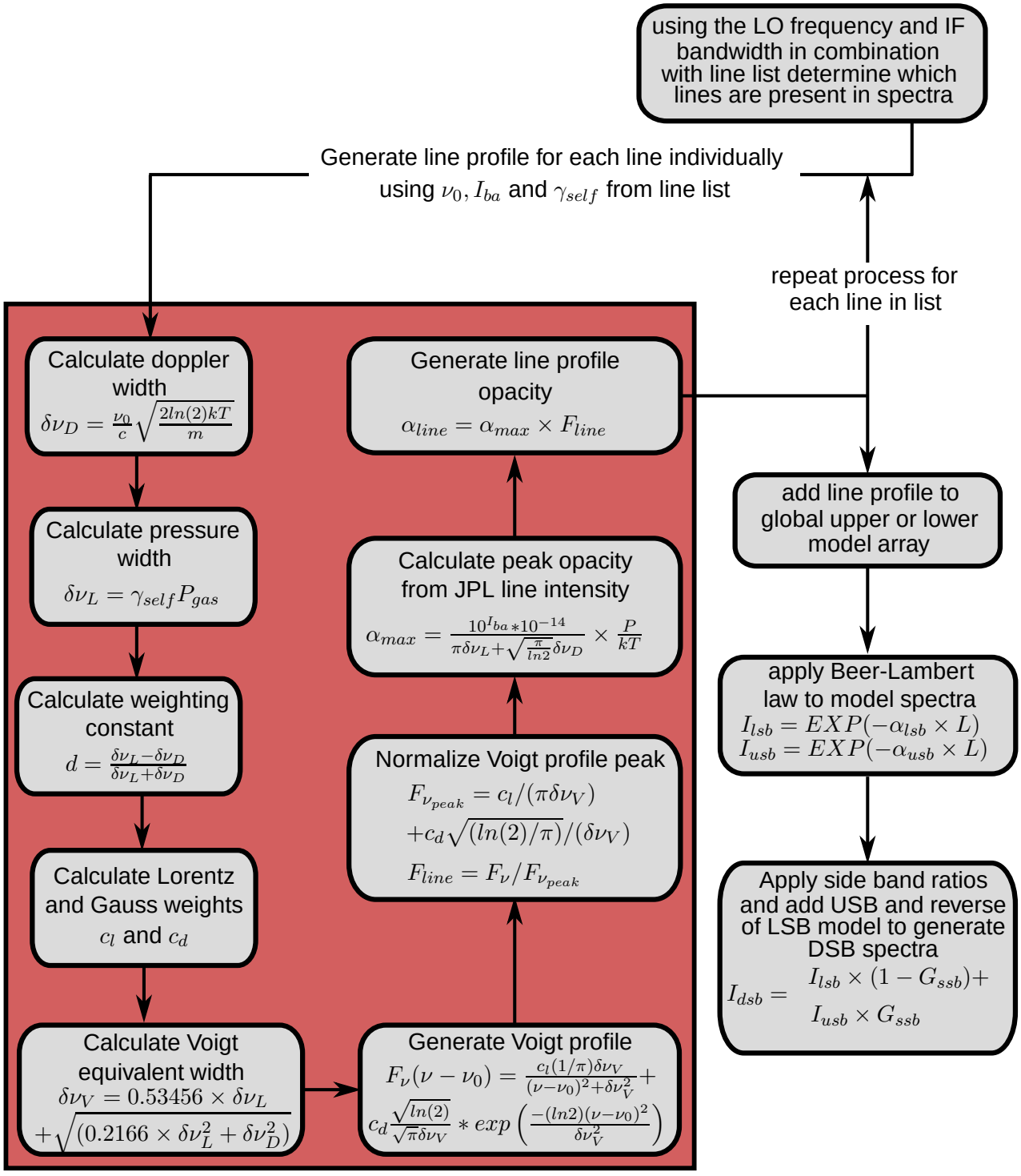

Figure 5.3: Process of generating double side band spectral line model.

5.4 Side band ratio extraction: simple molecules

5.4.1 Introduction

In this section the extraction of the side band ratio is described. By comparing a model spectrum to the measured spectrum it is possible to determine the side band ratio. The use of a model allows additional non saturated lines to be included in the analysis. This section describes the analysis of 4 simple molecules ^{12}CO,^{13}CO, OCS and H_2O. Each of these molecules have complete line lists available through the JPL and HITRAN spectroscopy catalogs.

The code used to generate the spectral line model is given in Appendix A. The code presented is the core of the gas cell model script a number of ancillary scripts for importing the gas cell data and importing the JPL and HITRAN databases are not included in the appendix but are referred to the the gas cell code. The code is written as a python class which interacts with the fitting routines available in the HCSS software. Within the code there are 3 variants of the model generation. One version is the `generateLineModelSBR` which leaves the normalized side band ratio, G_{ssb}, as the only free variable in the model. The fitting routine then varies this variable until the best fit between the model and data is found. As there is some uncertainty in the measured gas cell pressure the most commonly used routine is the `generateLineModelSBRPressure` function. In this case both the pressure and G_{ssb} are left as free variables. The fitted gas cell pressure is limited to within $\pm$ 5% of the measured gas cell pressure. The molecules discussed in this section have pressure broadening parameters, γ_{self}, available for each transition. However for more complex molecules such as CH_3OH, γ_{self} data is not available and hence for this data the γ_{self} variable is fitted using the `generateLineModelPSelfSBR`. In this function both the pressure broadening and normalized side band ratio are fitted while the gas cell pressure is taken as the measured pressure. An additional function is available, `generateLineModelPSelf`, which fits the pressure broadening only. This is useful for checking the published γ_{self} against the measured γ_{self}.

5.4.2 ^{12}CO, ^{13}CO

Section 5.3 demonstrated the generation of a double side spectral line model using the gas cell properties and line parameters taken from the JPL and HITRAN spectroscopy database. Figure 5.2 showed a comparison between a model and the measured ^{12}CO spectrum in band 2a showing good agreement. This example data was chosen as the mixer side band gain was balanced for this LO frequency. This provided a good test case for an ideal mixer gain scenario. ^{12}CO was also chosen as a test case as the line frequency intensities and pressure broadening parameters were well known for the lines observed in the gas cell campaign. For the CO analysis the line frequencies were taken from the JPL catalog which based its line list on the work of Goorvitch & Chackerian [38] (line intensities) and Winnewisser et al. [127] (line frequencies). The JPL catalog does not supply the pressure broadening parameters and they were taken from

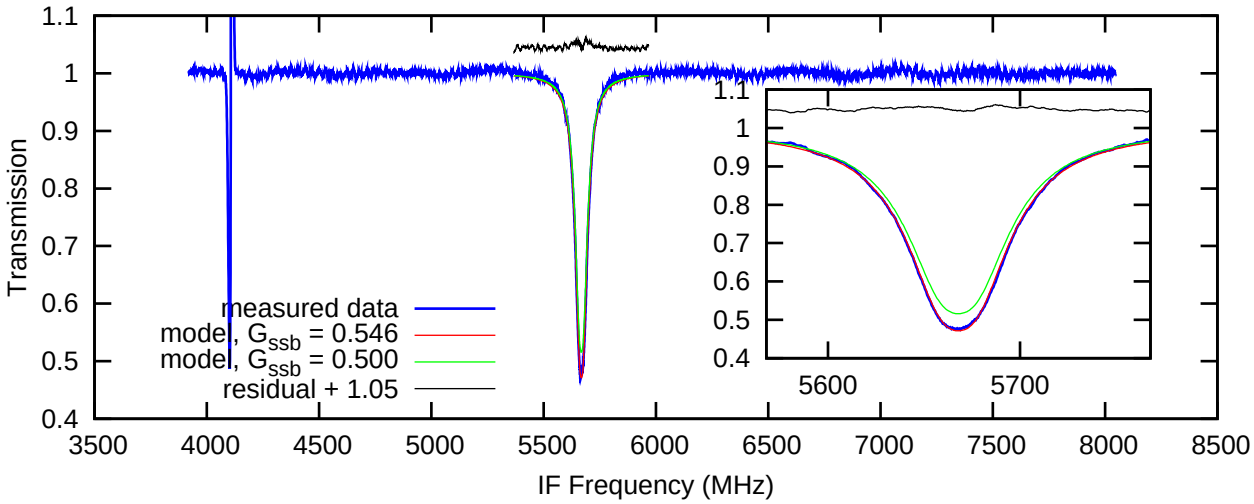

Figure 5.4: Double side band model spectra for a ^{12}CO gas cell observation at a gas cell pressure of 5.54mbar. Spectrum was taken at an LO frequency 570.6 GHz. The model spectra for side band gain balanced state is shown in green (G_{ssb} =0.5). The fitted profile with a side band ratio of 0.546 is plotted in red. The residual to the fitted data is shown in black with an offset.

the HITRAN database which took the data from the work of Brault et al. [9].

Figure 5.4 shows an example of a model spectrum when the side band ratio, G_{ssb}, is allowed to vary. The fitted value is calculated as 0.546. Hence for this IF frequency at this LO frequency the upper side band intensity is 54.6% of the total double side band intensity. The model spectra for a gain balanced mixer (G_{ssb} = 0.5) is also plotted for comparison. For this example only the region around the line is included in the fitting routine which improves the computation speed and quality of the final fit as opposed to including the whole 4GHz IF band which can take longer to reach a solution.

The residual between the model and fit provide a useful filter property for quickly determining the quality of the fit. For each fit the mean and standard deviation of the residual are recorded. Figure 5.5 shows an overview of the mean residual for all ^{12}CO spectra fitted in band 1b where the error bars are the standard deviation of the residual. From this plot one can see outlier points for the H mixer. The corresponding model fit for spectrum number 50 is shown in figure 5.6. From the plot one can see that the spectral line frequency doesn't correspond to the model frequency. The V mixer spectrum taken at the same time is shown in figure 5.4 which shows no frequency disparity.

On first inspection it seems that the commanded and actual LO frequency are not the same. However the V mixer spectrum has the spectral line at the correct IF position while the H mixer does not. The source of this problem was eventually tracked to the frequency calibration of the spectrometer. The WBS spectrometer uses a local signal source called the comb which is used to calibrated the CCD channel corresponding frequency. For this example the comb was not generated for the H mixer but was generated for the V mixer. The pipeline still generated data but with a default frequency calibration. At the time of the gas cell observation the level 0

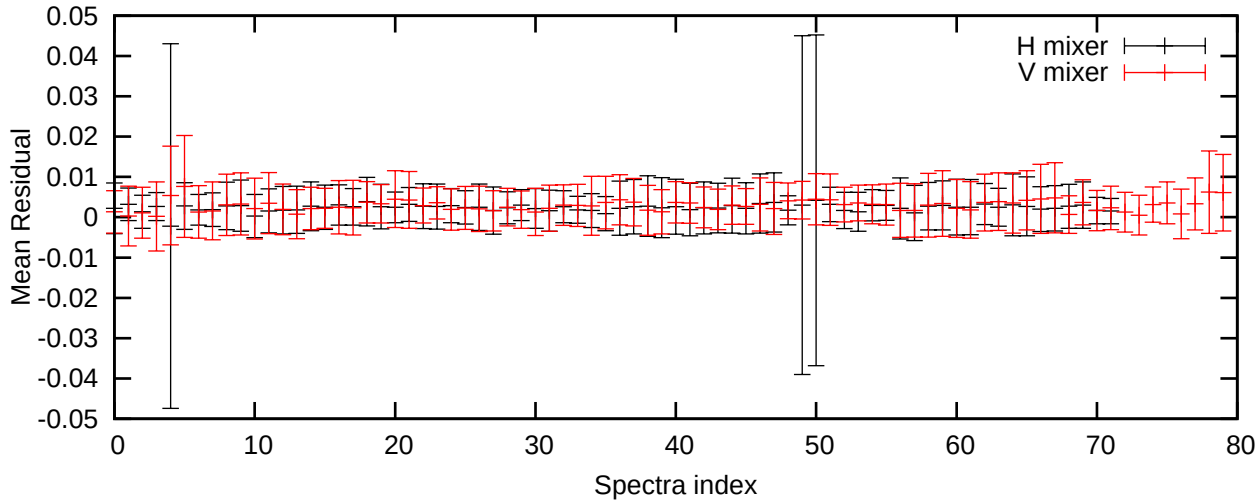

Figure 5.5: Mean of model residual for all ^{12}CO spectra taken in band 1b. The error bar is the standard deviation of the model residual. Note the outlier for the H mixer at 4th, 49th and 50th spectra.

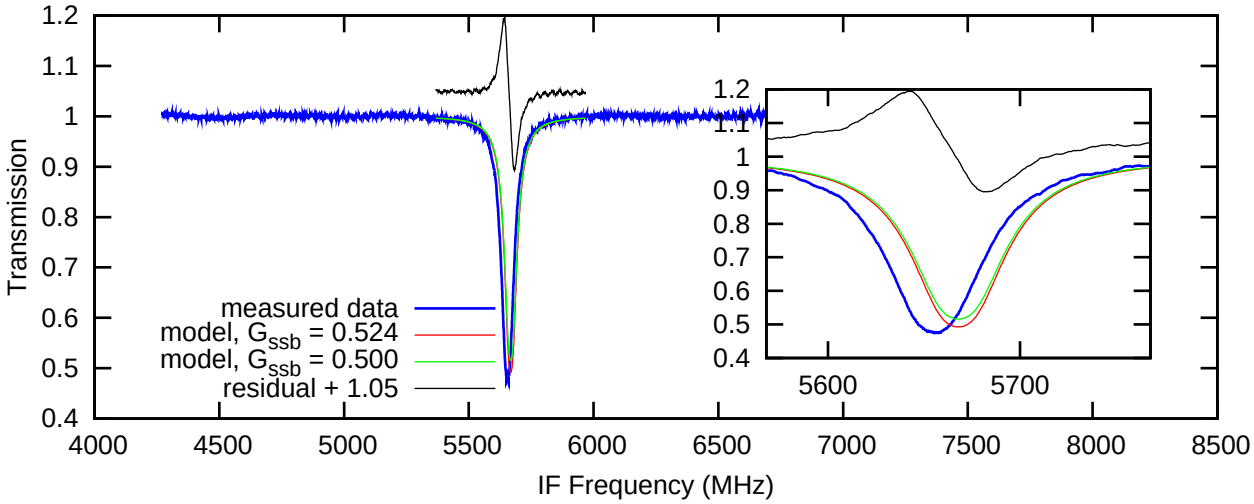

Figure 5.6: Model fit with high residual due to a frequency calibration error due to missing WBS-H backend comb.

pipeline was still at an early stage of development and not programmed to flag poor frequency calibration. The pipeline has since been updated to flag such behaviour.

The same procedure of model generation is repeated for all ^{12}CO and ^{13}CO spectra taken during the gas cell campaign and the results recorded. Using the fit residual in combination with the baseline quality and noise provide useful properties to filter the data. The results are summarized at the end of this section following a description of the OCS and H_2O analysis.

5.4.3 OCS

The OCS analysis follows a similar process to the CO analysis discussed previously. The line frequencies and intensities are taken from the JPL catalog. The line frequencies are sourced from the work of Dubrulle et al. [28] while the dipole moment was taken from Reinartz & Dymanus

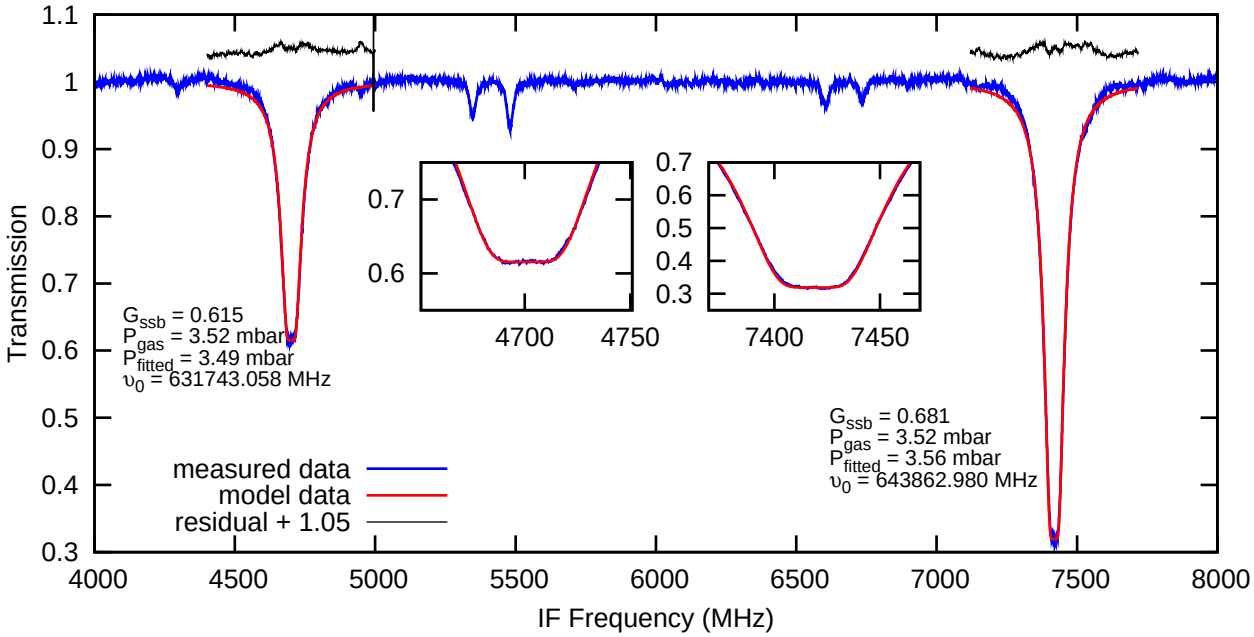

Figure 5.7: OCS spectrum observed at 636.444 GHz showing a large side band ratio imbalance. Each line is fitted individually and the parameters of each fit are given beside the model.

[103]. The self broadening parameter was taken from the work of Koshelev & Tretyakov [67]. The HITRAN database provides another similar set of pressure broadening parameters but the Koshelev & Tretyakov [67] work was more up to date.

The fitting procedure is similar to the CO procedure discussed in the previous section. However OCS has 2 spectral lines in the IF band. Initial fitting efforts tried to fit the side band ratio for both lines simultaneously. Whereby a spectral line model of the entire IF band was generated and the a model of the side band ratio across the IF band was fitted. With this approach the side band ratio was assumed to vary linearly across the IF band. This approach was very rigid and a good fit, particularly towards the band edges, was difficult. The final approach was to model each spectral line separately and fit the side band ratio for each line individually. Additionally, the gas cell pressure was left as a free variable and the `generateLineModelSBRPressure` fitting procedure in the gas cell code was used. For the CO analysis the pressure was left as that measured in the gas cell. However for OCS the resulting fit was poor and failed to properly fit the line peak therefore producing a poor side band ratio measurement. Leaving the gas cell pressure free to vary ± 20% of the measured pressure produced a better fit. The resulting fitted pressure doesn't vary more than 5% from the measured gas cell pressure. The deviation for OCS may be indicative of uncertainty in the published pressure broadening as opposed to a measurement error in the gas cell pressure.

Figure 5.7 shows an example of an OCS line fit. A region ± 300 MHz around each line is extracted and a line model is generated. The fit parameters are given beside each spectral line along with the sky frequency of the observed line. From this one can see that the spectral line at the lower IF frequencies is observed in the lower side band while the line in the higher

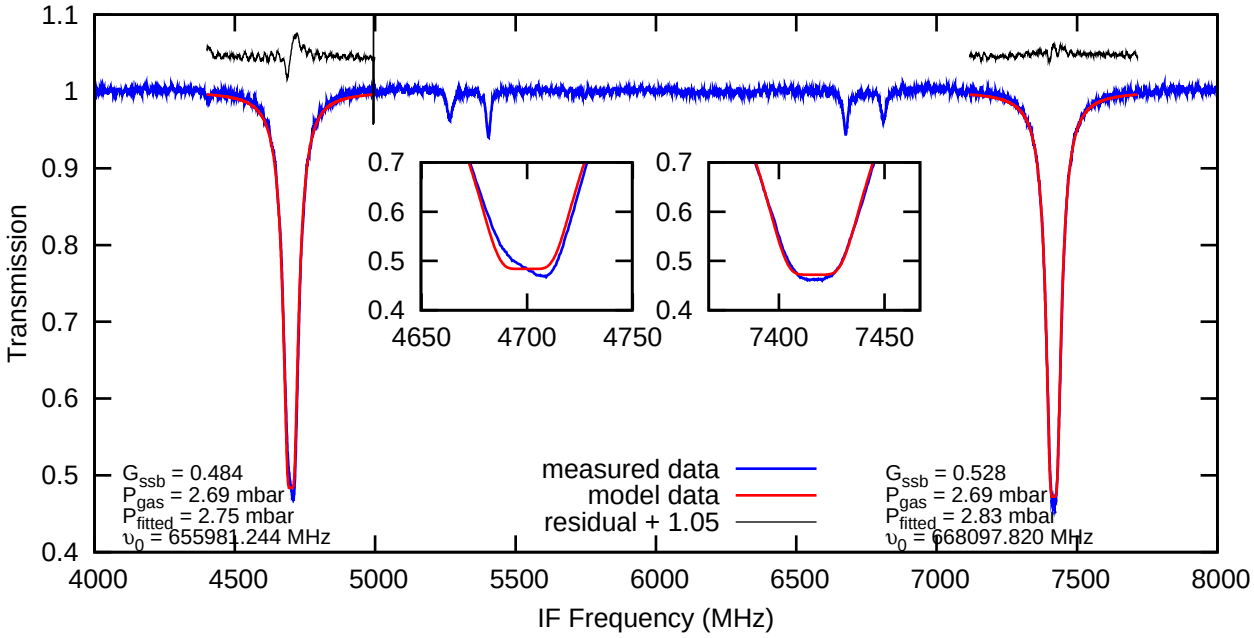

Figure 5.8: OCS spectrum observed at 660.681 GHz showing peculiar line profile and extreme side band ratio behaviour.

IF frequencies is observed in the upper side band. The fitted side band ratios shows that the upper side band gain is larger than the lower side band gain ($G_{ssb} > 0.5$). The advantage of OCS is that 2 simultaneous measurements of the side band ratio are taken at 2 different parts of the IF band. From this one can extract the slope of the side band ratio across the IF band. In this example a significant slope can be seen in the side band ratio variation across the IF band, the side band gain at an IF frequency of 4.6 GHz is 0.615 while at higher IF frequencies (7.45GHz) it is 0.681. This is 10% variation across the IF band. The is an extreme example and is consistent with the FTS model side band gain ratio generated at similar frequencies towards the band edge in figure 2.16(a) on page 36.

Figure 5.8 shows a line fit to a peculiar OCS line profile. This example was shown previously in figure 4.39 on page 163. In this example the side band ratio goes from an upper side band dominated region ($G_{ssb} > 0.5$) to a lower side band dominated region ($G_{ssb} < 0.5$) over 3 GHz of the IF band. This variation is not feasible and was not predicted by the side band ratio model in section 2.3.2.2. It was hoped that the spectral line model approach could recover the side band ratio as it fits the line wings as well as the line peak giving a better measure of the side band ratio. However the extreme variations are still evident with a G_{ssb} value of 0.484 seen in the lower IF band and 0.528 seen at the higher IF band frequencies. The source of this skewed side band ratio variation is the pointed line profile seen in the lower side band line profile. This is evident in the residual between the model and measured line profile. The upper IF frequency line appears the more credible side band ratio measure. As with the previous analysis in section 4.4 spectral lines exhibiting this behaviour are not included in the side band ratio measurement. One of the useful traits of the spectral line model approach is that the residual between the

measured and model spectrum provides a useful flag for the extreme spectral lines discussed here.

The analysis up to now has concentrated on the saturated lines of CO and OCS. The original motivation to develop a spectral line model of the gas in the gas cell was to extract the side band ratio for non-saturated lines as well. Observations of OCS were made above 800 GHz where the OCS lines were not saturated (see figure 4.1(c) on page 112) and hence were not included in the saturated line analysis described in chapter 4.

The extraction of the side band ratio for a non saturated line follows the same procedure as that described in the previous sections. Unfortunately the bands 3 and 4 data were beset with problems. For the band 3 and 4 data, the gas cell pressure wasn't measured during the observation so the gas cell pressure was left to vary within acceptable limits. The P_{gas} quoted in the following figures are the best guest pressure. More detrimental to the extraction of the side band ratio was the diplexer mistuning problem. This was seen previously in ^{12}CO data taken in band 3b, see figure 4.19 on page 139. The problem becomes more apparent when observing 2 spectral lines from 2 side bands.

Figure 5.9 shows an example of an OCS observation in band 3a. The side band ratio measured for the upper and lower side band line shows an extreme variation in side band ratio. Returning to figure 4.38 on page 162 this type of extreme change in side band ratio is not expected from the FTS measurements. This behaviour is indicative of a diplexer mistuning. A diplexer mistuning occurs when the difference in length between the 2 arms of the diplexer is not correct for the LO frequency being observed, this results in a mismatch between the upper and lower side band gain leading to a large slope in the side band gain ratio, see section 2.3.2.3 on page 38 for further discussion.

Figure 5.10 shows the side band ratios determined for bands 2-4 using the line model approach. From this one can see that in band 2 the side band ratios measured for the upper and lower side at the same LO frequencies are roughly consistent. The difference between the 2 measurements indicating a slope in the side band ratio across the IF band. For almost all OCS lines measured in band 2 the side band ratios for both lines are either greater than or less than than 0.5 as predicted by the FTS data simulation. Any observation where the side band measured with the upper and lower side band lines are on opposite sides of 0.5 are flagged. Examples of this behaviour were seen in the saturated line analysis of OCS, see figure 4.39 on 163 and were attributed to strange line profiles and discarded.

The analysis of Bands 3 and 4 show this type of extreme side band behaviour in all observations. Figure 5.9 shows an example of this behaviour. The lower side band line has a normalized side band ratio, G_{ssb}, of 0.603 while the upper side band line has a value of 0.394. On first inspection is was thought that the line intensity or pressure broadening parameters were incorrect, however this would have also been apparent in bands 1 and 2 data. The most likely culprit here is a diplexer mistuning, this was was seen to occur in ^{12}CO data taken in band 3b. As shown in figure 4.19(c) on page 139, it is possible to correct the spectral line data

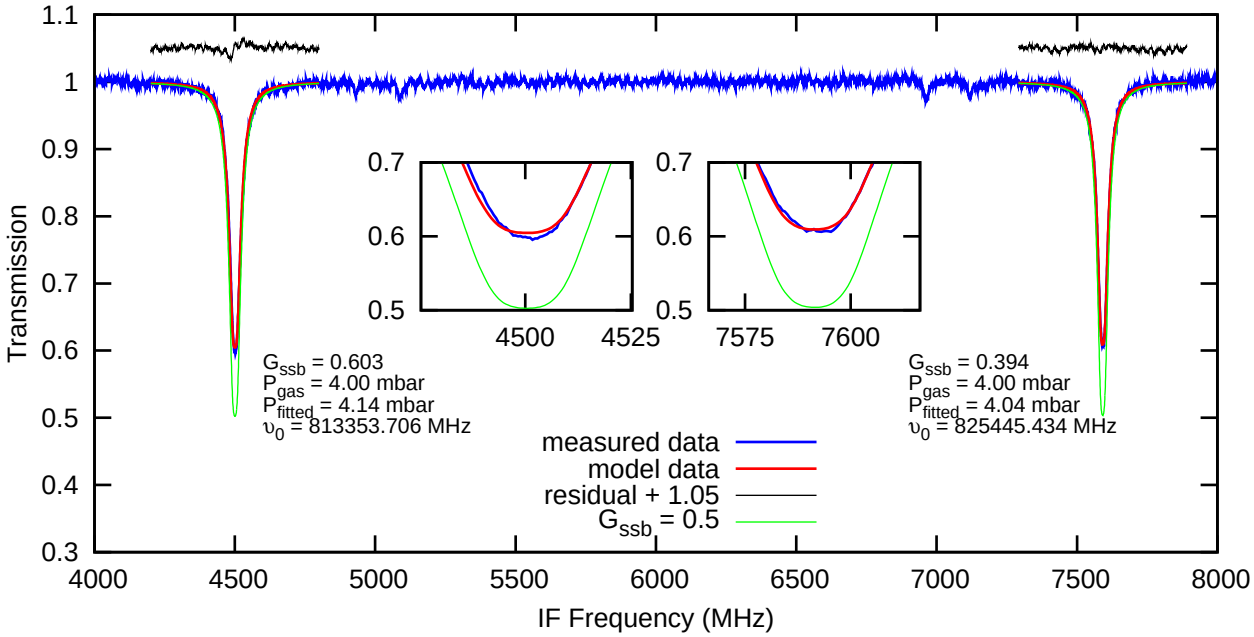

Figure 5.9: OCS spectrum observed at 817.854 GHz showing a large difference in side band ratio between measurement from the upper side band and lower side band. This extreme is due to a diplexer mistuning during this phase of the gas cell tests. The line profile for a side band gain balanced mixer is shown in green.

by estimating the degree of diplexer mistuning.

For the ^{12}CO data multiple observations were taken at different LO frequencies tracking the line across the IF band. By plotting the fitted side band gain ratio against the IF frequency of the line it was possible to fit a diplexer gain model and from that extract the diplexer tuning error. A similar procedure is followed for the OCS data. For OCS there are 2 measurements of G_{ssb} at opposite ends of the IF band so the diplexer mistuning can be determined for each LO frequency and doesn't require multiple LO frequency observations like the ^{12}CO data. Figure 5.11 shows some examples of the OCS diplexer fitting procedure for band 3. The ^{12}CO data data from band 3b is also shown along with ^{12}CO data from band 3a. The band 3a data showed no evidence of diplexer mistuning and is repeated here for comparison. The side band ratios extracted from the data in figure 5.9 are shown in the top left figure.

The fitting procedure has 2 free variables, the diplexer mistuning, Δ_{dip}, and the mean side band ratio, $G_{ssb,fit}$. From the discussion in section 2.3.2.3 on page 38 it was shown that while a diplexer mistuning has a detrimental effect on the gain towards the band edges the central IF frequency is not effected. So a line placed at the IF band center would be representative of the RF side band gain and not be affected by a mistuned diplexer. As we saw in the ^{12}CO the diplexer gain curve was superimposed on the mixer RF side band ratio, the offset for the diplexer model was then taken as the side band ratio. The same procedure is followed here. The dashed line in figure 5.11 represents this mean offset and is taken as a corrected measure of the mean side band ratio at that LO frequency.

The data presented in figure 5.11 is taken from the V mixer. As shown with ^{13}CO (see

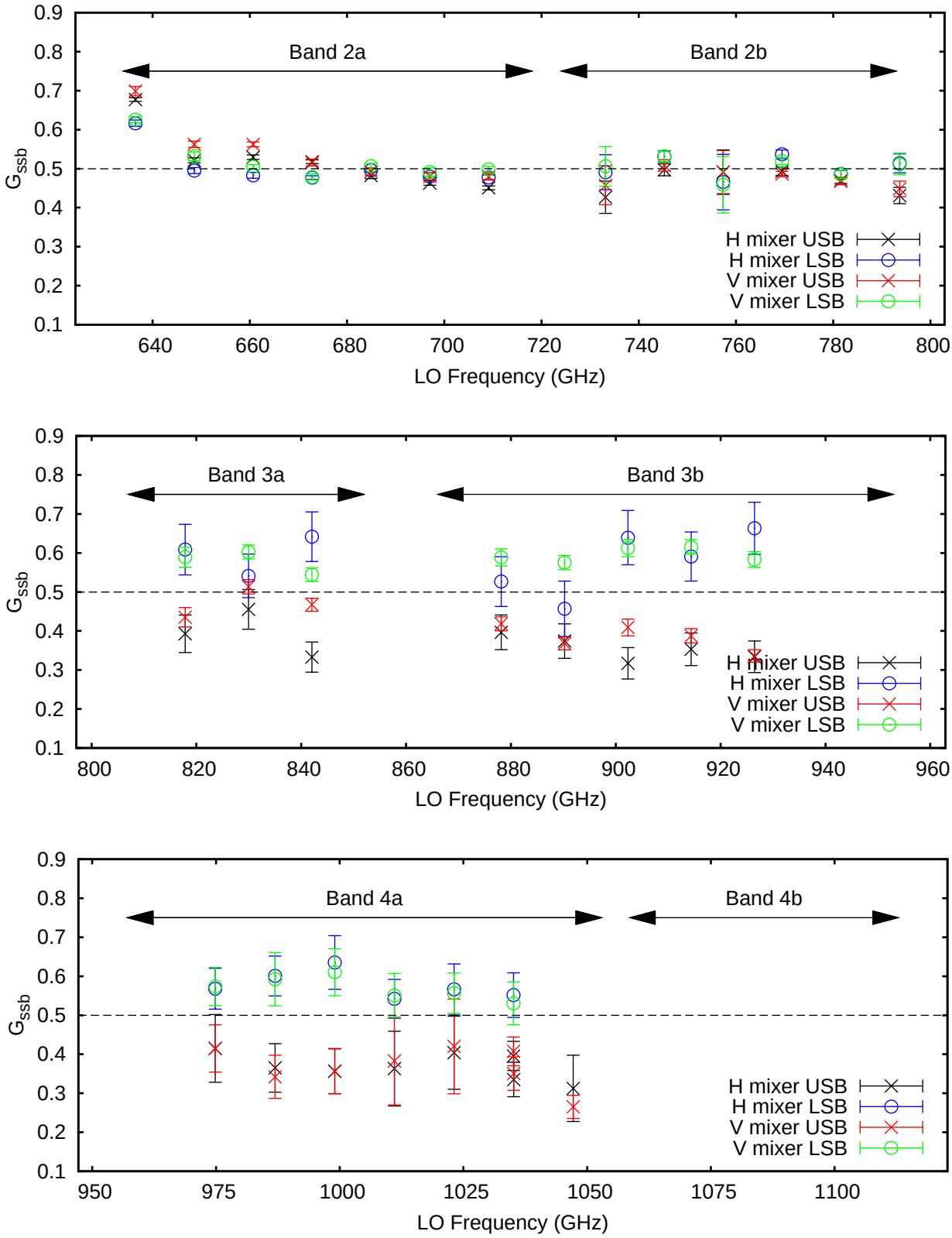

Figure 5.10: Overview of side band ratio in bands 2-4 extracted using the spectral model approach for OCS.

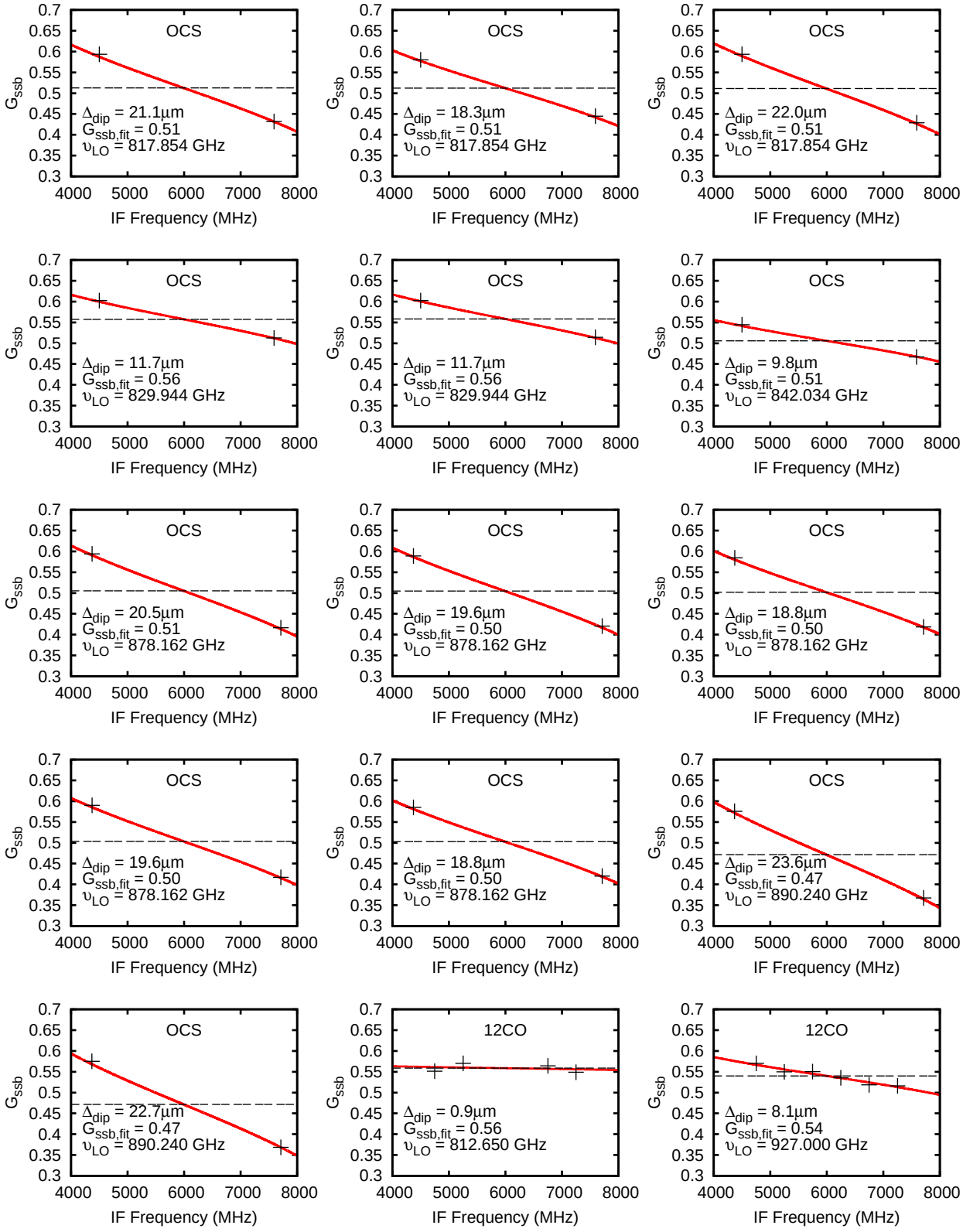

Figure 5.11: Extracting diplexer misalignment from OCS data in band 3a

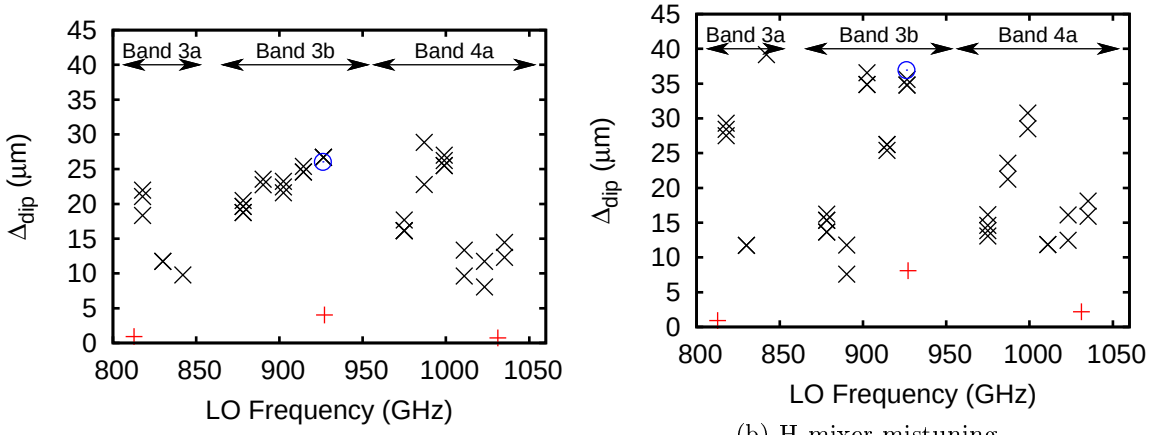

(a) V mixer mistuning

(b) H mixer mistuning

Figure 5.12: Diplexer mistuning extracted from OCS and ^{12}CO data.

figure 4.28 on page 150) and CH_3CN observations (see figure 4.43 on page 166) the H mixer is more effected by standing waves which introduces added uncertainty in determining the degree of diplexer mistuning. The one outstanding point garnered from figure 5.11 is that the diplexer mistuning is not the same for all LO frequency settings and shows there is some trend between diplexer mistuning and LO frequency.

Figure 5.12 provides an overview of the degree of diplexer mistuning vs LO frequency. Only OCS and ^{12}CO data are plotted as these were the only data sets from which the diplexer mistuning could be calculated. On first inspection it appears that there is a large discrepancy in diplexer mistuning seen between the 2 gases. Only the 3b ^{12}CO data shows evidence of a diplexer mistuning. The other ^{12}CO observations in bands 3a and 4a show scatter consistent with the standing wave modulation but no evidence of a gain slope across the IF band. The OCS data on the other hand shows some degree of diplexer mistuning for all observations. Both sets of data were taken within 7 hours of each other on the 3^{rd} of May 2007 so the same diplexer look up table was used for both sets of observations. The question remains why is the OCS diplexer settings so extreme? Perhaps the method of generating the line profile for OCS was wrong?

Fortunately there was one ^{12}CO observation which appears to be taken with the same diplexer settings as the OCS data. This ^{12}CO observation was mentioned previously in the saturated line analysis of chapter 4. Figure 4.19(a) on page 139 shows the observation in question. 2 observations were taken of ^{12}CO at an LO frequency of 926.05 GHz with different diplexer settings. In the saturated line analysis the observation with the extreme side band ratio was discarded however this observation now appears consistent with the diplexer setting observed in the OCS data. From this single ^{12}CO observation it is possible to estimate the level of diplexer mistuning albeit with some error as more than 2 points are needed to accurately establish the gain slope across the IF. For this example the mixer is assumed to be side band gain balanced and hence has a gain of 0.5 at the band center. Based on this assumption a diplexer

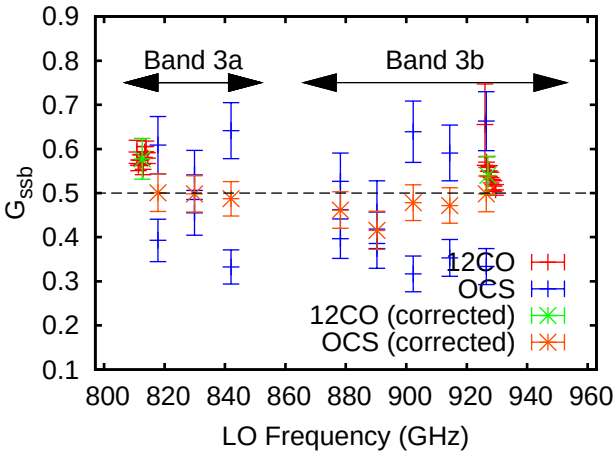

(a) band 3, H mixer

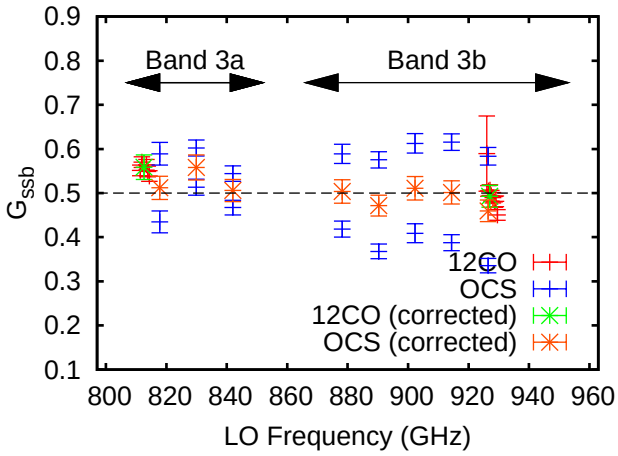

(b) band 3, V mixer

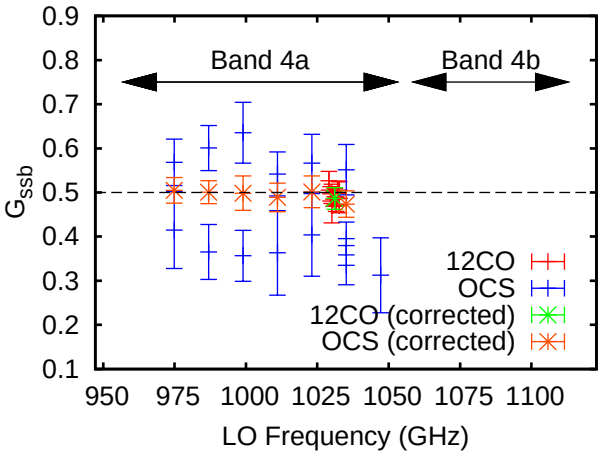

(c) band 4, H mixer

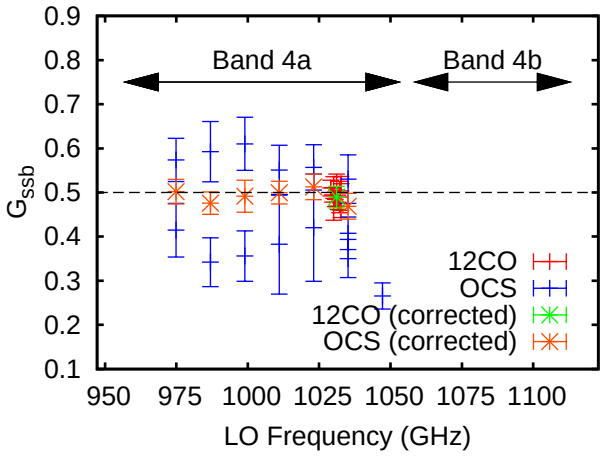

(d) band 4, V mixer

Figure 5.13: Side band gain ratio data from OCS and ^{12}CO before and after correction for diplexer gain slope in bands 3 and 4

mistuning can be determined for the outlier ^{12}CO observation. The diplexer mistuning is plotted in figure 5.12 as a blue circle which is consistent for both the H and V diplexer mistuning measured from OCS. This supports the thesis that in fact 2 different diplexer models were used to set the diplexer for the majority of ^{12}CO observations and the OCS data. For only one observation was the same diplexer setting used for both gases. What caused this change in diplexer settings requires further investigation.

Now the integrity of the OCS measurements and diplexer mistuning has been established, the results in figure 5.12 are quite alarming. The first evidence of diplexer misalignment was seen in the saturated ^{12}CO 3b data. From this a diplexer IF gain slope was generated with which it was assumed all data taken in the band could be corrected, see Jellema [50] for further discussion. However from the OCS data it is apparent that the diplexer mistuning is LO frequency dependent. Unless the mistuning is known for a given LO frequency applying a fixed diplexer mistuning tuning would further corrupt the data. The source of this LO

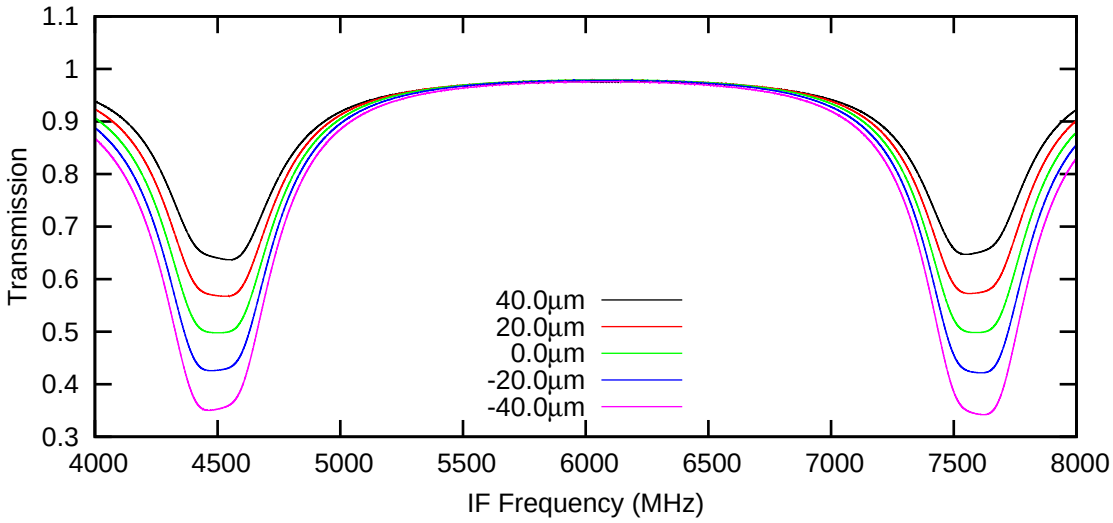

Figure 5.14: Model OCS spectra at a gas cell pressure of 40mbar at an LO frequency of 817.854 GHz showing the effect of diplexer mistuning on the line strength of an upper and lower side band spectral line. The gas cell pressure is increased for the model to highlight the effect of diplexer misalignment on the line intensity.

frequency dependence is a concern and may indicate that the basis of the diplexer model is incorrect. Flight tests have shown that there is no evidence of diplexer mistuning and perhaps this frequency dependence is an artifact of the ILT set up.

While it may not be possible to correct all diplexer band data with a common diplexer mistuning it is possible to correct data where the diplexer mistuning is known. Figure 5.13 shows a comparison of before and after correction of the data for side band ratio for OCS and ^{12}CO data where the diplexer mistuning is known. For the OCS data the plotted side band ratio is the average of the 2 corrected points. The data is reasonably consistent however there is still a large degree of uncertainty in the diplexer bands due to the standing wave effects.

As stated previously OCS is a useful gas for calibration. The regular occurrence of spectral lines every 12GHz provides a useful probe of the instrument behaviour. However OCS in combination with a diplexer mistuning presents an interesting problem. In the previous OCS analysis for bands 1 and 2, when the 2 OCS spectral lines had a similar line peak intensity this was indicative of balanced side band gain ratio. Figure 4.35 on page 159 shows an example of a balanced side band gain in band 2 showing similar peak intensity for the upper and lower line. For the diplexer band this approach wasn't sufficient. The diplexer mistuning had the effect of decreasing or increasing the line intensity of both spectral lines equally. The IF gain profile introduced by the diplexer mistuning is symmetric about the center of the IF band so a spectral line in the upper side band would have an increased gain in the lower part of the IF band and decreased towards the lower part of the IF band. When 2 lines are observed in both the upper and lower side band such as OCS, the diplexer mistuning has an equal effect on both spectral lines. This results in the 2 lines having the same relative intensity but incorrect absolute intensity.

Figure 5.14 shows an example of a OCS model DSB spectrum at an LO frequency of 817.854 GHz, a gas cell pressure of 40mbar for a variety of diplexer mistunings. The gas cell pressure is purposely left large for illustrative purposes, the typical OCS gas cell spectra was observed at a pressure of 2mbar. From the model one can see that the line intensity is increased or decreased equally for both spectral lines depending on the extent of mistuning. This effect is deceiving and on first impression appears like the side band gain ratio is balanced while in fact there is a large slope across the IF band. This LO frequency corresponds to the observation shown in figure 5.9 on page 189, which spurred the diplexer mistuning investigation. The spectrum shown in figure 5.14 is at the same LO frequency and from this one we see that the only viable explanation for the decreased line intensity observed in the gas cell data is a diplexer mistuning of $\sim 20\mu$m.

Unfortunately the analysis of the non saturated OCS data in the diplexer bands was dominated by the diplexer mistuning issue. However using the spectral line model approach a new set of measurements were included in the side band ratio analysis which was not possible using only saturated spectral lines. The side band ratios returned from the non saturated lines are close to 0.5 which shows that method of using a spectral line model to estimate the side band ratio from non-saturated lines is viable.

5.4.4 H_2O

The observation of H_2O in the ISM is a key science goal of the HIFI instrument. An accurate picture of the side band gain ratio around the important water lines is key to returning accurate measurement of water emission in the interstellar medium. Water was observed in the latter stages of the gas cell campaign and this is reflected in the quality of data. The majority of lines observed during the gas cell campaign were saturated and so the development of a line model is not entirely necessary. However the comparison between data and model helps shed new light on some calibration problems.

As with the previous molecules accurate knowledge of the line intensities, frequency and pressure broadening parameters is crucial to developing an accurate model spectrum and extracting the instrument response. The line data is again taken from a combination of the JPL catalog and the HITRAN catalog. The line frequencies taken from the JPL catalog are based on the work of Pickett et al. [96] while the line intensities are based on the calculations of Camy-Peyret et al. [13]. The pressure broadening data is taken from the HITRAN database and is based on the work of numerous authors [51, 37, 119, 15, 66, 48, 72, 10].

Figure 5.15 shows an example of a H_2O observation at an LO frequency of 563.436 GHz at a gas cell pressure of 2.23. From this one can see that the spectral line is saturated. The model shows excellent agreement with the observed data. The side band ratio is calculated to be 0.431. The gas cell pressure is left as a free variable and is fitted to within 0.5% of the measured value. The spike at the center of the spectral line occurs when the gas cell is not

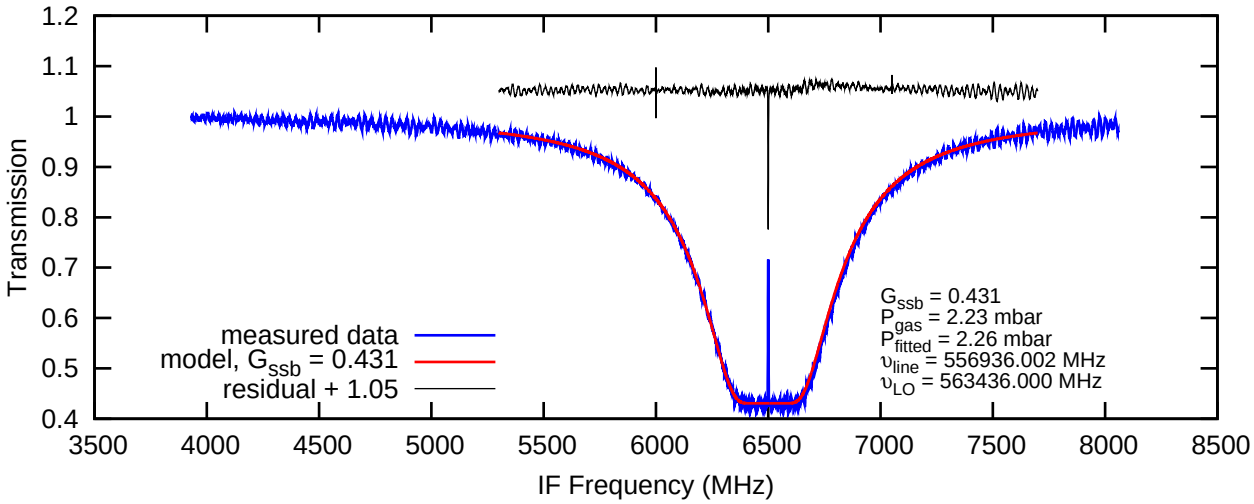

Figure 5.15: H_2O observed at an LO frequency of 563.436 GHz and a gas cell pressure of 2.23 mbar with the model spectrum over plotted.

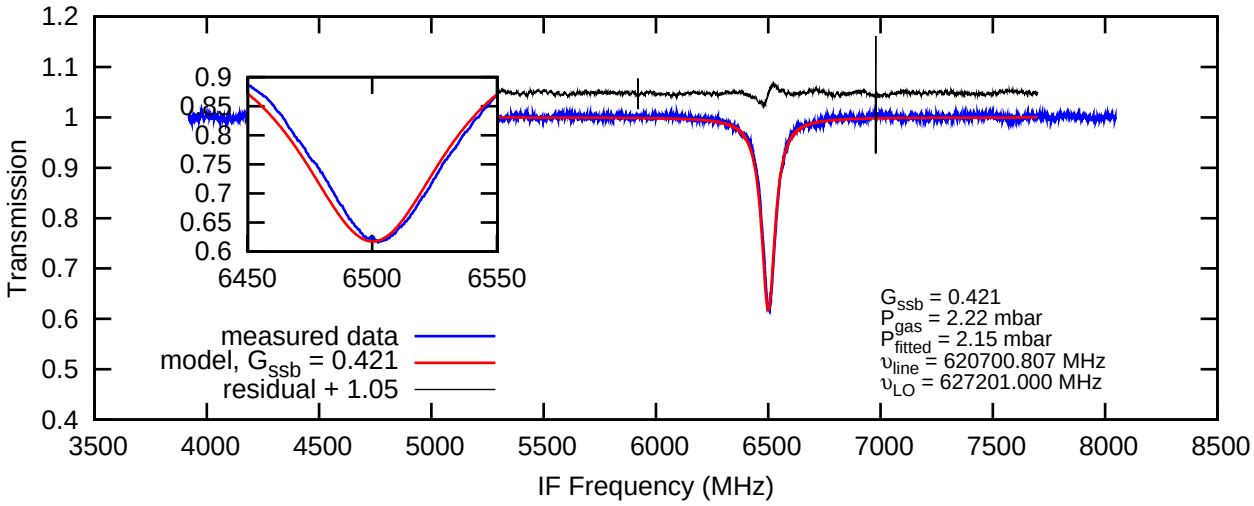

Figure 5.16: H_2O observed at an LO frequency of 627.201 GHz and a gas cell pressure of 2.21 mbar with the model spectrum over plotted. This spectral line is not saturated.

completely emptied during the empty phase of the gas cell observation. As water is a strong emitter at these frequencies even at low pressure water vapor can have significant emission.

Figure 5.16 shows an example of a spectral line that is not saturated. Hence, this spectral line was not included in the analysis of chapter 4. The residual between the model and the data is interesting. This type of residual indicates that there is a frequency disparity between the model and the observed spectrum. The source of this disparity could be from the catalog data or perhaps there was a difference between the commanded and actual LO setting. Bar this the fit is accurate and was not discarded.

The H_2O data in band 2b is of similar quality to the data already presented for band 1 and there is excellent agreement with the model spectrum. The data in bands 3 and 4 however are problematic and it appears that even at the latter stages of the gas cell campaign the diplexer was mistuned. All the H_2O lines observed in bands 3 & 4 were taken at the same IF frequency

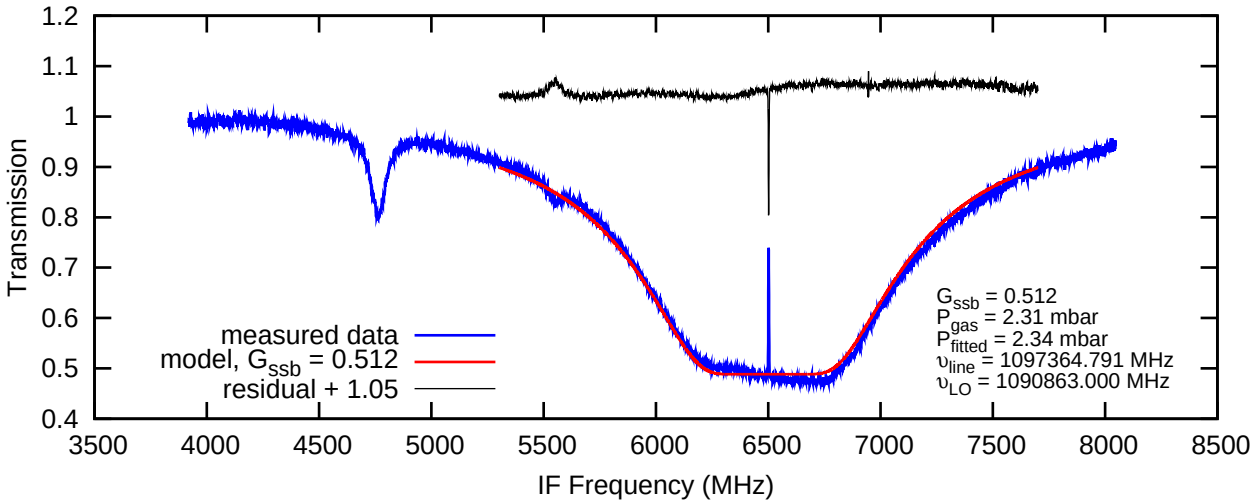

Figure 5.17: H_2O observed at an LO frequency of 1090.863 GHz and a gas cell pressure of 2.31 mbar with the model spectrum over plotted. There is noticeably slope on the saturated peak of line indicating a slope across the IF band consistent with a diplexer mistuning

and the line wasn't tracked across the IF like some of the ^{12}CO. It is then hard to establish the degree of diplexer mistuning present. However for some saturated spectral lines with a large region of saturation such as in figure 5.17 it is possible to see a large slope in the flat peak region. This topic was discussed previously in section 4.4.5 with some examples shown in figure 4.33 on page 156. This was originally thought to be a standing wave effect on the line profile however following the analysis of the OCS data it is apparent that the diplexer IF gain slope is the lightly source of the distortion. The OCS model spectra shown in figure 5.14 also shows evidence of this slanting of the saturated peak region due to the diplexer IF gain slope.

It is possible however to extract the diplexer mistuning for lines with large saturated regions. By extracting the saturated region and comparing the slope to various diplexer mistuning gain slopes it is possible to determine the level of mistuning. This is similar to the process used to determine the diplexer mistuning for OCS where there were 2 side band gain measurements at the IF band edges. For this example we have multiple measurements over a short frequency range. Figure 5.18 shows some examples of the diplexer mistuning extraction for H_2O observations in band 4. Care must be taken to apply the correct gain to the correct side band. No large saturated lines were observed in band 3.

The H_2O spectral line at 987.9 GHz was observed in both the upper and lower side band at the same IF frequencies and provides a useful example of the difference in slopes introduced by the diplexer IF gain depending on the side band. One would expect that if the diplexer IF gain shape is the same for both observations that the slope on the line peak when observed in the upper side band would be in the opposite direction in the lower side band (see figure 5.14 for example), this is indeed what we see for the H mixer observations at the LO frequencies of 981.4 and 994.4 GHz (2 figures in upper left corner of figure 5.18). However the spectral line slope of the V mixer is not consistent between the 2 observations and suggests that the diplexer

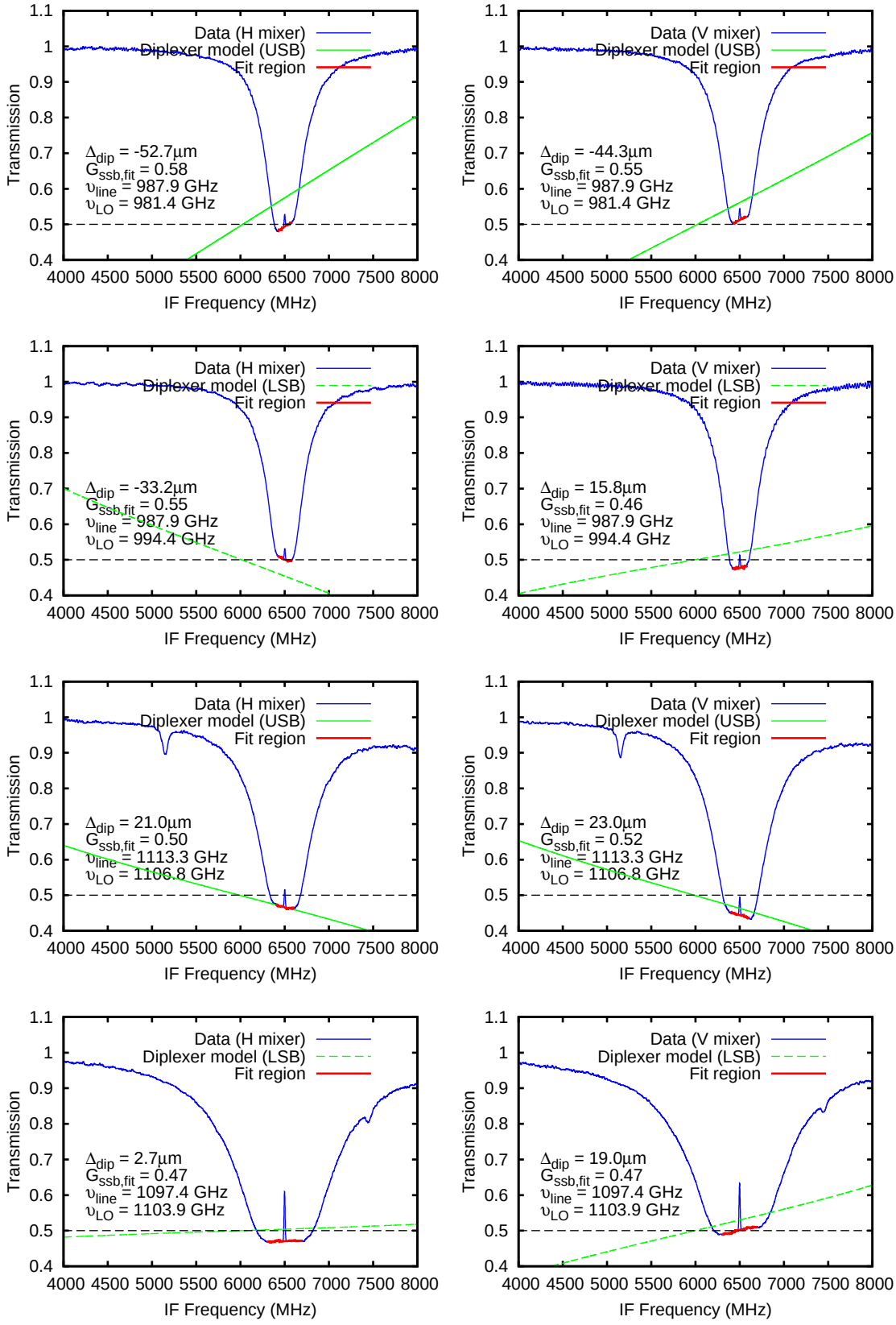

Figure 5.18: Extraction of diplexer mistuning from saturated H_2O data. H mixer spectra are shown on the left hand side while the corresponding V mixer spectra are shown on the right right side.

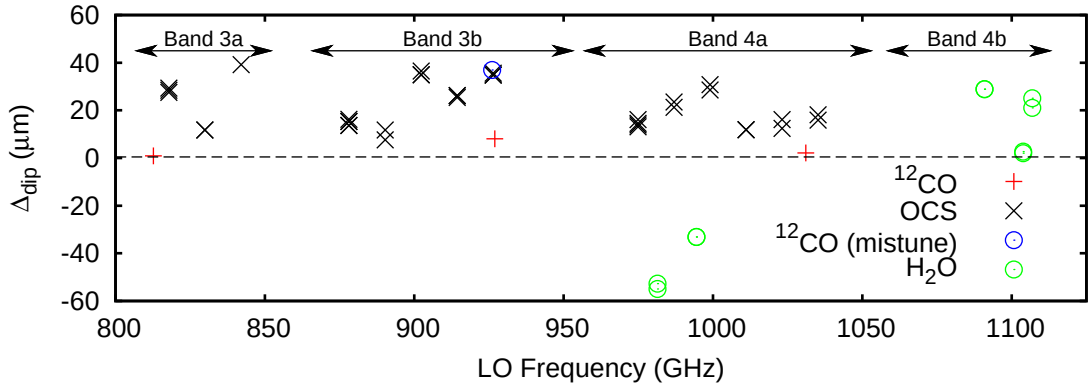

(a) Diplexer mistuning, H mixer

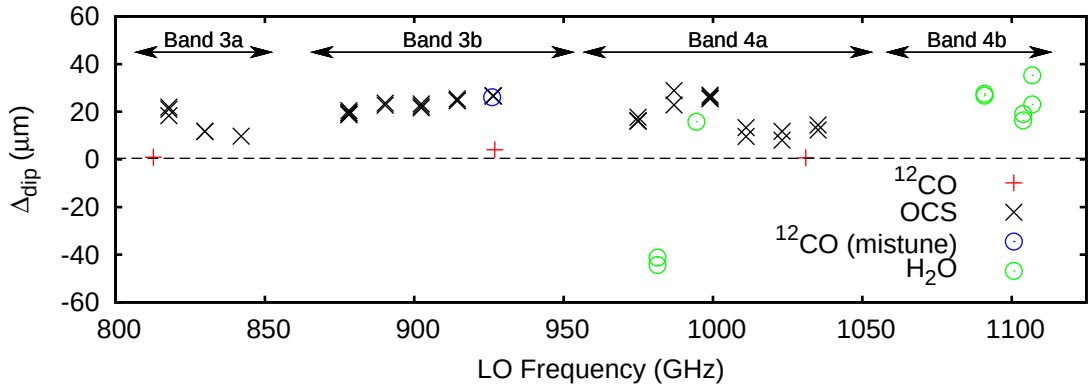

(b) Diplexer mistuning, V mixer

Figure 5.19: Level of diplexer mistuning as measured from the spectral line data of ^{12}CO, OCS and H_2O.

mistuning goes from a positive to negative value over the 13GHz difference in LO frequency between the 2 spectra.

The diplexer mistuning has been determined for four LO frequencies using the methods shown in figure 5.18. Figure 5.19 shows a comparison between the H_2O determined diplexer mistuning and those determined earlier for OCS and CO observations. It should be noted that the diplexer look up table changed between the ^{12}CO, OCS observations and the H_2O observations. Hence the variation in measured mistuning. The H_2O data does however provide further evidence of a frequency dependent diplexer mistuning.

Figure 5.20 shows the side band gain determined for the H_2O line observed in band 4. The lines with a saturated line peak have being corrected by fitting the saturated plateau with a diplexer IF gain slope model. Using the determined diplexer mistuning it is possible to correct these spectral lines for the diplexer mistuning gain effect. Unfortunately the degree of scatter appears to increase for the corrected data. This is perhaps unveiling underlying structure in the side band ratio however this data should be viewed in the context of the other gases in order to draw any conclusions.

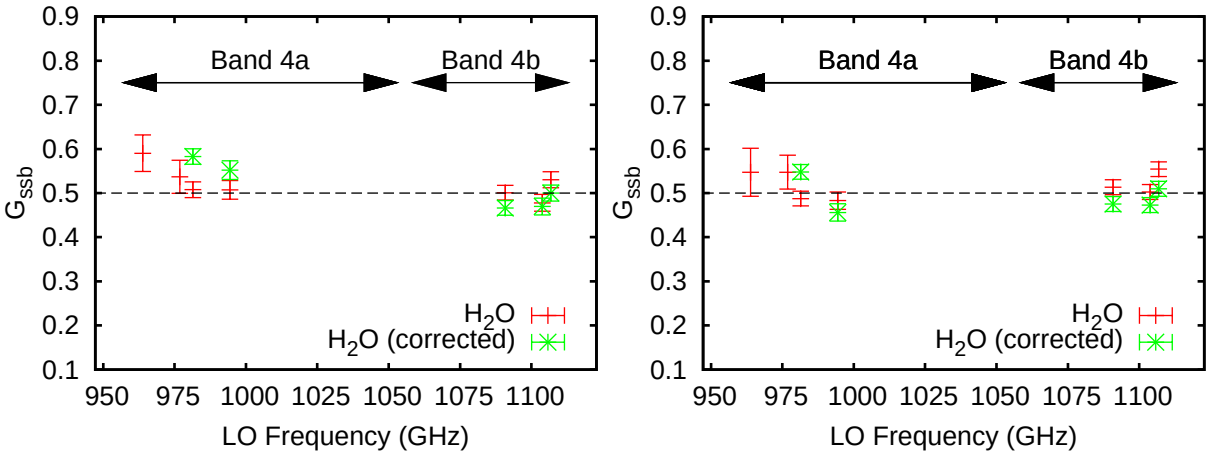

(a) H mixer (b) V mixer

Figure 5.20: Side band ratio before and after diplexer correction

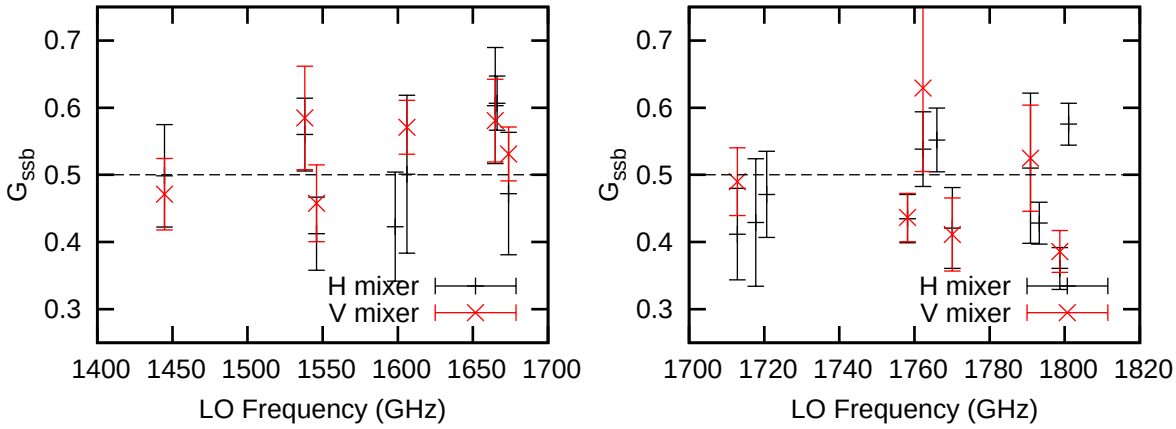

(a) Band 6 (b) Band 7

Figure 5.21: Side band ratio extracted for H_2O in the HEB bands

The spectral line model approach to side band ratio extraction introduces a number of additional non-saturated lines to the analysis in the HEB bands. The H_2O observing strategy shows some extra sophistication to the approach used for ^{12}CO and ^{13}CO. Numerous spectral lines are observed in both the upper and lower side band at the same IF frequencies. This is a useful exercise and ideally we should see the same side band ratio in both the upper and lower side band. From the FTS data the side band ratio gradient is expected to be the less severe in bands 6 & 7. Unfortunately the extracted side band ratios are not consistent with the expected variation and large differences are seen for the side band ratio measured with same line observed in the upper and lower side bands. This appears to be the pattern for all observations where the line is observed in the upper and lower side band. This could be evidence of a diplexer mistuning in bands 6 & 7 similar to band 3 and 4. Evidence of a possible diplexer mistuning in the HEB bands was seen in ^{12}CO data taken at multiple IF frequencies, see figure 4.26 on page 147.

Figure 5.21 shows the extracted side band ratio from H_2O measurements for the H and V mixer in the HEB bands. Most H_2O lines were observed in the upper and lower side band. One can see that there is a large scatter in the side band ratio. However there is a pattern present, the side band ratio is seen to alternate between greater than 0.5 and less than 0.5 when the same spectral line is measured in different side bands. A clear example of this behaviour is seen around 1545 GHz in band 6 and at 1760 GHz in band 7.

Figure 5.22 shows an example of the same spectral line observed in the upper and lower side band. The H_2O spectral line is at 1762.043 GHz. The spectrum with the line in the lower side band is shown in figure 5.22(a) where the LO frequency is set at 1758.146 GHz placing the spectral line at an IF frequency of 3.897 GHz. Figure 5.22(b) shows the same spectral line in the upper side band here the LO frequency is 1765.942 GHz and the spectral line is observed at an IF frequency of 3.899Ghz. If the only effect on the side band ratio was the RF mixer gain one would expect that the side band ratio observed for the spectral line in the upper side band would be very similar to that observed when the spectral line is in the lower side band given there is a relatively small frequency gap of 7.8 GHz between the 2 LO frequencies. For example if we take the upper side band observation as correct with a line peak of 0.56 and assume the side band gain ratio doesn't change between observation one would expect that the line peak of the same line in the lower side band would be 0.44. In reality we see the line measured in the lower side band has almost the same intensity as that measured in the upper side band.

Figures 5.22(d) and 5.22(d) show double side band spectral line models of H_2O at a gas cell pressure of 2.1mbar for various diplexer mistunings. From the model the diplexer would have to have being mistuned in the positive direction for the upper side band observation and in the negative direction for the lower side band. This may be feasible for one pair of LO frequencies but doesn't seem likely for the multiple observations which show this effect. Furthermore, the modeled spectra show significant slopes in the saturated line peak which is not seen in the data. Further investigation is needed.

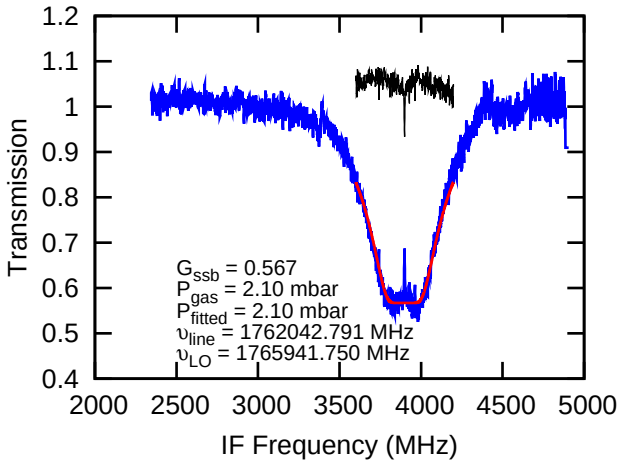

(a) H_2O line at 1762.043 observed in the upper side band at an LO frequency of 1765.942 GHz

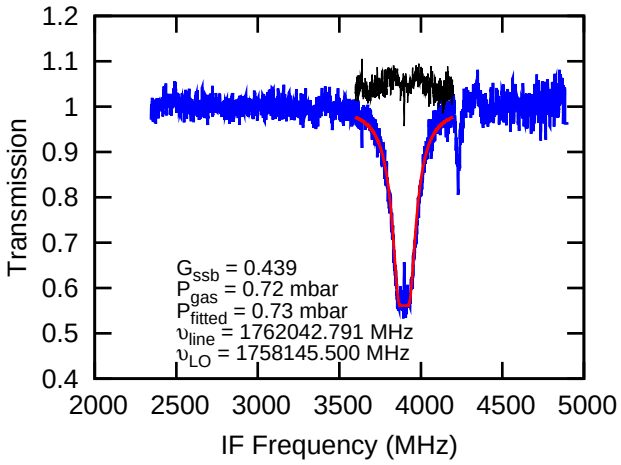

(b) H_2O line at 1762.043 observed in the lower side band at an LO frequency of 1758.146 GHz

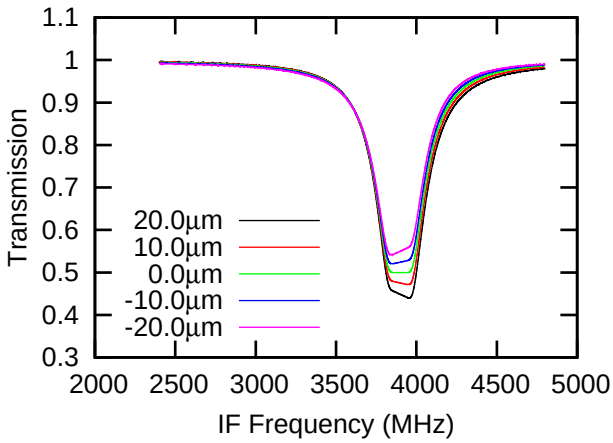

(c) Double side band model spectra of H_2O at an LO frequency of 1765.942 GHz at a gas cell pressure of 2.1mbar

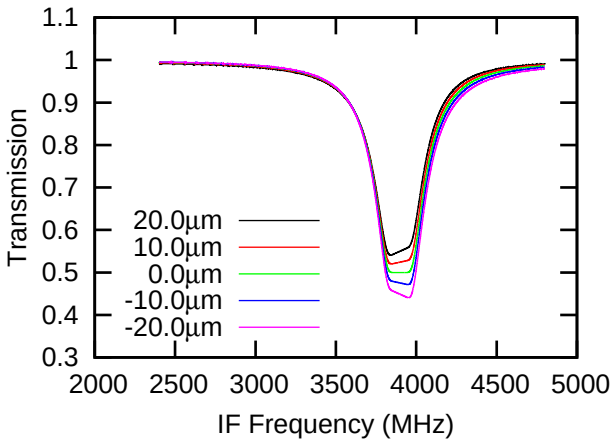

(d) Double side band model spectra of H_2O at an LO frequency of 1758.146 GHz at a gas cell pressure of 2.1mbar

Figure 5.22: Comparison of H_2O line at 1762.043 GHz taken at the same IF position but in different side bands. A model spectra of the same LO frequency is shown for different diplexer mistunings.

5.4.5 Summary

Figures 5.23 and 5.24 provide a summary of the side band ratios extracted for the H and V mixer mixers using the spectral line model approach. Using this approach a number of additional spectral lines are included in the analysis compared to the previous saturated line only analysis of chapter 4.

The analysis of the OCS data in the diplexer bands provided new insights into the diplexer mistuning previously discovered through ^{12}CO observations in band 3b. From the OCS data it was possible to determine the degree of diplexer mistuning. This was shown to be frequency dependent. Originally it was thought the diplexer mistuning would have a fixed offset for all LO frequencies in a given band however this wasn't the case. The H_2O data was also seen to have diplexer mistuning effects. By analyzing the slope of the saturated peak plateau it was possible to extract the degree of diplexer mistuning present. Again the degree of diplexer mistuning was shown to be frequency dependent. The outcome of the diplexer investigation has profound effects for the calibration accuracy of band 3 & 4 diplexer gas cell data as a global offset will not be sufficient to correct the data. More data is needed to investigate the diplexer mistuning problem. The frequency dependence of the diplexer mistuning may also have profound effects as to how the diplexer model is generated. It should be noted that no evidence of diplexer mistuned was seen from in flight data and this anomaly may be due to the ILT set up.

The HEB band shows a large degree of scatter even with the spectral model approach. The data quality is quite poor and a significant portion of data had to be discarded. Even when the data is of good quality there can still be a large degree of scatter in line peak intensity between observations taken at the same LO frequency subsequent to each other. Further work is needed in the HEB bands particularly for the H_2O analysis which showed an interesting variation in side band ratio which could possibly be due to a diplexer mistuning.

Even with the inclusion of the non saturated spectral lines a large part of the HIFI frequency range remains unsampled. The inclusion of methanol in the determination of side band ratio may help fill in the gaps in the side band ratio coverage. This is particularly applicable in the beamsplitter SIS bands (1,2,5) where the simple molecule analysis provides a solid measure of the side band ratios at particular frequencies. Using the side band ratios calculated from the analysis presented so far it may be possible to fill in the gaps in coverage using strong methanol lines. However a number of challenges exist for the the methanol data, the primary one being the lack of pressure broadening available currently for this molecule. The next section will discuss the extraction of the pressure broadening parameter from methanol and the determination of the side band ratio for a small portion of the HIFI frequency range.

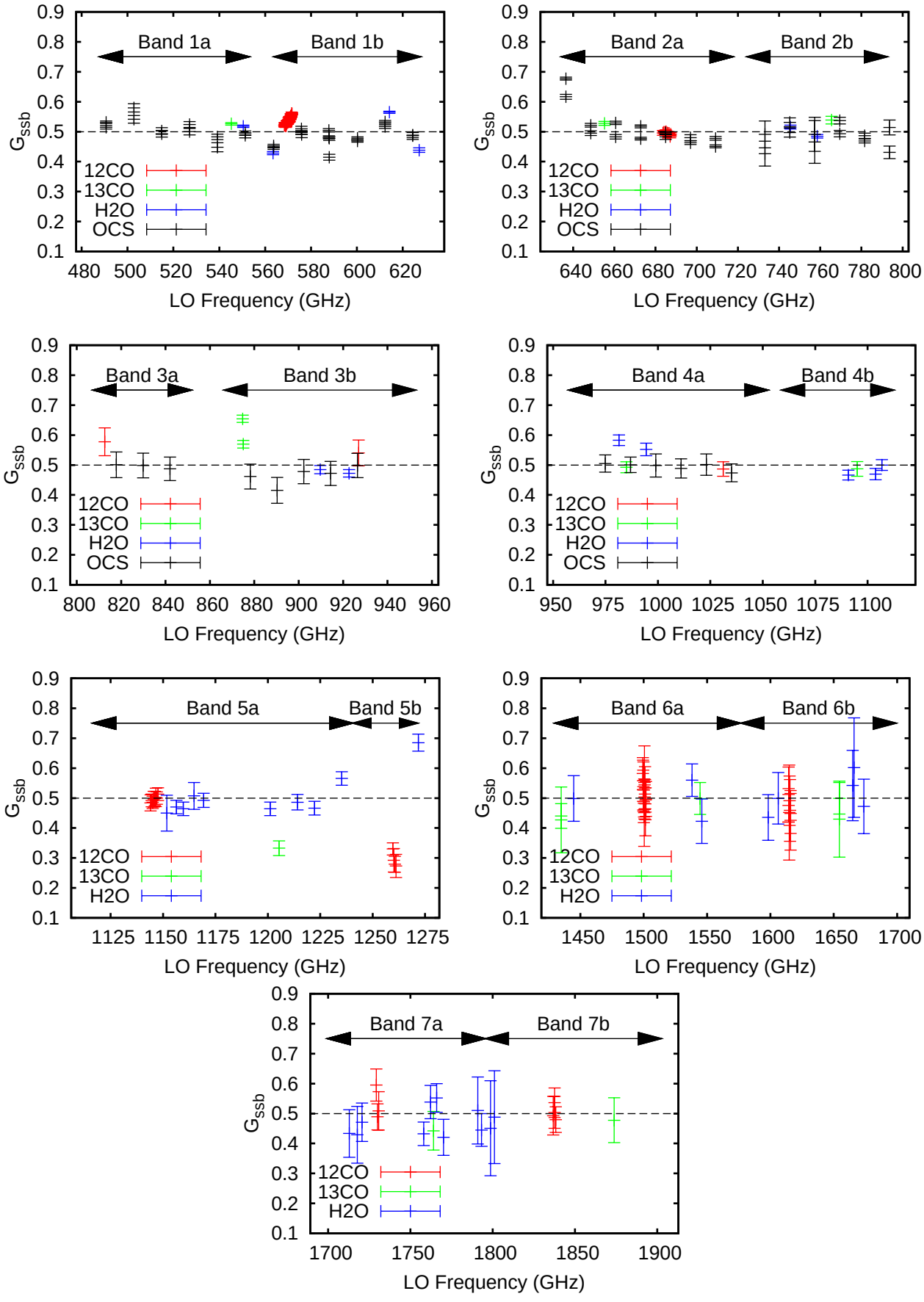

Figure 5.23: Overview of side band ratio for H mixer using ^{12}CO, ^{13}CO, H_2O, OCS.

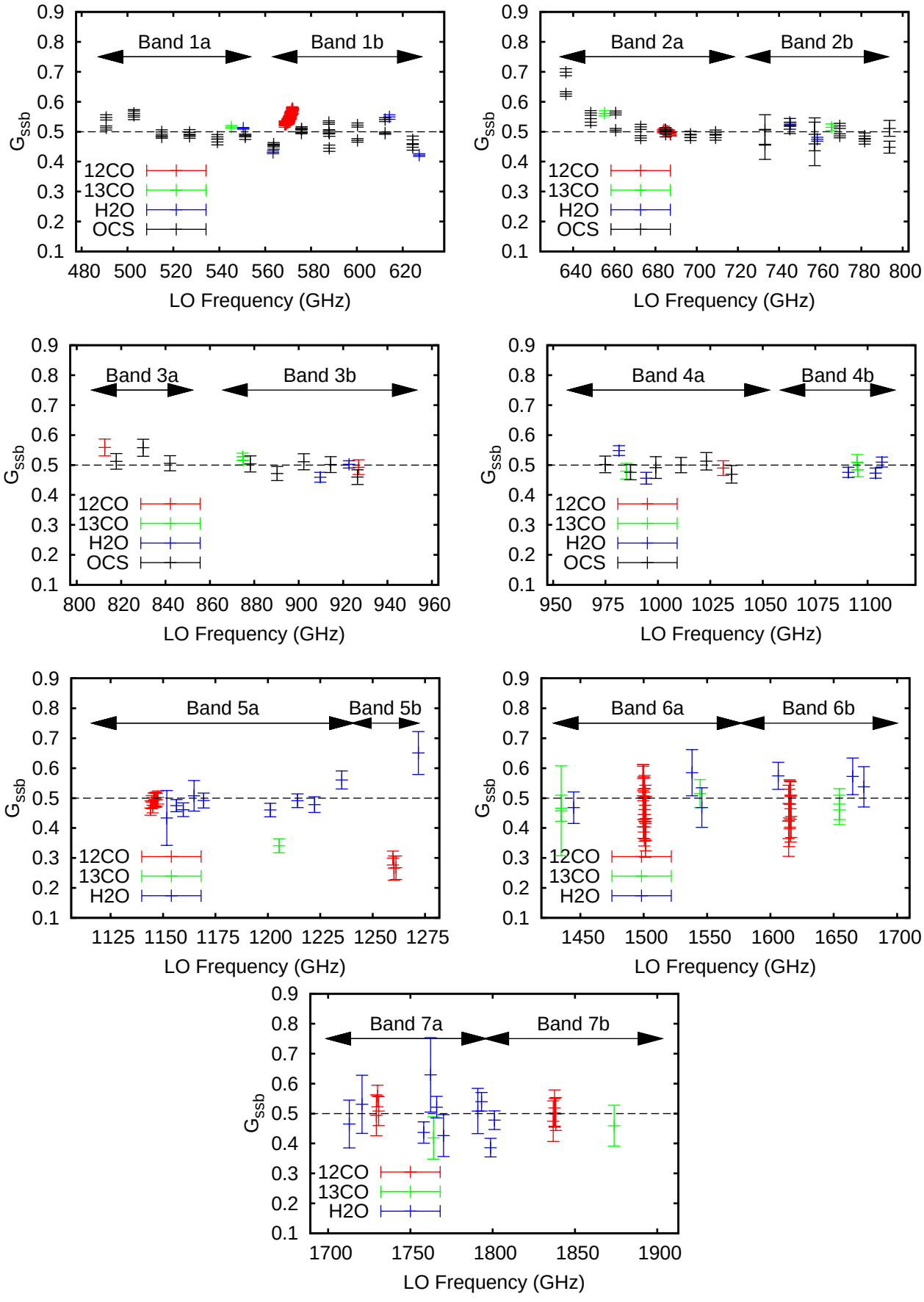

Figure 5.24: Overview of side band ratio for V mixer using ^{12}CO, ^{13}CO, H_2O, OCS.

5.5 CH_3OH analysis

5.5.1 Introduction

Methanol spectra account for 80% of the total spectra taken during the gas cell campaign. The extensive observation of methanol in the gas cell was primarily intended as a test data set for the deconvolution algorithm. The observation of methanol has a number of ancillary uses for HIFI calibration also. Methanol is the only gas observed during the test campaign which provides spectral lines at all frequency settings. Each spectrum provides a snap shot of the instrument behaviour at a given frequency. The rigorous analysis of each frequency setting is huge amount of work. The best approach is to use the simpler molecules as starting point for the analysis and expand from there. For example, the LO spur in band 5b observed in ^{12}CO spectrum (see figure 4.11 on page 126) is also apparent in the methanol spectrum observed at this frequency (see figure 4.12).

The analysis of the entire methanol dataset is beyond the scope of this thesis, the discussion will follow a similar pattern to the 5b spur investigation and focus on areas of interest uncovered in the simple molecule analysis summarized in figures 5.23 and 5.24. The analysis of methanol in this thesis will focus on the large side band ratio gain slope seen in the lower band edge of 2a where OCS, CH_3CN and ^{13}CO also showed that this region is upper side band dominated.

The analysis of methanol will follow a similar approach to that of OCS. Each spectral line will be modeled individually. Only lines that are not blended with other spectral lines are included in the analysis. One of the disadvantages of the methanol is that the pressure broadening terms are not available. These values will be extracted from the data using the `generateLineModelPSelfSBR` function of the gas cell line fitting code described in appendix A. The analysis presented here is of spectroscopic importance and is the first time such an extensive analysis of methanol has been undertaken over this frequency range.

5.5.2 Testing the deconvolution algorithm

The deconvolution algorithm is a key component in the processing of HIFI data particularly for line rich sources such as Orion KL[6, 19]. As HIFI observes a double side band spectrum, spectral lines from the upper and lower side band are seen in the final spectrum. The deconvolution algorithm is based on the property of double side band spectrum that as the LO frequency is changed spectral lines from the upper and lower side band move the same amount in opposite directions on the IF band. Using this property it is possible to reconstruct the singe side band spectrum from the double side band spectra. However multiple LO frequency observations of the same spectral line are needed (spectral scans) to deconvolve the upper and lower side bands from the double side band spectrum. The algorithm and its application to different observation modes is described in detail in Comito & Schilke [20].

A number of parameters exist within the deconvolution algorithm such as the number of

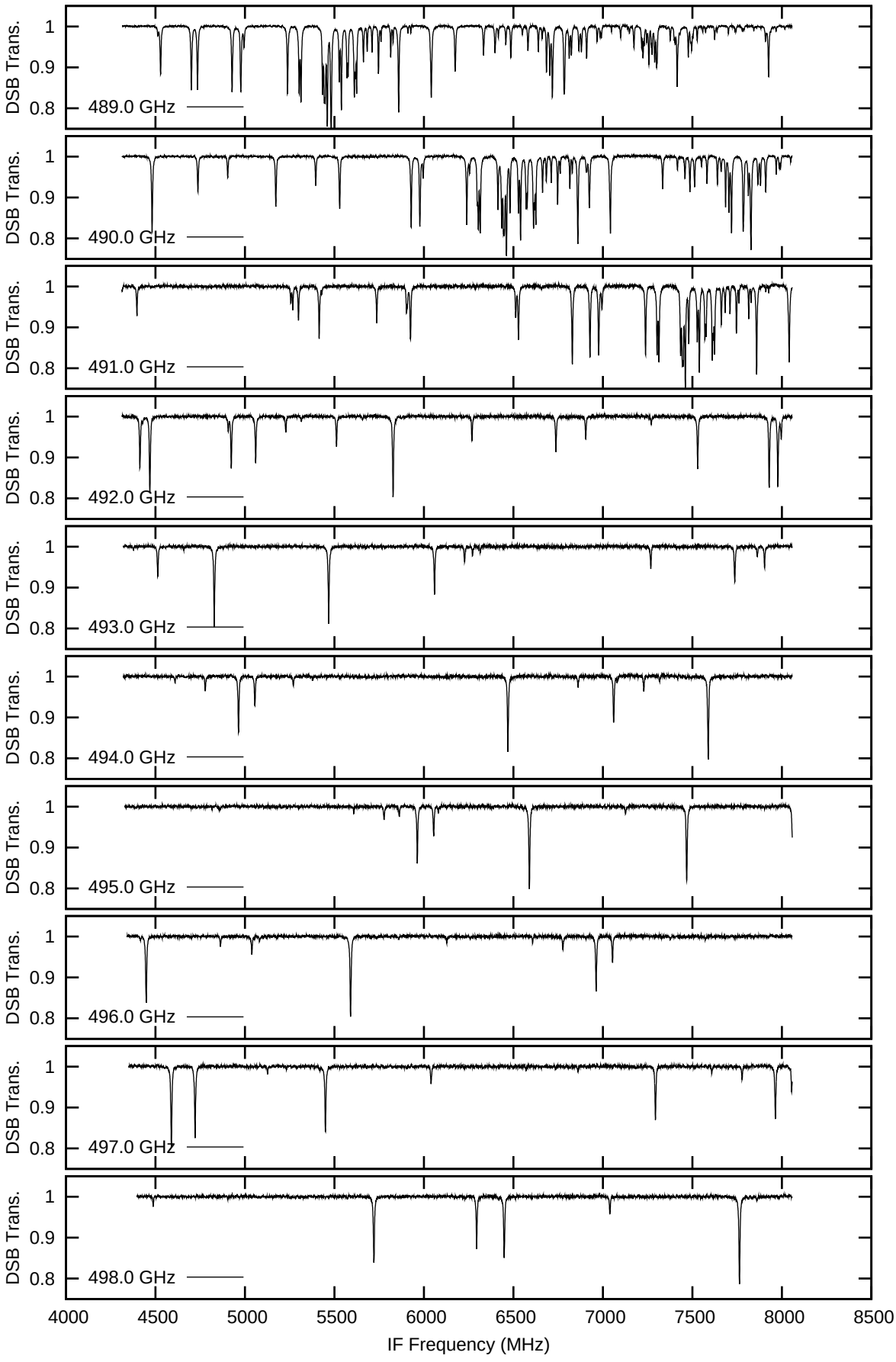

Figure 5.25: Double side band spectra of CH_3OH taken between 489 GHz to 498 GHz in steps of 1 GHz.

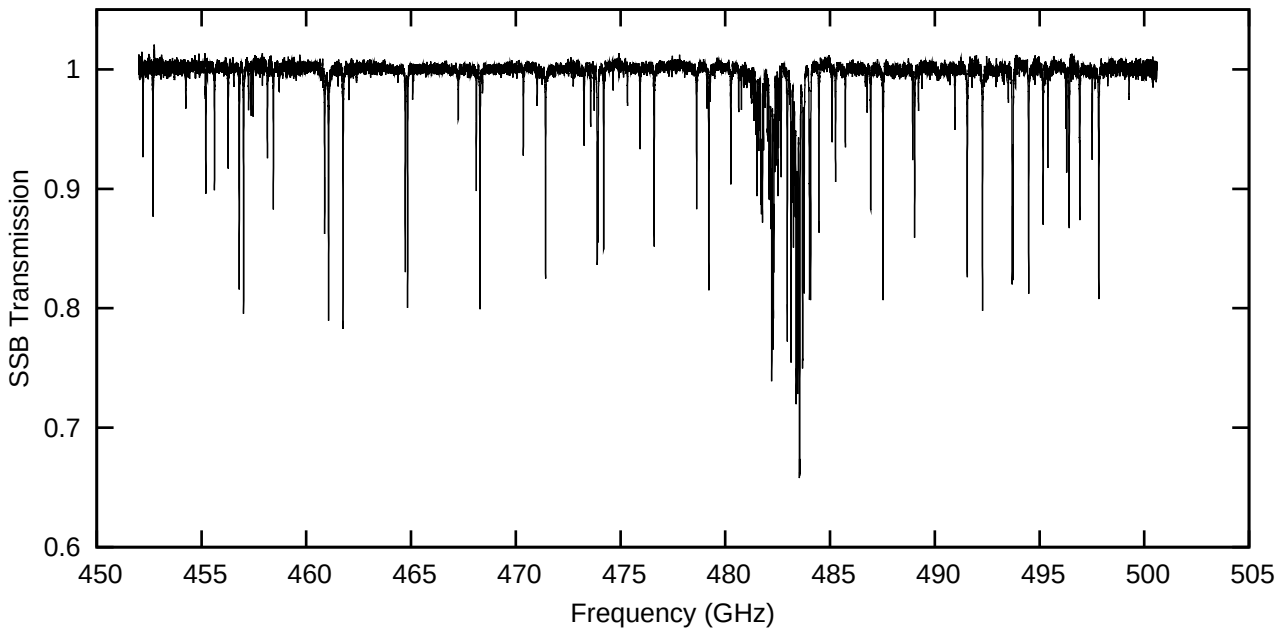

Figure 5.26: Deconvolved Methanol spectrum between 500.599 GHz and 452.0 GHz[18]

frequency steps (also known as the redundancy) which require testing. The methanol data was envisaged to provide a test ground to optimize the level of redundancy and also to develop the HCSS routines required. The original deconvolution algorithm was written in Fortran and the commonly used sub-mm astronomy software CLASS. All methanol spectra observed in the gas cell followed a similar routine and data was taken in frequency steps of 1GHz. Unfortunately the deconvolution algorithm needed a certain amount of scatter in the frequency stepping of the LO to avoid continuum platforming in the deconvolved spectrumComito & Schilke [20]. This was not taken into account for some gas cell spectral scans and this was reflected as a stepped continuum in the final deconvolved spectrum. This resulted in some of the data taken being not suitable for the deconvolution algorithm. Further problems with the data such as the poor quality of HEB data resulted in a further reduction in the amount of data available. Like much of the analysis in this thesis, bands 1 and 2 provide the best quality data and so deconvolution testing was limited to these bands.

Figure 5.26 shows an example of double side band CH_3OH data taken in band 1a. From this one can see the movement of spectral lines through the IF band with increasing LO frequency. The most noticeable feature being the branch of lines seen at an IF frequency of 5.5 GHz at an LO frequency of 489.0 GHz. This group of lines in the lower side band so as the LO frequency is increased the lines are seen to move to higher IF frequencies eventually leaving the IF band at an LO frequency of 492 GHz. Figure 5.26 shows the deconvolved single side band spectrum generated using the spectra shown in figure 5.25 as well as additional spectra at other LO frequencies not plotted. Note the line intensity is now in single side band transmission so it appears at twice the double side band transmission.

While a portion of the methanol gas cell data was not appropriate for the deconvolution

algorithm the data from bands 1 and 2 provided enough test data to optimize and develop the deconvolution algorithm. Based on the experience garnered from the gas cell survey the deconvolution algorithm was a functioning part of the instrument processing pipeline prior to the Herschel satellite launch. The first line rich source observed was the Orion KL data which was processed by the key program astronomer with little help needed from the dedicated deconvolution group. This level of maturity in data processing is unprecedented at the early stages of a space mission. The usage of the gas cell test data in the deconvolution development played a crucial role in achieving this level of data processing maturity at an early stage in the HIFI mission.

5.5.3 Pressure broadening extraction

In order to retrieve side band ratios from the methanol data, the pressure broadening parameter for each transition must be extracted. Unlike the other molecules analyzed so far this data was not available and had previously being estimated to range between 0.1 to 0.4 $cm^{-1}atm^{-1}$ (2.95 to 11.83 MHz/mbar)[106]. The line frequencies and intensities are however available through the JPL database and while certain transitions are the subject of research the vast majority are considered accurate, this is described in more detail in the JPL catalog documentation[52]. The extraction of methanol pressure broadening is of interest to the spectroscopy community also and this gas cell dataset is a unique opportunity to retrieve these parameter.

HIFI's large frequency range is unique among comparable heterodyne spectrometers. HIFI is also unique as a lab spectrometer given its large frequency resolution compared to the FTS systems commonly used in laboratory spectroscopy at these wavelengths. A standard pressure broadening investigation normally focuses on a small frequency range limited by the spectrometer. For a typical pressure broadening investigation the pressure is increased and for each measurement the line width is extracted. The slope between the increasing pressure and line width is then taken as the pressure broadening term, see [67]. For the HIFI methanol observations the pressure was kept relatively constant throughout the test campaign to suit the deconvolution algorithm.

The approach used here to extract the pressure broadening parameter is far from ideal. Each line transition that is not confused with another line is fitted using the line intensity taken from the JPL catalog and the gas cell pressure measured during the observation. The pressure broadening term and side band ratio are left as free variables in the model routine (see `generateLineModelPSelfSBR` function in Appendix A). Each line is measured at least 8 times, 4 in the upper side band and 4 in lower side band. Barring confusion with other spectral lines this gives 8 measures of the pressure broadening. The method depends on the accuracy of the pressure measurement which based on the fitted and measured pressure of the H_2O and CO analysis is close to 5%.

As a assessment of the `generateLineModelPSelfSBR` routine the analysis is first tested on

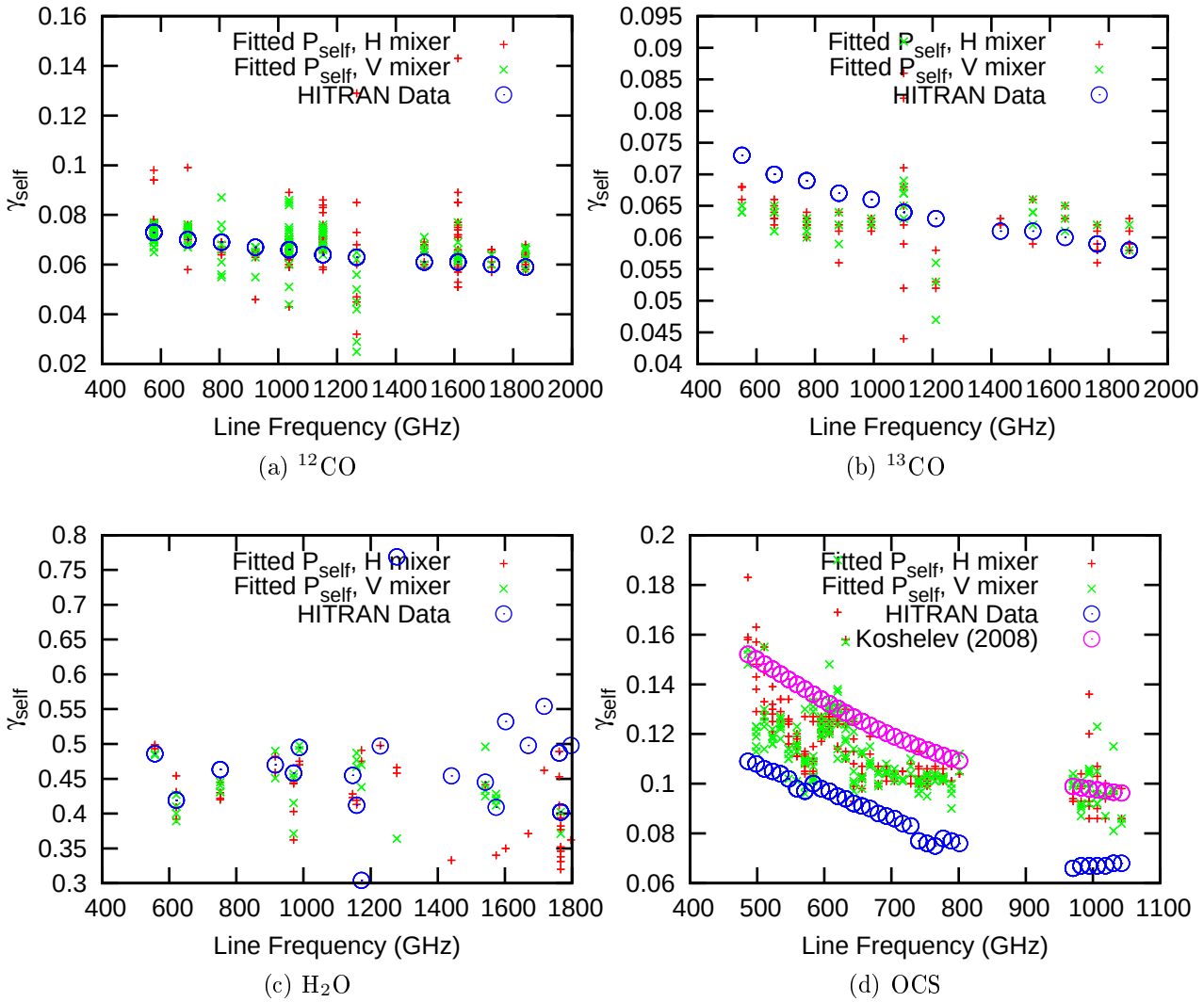

(a) ^{12}CO (b) ^{13}CO

(c) H_2O (d) OCS

Figure 5.27: Comparison between fitted pressure broadening parameter, γ_{self} and published data for ^{12}CO, ^{13}CO, OCS and H_2O.

molecules where the pressure broadening parameter is well known such as H_2O, ^{12}CO, ^{13}CO and OCS. The fitted pressure broadening is then compared to the published pressure broadening parameters. Figure 5.27 shows a comparison between the fitted pressure broadening parameters and the published data taken from the HITRAN catalog. The measured and published data show best agreement in bands 1 and 2 which is to be expected given the variety of instrument problems in the higher frequency bands. For ^{13}CO data there appears to be a marked offset between the measured and published data. No uncertainty was given in the HITRAN database so its difficult to determine if the measured data is within the error bars of the published data. OCS is plotted against 2 sets of published data, those from the HITRAN database and those from Koshelev & Tretyakov [67]. The measured data appears to lie between the 2 sets of data. At higher frequencies the measured data shows good agreement with the data of Koshelev & Tretyakov [67]. There is a gap in the OCS coverage where the band 3 data should lie. Unfortunately for these observations the gas cell pressure was not known and hence it was neglected in this analysis. The H_2O data shows good agreement between the fitted and published data in the lower frequency bands. There are a number of outlier points towards higher frequencies, in particular for band 5. On closer inspection these spectra appear to have LO spur problems and hence are not returning an accurate line profile. This effect is also seen in the ^{12}CO band 5 data.

From figure 5.27 one can see that measured pressure broadening is on average within $\pm$ 10% of the published data. These results provide limits on the accuracy of any pressure broadening data extracted from the methanol data and also illustrates the ability of the `generateLineModelPSelfSBR` function to extract the pressure broadening parameters.

The presentation of the entire methanol pressure broadening analysis is beyond the scope of this thesis. Here only select branches of methanol with strong emission lines are presented. The variation of the pressure broadening parameter with line frequency and J number is of interest to the spectroscopy community. For the pressure broadening analysis presented here only lines that are not confused with other spectral lines are chosen for analysis. Therefore dense regions of line emission such at the 483 GHz region of figure 5.26 are ignored in this analysis and only stand alone lines are considered.

Figure 5.32 shows an example of the pressure broadening extraction for a single line transition. The methanol transition is described using the following notation, $12_{1+,0} \rightarrow 11_{1+,0}$ which occurs at a frequency of 574868.45 MHz. Given the complexity of the methanol emission the description of the emission process for each transition is complicated. The definition of the different transitions and their notation is discussed in Xu et al. [128] and in the online JPL catalog manual[95]. The notation follows the template $J_{k,vt}$ where J is typical J number associated with microwave transitions while k and vt are unique to methanol. With these 3 variables a single transition can be described. k is occasionally preceded or followed by a '+' or '-' sign which further describes the nature of the transition.

In total the 574868.45 MHz line transition was observed 12 times at different IF frequencies

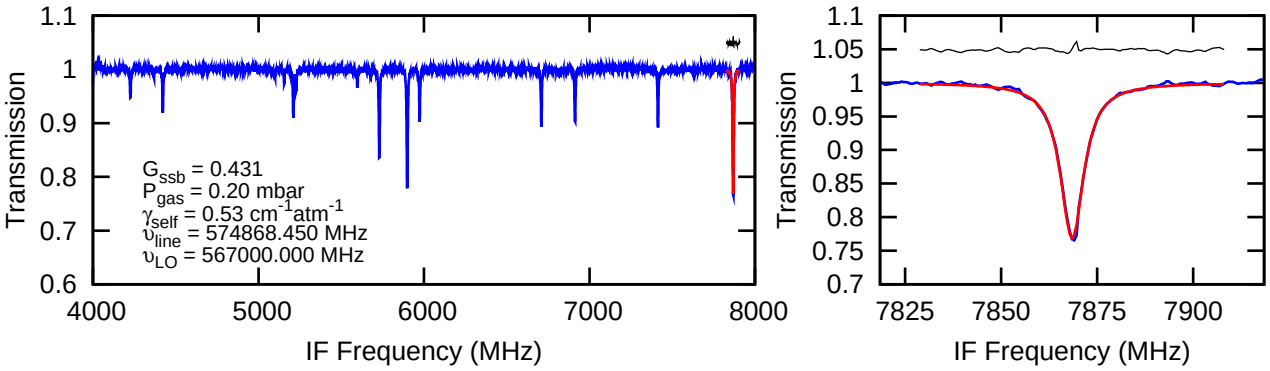

(a) CH_3OH at an LO frequency of 567 GHz

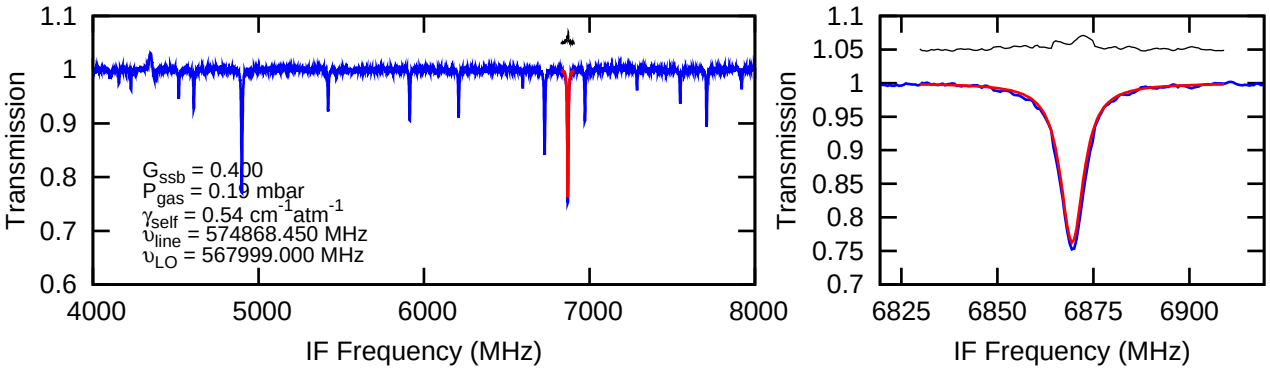

(b) CH_3OH at an LO frequency of 567.99 GHz

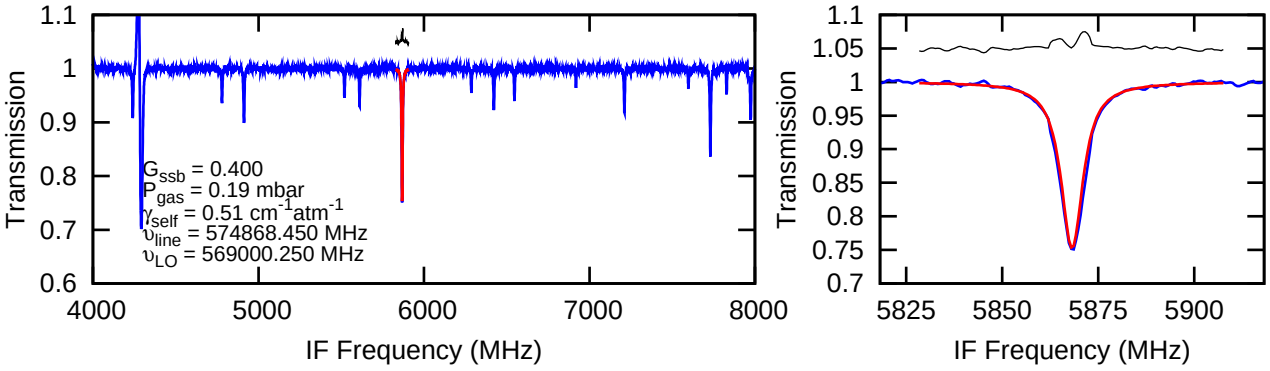

(c) CH_3OH at an LO frequency of 569 GHz

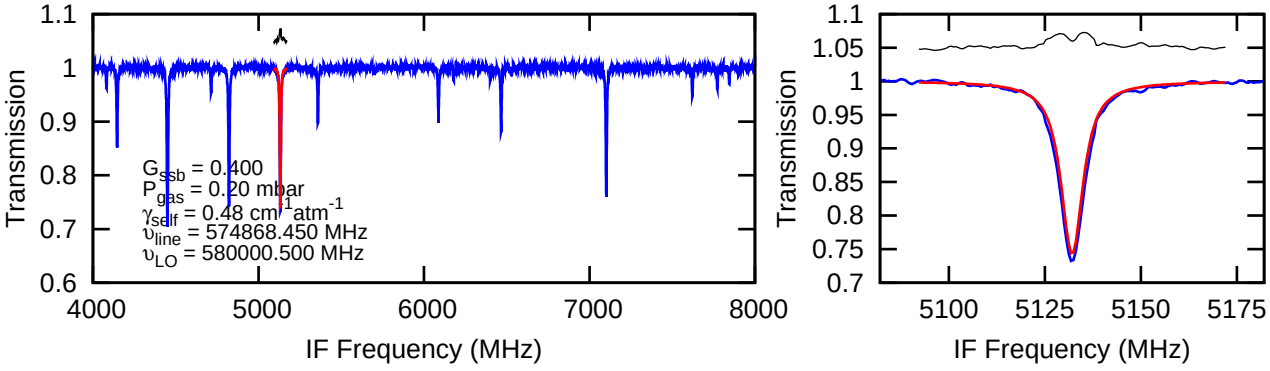

(d) CH_3OH at an LO frequency of 580 GHz

Figure 5.28: Determination of γ_{self} for the CH_3OH spectral line at 574868.45 MHz for multiple LO frequency observations.

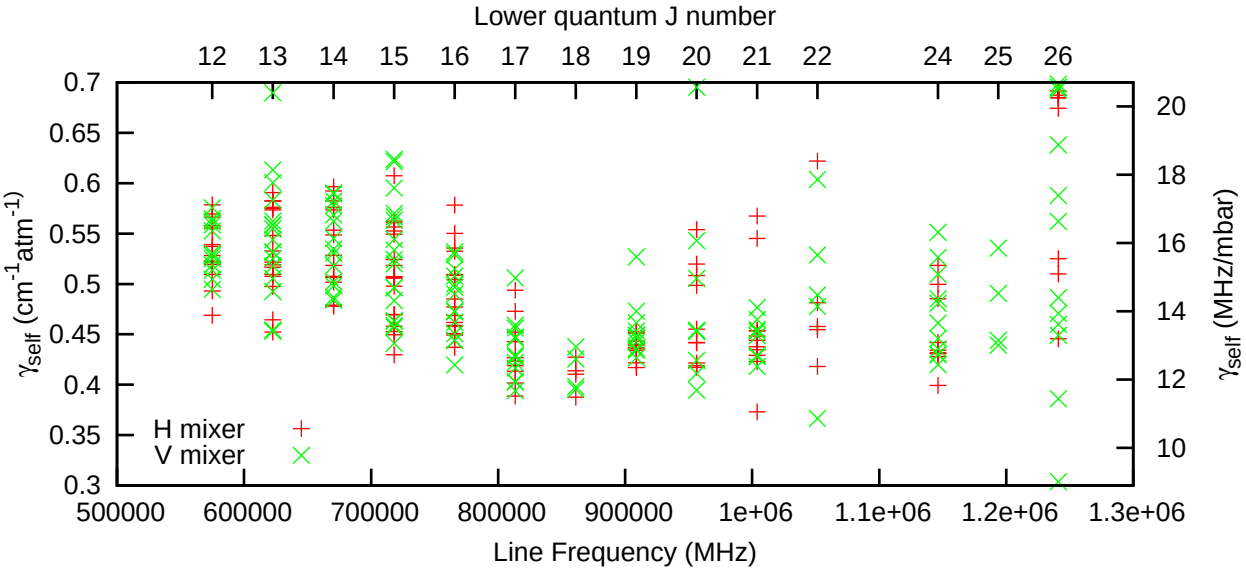

Figure 5.29: Overview of γ_{self} for the transition branch $J_{1+,0} \rightarrow J_{1+,0}$

and in different side bands. The self broadening parameter is then calculated as the average of the 12 measurements and the standard deviation taken as level of uncertainty in the measurement. Figure 5.29 shows an overview of the pressure broadening parameter extracted along with other transitions from the $J_{lower1+,0} \rightarrow J_{upper1+,0}$ branch of lines. The 574868.45 MHz line transition is seen at the J number 12. From the data one can see that there is a frequency or perhaps J number dependence for the pressure broadening term. Note the degree of scatter increases towards higher frequencies particularly in band 5 with the signal to noise ratio is high. The is due to a combination of decreasing line strength and increasing noise.

Figure 5.30 presents further pressure broadening data for other methanol line branches. Similar to figure 5.29 there appears to be a significant frequency dependence for the pressure broadening parameters. The line branch $J_{2-,0} \rightarrow J_{1-,0}$ in particular shows a significant variation in pressure broadening with line frequency, see figure 5.30(c). The significance of these variations requires further investigation beyond the scope of this thesis.

This section presented a unique first look into the variation of the pressure broadening parameter for methanol. The frequency range coupled to the frequency resolution of the data is unprecedented for a lab spectrometer and allows such an analysis as that presented in figure 5.29. The process of extracting the pressure broadening was presented in this section and has been calibrated for known gases for the simpler molecules as shown in figure 5.27. Further work is needed to extract the maximum spectroscopic return from this unique dataset.

5.5.4 Side band ratio extraction

The extraction of the side band ratio is the ultimate goal of the gas cell test campaign. The methanol data provide the best source of side band ratio information. Due to the line rich nature of methanol it provided spectral line at multiple positions in the IF band at all LO frequencies.

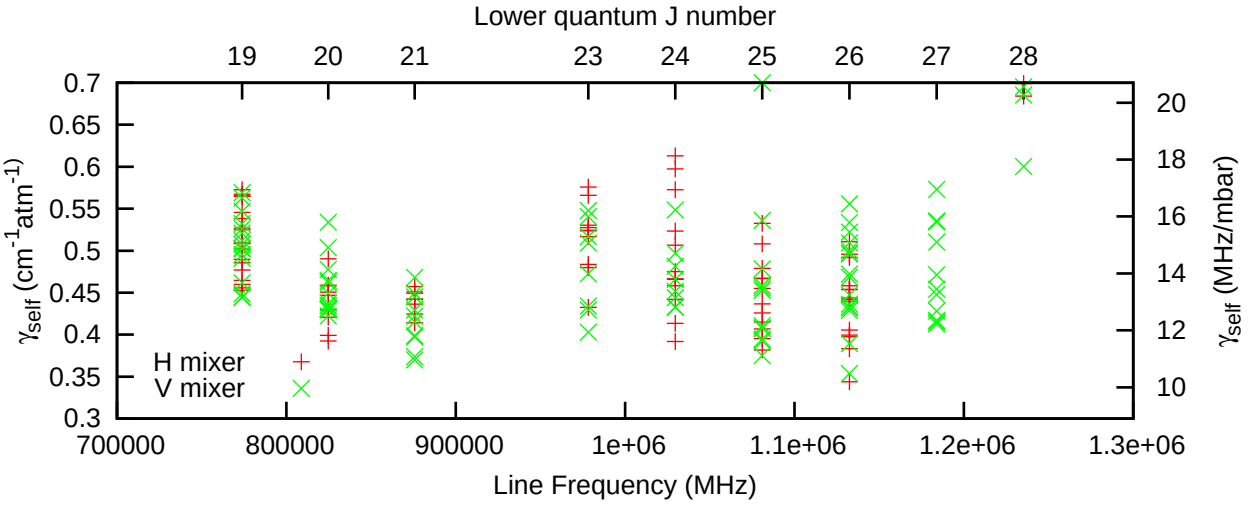

(a) $J_{-1,0} \rightarrow J_{0,0}$

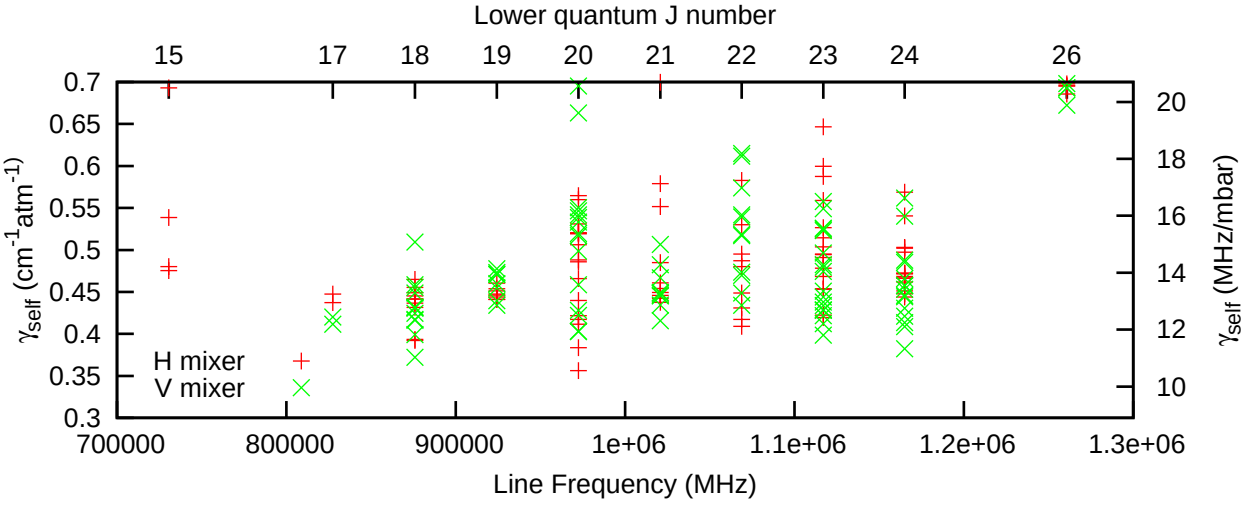

(b) $J_{1-,0} \rightarrow J_{1-,0}$

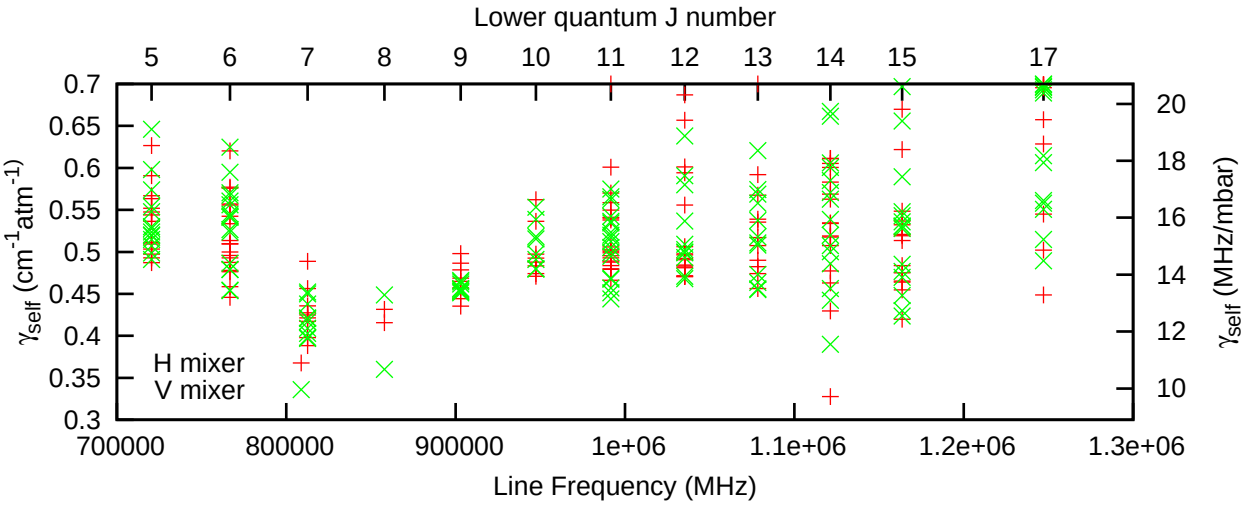

(c) $J_{2-,0} \rightarrow J_{1-,0}$

Figure 5.30: Example of pressure broadening variation for different methanol line branches

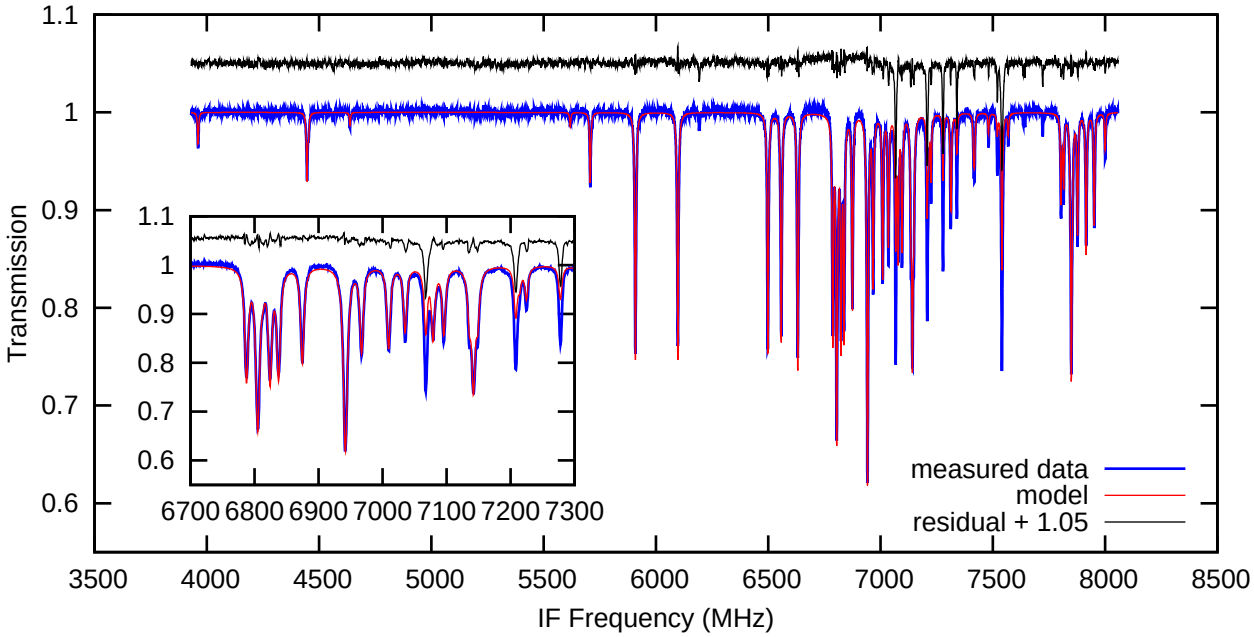

Figure 5.31: Example of a CH_3OH at 587 GHz with a model spectrum assuming a pressure broadening parameter for all lines of 0.41 $cm^{-1}atm^{-1}$ and a gas cell pressure of 0.22mbar and a side band ratio, G_{ssb}, of 0.46

Unfortunately the extraction of the side band ratio data from the methanol spectra is not trivial and requires an accurate knowledge of the pressure broadening parameter as well as an accurate line list containing the correct frequencies and intensities. In the previous section the method of extracting the pressure broadening from the data was detailed. However there is a large scatter in the determining the pressure broadening making it difficult to accurately determine the side band ratio.

Figure 5.31 shows a comparison between the model spectrum and the measured spectrum. For this spectrum a pressure broadening of 0.41 $cm^{-1}atm^{-1}$ is assumed for all transitions. This assumption provides a reasonable fit for most stand alone lines however the residuals are large where blended lines are modeled. The source of these large residuals could be uncertainty in the line intensity or perhaps the pressure broadening does vary wildly for these transitions.

In this section only a small region of the HIFI frequency coverage is analyzed. The region discussed is the lower band edge of band 2a. This is a region of known side band ratio imbalance observed through OCS, CH_3CN and ^{13}CO observations. For this analysis a select group of stand alone methanol lines are analyzed. The criteria for selection is a line intensity greater than -3.15 (JPL intensity units [52]). Similar to the analysis of the pressure broadening the line is fitted individually over a short range around the line peak. The same fitting function used for the pressure broadening analysis is used here, `generateLineModelPSelfSBR`. In this routine both the side band ratio and pressure broadening are fitted simultaneously. For the pressure broadening analysis large limits were placed on the fitting routine. For this analysis the side band ratio is known from previous measurements. The side band ratio extracted from the OCS and CH_3CN analysis is used as a best guess for the fitting routine and the fit is restricted to

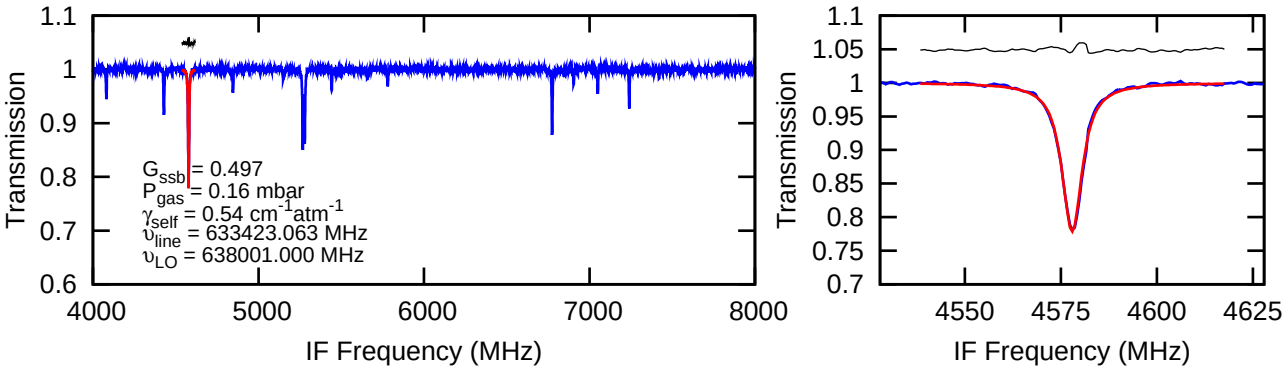

(a) CH_3OH at an LO frequency of 638.001 GHz

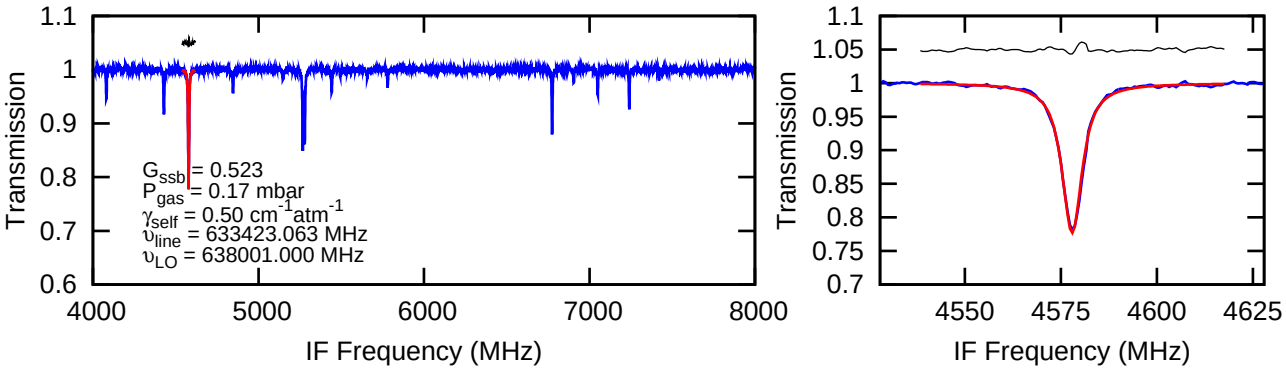

(b) CH_3OH at an LO frequency of 638.001 (separate observation to above figure) GHz

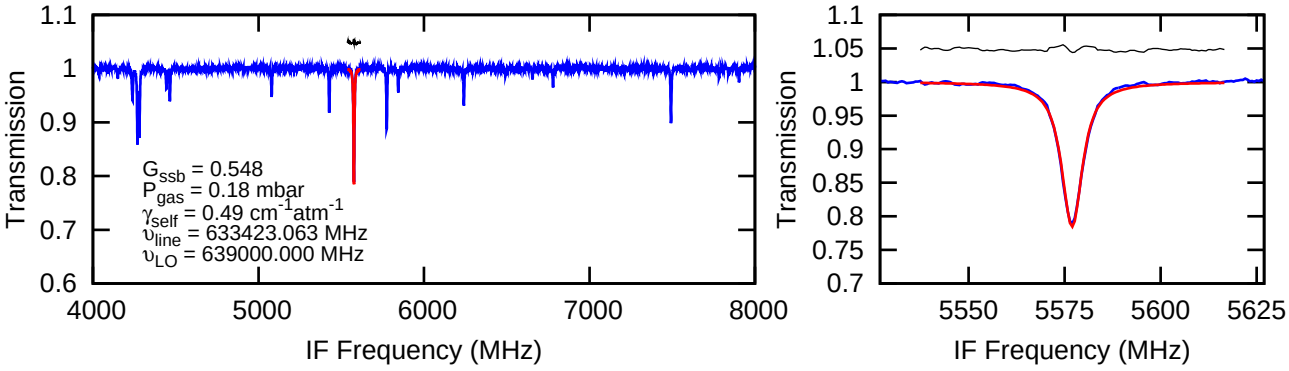

(c) CH_3OH at an LO frequency of 639.000 GHz

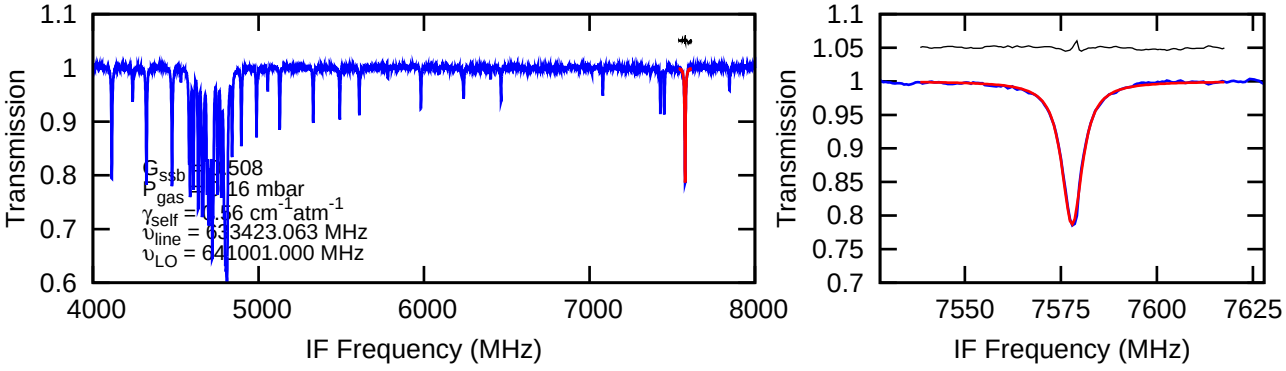

(d) CH_3OH at an LO frequency of 641.000 GHz

Figure 5.32: Observations of the spectral line 656168.960 MHz at multiple LO frequencies.

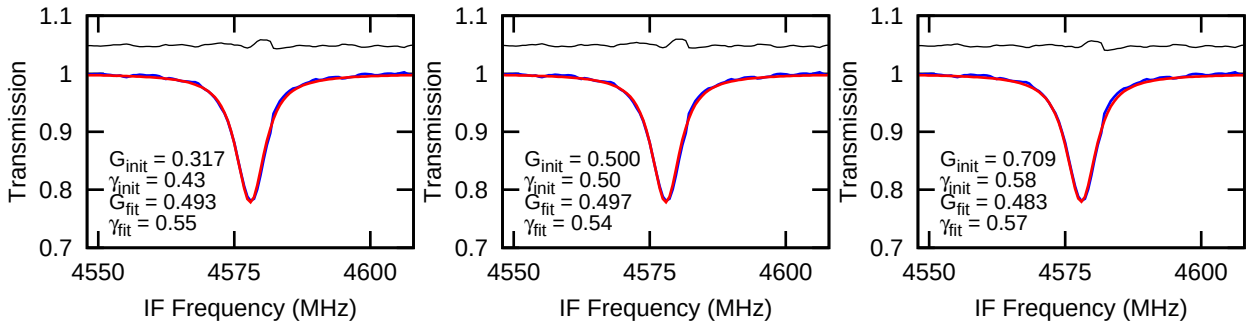

Figure 5.33: Different possible fits for the spectral line 633423.063 MHz at an LO frequency of 638 GHz depending on the fit initial parameters.

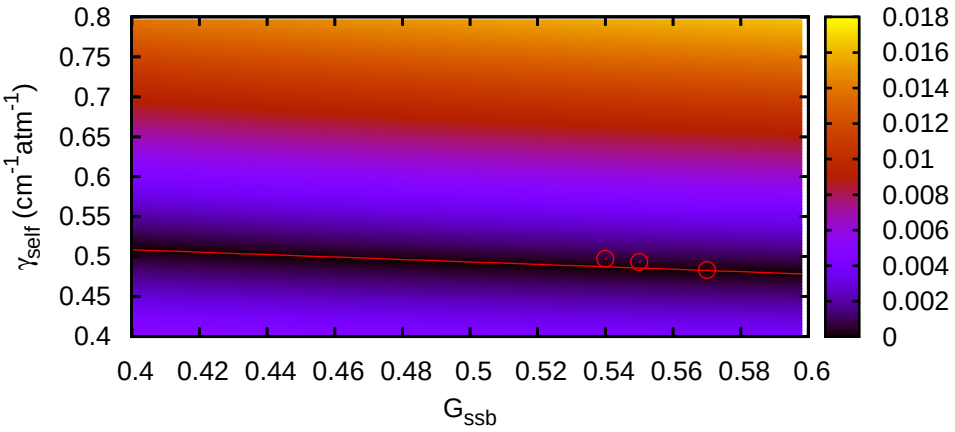

Figure 5.34: Contour plot of the chi-squared residual between the model and data for 633423.063 MHz methanol line using a range of G_{ssb} and γ_{self} values. A trough is seen across the residual showing a variety of G_{ssb} and γ_{self} values which provide a reasonable fit. The fitted parameters from the 3 models in figure 5.33 are plotted with red circles.

within ± 10% of these values.

Figure 5.32 shows an overview of the spectral line fitting for a single methanol line at different IF positions. There is large degree of scatter seen in the extracted side band ratio and over a short range of 4 GHz the side band ratio is seen to vary between 0.49 and 0.56. The line fit residuals however are good and don't indicate a poor quality fit. On closer inspection there appears to be a large degree of scatter even for near identical spectrum such as that shown in figures 5.32(a) and 5.32(b). Both spectra were taken at the same LO frequency and similar gas cell pressure. On visual inspection the spectra appear almost identical. However a side band ratio of 0.497 is extracted for figure 5.32(a) while a side band ratio of 0.518 is extracted for figure 5.32(b). There appears to be a repeatability problem with the fitting routine.

The fitting routine used is a standard Amoeba fitting algorithm. The side band ratio and pressure broadening are left as free parameters to vary within limits set by previous observations of the side band ratio at that LO frequency and the expected pressure broadening

parameters. However the results returned by the fitting routine are dependent on the fitting initial parameter. Figure 5.33 shows an example of fitting a spectral line with different initial parameters. Each fit returns a small residual between the model and measured data. However there is a large variation between the final fit parameters for the three different sets of initial parameters, the question remains which of the fit parameters are the correct results.

Figure 5.34 shows a contour plot of the chi squared residual for a range of G_{ssb} and γ_{self} values for the model fit of the 633423.063 MHz spectral line. The parameters from the 3 fits shown in figure 5.33 with red circles. From the plot it is apparent that a range of G_{ssb} and γ_{self} (highlighted by the red diagonal line) provide a good fits to the measure data. This helps explain the variability in the fitting seen from the `generateLineModelPSelfSBR` so far. From the contour plot it is apparent that the limits set for the model fitting must be tightly constrained otherwise a large scatter will be seen in the fitted side band gain and pressure broadening data.

However as shown in figure 5.30 there is a large degree of scatter seen in the extracted γ_{self} of $\pm 10\%$. From the red line in figure 5.34 it is apparent that a large range of side band ratios can provide a viable model spectrum. The extraction of side band ratio from the gas cell data must follow a chicken and egg approach. The pressure broadening must first be accurately established in areas where the side band ratio has been established through observation of other simpler gases. Using the measured pressure broadening the side band ratio coverage can be expanded. For example using the OCS observations at 630 GHz to fix the side band ratio the pressure broadening can be then accurately established for strong lines observed at the same LO frequency. As each of these lines are observed at multiple LO frequencies one can expand the region of side band ratio coverage to $\pm$ 4 GHz of the original OCS observation. Knowledge of the pressure broadening of these methanol lines can then be used to further calibrate the pressure broadening of other lines not covered by the OCS observation but close by in frequency further expanding the side band ratio coverage.

This approach has not been implemented for the analysis presented here. The analysis presented has a large degree of variability as the model limits were relaxed to within 10% of the nearest side band ratio measurement. Tighter constraints are needed to improve the results. As stated in the beginning of this section the analysis presented here concentrated on the lower edge of band 2a. The results of this first pass analysis of methanol are shown in Figure 5.35. The data is presented from 3 perspectives. Figure 5.35(a) shows the side band ratio extracted for each line frequency. The side ratio is then plotted against the line frequency and shows the degree of scatter seen for the side band ratio of each line measured. Figure 5.35(b) shows the side band ratios plotted against the LO frequency. From this again one can see the degree of scatter for each LO frequency setting. Ideally if the side band ratio for a given LO frequency was plotted against the IF frequency of line measured it would be expected to see a slope down from the upper IF frequencies to the lower IF frequencies (see figure 2.16 on page 36) however due to the large degree of scatter no such pattern is seen. Figure 5.35(c) shows the side band

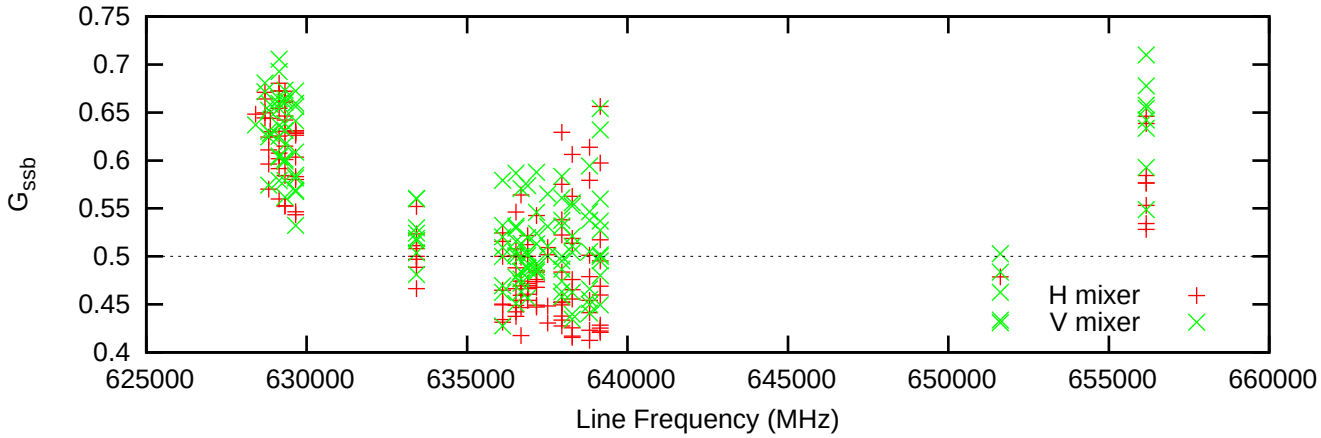

(a) Side band ratio vs line frequency

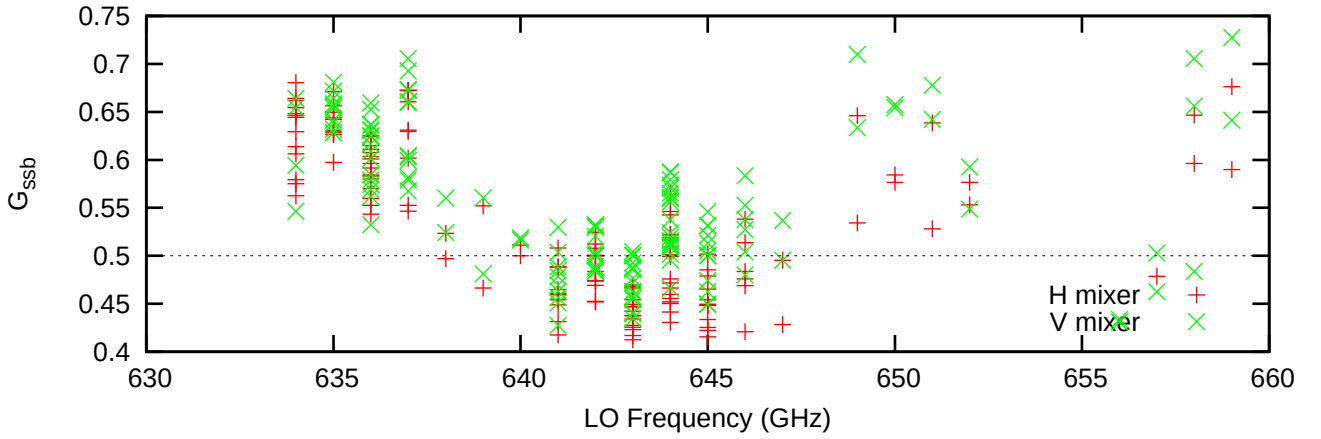

(b) Side band ratio vs LO frequency

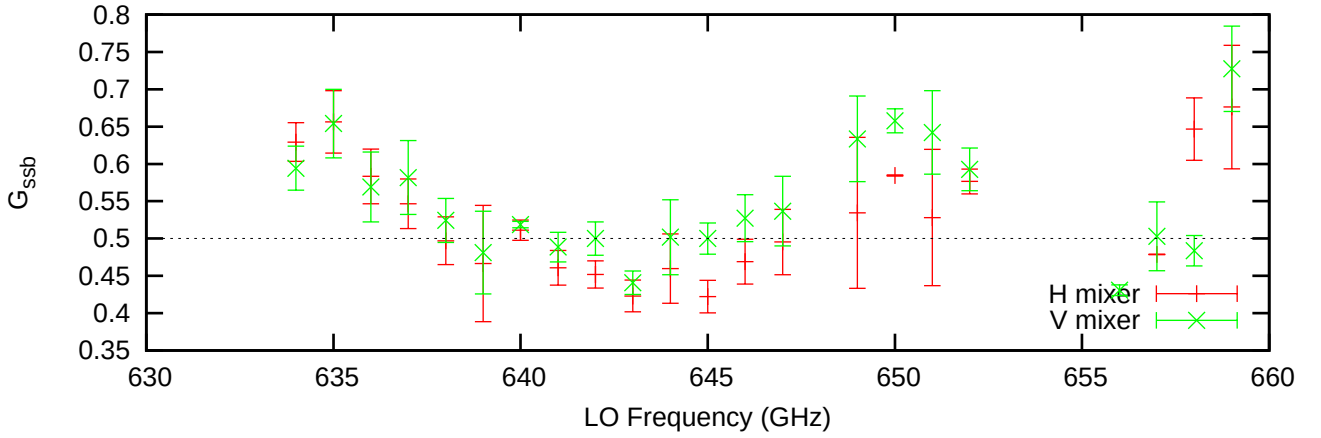

(c) Averaged Side band ratio vs LO frequency

Figure 5.35: Side band ratio extracted from methanol for the lower edge of band 2a.

ratio averaged for each LO frequency setting. This appears to show a trend of decreasing side band ratio consistent with variation observed for the other gases.

Figure 5.36 shows a comparison between the side band ratio previously extracted from the simple molecules. The measured methanol data shows reasonable agreement with the data measured using other gases however further analysis is needed to reduce the amount of scatter seen in the data.

5.5.5 Summary

In this section the process of extracting the side band ratio from the methanol data using a spectral line model has being detailed. The first step in extracting the side band ratio was the extraction of the pressure broadening parameter from the data. Only a small portion of the entire dataset was presented. The analysis concentrated on unconfused spectral lines. The data is grouped together into the different methanol line branches observed. The complete analysis of the pressure broadening variation is beyond the scope of this thesis. The four line branches presented showed a marked structure and there seems to be a frequency dependence. Further work is needed in collaboration with the spectroscopy community to extract the maximum potential from this dataset

The first steps in extracting the side band ratio from the dataset was presented here also. On closer inspection the data showed a large degree of scatter in the extracted side band ratio for spectral lines that were almost identical. Further investigation showed that the fitted side band ratio was sensitive to the initial parameter of the fit routine. It was shown for a single spectral line that a range of combinations of pressure broadening and side band ratios could return a good fit. It is proposed that the next phase of the methanol analysis should concentrate primarily on the regions where the side band ratio has been established using other gas observations. By fixing the side band ratio the pressure broadening can be established for spectral lines around the region of known side band ratio. Since each methanol spectral line is on average observed over an LO range of 16GHz (from the edge of the LSB to the upper edge of the USB) using this method the side band ratio coverage around a simply molecule can be expanded.

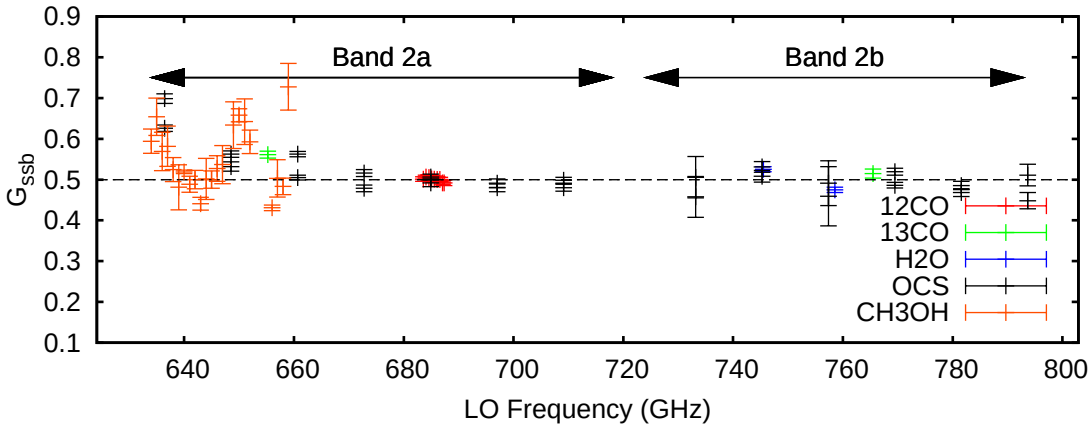

(a) side band ratio V mixer, band 2

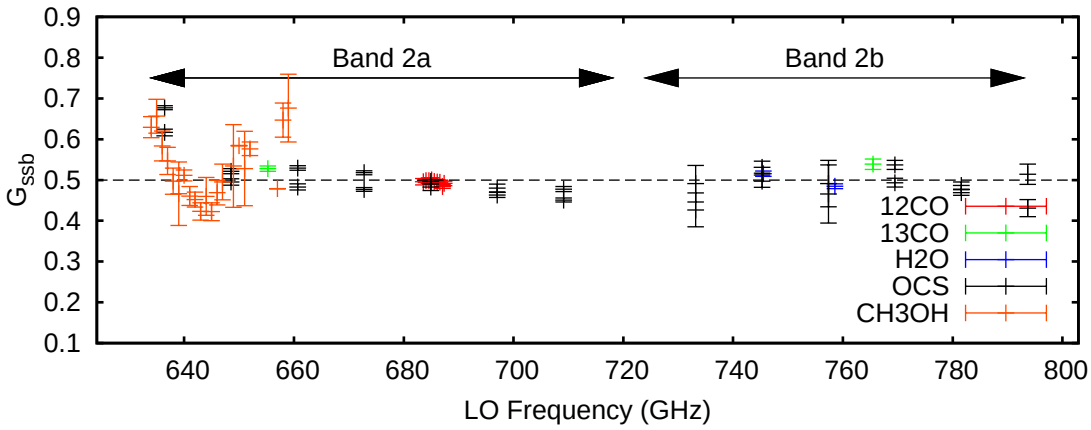

(b) side band ratio H mixer, band 2

Figure 5.36: Comparison of side band ratios extracted from methanol compared to values extracted earlier from the simply molecules

5.6 Gas cell calibration of a QCL heterodyne receiver

5.6.1 Introduction

The development of astronomical heterodyne receivers is on going. The state of art performance of HIFI is being confined to the past with new receivers providing high frequency coverage and lower noise performance at the same frequencies[131]. A new frontier in sub-mm heterodyne spectroscopy is the development of local oscillator sources operating around 2THz. A number of interesting astronomical lines exist about this barrier. An early iteration of the HIFI design included an 8th band which was designed to operate from 2.4 to 2.7 THz this was eventually descoped due to development issues with the gas laser LO source. Recent developments have attempted to develop alternate sources for LO frequencies above 2 THz to much success. This section briefly describes the development of a quantum cascade laser (QCL) LO source and the usage gas cell observations of methanol to calibration the instrument. The gas cell code described in this chapter was used to calibrate the QCL frequency. The results of these tests and gas cell modeling efforts were published in Ren et al. [104].

5.6.2 THz QCL lasers

The concept of a quantum cascade laser was first proposed by Kazarinov & Suris [58]. A quantum cascade laser was first demonstrated in 1994 and published by Faist et al. [32]. The mechanics of a quantum cascade laser are beyond the scope of this thesis. The basic premise is that through careful selection of a semiconducting material in combination with a specific layering and geometry of the QCL material coupled to a voltage source an infra signal at a specific frequency can be produced.

QCL lasers initially operated at mid-infrared wavelengths however they have recently been developed to operate at THz wavelengths[126]. A number of milestones for using a QCL as a LO source have being reached such as a phase locking capability[60], narrow intrinsic line width[2], and excellent power stability[35]. A remaining key step in the development of a QCL as a viable LO source is the observation of spectral lines. The obvious next set up is the use of a QCL in combination with a mixer observing a hot and load source through a gas cell.

5.6.3 Gas cell observation

A gas cell test setup was developed at TU Delft to demonstrate the performance of the QCL laser as an LO source. The test set up is much simpler than the HIFI gas cell test set up, as the components involved are separated and don't require any special optics to modify the beams. Figure 5.38 shows the experimental set up. A NbN HEB mixer with a bandwidth of 0.7 to 2.2 GHz is used for down converting the signal. The IF signal is recorded with a Fourier Transform Spectrometer (FTS).

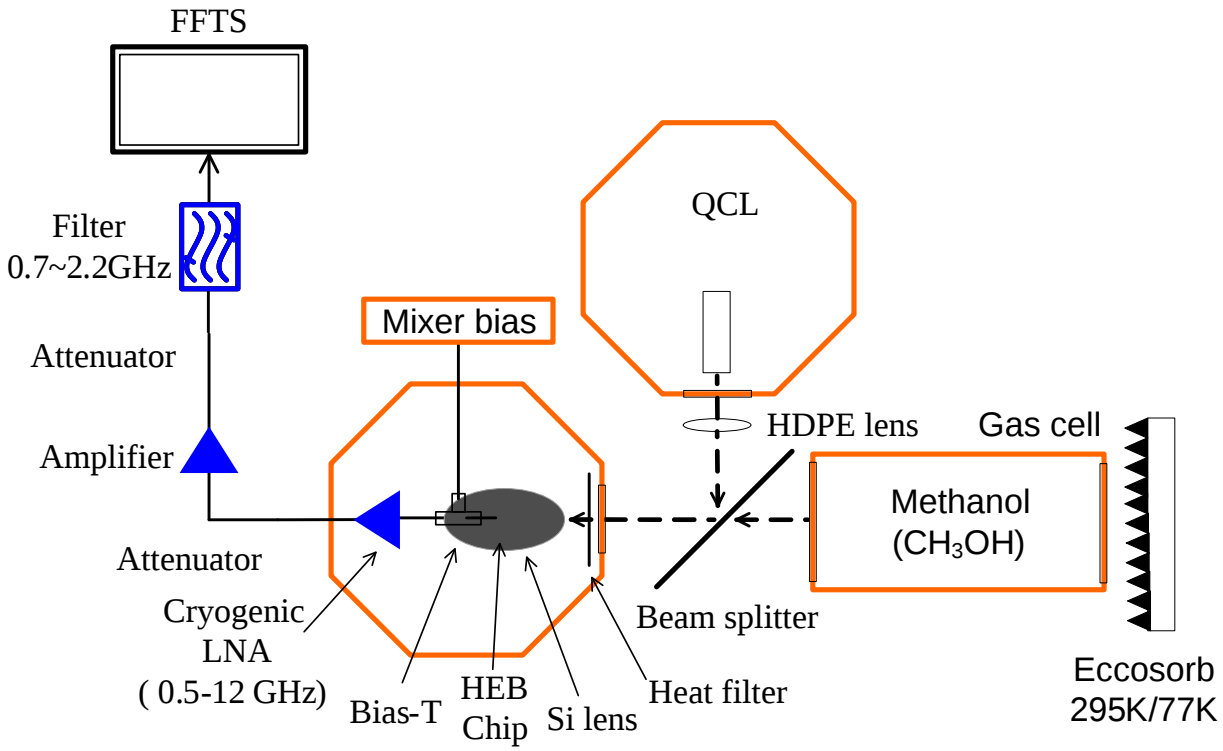

Figure 5.37: Experimental set up of QCL gas cell test set up[104].

The test procedure follows a similar process to the HIFI gas cell tests. A chopper is used to chop between a hot and cold load source. No hot empty data was taken which increases the noise compared the four phase calibration of the HIFI gas cell test. The data is calibrated differently and is plotted as an emission spectrum which is more intuitive as opposed to the absorption plot used for HIFI data. The 3 phases data is temperature calibrated using the following equation:

$$T_{gas}(f) = T_{cold} + 2(T_{hot} - T_{cold})\frac{CF - CE}{HF - CE} \tag{5.20}$$

where T_{cold} and T_{hot} are the cold and hot load temperatures respectively, CF is the IF signal for the test phase looking though a methanol filled gas cell with the cold load as a background, CE is the IF signal looking through an empty gas cell at the cold load and HF is the IF signal looking through the filled gas cell at the hot load.

Figure 5.38 shows example spectra at different gas cell pressures. These plot shows that the effect of increasing gas cell pressure on the line profile. This is a simple but useful test to establish the spectroscopy credentials of the QCL laser set-up. From the data one can see the increasing line width with increasing pressure. A critical demonstration of the QCL laser frequency stability is that the line width is consistent with the pressure broadening and not affected by any additional effects such as LO frequency jitter in the QCL signal. From the data the pressure broadening was extracted from the data by fitting a Lorentzian profile to the line profile and compared to comparable data at 2.519THz taken using a QCL as an active tuning source[47]. There was large disparity seen between the results.

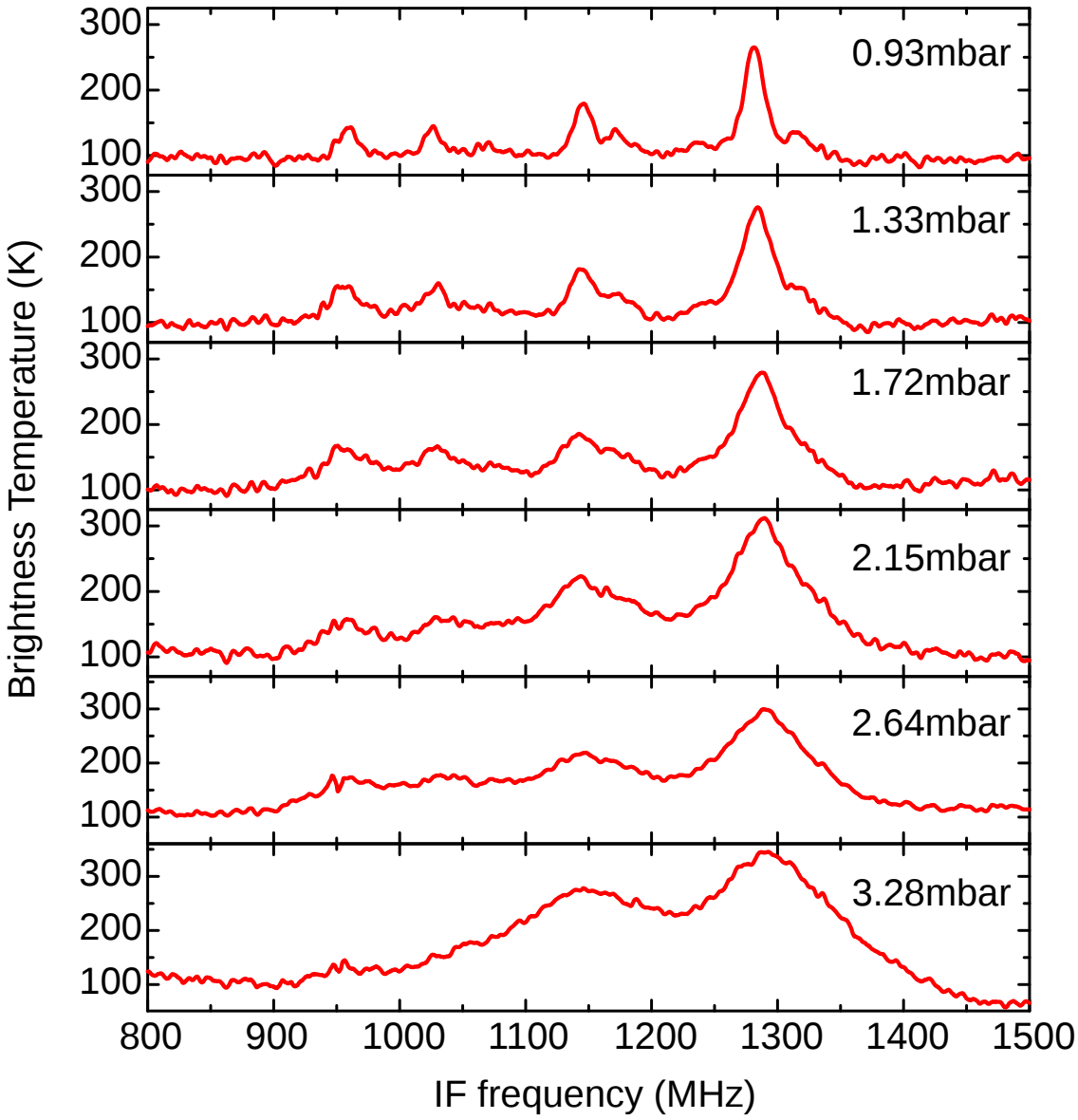

Figure 5.38: Calibrated spectra taken using the QCL coupled to a HEB mixer at an LO frequency of 2915.6 GHz [104].

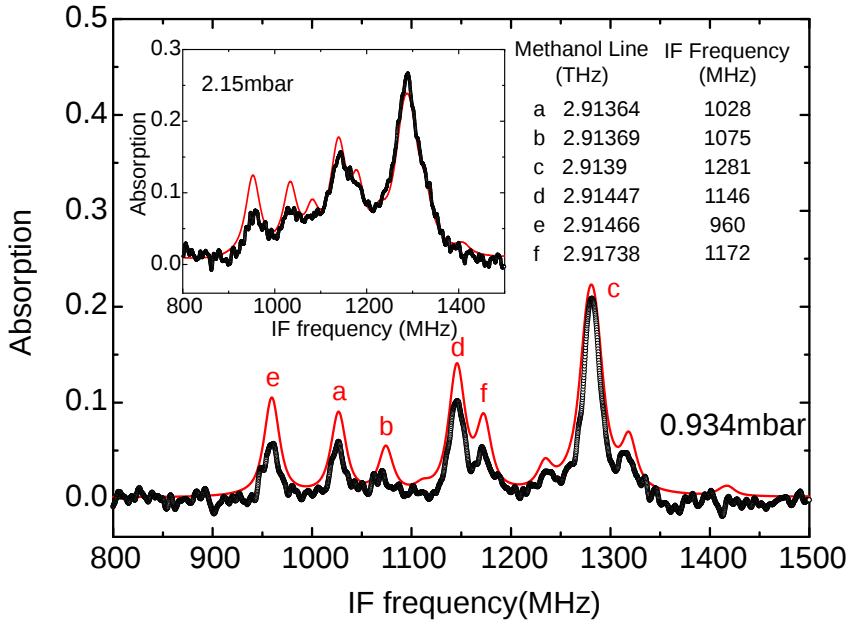

Figure 5.39: Measured and modeled methanol spectrum at 2 different gas cell pressure taken at an LO frequency of 2.9156THz[104]

The author was tasked with developing a model of the line emission using the gas cell properties in combination with the JPL catalog which provided methanol line frequencies and intensities up to 4THz. The TU Delft gas cell has a shorter path length of 50cm compared to the HIFI multi-path length of 102.5 cm. The most noticeable difference between HIFI and the QCL source is that that LO frequency is not as accurately known. For HIFI the frequency is known to within kHz however for the QCL the exact LO frequency was not known and was accurate only to the resolution of the FTS spectrometer used to measure the THz signal. The QCL LO frequency was measured using the FTS to be 2.9176 $\pm$ 0.6 GHz.

The first step in developing a model spectrum was the determination of the LO frequency. This followed a rather crude approach where a model spectrum was generated with the measured gas cell pressure and an average pressure broadening. This spectrum was then compared to the measured spectrum. The process was repeated for multiple LO frequency settings within the predicted frequency range. The residual between the modeled and measured spectra were visually inspected until a matching LO frequency was established. Additional spectra were measured at slightly different LO frequencies, since spectral lines move in different directions on the IF band it could be established which lines were from the upper and lower side bands. The LO frequency was eventually determined to be 2.9156 THz. Once the LO frequency was established the pressure broadening value could be extracted. The fitting was preferenced towards the strong spectral line in the band center. The pressure broadening was finally determined to be $\sim$0.25 $cm^{-1}atm^{-1}$ (7.4 MHz/mbar). The modeled QCL double side band spectrum at 2.9156THz is shown in figure 5.39.

The model and measured spectra show good agreement returning a viable value for the

pressure broadening parameter. The deviation from the value of Hübers et al. [47] was determined to be due to different approaches to measuring the pressure broadening. Instrumental papers commonly measure the pressure broadening of a line profile using a straight Lorentzian fit to the data and taking the half-width half-maximum as the pressure broadening value. They neglect the effect of opacity broadening and hence the extracted value is not the true pressure broadening term as defined in section 5.2.4 and not directly comparable with other pressure broadening extracted from other gas cell tests.

The spectra shown in figure 5.39 demonstrate the applicability of QCL as an LO source in heterodyne spectroscopy. Tentative steps have recently being made to develop a tunable QCL which could cover a larger frequency range. Recent tests have pushed heterodyne spectroscopy to higher LO frequencies with observations of methanol up to 3.4THz[105]. The methods developed in this chapter provide a vital tool in the calibration of the QCL output frequency.

5.7 Conclusions

In this chapter the main line broadening mechanisms evident in a gas cell spectrum were described. These line broadening mechanisms were developed into a Jython[2] code which produces a double side band transmission spectrum for a given gas cell set up and receiver LO frequency. By comparing the model gas cell spectra to measured spectra it was shown that for simple molecules (^{12}CO,^{13}CO,OCS and H_2O) where the pressure broadening parameter was known the side band ratio could be extracted from the data.

This approach was applied to both saturated and not saturated lines. The side band ratio extracted for saturated lines was in good agreement with the values determined using the line peak extraction approach described in chapter 4. A number of side band ratio measurement were added for un-saturated lines. The analysis of the OCS data in the diplexer bands 3 & 4 showed large variations in side band ratio with diplexer mistuning being the likely culprit. Based on the previous analysis of ^{12}CO this was thought to be a fixed offset, this assumption was shown to be false as the OCS data showed a frequency dependent mistuning. From the OCS data it was possible to correct the data for the diplexer IF gain slope and the extracted side band ratio was seen to be close unity, $G_{ssb} = 0.5$. Similarly diplexer mistunings were seen in the H_2O.

By same line modeling approach was applied to the methanol dataset. The pressure broadening parameters were not known before the analysis and these were extracted from the data. The pressure broadening parameter and side band ratio were fitted simultaneously. This method was found to be prone to finding false fit results unless tightly constrained. The fitted pressure broadening had a large scatter. However for the methanol line branches fitted there was a distinct variation with line frequency the significance of which remains to be explored.

The side band ratios extracted from the methanol data showed large scatter much like the pressure broadening data. It was shown that different initial parameters in the fitting algorithm resulted in different fit parameters. On closer inspection it was shown that having two free parameters, the side band ratio and the pressure broadening resulted in multiple viable solutions to the line fit. Future analysis should concentrate on regions where the side band ratio is accurately known. This can be used as a constraint to fit the pressure broadening parameter of the methanol line observed at that LO frequency. Once the pressure broadening is established for a given line, this line can be tracked through the IF band at different LO frequencies and expand the coverage around known regions of side band ratio until eventually the whole band is covered with methanol lines observations. Further work is needed on an intelligent algorithm that uses the simple molecule analysis to constrain the pressure broadening and then using this information constrain the side ratio at other LO frequencies.

The final section in this chapter discussed the analysis of quantum cascade laser heterodyne gas cell observations. The methods developed in this thesis were applied to spectra taken

[2]Jython, successor of JPython, is an implementation of the Python programming language written in Java.

an LO frequency of 2915.6 GHz. Using the gas cell spectrum model the LO frequency was accurately established and a model double side band spectrum was generated. This model showed good agreement with the measured data. The observation of molecular spectra using a QCL heterodyne system is a crucial step in the development of the QCL as a viable LO source above 2 THz. The gas cell code developed in this thesis played an important role in verifying the QCL's future potential.

Chapter 6

Conclusions

In this thesis the major sources of intensity uncertainty in the Herschel/HIFI instrument were described and investigated. The HIFI instrument has very ambitious calibration goals of 3% uncertainty. In line with these goals an extensive ground test campaign was undertaken to quantify the system response prior to launch on the Herschel Space Observatory. A central part of this ground test campaign was the gas cell test apparatus.

By observing known gases at low pressures through a gas cell of suitable optical path length it was hoped to quantify the instrument response and behavior. The primary goal of the gas cell test campaign was the determination of the side band ratio. HIFI is a double side band receiver with intensity detected from an upper and lower side band. The ratio of the upper and lower side intensity of the total intensity was foreseen as source of uncertainty in the determination of spectral line intensity particular towards LO band edges. Through observation of saturated gas lines the side band ratio was measured at particular frequencies. In total 4 gases provided saturated lines in the gas cell test campaign. Using these saturated lines the side band ratio was sparsely measured across the HIFI frequency coverage. The highest resolution coverage was in bands 1 and 2. For some regions the side band ratio was seen to vary significantly from unity. The lower edge of band 2 was seen through the observation of 3 different gases to have an upper side band dominated spectra over the region of 630 to 660 GHz.

Saturated lines however only covered a small fraction of the total HIFI frequency coverage. Other gases were also observed which provided un-saturated spectral lines. In order to extract the side band ratio information a spectral line model was developed to predict the gas opacity for a given pressure, optical depth and temperature using the JPL and HITRAN spectral line catalogs as a starting point. This method was tested on the saturated lines and showed excellent agreement between the measured and modeled data. By comparing the expected model data for a side band gain balanced system with the measured data the side band gain ratio could be extracted from the data.

The spectral model approach was applied to the OCS data in bands 3 and 4. The extracted side band ratio shows an extreme variation not consistent with the side band ratio variation due to the mixer antenna response. On closer inspection the source of the extreme side band ratio

was due to a diplexer mistuning. The mistuned diplexer introduced a significant gain slope on IF band. Using a model of the diplexer gain variation due to different levels of mistuning it was possible to extract the degree of mistuning from the data and correct the side band ratio for this effect. This diplexer mistuning was seen in all data in bands 3 and 4 where sufficient data coverage was available. This had a detrimental effect on the overall accuracy of the side band measurement through gas cell observations. Follow-up flight observations have shown that the issue of diplexer mistuning was an artifact of the ground based test campaign and no evidence of a mistuning have been seen in flight data.

The gas cell observations in the HEB bands were beset with standing wave issues. This was indicative of the overall performance and has followed HIFI into orbit. Due to a non-optimal IF chain design an impedance mismatch between the mixer and the first amplifier exists. The mixer unit impedance is extremely sensitive to LO power variations. A slight change in LO power or mixer state over the course of an observation can result in poor baseline performance. In this thesis a method was developed using a catalog of standing waves to correct the poor baselines. This approach used to correct gas cell data and was also applied to in-flight observations. The HEB bands are of vital importance to the HIFI instrument accounting for 30% of the frequency coverage and 33% of the observing time. The development of the baseline correction routine will form a crucial part of the data processing for these bands.

The molecules with saturated lines make up only 20% of the total observations taken during the gas cell test campaign. The most observed gas was methanol which accounted for 80% of the observation taken. Methanol was observed every 1 GHz over the entire range of the HIFI frequencies. The extraction of the side band ratio would provide a complete picture of the side band ratio variation across the HIFI bands. The extraction of the side band ratio was problematic as the pressure broadening parameter of the methanol line frequencies were not known prior to the analysis. The spectral line model developed to extract the side band ratio from non-saturated lines was adapted to fit both the side band ratio and the pressure broadening. This approach however was problematic and the model fit was dependent on the initial parameters. On closer inspection it was shown that multiple different combinations of the side band ratio and pressure broadening would produce a viable fit to the data. It was concluded that the extraction of the side band ratio from the methanol data would require the use of the side band ratio determined from the saturated line analysis as a starting point. Using this approach the coverage of the side band ratio around these known points could be expanded to eventually recover the entire band.

A first pass analysis of methanol was undertaken towards the edge of band 2a. The data was extracted leaving the side band ratio and pressure broadening to vary within large limits. This method was prone to false fits and the resulting data shows a great deal of scatter. However the extracted pressure broadening did show some structure and the extracted pressure broadening, while having a large scatter, was consistent with published predicted values. The extracted side band ratio was shown to be consistent with the measured OCS data towards the band edge

albeit with a large degree of scatter. The increased level of frequency resolution however was encouraging for the future determination of the side band ratio.

Bibliography

[1] J. Baars (2003). 'Characteristics of a reflector antenna'. *ALMA Memo 456* .

[2] A. Barkan, et al. (2004). 'Linewidth and tuning characteristics of terahertz quantum cascade lasers'. *Opt. Lett.* **29**(6):575–577.

[3] J. J. A. Baselmans, et al. (2005). 'Direct detection effect in small volume hot electron bolometer mixers'. *Applied Physics Letters* **86**(16):163503.

[4] M. Belgacem, et al. (2004). 'The high resolution versatile digital spectrometer of HIFI-HSO'. *New Astronomy* **9**(1):43 – 50.

[5] T. Berg, et al. (2005). 'IF Impedance Optimization of HEB's for Band 6 at the Herschel Space Observatory'. In *Sixteenth International Symposium on Space Terahertz Technology*, pp. 474–+.

[6] E. A. Bergin, et al. (2010). 'Herschel observations of EXtra-Ordinary Sources (HEXOS): The present and future of spectral surveys with Herschel/HIFI'. *A&A* **521**:L20+.

[7] S. M. Birkmann, et al. (2004). 'Characterization of high- and low-stressed Ge:Ga array cameras for Herschel's PACS instrument'. In J. C. Mather (ed.), *Society of Photo-Optical Instrumentation Engineers (SPIE) Conference Series*, vol. 5487 of *Society of Photo-Optical Instrumentation Engineers (SPIE) Conference Series*, pp. 437–447.

[8] C. Borys, et al. (2008). 'Detection and characterization of spurs in ILT gas-cell observation'. Tech. rep. NHSC-JPL-HIFI-technote.

[9] J. Brault, et al. (2003). 'Self-broadened 12C16O line shapes in the v=2<–0 band'. *Journal of Molecular Spectroscopy* **222**(2):220 – 239.

[10] A. Bruno, et al. (2002). 'Self-, Nitrogen-, and Oxygen-Broadening Coefficient Measurements in the [nu]1 Band of H2O Using a Difference Frequency Generation Spectrometer at 3 [mu]m'. *Journal of Molecular Spectroscopy* **215**(2):244 – 250.

[11] P. J. Burke (1997). *High-Frequency Electron Dynamics in Thin Film Superconductors and Applications to Fast, Sensitive Thz Detectors*. Ph.D. thesis, Yale University.

[12] P. J. Burke, et al. (1996). 'Length scaling of bandwidth and noise in hot-electron superconducting mixers'. *Applied Physics Letters* **68**(23):3344–3346.

[13] C. Camy-Peyret, et al. (1985). 'The high-resolution spectrum of water vapor between 16500 and 25250 cm-1'. *Journal of Molecular Spectroscopy* **113**(1):208 – 228.

[14] G. Cazzoli & C. Puzzarini (2006). 'The Lamb-dip spectrum of methylcyanide: Precise rotational transition frequencies and improved ground-state rotational parameters'. *Journal of Molecular Spectroscopy* **240**(2):153 – 163.

[15] G. Cazzoli, et al. (2008). 'Pressure-broadening in the THz frequency region: The 1.113 THz line of water'. *Journal of Quantitative Spectroscopy and Radiative Transfer* **109**(9):1563 – 1574.

[16] S. Cherednichenko, et al. (2008). 'Hot-electron bolometer terahertz mixers for the Herschel Space Observatory'. *Review of Scientific Instruments* **79**(3):034501–+.

[17] P. A. Collins, et al. (2003). 'A Ground Calibration Facility for Herschel-SPIRE'. In J. C. Mather (ed.), *Society of Photo-Optical Instrumentation Engineers (SPIE) Conference Series*, vol. 4850 of *Society of Photo-Optical Instrumentation Engineers (SPIE) Conference Series*, pp. 628–637.

[18] C. Comito (2011). private communication.

[19] C. Comito, et al. (2009). 'Spectral Surveys of Star-forming Regions with Herschel/HIFI'. In D. C. Lis, J. E. Vaillancourt, P. F. Goldsmith, T. A. Bell, N. Z. Scoville, & J. Zmuidzinas (ed.), *Astronomical Society of the Pacific Conference Series*, vol. 417 of *Astronomical Society of the Pacific Conference Series*, pp. 95–+.

[20] C. Comito & P. Schilke (2002). 'Reconstructing reality: Strategies for sideband deconvolution'. *A&A* **395**:357–371.

[21] M. W. de Graauw, et al. (1998). 'Heterodyne instrument for FIRST (HIFI): preliminary design'. vol. 3357, pp. 336–347. SPIE.

[22] T. de Graauw, et al. (2010). 'The Herschel-Heterodyne Instrument for the Far-Infrared (HIFI)'. *A&A* **518**:L6+.

[23] T. de Graauw, et al. (2008). 'The Herschel-Heterodyne Instrument for the Far-Infrared (HIFI):instrument and pre-launch testing'. In J. M. Oschmann, Jr., M. W. M. de Graauw, & H. A. MacEwen (eds.), *Space Telescopes and Instrumentation 2008: Optical, Infrared, and Millimeter*, vol. 7010, p. 701004. SPIE.

[24] G. de Lange, et al. (2003). 'Development of the HIFI Band 3 and 4 Mixer Units'. In C. Walker & J. Payne (ed.), *Fourteenth International Symposium on Space Terahertz Technology*, pp. 447–+.

[25] Y. Delorme, et al. (2005). 'Space-qualified SIS mixers for Herschel Space Observatory's HIFI Band 1 instrument'. In *Sixteenth International Symposium on Space Terahertz Technology*, pp. 444–448.

[26] P. Dieleman (2004). 'FP QM MA tests Band 3: HIFI Consortium meeting (September 6-7 2004, Leiden)'. Tech. rep., SRON Groningen.

[27] P. Dieleman, et al. (2008). 'HIFI Flight Model Testing at Instrument and Satellite Level'. In W. Wild (ed.), *Ninteenth International Symposium on Space Terahertz Technology*, pp. 106–+.

[28] A. Dubrulle, et al. (1980). 'The Millimeter Wave Rotational Spectra of Carbonyl Sulfide'. *Zeitschrift Naturforschung Teil A* **35**:471–+.

[29] H. Ekström, et al. (1997). 'Gain and noise bandwidth of NbN hot-electron bolometric mixers'. *Applied Physics Letters* **70**(24):3296–3298.

[30] D. Emerson (1997). *Interpreting Astronomical Spectra*. Wiley-Interscience.

[31] ESOC (2010). 'Herschel Products Definitions Document - Part I (HERSCHEL-HSC-DOC-0959)'. Tech. rep., ESA.

[32] J. Faist, et al. (1994). 'Quantum Cascade Laser'. *Science* **264**(5158):553–556.

[33] D. T. Frayer, et al. (2007). 'Tools for the Herschel Space Observatory: Observation Planning and Data Processing'. In *Bulletin of the American Astronomical Society*, vol. 38 of *Bulletin of the American Astronomical Society*, pp. 108–+.

[34] U. Frisk, et al. (2003). 'The Odin satellite. I. Radiometer design and test'. *A&A* **402**:L27–L34.

[35] J. R. Gao, et al. (2005). 'Terahertz heterodyne receiver based on a quantum cascade laser and a superconducting bolometer'. *Applied Physics Letters* **86**(24):244104.

[36] P. Goldsmith (1998). *Quasioptical Systems*. IEEE.

[37] G. Golubiatnikov, et al. (2008). 'Pressure shift and broadening of 110-101 water vapor lines by atmosphere gases'. *Journal of Quantitative Spectroscopy and Radiative Transfer* **109**(10):1828 – 1833.

[38] D. Goorvitch & C. Chackerian, Jr. (1994). 'Rovibrational intensities of the minor isotopes of the CO X $^1\Sigma^+$ state for v less than or equal to 20 and J less than or equal to 150'. *ApJS* **92**:311–321.

[39] W. Gordy & R. Cook (1984). *Microwave Molecular Spectra*. Wiley-Interscience.

[40] Y. P. Gousev, et al. (1994). 'Broadband ultrafast superconducting NbN detector for electromagnetic radiation'. *Journal of Applied Physics* **75**:3695–3697.

[41] M. J. Griffin, et al. (2010). 'The Herschel-SPIRE instrument and its in-flight performance'. *A&A* **518**:L3+.

[42] R. Güsten, et al. (2006). 'The Atacama Pathfinder EXperiment (APEX) - a new submillimeter facility for southern skies -'. *A&A* **454**:L13–L16.

[43] R. Higgins (2009). 'Settling time between Frequency switch changes'. Tech. rep. ICC/2009-NA.

[44] R. D. Higgins & J. W. Kooi (2009). 'Electrical standing waves in the HIFI HEB mixer amplifier chain'. In *Society of Photo-Optical Instrumentation Engineers (SPIE) Conference Series*, vol. 7215 of *Society of Photo-Optical Instrumentation Engineers (SPIE) Conference Series*.

[45] R. D. Higgins, et al. (2010). 'Calibration of the Herschel HIFI Instrument Using Gas Cell Measurements'. In *Twenty-First International Symposium on Space Terahertz Technology*, pp. 390–397.

[46] S. Hiyama (1998). 'Seitenbandkalibration radioastronomischer Linienbeobachtungen'. Master's thesis, Universität zu Köln.

[47] H.-W. Hübers, et al. (2006). 'High-resolution gas phase spectroscopy with a distributed feedback terahertz quantum cascade laser'. *Applied Physics Letters* **89**(6):061115.

[48] N. Ibrahim, et al. (2008). 'Line parameters of H2O around 0.8Âă[mu]m studied by tuneable diode laser spectroscopy'. *Journal of Quantitative Spectroscopy and Radiative Transfer* **109**(15):2523 – 2536.

[49] B. Jackson (2003). 'IF1-Low Design Description'. Tech. rep. SRON-G/FPU/TN/2003.

[50] W. Jellema (2008). 'Diplexer calibration: LO subband dependence and IF passband shape'. Tech. rep. SRON-G/HIFI/TN/2008-24.

[51] A. Jenouvrier, et al. (2007). 'Fourier transform measurements of water vapor line parameters in the 4200-6600cm-1 region'. *Journal of Quantitative Spectroscopy and Radiative Transfer* **105**(2):326 – 355.

[52] JPL (2011). 'CH3OH catalog note @ `http://spec.jpl.nasa.gov/ftp/pub/catalog/doc/d032003.pdf`'.

[53] B. Karasik, et al. (1999). 'Optimal choice of material for HEB superconducting mixers'. *Applied Superconductivity, IEEE Transactions on* **9**(2):4213 –4216.

[54] B. S. Karasik, et al. (1996). 'Diffusion cooling mechanism in a hot-electron NbC microbolometer mixer'. *Applied Physics Letters* **68**(16):2285–2287.

[55] C. Karmer (2008). 'Spatial response framework document'. Tech. rep. SRON-G/HIFI/TR/2008-010, Issue 1.9.

[56] A. Karpov, et al. (2007). 'Low Noise 1 THz-1.4 THz Mixers Using Nb/Al-AlN/NbTiN SIS Junctions'. *Applied Superconductivity, IEEE Transactions on* **17**(2):343–346.

[57] J. Kawamura, et al. (2003). '1.8 THz superconductive hot-electron bolometer mixer for Herschel'. vol. 4855, pp. 355–360. SPIE.

[58] R. Kazarinov & R. Suris (1971). 'Possibility of amplification of electromagnetic waves in a semiconductor with a superlattice'. *Sov. Phys. Semicond.* **5**:707–709.

[59] D. J. M. Kester, et al. (2003). 'SWS Fringes and Models'. In L. Metcalfe, A. Salama, S. B. Peschke, & M. F. Kessler (ed.), *The Calibration Legacy of the ISO Mission*, vol. 481 of *ESA Special Publication*, pp. 375–+.

[60] P. Khosropanah, et al. (2009). 'Phase locking of a 2.7 THz quantum cascade laser to a microwave reference'. *Opt. Lett.* **34**(19):2958–2960.

[61] J. Kooi (2007). 'HIFI Instrument Stability as measured during the ILT phase'. Tech. rep. FPSS-01201.

[62] J. Kooi (2008). *Advanced receivers for submillimeter and far infrared astronomy.* Ph.D. thesis, Rijksuniversiteit Groningen.

[63] J. W. Kooi, et al. (2006). 'Stability of heterodyne terahertz receivers'. *Journal of Applied Physics* **100**(6):064904.

[64] J. W. Kooi, et al. (2007). 'IF impedance and mixer gain of NbN hot electron bolometers'. *Journal of Applied Physics* **101**(4):044511.

[65] J. W. Kooi, et al. (2008). 'HIFI Stability as Measured During ILT Phase'. In W. Wild (ed.), *Ninteenth International Symposium on Space Terahertz Technology*, pp. 111–+.

[66] M. Koshelev, et al. (2007). 'Broadening and shifting of the 321-, 325- and 380-GHz lines of water vapor by pressure of atmospheric gases'. *Journal of Molecular Spectroscopy* **241**(1):101 – 108.

[67] M. A. Koshelev & M. Y. Tretyakov (2009). 'Collisional broadening and shifting of OCS rotational spectrum lines'. *Journal of Quantitative Spectroscopy and Radiative Transfer* **110**(1-2):118 – 128.

[68] M. L. Kutner & B. L. Ulich (1981). 'Recommendations for calibration of millimeter-wavelength spectral line data'. *ApJ* **250**:341–348.

[69] W. Langer, et al. (2010). 'GOT C+: A Herschel Space Observatory Key Program to Study the Diffuse ISM'. In *American Astronomical Society Meeting Abstracts #215*, vol. 42 of *Bulletin of the American Astronomical Society*, p. 440.

[70] B. Larsson & D. Teyssier (2008). 'HIFI FM Radiometry measurements'. Tech. rep. SRON-G/HIFI/TR/2008-001.

[71] E. Lellouch (2010). 'Mars brightness model'. http://www.lesia.obspm.fr/perso/emmanuel-lellouch/mars/.

[72] D. Lisak, et al. (2004). 'An accurate comparison of lineshape models on H2O lines in the spectral region around 3Âă[mu]m'. *Journal of Molecular Spectroscopy* **227**(2):162 – 171.

[73] Y. Liu, et al. (2001). 'Simple empirical analytical approximation to the Voigt profile'. *Journal of the Optical Society of America B Optical Physics* **18**:666–672.

[74] I. Lopez-Fernandez, et al. (2003). 'Wideband ultra-low noise cryogenic InP IF amplifiers for the Herschel mission radiometers'. vol. 4855, pp. 489–500. SPIE.

[75] A. Maestrini, et al. (2004). 'A 1.7-1.9 THz local oscillator source'. *Microwave and Wireless Components Letters, IEEE* **14**(6):253 – 255.

[76] A. Maestrini, et al. (2005). 'Local oscillator chain for 1.55 to 1.75THz with 100- mu;W peak power'. *Microwave and Wireless Components Letters, IEEE* **15**(12):871 – 873.

[77] J. Mangum (1993). 'Main-beam efficiency measurements of the Caltech Submillimeter Observatory'. *PASP* **105**:117–122.

[78] A. Marston (2011). 'HIFI observers manual'. Tech. rep., ESA.

[79] J. D. Mill, et al. (1994). 'Midcourse space experiment: Introduction to the spacecraft, instruments, and scientific objectives'. *Journal of Spacecraft and Rockets* **31**:900–907.

[80] R. Morena (2009). 'COP Beam efficiency test report'. Tech. rep. SRON-G/HIFI/TR/2009-xxx.

[81] P. Morris (2010). 'HIFI Observers' Manual'. Tech. rep. HERSCHEL-HSC-DOC-0784.

[82] P. Morris & C. Borys (2009). 'HIFI AOT Configurations in GTKPs'. Tech. rep. ICC/2007-nnn.

[83] R. S. Nebosis, et al. (1996). 'Rigorous Analysis of a Superconducting Hot-Electron Bolometer Mixer: Theory and Comparison with Experiment'. In *Seventh International Symposium on Space Terahertz Technology*, pp. 601–+.

[84] O. Okunev, et al. (1994). 'NbN Hot Electron Waveguide Mixer for 100 GHz Operation'. In *Fifth International Symposium on Space Terahertz Technology*, pp. 214–+.

[85] J. Olivero & R. Longbothum (1977). 'Empirical fits to the Voigt line width: A brief review'. *Journal of Quantitative Spectroscopy and Radiative Transfer* **17**(2):233 – 236.

[86] V. Ossenkopf (2003). 'The Intensity Calibration Framework for HIFI'. *ALMA Memo 442* .

[87] V. Ossenkopf (2008). 'The stability of spectroscopic instruments: a unified Allan variance computation scheme'. *A&A* **479**:915–926.

[88] P. T. Peacocke (2006). 'Herschel Telescope Beam Patterns'. Tech. rep. NUIM-HIFI-TEL-001.

[89] P. T. Peacocke (2007). 'Optical Analysis of the Heterodyne Instrument for the Far Infrared: Methods and Results'. Master's thesis, NUI Maynooth.

[90] J. Pearson (2008). 'Detection strategy for spurious response from the house keeping data'. Tech. rep. JPL/HIFI/TN/2008-006.

[91] J. C. Pearson, et al. (2000). 'Local oscillator system for the heterodyne instrument for FIRST (HIFI)'. In J. B. Breckinridge & P. Jakobsen (ed.), *Society of Photo-Optical Instrumentation Engineers (SPIE) Conference Series*, vol. 4013 of *Presented at the Society of Photo-Optical Instrumentation Engineers (SPIE) Conference*, pp. 264–274.

[92] Perrin, N. & Vanneste, C. (1987). 'Dynamic behaviour of a superconductor under time-dependent external excitation'. *J. Phys. France* **48**(8):1311–1316.

[93] T. G. Phillips & K. B. Jefferts (1973). 'A Low Temperature Bolometer Heterodyne Receiver for Millimeter Wave Astronomy'. *Review of Scientific Instruments* **44**(8):1009–1014.

[94] H. Pickett, et al. (1998). 'Submillimeter, millimeter, and microwave spectral line catalog'. *Journal of Quantitative Spectroscopy and Radiative Transfer* **60**(5):883–890. cited By (since 1996) 343.

[95] H. M. Pickett, et al. (2003). 'Submillimeter, Millimeter, and Microwave Spectral Line Catalog'. Tech. rep., JPL.

[96] H. M. Pickett, et al. (2005). 'Use of Euler series to fit spectra with application to water'. *Journal of Molecular Spectroscopy* **233**:174–179.

[97] D. Pierot (2002). 'Herschel telescope optical design justification'. Tech. rep. HER.NT.0183.T.ASTR.

[98] G. L. Pilbratt, et al. (2010). 'Herschel Space Observatory. An ESA facility for far-infrared and submillimetre astronomy'. *A&A* **518**:L1+.

[99] J. Pineda (2011). private communication.

[100] A. Poglitsch, et al. (2010). 'The Photodetector Array Camera and Spectrometer (PACS) on the Herschel Space Observatory'. *A&A* **518**:L2+.

[101] D. E. Prober (1993). 'Superconducting terahertz mixer using a transition-edge microbolometer'. *Applied Physics Letters* **62**:2119–2121.

[102] G. Rebeiz (1992). 'Millimeter-wave and terahertz integrated circuit antennas'. *Proceedings of the IEEE* **80**(11):1748 –1770.

[103] J. Reinartz & A. Dymanus (1974). 'Molecular constants of OCS isotopes in the (0110) vibrational state measured by molecular-beam electric-resonance spectroscopy'. *Chemical Physics Letters* **24**(3):346 – 351.

[104] Y. Ren, et al. (2010a). 'Terahertz heterodyne spectrometer using a quantum cascade laser'. *Applied Physics Letters* **97**(16):161105.

[105] Y. Ren, et al. (2010b). 'Tunable terahertz quantum cascade laser for high resolution heterodyne spectroscopy'. *Applied Physics Letters* in press.

[106] L. S. Rothman, et al. (2009). 'The HITRAN 2008 molecular spectroscopic database'. *Journal of Quantitative Spectroscopy and Radiative Transfer* **110**:533–572.

[107] R. Schieder (1993). 'The usefulness of a gas cell for performance testing'. Tech. Rep. SWAS/TM-4027.

[108] R. Schieder & C. Kramer (2001). 'Optimization of heterodyne observations using Allan variance measurements'. *A&A* **373**:746–756.

[109] R. T. Schieder, et al. (2003). 'Toward very large bandwidth with acousto-optical spectrometers'. vol. 4855, pp. 290–300. SPIE.

[110] A. D. Semenov, et al. (1995). 'Analysis of the nonequilibrium photoresponse of superconducting films to pulsed radiation by use of a two-temperature model'. *Phys. Rev. B* **52**(1):581–590.

[111] I. Siddiqi & D. E. Prober (2004). 'Nb–Au bilayer hot-electron bolometers for low-noise THz heterodyne detection'. *Applied Physics Letters* **84**(8):1404–1406.

[112] I. Siddiqi, et al. (2002). 'Heterodyne mixing in diffusion-cooled superconducting aluminum hot-electron bolometers'. *Journal of Applied Physics* **91**(7):4646–4654.

[113] O. Siebertz, et al. (2007). 'The Impact of Standing Waves in the LO path of a Heterodyne Receiver'. In *18th International Symposium of Space Terahertz Technology, California Institute of Technology, Pasadena, California*, pp. 117–122.

[114] M. F. Skrutskie, et al. (2006). 'The Two Micron All Sky Survey (2MASS)'. *AJ* **131**:1163–1183.

[115] K. Tchernyshyov (2010). private communication.

[116] R. Teipen, et al. (2005). 'Results and Analysis of HIFI Band 2 Flight Mixer Performance'. In *Sixteenth International Symposium on Space Terahertz Technology*, pp. 199–204.

[117] D. Teyssier, et al. (2004). 'A Multi-path Far-Infrared and Sub-millimetre Gas Cell for Spectral Tests of Herschel-HIFI'. In *15th International Symposium of Space Terahertz Technology, Northampton, Massachusetts*, pp. 306–312.

[118] V. Tolls, et al. (2004). 'Submillimeter Wave Astronomy Satellite Performance on the ground and in orbit'. *ApJS* **152**:137–162.

[119] R. A. Toth (2005). 'Measurements and analysis (using empirical functions for widths) of air- and self-broadening parameters of H2O'. *Journal of Quantitative Spectroscopy and Radiative Transfer* **94**(1):1 – 50.

[120] N. Trappe, et al. (2007). 'Analysis of standing waves in submillimeter-wave optics'. vol. 6472, p. 64720B. SPIE.

[121] N. Trappe, et al. (2003). 'Quasi-optical analysis of the HIFI instrument for the Herschel Space Observatory'. vol. 4876, pp. 1091–1099. SPIE.

[122] C. Vastel (2010). *Formalism for the CASSIS software*. CESR, Toulouse.

[123] J. Ward, et al. (2005). 'Local Oscillators from 1.4 to 1.9 THz'. In *Sixteenth International Symposium on Space Terahertz Technology*, pp. 374–377.

[124] N. Whyborn (2002). 'Band 6 IF change impact assessment'. Tech. rep., SRON-Groningen. SRON-U/HIFI/RP/2002-005.

[125] Wikipedia (2011). 'Acousto Optical Spectrometer @ `http://en.wikipedia.org/wiki/Acousto_Optical_Spectrometer`'.

[126] B. S. Williams (2007). 'Terahertz quantum-cascade lasers'. *Nature Photonics* **1**:517–525.

[127] G. Winnewisser, et al. (1997). 'Sub-Doppler Measurements on the Rotational Transitions of Carbon Monoxide'. *Journal of Molecular Spectroscopy* **184**:468–472.

[128] L. Xu, et al. (2008). 'Torsion rotation global analysis of the first three torsional states (ν_t = 0, 1, 2) and terahertz database for methanol'. *Journal of Molecular Spectroscopy* **251**:305–313.

[129] P. Yagoubov, et al. (1996). 'The Bandwidth of HEB Mixers Employing Ultrathin NbN Films on Sapphire Substrate'. In *Seventh International Symposium on Space Terahertz Technology*, pp. 290–+.

[130] P. Yagoubov, et al. (2006). '550-650 GHz spectrometer development for TELIS'. In A. Hedden, M. Reese, D. Santavicca, L. Frunzio, D. Prober, P. Piitz, C. Groppi, & C. Walker (ed.), *Seventeenth International Symposium on Space Terahertz Technology*, pp. 338–341.

[131] W. Zhang, et al. (2010). 'Quantum noise in a terahertz hot electron bolometer mixer'. *Applied Physics Letters* **96**(11):111113.

[132] J. Zmuidzinas & P. Richards (2004). 'Superconducting detectors and mixers for millimeter and submillimeter astrophysics'. *Proceedings of the IEEE* **92**(10):1597–1616.

Appendix A

Gas cell model code

```
class GascellLineFitter(NonLinearPyModel):

        # pressure, SBR   #
    def __init__(self, npar = 1):
        # Constructor
        self.npar = npar
        NonLinearPyModel.__init__( self, self.npar )

    # define data to be fitted
    def setDataset(self, value, model = 'pressure_sbr'):
        self.dataset       = value
        self.lo_freq       = self.dataset['LoFrequency'].data[0]*1E3
        if self.dataset.hasName('frequency_1'):
            self.if_freq       = self.dataset.getWave(1).get(0)
            self.flux          = self.dataset.getFlux(1).get(0)
        else:
            self.if_freq       = self.dataset.getWave().get(0)
            self.flux          = self.dataset.getFlux().get(0)
        self.obsid         = self.dataset['obsid'].data[0]
        self.backend       = self.dataset.getMeta()['backend'].value
        self.band          = self.dataset.getMeta()['Band'].value
        self.gas, self.p_measure = getGasType(self.obsid)
        self.line_table    = getLinesFromCatalogWithIFFreqeuncy(ds = self.
            dataset, gas = self.gas)
        self.line_model    = 'voigt' # lorentz
        self.line_freq     = 0.0
        self.line_int      = 0.0

    def Plotdata(self):
```

```
        PlotXY(self.if_freq, self.flux)

#   def SetLineProperties(self, line_freq, line_int):
#       model.line_freq = line_freq
#       model.line_int = line_int

    def generateLineModelPSelf(self,x,p):
        # check if_freq state
        if str(x.__class__) == 'org.python.core.PyFloat':
            freq       = Double1d([x])
            nb         = 1
        else:
            freq       = x
            nb         = len(freq)
        # constants
        c = 29979245800.0       # cm/s
        #
        k = 1.38E-16
        T = 300
        L = 102.54
        pi = Math.PI
        #
        #model.line_freq  = ABS(self.line_table['if_freq'].data[0])
        #model.line_int   = self.line_table['LGINT'].data[0]
        pressure    = self.p_measure*1e-3
        p_atm       = pressure / 1.01325
        #
        w_l         = p[0]  * p_atm * c / 1E6
        # calculate doppler broadening
        line_freq_ssb = model.line_table['line_freq'].data[0]
        m           = getMolecularWeight(self.gas)
        avagado     = 6.02214179E23      # 1/mol
        m_g         = m / avagado          # grammes
        k           = 1.38E-16           # ergâĂĽKâĹŠ1
        w_d         = (line_freq_ssb / c) * SQRT(2 * LOG(2) * k * T / m_g)  #
            MHz, HWHM due to doppler broadening
        # generate voigt profile from nuerical approximation, from olivero
           & longbothom (1977)
        d       = (w_l - w_d)/(w_l + w_d)                                   #
            ratio of pressure and doppler broadening
        #
```

```
        c_l     = 0.68188 + 0.61293*d - 0.18382*d**2 - 0.11568*d**3     #
            weighting constants
        c_d     = 0.32460 - 0.61825*d + 0.17681*d**2 + 0.12109*d**3
        w_v     = 0.53456*w_l + SQRT(0.2166*w_l**2 + w_d**2)            #
            voigt width
        # voigt profile,liu et al (2001)
        peak_v = c_l*1.0/(pi*w_v) + c_d*SQRT(LOG(2)/pi)/(w_v)           #
            voigt peak
        f_p    = c_l*(1/pi)*w_v/((freq - model.line_freq)**2 + w_v**2) + c_d
            *((SQRT(LOG(2)))/(SQRT(pi)*w_v))*EXP((-LOG(2)*(freq - model.
            line_freq)**2)/(w_v**2))
        v_p    = f_p/peak_v
        # line model, lorentz simplification
        if self.line_model == 'lorentz':
            self.model      = EXP(-10**model.line_int*10**-14.0*((pressure
                *10**6)/(k*T*pi))*L*(w_l/((freq-model.line_freq)**2+w_l**2))
                )
        # line model, full vogit
        elif self.line_model == 'voigt':
            self.model      = EXP(-10**model.line_int*10**-14.0*((pressure
                *10**6)/(k*T))*L* v_p /(pi*w_l + SQRT(pi/LOG(2))*w_d))
#        print self.model
        if str(x.__class__) == 'org.python.core.PyFloat':
            return (1.0-self.model[0])*-0.5+1.0
        else:
            return (1.0-self.model)*-0.5+1.0


    def generateLineModelPSelfSBR(self,x,p):
        # check if_freq state
        if str(x.__class__) == 'org.python.core.PyFloat':
            freq        = Double1d([x])
            nb          = 1
        else:
            freq        = x
            nb          = len(freq)
        # constants
        c = 29979245800.0       # cm/s
        #
        k = 1.38E-16
        T = 300
```

```
L = 102.54
pi = Math.PI
#
#model.line_freq  = ABS(self.line_table['if_freq'].data[0])
#model.line_int   = self.line_table['LGINT'].data[0]
pressure   = self.p_measure*1e-3
p_atm      = pressure / 1.01325
#
w_l        = p[0]  * p_atm * c / 1E6
# calculate doppler broadening
line_freq_ssb = model.line_table['line_freq'].data[0]
m          = getMolecularWeight(self.gas)
avagado    = 6.02214179E23      # 1/mol
m_g        = m / avagado          # grammes
k          = 1.38E-16           # ergâĂĽKâĹŠ1
w_d        = (line_freq_ssb / c) * SQRT(2 * LOG(2) * k * T / m_g)  #
    MHz, HWHM due to doppler broadening
# generate voigt profile from nuerical approximation, from olivero
   & longbothom (1977)
d      = (w_l - w_d)/(w_l + w_d)                                    #
    ratio of pressure and doppler broadening
#
c_l    = 0.68188 + 0.61293*d - 0.18382*d**2 - 0.11568*d**3    #
    weighting constants
c_d    = 0.32460 - 0.61825*d + 0.17681*d**2 + 0.12109*d**3
w_v    = 0.53456*w_l + SQRT(0.2166*w_l**2 + w_d**2)           #
    voigt width
# voigt profile,liu et al (2001)
peak_v = c_l*1.0/(pi*w_v) + c_d*SQRT(LOG(2)/pi)/(w_v)         #
    voigt peak
f_p    = c_l*(1/pi)*w_v/((freq - model.line_freq)**2 + w_v**2) + c_d
    *((SQRT(LOG(2)))/(SQRT(pi)*w_v))*EXP((-LOG(2)*(freq - model.
    line_freq)**2)/(w_v**2))
v_p    = f_p/peak_v
# line model, lorentz simplification
if self.line_model == 'lorentz':
    self.model      = EXP(-10**model.line_int*10**-14.0*((pressure
        *10**6)/(k*T*pi))*L*(w_l/((freq-model.line_freq)**2+w_l**2))
        )
# line model, full vogit
elif self.line_model == 'voigt':
```

```
            self.model      = EXP(-10**model.line_int*10**-14.0*((pressure
                *10**6)/(k*T))*L* v_p /(pi*w_l + SQRT(pi/LOG(2))*w_d))
#         print self.model
        if str(x.__class__) == 'org.python.core.PyFloat':
            return (1.0-self.model[0])*-p[1]+1.0
        else:
            return (1.0-self.model)*-p[1]+1.0

    def generateLineModelSBR(self,x,p):
        # check if_freq state
        if str(x.__class__) == 'org.python.core.PyFloat':
            freq       = Double1d([x])
            nb         = 1
        else:
            freq       = x
            nb         = len(freq)
        # constants
        c = 29979245800.0       # cm/s
        #
        k = 1.38E-16
        T = 300
        L = 102.54
        pi = Math.PI
        #
        #model.line_freq  = ABS(self.line_table['if_freq'].data[0])
        #model.line_int   = self.line_table['LGINT'].data[0]
        pressure    = self.p_measure*1e-3
        p_atm       = pressure / 1.01325
        #
        p_self     = model.line_table['p_self'].data[0]
        if IS_FINITE(p_self):
            w_l        = p_self  * p_atm * c / 1E6
        else:
            print 'no pself data found for %s' % (model.gas)
            print shit
        # calculate doppler broadening
        line_freq_ssb = model.line_table['line_freq'].data[0]
        m          = getMolecularWeight(self.gas)
        avagado    = 6.02214179E23      # 1/mol
        m_g        = m / avagado          # grammes
        k          = 1.38E-16           # ergâĂĽKâĹŠ1
```

```
        w_d       = (line_freq_ssb / c) * SQRT(2 * LOG(2) * k * T / m_g)  #
            MHz, HWHM due to doppler broadening
        # generate voigt profile from nuerical approximation, from olivero
           & longbothom (1977)
        d       = (w_l - w_d)/(w_l + w_d)                                  #
            ratio of pressure and doppler broadening
        #
        c_l     = 0.68188 + 0.61293*d - 0.18382*d**2 - 0.11568*d**3        #
            weighting constants
        c_d     = 0.32460 - 0.61825*d + 0.17681*d**2 + 0.12109*d**3
        w_v     = 0.53456*w_l + SQRT(0.2166*w_l**2 + w_d**2)               #
            voigt width
        # voigt profile,liu et al (2001)
        peak_v = c_l*1.0/(pi*w_v) + c_d*SQRT(LOG(2)/pi)/(w_v)              #
            voigt peak
        f_p    = c_l*(1/pi)*w_v/((freq - model.line_freq)**2 + w_v**2) + c_d
            *((SQRT(LOG(2)))/(SQRT(pi)*w_v))*EXP((-LOG(2)*(freq - model.
            line_freq)**2)/(w_v**2))
        v_p    = f_p/peak_v
        # line model, lorentz simplification
        if self.line_model == 'lorentz':
            self.model      = EXP(-10**model.line_int*10**-14.0*((pressure
                *10**6)/(k*T*pi))*L*(w_l/((freq-model.line_freq)**2+w_l**2))
                )
        # line model, full vogit
        elif self.line_model == 'voigt':
            self.model      = EXP(-10**model.line_int*10**-14.0*((pressure
                *10**6)/(k*T))*L* v_p /(pi*w_l + SQRT(pi/LOG(2))*w_d))
#        print self.model
        if str(x.__class__) == 'org.python.core.PyFloat':
            return (1.0-self.model[0])*-p[0]+1.0
        else:
            return (1.0-self.model)*-p[0]+1.0


    def generateLineModelSBRPressure(self,x,p):
        # check if_freq state
        if str(x.__class__) == 'org.python.core.PyFloat':
            freq       = Double1d([x])
            nb         = 1
        else:
```

```
        freq       = x
        nb         = len(freq)
    # constants
    c = 29979245800.0       # cm/s
    #
    k = 1.38E-16
    T = 300
    L = 102.54
    pi = Math.PI
    #
    #model.line_freq  = ABS(self.line_table['if_freq'].data[0])
    #model.line_int   = self.line_table['LGINT'].data[0]
#     pressure    = self.p_measure*1e-3
    pressure    = p[1]
    p_atm       = p[1] / 1.01325
    #
    p_self    = model.line_table['p_self'].data[0]
    if IS_FINITE(p_self):
        w_l       = p_self  * p_atm * c / 1E9
    else:
        print 'no pself data found for %s' % (model.gas)
        print shit
    # calculate doppler broadening
    line_freq_ssb = model.line_table['line_freq'].data[0]
    m         = getMolecularWeight(self.gas)
    avagado   = 6.02214179E23      # 1/mol
    m_g       = m / avagado          # grammes
    k         = 1.38E-16           # ergâĂĽKâĹŠ1
    w_d       = (line_freq_ssb / c) * SQRT(2 * LOG(2) * k * T / m_g)  #
        MHz, HWHM due to doppler broadening
    # generate voigt profile from nuerical approximation, from olivero
       & longbothom (1977)
    d       = (w_l - w_d)/(w_l + w_d)                                  #
        ratio of pressure and doppler broadening
    #
    c_l     = 0.68188 + 0.61293*d - 0.18382*d**2 - 0.11568*d**3     #
        weighting constants
    c_d     = 0.32460 - 0.61825*d + 0.17681*d**2 + 0.12109*d**3
    w_v     = 0.53456*w_l + SQRT(0.2166*w_l**2 + w_d**2)             #
        voigt width
    # voigt profile,liu et al (2001)
```

```
        peak_v = c_l*1.0/(pi*w_v) + c_d*SQRT(LOG(2)/pi)/(w_v)          #
            voigt peak
        f_p    = c_l*(1/pi)*w_v/((freq - model.line_freq)**2 + w_v**2) + c_d
            *((SQRT(LOG(2)))/(SQRT(pi)*w_v))*EXP((-LOG(2)*(freq - model.
            line_freq)**2)/(w_v**2))
        v_p    = f_p/peak_v
        # line model, lorentz simplification
        if self.line_model == 'lorentz':
            self.model      = EXP(-10**model.line_int*10**-14.0*((pressure
                *10**3)/(k*T*pi))*L*(w_l/((freq-model.line_freq)**2+w_l**2))
                )
        # line model, full vogit
        elif self.line_model == 'voigt':
            self.model      = EXP(-10**model.line_int*10**-14.0*((pressure
                *10**3)/(k*T))*L* v_p /(pi*w_l + SQRT(pi/LOG(2))*w_d))
#        print self.model
        if str(x.__class__) == 'org.python.core.PyFloat':
            return (1.0-self.model[0])*-p[0]+1.0
        else:
            return (1.0-self.model)*-p[0]+1.0


    def pyResult(self, x, p): # the function value
        #
        if self.fittype == 'PSelfSBR':
            return self.generateLineModelPSelfSBR(x,p)
        elif self.fittype == 'PSelf':
            return self.generateLineModelPSelf(x,p)
        elif self.fittype == 'SBR':
            return self.generateLineModelSBR(x,p)
        elif self.fittype == 'SBRPressure':
            return self.generateLineModelSBRPressure(x,p)


    #
    def myName( self ): # Explicatory string
        # Return an explicatory name (String). Optional.
        return "fitting P_self"
```

Appendix B

Paper 1: Electrical standing waves in the HIFI HEB mixer amplifier chain

Conference proceedings of SPIE Photonics west conference, San Jose, CA., February 10th 2009[44].

Electrical standing waves in the HIFI HEB mixer amplifier chain

Ronan D. Higgins[a,b] and Jacob W. Kooi[c]

[a]National University of Ireland, Maynooth, Co. Kildare, Ireland
[b]SRON Netherlands Institute for Space Research, PO Box 800, Groningen, the Netherlands
[c]California Institute of Technology, MS 320-47, Pasadena, California 91125, U.S.A.

1. ABSTRACT

The Heterodyne Instrument for the Far-Infrared (HIFI) is one of three instruments to be launched aboard the Herschel Space Observatory (HSO) in 2009. HIFI will provide unprecedented spectral sensitivity and resolution between 490–1250 GHz and 1410–1910 GHz. In this paper, we report on the analysis of electrical standing waves that are present between the hot electron bolometer (HEB) heterodyne mixing element and the first low noise amplifier in the HIFI instrument. We show that the standing wave shape is not a standard sinusoid and difficult to remove from the resulting spectrum using standard fitting methods. We present a method to remove the standing waves based on data taken during the HIFI instrument level test, and anticipate the use of a similar calibration procedure in actual flight. Using the standing wave profile we obtain direct evidence of the complex IF output impedance of the HEB mixer.

Keywords: HIFI, Herschel, HEB mixer, standing wave, impedance

2. INTRODUCTION

The Heterodyne Instrument for the Far-Infrared (HIFI) is one of three instruments to be flown on the Herschel Space Observatory.[1] HIFI will observe at high spectral resolution the complete range of frequencies from 480–1250 GHz and 1410–1910 GHz for two polarizations, divided over seven bands. This range of the electromagnetic spectrum is unique as it has never been comprehensively observed before. Observation at these wavelengths will answer numerous questions in the area of galaxy evolution and star and planet formation.

This range of the electromagnetic spectrum is also unique from an instrumentation point of view in that it falls between conventional operating limits of electronic and photonic devices. At millimeter and longer wavelengths low noise high electron mobility transistors are the back bone of radio astronomy. However, due to the finite electron mobility of $III-V$ materials, their performance degrades rapidly as the wavelengths get shorter. At optical wavelengths down through to the mid-infrared, observations using quantum electronics are ideal as the higher photon energy allows efficient detection. At far infrared wavelengths the performance of quantum devices becomes problematic however due to the low photon energy. For this reason low energy gap superconducting materials are used for high sensitivity applications. In the case of low spectral resolution observations superconducting transition-edge bolometers (TES) have achieved very high sensitivity. To achieve near quantum limited high spectral resolution observations, heterodyne techniques based on superconducting-insulator-superconducting (SIS) tunnel junctions and hot electron bolometers (HEBs) need to be employed.

The heterodyne technique works by multiplying (mixing) of the incoming sky signal with a monochromatic local signal (the Local Oscillator, LO) by means of a highly non-linear mixing element sensitive to the beat term between the two signals. The HIFI instrument uses this technique to down-convert terahertz radiation to the microwave frequency domain where it can be sampled and recorded using conventional electronics. At the output of the mixer

Further author information: (Send correspondence to R.D.H)
R.D.H.: E-mail: daniel.r.higgins@nuim.ie, Telephone: +353-1-708-3641
J.W.K.: E-mail: kooi@submm.caltech.edu, Telephone: +1-626-395-4286

the beat term between the LO frequency and the signal frequency (also known as the intermediate frequency or IF) is then typically fed to a spectrometer where the spectral information is analyzed. In this way very high resolution observations (defined as $R = \nu/\Delta\nu \geq 10^6$–$10^7$) may be obtained. The mixer has a IF bandwidth determined by the geometry and superconducting material used. In the case of HIFI an upper and lower sideband at the LO frequency is down converted and fed to the backends. No sideband separation is present in HIFI and hence the output spectra contains both the upper and lower sidebands. The double side band spectra are separated in the instrument pipeline using a deconvolution algorithm.[2]

HIFI uses two types of mixing elements. Superconductor-Insulator-Superconductor (SIS) mixers are used from 480–1250 GHz (bands 1–5) and Hot Election Bolometer (HEB) mixers from 1410–1910 GHz (bands 6–7). Both mixers use superconducting principles to mix the incoming terahertz sky signal with the LO signal, albeit with completely different mechanisms.

The HEB mixer technology used in mixer bands 6–7 was first proposed in the early 1970's[3] but then superseded by SIS mixer technology in the 1980's. The range of frequencies of SIS mixers are however limited by the energy gap of the superconducting material (above this frequency absorption loss in the superconducting film, due to the breaking of Cooper pairs, increases dramatically). SIS mixer techniques are a key technology of submillimeter spectroscopy and have being used extensively in ground based telescopes for the last twenty years.[4,5] At the time of HIFI development HEB mixers were seen as the only option for mixing above 1.25 THz. The two mixer types were envisaged to produce a common 4–8 GHz bandwidth and hence used an identical IF chain and output to the same backend spectrometers*. Due to development issues with the HEB mixers, the original 4–8 GHz IF bandwidth had to be reduced to 2.4–4.8 GHz. The IF chain configuration was subsequently changed to match the new mixer bandwidth however without the use of an isolator between the mixer and first Low Noise Amplifier (LNA), as shown in Fig. 1. This was due to the lack of availability of an appropriate (space qualified) isolator for the new bandwidth. As a result of this configuration change the impedance mismatch between the HEB mixer and the first cryogenically cooled LNA becomes very important.

This paper will discuss the resulting power reflection (standing waves) between the HEB mixer and the first LNA. Section 3 describes the problem of HEB bandwidth and the missing isolators in the IF chain. Section 4 details how the standing wave affects in-flight observations and how a standard fitting approach fails to remove, to a satisfactory level, the effect. Section 5 describes the current HEB impedance mixer theory and how, using this theory, a fit to the IF standing wave is possible. This approach facilitates baseline correction but also allows the extraction of physically relevant device parameters, such as the electron temperature in the hot electron bolometer bridge. Finally, section 6 presents the proposed solution of using the calibration data taken during the HIFI instrument level tests of 2007 to remove the IF standing wave.

3. HEB IF CHAIN

The IF chain is used to amplify the mixer output signal with as little added noise as possible, and provide a link to the back-end spectrometers. The IF chain passband is designed to transmit the signal equally over the entire IF bandwidth and to minimize reflection loss between the individual components. The latter is typically accomplished by careful matching of the impedance between components. To further reduce reflections between the IF components fixed 3 dB attenuators have been added at certain crucial locations, as indicated in Fig. 1

When HIFI was originally proposed in 1998 it was envisaged that the two bands above 1250 GHz would use HEB mixer technology. At the time two mixer technologies were proposed: a baseline goal of diffusion-cooled Nb HEBs and a goal of diffusion-cooled Al HEBs. Diffusion cooled HEBs were chosen over phonon cooled NbN HEBs on the basis of potentially superior sensitivity and higher IF bandwidth. It was argued that the diffusion-cooled technology could reach the higher IF bandwidth simply by reducing the length of the superconducting bolometer element whereas the phonon-cooled technology's maximum IF bandwidth is more dependent on intrinsic material properties, and thus not easily extendable. Initial results proved promising[6] but the diffusion cooled HEB didn't produce repeatable results for subsequent mixer batches. In 2002 the decision was made to switch from the use of

*HIFI has two backend spectrometers, the Wide Band Spectrometer (WBS) and the High Resolution Spectrometer (HRS)

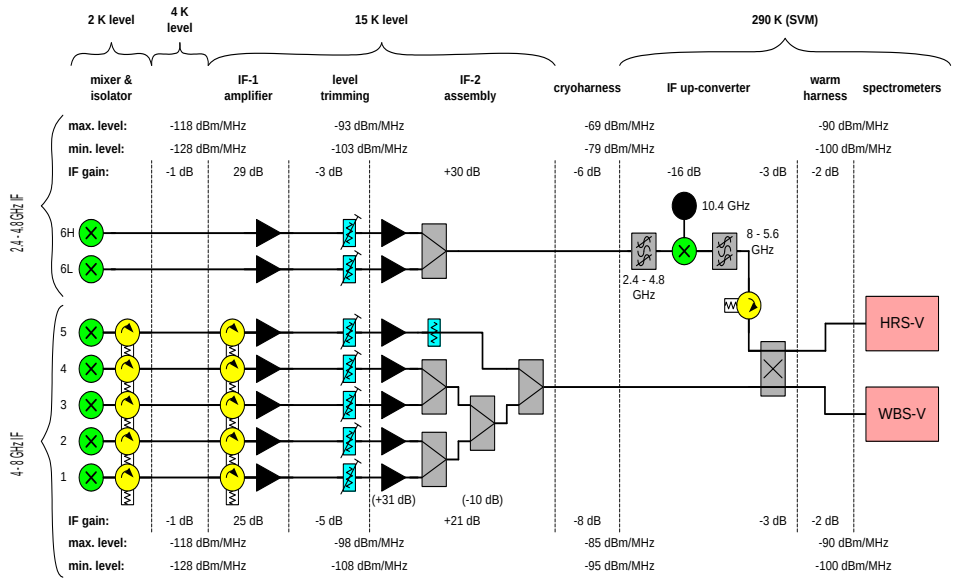

Figure 1. Block diagram of the HIFI signal chain showing all components for one polarization[1]

diffusion cooled HEBs to the (by then) proven phonon cooled HEB mixer technology.[7] This required a redesign of the IF chain to match the reduced bandwidth.[8]

As we have stated, in the original IF chain design it was envisaged that the seven HIFI bands would have the same IF bandwidth (4–8 GHz) and therefore have a common IF chain design. However due to the change in HEB bandwidth a new IF chain design was necessary for bands 6 & 7. The first and second amplifiers were redesigned to accommodate the new bandwidth and a 10.4 GHz oscillator was added after the second amplifier to up-convert the 2.4–4.8 GHz bandwidth to a spectrometer compatible bandwidth of 8–5.6 GHz. Due to time and mass/volume constraints it was not possible to develop and procure a new cryogenic isolator, and it was decided to remove the isolators from the HEB IF chain. Initially it was believed that the IF chain could be designed to work without isolators due to the supposed benign (50 Ω) output impedance of the HEB mixer, but this proved to be false. The first IF design had noise temperatures in excess of 10,000 K and a large 300 MHz ripple due to power reflections between the mixer and first LNA. After a careful analyzes of the actual HEB mixer IF output impedance[9] a redesign of the HEB mixer unit IF board and matching circuit was judged needed. Subsequent measurements showed that the large excess noise was eliminated, however there remained (not unexpected) a significant IF standing wave. The final IF chain design is shown in Fig. 1.

4. STANDING WAVE PROFILE

Optical standing waves are a common feature in submm instruments. They occur when the signal wavelength is comparable with the instrument dimensions. Standing waves occur between two surfaces when a fraction of the incoming radiation is reflected back along the path of the incoming radiation, and the reflected electromagnetic wave interferes with the incoming signal. Depending on the relative phase of the incoming and reflected signal this effect can either add or subtract the total signal detected. This effect produces a sinusoid on the backend spectrometer baseline, the period, P, of this sinusoid a function of the distance, d, between the two reflecting surfaces and the speed of light, c, in the propagation medium, see equation 1. The amplitude is a function of the beam coupling between the two surfaces.[10]

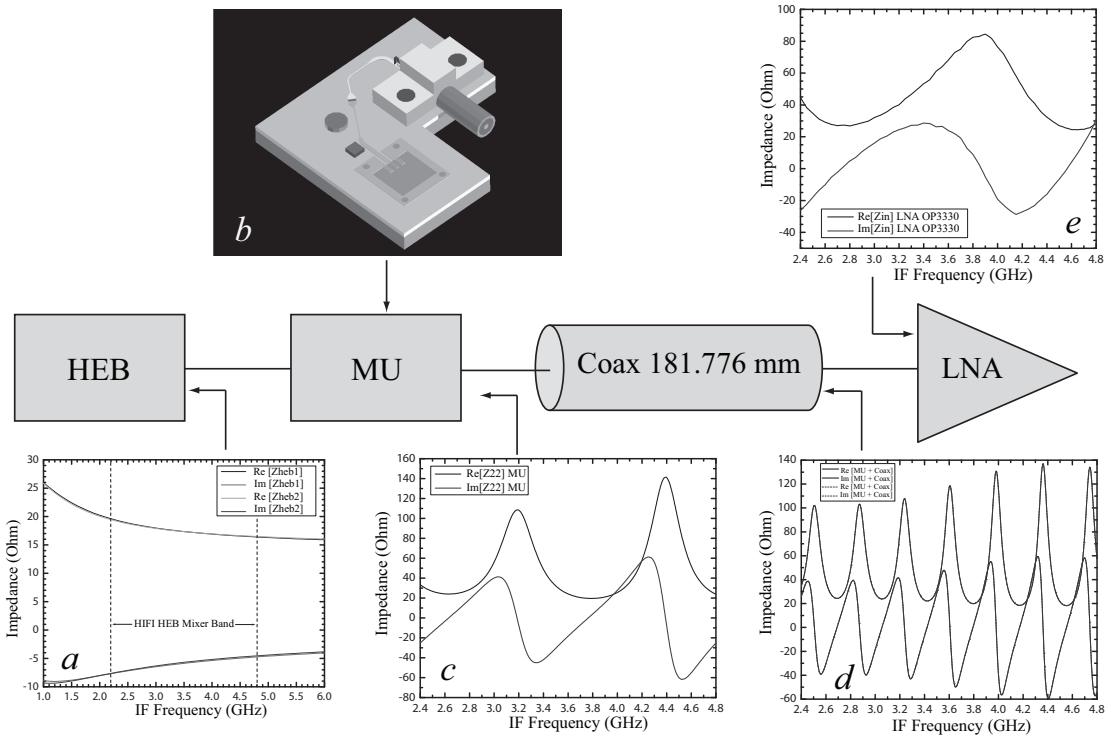

Figure 3. The HIFI instrument band 6 & 7 IF chain. *a*) The modeled real and complex part of the HEB mixer IF output impedance (see text for details). This impedance is then transformed by the 'mixer unit', depicted in *b*, to yield an IF impedance as shown in panel *c*. The complex nature of space qualified hardware made it impossible to alter the mixer unit physical layout, hence the non-ideal impedance (note that the locus is around 50 Ω). After passing through a ∼ 182 mm (effective length obtained from a fit to the data) 50 Ω semi-ridged coax cable the IF impedance is then transformed to that shown in panel *d*. The IF chain having no isolator connects directly to the first LNA, whose measured input impedance is shown in panel *e*. The result is a ∼ 300 MHz standing wave in the IF passband (Fig. 5).

temperature. To make matters worse, changes in voltage reflections at the mixer IF output port cause a small change in the hot electron bolometer distributed temperature profile,[13] thus providing a positive feedback mechanism. This is known as electro-thermal feedback. These small changes in impedance result in a non-perfect cancellation of instrument effects and the observer is left with a distorted baseline. Since the LNA is kept in a fixed state during observations the amplitude of the residual standing wave is a measure of how far the mixer impedance has drifted between two observations.

To understand how the frequency dependent IF output impedance of the HEB mixer modulates the standing wave consider the model of the HIFI IF chain shown in Fig. 3. As stated in section 3, due to the complex nature of space qualified hardware it was not possible to change the layout of the mixer unit, hence the somewhat non-optimal design.

To better comprehend the nature and frequency dependence of the HEB mixer output impedance we follow the analyzes of Nebosis and Kooi *et al.*[9,14] A HEB mixer operates in principle very close to the critical temperature of the superconducting material used. For NbN films this is around 10 K. Both LO power and bias are used to bring the HEB bridge temperature close to the ideal transition, or operating temperature. Since the local oscillator frequency is well above the energy gap of the superconducting film, heating in the film may be considered uniform. To describe the thermal balance in the HEB bridge we have to consider the phonon-electron interaction time (τ_{eph}), the phonon escape time (τ_{esc}) to the lattite (substrate), and the temperature of the quasi-particles (T_e). The electron-electron interaction time is assumed must faster then the above mentioned time constants.

Diffusion loss via the normal conducting (Au) contact pads may be neglected for the predominantly 'phonon' cooled HEB mixer we consider ourselves with.

Using the two temperature electron cooling model with associated heat balance equations of a thin 2D film as described by Perrin-Vanneste (PV),[15] and expanded upon by Nebosis, Semenov, Gousev, and Renk (NSGR),[14] while making the assumption that at IF frequencies the temporal response is predominantly governed by the electron temperature dependent change in resistance ($\partial R/\partial T_e$) we obtain the complex IF impedance

$$Z(\omega) = R_0 \cdot \frac{\Psi(\omega) + C}{\Psi(\omega) - C} \ . \tag{2}$$

In the above equation $\Psi(\omega)$ represents the time dependent modulation of the electron temperature and is defined by three time constants, τ_1, τ_2, τ_3

$$\Psi(\omega) = \frac{(1 + i\omega\tau_1)(1 + i\omega\tau_2)}{(1 + i\omega\tau_3)}. \tag{3}$$

C is the self heating parameter and can be described as

$$C = \frac{I^2}{V}\frac{\partial R}{\partial T_e}\left(\frac{\tau_{eph}}{c_e} + \frac{\tau_{esc}}{c_{ph}}\right) . \tag{4}$$

In the above equations R_0 is the dc resistance at the operating point of the mixer ($\sim 15\ \Omega$). The differential resistance at the operating point, $\partial R/\partial V$, is under normal bias conditions $\sim 60\ \Omega$.[7] c_e and c_{ph} are the respective heat capacities of the electrons and phonons. The time constants τ_1, τ_2, τ_3 depend on τ_{eph}, τ_{esc}, c_e/c_{ph} which are derived from the empirical relationship that for thin NbN films $\langle\tau_{esc}\rangle \sim\ 10.5\ d$ (ps/nm)[16],[17] $\tau_{eph} \approx 500\ T^{-1.6}$ (ps·K)[18] and that $c_e/c_{ph} \approx 18.77\ T^{-2}$.[17] In the previous equation d is the thickness of the (NbN) film in the HEB bridge. In Fig. 4 we show τ_1, τ_2, τ_3 as a function of electron temperature. From a fit of the model against the measurement we obtain an electron temperature of ~ 10 K, consistent with the outlined theory.

$$\tau_1^{-1}, \tau_2^{-1} = \frac{\Omega}{2}\left(1 \mp \sqrt{1 - \frac{4{\tau_{eph}}^{-1}{\tau_{esc}}^{-1}}{\Omega^2}}\right) \ , \tag{5}$$

with

$$\Omega = \left(1 + \frac{c_e}{c_{ph}}\right) \cdot \tau_{eph}^{-1} + \tau_{esc}^{-1} \ , \tag{6}$$

and

$$\tau_3^{-1} = \frac{c_e}{c_{ph}}{\tau_{eph}}^{-1} + {\tau_{esc}}^{-1} \ . \tag{7}$$

As the local oscillator power or bias voltage changes,[9] the electron temperature in the bridge changes, effecting the physical parameters and thereby τ_1, τ_2, τ_3. This is illustrated in Fig. 4. The change in IF output impedance is small, but not negligible (Fig. 3a).

To calculate the effect of the HEB mixer IF output impedance on the instrument we first transform the derived HEB impedance to the mixer unit (MU) output. This is accomplished via a S-parameter model (Fig. 3) derived from electromagnetic finite element analysis.[19] In this model the IF bond wires are included. Next we transform the mixer unit output impedance via an effective 181.776 mm (derived from a fit against the data) electrical length

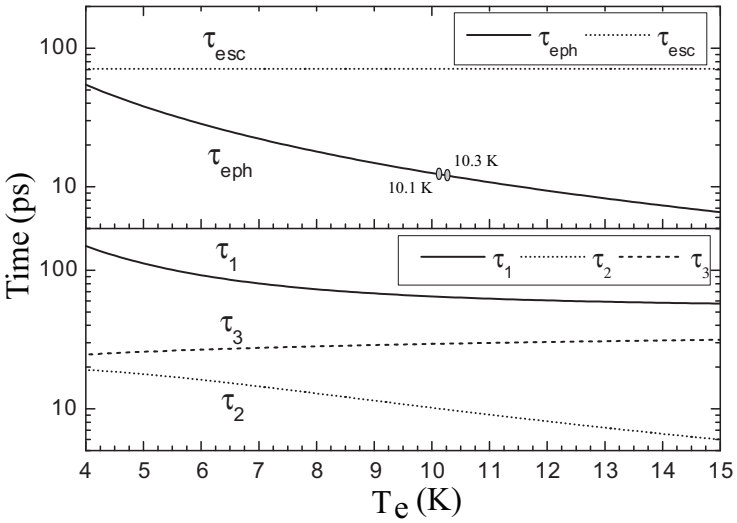

Figure 4. Discussed time constants and their electron temperature relationship. The NbN τ_{eph}, τ_{esc}, and the heat capacity ratio c_e/c_{ph} (not shown) are obtained from literature and serve to constrain the impedance and mixer gain models. From a fit of the model against measurement (Fig 3) we derive a 6.4 nm thick NbN film. The electron temperature of the 'on' and 'off' source signals are 10.1 & 10.3 K respectively. The redistribution of the electron temperature is due to a small change in LO power (optical standing wave, LO power drift) and/or bias change. This results in a slight change in the mixer output impedance (Fig. 3a), and a non-prefect 'on' – 'off' subtraction, and hence a residual IF standing wave in thus obtained spectrum.

coaxial cable to the input of the first low noise amplifier. Using a linear circuit simulator[20] we calculate the overall gain of the system. If we next allow the electron temperature of the bridge to vary to mimic an actual 'off' position observation we than obtain the normalized *Off/On* spectrum with the residual standing wave. By varying τ_{eph}, τ_{esc}, and c_e/c_{ph} in our HEB model, we can 'fit' the measurement and thus extract information on the actual electron temperature of the bridge. The thus obtained parameters are shown in Table 1. The quality of the depicted fit provides a nice confirmation of the 'NSGR' model.[14] It does however also show that there are some lower order residuals present that cannot be accounted for by the model, thereby limiting the accuracy of the *Off/On* correction. To improve the quality and numerical calculation overhead of the IF standing wave removal we now introduce a new technique as outlined in Section 6.

Table 1. Derived HEB mixer parameters for the 'On' and 'Off' source observations as based on the outlined impedance model. Units of R_o is in Ω, τ_{esc} and τ_{eph} in ps, and T_e in Kelvin.

mode	R_o	C	τ_{esc}	τ_{eph}	c_e/c_{ph}	T_e
On	14.394	0.3995	71.701	12.108	0.1978	10.1
Off	14.715	0.4007	73.397	12.314	0.2297	10.3

6. STANDING WAVE SOLUTION

We have shown in section 5 that a fitting approach based on the fundamental physics of the HEB mixer coupled with a model of the coaxial cable and the first LNA provides a good first order fit to the standing wave profile. However this approach is computationally expensive given that four free parameters are used for each calibration phase. In the example spectra shown we have used a 2 phase calibration, *Off/On*, to remove system artifacts from the spectra. For HIFI operation the observed spectra will be temperature calibrated using a four phase calibration routine incorporating the HIFI internal hot and cold loads. The four phase calibration equation is as follows:

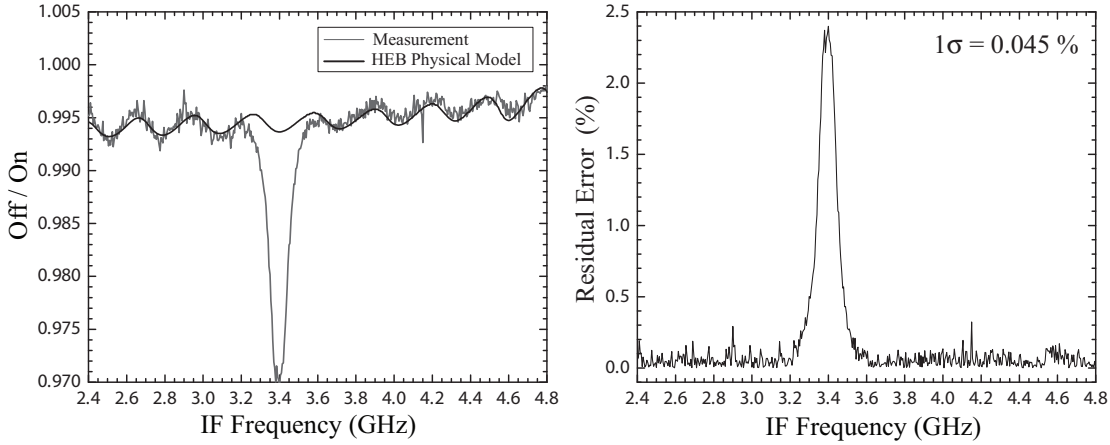

Figure 5. *Left*) Measured and modeled *Off/On* IF standing wave. The impedance model was fit against the measurement, from which the physical constants τ_{eph}, τ_{esc}, and c_e/c_{ph} are estimated. From the empirical relationship to the electron temperature in literature we obtain an estimate of the actual electron temperature during the (gas-cell) observation. The thus obtained parameters are compiled in Table 1. *Right*) Residual error of the measurement minus the model. The region around the absorption line has been omitted during the fitting routine.

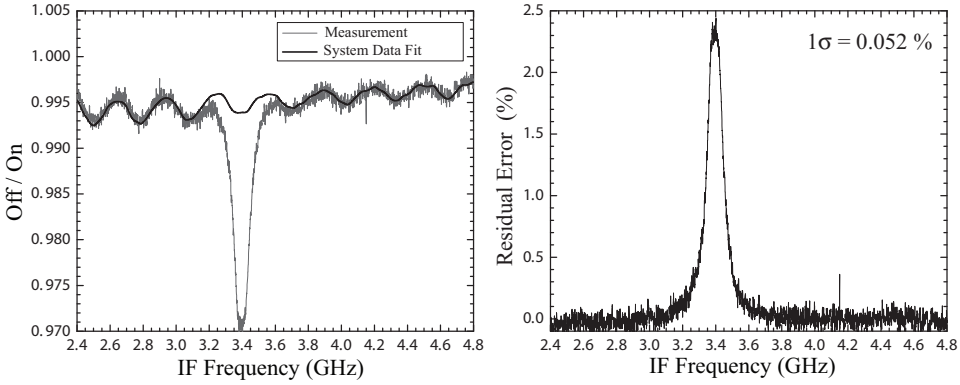

Figure 6. 12CO data fitted with a smoothed mixer current equivalent spectra taken from the HIFI stability test data.

$$\frac{On - Off}{Hot - Cold}. \tag{8}$$

Fitting the standing wave for a four phase calibration using the HEB model becomes problematic as the amount of parameters increases to 16. Additionally, HIFI will take multiple spectra during routine operation, which are calibrated individually using equation 8. This further increases the computation time for removal of the HEB standing wave. For a one minute integration time and a nominal WBS mode of 4 second readout this would generate up to 15 calibrated spectra which would be computationally very time consuming using the method proposed in section 5.

As part of our investigation into the standing wave effect in the HEB bands we noticed a correlation between the mixer current and the amplitude of the standing wave present in the spectra. It was seen that the greater the difference in mixer current, ΔI_{mix}, between two calibration phases the larger the residual standing wave present in the calibrated spectra. This correlation between ΔI_{mix} and the residual standing wave was expected since I_{mix} can be taken as a measure of the mixer impedance given that the mixer bias voltage, V, is a fixed parameter.

Furthermore, it was seen that there was a remarkable stability in the standing wave profile for a given ΔI_{mix} between two calibration phases at a given I_{mix} when compared to equivalent spectra taken at different times and LO frequencies for the same HEB mixer unit. Using this standing wave stability we devised a method to match the gas cell spectra with equivalent stability test data spectra. The stability test data, particularly the LO warm up data, provide a large sample of spectra at different mixer currents at the same LO frequency. Using this LO warm up data we matched the mixer current seen in the gas cell phases with an equivalent stability spectra, the results are shown in figure 6.

This approach has proved effective as a method to remove the electrical standing wave from the spectra of HEB band observations. Significantly this method is easier to implement than the HEB impedance model method presented in section 5 and less computationally extensive. This method will be included as a module in the HIFI instrument pipeline. Further tests are to be undertaken as part of the commissioning phase of HIFI in order to generate a complete catalog of standing wave spectra for a range of mixer currents for each of the four HEBs present in HIFI.

7. CONCLUSIONS

In this paper, we presented a method to fit the electrical standing waves present in the HEB mixer IF chain of the Herschel HIFI spectrometer. We have shown that the standing wave can be removed by using equivalent mixer impedance data taken from the calibration data with no spectral line data. This method will be included in the HIFI instrument pipeline.

In addition, we have shown that the current HEB impedance model generates a good first order fit to the standing wave profile. The fit parameters returns information about the conditions at the mixer bridge which have previously not been directly observed. This fit supports the HEB impedance model presented by Kooi *et al* and Nebosis.[9,14]

Acknowledgements

The authors thanks the gas cell team for providing the data presented in this paper and Bertrand Delforge for generating the gas cell database and the tools to access it. Additionally the authors would like to thanks David Teyssier, Pourya Khosropanah, Willem Jellema, Gert de Lange and Pieter Dieleman for their insights on HIFI and the HEB IF chain.The authors would like to acknowledge the financial support of Enterprise Ireland (Prodex).

REFERENCES

[1] de Graauw, T., Whyborn, N., Helmich, F., Dieleman, P., Roelfsema, P., Caux, E., Phillips, T., Stutzki, J., Beintema, D., Benz, A., Biver, N., Boogert, A., Boulanger, F., Cherednichenko, S., Coeur-Joly, O., Comito, C., Dartois, E., de Jonge, A., de Lange, G., Delorme, I., DiGiorgio, A., Dubbeldam, L., Edwards, K., Fich, M., Güsten, R., Herpin, F., Honingh, N., Huisman, R., Jacobs, H., Jellema, W., Kawamura, J., Kester, D., Klapwijk, T., Klein, T., Kooi, J., Krieg, J.-M., Kramer, C., Kruizenga, B., Laauwen, W., Larsson, B., Leinz, C., Liseau, R., Lord, S., Luinge, W., Marston, A., Merkel, H., Moreno, R., Morris, P., Murphy, A., Naber, A., Planesas, P., Martin-Pintado, J., Olberg, M., Orleanski, P., Ossenkopf, V., Pearson, J., Perault, M., Phillip, S., Rataj, M., Ravera, L., Saraceno, P., Schieder, R., Schmuelling, F., Szczerba, R., Shipman, R., Teyssier, D., Vastel, C., Visser, H., Wildeman, K., Wafelbakker, K., Ward, J., Higgins, R., Aarts, H., Tielens, X., and Zaal, P., "The Herschel-Heterodyne Instrument for the Far-Infrared (HIFI):instrument and pre-launch testing," *Space Telescopes and Instrumentation 2008: Optical, Infrared, and Millimeter* **7010**(1), 701004, SPIE (2008).

[2] Comito, C. and Schilke, P., "Reconstructing reality: Strategies for sideband deconvolution," A&A **395**, 357–371 (Nov. 2002).

[3] Phillips, T. G. and Jefferts, K. B., "A low temperature bolometer heterodyne receiver for millimeter wave astronomy.," *Review of Scientific Instruments* **44**, 1009–1014 (1973).

[4] Zmuidzinas, J. and Richards, P., "Superconducting detectors and mixers for millimeter and submillimeter astrophysics," *Proceedings of the IEEE* **92**, 1597–1616 (Oct. 2004).

[5] Kooi, J. W., Kovács, A., Sumner, M. C., Chattopadhyay, G., Ceria, R., Miller, D., Bumble, B., Leduc, H. G., Stern, J. A., and Phillips, T. G., "A 275-425 GHz Tunerless Waveguide Receiver Based on AlN-Barrier SIS Technology," *IEEE Transactions on Microwave Theory Techniques* **55**, 2086–2096 (Oct. 2007).

[6] Kawamura, J., Bumble, B., Harding, D. G., McGrath, W. R., Focardi, P., and LeDuc, R., "1.8 THz superconductive hot-electron bolometer mixer for Herschel," in [*Society of Photo-Optical Instrumentation Engineers (SPIE) Conference Series*], Phillips, T. G. and Zmuidzinas, J., eds., *Society of Photo-Optical Instrumentation Engineers (SPIE) Conference Series* **4855**, 355–360 (Feb. 2003).

[7] Cherednichenko, S., Drakinskiy, V., Berg, T., Khosropanah, P., and Kollberg, E., "Hot-electron bolometer terahertz mixers for the Herschel Space Observatory," *Review of Scientific Instruments* **79**, 034501–+ (Mar. 2008).

[8] Whyborn, N., "Band 6 IF change impact assessment," tech. rep., SRON (2002).

[9] Kooi, J. W., Baselmans, J. J. A., Hajenius, M., Gao, J. R., Klapwijk, T. M., Dieleman, P., Baryshev, A., and de Lange, G., "IF impedance and mixer gain of NbN hot electron bolometers," *Journal of Applied Physics* **101**(4), 044511 (2007).

[10] Trappe, N., Finn, T., Murphy, J. A., Withington, S., and Jellema, W., "Analysis of standing waves in submillimeter-wave optics," in [*Society of Photo-Optical Instrumentation Engineers (SPIE) Conference Series*], Hwu, R. J. and Linden, K. J., eds., *Society of Photo-Optical Instrumentation Engineers (SPIE) Conference Series* **6120**, 107–116 (Mar. 2006).

[11] Kester, D. J. M., Beintema, D. A., and Lutz, D., "SWS Fringes and Models," in [*The Calibration Legacy of the ISO Mission*], Metcalfe, L., Salama, A., Peschke, S. B., and Kessler, M. F., eds., *ESA Special Publication* **481**, 375–+ (2003).

[12] Siebertz, O., Honingh, C., Tils, T., Gal, C., and Olbrich, M., "The impact of standing waves in the LO path of a heterodyne receiver," *IEEE Transactions on Microwave Theory Techniques* **50**(1) (2002).

[13] Klapwijk, T. M., Barends, R., Gao, J., Hajenius, M., and Baselmans, J. J. A., "Improved superconducting hot-electron bolometer devices for the THz range," in [*Society of Photo-Optical Instrumentation Engineers (SPIE) Conference Series*], Bradford, C. M., Ade, P. A. R., Aguirre, J. E., Bock, J. J., Dragovan, M., Duband, L., Earle, L., Glenn, J., Matsuhara, H., Naylor, B. J., Nguyen, H. T., Yun, M., and Zmuidzinas, J., eds., *Society of Photo-Optical Instrumentation Engineers (SPIE) Conference Series* **5498**, 129–139 (Oct. 2004).

[14] Nebosis, R. S., Semenov, A. D., Gousev, Y. P., and Renk, K. F., "Rigorous Analysis of a Superconducting Hot-Electron Bolometer Mixer: Theory and Comparison with Experiment," *Proc. 7th Int. Symp. on Space Terahertz Tech.* , 601–613 (March 1996).

[15] Perrin, N. and Vanneste, C. , "Dynamic behaviour of a superconductor under time-dependent external excitation," *Journal de Physique* **48**(8), 1311–1316 (1987).

[16] Kaplan, S. B., "Acoustic matching of superconducting films to substrates," *Journal of Low Temperature Physics* **37**, 343–365 (Nov. 1979).

[17] Semenov, A. D., Nebosis, R. S., Gousev, Y. P., Heusinger, M. A., and Renk, K. F., "Analysis of the nonequilibrium photoresponse of superconducting films to pulsed radiation by use of a two-temperature model," Phys. Rev. B **52**, 581–590 (July 1995).

[18] Gousev, Y. P., Gol'Tsman, G. N., Semenov, A. D., Gershenzon, E. M., Nebosis, R. S., Heusinger, M. A., and Renk, K. F., "Broadband ultrafast superconducting NbN detector for electromagnetic radiation," *Journal of Applied Physics* **75**, 3695–3697 (Apr. 1994).

[19] "Ansoft Corporation, Pittsburgh, PA 15219, USA.," (November 2008).

[20] "Microwave office, Applied Wave Research Inc. El Segundo, CA 90245, USA.," (November 2008).

Appendix C

Paper 2: Calibration of the Herschel HIFI Instrument using Gas Cell Measurements

Conference proceedings of the 21st International Symposium on Space Terahertz Technology, 23rd - 25th March 2010, University of Oxford and STFC Rutherford Appleton Laboratory[45].

Calibration of the Herschel HIFI Instrument using Gas Cell Measurements

Ronan D. Higgins*§, David Teyssier†, John C. Pearson‡, Christophe Risacher** and Neil A. Trappe*

* Dept. of Experimental Physics, National University of Ireland, Maynooth, Co. Kildare, Ireland

†Herschel Science Centre, European Space Astronomy Centre (ESAC), 28691 Villanueva de la Cãnada, Madrid, Spain.

‡Jet Propulsion Laboratory, California Institute of Technology, Pasadena, CA 91109, USA

** SRON (Netherlands Institute for Space Research), Landleven 12, 9747 AD, Groningen, the Netherlands

§Email: daniel.r.higgins@nuim.ie

***Abstract*—The Heterodyne Instrument for the Far-Infrared (HIFI) was launched aboard the Herschel space telescope on the 14th of May 2009. HIFI's frequency range is spread over 7 mixer bands. Bands 1-5 (480-1270 GHz) use Superconducting-Insulator-Superconducting (SIS) mixer technology while bands 6 & 7 (1410-1910 GHz) use Hot Electron Bolometer (HEB) mixer technology. HIFI is a double sideband instrument and hence contains both the upper and lower sideband of the down converted sky signal. The gain in the upper and lower sideband is not always equal. This effect introduces a calibration uncertainty that must be understood in order to achieve the HIFI calibration goal of 3%.**

To determine the frequency dependent sideband ratio for each mixer band, a gas cell test set up was developed [1]. During the instrument level testing a number of simple (^{12}CO, ^{13}CO and OCS) and complex (CH_3CN and CH_3OH) molecules were observed using the HIFI instrument. Using a radiative transfer model with the measured pressure and optical path length of the gas cell and molecular line parameters taken from the JPL and HITRAN catalogs, model spectra can be generated. By comparing the generated spectra with the observed spectra the sideband gain can be determined.

In this paper we present the analysis of ^{12}CO gas cell data in bands 1 & 2 and the application of the determined side gain ratios to flight data.

I. Introduction

HIFI is a one of three instruments on board the Herschel Space Observatory. Using heterodyne techniques it provides very high spectral resolution ($R = \nu/\Delta\nu \geq 10^6$–$10^7$) from 480–1270 GHz and 1410–1910 GHz for two polarizations. This high resolution promises to open a new window on the chemistry and kinematics of the cold universe [2].

The heterodyne technique achieves high resolution spectra by beating the sky signal with an instrument produced monochromatic signal of a similar frequency close to the sky frequency of interest. This local signal is typically known as the local oscillator (LO) signal. The two signals are added together at the mixer which reacts to the beat frequency of the two signals. This down converted signal is known as the intermediate frequency (IF). Depending on the mixer characteristics a 2.4 to 4GHz band of the sky signal is down converted either side of the LO frequency, these bands are known as the sidebands.

HIFI's frequency coverage is spread over 7 bands. Each band has two mixer blocks which detect orthogonal polarizations. Each mixer is coupled to two LO chains covering approximately half of the

mixer band frequency coverage. HIFI uses two types of mixing elements. Bands 1-5 (480–1270 GHz) use Superconductor-Insulator-Superconductor (SIS) technology and bands 6 & 7 use Hot-Electron-Bolometer technology to mix sky and LO signals. Both technology use superconducting techniques to downconvert the signal albeit via different mechanisms, for a review of mixer technology see [3].

HIFI aims to have unprecedented calibration accuracy for a heterodyne instrument. A major source of calibration error in ground based telescope is atmospheric perturbations. By going to space HIFI opens up new parts of the sub-mm spectrum but also the vacuum of space removes a large calibration error. The main calibration errors in HIFI will be from the telescope optics and the instrument itself. The main sources of calibration error for HIFI come from internal standing waves, hot and cold load coupling and temperature and mixer sideband gain ratio. Standing waves manifest themselves in numerous ways in a heterodyne systems and can be seen on the spectra baseline but also more subtlety in the mixer sensitivity due to internal reflection in the LO mixer cavity, see [4] for a review.

Side band gain ratio is a bi-product of the HIFI mixer set up. The HIFI mixers are double side band (DSB) mixers and hence have an upper and lower side band in the down converted spectra. The separation of side bands in the mixer setup is a common component in ground based telescope however at the time of HIFI development the technique was still in a development phase. HIFI separates the sideband in the data processing pipeline. Using the principle that by changing the LO frequency spectral lines in the upper and lower side band move in opposite directions it is possible to deconvolve DSB spectra into its SSB (single side band) components, see [5]. For wide band spectrometers such as HIFI the change in gain across the upper and lower side bands can introduce a significant calibration error. The side band gain effect can be removed during the deconvolution process however knowledge of the side band gain ratio is required.

This paper discusses the gas cell tests undertaken during instrument level testing (ILT) phase to determine the side band gain variation across the HIFI frequency coverage. The effect of side band ratio on calibration accuracy will be discussed in section 2. The gas cell set-up will be discussed in section 3. Section 4 details the gas cell line fitting and the extraction of the side band ratio from this data. Finally section 5 details the application of side band ratio to flight data taken during the performance verification phase of HIFI.

II. Calibration errors

As HIFI aims for unprecedented calibration accuracy in a heterodyne system all efforts were made in the instrument level tests to quantify and understand the sources of calibration error in the system. 2 of the main sources of calibration error within HIFI are standing waves and the mixer sideband ratio.

A. Standing waves

Standing waves are a common feature in radio and sub-mm telescopes as the telescope and instrument optics are comparable with the radiation wavelength. Standing waves occur when a signal is reflected between 2 surfaces. The reflected signal interferes with the incoming signal. Depending on the phase of the signal when reflection occurs, the interference can be constructive or destructive. When this interference is viewed from a broadband perspective it appears as sinusoidal intensity variation with frequency. From the period of this modulation one can determine the distance between 2 reflecting surfaces as follows:

$$d = c/2P \tag{1}$$

where P is the standing wave period in frequency, c is the speed of light and d is the distance between the 2 surfaces.

The main source of standing waves in ground based telescopes is from the secondary mirror. This was considered in the design of the Herschel secondary mirror and the inclusion of scattering cone has almost completely removed this effect. However even though great efforts were made to reduce standing waves they are still seen in the HIFI internal optics. Standing waves are seen in both the sky and local oscillator signal paths.

Standing waves in the sky path, be it from the calibration loads or the sky, appear as a modulation on the spectrometer output. The problem is complicated further by the double side band nature of HIFI. The standing wave in figure 1 is the result of the interference between the standing wave in the the upper and lower sideband signal.

Standing waves in the LO path are not as apparent as those in the sky signal path but can have a detrimental effect on certain observing modes such as frequency switch modes [6]. Standing waves in the LO path modulate the LO power and hence the sensitivity of the mixer. Figure 2 shows the effect of a standing wave on the mixer pump level. A fraction

of the LO power is reflected between the LO unit and mixer causing a modulation in the LO power and hence mixer sensitivity. The effect of standing waves in the LO signal path is discussed in detail in [4].

The standing wave seen in the HEB bands is of another form. Like the sky path standing wave it is seen as a broadband modulation on the spectrum baseline however the origin of the reflection cavity is not in the instrument optics but in the IF electrical amplification chain. Due to an impedance mismatch between the HEB mixer and the first amplifier not all of the signal is transmitted and some is reflected back and forth between the 2 component along 182mm of coaxial cable. In bands 1-5 an electrical isolator is present absorbing any reflected signal. However due to a late design change in IF bandwidth for the HEB band no suitable isolator was available and hence reflected signal become a problem. In an ideal system the standing waves would cancel in the calibration routine. However the HEB impedance is a very sensitive to small fluctuations in LO and sky power which change the standing wave shape and leads to a residual between the On and Off phases. The impedance of HEB and the proposed solution to remove this standing wave is discussed in reference [7].

Correcting baselines for the standing wave effects seen in figure 1 is a typical chore of a radio astronomer and a number of tools are available for this task. However complete removal of all standing wave effects is not entirely possible. Standing waves from the temperature loads can limit the absolute temperature calibration possible and the standing wave amplitude must be taken as a calibration error.

B. Side band ratio

As stated previously, HIFI is a double side band instrument and contains signal from both the upper and lower sideband. The basic HIFI calibration contains 4 different observation phases, (On source, Off source, Hot load, cold load) which when combined together in equation 2 remove the systematic effects (assuming the instrument is stable over the course of the data acquisition) and return a temperature calibrated DSB spectra.

$$\frac{On - Off}{Hot - Cold} \tag{2}$$

In an ideal mixer with an equal gain in both sidebands, the spectral line intensity for an unconfused line (i.e. not blended with a line from the other side band) can be calculated simply by multiplying the line intensity by 2. However the gain response across a mixer band is not necessarily uniform.

HIFI observes 2 sidebands of 4.0 (bands 1-5) or 2.4 GHz (bands 6 & 7) either side of the LO Frequency.At the upper end of the IF band a 16 GHz frequency difference is seen between the LSB and USB frequency channel summing together to make a single IF channel. A slope in the gain across the side bands can introduce a calibration error when converting DSB intensity to SSB intensities, see figure 3. As HIFI has a large IF band width this effect becomes significant. The effect must be understood

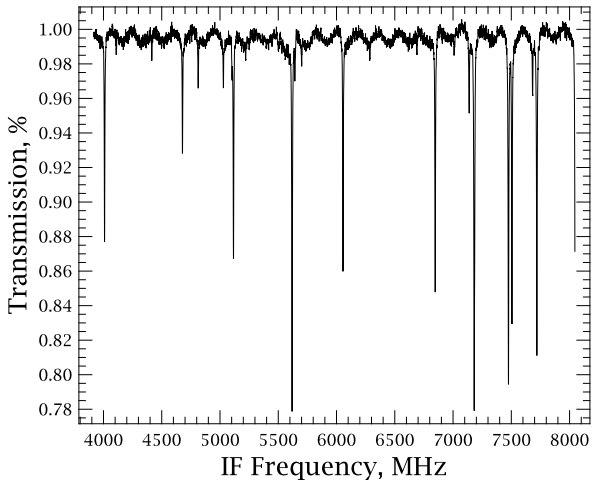

Figure 1. Plot of Methanol data taken at 645.999 GHz showing a 170 MHz period standing wave corresponding to internal reflection in a cavity of length $\sim$ 88cm

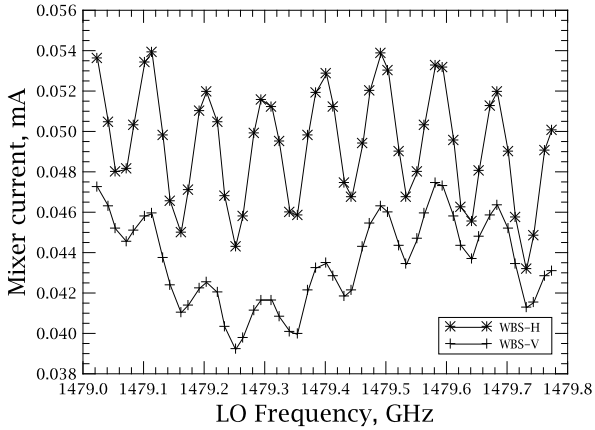

Figure 2. Plot of mixer currents for both H and V mixers. For this test the LO power is kept constant and the LO frequency is changed. In the mixer current vs. LO Frequency plot 2 standing waves are apparent, a 92MHz modulation corresponding to a distance between the LO source unit and the mixer focus and a 680 MHz period standing wave corresponding to an reflection between the diplexer rooftop mirror and the mixer focus.

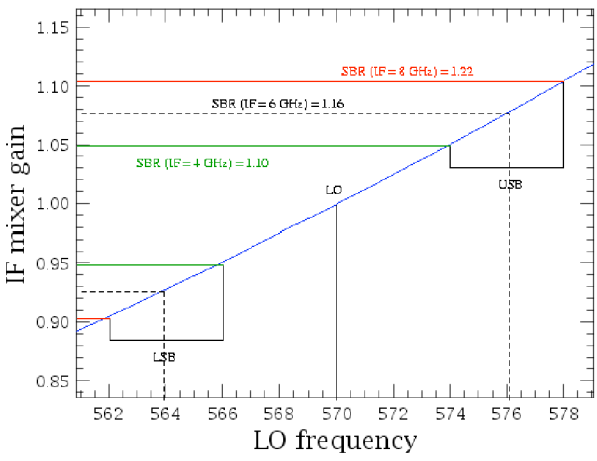

Figure 3. Example of linear mixer gain variation and the resulting side band ratios. The term SBR (side band ratio) is defined as USB gain divided by the LSB gain

in order to determine the calibration accuracy and eventually correct in the data processing pipeline.

The topic of intensity calibration is covered in detail in reference [8].

III. Gas cell test setup

A. Principles

Gas cell tests were used by the SWAS satellite [9] and the Odin satellite [10] in their ground testing. SWAS in particular used a gas cell set up to demonstrate a side band gain ratio of unity. The IF bandwidth of SWAS of 1.4 GHz is considerably less than HIFI and hence would be less susceptible to side band gain imbalances.

The basic concept of a gas cell calibration of a heterodyne receiver is to observe well understood molecules (known line frequencies, intensities, pressure broadening parameters) and then using a radiative transfer model generate a model line profile. By comparing the model line profile with the observed line profile it is possible to extract the instrumental effects.

A gas cell observation follows that of a standard observation detailed in equation 2. A typical observation observes the hot and cold calibration loads through both the filled and empty gas cell. By forming a ratio of filled and empty observations one can extract the side band ratio. For a single spectral line in the lower side band, the filled and empty phases of the gas cell observation would be as follows:

$$S_{filled} = G_u(J_h - J_c) + G_l(J_h - J_c)e^{-\tau} \quad (3)$$

$$S_{empty} = G_u(J_h - J_c) + G_l(J_h - J_c) \quad (4)$$

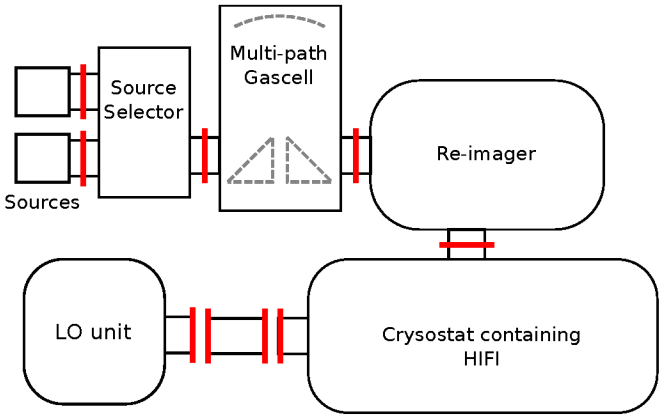

Figure 4. Gas test setup

where G_u and G_l are the frequency dependent upper and lower side band gain respectively, J_h and J_c are the effective hot and cold load temperature of a black body of temperature T at a given frequency. The $e^{-\tau}$ term represents the line opacity at the line center, see section IV. By rearranging equations 3 and 4 the side band ratio is given by:

$$R_G = \frac{G_l}{G_u} = \frac{1 - S_{filled}/S_{empty}}{S_{filled}/S_{empty} - e^{-\tau}} \quad (5)$$

For gases where the line intensity is saturated, $\tau \gg 1$, the above equation can be reduced to $S_{empty}/S_{filled} - 1$. For a gain balanced mixer S_{empty}/S_{filled} for a saturated line = 0.5 or an absorption line half the continuum level in a normalized spectra, see figure 6.

In the data processing pipeline the side band gains are applied to the DSB intensity to convert to single side band intensity. In an ideal gain balanced mixer this is simply a case of multiplying the intensity by two. Where the mixer sideband is not equal the intensity must be dividing by the side band gain factor which is defined for the upper side band as:

$$G_{ssb} = \frac{1}{1 + R_G} \quad (6)$$

and the lower side band gain factor is defined a $1 - G_{ssb}$, see reference [8].

B. Design

The design of the HIFI gas cell set up is detailed in reference [1]. The gas cell set up chosen was based on the recommendations from the SWAS gas cell setup [11]. The gas cell has a multi path optical set up which maximizes the optical path length while keeping the volume of the gas cell to minimum for ease of installation. The gas cell has a path length of

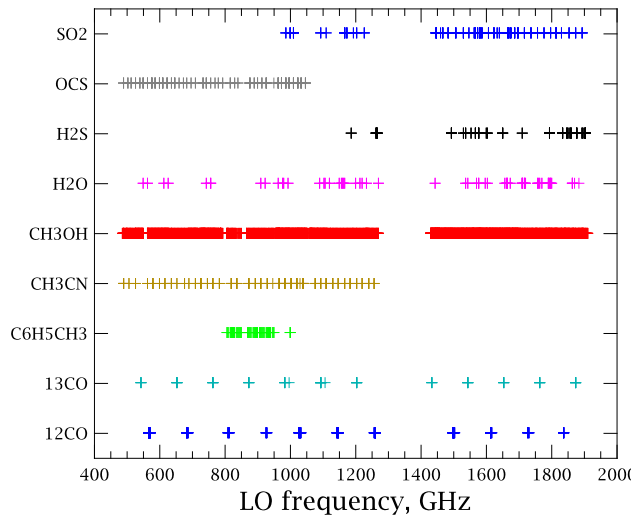

Figure 5. Summary plot showing LO frequency coverage of each gas used in the gas cell test campaign

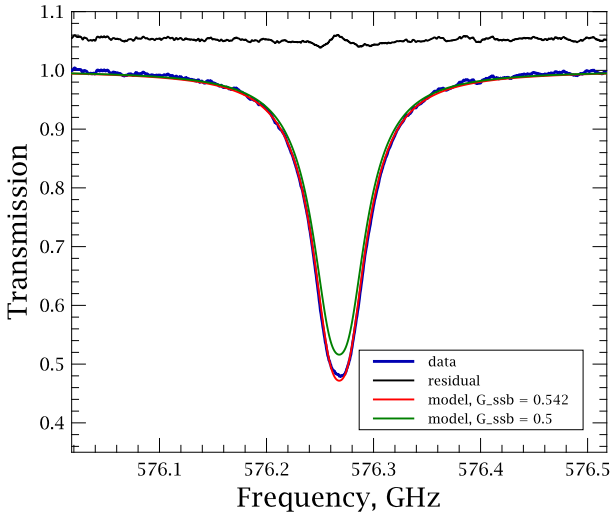

Figure 6. ^{12}CO gas cell data at 570.4 GHz (highlighted in blue on the left). Green line shows spectral line fit for a balanced mixer (G_{ssb} = 0.5), red line shows the fitted profile where G_{ssb} = 0.542

128cm which is contained in a cylindrical vessel of 15 cm diameter and 50cm height.

As HIFI has a large frequency coverage one single molecule will not provide saturated lines at all frequencies. For the HIFI gas cell a range of molecules were observed and hence the effect of cross contamination was considered in the material choice for the gas cell. A glass gas cell design was chosen over a metal one as certain molecules would stick to the metal walls particularly water. The gas cell was designed to operate at low pressures around 1 millibar. The final gas cell test set up showing the calibration loads, re-imager, LO and HIFI cryostat is shown in figure 4.

C. Calibration gases

The choice of gases for the test campaign was a trade off between a number of criteria. For side band measurement a saturated line was necessary. This limited the gas choice to molecules with line intensities of 10^{-2} to 10^{-3} in units of nm^{-2}.MHz. Lab safety was also considered and possible corrosive effects on the gas cell itself. Figure 5 summarizes the frequency coverage of the final gas choices.

IV. Gas cell line fitting

A. Line profile theory

The line profile seen in figure 6 is best described using a voigt profile. The voigt profile is a convolution of a lorentzian and gaussian profile. The lorenztian profile describes the line broadening effect due to the gas pressure and its half width half maximum is defined by the:

$$\delta\nu_L = \gamma_{self} P \tag{7}$$

where γ_{self} is the pressure broadening parameter MHz/mbar and P, the gas cell pressure, is in mbar. γ_{1self} is taken from the HITRAN database [12]. The gaussian profile describes the broadening effect due to the thermal motion of the gas. The width of a gaussian profile is a derived from the Boltzmann equation and is a function of the gas temperature and the line frequency. The half width half maximum is defined as:

$$\delta\nu_D = \frac{\nu_0}{c}\sqrt{\frac{2(ln2)kT}{m}} \tag{8}$$

where ν_0 is the line frequency, c is the speed of light, k is Boltzmann constant, T is the gas temperature and m is the molecular weight. The convolution of these 2 profiles gives the distribution of energy for that molecular transition. The integrated area of the voigt profile for that transition is then equal to the integrated intensity taken from the HITRAN or JPL catalogs for that line. The peak absorption is then defined as:

$$\alpha_{max} = \frac{I_{ba}}{\pi\delta\nu_L + \sqrt{\frac{\pi}{ln2}}}\frac{P}{kT} \tag{9}$$

where I_{ba} is the integrated intensity taken from the catalog. Using α_{max} the unit voigt profile peak is scaled. Combining the scaled voigt with the exponential opacity broadening effect (Beer-Lambert law)

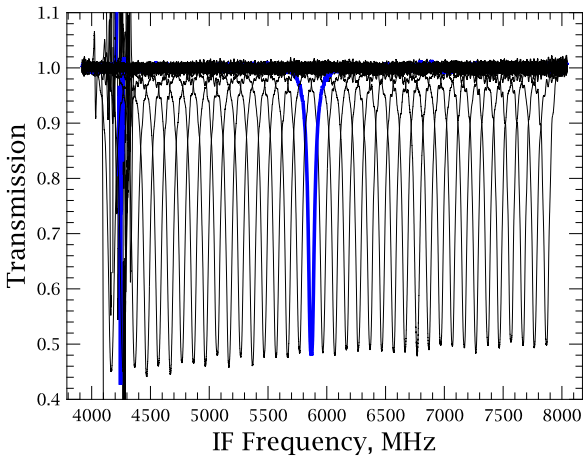

Figure 7. Plot of ^{12}CO (5-4) data taken with the V polarization wide band spectromoter (WBS) backend between 568.4 to 572.1 GHz in steps of 0.1 GHz at an average gas cell pressure of 6.5mbar. Traces of LO spurious signals can be seen between the LO frequencies of 570.7 and 568.4 GHz around the IF frequency of 4.3GHz. The spectra highlighted in blue is shown in more detail in figure 6

due to gas column length, the final line profile profile peak is:

$$e^{\alpha_{max} V(\nu-\nu_0,\delta\nu_D,\delta\nu_L) L} \tag{10}$$

where L is the gas cell column length. The residual between this line profile and the observed line is taken to be the side band gain ratio.

B. *Line profile fitting*

Figure 6 shows a example of the line fitting routine. The green profile shows the line profile for a balanced mixer while the red profile shows line profile where the side band gain is left as a free parameter which is fitted to match the observed line profile. The resulting side band ratio factor is 0.542, see equation 6.

Figure 7 shows an overview of the ^{12}CO 576.268 GHz spectral line for a range of LO Frequencies between 568.4 and 572.1 GHz. Each of spectra was fitted with a model spectral line where the side band gain was a free parameter. The resulting fitted side band ratio factor versus LO Frequency is shown in figure 8.

Note that the band 1b data presented here is an exceptional example with a large side band gain difference over 4GHz. This extreme example was chosen to demonstrate the gas cell method and is not typical of the side band ratio determined from ^{12}CO line fitting in other bands.

V. Correction of flight data

The main goal of the gas cell test campaign was to determine the side band ratio across each mixer band and eventually correct flight data for this effect. The main assumption made was that the side band ratio is an inherent part of the mixer set up and should remain the same over the instrument life time. The example presented here is an extreme side band ratio compared with other LO frequencies in HIFI. A 10% change in gain is seen across over 4 GHz of the IF band. This makes it an ideal region to compare the lab data presented here with a comparable spectral scan observed in space.

During the first performance verification phase of HIFI in July 2010 a number of spectral scan observations on strong sources were taken. Figure 9 shows a ^{12}CO line tracked across the IF band in steps of 0.4 GHz between the LO frequencies 568.535 and 571.932 GHz. In this plot it is apparent that the same slope in gain seen in the gas cell data is seen in the flight. Ideally the spectral line intensity should be the same across the IF band, however in figures 7 and 9 the line intensity is seen to decrease across the IF band indicating a side band gain imbalance. More significantly is that the slope in gain across the IF seen in flight data is consistent with that seen in the gas cell data.

Figure 10 shows the peak line intensity of the data show in figure 9 and also the peak line intensities when the side band gain shown in figure 8 is applied. From this plot one can see that before the gain correction is applied the peak intensity scatter is $\sim$10% while after gain correction it is greatly reduced to $\sim$3%.

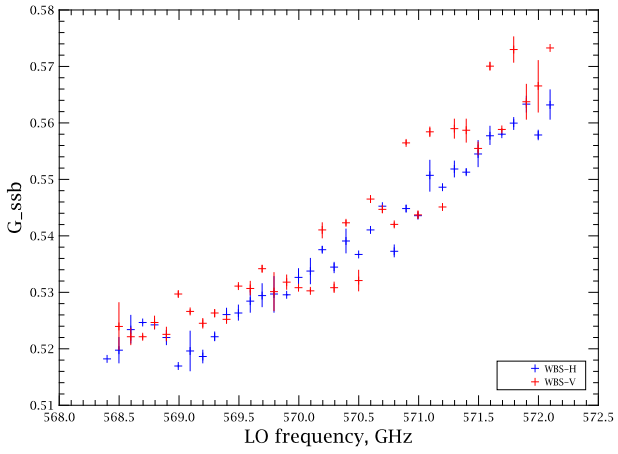

Figure 8. Fitted G_{ssb} for each line profile shown in figure 7 versus LO Frequency

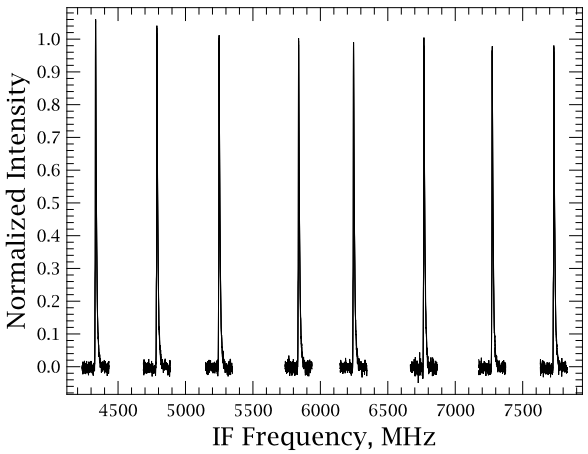

Figure 9. Flight data spectral scan showing the ^{12}CO (5-4) line for a range of LO frequencies from 568.535 to 571.932 GHz

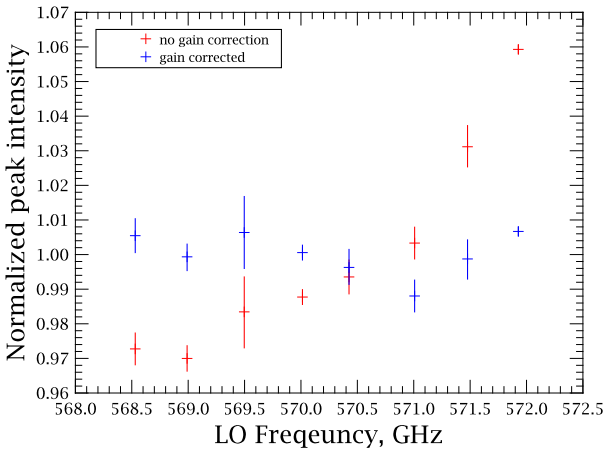

Figure 10. Peak line intensity with and without gain correction. Notice the variation is intensity scatter is reduced from 10% to 3%

VI. Conclusions

In this paper, the concept of calibrating a double side band heterodyne spectrometer using a gas cell test set up was described. It was shown how to generate a model spectra using radiative transfer methods taking into account the optical path length, gas pressure and temperature coupled with the JPL and HITRAN line catalogs. We described how by comparing model spectra to observed spectra the side band ratio at that IF frequency could be extracted. Using this extracted side band ratio data we showed that for the LO frequency range from 568 to 572 GHz the amount of scatter in a flight data could be reduced from the $\sim$10% to $\sim$3%.

VII. Future work

The data covered in this paper is only a small fraction of the total data taken during the gas cell campaign, see figure 5. Future work will involve the expansion of the methods demonstrated here to ^{12}CO and ^{13}CO in other mixer bands. The final goal of this work is to analyze the large CH_3OH and CH_3CN dataset taken and generate a more complete picture of the side band gain ratio, thereby improving the overall calibration accuracy of HIFI and finally helping produce exceptional science data.

VIII. Acknowledgments

A portion of this research was performed at the Jet Propulsion Laboratory, California Institute of Technology, under contract with the National Aeronautics and Space Administration.

References

[1] D. Teyssier, E. Dartois, D. Deboffle, J. Crussaire, Y. Longval, F. Boulanger, and M. Pérault, "A Multi-path Far-Infrared and Sub-millimetre Gas Cell for Spectral Tests of Herschel-HIFI," in *15th International Symposium of Space Terahertz Technology, Northampton, Massachusetts*, 2004, pp. 306–312.

[2] T. de Graauw, N. Whyborn, F. Helmich, P. Dieleman, P. Roelfsema, E. Caux, T. Phillips, J. Stutzki *et al.*, "The Herschel-Heterodyne Instrument for the Far-Infrared (HIFI):instrument and pre-launch testing," in *Space Telescopes and Instrumentation 2008: Optical, Infrared, and Millimeter*, J. M. Oschmann, Jr., M. W. M. de Graauw, and H. A. MacEwen, Eds., vol. 7010, no. 1. SPIE, 2008, p. 701004. [Online]. Available: http://link.aip.org/link/?PSI/7010/701004/1

[3] J. Zmuidzinas and P. Richards, "Superconducting detectors and mixers for millimeter and submillimeter astrophysics," *Proceedings of the IEEE*, vol. 92, no. 10, pp. 1597–1616, Oct. 2004.

[4] O. Siebertz, C. Honingh, T. Tils, C. Gal, M. Olbrich, R. Bieber, F. Schmuelling, and R. Schieder, "The Impact of Standing Waves in the LO path of a Heterodyne Receiver," in *18th International Symposium of Space Terahertz Technology, California Institute of Technology, Pasadena, California*, 2007, pp. 117–122.

[5] C. Comito and P. Schilke, "Reconstructing reality: Strategies for sideband deconvolution,"

A&A, vol. 395, pp. 357–371, Nov. 2002.

[6] J. Kooi and V. Ossenkopf, "HIFI Instrument Stability as Measured during the Thermal Vacuum Tests of the Herschel Space Observatory," in *20th International Symposium of Space Terahertz Technology, Charlottesville, Virginia*, 2009, p. 69.

[7] R. D. Higgins and J. W. Kooi, "Electrical standing waves in the HIFI HEB mixer amplifier chain," in *Society of Photo-Optical Instrumentation Engineers (SPIE) Conference Series*, ser. Society of Photo-Optical Instrumentation Engineers (SPIE) Conference Series, vol. 7215, Feb. 2009.

[8] V. Ossenkopf, "The Intensity Calibration Framework for HIFI," *ALMA Memo 442*, Jan. 2003.

[9] V. Tolls, G. J. Melnick, M. L. N. Ashby, E. A. Bergin, M. A. Gurwell, S. C. Kleiner, B. M. Patten, R. Plume *et al.*, "Submillimeter Wave Astronomy Satellite Performance on the ground and in orbit," ApJS, vol. 152, pp. 137–162, May 2004.

[10] U. Frisk, M. Hagström, J. Ala-Laurinaho, S. Andersson, J. Berges, J. Chabaud, M. Dahlgren, A. Emrich *et al.*, "The Odin satellite. I. Radiometer design and test," A&A, vol. 402, pp. L27–L34, May 2003.

[11] R. Schieder, "The usefulness of a gas cell for performance testing," Tech. Rep. SWAS/TM-4027, 1993.

[12] L. S. Rothman, I. E. Gordon, A. Barbe, D. C. Benner, P. F. Bernath, M. Birk *et al.*, "The HITRAN 2008 molecular spectroscopic database," *Journal of Quantitative Spectroscopy and Radiative Transfer*, vol. 110, pp. 533–572, Jun. 2009.

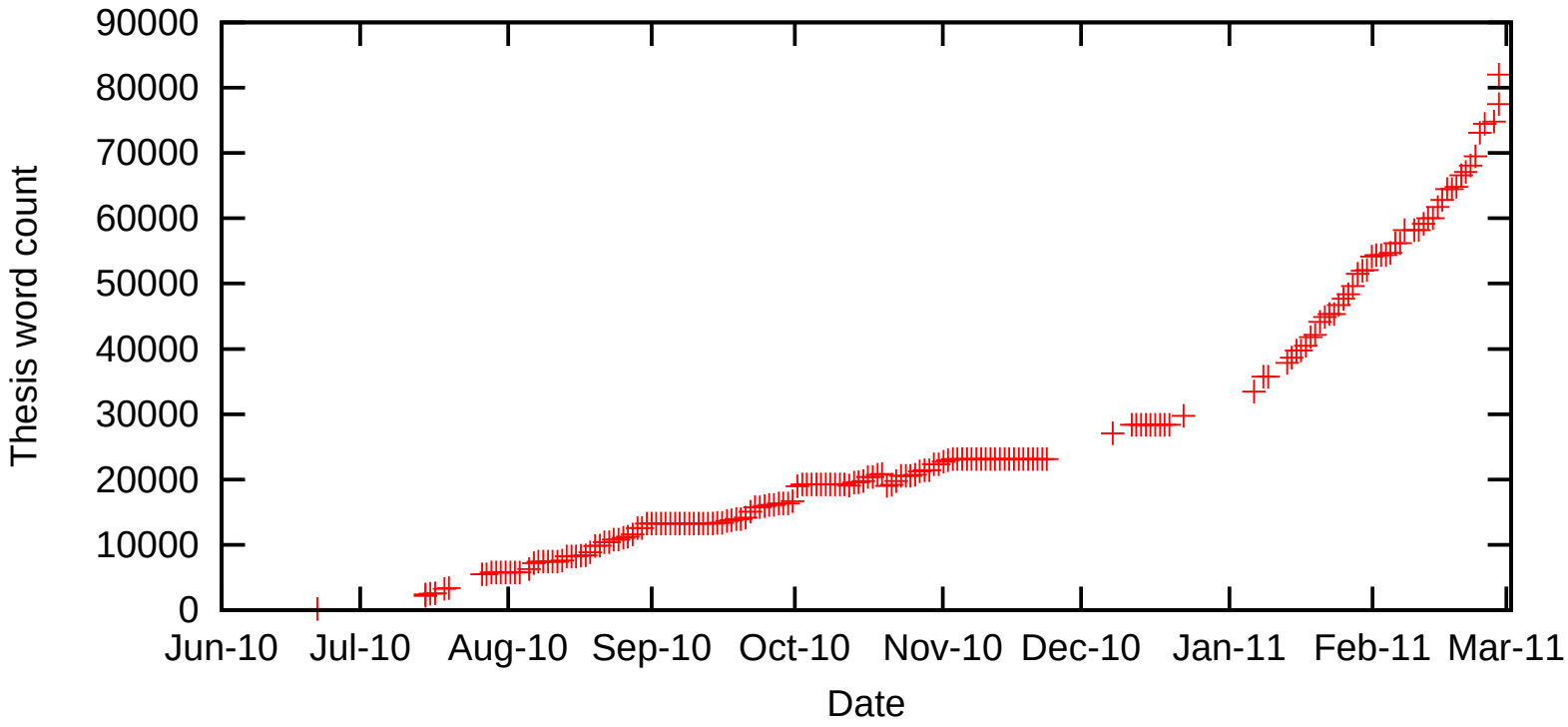
Thesis word count
90000
80000
70000
60000
50000
40000
30000
20000
10000
0
Jun-10
Jul-10
Aug-10
Sep-10
Oct-10
Nov-10
Dec-10
Jan-11
Feb-11
Mar-11
Date

There lies the port; the vessel puffs her sail:
There gloom the dark broad seas. My mariners,
Souls that have toiled, and wrought, and thought with me
That ever with a frolic welcome took
The thunder and the sunshine, and opposed
Free hearts, free foreheads you and I are old;
Old age had yet his honour and his toil;
Death closes all: but something ere the end,
Some work of noble note, may yet be done,
Not unbecoming men that strove with Gods.
The lights begin to twinkle from the rocks:
The long day wanes: the slow moon climbs: the deep
Moans round with many voices. Come, my friends,
'Tis not too late to seek a newer world.
Push off, and sitting well in order smite
The sounding furrows; for my purpose holds
To sail beyond the sunset, and the baths
Of all the western stars, until I die.
It may be that the gulfs will wash us down:
It may be we shall touch the Happy Isles,
And see the great Achilles, whom we knew.
Though much is taken, much abides; and though
We are not now that strength which in the old days
Moved earth and heaven; that which we are, we are,
One equal-temper of heroic hearts,
Made weak by time and fate, but strong in will
To strive, to seek, to find, and not to yield.

Ulysses
Alfred Lord Tennyson